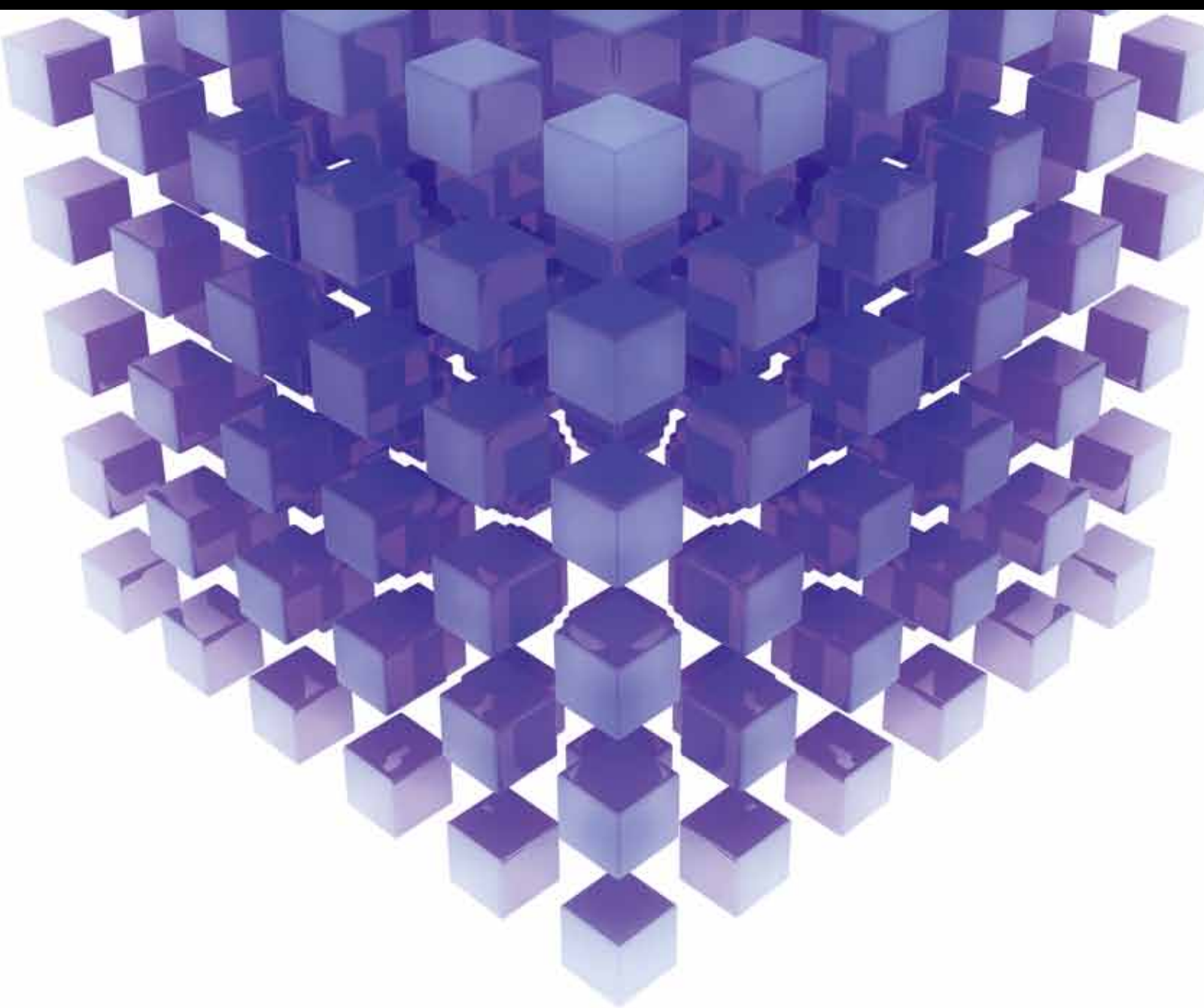


MATHEMATICAL PROBLEMS IN ENGINEERING

COMPUTATIONAL INTELLIGENCE IN CIVIL AND HYDRAULIC ENGINEERING

GUEST EDITORS: SHENGYONG CHEN, FEI KANG, SIAMAK TALATAHARI, SUNGHWAN KIM,
AND DOĞAN AYDIN





Computational Intelligence in Civil and Hydraulic Engineering

Mathematical Problems in Engineering

Computational Intelligence in Civil and Hydraulic Engineering

Guest Editors: Shengyong Chen, Fei Kang,
Siamak Talatahari, Sunghwan Kim, and Dogan Aydin



Copyright © 2013 Hindawi Publishing Corporation. All rights reserved.

This is a special issue published in “Mathematical Problems in Engineering.” All articles are open access articles distributed under the Creative Commons Attribution License, which permits unrestricted use, distribution, and reproduction in any medium, provided the original work is properly cited.

Editorial Board

Mohamed Abd El Aziz, Egypt
Eihab M. Abdel-Rahman, Canada
Rashid K. Abu Al-Rub, USA
Sarp Adali, South Africa
Salvatore Alfonzetti, Italy
Igor Andrianov, Germany
Sebastian Anita, Romania
W. Assawinchaichote, Thailand
Erwei Bai, USA
Ezzat G. Bakhoun, USA
José Manoel Balthazar, Brazil
R. K. Bera, India
Christophe Bérenguer, France
Jonathan N. Blakely, USA
Stefano Boccaletti, Spain
Stephane P. A. Bordas, USA
Daniela Boso, Italy
M. Boutayeb, France
Michael J. Brennan, UK
Salvatore Caddemi, Italy
Piermarco Cannarsa, Italy
Jose E. Capilla, Spain
Carlo Cattani, Italy
Marcelo Cavalcanti, Brazil
Diego J. Celentano, Chile
Mohammed Chadli, France
Arindam Chakraborty, USA
Yong-Kui Chang, China
Michael J. Chappell, UK
Xinkai Chen, Japan
Kui Fu Chen, China
Kue-Hong Chen, Taiwan
Jyh-Hong Chou, Taiwan
Slim Choura, Tunisia
Cesar Cruz-Hernandez, Mexico
Swagatam Das, India
Filippo de Monte, Italy
Maria de Pinho, Portugal
Antonio Desimone, Italy
Yannis Dimakopoulos, Greece
Baocang Ding, China
Joao B. R. Do Val, Brazil
Daoyi Dong, Australia
B. Dubey, India
Horst Ecker, Austria

M. Onder Efe, Turkey
Elmetwally Elabbasy, Egypt
Alex Elias-Zuniga, Mexico
Anders Eriksson, Sweden
Vedat S. Erturk, Turkey
Qi Fan, USA
Moez Feki, Tunisia
Ricardo Femat, Mexico
Robertt Fontes Valente, Portugal
Claudio Fuerte-Esquivel, Mexico
Zoran Gajic, USA
Ugo Galvanetto, Italy
Furong Gao, Hong Kong
Xin-Lin Gao, USA
Behrouz Gatmiri, Iran
Oleg V. Gendelman, Israel
Didier Georges, France
Paulo Batista Gonçalves, Brazil
Oded Gottlieb, Israel
Fabrizio Greco, Italy
Quang Phuc Ha, Australia
M. R. Hajj, USA
Thomas Hanne, Switzerland
Katica Hedrih, Serbia
M. I. Herreros, Spain
Wei-Chiang Hong, Taiwan
Jaromir Horacek, Czech Republic
Gordon Huang, Canada
Chuangxia Huang, China
Huabing Huang, China
Yi Feng Hung, Taiwan
Hai-Feng Huo, China
Asier Ibeas, Spain
Anuar Ishak, Malaysia
Reza Jazar, Australia
Zhijian Ji, China
Jun Jiang, China
J. J. Judice, Portugal
Tadeusz Kaczorek, Poland
Tamas Kalmar-Nagy, USA
Tomasz Kapitaniak, Poland
Hamid Reza Karimi, Norway
Metin O. Kaya, Turkey
Nikolaos Kazantzis, USA
Farzad Khani, Iran

Kristian Krabbenhoft, Australia
Ren-Jieh Kuo, Taiwan
Jurgen Kurths, Germany
Claude Lamarque, France
Marek Lefik, Poland
Stefano Lenci, Italy
Roman Lewandowski, Poland
Shanling Li, Canada
Ming Li, China
Jian Li, China
Shihua Li, China
Teh-Lu Liao, Taiwan
Panos Liatsis, UK
Jui-Sheng Lin, Taiwan
Yi-Kuei Lin, Taiwan
Shueei M. Lin, Taiwan
Wanquan Liu, Australia
Bin Liu, Australia
Yuji Liu, China
Paolo Lonetti, Italy
Vassilios C. Loukopoulos, Greece
Chien-Yu Lu, Taiwan
Junguo Lu, China
Alexei Mailybaev, Brazil
Manoranjan K. Maiti, India
Oluwale Daniel Makinde, South Africa
Rafael Martinez-Guerra, Mexico
Driss Mehdi, France
Roderick Melnik, Canada
Xinzhu Meng, China
Yuri V. Mikhlin, Ukraine
Gradimir Milovanovic, Serbia
Ebrahim Momoniat, South Africa
Trung Nguyen Thoi, Vietnam
Hung Nguyen-Xuan, Vietnam
Ben T. Nohara, Japan
Sotiris Ntouyas, Greece
Gerard Olivar, Colombia
Claudio Padra, Argentina
Bijaya Ketan Panigrahi, India
Francesco Pellicano, Italy
Matjaz Perc, Slovenia
Vu Ngoc Phat, Vietnam
Alexander Pogromsky, The Netherlands
Seppo Pohjolainen, Finland

Stanislav Potapenko, Canada
Sergio Preidikman, USA
Carsten Proppe, Germany
Hector Puebla, Mexico
Justo Puerto, Spain
Dane Quinn, USA
Kumbakonam Rajagopal, USA
Gianluca Ranzi, Australia
Sivaguru Ravindran, USA
G. Rega, Italy
Pedro Ribeiro, Portugal
J. Rodellar, Spain
Rosana Rodriguez-Lopez, Spain
Alejandro J. Rodriguez-Luis, Spain
Ignacio Romero, Spain
Hamid Ronagh, Australia
Carla Roque, Portugal
Rubén Ruiz García, Spain
Manouchehr Salehi, Iran
Miguel A. F. Sanjuán, Spain
Ilmar Ferreira Santos, Denmark
Nickolas S. Sapidis, Greece
Evangelos J. Sapountzakis, Greece
Bozidar Sarler, Slovenia
Andrey V. Savkin, Australia
Massimo Scalia, Italy
Mohamed A. Seddeek, Egypt
Alexander P. Seyranian, Russia
Leonid Shaikhet, Ukraine
Cheng Shao, China

Bo Shen, Germany
Daichao Sheng, Australia
Tony Sheu, Taiwan
Jian-Jun Shu, Singapore
Zhan Shu, UK
Dan Simon, USA
Luciano Simoni, Italy
Grigori M. Sisoiev, UK
Christos H. Skiadas, Greece
Davide Spinello, Canada
Sri Sridharan, USA
Rolf Stenberg, Finland
Jitao Sun, China
Xi-Ming Sun, China
Changyin Sun, China
Andrzej Swierniak, Poland
Yang Tang, Germany
Allen Tannenbaum, USA
Cristian Toma, Romania
Irina N. Trendafilova, UK
Alberto Trevisani, Italy
Jung-Fa Tsai, Taiwan
Kuppalapalle Vajravelu, USA
Victoria Vampa, Argentina
Josep Vehi, Spain
Stefano Vidoli, Italy
Dan Wang, China
Youqing Wang, China
Yongqi Wang, Germany
Moran Wang, China

Cheng C. Wang, Taiwan
Yijing Wang, China
Xiaojun Wang, China
Gerhard-Wilhelm Weber, Turkey
Jeroen Witteveen, USA
Kwok-Wo Wong, Hong Kong
Zheng-Guang Wu, China
Ligang Wu, China
Wang Xing-yuan, China
X. Frank Xu, USA
Xuping Xu, USA
Xing-Gang Yan, UK
Jun-Juh Yan, Taiwan
Suh-Yuh Yang, Taiwan
Mahmoud T. Yassen, Egypt
Mohammad I. Younis, USA
Huang Yuan, Germany
S. P. Yung, Hong Kong
Ion Zaballa, Spain
Ashraf Zenkour, Saudi Arabia
Jianming Zhan, China
Yingwei Zhang, China
Xu Zhang, China
Lu Zhen, China
Liancun Zheng, China
Jian Guo Zhou, UK
Zexuan Zhu, China
Mustapha Zidi, France

Contents

Computational Intelligence in Civil and Hydraulic Engineering, Shengyong Chen, Fei Kang, Siamak Talatahari, Sunghwan Kim, and Dogan Aydin
Volume 2013, Article ID 935158, 2 pages

Rainfall Reliability Evaluation for Stability of Municipal Solid Waste Landfills on Slope, Fu-Kuo Huang, Grace S. Wang, and Yueh-Lin Tsai
Volume 2013, Article ID 653282, 10 pages

A Nonlinear Optimization Technique of Tunnel Construction Based on DE and LSSVM, Xing Jun, Jiang Annan, Wen Zhiwu, and Qiu Jingping
Volume 2013, Article ID 980154, 11 pages

Settlement Analysis of a Confined Sand Aquifer Overlain by a Clay Layer due to Single Well Pumping, Wen-jie Niu, Zhenyu Wang, Feng Chen, and Hongran Li
Volume 2013, Article ID 789853, 13 pages

Lévy-Flight Krill Herd Algorithm, Gaige Wang, Lihong Guo, Amir Hossein Gandomi, Lihua Cao, Amir Hossein Alavi, Hong Duan, and Jiang Li
Volume 2013, Article ID 682073, 14 pages

Simultaneous Topology, Shape, and Sizing Optimisation of Plane Trusses with Adaptive Ground Finite Elements Using MOEAs, Norapat Noilublao and Sujin Bureerat
Volume 2013, Article ID 838102, 9 pages

A Simple Generation Technique of Complex Geotechnical Computational Model, Hang Lin, Taoying Liu, Jiangteng Li, and Ping Cao
Volume 2013, Article ID 863104, 8 pages

Mathematical and Metaheuristic Applications in Design Optimization of Steel Frame Structures: An Extensive Review, Mehmet Polat Saka and Zong Woo Geem
Volume 2013, Article ID 271031, 33 pages

Accelerated Particle Swarm for Optimum Design of Frame Structures, S. Talatahari, E. Khalili, and S. M. Alavizadeh
Volume 2013, Article ID 649857, 6 pages

E-Block: A Tangible Programming Tool with Graphical Blocks, Danli Wang, Yang Zhang, and Shengyong Chen
Volume 2013, Article ID 598547, 10 pages

Factors Influencing Quasistatic Modeling of Deformation and Failure in Rock-Like Solids by the Smoothed Particle Hydrodynamics Method, X. W. Tang, Y. D. Zhou, and Y. L. Liu
Volume 2013, Article ID 852875, 13 pages

Combined Data with Particle Swarm Optimization for Structural Damage Detection, Fei Kang, Junjie Li, and Sheng Liu
Volume 2013, Article ID 416941, 10 pages

Inverse Parametric Analysis of Seismic Permanent Deformation for Earth-Rockfill Dams Using Artificial Neural Networks, Xu Wang, Fei Kang, Junjie Li, and Xin Wang
Volume 2012, Article ID 383749, 19 pages

Intelligent Risk Assessment for Dewatering of Metro-Tunnel Deep Excavations, X. W. Ye, L. Ran, T. H. Yi, and X. B. Dong

Volume 2012, Article ID 618979, 13 pages

Prediction of Optimal Design and Deflection of Space Structures Using Neural Networks,

Reza Kamyab Moghadas, Kok Keong Choong, and Sabarudin Bin Mohd

Volume 2012, Article ID 712974, 18 pages

Adaptive Parameters for a Modified Comprehensive Learning Particle Swarm Optimizer, Yu-Jun Zheng, Hai-Feng Ling, and Qiu Guan

Volume 2012, Article ID 207318, 11 pages

Combination of Interacting Multiple Models with the Particle Filter for Three-Dimensional Target Tracking in Underwater Wireless Sensor Networks, Xin Wang, Mengxi Xu, Huibin Wang, Yan Wu, and Haiyan Shi

Volume 2012, Article ID 829451, 16 pages

Optimal Placement of Passive Energy Dissipation Devices by Genetic Algorithms, Ji-ting Qu and Hong-nan Li

Volume 2012, Article ID 474282, 21 pages

Sludge Bulking Prediction Using Principle Component Regression and Artificial Neural Network, Inchio Lou and Yuchao Zhao

Volume 2012, Article ID 237693, 17 pages

Particle Swarm Optimization Algorithm Coupled with Finite Element Limit Equilibrium Method for Geotechnical Practices, Hongjun Li, Hong Zhong, Zuwen Yan, and Xuedong Zhang

Volume 2012, Article ID 498690, 14 pages

Freshwater Algal Bloom Prediction by Support Vector Machine in Macau Storage Reservoirs, Zhengchao Xie, Inchio Lou, Wai Kin Ung, and Kai Meng Mok

Volume 2012, Article ID 397473, 12 pages

Artificial Intelligence in Civil Engineering, Pengzhen Lu, Shengyong Chen, and Yujun Zheng

Volume 2012, Article ID 145974, 22 pages

Optimum Design of Gravity Retaining Walls Using Charged System Search Algorithm, S. Talatahari, R. Sheikholeslami, M. Shadfaran, and M. Pourbaba

Volume 2012, Article ID 301628, 10 pages

Investment Decision Support for Engineering Projects Based on Risk Correlation Analysis, Yan Liu, Ting-Hua Yi, and Cui-Qin Wang


Volume 2012, Article ID 242187, 14 pages

Histogram Modification and Wavelet Transform for High Performance Watermarking, Ying-Shen Juang, Lu-Ting Ko, Jwu-E Chen, Yaw-Shih Shieh, Tze-Yun Sung, and Hsi Chin Hsin

Volume 2012, Article ID 164869, 14 pages

Down-Hole Heat Exchangers: Modelling of a Low-Enthalpy Geothermal System for District Heating, M. Carlini, S. Castellucci, E. Allegrini, and A. Tucci

Volume 2012, Article ID 845192, 11 pages



Real-Time Simulation of Fluid Scenes by Smoothed Particle Hydrodynamics and Marching Cubes,
Weihong Wang, Zhongzhou Jiang, Honglin Qiu, and Wei Li
Volume 2012, Article ID 635631, 9 pages

Numerical Solution of Nonlinear Volterra Integral Equations System Using Simpson's 3/8 Rule,
Adem Kılıçman, L. Kargaran Dehkordi, and M. Tavassoli Kajani
Volume 2012, Article ID 603463, 16 pages

Analysis of a T-Frame Bridge, Pengzhen Lu, Fangyuan Li, and Changyu Shao
Volume 2012, Article ID 640854, 14 pages

Statistical Analysis and Calculation Model of Flexibility Coefficient of Low- and Medium-Sized Arch Dam, Su Huaizhi, You Ting, and Wen Zhiping
Volume 2012, Article ID 860760, 20 pages

Editorial

Computational Intelligence in Civil and Hydraulic Engineering

Shengyong Chen,¹ Fei Kang,² Siamak Talatahari,³ Sunghwan Kim,⁴ and Dogan Aydin⁵

¹ College of Computer Science & Technology, Zhejiang University of Technology, Hangzhou 310023, China

² Faculty of Infrastructure Engineering, Dalian University of Technology, Dalian 116024, China

³ Marand Faculty of Engineering, University of Tabriz, Tabriz 51368, Iran

⁴ Department of Civil, Construction, and Environmental Engineering, Iowa State University, IA 50011, USA

⁵ Computer Engineering Department, Dumlupınar University, 43100 Kutahya, Turkey

Correspondence should be addressed to Shengyong Chen; sy@ieee.org

Received 30 April 2013; Accepted 30 April 2013

Copyright © 2013 Shengyong Chen et al. This is an open access article distributed under the Creative Commons Attribution License, which permits unrestricted use, distribution, and reproduction in any medium, provided the original work is properly cited.

Computational intelligence (CI) is a set of nature-inspired computational methodologies and approaches that address complex problems of the real-world applications to which traditional methodologies and approaches are ineffective or infeasible. CI methods and techniques, including neural networks, evolutionary computation, and fuzzy logic systems, have rapidly evolved over the last decades, and they have already been applied in various fields of civil and hydraulic engineering. The focus of this special issue is the mathematical analysis and real-world application in civil and hydraulic engineering of computational intelligence. It is mostly interested in the related new development of both theoretical study and practical implementation, either with modeling, prediction, and optimization in geotechnical engineering, transportation engineering or structural design, diagnostics, and health monitoring.

The papers selected for this special issue represent a good panel in recent challenges. The topics of the research papers and review papers are connected with the computational intelligence methods and their application in civil and hydraulic infrastructure engineering, for example, structure optimization using evolutionary algorithms, damage detection using swarm intelligence, civil infrastructure performance prediction using neural networks, numerical simulation of intelligence algorithms, and civil infrastructures.

This special issue contains 29 papers. In the category of civil infrastructure engineering optimization design, M. Polat Saka and Z. Woo Geem present an extensive review

of mathematical and metaheuristic applications in design optimization of steel frame structures. X. Jun et al. present a nonlinear optimization technique for tunnel construction based on DE and LSSVM. H. Li et al. present a particle swarm optimization algorithm coupled with finite element limit equilibrium method for geotechnical practices. J.-T. Qu and H. Li present a report on optimal placement of passive energy dissipation devices by genetic algorithms. X. Wang et al. present a method for three-dimensional target tracking in underwater wireless sensor networks using combination of interacting multiple models with the particle filter. N. Noilublaio and S. Bureerat present a report on simultaneous topology, shape, and sizing optimisation of plane trusses with adaptive ground finite elements using MOEAs. S. Talatahari et al. present accelerated particle swarm optimization algorithm for optimal design of frame structures. S. Talatahari et al. present a report on optimum design of gravity retaining walls using charged system search algorithm. D. Wang et al. present a tangible programming tool with graphical blocks, that is, E-Block. Y.-S. Juang et al. present a report on histogram modification and wavelet transform for high-performance watermarking.

In the category of neural network in civil engineering, F.-K. Huang et al. present a report on rainfall reliability evaluation using artificial neural networks for stability of municipal solid waste landfills on a slope. X. Wang et al. present a report on inverse parametric analysis of seismic permanent deformation for earth-rockfill dams using artificial neural networks. R. K. Moghadas et al. present a report

on the prediction of optimal design and deflection of space structures using neural networks. P. Lu et al. give a review on artificial intelligence in civil engineering. Z. Xie et al. present a report on freshwater algal bloom prediction by a supporting vector machine in macau storage reservoirs. I. Lou and Y. Zhao present a sludge bulking prediction method using principle component regression and artificial neural network.

In the category of numerical simulation of infrastructure engineering problems, F. Kang et al. present a structural damage detection method using combined data with particle swarm optimization. X.-W. Ye et al. present an intelligent risk assessment for dewatering of metro-tunnel deep excavations. Y.-J. Zheng et al. present a report on adaptive parameters for a modified comprehensive learning particle swarm optimizer. H. Lin et al. present a simple generation technique of complex geotechnical computational model. X. Tang et al. present a report on factors influencing quasistatic modeling of deformation and failure in rock-like solids by the smoothed particle hydrodynamics method. W.-J. Niu et al. present a report on settlement analysis of a confined sand aquifer overlain by a clay layer due to single-well pumping. P. Lu et al. present a report on analysis of a T-frame bridge. S. Huaizhi et al. present a report on statistical analysis and calculation model of flexibility coefficient of low-and medium-sized arch dam. M. Carlini et al. present a report on down-hole heat exchangers: modeling of a low-enthalpy geothermal system for district heating. W. Wang et al. present a method for real-time simulation of fluid scenes by smoothed particle hydrodynamics and marching cubes. A. Kiliçman et al. present a report on numerical solution of nonlinear Volterra integral equations system using Simpson's 3/8 rule. Y. Liu et al. present a report on investment decision support for engineering projects based on risk correlation analysis. G. Wang et al. present a Lévy-Flight krill herd algorithm for solving optimization tasks within limited computing time.

Of 72 submissions, 29 papers are selected in this special issue. Of course, the topics and papers are not an exhaustive representation of the area of computational intelligence in civil infrastructure engineering. It can be seen that although some solutions and models become available, most problems remain open and research is highly active in this field. In the near future, we expect more contributions that will address all of the key aspects previously mentioned. Nonetheless, the special issue represents the recent concerns in the community and we have the pleasure of sharing them with the readers.

Acknowledgment

We would like to thank the authors for their excellent contributions and the reviewers in helping improving the papers.

*Shengyong Chen
Fei Kang
Siamak Talatahari
Sunghwan Kim
Dogan Aydin*

Research Article

Rainfall Reliability Evaluation for Stability of Municipal Solid Waste Landfills on Slope

Fu-Kuo Huang,¹ Grace S. Wang,² and Yueh-Lin Tsai³

¹ Department of Water Resources and Environmental Engineering, Tamkang University, New Taipei City 25137, Taiwan

² Department of Construction Engineering, Chaoyang University of Technology, Taichung City 41349, Taiwan

³ Project Department, GeoTech Science Corporation Ltd., New Taipei City 22103, Taiwan

Correspondence should be addressed to Fu-Kuo Huang; fkhuang@mail.tku.edu.tw

Received 5 November 2012; Revised 12 February 2013; Accepted 28 February 2013

Academic Editor: Sunghwan Kim

Copyright © 2013 Fu-Kuo Huang et al. This is an open access article distributed under the Creative Commons Attribution License, which permits unrestricted use, distribution, and reproduction in any medium, provided the original work is properly cited.

A method to assess the reliability for the stability of municipal solid waste (MSW) landfills on slope due to rainfall infiltration is proposed. Parameter studies are first done to explore the influence of factors on the stability of MSW. These factors include rainfall intensity, duration, pattern, and the engineering properties of MSW. Then 100 different combinations of parameters are generated and associated stability analyses of MSW on slope are performed assuming that each parameter is uniform distributed around its reason ranges. In the following, the performance of the stability of MSW is interpreted by the artificial neural network (ANN) trained and verified based on the aforementioned 100 analysis results. The reliability for the stability of MSW landfills on slope is then evaluated and explored for different rainfall parameters by the ANN model with first-order reliability method (FORM) and Monte Carlo simulation (MCS).

1. Introduction

The response of municipal solid waste (MSW) landfills during earthquakes has gained much attention during the past years (Anderson and Kavazanjian [1], Anderson [2], Augello et al. [3], Idriss et al. [4], Kavazanjian and Matasovic [5], Kavazanjian et al. [6], Krinitzsky et al. [7], and Pinto [8]). However, there were many failure events of MSW landfills on slope resulted from rainfall situations (Huvaj-Sarihan and Stark [9], Liu [10]). Thus, the stability of MSW landfills on slope due to rainfall infiltration is another important topic worthy of further studied.

As to stability evaluation of MSW landfills on slope, safety factors are common used in engineering practice. The critical state of failure is usually regarded as reached when the factor of safety, FS, is equal to 1.0 based on this approach. This deterministic approach not only does not consider the influence of randomness and uncertainties of soil properties, analysis model, and associated parameters on the analysis results but also has not any implications about the failure probability of the critical state according to the factor of safety. In other

words, factors of safety are usually selected based on past experience empirically. The relationship between the factor of safety and the probability of failure is often unclear and needs to be established. If uncertainties of associated analysis parameters are greater than anticipated, an unstable situation of the MSW landfills may be encountered by using the deterministic factor-of-safety approach. Conversely, overdesigning can probably be done to some extent when uncertainties are smaller than anticipated. Accordingly, the reliability-based design (RBD) or performance-based design (PBD) approach that can evaluate the ultimate or serviceability performance of the MSW landfills on slope probabilistically is preferred in landfill and slope engineering.

The researches of reliability in geotechnical engineering are growing rapidly in these years. H. D. Lin and C. P. Lin [11] applied it to drilled piles while Shou and Chen [12] to spatial risk analysis of landslide. For deep excavation, Tang et al. [13] first performed a reliability analysis and design of braced excavation systems with FOSM method. Low [14] adopted FORM and MCS method by spreadsheet to reliability-based design for retaining walls using explicit

performance function. Owing to the performance function which is usually implicit in geotechnical engineering, Goh and Kulhawy [15] thus introduced artificial neural network to model the limit state surface of displacements for reliability analysis.

This paper will explore the application of artificial neural network to reliability analysis for rainfall stability of MSW landfills on slope. After modeling the limit state surface of concerned response parameters (factor of safety, FS) obtained from finite element program executed in this study, ANN-based FORM and ANN-based MCS are then performed to assess the reliability of rainfall stability of MSW landfills on slope. Emphasis is focused on the influence of rainfall characteristics, such as rainfall intensity, duration, and pattern on the reliability.

2. Reliability Analysis Method

2.1. Performance Function and Reliability. The reliability of an engineering system is defined as the probability of performing its intended function or mission (Ang and Tang [16]). The probability will depend on the properties of the system and the requirements of the level of performance. If we define a performance function, or state function,

$$g(\mathbf{X}) = g(X_1, X_2, \dots, X_n), \quad (1)$$

where $\mathbf{X} = (X_1, X_2, \dots, X_n)$ is a vector of design variables of the system. The performance or state of the system will be determined by the function $g(\mathbf{X})$. Thus, the "limit-state" of the system may be defined as $g(\mathbf{X}) = 0$. If $g(\mathbf{X}) > 0$ stands for the "safe state", $g(\mathbf{X}) < 0$ will be the "failure state" or "unsatisfactory performance state".

Geometrically, the limit-state function, $g(\mathbf{X}) = 0$, is an n -dimensional surface that represents the "failure surface". If the joint probability density function of the design variables X_1, X_2, \dots, X_n is $f_{X_1, \dots, X_n}(x_1, \dots, x_n)$, abbreviated as $f_{\mathbf{X}}(x)$, the probability of the failure state of the system would be the corresponding volume integral over the failure region $g(\mathbf{X}) < 0$ [16]:

$$P_f = \int_{g(\mathbf{X}) < 0} f_{\mathbf{X}}(x) dx. \quad (2)$$

To evaluate the previous equation is generally a formidable task, especially, when the failure surface cannot be represented by explicit function. The practical methods for evaluating P_f are often those of FOSM, FORM, or MCS, in which the failure probability, P_f , is estimated by reliability index in FOSM:

$$\beta = \frac{\mu_g}{\sigma_g}, \quad (3)$$

where μ_g and σ_g are mean and standard deviation of the performance function $g(\mathbf{X})$, respectively. Based on the definition, the β value may be different for two equivalent performance functions in FOSM, and thus restrict its usage. For

FORM Ditlevsen [17] uses the matrix formulation of Hasofer-Lind index [18], another interpretation of reliability index:

$$\beta = \min_{\mathbf{X} \in F} \sqrt{(\mathbf{X} - \boldsymbol{\mu})^T \mathbf{C}^{-1} (\mathbf{X} - \boldsymbol{\mu})}, \quad (4a)$$

or, equivalently (Low [14]),

$$\beta = \min_{\mathbf{X} \in F} \sqrt{\left(\frac{\mathbf{X}_i - \boldsymbol{\mu}_i}{\boldsymbol{\sigma}_i} \right)^T \mathbf{R}^{-1} \left(\frac{\mathbf{X}_i - \boldsymbol{\mu}_i}{\boldsymbol{\sigma}_i} \right)}, \quad (4b)$$

in which \mathbf{X} is a vector representing the set of random variables \mathbf{X}_i , $\boldsymbol{\mu}$ is the vector of mean values $\boldsymbol{\mu}_i$, \mathbf{C} is the covariance matrix, \mathbf{R} is the correlation matrix, $\boldsymbol{\sigma}_i$ is the standard deviation, and F is the failure domain (i.e., $g(\mathbf{X}) < 0$ region). It is worthwhile to note that the variables \mathbf{X} must follow the normal distributions. Otherwise, a transformation, such as R & F method (Rackwitz and Flessler [19]), must be carried out. If \mathbf{X} follows normal distributions and the performance function is linear, the failure probability, P_f , can be estimated by

$$P_f = \Phi(-\beta) \quad (5)$$

and approximated otherwise, in which Φ is the cumulative distribution of the standard normal variate.

Low [14] has shown that the quadratic form of reliability index β (4b) in the original space of the variables may be interpreted geometrically as the perspective of an ellipsoid. For two-dimensional case, the quadratic form is an ellipse. As shown in Figure 1, the reliability index β is the axis ratio (R/r) of the ellipse that touches the limit state surface (β -ellipse) and the one-standard-deviation dispersion ellipse [14]. The design point, being the first point of contact between the expanding ellipsoid and the limit state surface, is the most probable failure point with respect to the safe mean-value point at the center of the expanding ellipsoid. The ellipsoidal method can be used to perform the minimization and determine β . This optimization process will be efficiently carried out in a spreadsheet environment such as Microsoft Excel [14]. It does not involve the complicated iteration procedure and does not need coordination transformation. Thus, the method will be used in the following reliability analysis.

2.2. Approximator of the Implicit Response of System. Though Monte Carlo simulation is a powerful tool for reliability analysis, it will be too computationally extensive when the performance of the system cannot be represented by an explicit expression and need numerical analyses, such as finite element method (FEM), to evaluate its response. The explicit expression of the system response is also necessary for FORM. Thus, many researchers utilize the response surface model or artificial neural network [20] as an alternative to improve the modeling of the performance function (Box and Darper [21]; Goh and Kulhawy [15]). ANN is a special form of response surface and possesses many advantages. It will be used as the universal approximator of the implicit rainfall stability of MSW landfills on slope system in this study.

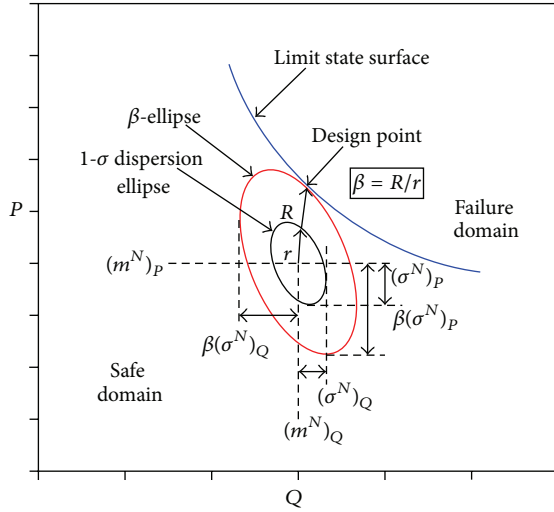


FIGURE 1: Relationship between 1- σ dispersion ellipse, β -ellipse, and reliability index β [14].

2.3. Procedures of the Reliability Analysis. The procedures of the reliability analysis for rainfall stability of municipal solid waste landfills on slope are shown in Figure 2. It includes the following seven steps: (1) identification of failure modes due to rainfall infiltration of MSW landfills on slope; (2) determination of design variables and its statistical properties; (3) preparation of training patterns and validation patterns for ANN inputs; (4) numerical analysis (e.g., FEM) of rainfall stability of MSW landfills on slope; (5) determination of ANN topology, and training and validation of ANN; (6) definition of performance function or limit state function; and (7) reliability analysis by FORM or MCS.

3. Safety Requirements of MSW Landfills on Slope and Analysis Method

After studying the failure modes of MSW landfills on slope (Bagchi [22]), it is found out that the internal rotational (circular) failure of solid waste and translational (block) failure along the liner interface are the two most common failure modes, which will be considered in this research. If factor of safety against rotational slide is denoted by FS_c and against translational failure is denoted by FS_t , the final governing factor of safety of MSW landfill against failure (FS) is determined by the following formula and shown as Figure 3:

$$FS = \min (FS_c, FS_t). \quad (6)$$

Though landfill covers were designed to prevent or control the infiltration of precipitation into the waste, some imperfections or disrupted will let the covers lose its function. Rainfall infiltration to MSW landfill will lead it to unstable situations. In Taiwan, the minimum requirement of factor of safety against slope failure under storm circumstances is $FS \geq 1.20$ [23].

The stability of MSW landfill on slope affected by rainfall has close relationship to the seepage pressure in response to

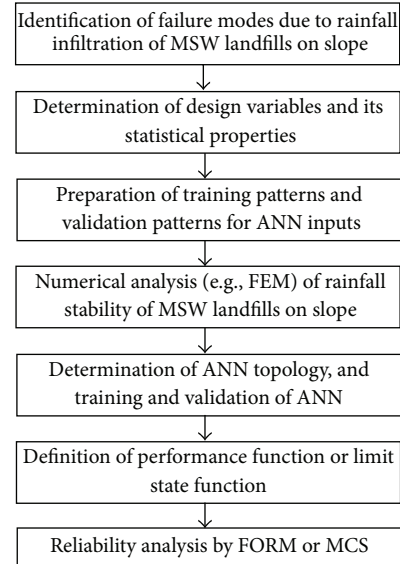


FIGURE 2: Flowchart of reliability analysis.

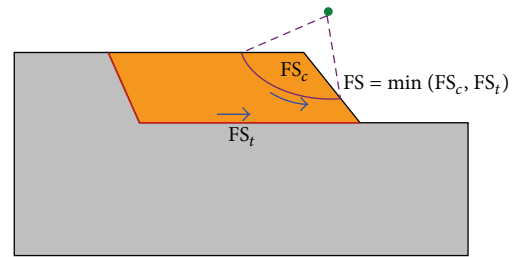


FIGURE 3: Failure modes of MSW landfills considered in this research and associated factor of safety against failure.

rainfall scenarios and related geological and geomorphologic conditions, physical and mechanical parameters. In this research, there will include both seepage analyses and slope stability analyses. The commercial finite element software-GeoStudio package of a coupled hydrological slope stability modeling tool will be used. The SEEP/W (GEO-SLOPE International Ltd. [24]) of the GeoStudio package is used to investigate how seepage will occur in a slope under different rainfall conditions, whereas SLOPE/W (GEO-SLOPE International Ltd. [25]) can be used to study the effect of different seepage conditions (as predicted by SEEP/W) on the factor of safety of the MSW landfill on slope. SEEP/W adopts an implicit numerical solution to solve Darcy's equation for saturated and unsaturated flow conditions, describing pore-water pressure and movement patterns within porous materials over space and time. The results obtained from seepage modeling can be directly linked into SLOPE/W, a limit equilibrium slope stability model, where the factor of safety is computed with the Morgenstern-Price method in this study.

In the analyses of SEEP/W, the permeability function, soil-water characteristic (SWC) curve, boundary flux, and initial hydraulic head are defined appropriate for the situations of MSW landfills on slope in advance.

4. Case Study of a Hypothetical Site

4.1. Description of the Hypothetical Site. Now, a hypothetical site that may exist in real-world situations subject to rainfall infiltration, as shown in Figure 4, is illustrated as an example for reliability analysis of the rainfall stability of MSW landfills on slope. The representative values of the parameters for the hypothetical site are shown in Table 1. These factors include the geometry and material properties of MSW landfills, including height of landfill (H), length of landfill (L), slope angle of the back (α), and slope angle of the waste body (β); and unit weight of waste (γ_1), unit weight of geomembrane (γ_2), unit weight of soft rock (γ_3), cohesion of waste (c_1), cohesion of geomembrane (c_2), cohesion of soft rock (c_3), friction angle of waste (ϕ_1), interfacial friction angle of geomembrane (ϕ_2), and friction angle of soft rock (ϕ_3). The properties of soft rock are drawn from Wang [26]. As to the rainfall characteristics that will be considered, it contains rainfall intensity (I), rainfall duration (T), and rainfall pattern (RP).

4.2. Analyses of the Rainfall Stability of MSW Landfills on Slope. According to the analysis method aforementioned, coupled SEEP/W-SLOPE/W analyses have been employed to evaluate the rainfall stability of MSW landfills on slope. The rainfall patterns considered here include seven types shown in Table 2: uniform, peak at the first section, peak at the first quarter section, peak at center, peak at the third quarter section, peak at the last section, and double peak. Different rainfall patterns can be assigned in analyses by specified associated function of water unit flux versus time over the top surface boundary of the model shown in Figure 4 in SEEP/W software [24].

After parametric study, it revealed that the interfacial friction angle of geomembrane (ϕ_2) and height of landfill (H) had major influences on the rainfall stability of MSW landfills. Although other factors have minor influences on slope stability relative to ϕ_2 and H , all the parameters except for those of soft rock shown in Table 1 will be used as design variables for reliability analysis in the following.

4.3. Training and Validation of the Artificial Neural Network (ANN). The factor of safety against slope failure is highly dependent on the geometry and material properties of MSW landfills and rainfall characteristics. The artificial neural network can provide a mapping relationship between these associated parameters. Considering the important factor that influences the stability or performance of the MSW landfills, thirteen parameters shown in Figure 5 are selected as the input neurons of the network. On the other hand, the factor of safety against slope failure, FS, from (6) is selected as the output neuron of the network.

The number of sampling points required to accurately model the mapping function of ANN is dependent on the number of design variables and the nonlinearity of the problem considered. In this paper, 100 sampling points were first randomly generated for each design variable (i.e., the 13 input neurons) assuming that it is uniform distributed around its reason range shown in Table 3. In the following, 100 data

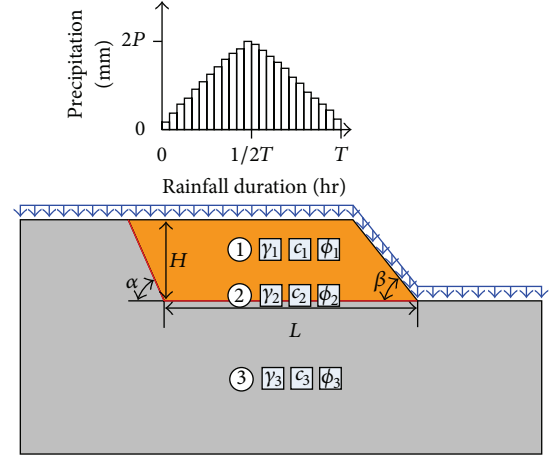


FIGURE 4: The hypothetical site and associated analysis parameters.

TABLE 1: Representative values of the parameters for the hypothetical site of MSW landfill on slope.

Parameter type	Name	Value
Geometry parameter	H (m)	20
	L (m)	30
	α (°)	60
	β (°)	30
Material parameter	γ_1 (kN/m ³)	7
	γ_2 (kN/m ³)	20
	γ_3 (kN/m ³)	24
	c_1 (kPa)	34
	c_2 (kPa)	0.35
	c_3 (kPa)	245.25
	ϕ_1 (°)	35
	ϕ_2 (°)	23
	ϕ_3 (°)	0

sets are obtained from the combinations of these sampling points and then used to evaluate the corresponding value of FS by performing the coupled SEEP/W-SLOPE/W analyses. These 100 patterns including input and output are divided into two parts, each with 75 and 25 patterns, to train and validate the artificial neural network.

Analyses of ANN in this paper are based on the popular back-propagation neural network algorithm (Goh and Kulhawy [15]) for demonstration, whereas other newer learning algorithm like extreme learning machine (ELM) [27–29] may also be used in such applications. The topology of ANN in this case is shown in Figure 5, with 13 input neurons, 14 hidden neurons, and 1 output neuron. After suitable training, the mapping function of the implicit response of the MSW landfills on slope is well established. It can be seen from the scatter diagram of Figure 6 that the relationship between network outputs and training targets for variable FS in the recalling phase, using the separate 25 patterns, is almost linear. Its coefficient of determination, R^2 , is greater than 0.9. Thus, the generalization capabilities of the trained network

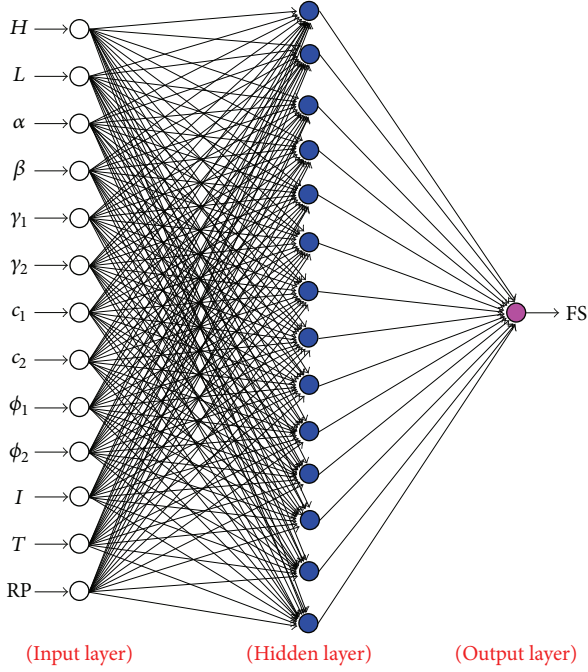


FIGURE 5: ANN topology in the case of MSW landfill on slope.

are validated. Therefore, the trained ANN can be used as a universal approximator of the implicit response (i.e., factor of safety against slope failure, FS) of the MSW landfills on slope that relates the parameters of output and input and can be employed in the following reliability analysis.

4.4. Definition of Performance Function or Limit State Function. The performance function is defined before reliability analysis for the rainfall stability of MSW landfills on slope:

$$g(\mathbf{X}) = \text{FS}(X_1, X_2, \dots, X_n) - \text{FS}_r, \quad (7)$$

where X_1, X_2, \dots, X_n are design variables. $\text{FS}(X_1, X_2, \dots, X_n)$ is FS determined from the trained ANN given a data set of X_1, X_2, \dots, X_n . FS_r is the required factor of safety against slope failure corresponding to the requirement for code or a certain limit state.

The statistical properties for reliability analysis of the thirteen parameters of ANN input neurons are shown in Table 4. Mean values μ drawn from Table 1 are regarded as the best estimated values of these parameters. Mean rainfall intensity and duration are assumed to be $I = 50$ mm/hr and $T = 36$ hr, respectively. The values of coefficient of variation (COV) are partly from the suggestions of Phoon and Kulhawy [30] and Duncan [31], and partly from writers' experience. Thus, the standard deviation is easily obtained from the mean value and corresponding COV.

4.5. Reliability Analysis: Monte Carlo Simulation (MCS). The reliability analysis evaluated by ANN-based MCS is illustrated first. The percentage errors of the results of the Monte Carlo simulations can be calculated by (8) (Shoorman

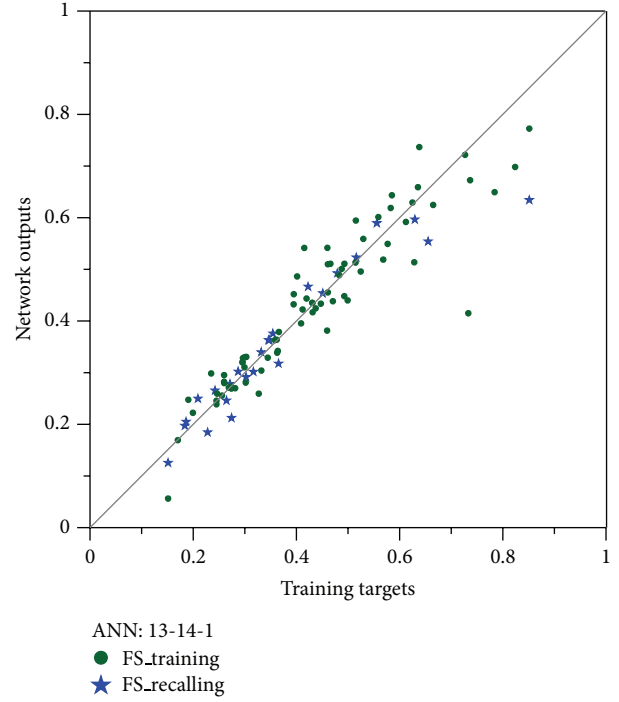


FIGURE 6: Scatter diagram of network outputs versus training targets in the recalling phase.

[32]), which is based on the 95% confidence interval for the probability of unsatisfactory performance:

$$\% \text{ error} = 200 \sqrt{\frac{1 - P_f}{N_M P_f}}, \quad (8)$$

where N_M is the total number of Monte Carlo trails. For example, if $N_M = 600,000$ and $P_f = 0.001$, (8) then yields 8.2% error. Therefore it is 95% likely that the actually failure probability will be within 0.001 ± 0.000082 . Since the error is relatively small, the number 600,000 will be used in this study.

Reliability of MSW landfills on slope is assessed first based on the assumptions that the input variables shown in Table 4 are all following normal distribution $N(\mu, \sigma)$, and the Uniform rainfall pattern shown in Table 2 is adopted. The input variables are supposed to be independent each other. The histogram of factor of safety (FS) obtained from MCS is shown in Figure 7. As depicted, the distribution of FS is close to normal distribution also. The mean value of FS is 1.732. Once the required factor of safety, FS_r , is specified, the associated failure probability, $P_f = P[\text{FS} < \text{FS}_r]$, can be calculated immediately. Figure 8 is the analysis results for both normal and log-normal input variables for different required factors of safety FS_r .

It is apparent that the failure probability P_f is both from small to large when required factor of safety FS_r becomes larger for input variables with normal or log-normal distribution. It is a reasonable trend regarding to the practical application.

TABLE 2: The pattern type of rainfall.

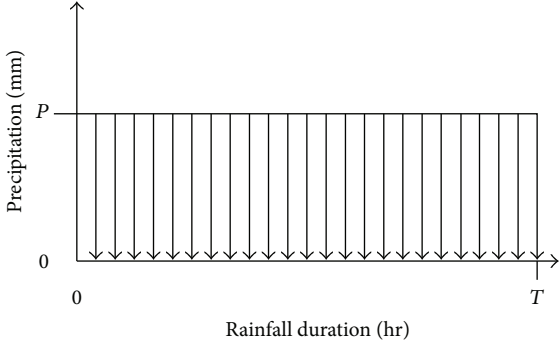
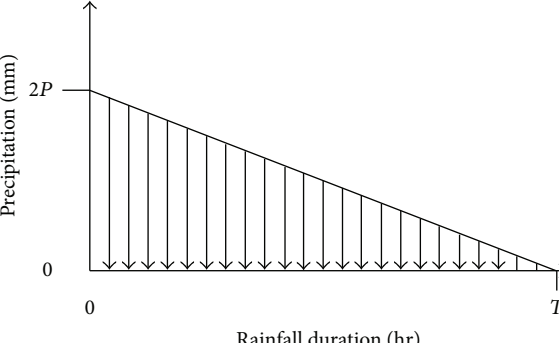
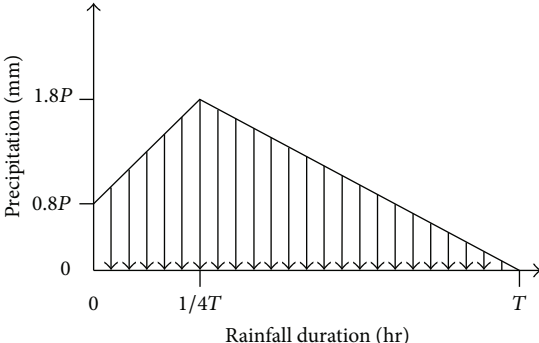
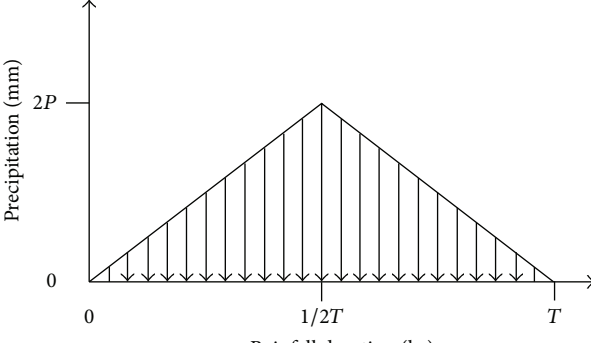
Number	Pattern type	Illustration
1	Uniform	 <p>The graph shows a constant precipitation rate of P mm over a duration of T hours. The y-axis is labeled 'Precipitation (mm)' with values 0 and P. The x-axis is labeled 'Rainfall duration (hr)' with values 0 and T. The area under the curve is filled with vertical lines, and horizontal arrows point downwards from the curve to the x-axis, indicating a constant rate of rainfall.</p>
2	Peak at the first section	 <p>The graph shows a linear decrease in precipitation rate from $2P$ mm at $t=0$ to 0 mm at $t=T$. The y-axis is labeled 'Precipitation (mm)' with values 0 and $2P$. The x-axis is labeled 'Rainfall duration (hr)' with values 0 and T. The area under the curve is filled with vertical lines, and horizontal arrows point downwards from the curve to the x-axis, indicating a decreasing rate of rainfall.</p>
3	Peak at the first quarter section	 <p>The graph shows a triangular rainfall pattern peaking at $1.8P$ mm at $t=1/4T$ hours. The y-axis is labeled 'Precipitation (mm)' with values 0, $0.8P$, and $1.8P$. The x-axis is labeled 'Rainfall duration (hr)' with values 0, $1/4T$, and T. The area under the curve is filled with vertical lines, and horizontal arrows point downwards from the curve to the x-axis, indicating a peak in the first quarter of the duration.</p>
4	Peak at center	 <p>The graph shows a triangular rainfall pattern peaking at $2P$ mm at $t=1/2T$ hours. The y-axis is labeled 'Precipitation (mm)' with values 0 and $2P$. The x-axis is labeled 'Rainfall duration (hr)' with values 0, $1/2T$, and T. The area under the curve is filled with vertical lines, and horizontal arrows point downwards from the curve to the x-axis, indicating a peak at the center of the duration.</p>

TABLE 2: Continued.

Number	Pattern type	Illustration
5	Peak at the third quarter section	
6	Peak at the last section	
7	Double peak	

4.6. *Reliability Analysis: First-Order Reliability Method (FORM).* In the following, the reliability analysis evaluated by ANN-based FORM is illustrated using the same case. The β -ellipse technique carried out in a spreadsheet environment, such as Microsoft Excel, proposed by Low [14] is used in the analyses.

The results obtained by ANN-based FORM are also shown in Figure 8. Comparing the results of FORM with those of MCS, it can be found that the failure probability obtained from FORM is less than that obtained from MCS for small P_f value, and their differences are larger if the design variables are following log-normal distribution, whereas the differences are minor if the design variables are following normal distribution. Therefore, the two method—ANN-based FORM and ANN-based MCS—can get comparable results with limit differences for variables with normal distribution based on this case study. Furthermore, whatever for which method, in comparison to results obtained from variables

with different distributions, it can be found that P_f with normal distribution (denoted by P_{f-N}) are greater than those with log-normal distribution (denoted by P_{f-LN}), that is, $P_{f-N} > P_{f-LN}$, especially when failure probability is smaller. Thus, in view of the evaluation efficiency and consideration of conservative design, the ANN-based FORM method with input variables of normal distribution will be adopted in the following analyses to explore the influence of rainfall characteristics on the reliability of MSW landfills on slope.

Figure 9 is the relationship between required factor of safety FS_r and failure probability P_f for different rainfall intensity I with rainfall duration $T = 36$ hr. Obviously, failure probability increases with rainfall intensity. For example, if $I = 40$ mm/hr, when FS_r increases from 1.0 to 1.2, the associated P_f increases vastly from 0.000086 to 0.003233. The corresponding performance level will be from “above average” decreases to near “below average” according to the relationship of target reliability index and failure probability

TABLE 3: The probable range considered for each parameter in the hypothetical site of MSW landfill.

Parameter type	Name	Range
Geometry parameter	H (m)	10~30
	L (m)	10~50
	α (°)	30~75
	β (°)	15.95~60
Material parameter	γ_1 (kN/m ³)	4.9~9.8
	γ_2 (kN/m ³)	18~22
	γ_3 (kN/m ³)	24
	c_1 (kPa)	33.55~34.90
	c_2 (kPa)	0~0.7
	c_3 (kPa)	245.25
	ϕ_1 (°)	10~40
	ϕ_2 (°)	5~30
	ϕ_3 (°)	0
Rainfall parameter	I (mm/hr)	0~100
	T (hr)	0~72
	Rainfall pattern	1~7

TABLE 4: The statistical properties of the parameters for reliability analysis.

Parameter type	Name	Mean (μ)	Coefficient of variation (COV)	Standard deviation (σ)
Geometry parameter	H (m)	20	0.01	0.2
	L (m)	30	0.01	0.3
	α (°)	60	0.01	0.6
	β (°)	30	0.01	0.3
Material parameter	γ_1 (kN/m ³)	7	0.10	0.7
	γ_2 (kN/m ³)	20	0.05	1.0
	c_1 (kPa)	34	0.20	6.8
	c_2 (kPa)	0.35	0.20	0.07
	ϕ_1 (°)	35	0.10	3.5
	ϕ_2 (°)	23	0.10	2.3
	ϕ_3 (°)	0	0.00	0.00
Rainfall parameter	I (mm/hr)	50	0.02	1.0
	T (hr)	36	0.01	0.36
	Rainfall pattern	1~7	—	—

Subscript 1 stands for solid waste; subscript 2 stands for geomembrane.

suggested by U.S. Army Corps of Engineers [33]. Therefore, it is necessary to redesign the MSW landfills on slope to meet the performance requirements in this case. Thus, the reliability analyses will be beneficial to engineering design and provide a guideline to achieve the target reliability considering uncertainty.

Figure 10 is the relationship between FS_r and P_f for different rainfall durations with rainfall intensity $I = 50$ mm/hr. As expected, P_f increases with rainfall duration. Finally, Figure 11 is the relationship between rainfall pattern and P_f for different mean rainfall intensities under the same total amount of precipitation with rainfall duration $T = 36$ hr and

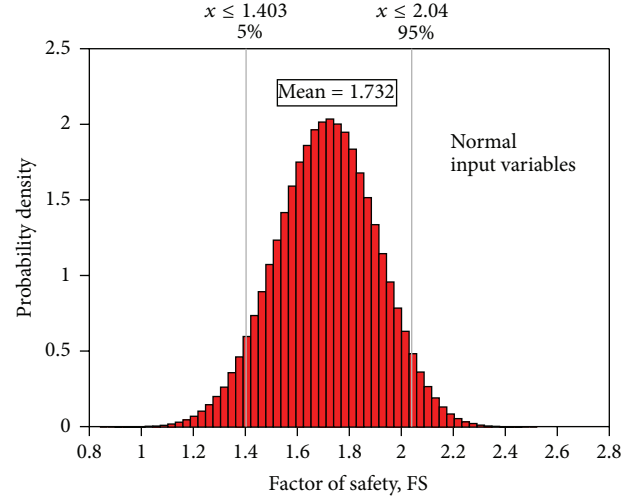


FIGURE 7: Histogram of factor of safety, FS, obtained from MCS assuming that the input variables are all following normal distribution and uniform rainfall pattern is adopted.

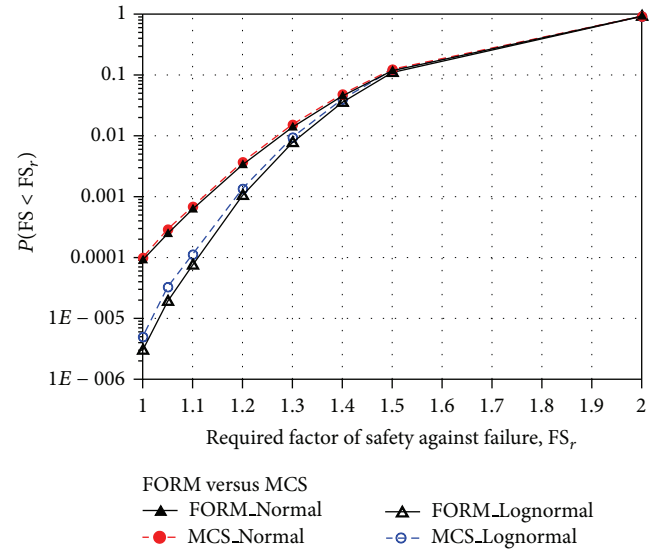


FIGURE 8: Comparisons of reliability analysis results between FORM method and MCS method.

$FS_r = 1.2$. It is shown that the Uniform pattern has the highest failure probability in the case. For other patterns, if the peak rainfall intensity occurs earlier, the cumulative amount of infiltrations will be larger with higher failure probability of P_f . The study of Jia et al. [34] draws similar conclusions and makes a recommendation that rainfall pattern should be taken into account in the performance assessment of landfill covers.

As to the effects of rainfall intensity and duration on the slope stability of MSW landfills and thus the failure probability, it can be attributed to the reduction in matrix suction of unsaturated landfills and consequent fall in shear strengths caused by the rise in pore water pressures. The higher the rainfall intensity and/or duration, the lower the

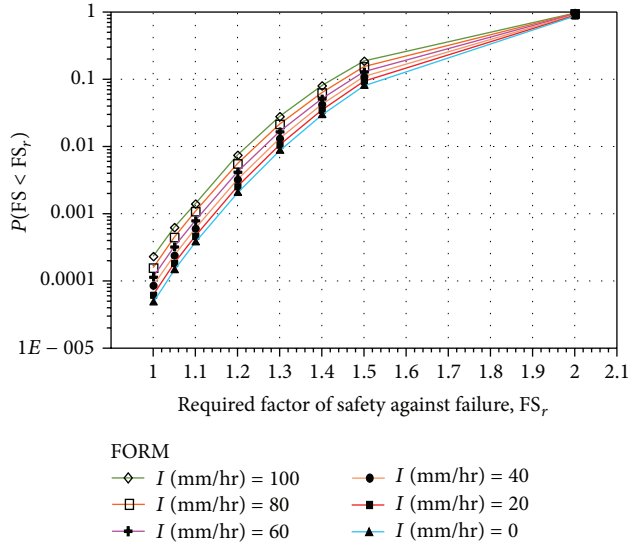


FIGURE 9: The relationship between required factor of safety and failure probability for different rainfall intensities ($T = 36$ hr).

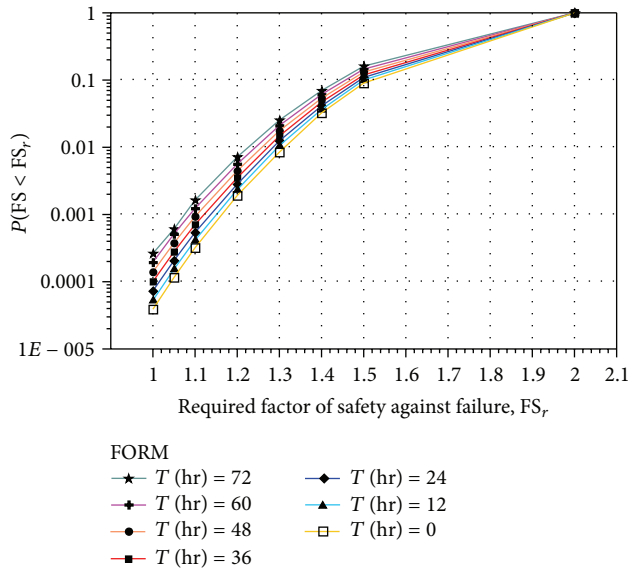


FIGURE 10: The relationship between required factor of safety and failure probability for different rainfall duration ($I = 50$ mm/hr).

matrix suctions behind the wetting front, and thus the higher the failure probability of the MSW landfills to be. The phenomena are the same as those studied by other researchers, such as Ng and Shi [35] and Li et al. [36].

5. Conclusions

In this study, two methods of reliability evaluation for the rainfall stability of MSW landfills on slope, ANN-based FORM and ANN-based MCS, are explored. By performing a case study of a hypothetical site, an analysis procedure for reliability analysis is proposed. The evaluation model of ANN-based FORM or ANN-based MCS is superior to traditional

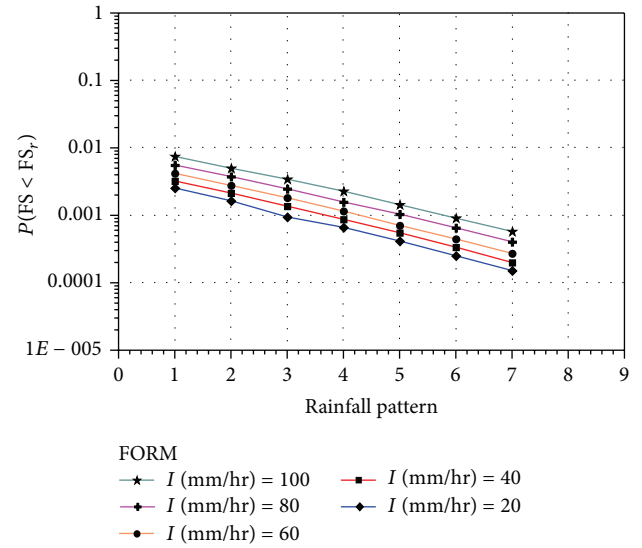


FIGURE 11: The relationship between rainfall pattern and failure probability for different rainfall intensities with $FS_r = 1.2$ ($T = 36$ hr).

reliability method in view of many aspects, such as system modeling, computational efficiency, and analysis precision. Based on these methods, the performance-based design (PBD) of MSW landfills on slope can be implemented easily.

According to the analysis results, it can be concluded that all the rainfall characteristics, including intensity, duration, and pattern, have obvious influence on the reliability for stability of MSW landfills on slope. Thus, the variation of rainfall condition should be investigated and considered in the analysis. By the quantitative reliability method proposed in this study, it will be beneficial to MSW landfills design and provide a guideline to achieve the target reliability considering rainfall scenarios.

Acknowledgment

The authors would like to thank the anonymous referees for their valuable comments and suggestions on earlier drafts of this paper.

References

- [1] D.G. Anderson and E. Kavazanjian, "Performance of landfills under seismic loading," in *Proceedings of the 3rd International Conference on Recent Advances in Geotechnical Earthquake Engineering and Soil Dynamics*, Rolla, Mo, USA, 1995.
- [2] R. L. Anderson, "Earthquake related damage and landfill performance," *Earthquake Design and Performance of Solid Waste Landfills*, ASCE Geotechnical Special Publication, vol. 54, pp. 1–16, 1995.
- [3] A. J. Augello, N. Matasovic, J. D. Bray E, Jr. Kavazanjian, and R. B. Seed, "Evaluation of solid waste landfill performance during the Northridge earthquake," *Earthquake Design and Performance of Solid Waste Landfills*, ASCE Geotechnical Special Publication, vol. 54, pp. 17–50, 1995.

- [4] I. M. Idriss, G. L. Fiegel, M. B. Hudson, P. K. Mundy, and R. Herzig, "Seismic response of the operating industries landfill," *Earthquake Design and Performance of Solid Waste Landfills*, ASCE Geotechnical Special Publication, vol. 54, pp. 83–118, 1995.
- [5] E. Kavazanjian Jr. and N. Matasovic, "Seismic analysis of solid waste landfills," *Geoenvironment 2000*, V. 2, ASCE Geotechnical Special Publication, vol. 46, pp. 1066–1081, 1995.
- [6] E. Kavazanjian Jr., N. Matasovic, R. Bonaparte, and G. R. Schmertmann, "Evaluation of MSW properties for seismic analysis," *Geoenvironment 2000*, V. 2, ASCE Geotechnical Special Publication, vol. 46, pp. 1126–1141.
- [7] E. L. Krinitzsky, M. E. Hynes, and A. G. Franklin, "Earthquake safety evaluation of sanitary landfills," *Engineering Geology*, vol. 46, no. 2, pp. 143–156, 1997.
- [8] P. S. S. Pinto, "Static and seismic analysis of solid waste landfills," in *Proceedings of the International Symposium on Geoenvironmental Engineering (ISGE '09)*, Hangzhou, China, September 2009.
- [9] N. Huvaj-Sarihan and T. D. Stark, "Back-analyses of landfill slope failures," in *Proceedings of the 6th International Conference on Case Histories in Geotechnical Engineering*, pp. 11–16, Arlington, Va, USA, August 2008.
- [10] X. L. Liu, *Study on stability of landfill due to rainfall infiltration [Ph.D. thesis]*, Tianjin University, Tianjin, China, 2006.
- [11] H. D. Lin and C. P. Lin, "A preliminary study on resistance and load factors for drilled piles," *Journal of the Chinese Institute of Civil and Hydraulic Engineering*, vol. 11, no. 1, pp. 13–21, 1999.
- [12] K. J. Shou and Y. L. Chen, "Spatial risk analysis of the Li-Shan landslide," in *Proceedings of the 11th Conference on Current Researches in Geotechnical Engineering in Taiwan*, pp. C04-4–C04-8, Wanli, Taiwan, September 2005.
- [13] W. H. Tang, M. S. Yuceman, and A. H. S. Ang, "Reliability analysis and design of braced excavation systems," in *Proceedings of the 1st International Conference on Applications of Statistics and Probability in Soil and Structural Engineering*, pp. 187–202, Hong Kong, 1971.
- [14] B. K. Low, "Reliability-based design applied to retaining walls," *Geotechnique*, vol. 55, no. 1, pp. 63–75, 2005.
- [15] A. T. C. Goh and F. H. Kulhawy, "Neural network approach to model the limit state surface for reliability analysis," *Canadian Geotechnical Journal*, vol. 40, no. 6, pp. 1235–1244, 2003.
- [16] A. H. S. Ang and W. H. Tang, *Probability Concepts in Engineering Planning and Design. Decision, Risk and Reliability*, Vol. II, John Wiley & Sons, New York, NY, USA, 1984.
- [17] O. Ditlevsen, *Uncertainty Modeling: With Applications to Multidimensional Civil Engineering Systems*, McGraw-Hill, New York, NY, USA, 1981.
- [18] A. M. Hasofer and N. C. Lind, "An exact and invariant first-order reliability format," *Journal of Engineering Mechanics*, vol. 100, no. 1, pp. 111–121, 1974.
- [19] R. Rackwitz and B. Flessler, "Structural reliability under combined random load sequences," *Computers and Structures*, vol. 9, no. 5, pp. 489–494, 1978.
- [20] K. Hornik, "Approximation capabilities of multilayer feedforward networks," *Neural Networks*, vol. 4, no. 2, pp. 251–257, 1991.
- [21] G. P. Box and N. R. Draper, *Empirical Model-Building and Response Surface*, John Wiley & Sons, New York, NY, USA, 1987.
- [22] A. Bagchi, *Design of Landfills and Integrated Solid Waste Management*, John Wiley & Sons, New Jersey, NJ, USA, 3rd edition, 2004.
- [23] Taiwan Geotechnical Society, *Design Code and Specifications of Building Foundations*, 2001.
- [24] *Seepage Modeling with SEEP/W*, GEO-SLOPE International Ltd., Alberta, Canada, 2004.
- [25] *Stability Modeling with SLOPE/W*, GEO-SLOPE International Ltd., Alberta, Canada, 2004.
- [26] Y. Y. Wang, *Stability analysis of municipal solid waste landfills on slope [M.S. thesis]*, Department of Civil Engineering, National Chiao Tung University, Hsin-chu, Taiwan, 2007.
- [27] G. B. Huang, Q. Y. Zhu, and C. K. Siew, "Extreme learning machine: theory and applications," *Neurocomputing*, vol. 70, no. 1–3, pp. 489–501, 2006.
- [28] Y. Yuan, Y. Wang, and F. Cao, "Optimization approximation solution for regression problem based on extreme learning machine," *Neurocomputing*, vol. 74, pp. 2475–2482, 2011.
- [29] Y. Wang, F. Cao, and Y. Yuan, "A study on effectiveness of extreme learning machine," *Neurocomputing*, vol. 74, pp. 2483–2490, 2011.
- [30] K. K. Phoon and F. H. Kulhawy, "Characterization of geotechnical variability," *Canadian Geotechnical Journal*, vol. 36, no. 4, pp. 612–624, 1999.
- [31] J. M. Duncan, "Factors of safety and reliability in geotechnical engineering," *Journal of Geotechnical and Geoenvironmental Engineering*, vol. 126, no. 4, pp. 307–316, 2000.
- [32] M. L. Shooman, *Probabilistic Reliability: An Engineering Approach*, McGraw-Hill, New York, NY, USA, 1968.
- [33] U.S. Army Corps of Engineers, *Introduction to Probability and Reliability Methods for Use in Geotechnical Engineering*, Engineering Technical Letter no. 1110-2-547, U.S. Army Corps of Engineers, Washington, DC, USA, 1995.
- [34] G. W. Jia, T. L. T. Zhan, Y. M. Chen, and D. G. Fredlund, "Influence of rainfall pattern on the infiltration into landfill earthen final cover," in *Proceedings of the International Symposium on Geoenvironmental Engineering*, pp. 641–645, Hang-zhou, China, September 2009.
- [35] C. W. W. Ng and Q. Shi, "A numerical investigation of the stability of unsaturated soil slopes subjected to transient seepage," *Computers and Geotechnics*, vol. 22, no. 1, pp. 1–28, 1998.
- [36] W. C. Li, L. M. Lee, H. Cai, H. J. Li, F. C. Dai, and M. L. Wang, "Combined roles of saturated permeability and rainfall characteristics on surficial failure of homogeneous soil slope," *Engineering Geology*, vol. 153, pp. 105–113, 2013.

Research Article

A Nonlinear Optimization Technique of Tunnel Construction Based on DE and LSSVM

Xing Jun,¹ Jiang Annan,² Wen Zhiwu,² and Qiu Jingping¹

¹ School of Resources & Civil Engineering, Northeastern University, Shenyang 110004, China

² Highway and Bridge Engineering Institute, Dalian Maritime University, Dalian 116026, China

Correspondence should be addressed to Jiang Annan; jiangannan@163.com

Received 22 November 2012; Revised 10 February 2013; Accepted 23 February 2013

Academic Editor: Shengyong Chen

Copyright © 2013 Xing Jun et al. This is an open access article distributed under the Creative Commons Attribution License, which permits unrestricted use, distribution, and reproduction in any medium, provided the original work is properly cited.

Tunnel construction is a dynamic controlling system with observability and controllability; the feedback analysis requires identifying geophysics parameters and adjusting supporting parameters, and both of them are optimisation problems. The paper proposed a nonlinear optimization technique based on difference evolution arithmetic (DEA), least square support vector machine (LSSVM), and three dimensional numerical simulation. This method employs support vector machine with optimal architecture trained by the difference evolution arithmetic, instead of the time-consuming finite element analysis. Firstly, the three dimensional numerical simulation is used to create training and testing samples for LSSVM model construction. Then the nonlinear relationship between rock or anchoring parameters and displacement is constructed by support vector machine. Finally, the geophysics and supporting parameters are obtained by DE optimization arithmetic. The technique overcomes the conventional optimization method shortages of expending too much computing time and easily being limited in local optimal solution. This technique was verified by applying it to the feedback analysis of Dalian Metro in China, and the influence of the parameters of LSSVM and DE on the simulation ability of the algorithm was investigated.

1. Introduction

The geological body where the tunnel is constructed has uncertainty and complexity property, and there are two kinds of factors affecting the stability of surrounding rock. Some factors are inherent geophysical parameters of surrounding rock; the other factors are supporting parameters that human can adjust. The new Austrian tunnelling method points out the significance of surrounding rock displacements observation in construction process, and the posterior “information construction” and “observation construction” are also emphasizing the field monitoring information. Adjusting construction scheme based on identified rock mechanics parameters and obtaining the secure and economic scheme have important economic and scientific meaning.

The back analysis thinking is identifying rock parameters based on monitoring data, which had been firstly proposed by Sakurai and Takeuchi [1]. Mashimo summarized the update tunnel engineering techniques in Japan and proposed the concept of “redesign” [2]. Li proposed typical analogy

analysis method and developed BMP program combining the techniques of rock classification, monitoring measurement, and rock mechanics analysis, which had gotten good application results [3]. Zhu and He had optimized construction subsequence of Xiao Langdi engineering taking broken zone as appraising index and fitness value; the calculation results stated that the method is feasible [4]. Construction schemes and parameters are not only affecting the tunnel safety but also deciding the economic cost. Arends proposed a method for the evaluation of tunnel safety using probabilistic risk assessment. The framework includes three criteria: personal, societal, and economic risk [5]. Pérez-Romero et al., and so forth, made joint use of geotechnical investigation campaigns, convergence measurements, and numerical simulations, thereby contributing towards the optimisation of the cross-section of the tunneled area support and lining [6].

Both rock parameters back analysis and supporting parameters adjusting are optimization problems in essence. Yuegeng Tang presented a nonlinear optimization technique (NOT) for conducting the back analyses of geotechnical

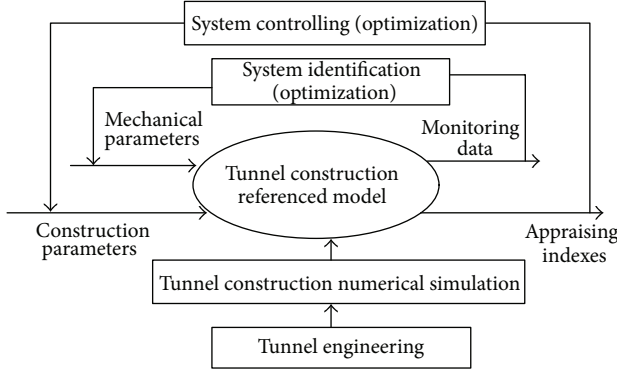


FIGURE 1: The adaptive control model of tunnel construction.

engineering problems based on the field observations. The developed NOT and additional auxiliary techniques are incorporated into a finite element code and then applied to the back analysis of excavation-induced wall deflection [7]. Hashash described and compared two inverse analysis approaches for an excavation project in downtown Chicago [8]. Along with the sensor techniques, tunnel monitoring developed from artificial, single information monitoring to automation, multiple information monitoring, genetic algorithm, and numerical method are also used in analysis of geotechnical problems [9–11]. The information science and intelligent methods are developed and applied in engineering [12–14] and overcome the shortcomings in conventional studies. Feng discussed how to establish the necessary quality and quantity of information required for rock engineering modelling and design [15]. Considering tunnel surrounding rock analysis being a complex nonlinear problem, the machine learning algorithms such as artificial neural network and support vector machine have been used in the rock displacement forecast or back analysis [16]. Jiang presented an integrated optimisation method for the feedback control of tunnel displacement; it combines the support vector machine (SVM), particle swarm optimisation (PSO), and 2D numerical analysis methods [17]. In that research, the method is applied only to control of the displacement objective and optimisation of the shotcrete parameters, ignoring the 3D space effect of tunnel heading face.

There are some problems in the tunnel construction optimization as follows. (1) Most methods are limited in surrounding rock parameters optimization and not including anchor parameters optimization. (2) Because the three dimensional numerical model expends too much time, the computing model is only limited in two dimensional space. (3) Because of the complex nonlinear characters of tunnel engineering, the conventional optimization method is easily limited in local optimum solution, and genetic algorithm has complex operation process and particle swarm optimization converges not steadily because of not having strictly convergence theory background. Aiming at the above problems, the paper constructed three dimensional feedback analysis method combining least square support vector machine (LSSVM) and difference evolution (DE) algorithm, and

applied the method into a metro tunnel engineering of Dalian City in China.

2. Tunnel Construction Nonlinear Optimization Method Based on DE-LSSVM

2.1. Tunnel Construction Optimization Problem Statement. In fact, the tunnel dynamic construction process is an adaptive controlling problem. The process includes two optimization processes. First is system identification, that is, utilizing the measurement data to back analyze rock mechanics parameters; second is system controlling, that is, selecting the optimal construction schemes in order to ascertain the surrounding rock stability with certain economical cost. The adaptive control system model with multi-input and multioutput is proposed as Figure 1.

On one hand, construction process has high requirement for construction speed. On the other hand, however, numerical calculation is nonexplicit and calculation time is long, so the conventional optimization method is limited. Considering tunnel construction being a dynamic system which takes anchoring parameters and surrounding rock mechanics parameters as input variables and takes observing and stability indices as output indices, a nonlinear optimization technique combining LSSVM and DE algorithm is proposed as follows.

2.2. LSSVM Theory. SVM has been proposed for solving pattern recognition and function estimation problems in 1995 [18]. The SVM method is based on statistical learning theory and makes use of the principle of structural risk minimization, avoiding the extra learning problem of conventional learning method based on empirical risk minimization. Suykens proposed LSSVM which greatly simplifies the problem and has efficiency and accuracy in classifiers and regression [19, 20], LSSVM selects the different slack variable as the second norm of ξ , while the standard SVM adopts the ξ . Consider the problem of approximation in the set of N samples and corresponding response is presented in

$$D = \{(x^1, y^1), (x^2, y^2), \dots, (x^l, y^l), \dots, (x^N, y^N)\}, \quad (1)$$

$$x^l \in R^n, \quad y^l \in R.$$

The classifier model of primal space can be presented as follows:

$$y(x) = \text{sign}(w^T \varphi(x) + b). \quad (2)$$

The optimization problem in primal weigh space can be expressed as

$$\min_{w, b, \varepsilon} J(w, \varepsilon) = \frac{1}{2} W^T W + \frac{1}{2} \gamma \sum_{i=1}^N \varepsilon_i^2. \quad (3)$$

Such at

$$y_l = w^T \varphi(x_l) + b + \varepsilon_l, \quad l = 1, 2, \dots, N, \quad (4)$$

$\varphi(\cdot) = R^n - R^{nh}$ is a kernel that maps the input space into hyperspace (infinite space). $w \in R^n$ is weight vector in primal space, $\varepsilon_1 \in R$ is error variable, and b is bias term. The relative importance of ERM and SRM terms is determined by positive constant γ .

Then, according to (3), the Lagrangian description mapping to the SVM optimization problem is defined as follows:

$$l(w, b, \varepsilon, a) = J(w, \varepsilon) - \gamma \sum_{i=1}^n a_i \{w^T \varphi(x_i) + b + \varepsilon_i - y_i\}. \quad (5)$$

With Lagrangian multiplier a , the criterions for optimization problems can be written as

$$\begin{aligned} \frac{\partial (l(w, b, \varepsilon, a))}{\partial w} = 0 &\implies w = \sum_{i=1}^N a_i \varphi(x_i) \\ \frac{\partial (l(w, b, \varepsilon, a))}{\partial b} = 0 &\implies \sum_{i=1}^N a_i = 0 \\ \frac{\partial (l(w, b, \varepsilon, a))}{\partial \varepsilon} = 0 &\implies a_i = \gamma \varepsilon_i \\ \frac{\partial (l(w, b, \varepsilon, a))}{\partial a} = 0 &\implies w^T \varphi(x_i) + b + \varepsilon_i - y_i = 0. \end{aligned} \quad (6)$$

After elimination of w and a , the solution is obtained as

$$\begin{bmatrix} 0 & I^T \\ I & \Gamma + \frac{1}{\gamma} I \end{bmatrix} \begin{bmatrix} b \\ a \end{bmatrix} = \begin{bmatrix} 0 \\ y \end{bmatrix}, \quad (7)$$

where $y = [y_1, y_2, \dots, y_N]$, $I = [1, 1, \dots, 1]$, and $a = [a_1, a_2, \dots, a_N]$.

Based on Mercer's condition, the kernel function can be expressed as

$$K(x_i, x_j) = \varphi(x_i)^T \varphi(x_j), \quad \text{for } i, j = 1, 2, \dots, N. \quad (8)$$

The result LSSVM model for function estimation is obtained as follows:

$$y(x) = \sum_{i=1}^N a_i K(x, x_i) + b. \quad (9)$$

The optimization problem is translated to solving the linear equations by least square method; therefore, the LSSVM is named. Normally, the kernel function has three kinds: polynomial kernel function, radial basis kernel function, and sigmoid kernel function. The paper adopts radial basis kernel function as follows:

$$k(x, x_i) = \exp\left(-\frac{|x - x_i|^2}{2\sigma^2}\right). \quad (10)$$

2.3. The DE-LSSVM Nonlinear Model Describing Tunnel Construction. The anchoring parameters are controllable and surrounding rock parameters are inherent but not assured

before excavation. Firstly, use monitoring data and anchoring parameters before heading face of tunnel to identify rock mechanics parameters. Then based on the identified rock mechanics parameters, optimize the anchoring parameters after heading face. The tunnel construction system can be described by numerical simulation; however, the three dimensional numerical simulation expends too much computing time; therefore, the LSSVM is introduced to replace the numerical simulation:

$$\begin{aligned} Y &= \text{LSSVM}(R), & Y &= \text{LSSVM}(M), \\ R &= (r_1, r_2, r_3, \dots, r_a), \\ M &= (m_1, m_2, m_3, \dots, m_b), \\ Y &= (y_1, y_2, y_3, \dots, y_l), \end{aligned} \quad (11)$$

where Y is displacements of surrounding rock, R and M are rock mechanics parameters and anchoring parameters, respectively. a is the number of rock mechanics variables, b is the number of anchoring parameters, and l is the number of outputting variables. Constructs orthogonal schemes of parameters combination and carries out three dimensional numerical simulation. Then obtains the data samples and trains support vector machine.

Some studies stated that different penal factor c and kernel parameter σ are corresponding to different LSSVM model and different forecast precision. LSSVM did not provide the theory of selecting the above parameters. DE optimization algorithm was proposed by Price and Storm of USA for solving Chebyshev Polynomial Polynomial Expression [21, 22]. It is simple, efficient and has good global optimization character [23]. The DE arithmetic is introduced and combined with LSSVM, and the DE-LSSVM model is constructed, which can solve the parameters selection problem of LSSVM. The DE-LSSVM algorithm computing process is as follows.

- (1) *Initial Population Generation.* Get learning samples and test samples ready for LSSVM model, take penal factor and kernel parameter as two dimensional solution vector, and randomly generate N_p two dimensional vectors according to the upper and lower boundaries, the formula is as follows:

$$\begin{aligned} X_{ij(0)} &= \text{rand} \times (x_{ijU} - x_{ijL}) + x_{ijL}, \\ i &= 1, 2, \dots, N_p; \quad j = 1, 2, \end{aligned} \quad (12)$$

where x_{ijU} , x_{ijL} are, respectively, upper and lower boundary of the j component, and rand is the random between $[0, 1]$. N_p is population scale; the vector dimension number is corresponding to the number of parameters which to be optimized, in this state it is adopted as 2.

- (2) *Mutation Operation.* Reduce or magnify the error between arbitrary two vector individuals and add it to the third vector, in order to produce new variation

variable. For the $G + 1$ generation, the j th component of the i th variation vector is

$$V_{i,j}(G + 1) = x_{r1j}(G) + F \times (x_{r2j}(G) - x_{r3j}(G)), \quad (13)$$

where the suffixes $r1$, $r2$, $r3$ are random integral numbers and different, and F is scaling factor, which is used to adjust the step amplitude value of difference between vectors; the value is between 0 and 2.

- (3) *Crossing Operation*. Cross the objective vector $x_i(G)$ with variation vector $v_i(G + 1)$, produce new sample vector $u_i(G + 1)$, the j th component is expressed as:

$$u_{ij}(G + 1) = \begin{cases} v_{ij}(G + 1), & r_j \leq CR \\ x_{ij}(G), & r_j > CR, \end{cases} \quad j = rn_i, \quad (14)$$

where $r_j \in [0, 1]$ is the random corresponding to the j th component of vector, and $CR \in [0, 1]$ is crossing probability constant. rn_i is random integral number selected from $1, 2, \dots, D$, which ensuring at least one component of $v_i(G + 1)$ is used by $u_i(G + 1)$.

- (4) *Selection*. Taking the sample vector as parameters of LSSVM, train LSSVM model by learning samples and forecast the test samples with the trained LSSVM model and take the maximal forecast error as the fitness value of difference evolution. Compare sample vector $u_i(G + 1)$ with objective vector $x_i(G)$, if $u_i(G + 1)$ is responding to smaller objective function value, select $u_i(G + 1)$, on the contrary, if $x_i(G)$ is responding to smaller objective function value, keep $x_i(G)$.
- (5) *Cyclic Iteration*. Repeat the computation from (2) to (4), until i has circulated from 1 to N_p , and j has circulated from 1 to n ; that is, one iteration of population has been finished. Circularly computing until the iteration number reaches the maximal step number or fitness value is less than the setting value, and the iteration is ended. Output the SVM parameters which is responding to the optimal LSSVM model expressing the data samples.

2.4. Tunnel Construction Optimization Objective Functions and Solving Procedure. The construction optimization procedure includes rock parameters identification and anchoring parameters optimization. For rock parameters identification: select a group of surrounding rock parameters and compute the surrounding rock displacements by the above trained LSSVM model, which compares with monitoring displacement data, until the error between computing and monitoring is minor enough, and the corresponding parameters are identified results. The LSSVM model is used to express the relation between surrounding rock parameters and monitoring displacements. For rock parameters identification, the constrained optimization problem is expressed by the following formula:

$$\begin{aligned} \min \quad & \frac{1}{m} \sum_{i=1}^m (|LSSVM_i(X) - Y_i^0|) \\ \text{s.t.} \quad & X \in [X_l, X_u], \end{aligned} \quad (15)$$

where Y_i^0 is the observed value of surrounding rock, and $LSSVM_i$ is the LSSVM forecast surrounding rock displacement corresponding to observation point i . m is the number of observation points, x_i is the i th parameter, n is the number of parameters, and X_l and X_u are, respectively, the lower and upper boundary of the solution vector.

For anchoring parameters optimization mainly based on the surrounding rock mechanics parameters identification, LSSVM model is also used to express the relation between anchoring parameters and surrounding rock displacements. The optimization function is as follows:

$$\begin{aligned} \min \quad & \text{Cost}(M) \\ \text{s.t.} \quad & LSSVM_j(M) < Y_{j\max}, \end{aligned} \quad (16)$$

where $LSSVM_j$ is the displacement forecast of surrounding rock control point j corresponding to anchoring parameter M . $Y_{j\max}$ is the limit displacement corresponding to surrounding rock control point j . $\text{Cost}(M)$ is the supporting cost corresponding to the anchoring parameter M . The LSSVM models in (15) and (16) were gotten by (9) and (10). And the objective functions are all solved by DE as follows.

- (1) According to prior surveying and design information, respectively, assure the value scope of back analyzed rock mechanics parameter and anchoring parameter and construct calculation schemes by orthogonal test and uniformity test theory.
- (2) Construct three dimensional numerical model and calculate. Carry out numerical simulation for each parameters combination and obtain monitoring information of key points corresponding to each parameters combination, which becomes a learning sample.
- (3) Search the optimal support vector machine parameters by difference evolution.
- (4) Adopting the optimized parameters and training the support vector machine with the above learning samples, obtain the DE-LSSVM nonlinear model mapping the relation between mechanics parameters (or anchoring parameters) and rock displacements.
- (5) Substitute the above nonlinear mapping model and monitoring displacement in the objective function of (15). Search the identification parameters by difference evolution algorithm.
- (6) Based on the identified parameters, take anchoring parameters as variables, repeat (2)–(4), and take formula (16) as objective function, optimized anchoring parameters by DE again. The feedback analysis process of tunnel construction based on DE-LSSVM is shown in Figure 2.

3. Engineering Application

3.1. Engineering Introduction. Applied the method to Dalian Metro 1# line tunnel engineering, and studied the running tunnel from Xueyuan Square to Dalian Maritime University.

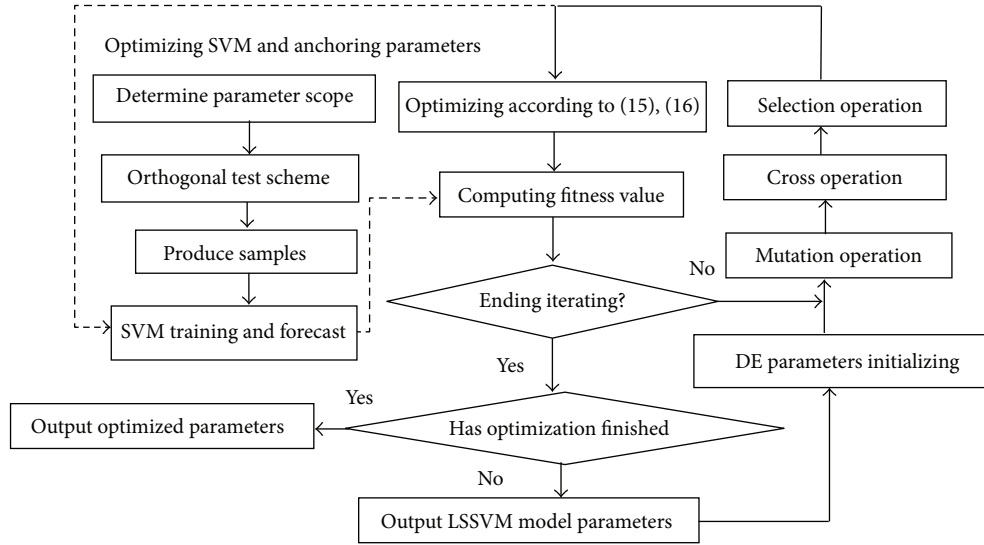


FIGURE 2: Tunnel construction optimization solving procedure based on DE-LSSVM.

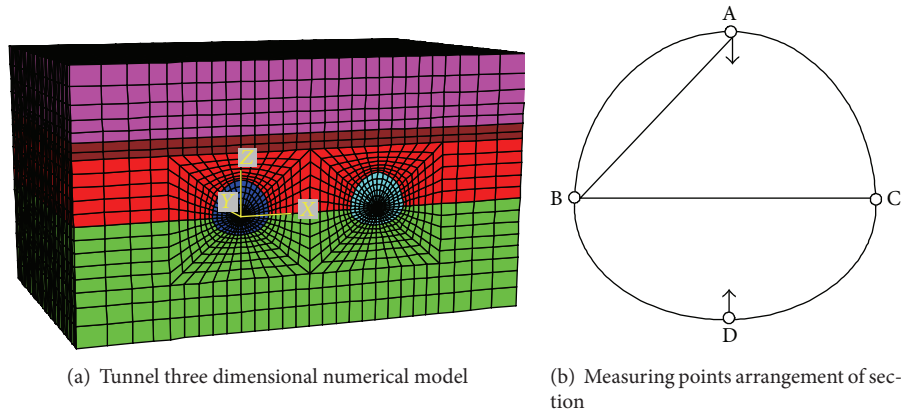


FIGURE 3: The three dimensional numerical model and monitoring section.

The geological strata are, respectively, artificial accumulation horizon of quaternary Holocene Series (Q_4^{ml}), quaternary Alluvium and Diluvium (Q_4^{al+pl}), and Changlinzi group slate of Sinian system (Zwhc). The tunnel belongs to super shallow buried tunnel and the distance from arc top to surface is 12 meters and the surrounding rock is IV class. According to the original design scheme, the tunnel has the width of 5.6 m, height of 6 m and adopts system grouted bolts. The bolt has length of 3.0 m, diameter of 22 mm, and space of 1 m; the thickness of shotcrete layer is 30 cm. It adopts benching tunneling construction method. The study region is from AK19 + 288 to AK19 + 318 of the mileage and there are two different strata slates with different weathering degree surrounding the tunnel.

The three dimensional numerical model is constructed and the model adopts artesian coordinate system and has 71859 nodes and 70000 elements, and the calculation scope is 45.8 m \times 30 m \times 29.8 m. The x direction is vertical to the main tunnel axis, z direction is vertical, and y direction is

along the main tunnel axis. The bolts are simulated by cable elements and shotcrete layer is simulated by shell elements. The null model is adopted for excavation and Mohr-Coulomb yield criterion is used for plastic damage. The model is shown in Figure 3(a). In the construction process, the typical monitoring section is shown in Figure 3(b). The convergence lines of AB and BC, and the sedimentation of A and rising of D should be monitored.

3.2. Rock Mechanics Parameters Identification. According to prior explore and laboratory tests, the self-weight stress is adopted, $\sigma_x = k * \sigma_z$, σ_x is horizontal ground stress, and σ_z is vertical groundstress. k is side pressure coefficient; the surrounding rock parameters are Young's modulus and Poisson ratio. The scope of rock mechanics parameters are Young's modulus of serious weathered slate E_1 that adopts 20~100 MPa, Poisson ratio of serious weathered slate μ_1 that adopts 0.27~0.35, and Young's modulus of middle weathered

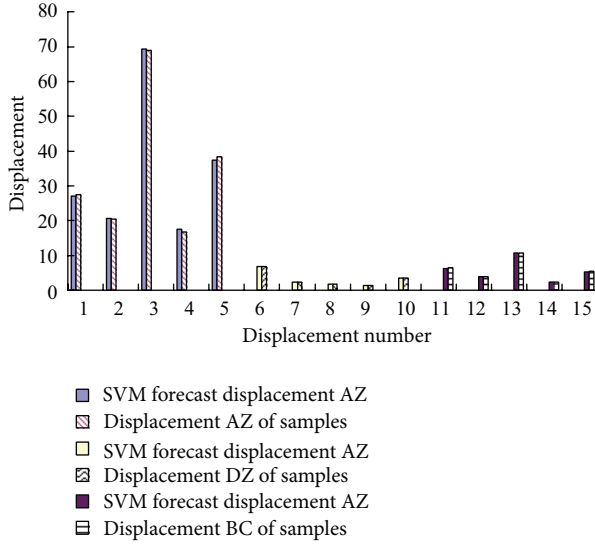


FIGURE 4: The forecast effect test of LSSVM ($C = 23.5$, $\delta = 56$).

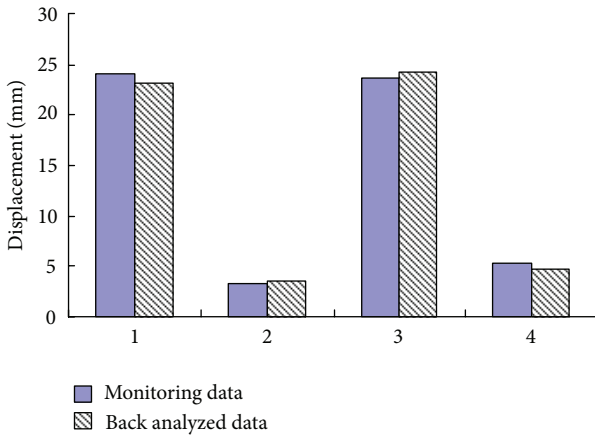


FIGURE 5: Optimized calculation and monitoring displacement.

slate E_2 that adopts 0.2~1 GPa, Poisson ratio of middle weathered slate u_2 that adopts 0.23~0.31. The monitoring indices are arc top sedimentation AZ, the rising of bottom DZ, and the convergence displacements of AB and BC. Selected orthogonal design table of $L_{25}(5^6)$ and uniform design table of $U_5 * (5^4)$ for E_1 , u_1 , E_2 , and u_2 between parameters scope, which construct 25 orthogonal schemes and 5 uniform schemes, carried out numerical simulation and obtained 25 learning samples and 5 test samples. The learning samples are shown in Table 1. Through the DE-LSSVM calculation as 2.3, the LSSVM has been trained by inputting samples, and the nonlinear mapping models between surrounding rock parameters and monitoring displacements are obtained. Figure 4 shows the forecast error of LSSVM model for the test samples, and it can be found that the error is minor and

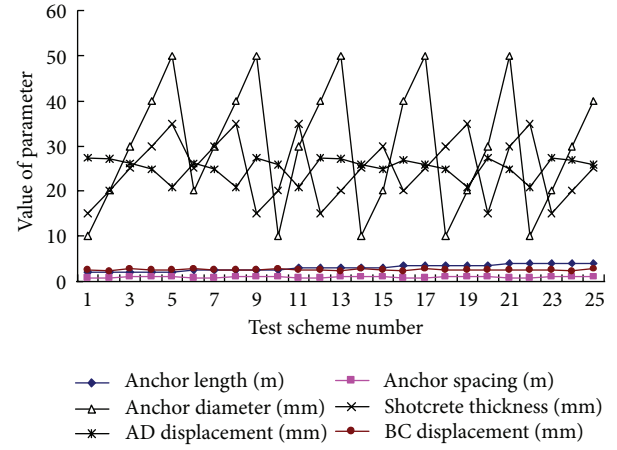


FIGURE 6: The parameters and displacements of orthogonal schemes.

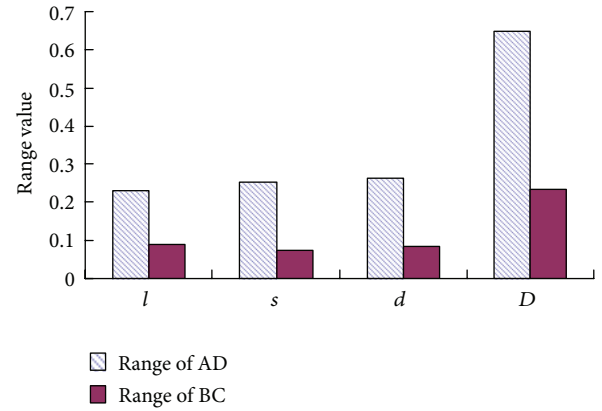
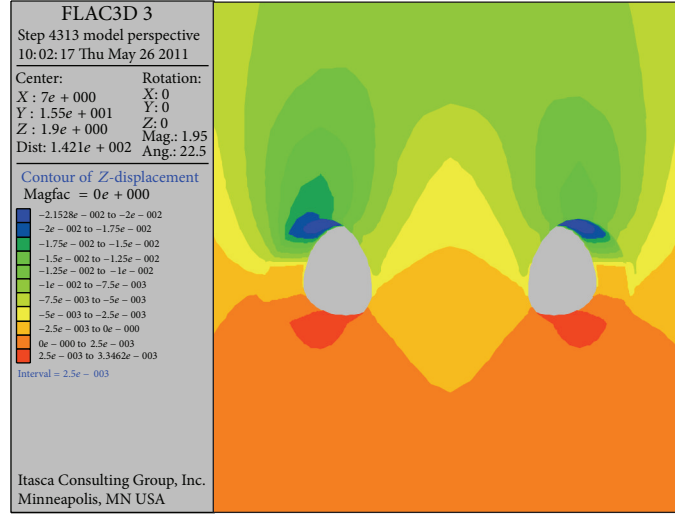


FIGURE 7: The sensibility analysis of anchoring parameters.

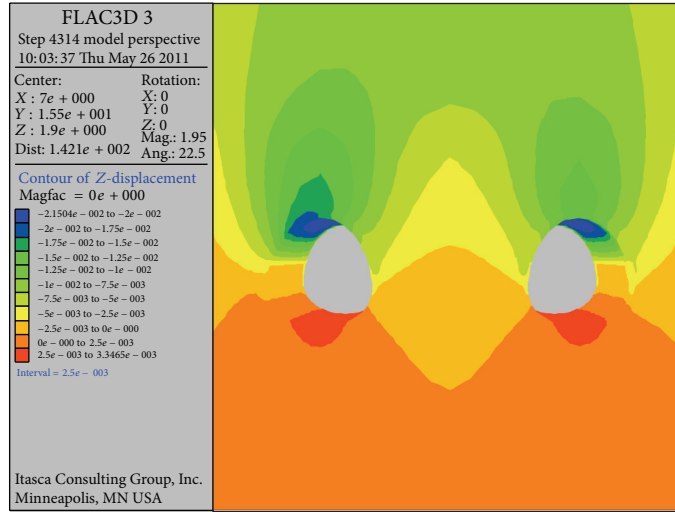
the trained LSSVM model can reflect the relation between mechanics parameters and displacements well.

The monitored displacements are as follows: AZ is 24.0 mm, DZ is 3.2 mm, AB is 23.6 mm, and BC is 5.4 mm. Substitute the monitored data to formula (15), using above trained LSSVM model, which identified the surrounding rock mechanics parameters by DE arithmetic. It is shown from Figure 5 that the trained LSSVM model has well forecast ability. The DE original parameters are set as follows. The number of optimal variables is 4, the population scale is 20, and the iteration number is 500. While the DE curve converges, the corresponding optimal mechanics parameters E_1 , E_2 , u_1 , and u_2 are 58.6 MPa, 347 MPa, 0.31, and 0.27, respectively.

In order to verify the rationality of the identified parameters, which inputted the identified parameters to the three dimensional numerical model and carried out calculation with finite difference method, the comparison between calculated results and monitoring data is shown in Figure 5. The maximal relative error between feedback calculated value and monitoring data is only 9.375%, and the maximal absolute error is 0.90 mm; therefore, the accuracy is satisfied.



(a) The original scheme



(b) The optimized scheme

FIGURE 8: The Z-displacement contour comparison between original and optimized schemes.

3.3. Anchoring Parameters Optimization. Cable and shotcrete layer are main reinforcement measures for controlling the surrounding rock stability of the tunnel. Based on the identified rock mechanics parameters of surrounding rock, the anchoring parameters should be optimized according to formula (16). The parameters to be optimized in this study are cable length l with the range of 2.0~4.0 m, cable diameter d with the range of 10~50 mm, cable space s with the range of 0.7~1.1 m, and shotcrete thickness D with the range of 15~35 cm. According to the orthogonal design table of $L_{25}(5^6)$ and the uniform design table of $U5 * (5^4)$, which arrange numerical test, take calculation results of 25 orthogonal schemes as learning samples and take calculation results of 5 uniform schemes as test samples.

Calculated above supporting schemes using the constructed three dimensional numerical model, and used the displacements of AD and BC as surrounding rock stability

indices. The anchoring parameters combination and the corresponding displacements of AD and BC are shown in Figure 6. Based on the above calculation results, the parameters were studied by the range analysis, and the sensibility of the anchoring parameters is shown by Figure 7. It is shown from Figure 7 that the sequence of the parameters sensibility affecting surrounding rock displacements AD and BC are D, l, d , and s in turn.

Set the optimized variables as $M = \{m_1, m_2, m_3, m_4\}$, the length of cable is m_1 , the space of cables is m_2 , the diameter of cable is m_3 , and the thickness of shotcrete is m_4 . The optimization objective is the minimal supporting cost according to the stability condition that is, displacement condition, just expressed as formula (16). The nonlinear relation of LSSVM_j between anchoring parameters and surrounding rock displacements has been trained by orthogonal schemes dataset. The relation between anchoring parameters and cost

can be pressed by experience calculation formula. Considering the safety demand set the limit displacement of AD is 25 mm, and the limit displacement of BC is 2.6 mm. Using DE arithmetic to optimize the anchoring parameters, set the original parameters as follows: the number of optimization variables is 4, the population scale is 20, and the iteration number is 500.

Run the DE-LSSVM optimization program, while the curve has converged; the optimal anchoring parameters are obtained. The optimized scheme, original design scheme, and part of the orthogonal schemes are all listed in Table 2.

The optimized supporting parameters are anchor length of 2.3 m, anchors space of 0.97 m, anchor diameter of 19 mm, and shotcrete thickness of 30 cm. The corresponding supporting cost is 10482.61 Yuan each running meter and economized 1382.76 Yuan each running meter. For the interval tunnel is about 1000 meters, the saved cost is about 1382760 Yuan. Input the optimized supporting parameters into the numerical model and carried out the simulation. Figure 8 is The Z-displacement contour comparison between original and optimized schemes. There are minor difference between the Z displacements of the two schemes, that means that the optimized scheme also ensures the tunnel stability well.

4. Discussion

4.1. Kernel Parameters Affecting LSSVM Model. Reflecting relation between rock mechanics parameters (or anchoring parameters) and surrounding rock displacements is a key problem affecting the optimization result. In the above optimisation process, the kernel parameter σ and the penal coefficient c are important factors that affect the generational performance of LSSVM. The effects of LSSVM parameters on the forecast result are shown in Figure 9.

The xy coordinates in Figure 9 are, respectively, the kernel parameter, σ and the penal factor, c , and the z coordinate is relative forecast error. For values of c below 20, the magnitude of the forecast error approaches 0.2; when c increases to more than 20, the corresponding forecast error is reduced to 0.05, while c increases to more than 30, the corresponding forecast error has increased more than 0.2. When σ is less than 40 and more than 60, the magnitude of the corresponding forecast errors are 0.2 and 0.1, respectively. And when σ is about 56, the corresponding forecast error is reduced to 0.047. Variations in the penal factor, c , and the kernel parameter, σ , will change the LSSVM forecast error, which shows that it is imperative to select proper parameters to guarantee the forecast performance. Because LSSVM does not have a method for selecting these parameters, optimizing parameters through DE arithmetic can avoid blind parameter selection. Therefore, the proposed DE-LSSVM method has high computing efficiency for LSSVM parameter selection.

4.2. DE Optimization Convergence Property. Compare the proposed optimization method with that of literature 17, firstly, three dimensional numerical model has been used to simulate tunnel, which can fully reflect the space effect of tunnel heading face, overcoming the shortage of two dimensional

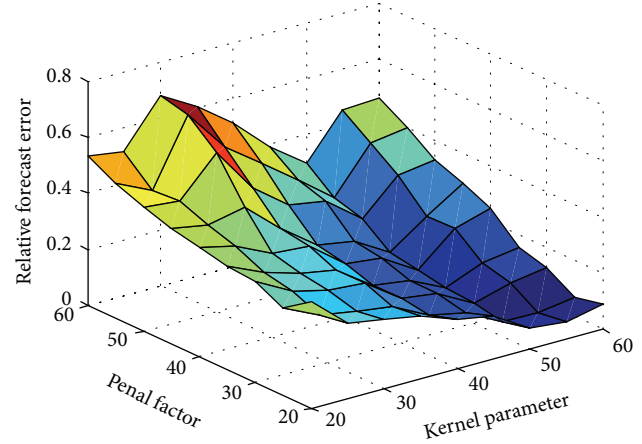


FIGURE 9: The forecast relative error changing according to C and σ .

model. Secondly, in this study the parameters of shotcrete thickness and cables have been synthetically optimized using surrounding rock displacements as constraint conditions and economic indices as objective function, which is more reasonable than only considering the shotcrete parameter and displacement controlling. Finally, the DE algorithm is selected replacing the PSO algorithm in this study.

In the optimization process of DE, different scaling factor F and crossing probability constant CR will affect the arithmetic converging property. For the examples of identifying surrounding rock mechanics parameters above, while F equates 0.8, CR changes from 0.5 to 0.9, and the corresponding converging curves are shown in Figure 10.

It is shown that while CR equates 0.5, the converging property is optimal; it has converged at about 100 step. Next CR adopted 0.7, 0.9, and 0.6 in order. It converges slowly while CR equates 0.8, and the corresponding converging step is 120. As a whole, the curves of different parameters can converge quickly and the searching property of DE arithmetic is good. While DE curve converges, the corresponding solution is the optimized parameters.

Figure 11 shows the converging curves of DE, PSO, and improved PSO (IPSO) in the optimizing process of identifying surrounding rock mechanics parameters. It is shown that for the optimizing case the converging property of the DE is better than normal PSO and IPSO. Because the DE arithmetic has more strict math theory background than PSO, it has better converging speed and optimizing property. Totally, it is observed that the proposed optimizing technique has more advantages than the former techniques.

5. Conclusion

The study presented a nonlinear optimization technique of tunnel construction based on DE, LSSVM, and three dimensional numerical simulation. This method can be divided into two main sections: feedback analysis of the surrounding rock mechanical parameters and optimisation of support parameters. The method only took use of scheme

TABLE 1: Orthogonal scheme and calculated displacements.

Factor	E_1 (MPa)	u_1	E_2 (GPa)	u_2	AZ (mm)	DZ (mm)	AB (mm)	BC (mm)
1	20	0.27	0.2	0.23	70.05	7.137	67.78	10.795
2	20	0.29	0.4	0.25	69.50	3.541	66.74	10.050
3	20	0.31	0.6	0.27	69.18	2.341	66.13	10.230
4	20	0.33	0.8	0.29	68.91	1.740	65.54	10.806
5	20	0.35	1.0	0.31	68.65	1.377	64.92	11.537
6	40	0.27	0.4	0.27	38.30	3.498	36.94	5.596
7	40	0.29	0.6	0.29	38.07	2.312	36.52	5.503
8	40	0.31	0.8	0.31	37.91	1.715	36.22	5.614
9	40	0.33	1.0	0.23	37.72	1.408	36.00	5.675
10	40	0.35	0.2	0.25	38.48	6.985	36.73	8.816
11	60	0.27	0.6	0.31	26.73	2.288	25.75	3.839
12	60	0.29	0.8	0.23	26.55	1.763	25.48	3.641
13	60	0.31	1.0	0.25	26.45	1.398	25.27	3.785
14	60	0.33	0.2	0.27	27.30	6.941	26.23	6.554
15	60	0.35	0.4	0.29	26.68	3.438	25.36	5.531
16	80	0.27	0.8	0.25	20.58	1.752	19.83	2.745
17	80	0.29	1.0	0.27	20.49	1.390	19.66	2.836
18	80	0.31	0.2	0.29	21.43	6.898	20.71	5.392
19	80	0.33	0.4	0.31	20.79	3.412	19.85	4.382
20	80	0.35	0.6	0.23	20.47	2.333	19.44	3.832
21	100	0.27	1.0	0.29	16.79	1.381	16.17	2.261
22	100	0.29	0.2	0.31	17.79	6.846	17.28	4.763
23	100	0.31	0.4	0.23	17.05	3.508	16.36	3.295
24	100	0.33	0.6	0.25	16.82	2.321	16.04	3.122
25	100	0.35	0.8	0.27	16.67	1.726	15.83	3.095

TABLE 2: The results of optimization compared with original and orthogonal schemes.

	Anchor length (m)	Anchors space (m)	Anchor diameter (mm)	Shotcrete thickness (cm)	AD (mm)	BC (mm)	Supporting cost (Yuan)
Optimized value	2.3	0.97	19	30	24.83	2.53	10482.61
Original scheme	3.0	1.0	22	30	24.80	2.52	11865.37
Scheme 4	2.0	1.0	40	30	24.83	2.53	26063.87
Scheme 8	2.5	0.9	40	35	20.89	2.59	35783.16
Scheme 19	3.5	1.0	20	35	20.86	2.58	14684.19

samples calculated by three dimensional numerical simulation; it employs LSSVM with optimal architecture trained by the difference evolution arithmetic, instead of the time-consuming finite element analysis, overcoming the shortages of expending too much time and easily being limited in local optimization solution of conventional back analysis method.

The three dimensional numerical model was used to simulate tunnel, which can fully reflect the space effect of tunnel heading face, overcoming the shortage of two dimensional model. Representative samples for LSSVM training and factor sensitivity analysis were given by the orthogonal experimental design method, which efficiently reduced the number of numerical simulations. The LSSVM method was based on statistical learning theory and made use of

the principle of structural risk minimization, overcoming empirical risk minimization of conventional statistic learning method (such as artificial neural network) and improving the generalizing ability for limited learning samples.

This study provided a real time, quantitative and powerful means to inform construction activities and can adjust construction schemes dynamically. Because LSSVM does not have a method for selecting these parameters, optimizing LSSVM parameters through DE arithmetic can avoid blind parameter selection. The parameters of lining and cables were synthetically optimized using surrounding rock displacements as constraint conditions and economic indices as objective function, which was more reasonable than former methods. DE converged quickly and had good

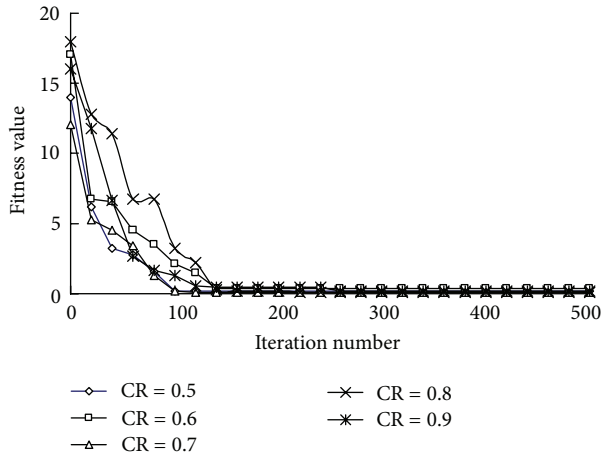
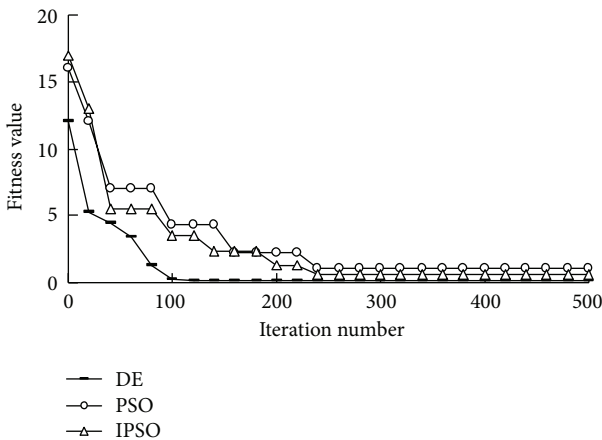
FIGURE 10: The DE converging curve ($F = 0.8$).

FIGURE 11: The converging curves of different algorithms.

global optimization characters, guaranteeing the rationality of the parameters identification and anchoring parameters optimization. The case study demonstrated that the displacements predicted by the identified parameters were in good agreement with field measurements and that the obtained supporting parameters were an acceptable control for achieving the stability and economic objective.

Acknowledgments

The authors deeply appreciate support from Fundamental Research Funds for the Central Universities (2011JC012, 2012TD015), National Natural Science Foundation (51079010), and National "Twelfth Five-Year" Plan for Science and Technology Support (2012BAJ17B01, 2012BAJ17B02).

References

- [1] S. Sakurai and K. Takeuchi, "Back analysis of measured displacements of tunnels," *Rock Mechanics and Rock Engineering*, vol. 16, no. 3, pp. 173–180, 1983.
- [2] H. Mashimo, "State of the road tunnel safety technology in Japan," *Tunnelling and Underground Space Technology*, vol. 17, no. 2, pp. 145–152, 2002.
- [3] S. H. Li, *New Theory of Tunnel Supporting: The Application and Theory of Typical Similar Supporting Design*, China Science Press, Beijing, China, 1999.
- [4] W. S. Zhu and M. C. He, *Surrounding Rock Stability of Complex Condition and Rock Mass Dynamic Construction Mechanics*, China Science Press, Beijing, China, 1995.
- [5] B. J. Arends, S. N. Jonkman, J. K. Vrijling, and P. H. A. J. M. van Gelder, "Evaluation of tunnel safety: towards an economic safety optimum," *Reliability Engineering and System Safety*, vol. 90, no. 2-3, pp. 217–228, 2005.
- [6] J. Pérez-Romero, C. S. Oteo, and P. de la Fuente, "Design and optimisation of the lining of a tunnel in the presence of expansive clay levels," *Tunnelling and Underground Space Technology*, vol. 22, no. 1, pp. 10–22, 2007.
- [7] Y. G. Tang and G. T. C. Kung, "Application of nonlinear optimization technique to back analyses of deep excavation," *Computers and Geotechnics*, vol. 36, no. 1-2, pp. 276–290, 2009.
- [8] Y. M. A. Hashash, S. Levasseur, A. Osouli, R. Finno, and Y. Malecot, "Comparison of two inverse analysis techniques for learning deep excavation response," *Computers and Geotechnics*, vol. 37, no. 3, pp. 323–333, 2010.
- [9] S. C. Lim, C. H. Eab, K. H. Mak, M. Li, and S. Y. Chen, "Solving linear coupled fractional differential equations by direct operational method and some applications," *Mathematical Problems in Engineering*, vol. 2012, Article ID 653939, 28 pages, 2012.
- [10] H. L. Liu, P. Li, and J. Y. Liu, "Numerical investigation of underlying tunnel heave during a new tunnel construction," *Tunnelling and Underground Space Technology*, vol. 26, no. 2, pp. 276–283, 2011.
- [11] F. S. Zhang, X. X. Xie, and H. W. Huang, "Application of ground penetrating radar in grouting evaluation for shield tunnel construction," *Tunnelling and Underground Space Technology*, vol. 25, no. 2, pp. 99–107, 2010.
- [12] Y. Xu, X. Y. Chen, and Q. H. Li, "INS/WSN-integrated navigation utilizing LSSVM and H_∞ filtering," *Mathematical Problems in Engineering*, vol. 2012, Article ID 707326, 19 pages, 2012.
- [13] P. Z. Lu, S. C. Chen, and Y. J. Zheng, "Artificial intelligence in civil engineering," *Mathematical Problems in Engineering*, vol. 2012, Article ID 145974, 22 pages, 2012.
- [14] C. Carlo, S. Y. Chen, and A. Gani, "Information and modeling in complexity," *Mathematical Problems in Engineering*, vol. 2012, Article ID 868413, 4 pages, 2012.
- [15] X. T. Feng, Z. Zhang, and Q. Sheng, "Estimating mechanical rock mass parameters relating to the Three Gorges Project permanent shiplock using an intelligent displacement back analysis method," *International Journal of Rock Mechanics and Mining Sciences*, vol. 37, no. 7, pp. 1039–1054, 2000.
- [16] A. N. Jiang, "Forecasting nonlinear time series of surrounding rock deformations of underground cavern based on PSO-SVM," *Rock and Soil Mechanics*, vol. 28, no. 6, pp. 1176–1180, 2007 (Chinese).
- [17] A. N. Jiang, S. Y. Wang, and S. L. Tang, "Feedback analysis of tunnel construction using a hybrid arithmetic based on Support Vector Machine and Particle Swarm Optimisation," *Automation in Construction*, vol. 20, no. 4, pp. 482–489, 2011.
- [18] V. N. Vapnik, *The Nature of Statistical Learning Theory*, Springer, New York, NY, USA, 1995.

- [19] J. A. K. Suykens, T. van Gestel, and J. de Brabanter, *Least Squares Support Vector Machines*, World Scientific, Singapore, 2002.
- [20] J. A. K. Suykens and J. Vandewalle, "Least squares support vector machine classifiers," *Neural Processing Letters*, vol. 9, no. 3, pp. 293–300, 1999.
- [21] R. Storn and K. Price, "Differential evolution," 2008, <http://www1.icsi.berkeley.edu/~storn/code.html>.
- [22] A. W. Mohamed, H. Z. Sabry, and M. Khorshid, "An alternative differential evolution algorithm for global optimization," *Journal of Advanced Research*, vol. 3, no. 2, pp. 149–165, 2012.
- [23] J. Ilonen, J. K. Kamarainen, and J. Lampinen, "Differential evolution training algorithm for feed-forward neural networks," *Neural Processing Letters*, vol. 17, no. 1, pp. 93–105, 2003.

Research Article

Settlement Analysis of a Confined Sand Aquifer Overlain by a Clay Layer due to Single Well Pumping

Wen-jie Niu,¹ Zhenyu Wang,² Feng Chen,² and Hongran Li³

¹ College of Mechanics and Engineering Department, Liaoning Technical University, Fuxin, Liaoning 123000, China

² College of Civil Engineering and Architecture, Zhejiang University, Hangzhou, Zhejiang 310058, China

³ Shanghai Geotechnical Investigations & Design Institute Co., Ltd., Shanghai 200031, China

Correspondence should be addressed to Zhenyu Wang; wzyu@zju.edu.cn

Received 21 November 2012; Revised 16 January 2013; Accepted 17 January 2013

Academic Editor: Fei Kang

Copyright © 2013 Wen-jie Niu et al. This is an open access article distributed under the Creative Commons Attribution License, which permits unrestricted use, distribution, and reproduction in any medium, provided the original work is properly cited.

This paper proposes a simplified analytical solution to determine the primary consolidation settlement of a confined sand aquifer overlain by a clay layer due to single well dewatering. After single well pumping in a steady state, the Dupuit equation predicts the confined sand aquifer water head drawdown. The confining pressure on the underlain confined sand aquifer top surface is determined using the principle of vertical force equilibrium. Additional vertical stresses in each layer of the confined sand aquifer are then computed with the Boussinesq solution. The overall aquifer consolidation deformation is then determined with the e - $\lg p$ curve from the one-dimensional consolidation test and the applied vertical stress with the integral method. The proposed analytical solution is validated using the ADINA software, where porous media are simulated with the Biot model and solved with the 3D finite element method. This proposed analytical solution is used to simulate the primary consolidation settlement due to well pumping, using the fourth confined aquifer in the Pudong New Area of Shanghai from 1980 to 1995 as a case study. The predicted settlement compares reasonably well with the actual measured settlement in Shanghai.

1. Introduction

With ever-increasing groundwater demands for domestic and industrial uses, loss of land due to well pumping has become a disastrous phenomenon in many cities worldwide [1, 2]. The consequences of well pumping include damage to underground utility lines, seawater intrusion, destabilisation of existing infrastructure, and ground fractures. Therefore, land subsidence by well pumping is a worldwide problematic issue that must be promptly addressed [3–7].

As a generalisation, land subsidence induced by well pumping is explained by groundwater flow and subsidence models [5, 8]. Previous subsidence research was concerned mainly with the compression of clay layers. Most models have represented compaction by incorporating Terzaghi's one-dimensional compaction principle into the groundwater flow equation [9–12]. However, because Terzaghi's one-dimensional compaction principle is valid only for a one-dimensional compaction case and was originally concerned with the dissipation of pore water pressure, the Biot theory

remains the only suitable fully coupled land subsidence model [13, 14]. Various aspects of compaction, such as stress-dependent storage properties, dependence of hydraulic conductivity on compaction [15], and the effects of moving water tables [16], may also be included in Terzaghi's model or the Biot model.

However, the extraction of a sand aquifer water could also give rise to land subsidence. For example, since the 1980s, the fourth confined aquifer of Shanghai city has been the main confined aquifer for groundwater extraction and has contributed greatly to the total subsidence of Shanghai. In predicting the settlement of a sand aquifer, the fully coupled Biot model, while appropriate, is inconvenient to use and may not be the best choice because of its many parameters and reliance on advanced software for computation. Moreover, applying Terzaghi's 1D compaction principle to a sand aquifer is meaningless because the sand aquifer consolidates instantaneously and Terzaghi's 1D compaction principle is suitable only for low permeability soils (e.g., clay).

For a confined sand aquifer overlain and confined by an impermeable clay layer, seepage of groundwater forms a depression cone when groundwater is pumped from a well [17]. The vertical hydraulic pressure in the confined sand aquifer against the bottom of the upper confining layer decreases during pumping. Increases in intergranular pressure among sand particles in confined sand aquifers are generated due to the pressure from the overlain confining impermeable clay layer [18]. Compression of sand particles gives rise to confined aquifer compressive deformation and contributes to the total subsidence of all layers.

Corresponding research on settlement analysis of confined aquifers can be found in the following references. Sun et al. used the storativity, specific storage, and hydrological information to estimate the elastic and inelastic compaction of the soil layers due to fluid withdrawal with a series of equations [19]. Chen et al. proposed a three-dimensional numerical model that couples the groundwater flow and soil consolidation to investigate the mechanisms of ground settlement [20]. Roy and Robinson performed a series of in situ soil experiments to calibrate the prediction model and used computer program SEEP/W version 4.23 in the seepage analyses [21]. Li et al. used the statistical procedure and fractal concept to analyse land subsidence caused by groundwater exploitation in the Hangzhou-Jiaxing-Huzhou plain in China [22]. Shi et al. obtained groundwater level and subsidence monitoring data from 27 extensometer groups and more than 1,000 observation wells in the Shanghai area. The relationship between the deformation and the groundwater level was analysed [23]. Wu et al. developed a nonlinear coupled regional land subsidence model. The coupled model consists of a three-dimensional groundwater flow model and a one-dimensional vertical deformation model based on viscoelastoplastic constitutive laws, called the modified merchant model, and then is solved using a multiscale iterative finite element method. The calibrated and evaluated model is then used to assess the future evolution of land subsidence under two groundwater pumping scenarios [24]. Solutions to the above models of confined aquifers are either numerical solutions or statistical analyses of field monitoring data. A simple, cost-effective method for engineers to predict confined sand aquifer settlement by well pumping would indeed prove valuable, although such simplified formulations are not well illustrated in the literature [25].

This paper proposes an approximate analytical solution for land subsidence induced by the confined sand aquifer consolidation due to single well pumping. In the model, a confined sand aquifer is overlain by a low permeability clay layer, and the confined aquifer is pumped by a single well. The water head drawdown in the confined sand aquifer is predicted with the Dupuit equation. The confined sand aquifer consolidates transiently due to the pressure from the impermeable confining layer, and the primary consolidation settlement manifests immediately. The resultant effective stress increase in the confined sand aquifer due to the pressure from the upper impermeable confining layer is determined using the Boussinesq solution [26]. The primary consolidation settlement of the confined sand aquifer is determined using the e -lgp curve method [27]. The proposed

analytical solution is compared to the numerical result found via the ADINA software where the porous medium is simulated with the Biot model and solved with the 3D finite element method. The Shanghai fourth confined sand aquifer settlement induced by well pumping from 1980 to 1995 is reasonably well predicted with the proposed analytical solution.

2. Theory of the Analytical Solution for Predicting a Confined Aquifer Consolidation Settlement at a Single Well in a Steady Seepage State

The method is based on an assumption of steady state, axisymmetric drawdown around a single well. Water head drawdown is predicted with the Dupuit equation, and then the confining pressure on the confined aquifer is determined. Additional vertical stress in the confined aquifer is computed using a 2D Boussinesq expression in terms of radial and depth variables. The void ratio change under the vertical stress is determined with the e -lgp curve from a one-dimensional consolidation test. The vertical element's consolidation deformation is then determined from the void ratio change. The overall consolidation settlement of the confined aquifer is then determined with the integral method. Details are presented below.

2.1. 2D Seepage Analysis and Water Head Prediction of the Confined Aquifer. In theory, an area is dewatered by a single well. The single well penetrates through the upper confining clay layers into a confined sand aquifer with an impervious bottom layer. The water head drawdown of the confined sand aquifer is presented in Figure 1. Under these conditions, ground subsidence occurs. Before studying the subsidence, the water head in the confined sand aquifer in Figure 1 must first be determined. The model for studying the water head variation in the confined sand aquifer induced by single well dewatering is presented in Figure 2. For the confined aquifer in Figure 2, the radial flow to the pumped well is steady state [28]. The pumped district boundary is surrounded with potential sources of recharge water (e.g., a large lake, a river, or the sea) that remain at a constant level. A balance exists between the pumping water and the recharge water for the confined aquifer in Figure 2.

A systematic analysis of the water head is expressed in Figure 2. With the Dupuit-Forchheimer approximation, where the vertical resistance to flow is neglected, water head drawdown s at a point with horizontal distance r to the well is given as follows [29–31]:

$$s = H_0 - h = \frac{Q}{2\pi KM} \ln \frac{R}{r}, \quad (1)$$

where Q denotes the well discharge, K denotes the confined aquifer hydraulic conductivity, M denotes the saturated confined aquifer thickness, and R denotes the confined aquifer radius. If the model in Figure 2 cannot be found in the field, the Sichardt equation to determine the influence radius $R = 3000s_w \sqrt{K}$ can be used instead [28], where s_w denotes the water head drawdown at the well.

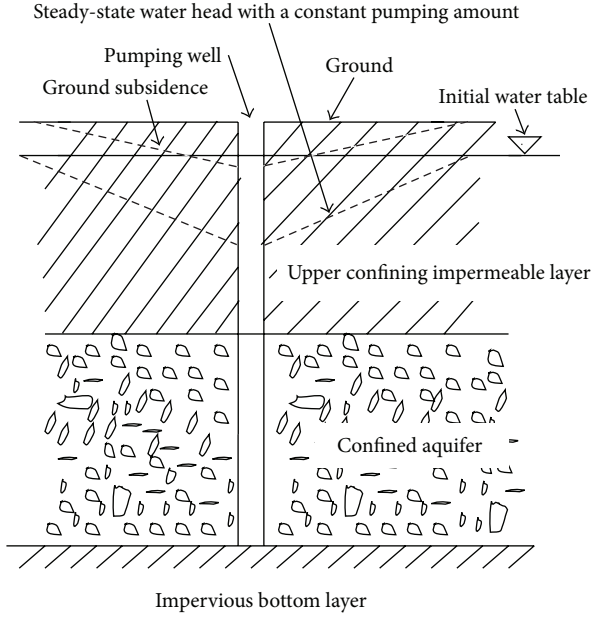


FIGURE 1: Dewatering in a confined sand aquifer overlain by a low permeability clay layer.

In Figure 2, the water head at distance r can also be derived as follows [29, 30]:

$$h - h_w = \frac{Q}{2\pi KM} \ln \frac{r}{r_w}, \quad (2)$$

where h_w denotes the water head at the well face and r_w denotes the well radius. Equation (2) can be transformed as follows:

$$s = H_0 - h_w - \frac{Q}{2\pi KM} \ln \frac{r}{r_w} = s_w - \frac{Q}{2\pi KM} \ln \frac{r}{r_w}. \quad (3)$$

In the remainder of this paper, the water head drawdown s in the confined aquifer is predicted with (1) because the hydraulic boundary is circular or could be assumed as circular with the assistance of the influence radius [32]. If the confined aquifer recharge water boundary geometry is complex, a 2D finite element program can be employed to study the water head drawdown due to well pumping [33].

2.2. Initial Effective Stress in the Confined Aquifer before Pumping. The initial confining pressure on the confined aquifer induced by the self-weight of the upper confining impermeable clay layer in Figure 2 is given as follows:

$$p_1 = D\gamma_1, \quad (4)$$

where D denotes the thickness of the confining layer and γ_1 denotes the confining layer impermeable clay unit weight. Figure 3 is a detailed presentation of Figure 2.

According to Karl von Terzaghi's Principle, if it is assumed that normal consolidation occurs in the confined aquifer before pumping in Figure 3 where Q is zero, the initial

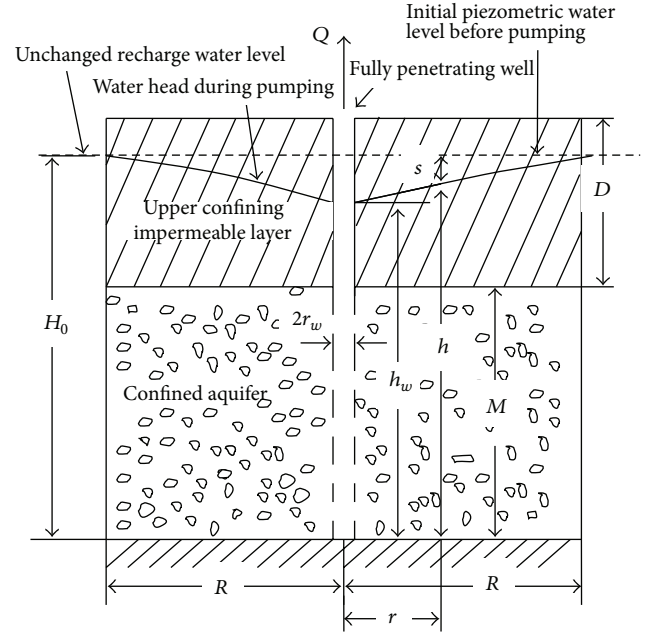


FIGURE 2: An idealised model for the determination of water head drawdown in a confined aquifer pumped by a well.

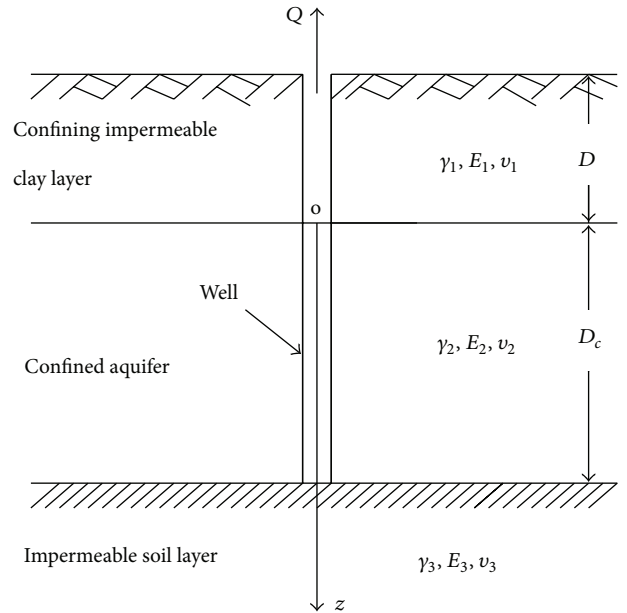


FIGURE 3: A simplified analysis scheme for the confined aquifer pumped by a well.

effective stress in the confined aquifer at a point of depth z is given by

$$p_0 = D\gamma_1 + z\gamma_2 - (H_0 - D_c + z)\rho_w g, \quad (5)$$

where D_c denotes the confined aquifer thickness, γ_2 denotes the confined aquifer sand unit weight in Figure 3, and z denotes the depth of the studied point in the confined aquifer, as shown in the z - r cylindrical coordinate system in Figure 4.

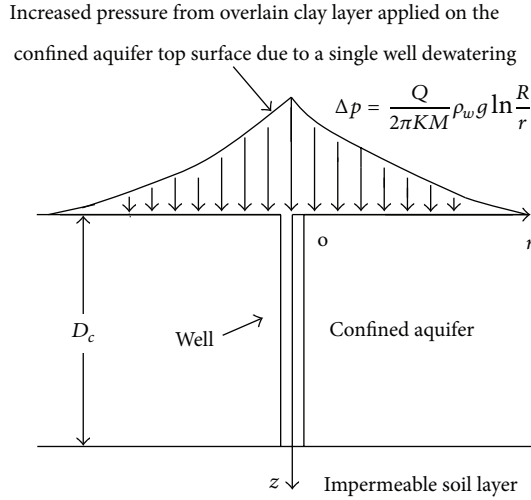


FIGURE 4: Increased pressures applied on the confined aquifer in a 2D view.

The origin o of the z - r cylindrical coordinate system in a single well is on the contact surface between the upper confining layer and the confined aquifer. Figure 4 is a detailed presentation of Figure 3.

2.3. Effective Stress Increase in the Confined Aquifer

2.3.1. Confining Pressure from the Overlying Layer on the Confined Aquifer Upper Surface Induced by Pumping. Because of water head drawdown, the upward hydraulic pressure against the bottom of the upper confining layer decreases, and the intergranular pressure increases [18]. According to the principle of vertical force equilibrium, the increased pressure applied on the confined aquifer top surface due to pumping in Figure 3 can be derived as follows:

$$\Delta p = s \rho_w g, \quad (6)$$

where ρ_w denotes the water density, s denotes the water head drawdown, and g denotes gravitational acceleration.

As mentioned in (1), the water head drawdown s can be predicted. By combining (1) and (6), the increased pressure applied on the confined aquifer top surface due to single well pumping can be derived as follows:

$$\Delta p = \frac{Q}{2\pi KM} \rho_w g \ln \frac{R}{r}. \quad (7)$$

Figures 4 and 5 demonstrate the applied pressure on the confined aquifer in 2D and 3D views, where A is defined as $(Q/2\pi KM)\rho_w g$.

2.3.2. Vertical Stress in the Confined Aquifer. For the sake of simplicity, it is assumed that primary consolidation in the confined aquifer occurs immediately after water head drawdown. The increased intergranular stress (also called the final effective stress increase) in the confined aquifer due to the single well pumping is equivalent to the additional

Increased pressure from overlain clay layer applied on the confined aquifer top surface due to a single well dewatering

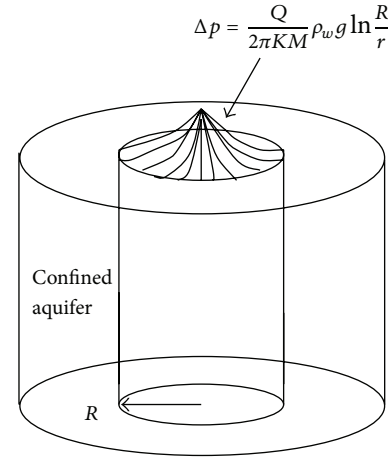


FIGURE 5: Increased pressures applied on the confined aquifer in a 3D view.

total stress acted on the soil particles (combination of soil skeleton and pore water), which can be determined with the Boussinesq solution if $E_2 = E_3$ and $\nu_2 = \nu_3$ in Figure 3.

The fundamental Boussinesq solution gives the vertical stress at point (z, r) in the z - r cylindrical coordinate system of Figure 4 as follows:

$$\sigma_z = \frac{3}{2\pi} \frac{1}{[1 + (r/z)^2]^{5/2}} \frac{p}{z^2}. \quad (8)$$

If the well radius is very small compared to the analysis region and can be assumed to be infinitely small for analysis simplification, with the external applied pressure on the confined aquifer top surface given in (7), the resultant vertical stress σ_{zr} at $r = 0$ at different depths z can be approximated via the integral method:

$$\sigma_{zr} = \int_{r_w}^R \frac{3A}{z^2} \frac{r \ln(R/r)}{[1 + (r/z)^2]^{5/2}} dr, \quad (9)$$

where $A = (Q/2\pi KM)\rho_w g$, as defined above. As discussed above, σ_{zr} is the additional total stress in the confined aquifer due to external applied pressure on the confined aquifer top surface given in (7) and is equal to the final effective stress increase.

2.4. Primary Consolidation Settlement Calculation Theories

2.4.1. Void Ratio Change and Intergranular Pressure. In the one-dimensional consolidation test, when the intergranular pressure increases from p_0 to $p_0 + \sigma_{zr}$, according to the e - $\lg p$ curve and the definition of the compression index C_c , the void ratio change Δe is calculated as follows [18]:

$$\Delta e = e_0 - e = C_c \lg \frac{p_0 + \sigma_{zr}}{p_0}, \quad (10)$$

where C_c is the compression index.

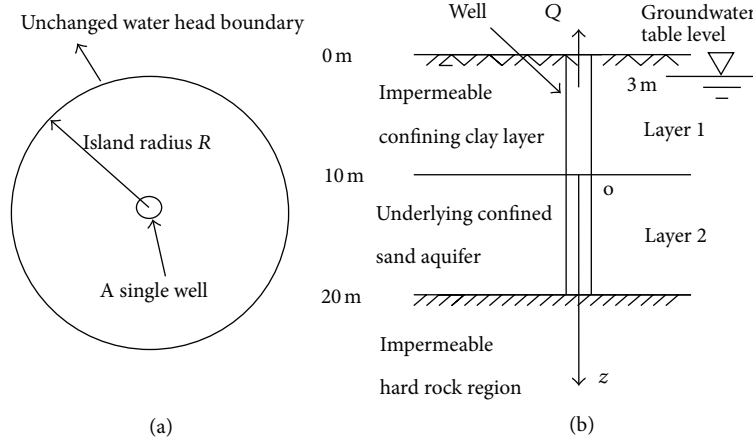


FIGURE 6: A single well pumping in an idealised island: (a) plan view; (b) sectional drawing.

2.4.2. Compacted Deformation in a Soil Layer with Thickness dz . In the one-dimensional consolidation test, the settlement $d\eta$ due to consolidation of a certain layer of thickness dz because of a reduction in the void ratio from e_0 to e , in conjunction with an effective stress increase from p_0 to $p_0 + \sigma_{zr}$, can be derived from the following expression [20, 34]:

$$d\eta = \frac{\Delta e}{1 + e_0} dz = C_c \frac{1}{1 + e_0} \lg \frac{p_0 + \sigma_{zr}}{p_0} dz. \quad (11)$$

2.4.3. Total Consolidation Settlement of the Confined Aquifer due to Single Well Pumping. The consolidation settlement of the confined sand aquifer at point $(0, 0)$ in the (r, z) coordinate system of Figure 4 is found from the summation of deformations in each layer of the confined aquifer with the integration method:

$$\eta = \int_0^{D_c} d\eta = \int_0^{D_c} C_c \frac{1}{1 + e_0(z)} \lg \frac{p_0 + \sigma_{zr}}{p_0} dz. \quad (12)$$

In the above equation, C_c is the compression index, and $e_0(z)$ is the initial void ratio at depth z in the midpoint of the $d\eta$ soil layer. Note that variable D_c in Figure 3 is M in Figure 2. Combine (5) and (9) and then (12) can be transformed as follows:

$$\eta = \int_0^{D_c} C_c \frac{1}{1 + e_0(z)} \lg \left[\left(D\gamma_1 + z\gamma_2 - (H_0 - D_c + z) \rho_w g \right. \right. \\ \left. \left. + \int_{r_w}^R \frac{3A}{z^2} \frac{r \ln(R/r)}{[1 + (r/z)^2]^{5/2}} dr \right) \right. \\ \left. \times (D\gamma_1 + z\gamma_2 - (H_0 - D_c + z) \times \rho_w g)^{-1} \right] dz. \quad (13)$$

The soil vertical compression strain at point $(0, z)$ derived from (11) is given as follows:

$$\varepsilon(0, z) = C_c \frac{1}{1 + e_0} \lg \left[\left(D\gamma_1 + z\gamma_2 - (H_0 - D_c + z) \rho_w g \right. \right. \\ \left. \left. + \int_{r_w}^R \frac{3A}{z^2} \frac{r \ln(R/r)}{[1 + (r/z)^2]^{5/2}} dr \right) \right. \\ \left. \times (D\gamma_1 + z\gamma_2 - (H_0 - D_c + z) \times \rho_w g)^{-1} \right]. \quad (14)$$

3. Validation of the Proposed Analytical Solution

3.1. An Example. The radius of the single well in the idealised island in Figure 6 is 0.3 metres. The island radius R as described in (1) is 100 metres. The overlying impermeable clay layer (layer 1) and confined sand aquifer (layer 2) are 10 metres each. The initial groundwater level is 17.0 metres as measured from the impermeable hard rock top surface. The soil properties in Figure 6 of the example are presented in Table 1. The compression index C_c of the confined sand aquifer is 0.13, while the initial void ratio e_0 is 0.6.

After an extensive period of single well pumping with pumping rate Q equal to approximately $0.00757 \text{ m}^3/\text{s}$, water flow is steady around the well, while the single well water level in Figure 6 decreases by 7 metres. The primary consolidation settlement at the single well due to well pumping in the confined sand aquifer is determined numerically and is presented analytically below.

TABLE 1: Material properties of the soil layers in the example of Figure 6.

Layer number	Average unit weight (kN/m ³)	Elastic modulus (MPa)	Poisson's ratio	Cohesive strength (kPa)	Angle of internal friction (°)	Horizontal hydraulic conductivity K_h (m/s)	Vertical hydraulic conductivity K_v (m/s)
1	18.0	20	0.3	15	16	3.0×10^{-9}	5.0×10^{-9}
2	20.0	40	0.22	2	31	1.0×10^{-4}	1.0×10^{-4}

3.2. Numerical Solution with ADINA

3.2.1. Numerical Model Computing Region. A square region with side lengths of 200 metres is analysed in the numerical model and shown in Figure 7. In the following numerical simulation with the model built within ADINA, the influence radius of the single well in the square region of Figure 7 is approximately 98.3 metres, which is quite similar to the island radius R in Figure 6. Therefore, the computational region selection of the square analysis region with side lengths of 200 metres in the numerical simulation produces negligible error regarding the settlement. In the ADINA computation process, the 20 metres depth soil layer in Figure 6(b) is divided into three layers as in Figure 7: the “waterless layer” (refers to the no water region) is 3.0 metres in depth, an “impermeable clay layer” is 7.0 metres in depth, and an “underlying confined sand aquifer layer” is 10.0 metres in depth.

The layers in Figure 7 are laterally constrained and are permeable in areas except for the rock bottom board. Neither displacements nor water flows at any direction are allowed at the rock bottom board. 3D element meshes of the porous media in the ADINA simulation process are generated and presented as in Figure 8.

3.2.2. Material Properties. The properties of the materials composing the “waterless” and “impermeable clay” layers in Figure 7 are all retrieved from the information on layer 1 in Table 1, with an exception that the “waterless” layer permeability is set as zero. The material properties of the “underlying confined sand” layer in Figure 7 are completely retrieved from the layer 2 information in Table 1.

The deformable continuous media material in the three soil layers as in Figure 7 is simulated with the Mohr-Coulomb model, which is based on linearly elastic and perfectly plastic yield behaviours. The yield function is defined by the Mohr-Coulomb criterion. The potential function is defined by the Drucker-Prager criterion. A piecewise tension cutoff analysis and a nonassociative flow rule are embedded in ADINA.

3.2.3. Computing Process with ADINA Software. The time step in the ADINA's computing is 0.1 day. The decrease of the water level in the single well totaled 7 metres, and the total computing time lasts for 108 days with 100 days for single well pumping and 8 days for stabilising the computed results. During pumping, the water level in the single well decreases by 0.07 metres per day.

3.2.4. Pore Pressures. Figure 9 gives the results of the excessive pore pressures around the well. From Figure 9, the maximum excessive pore pressure is 70000 Pa at the single well, which means that the water level of the single well in

the confined aquifer decreases by approximately 7 metres. At the end of the computation, the influence radius in the computing region is approximately 98.3 metres, which is very close to 100 metres. Therefore, ADINA reasonably simulated the problem as in Figure 6.

3.2.5. Settlements. From Figure 10 and the resulting files from the ADINA software, the maximum settlements in all three soil layers in Figure 7 occur at the contact point between the “waterless” and “impermeable clay” layers with negligible deformation in the “waterless” layer. The maximum settlement of the confined sand aquifer occurs at the top surface of the confined sand aquifer at the single well. Its value is 70.43 mm.

3.3. Proposed Analytical Solution. The proposed analytical solution mainly concerns the settlement of the confined sand aquifer (layer 2) in Figure 6 when water flow around the single well is steady, and the water level at the single well decreases by 7 metres. The total consolidated compressive deformation of layer 2 is determined with (14) using the parameters given in the example. The settlement results for different depth points in the confined aquifer at the single well are presented in Figure 11 for the analytical solution and ADINA. The maximum settlement of 76.8 mm in layer 2 at the single well in the top surface of layer 2 is similar to the 70.43 mm settlement calculated by ADINA. According to the detailed comparison between the proposed analytical solution and the numerical result obtained with the ADINA software in Figure 11, the settlements of layer 2 determined by the two methods are almost equal. Therefore, the proposed analytical solution is applicable under certain boundary conditions, as in the example in Figure 6. The excessive pore water pressures determined using ADINA and the proposed analytical solution are presented in Figure 12. It is obvious that they almost coincide with each other. The deformation of the impermeable clay layer (layer 1, which includes “waterless” and “impermeable clay” layers) in Figure 6 is not presented in the analytical solution.

4. Case Study

The settlement prediction of the fourth confined sand aquifer in Shanghai city is performed with the above-proposed analytical solution. The detailed process is as follows.

4.1. Study Area. As the country's most densely populated and developed area, Shanghai city encounters land subsidence problems due to well pumping. Many large residential districts and business firms are located in Shanghai, and there is an extensive groundwater exploitation in this area. When

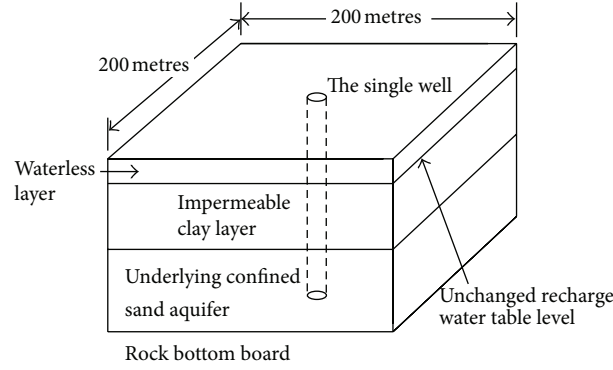


FIGURE 7: Analysis region in ADINA.

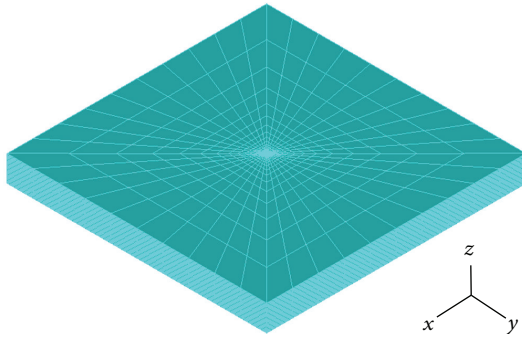


FIGURE 8: Mesh generation with ADINA.

groundwater is extracted at a constant rate in Pudong New Area of Shanghai, the study area can be recharged with water from the Huangpu River, Yellow Sea, and East China Sea, as shown in Figure 13. A balance can exist between the confined aquifer and the supply water system after some time for given pumping conditions (e.g., pumping rate, well radius, etc.).

A sectional drawing of the corresponding earth layer is shown in Figure 14(a). Before the 1980s, the Shanghai second and third confined sand aquifers were the main groundwater extraction layers [25]. Since the 1980s, the fourth confined aquifer has been the main confined aquifer for groundwater extraction. From 1980 to 1995, the fourth confined aquifer contributed a total settlement of approximately 30 mm to the total subsidence [24, 25].

Because the fourth confined aquifer is mainly composed of sand and has been the main confined aquifer for groundwater extraction since the 1980s, the fourth confined aquifer is isolated as the research layer, as shown in Figure 14(b). In the analytical solution, the earth layers (layers with a depth of less than 160 metres) above the roof of the fourth confined aquifer and the earth layers (layers with a depth greater than 240 metres) below the floor of the fourth confined aquifer are all equivalently transformed to impermeable layers in Figure 14(b).

The fourth confined sand aquifer, shown in Figure 14, is fully penetrated by a single well and generates consolidation settlement as a result of single well pumping. As water flows

TABLE 2: Upper confining clay layer parameters in the settlement simulation.

Earth layer name	Thickness D (m)	Average unit weight γ_1 (kN/m ³)	Initial ground water level H_0 (m)
Confining impermeable layer	160	18.0	228

into the well at a constant rate, equations (1), (2), (3), and the proposed analytical solution can be applied to the settlement simulation of the fourth confined aquifer of Shanghai.

4.2. Parameters Adopted for the Proposed Analytical Solution.

The pumping well radius r_w in this study is 0.3 metres with a pumping rate Q of 0.121 m³/s [35]. From 1980 to 1995, the water head drawdown s_w at the well was approximately 18 metres [24, 25]. The Shanghai ground height above sea level is approximately 2 metres. The soil parameters are presented in Tables 2 and 3 [24, 25, 36].

According to the Sichardt equation, the influence radius R of Figures 4 and 5 for the pumping well in this case study can be determined empirically as $R = 540$ metres [32]. A in (9) for the settlement simulation is determined to be 24014 Pa.

4.3. Predictions

4.3.1. Vertical Compression Stress in the Fourth Confined Sand Aquifer of Shanghai.

In the proposed analytical solution, the resultant vertical stress σ_{zr} at $r = 0$ induced by single well pumping and the consequent pressure from the overlying impermeable layer is determined by (9). After substituting the parameters in the above example for the settlement simulation of the fourth confined aquifer of Shanghai, the results are presented in Figure 15. First, σ_{zr} increases and then decreases. Its maximum value is reached when the soil layer depth is approximately 161 metres, measured from the ground downwards, as shown in Figure 14(b). The fourth confined sand aquifer of Shanghai consolidates immediately after its water is extracted during single well pumping. Here, σ_{zr} is the final effective stress increase in the fourth confined aquifer of Shanghai at the point $r = 0$ as determined by (9).

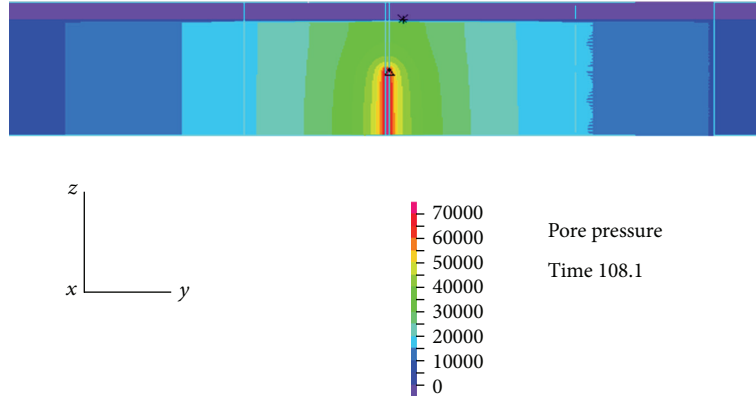


FIGURE 9: Pore pressures analysed with the ADINA software.

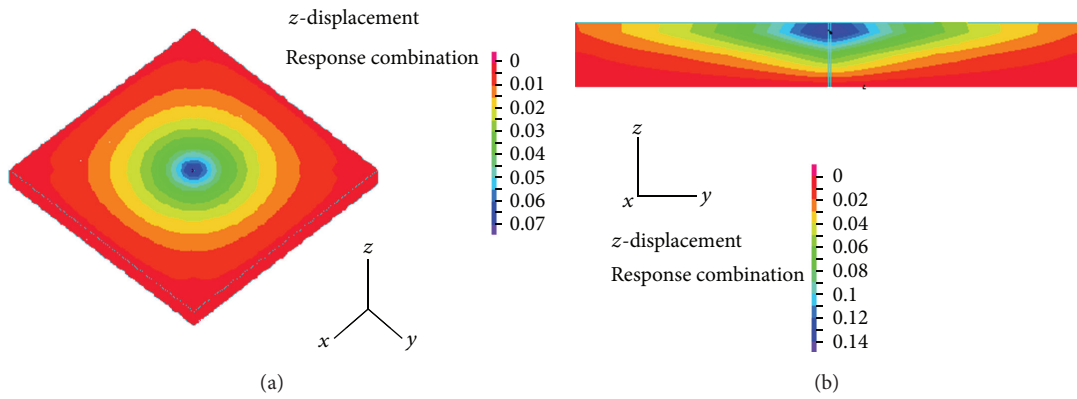


FIGURE 10: Settlements analysed with the ADINA software: (a) three-dimensional view of layer 2; (b) sectional drawing of layer 1 and layer 2.

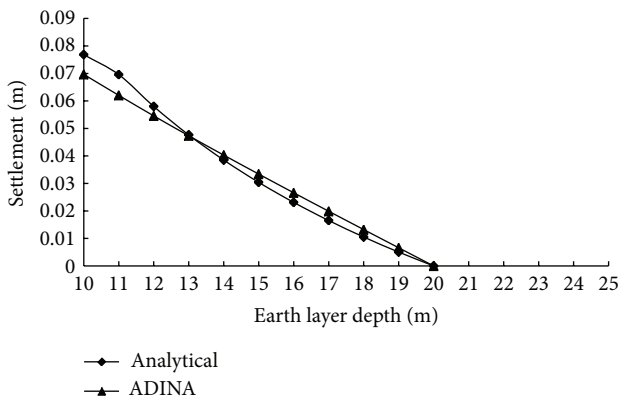


FIGURE 11: Settlements of different depth points in the underlying confined sand aquifer (layer 2) at the single well.

4.3.2. Vertical Compression Strain in the Fourth Confined Sand Aquifer of Shanghai. The vertical compression strain $\varepsilon(0, z)$ is determined using (14). The soil vertical compression strain $\varepsilon(0, z)$ at point $(0, z)$ is presented in Figure 16. First, $\varepsilon(0, z)$ increases, and then it decreases. Its maximum value is reached when the soil layer depth is approximately 161 metres measured from the ground downwards, as shown in Figure 14(b).

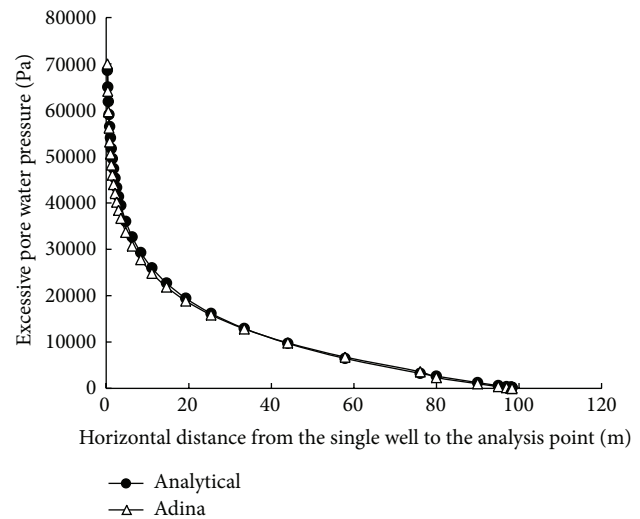


FIGURE 12: Excessive pore water pressures at the analysis points at different distances to the single well in the centre of the horizontal radial plane.

4.3.3. Prediction of the Consolidation Settlement of the Fourth Confined Sand Aquifer of Shanghai. According to (13), the primary consolidation settlement of the fourth confined sand



FIGURE 13: The Pudong New Area of Shanghai city as a case study.

TABLE 3: Fourth confined sand aquifer parameters in the settlement simulation.

Earth layer name	Compression index C_c	Thickness $M = D_c$ (m)	Saturated sand unit weight γ_2 (kN/m ³)	Hydraulic conductivity K (m/s)	Initial void ratio e_0
Fourth confined sand aquifer	0.05	80	20.0	1.0×10^{-4}	0.8

aquifer of Shanghai at the single well due to single pumping can be determined via the numerical integration method. The derived values for the proposed analytical solution were presented in Figure 17, and the maximum settlement is 41.5 mm. Only the subsidence induced by the compression of the fourth confined aquifer is included in the proposed analytical solution because the fourth confined aquifer has been the main confined aquifer for groundwater extraction since the 1980s [25].

4.4. Comparing the Fourth Confined Aquifer Predicted Settlement with In Situ Measured Values. Seepage monitoring records are presented in Figure 18 according to reference [23]. The deformation-groundwater level (m above sea level) in the fourth confined aquifer according to Wu et al. is presented in Figure 19 [24]. According to Wu et al. [24] and Wei et al. [25], from 1980 to 1995, there was a total settlement of approximately 30 mm contributed by the fourth confined aquifer. The maximum subsidence of 41.5 mm at

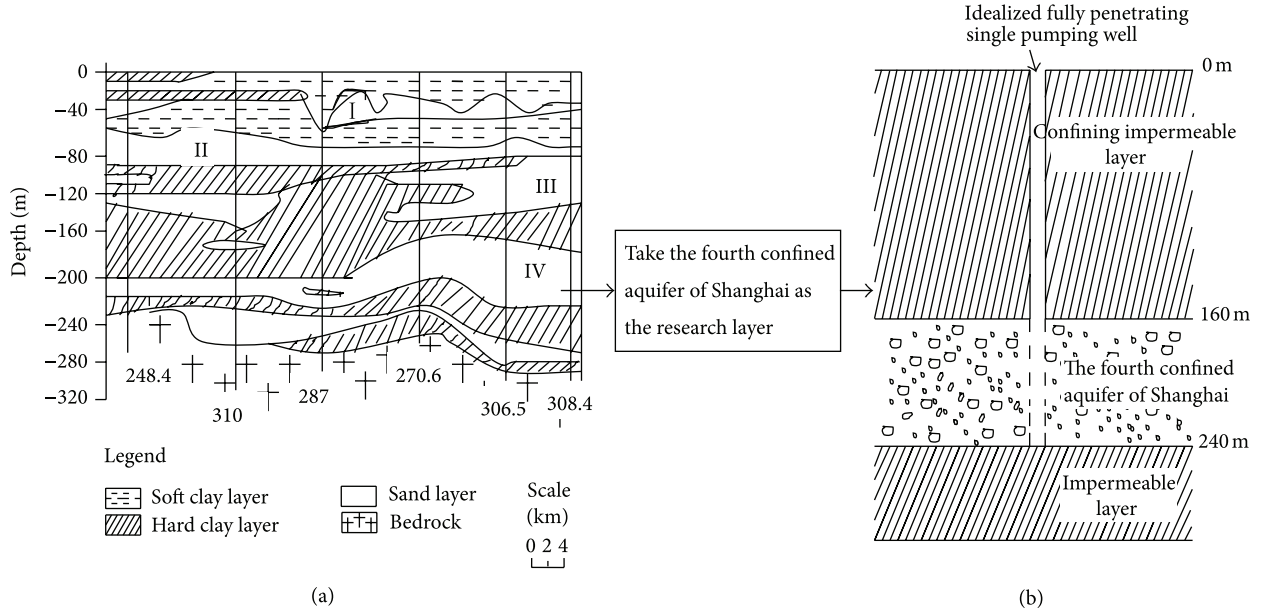


FIGURE 14: (a) Shanghai quaternary period earth layer characteristics where I, II, III, and IV are the first, second, third, and fourth confined aquifers of Shanghai, respectively. (b) The fourth confined aquifer as the research layer in the analytical solution.

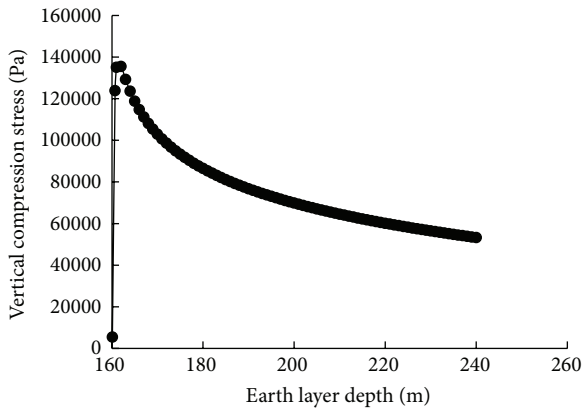


FIGURE 15: Vertical compression stress in the fourth confined sand aquifer of Shanghai.

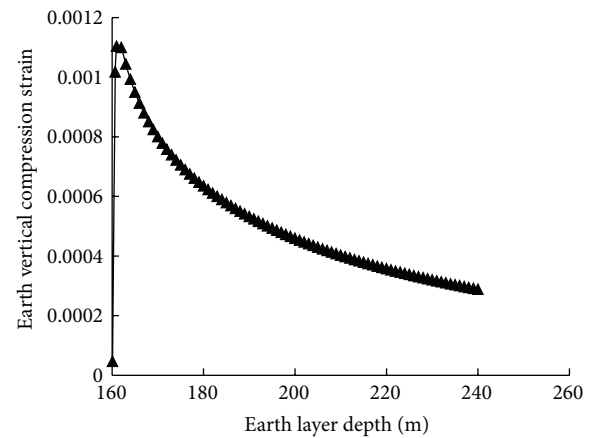


FIGURE 16: Vertical compression strain in the fourth confined sand aquifer of Shanghai at the single well.

the Shanghai's fourth confined aquifer from 1980 to 1995 predicted with the analytical solution (13) is very close to the in situ measurements of Wu et al. [24] and Wei et al. [25].

5. Discussion

5.1. Assumptions in the Theory of the Proposed Analytical Solution. If the influence radius R shown in Figure 2 is difficult to determine in practical situations, the Sichardt equation can be used to determine R empirically [32]. In order to use (1) or, consequently, (6), the condition $s_w \leq H_0 - D_c$ must be satisfied. Equation (8) is the basic Boussinesq solution, which can only be used if $E_2 = E_3$ and $\nu_2 = \nu_3$ and the single well radius remains infinitely small. The proposed analytical solution is fundamentally applicable for the

proposed analytical solution for the use in the prediction of the fourth confined aquifer of Shanghai.

This paper does not incorporate the Terzaghi equation or the Biot equation in the prediction process because the Terzaghi equation and the Biot equation are mainly intended to predict pore water pressure and the corresponding consolidation degree for low permeability soils. However, the confined aquifer is composed of sand, and sand aquifers consolidate immediately after water extraction.

5.2. Limits of the Present Analytical Solution and Possible Future Modifications for the Prediction of Consolidation Settlement. Equation (10) implies the following:

$$\Delta u = \Delta \sigma_1 = \sigma_z, \quad (15)$$

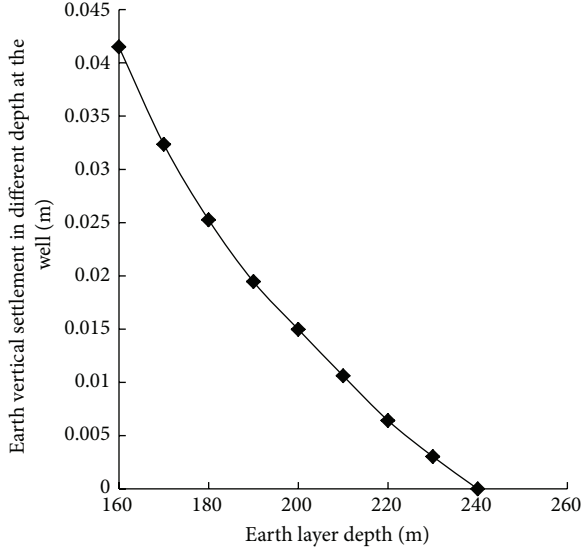


FIGURE 17: Total settlements of different depth points in the Shanghai fourth confined sand aquifer at the single well from 1980 to 1995.

Δu , $\Delta\sigma_1$, and σ_z are physical quantities representing the physical process of the one-dimensional consolidation test where the external compressive load is exerted vertically and axially. The soil sample for test is saturated. σ_z is the vertical axial additional total stress acting on the soil particles in the soil sample due to the vertical external compressive load. Δu denotes the initial excess pore water pressure induced by vertical axial external load. $\Delta\sigma_1$ is the intergranular vertical pressure increase (also called the final vertical effective stress increase) because the overall dissipation of the initial excess pore water pressure Δu after primary consolidation is completed. This equation is only accurate for the one-dimensional consolidation test where there is no lateral yielding of the soil specimen and the ratio of the minor to major principal effective stresses, K_0 , remains constant [34].

Skempton and Bjerrum gave the final vertical compression of a soil element of thickness dz caused by the initial generated and final completed dissipation of excess pore water pressure where the soil element is substantial in triaxial compression tests (e.g., soil triaxial shear test [37, 38]). The initial excess pore water pressure is obtained from a three-dimensional analysis, while the consolidation settlement due to completed dissipation of excess pore water pressure is determined according to the void ratio pressure curve in the one-dimensional consolidation test. In the one-dimensional consolidation test, the soil specimen is restrained laterally and loaded vertically axially. The equation by Skempton and Bjerrum is as follows:

$$dS_c = \left(\frac{1}{Es} \right) \Delta\sigma_1 \left[B + \frac{\Delta\sigma_3}{\Delta\sigma_1} (1 - B) \right] dz, \quad (16)$$

dS_c denotes the vertical axial consolidation settlement when the soil sample in the experiment is in triaxial compression (i.e., soil triaxial shear test), Es is the soil compression modulus when the soil specimen is restrained laterally and loaded

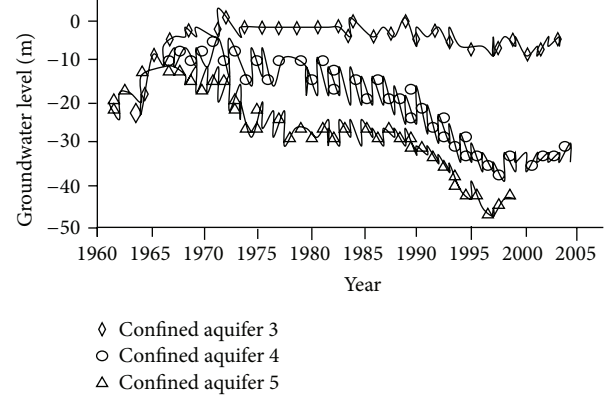


FIGURE 18: History of the groundwater level (m above sea level) for the confined aquifers in Shanghai [23].

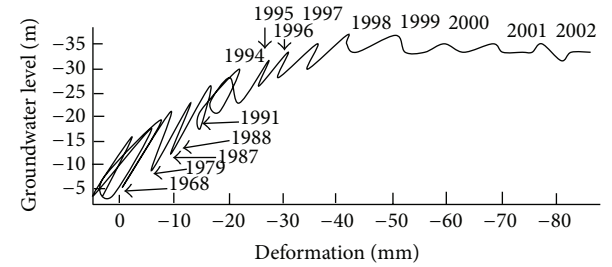


FIGURE 19: Deformation-groundwater level (m above sea level) curve of the fourth confined aquifer in Shanghai [24].

vertically axially in the one-dimensional consolidation test, $\Delta\sigma_1$ is the vertical axial stress increase in the soil specimen (in the soil triaxial shear test), $\Delta\sigma_3$ is the horizontal stress increase in the soil specimen (in the soil triaxial shear test), and B is the pore-pressure coefficient under differential stress ($\Delta\sigma_1 - \Delta\sigma_3$).

This analysis suggests that (10) and the derived analytical solution (13) are just approximate solutions and could be improved with (16) to include the influence of triaxial stress on the initial excess pore water pressure. It means that σ_{zr} is not the final effective stress increase in the Skempton and Bjerrum theory. The final effective stress increase should be determined with three-dimensional stress analysis with the Boussinesq solution, consequent principle stress analysis and that soil triaxial shear test. This point could be improved in the future.

6. Conclusions

This paper proposes a simplified analytical solution for determining the primary consolidation settlement of a confined sand aquifer overlain by an impermeable clay layer at the single well induced by single well pumping in a confined sand aquifer. For the sand aquifer, because the initial immediate settlement occurs before pumping, and the secondary compression is usually negligible, primary consolidation settlement can be regarded as the final settlement.

The method is constituted by a series of fundamental equations. First, with an assumption of steady state, axisymmetric drawdown around a single well, the radial water head drawdown is predicted with the Dupuit equation. Then, the confining pressure on the underlain confined aquifer is determined with the assumption that the loss of confined aquifer water head against the upper confining impermeable layer converts to equivalent confining pressure according to the principles of equilibrium of forces in the vertical direction. With the obtained confining pressure on the underlain confined aquifer, the vertical additional stress in the confined aquifer is computed using the Boussinesq solution. After that, the void ratio change under the vertical stress is determined by the compression index from the e - $\lg p$ curve from a one-dimensional consolidation test. Then, the vertical strain of soil can be obtained. The consolidation deformation of the vertical element layer in the aquifer is then derived using the strain and the element layer thickness. With the integral method, the overall consolidation settlement, which is the sum of the settlements of all vertical element layers, can be obtained. Validation of the proposed analytical solution with the ADINA software is presented as an example. The analytical solution is found to be applicable and cost-effective in predicting the settlement of a confined sand aquifer overlain by an impermeable clay layer.

The proposed analytical solution is then used to predict the fourth confined sand aquifer settlement due to water head drawdown in the Pudong New Area of Shanghai. The predicted value of 41.5 mm calculated using the proposed analytical solution in (13) is close to the in situ measured settlement of 30 mm for the fourth confined aquifer of Shanghai due to water extraction from 1980 to 1995, according to the measurements of Wu et al. [24] and Wei et al. [25].

Conflict of Interests

The authors declare that they have no financial and personal relationships with other people or organisations that could inappropriately influence their work. The authors of this paper have chosen not to furnish the paper and its readers with information that might present a potential conflict of interests.

Acknowledgments

The first author was supported by the 47th Chinese Postdoctoral Scientific Fund (no. 113000-X91001) and is supported by the Scientific Research Starting Funds at Liaoning Technical University (no. 11-415). The second author is supported by the National Natural Science Foundation of China (no. 51079127, no. 51179171, and no. 51279180). Comments from the reviewers are greatly appreciated.

References

- [1] M. Budhu and I. B. Adiyaman, "Mechanics of land subsidence due to groundwater pumping," *International Journal for Numerical and Analytical Methods in Geomechanics*, vol. 34, no. 14, pp. 1459–1478, 2010.
- [2] R. L. Hu, Z. Q. Yue, L. C. Wang, and S. J. Wang, "Review on current status and challenging issues of land subsidence in China," *Engineering Geology*, vol. 76, no. 1-2, pp. 65–77, 2004.
- [3] J. H. Kihm, J. M. Kim, S. H. Song, and G. S. Lee, "Three-dimensional numerical simulation of fully coupled groundwater flow and land deformation due to groundwater pumping in an unsaturated fluvial aquifer system," *Journal of Hydrology*, vol. 335, no. 1-2, pp. 1–14, 2007.
- [4] A. I. Calderhead, R. Therrien, A. Rivera, R. Martel, and J. Garfias, "Simulating pumping-induced regional land subsidence with the use of InSAR and field data in the Toluca Valley, Mexico," *Advances in Water Resources*, vol. 34, no. 1, pp. 83–97, 2011.
- [5] X. Shi, J. Wu, S. Ye et al., "Regional land subsidence simulation in Su-Xi-Chang area and Shanghai City, China," *Engineering Geology*, vol. 100, no. 1-2, pp. 27–42, 2008.
- [6] A. M. Wilson and S. Gorelick, "The effects of pulsed pumping on land subsidence in the Santa Clara Valley, California," *Journal of Hydrology*, vol. 174, no. 3-4, pp. 375–396, 1996.
- [7] O. J. Santos Jr. and T. B. Celestino, "Artificial neural networks analysis of São Paulo subway tunnel settlement data," *Tunnelling and Underground Space Technology*, vol. 23, no. 5, pp. 481–491, 2008.
- [8] C. Chen, S. Pei, and J. J. Jiao, "Land subsidence caused by groundwater exploitation in Suzhou City, China," *Hydrogeology Journal*, vol. 11, no. 2, pp. 275–287, 2003.
- [9] J. Hoffmann, D. L. Galloway, and H. A. Zebker, "Inverse modeling of interbed storage parameters using land subsidence observations, Antelope Valley, California," *Water Resources Research*, vol. 39, no. 2, p. 1231, 2003.
- [10] D. Bernaud, L. Dormieux, and S. Maghous, "A constitutive and numerical model for mechanical compaction in sedimentary basins," *Computers and Geotechnics*, vol. 33, no. 6-7, pp. 316–329, 2006.
- [11] Y. Liu and D. C. Helm, "Inverse procedure for calibrating parameters that control land subsidence caused by subsurface fluid withdrawal: 1. Methods," *Water Resources Research*, vol. 44, no. 7, pp. 1–15, 2008.
- [12] T. Keller, M. Lamande, S. Peth et al., "An interdisciplinary approach towards improved understanding of soil deformation during compaction," *Soil & Tillage Research*, vol. 128, pp. 61–80, 2013.
- [13] T. J. Burbey, "Stress-strain analyses for aquifer-system characterization," *Ground Water*, vol. 39, no. 1, pp. 128–136, 2001.
- [14] T. J. Burbey, "Use of vertical and horizontal deformation data with inverse models to quantify parameters during aquifer testing," in *Proceedings of the 7th International Symposium on Land Subsidence*, Shanghai, China, 2005.
- [15] D. L. Rudolph and E. O. Frind, "Hydraulic response of highly compressible aquitards during consolidation," *Water Resources Research*, vol. 27, no. 1, pp. 17–30, 1991.
- [16] S. A. Leake and D. L. Galloway, *MODFLOW Ground-Water Model-User Guide to the Subsidence and Aquifer-System Compaction Package (SUB-WT) for Watertable Aquifers*, Techniques and Methods 6-A23, US. Geological Survey, 2007.
- [17] S. Q. Wang, Y. P. Wee, and G. Ofori, "DSSDSS: a decision support system for dewatering systems selection," *Building and Environment*, vol. 37, no. 6, pp. 625–645, 2002.
- [18] H. Bouwer, "Land subsidence and cracking due to ground-water depletion," *Ground Water*, vol. 15, no. 5, pp. 358–364, 1977.

- [19] H. Sun, D. Grandstaff, and R. Shagam, "Land subsidence due to groundwater withdrawal: potential damage of subsidence and sea level rise in southern New Jersey, USA," *Environmental Geology*, vol. 37, no. 4, pp. 290–296, 1999.
- [20] C. Chen, S. Pei, and J. J. Jiao, "Land subsidence caused by groundwater exploitation in Suzhou City, China," *Hydrogeology Journal*, vol. 11, no. 2, pp. 275–287, 2003.
- [21] D. Roy and K. E. Robinson, "Surface settlements at a soft soil site due to bedrock dewatering," *Engineering Geology*, vol. 107, no. 3–4, pp. 109–117, 2009.
- [22] C. Li, X. Tang, and T. Ma, "Land subsidence caused by groundwater exploitation in the Hangzhou-Jiaxing-Huzhou plain, China," *Hydrogeology Journal*, vol. 14, no. 8, pp. 1652–1665, 2006.
- [23] X. Shi, Y. Xue, J. Wu et al., "Characterization of regional land subsidence in Yangtze Delta, China: the example of Su-Xi-Chang area and the city of Shanghai," *Hydrogeology Journal*, vol. 16, no. 3, pp. 593–607, 2008.
- [24] J. Wu, X. Shi, S. Ye et al., "Numerical simulation of viscoelastoplastic land subsidence due to groundwater overdrafting in Shanghai, China," *Journal of Hydrologic Engineering*, vol. 15, no. 3, pp. 223–236, 2010.
- [25] Z. X. Wei, G. F. Yang, and J. Y. Yu, "Stress-strain characteristic of the confined aquifer system and land subsidence controlling countermeasures in Shanghai," *The Chinese Journal of Geological Hazard and Control*, vol. 16, no. 1, pp. 5–8, 2005 (Chinese).
- [26] S. van Asselen, E. Stouthamer, and T. W. J. van Asch, "Effects of peat compaction on delta evolution: a review on processes, responses, measuring and modeling," *Earth-Science Reviews*, vol. 92, no. 1–2, pp. 35–51, 2009.
- [27] A. S. Gregory, W. R. Whalley, C. W. Watts, N. R. A. Bird, P. D. Hallett, and A. P. Whitmore, "Calculation of the compression index and precompression stress from soil compression test data," *Soil and Tillage Research*, vol. 89, no. 1, pp. 45–57, 2006.
- [28] S. Silliman and D. Higgins, "An analytical solution for steady-state flow between aquifers through an open well," *Ground Water*, vol. 28, no. 2, pp. 184–190, 1990.
- [29] M. Bakker and K. Hemker, "A Dupuit formulation for flow in layered, anisotropic aquifers," *Advances in Water Resources*, vol. 25, no. 7, pp. 747–754, 2002.
- [30] M. Bakker, "Simulating groundwater flow in multi-aquifer systems with analytical and numerical Dupuit-models," *Journal of Hydrology*, vol. 222, no. 1–4, pp. 55–64, 1999.
- [31] M. Li, N. R. Diao, and Z. H. Fang, "Analysis of seepage flow in a confined aquifer with a standing column well," *Journal of Hydrodynamics*, vol. 19, no. 1, pp. 84–91, 2007.
- [32] D. Bloomquist, A. A. Viala, and M. Gartner, *Development of a Field Permeability Apparatus: The Vertical And Horizontal Insitu Permeameter (VAHIP)*, Department of Civil and Coastal Engineering, University of Florida, Gainesville, Fla, USA, 2007.
- [33] W. J. Niu, "An approximated analytical solution to the problem of single well pumping within an irregular boundary," in *Proceedings of the Civil Engineering and Urban Planning (ASCE '12)*, pp. 88–92, Yantai, China, 2012.
- [34] M. M. Monkul and O. Önal, "A Visual Basic program for analyzing oedometer test results and evaluating intergranular void ratio," *Computers and Geosciences*, vol. 32, no. 5, pp. 696–703, 2006.
- [35] Z. W. Li, Y. Zhang, and C. L. Chen, "Disposal for pumping well in phreatic water aquifer in three-dimensional numerical simulation," *Journal of Water Resources and Architectural Engineering*, vol. 6, no. 2, pp. 121–126, 2008 (Chinese).
- [36] Y. S. Xu, S. L. Shen, C. P. Tang, and H. Jiang, "Three-dimensional analysis of land subsidence based on groundwater flow model," *Rock and Soil Mechanics*, vol. 26, pp. 109–112, 2005 (Chinese).
- [37] C. B. Zhanga, L. H. Chena, and Y. P. Liu, "Triaxial compression test of soil-root composites to evaluate influence of roots on soil shear strength," *Ecological Engineering*, vol. 36, pp. 19–26, 2010.
- [38] S. J. Lee, Y. M. A. Hashash, and E. G. Nezami, "Simulation of triaxial compression tests with polyhedral discrete elements," *Computers and Geotechnics*, vol. 43, pp. 92–100, 2012.

Research Article

Lévy-Flight Krill Herd Algorithm

Gaige Wang,^{1,2} Lihong Guo,¹ Amir Hossein Gandomi,³ Lihua Cao,¹ Amir Hossein Alavi,⁴ Hong Duan,⁵ and Jiang Li¹

¹ Changchun Institute of Optics, Fine Mechanics and Physics, Chinese Academy of Sciences, Changchun, Jilin 130033, China

² University of Chinese Academy of Sciences, Beijing 100039, China

³ Department of Civil Engineering, University of Akron, Akron, OH 443253905, USA

⁴ Department of Civil and Environmental Engineering, Engineering Building, Michigan State University, East Lansing, MI 48824, USA

⁵ School of Computer Science and Information Technology, Northeast Normal University, Changchun 130117, China

Correspondence should be addressed to Lihong Guo; guolh@ciomp.ac.cn

Received 3 November 2012; Accepted 20 December 2012

Academic Editor: Siamak Talatahari

Copyright © 2013 Gaige Wang et al. This is an open access article distributed under the Creative Commons Attribution License, which permits unrestricted use, distribution, and reproduction in any medium, provided the original work is properly cited.

To improve the performance of the krill herd (KH) algorithm, in this paper, a Lévy-flight krill herd (LKH) algorithm is proposed for solving optimization tasks within limited computing time. The improvement includes the addition of a new local Lévy-flight (LLF) operator during the process when updating krill in order to improve its efficiency and reliability coping with global numerical optimization problems. The LLF operator encourages the exploitation and makes the krill individuals search the space carefully at the end of the search. The elitism scheme is also applied to keep the best krill during the process when updating the krill. Fourteen standard benchmark functions are used to verify the effects of these improvements and it is illustrated that, in most cases, the performance of this novel metaheuristic LKH method is superior to, or at least highly competitive with, the standard KH and other population-based optimization methods. Especially, this new method can accelerate the global convergence speed to the true global optimum while preserving the main feature of the basic KH.

1. Introduction

In current competitive world, human beings make an attempt at extracting the maximum output or profit from a restricted amount of usable resources. In the case of engineering optimization, such as design optimization of tall steel buildings [1], optimum design of gravity retaining walls [2], water, geotechnical and transport engineering [3], and structural optimization and design [4, 5], engineers would attempt to design structures that satisfy all design requirements with the minimum possible cost. Most real-world engineering optimization problems could be converted into general global optimization problems. Therefore, the study of global optimization is of vital importance for the engineering optimization. In this issue, many biological intelligent techniques [6] as optimization tools have been developed and applied to solve engineering optimization problems for engineers. A general classification way for these techniques is considering the nature of the techniques, and optimization

techniques can be classified as two main groups: classical methods and modern intelligent algorithms. Classical methods such as hill climbing have a rigorous move and will generate the same set of solutions if the iterations start with the same initial starting point. On the other hand, modern intelligent algorithms often generate different solutions even with the same initial value. However, in general, the final solutions, though slightly different, will converge to the same optimal values within a given accuracy. The emergence of metaheuristic optimization algorithm as a blessing from the artificial intelligence and mathematical theorem has opened up a new facet to carry out the optimization of a function. Recently, nature-inspired metaheuristic algorithms perform powerfully and efficiently in solving modern nonlinear numerical global optimization problems. To some extent, all metaheuristic algorithms make an attempt at relieving the conflict between diversification/exploration/randomization (global search) and intensification/exploitation (local search) [7, 8].

Inspired by nature, these strong metaheuristic algorithms have been proposed to solve NP-hard tasks, such as UCAV path planning [9, 10], test-sheet composition [11], and parameter estimation [12]. These kinds of metaheuristic methods perform on a population of solutions and always find optimal or suboptimal solutions. During the 1960s and 1970s, computer scientists studied the possibility of formulating evolution as an optimization method and eventually this generated a subset of gradient free methods, namely, genetic algorithms (GAs) [13, 14]. In the last two decades, a huge number of techniques were developed on function optimization, such as bat algorithm (BA) [15, 16], differential evolution (DE) [17, 18], genetic programming (GP) [19], harmony search (HS) [20, 21], particle swarm optimization (PSO) [22–24], cuckoo search (CS) [25, 26], and, more recently, the krill herd (KH) algorithm [27] that is based on imitating the krill herding behavior in nature.

Firstly proposed by Gandomi and Alavi in 2012, inspired by the herding behavior of krill individuals, KH algorithm is a novel swarm intelligence method for optimizing possibly nondifferentiable and nonlinear complex functions in continuous space [27]. In KH, the time-dependent position of the krill individuals involves three main components: (i) movement led by other individuals, (ii) foraging motion, and (iii) random physical diffusion. One of the notable advantages of the KH algorithm is that derivative information is unnecessary, because it uses a random search instead of a gradient search use in classical methods. Moreover, comparing with other population-based metaheuristic methods, this new method needs few control variables, in principle only a separate parameter Δt (time interval) to tune, which makes KH easy to implement, more robust and fits for parallel computation.

KH is an effective and powerful algorithm in exploration, but at times it may trap into some local optima so that it cannot implement global search well. For KH, the search depends completely on random search, so there is no guarantee for a fast convergence. In order to improve KH in optimization problems, a method has been proposed [28], which introduces a more focused mutation strategy into KH to add the diversity of population.

On the other hand, many researchers have centralized on theories and applications of statistical techniques, especially of Lévy distribution. And recently huge advances are acquired in many fields. One of these fields is the applications of Lévy flight in optimization methods. Previously, Lévy flights have been used together with some metaheuristic optimization methods such as firefly algorithm [29], cuckoo search [30], krill herd algorithm [31], and particle swarm optimization [32].

Firstly presented here, an effective Lévy-flight KH (LKH) method is originally proposed in this paper, in order to accelerate convergence speed, thus making the approach more feasible for a wider range of real-world engineering applications while keeping the desirable characteristics of the original KH. In LKH, first of all, a standard KH algorithm is implemented to shrink the search space and select a good candidate solution set. And then, for more precise modeling of the krill behavior, a local Lévy-flight (LLF) operator is

added to the algorithm. This operator is applied to exploit the limited promising area intensively to get better solutions so as to improve its efficiency and reliability for solving global numerical optimization problems. The proposed method is evaluated on fourteen standard benchmark functions that have ever been applied to verify optimization methods in continuous optimization problems. Experimental results show that the LKH performs more efficiently and effectively than basic KH, ABC, ACO, BA, CS, DE, ES, GA, HS, PBIL, and PSO.

The structure of this paper is organized as follows. Section 2 gives a description of basic KH algorithm and Lévy flight in brief. Our proposed LKH method is described in detail in Section 3. Subsequently, our method is evaluated through fourteen benchmark functions in Section 4. In addition, the LKH is also compared with ABC, ACO, BA, CS, DE, ES, GA, HS, KH, PBIL, and PSO in that section. Finally, Section 5 involves the conclusion and proposals for future work.

2. Preliminary

At first, in this section, a background on the krill herd algorithm and Lévy flight will be provided in brief.

2.1. Krill Herd Algorithm. Krill herd (KH) [27] is a new metaheuristic optimization method [4] for solving optimization tasks, which is based on the simulation of the herding of the krill swarms in response to particular biological and environmental processes. The time-dependent position of an individual krill in 2D space is decided by three main actions presented as follows:

- (i) movement affected by other krill individuals,
- (ii) foraging action,
- (iii) random diffusion.

KH algorithm adopted the following Lagrangian model in a d -dimensional decision space as in the following (1):

$$\frac{dX_i}{dt} = N_i + F_i + D_i, \quad (1)$$

where N_i , F_i , and D_i are the motion led by other krill individuals, the foraging motion, and the physical diffusion of the i th krill individual, respectively.

In movement affected by other krill individuals, the direction of motion, α_i , is approximately computed by the target effect (target swarm density), local effect (a local swarm density), and a repulsive effect (repulsive swarm density). For a krill individual, this movement can be defined as

$$N_i^{\text{new}} = N^{\text{max}} \alpha_i + \omega_n N_i^{\text{old}}, \quad (2)$$

and N^{max} is the maximum induced speed, ω_n is the inertia weight of the motion induced in $[0, 1]$, and N_i^{old} is the last motion induced.

The foraging motion is estimated by the two main components. One is the food location and the other one is

TABLE 1: Benchmark functions.

Number	Name	Definition
F01	Ackley	$f(\vec{x}) = 20 + e - 20 \cdot e^{-0.2 \cdot \sqrt{(1/n) \sum_{i=1}^n x_i^2}} - e^{(1/n) \sum_{i=1}^n \cos(2\pi x_i)}$
F02	Fletcher-Powell	$f(\vec{x}) = \sum_{i=1}^n (A_i - B_i)^2, \quad A_i = \sum_{j=1}^n (a_{ij} \sin \alpha_j + b_{ij} \cos \alpha_j)$ $B_i = \sum_{j=1}^n (a_{ij} \sin x_j + b_{ij} \cos x_j)$
F03	Griewank	$f(\vec{x}) = \sum_{i=1}^n \frac{x_i^2}{4000} - \prod_{i=1}^n \cos\left(\frac{x_i}{\sqrt{i}}\right) + 1$
F04	Penalty #1	$f(\vec{x}) = \frac{\pi}{30} \left\{ 10 \sin^2(\pi y_1) + \sum_{i=1}^{n-1} (y_i - 1)^2 \cdot [1 + 10 \sin^2(\pi y_{i+1})] + (y_n - 1)^2 \right\} + \sum_{i=1}^n u(x_i, 10, 100, 4), \quad y_i = 1 + 0.25(x_i + 1)$
F05	Penalty #2	$f(\vec{x}) = 0.1 \left\{ \sin^2(3\pi x_1) + \sum_{i=1}^{n-1} [1 + \sin^2(3\pi x_{i+1})] + (x_n - 1)^2 [1 + \sin^2(2\pi x_n)] \right\} + \sum_{i=1}^n u(x_i, 5, 100, 4)$
F06	Quartic with noise	$f(\vec{x}) = \sum_{i=1}^n (i \cdot x_i^4 + U(0, 1))$
F07	Rastrigin	$f(\vec{x}) = 10 \cdot n + \sum_{i=1}^n (x_i^2 - 10 \cdot \cos(2\pi x_i))$
F08	Rosenbrock	$f(\vec{x}) = \sum_{i=1}^{n-1} \left[100(x_{i+1} - x_i^2)^2 + (x_i - 1)^2 \right]$
F09	Schwefel 2.26	$f(\vec{x}) = 418.9829 \times D - \sum_{i=1}^D x_i \sin\left(x_i ^{1/2}\right)$
F10	Schwefel 1.2	$f(\vec{x}) = \sum_{i=1}^n \left(\sum_{j=1}^i x_j \right)^2$
F11	Schwefel 2.22	$f(\vec{x}) = \sum_{i=1}^n x_i + \prod_{i=1}^n x_i $
F12	Schwefel 2.21	$f(\vec{x}) = \max_i \{ x_i , 1 \leq i \leq n\}$
F13	Sphere	$f(\vec{x}) = \sum_{i=1}^n x_i^2$
F14	Step	$f(\vec{x}) = 6 \cdot n + \sum_{i=1}^n \lfloor x_i \rfloor$

* In benchmark function F02, the matrix elements $\mathbf{a}_{n \times n}$, $\mathbf{b}_{n \times n} \in (-100, 100)$, and $\alpha_{n \times 1} \in (-\pi, \pi)$ are draw from uniform distribution.

* In benchmark functions F04 and F05, the definition of the function $u(x_i, a, k, m) = \{k(x_i - a)^m, x_i > a; 0, -a \leq x_i \leq a; k(-x_i - a)^m, x_i < -a\}$.

the prior knowledge about the food location. For the i th krill individual, this motion can be approximately formulated as follows:

$$F_i = V_f \beta_i + \omega_f F_i^{\text{old}}, \quad (3)$$

where

$$\beta_i = \beta_i^{\text{food}} + \beta_i^{\text{best}}, \quad (4)$$

and V_f is the foraging speed, ω_f is the inertia weight of the foraging motion between 0 and 1, F_i^{old} is the last foraging motion.

The random diffusion of the krill individuals can be considered to be a random process in essence. This motion can be described in terms of a maximum diffusion speed and a random directional vector. It can be indicated as follows:

$$D_i = D^{\text{max}} \delta, \quad (5)$$

where D^{max} is the maximum diffusion speed, and δ is the random directional vector and its arrays are random values in $[-1, 1]$.

Based on the three above-mentioned movements, using different parameters of the motion during the time, the position vector of a krill individual during the interval t to $t + \Delta t$ is expressed by the following equation:

$$X_i(t + \Delta t) = X_i(t) + \Delta t \frac{dX_i}{dt}. \quad (6)$$

It should be noted that Δt is one of the most important parameters and should be fine-tuned in terms of the specific real-world engineering optimization problem. This is because this parameter can be treated as a scale factor of the speed vector. More details about the three main motions and KH algorithm can be found in [27].

2.2. Lévy Flights. Usually, the hunt of food by animals takes place in the form of random or quasi-random. That is to say, all animals feed in a walk path from one location to another at random. However, the direction it selects relies only on a mathematical model [33]. One of the remarkable models is called Lévy flights.

Lévy flights are a class of random walk in which the steps are determined in terms of the step lengths, and the jumps are distributed according to a Lévy distribution. More recently, Lévy flights have subsequently been applied to improve and optimize searching. In the case of CS, the random walking steps of a cuckoo are determined by a Lévy flight [34]:

$$X_i^{t+1} = X_i^t + \beta L(s, \lambda), \quad (7)$$

$$L(s, \lambda) = \frac{\lambda \Gamma(\lambda) \sin(\pi\lambda/2)}{\pi} \frac{1}{s^{1+\lambda}}, \quad (s, s_0 > 0).$$

Here, $\beta > 0$ is the step size scaling factor, which should be related to the scales of the problem of interest. The random walk via Lévy flight is more efficient in exploring the search space as its step length is much longer in the long run. Some of the new solutions should be generated by Lévy walk around the best solution obtained so far; this will speed up the local search.

3. Our Approach: LKH

In general, the standard KH algorithm is adept at exploring the search space and locating the promising region of global optimal value, but it is not relatively good at exploiting solution. In order to improve the exploitation of KH, a new distribution Lévy flight performing local search, called local Lévy-flight (LLF) operator, is introduced to form a novel Lévy-flight krill herd (LKH) algorithm. In LKH, to begin with, standard KH algorithm with high convergence speed is used to shrink the search region to a more promising area. And then, LLF operator with good exploitation ability is applied to exploit the limited area intensively to get better solutions. In this way, the strong exploration abilities of the original KH and the exploitation abilities of the LLF operator can be fully extracted. The difference between LKH and KH is that the LLF operator is used to perform local search and fine-tune the original KH generating a new solution for each krill instead of random walks originally used in KH. As a matter of fact, according to the figuration of LKH, the original KH in LKH focuses on the exploration/diversification at the beginning of the search to evade trapping into local optima in a multimodal landscape; while later LLF operator encourages the exploitation/intensification and makes the krill individuals search the space carefully at the end of the search. Therefore, our proposed LKH method can fully exploit the merits of different search techniques and overcome the lack of the exploitation of the KH and solve the conflict between exploration and exploitation effectively. The detailed explanation of our method is described as follows.

To start with, standard KH algorithm utilizes three main actions to search the promising area in the solution space and use these actions to guide the generation of the candidate solutions for the next generation. It has been demonstrated that [27] KH performs well in both convergence speed and final accuracy on unimodal problems and many simple multimodal problems. Therefore, in LKH, we employ the merit of the fast convergence of KH to implement global search. In addition, KH is able to shrink the search region towards the promising area within a few generations. However, sometimes KH's performance on complex multimodal problems is unsatisfying; accordingly, another search technique with good exploitation ability is crucial to exploit the limited area carefully to get optimal solutions.

To improve the exploitation ability of the KH algorithm, genetic reproduction mechanisms have been incorporated into the standard KH algorithm. Gandomi and Alavi have proved that the KH II (KH with crossover operator only) performs the best among serials of KH methods [27]. In our present work, we use a more focused local search technique, local Lévy-flight (LLF) operator, in the local search part of the LKH algorithm, which can increase diversity of the population in an attempt to avoid premature convergence and exploit a small region in the later run phase to refine the final solutions. The main step of LLF operator used in the LKH algorithm is presented in Algorithm 1.

Here, $t \in [0, t_{\text{max}}]$ and t_{max} is the maximum of generations. d is the number of decision variables. NP is the size of the parent population. A is max Lévy-flight step size.

```

Begin
   $a = A/(t^2)$ ;           % Smaller step for local walk
  NoSteps =  $\lceil d * \text{exprnd}(2 * t_{\max}) \rceil$ ;
  Determine the next step size  $dx$  by performing Lévy flight as shown in Section 2.2;
   $r = \lceil NP * \text{rand} \rceil$ 
  for  $j = 1$  to  $d$  do
    if  $\text{rand} \leq 0.5$            % Random number to determine direction
       $V_i(j) = a \times dx(j) + X_{NP-r+1}(j)$ 
    else
       $V_i(j) = a \times dx(j) - X_{NP-r+1}(j)$ 
    end if
  end for  $j$ 
  Evaluate the offspring  $V_i$ 
  if  $V_i$  is better than  $X_i$  then
     $X_i = V_i$ 
  end if
End.

```

ALGORITHM 1: Local Lévy-flight (LLF) operator.

$X_i(j)$ is the j th variable of the solution X_i . V_i is the offspring. $\lceil d * \text{exprnd}(2 * t_{\max}) \rceil$ is a random integer number between 1 and $d * \text{exprnd}(2 * t_{\max})$ drawn from exponential distribution. $\text{exprnd}(2 * t_{\max})$ returns an array of random numbers chosen from the exponential distribution with mean parameter $2 * t_{\max}$. Similarly, $\lceil d * \text{rand} \rceil$ is a random integer number between 1 and d drawn from uniform distribution. And rand is a random real number in interval (0, 1) drawn from uniform distribution.

In addition, another important improvement is the addition of elitism strategy into the LKH. Clearly, KH has some fundamental elitism. However, it can be further improved. As with other population-based optimization algorithms, we combine some sort of elitism so as to store the optimal solutions in the population. Here, we use a more centralized elitism on the best solutions, which can stop the best solutions from being ruined by three motions and LLF operator in LKH. In the main cycle of the LKH, to start with, the *KEEP* best solutions are retained in a variable *KEEPKRILL*. Generally speaking, the *KEEP* worst solutions are substituted by the *KEEP* best solutions at the end of the every iteration. There is a guarantee that this elitism strategy can make the whole population not decline to the population with worse fitness than the former. Note that we use an elitism strategy to save the property of the krill that has the best fitness in the LKH process, so even if three motions and LLF operator corrupt their corresponding krill, we have retained it and can recuperate to its preceding good status if needed.

Based on the above analyses, the main steps of Lévy-flight krill herd method can be simply presented in Algorithm 2.

4. Simulation Experiments

In this section, the performance of our proposed method LKH is tested to global numerical optimization through a series of experiments implemented in benchmark functions.

To allow an unprejudiced comparison of CPU time, all the experiments were carried out on a PC with a Pentium IV

processor running at 2.0 GHz, 512 MB of RAM, and a hard drive of 160 GB. Our execution was compiled using MATLAB R2012b (8.0) running under Windows XP3. No commercial KH or other optimization tools were used in our simulation experiments.

Well-defined problem sets benefit for testing the performance of optimization algorithms proposed in this paper. Based on numerical functions, benchmark functions can be considered as objective functions to fulfill such tests. In our present study, fourteen different benchmark functions are applied to test our proposed metaheuristic LKH method. The formulation of these benchmark functions are given in Table 1 and the properties of these benchmark functions are presented in Table 2. More details of all the benchmark functions can be found in [35, 36]. We must point out that, in [35], Yao et al. have used 23 benchmarks to test optimization algorithms. However, for the other low-dimensional benchmark functions (such as $d = 2, 4$, and 6), all the methods perform almost identically with each other [37], because these low-dimensional benchmarks are too simple to clarify the performance difference among different methods. Therefore, in our present work, only fourteen high-dimensional complex benchmarks are applied to verify our proposed LKH algorithm.

4.1. General Performance of LKH. In order to explore the merits of LKH, in this section, we compared its performance on global numeric optimization problems with eleven population-based optimization methods, which are ABC, ACO, BA, CS, DE, ES, GA, HS, KH, PBIL, and PSO. ABC (artificial bee colony) [38] is an intelligent optimization algorithm based on the smart behavior of honey bee swarm. ACO (ant colony optimization) [39] is a swarm intelligence algorithm for solving optimization problems which is based on the pheromone deposition of ants. BA (bat algorithm) [16] is a new powerful metaheuristic optimization method inspired by the echolocation behavior of bats with varying

Begin

Step 1: Initialization. Set the generation counter $t = 1$; initialize the population P of NP krill individuals randomly and each krill corresponds to a potential solution to the given problem; set the foraging speed V_f , the maximum diffusion speed D^{\max} , and the maximum induced speed N^{\max} ; set max Lévy flight step size A and elitism parameter

KEEP: how many of the best krill to keep from one generation to the next.

Step 2: Fitness evaluation. Evaluate each krill individual according to its position.

Step 3: While the termination criteria is not satisfied or $t < \text{MaxGeneration}$ **do**

Sort the population/krill from best to worst.

Store the *KEEP* best krill as *KEEPKRILL*.

for $i = 1 : \text{NP}$ (all krill) **do**

Perform the following motion calculation.

Motion induced by the presence of other individuals

Foraging motion

Physical diffusion

Update the krill individual position in the search space by (6).

Fine-tune X_{t+1} by performing LLF operator as shown in Algorithm 1.

Evaluate each krill individual according to its new position X_{t+1} .

end for i

Replace the *KEEP* worst krill with the *KEEP* best krill stored in *KEEPKRILL*.

Sort the population/krill from best to worst and find the current best.

$t = t + 1$;

Step 4: end while

Step 5: Post-processing the results and visualization.

End.

ALGORITHM 2: Lévy-flight krill herd algorithm.

pulse rates of emission and loudness. CS (cuckoo search) [40] is a metaheuristic optimization algorithm inspired by the obligate brood parasitism of some cuckoo species by laying their eggs in the nests of other host birds. DE (differential evolution) [17] is a simple but excellent optimization method that uses the difference between two solutions to probabilistically adapt a third solution. An ES (evolutionary strategy) [41] is an algorithm that generally distributes equal importance to mutation and recombination and that allows two or more parents to reproduce an offspring. A GA (genetic algorithm) [13] is a search heuristic that mimics the process of natural evolution. HS (harmony search) [20] is a new metaheuristic approach inspired by behavior of musician' improvisation process. PBIL (probability-based incremental learning) [42] is a type of genetic algorithm where the genotype of an entire population (probability vector) is evolved rather than individual members. PSO (particle swarm optimization) [22] is also a swarm intelligence algorithm which is based on the swarm behavior of fish and bird schooling in nature. In addition, it should be noted that, in [27], Gandomi and Alavi have proved that, comparing all the algorithms, the KH II (KH with crossover operator) performed the best which confirms the robustness of the KH algorithm. Therefore, in our work, we use KH II as a standard KH algorithm.

In our experiments, we will use the same parameters for KH and LKH that are the foraging speed $V_f = 0.02$, the maximum diffusion speed $D^{\max} = 0.005$, the maximum induced speed $N^{\max} = 0.01$, and max Lévy-flight step size $A = 1.0$ (only for LKH). For ACO, DE, ES, GA, PBIL, and

PSO, we set the same parameters as [36, 43]. For ABC, the number of colony size (employed bees and onlooker bees) $\text{NP} = 50$, the number of food sources $\text{FoodNumber} = \text{NP}/2$, and maximum search times $\text{limit} = 100$ (a food source which could not be improved through "limit" trials is abandoned by its employed bee). For BA, we set loudness $L = 0.95$, pulse rate $r = 0.5$, and scaling factor $\varepsilon = 0.1$; for CS, a discovery rate $p_a = 0.25$. For HS, we set harmony memory accepting rate = 0.75 and pitch adjusting rate = 0.7.

We set population size $\text{NP} = 50$ and maximum generation $\text{Maxgen} = 50$ for each method. We ran 100 Monte Carlo simulations of each method on each benchmark function to get representative performances. Tables 3 and 4 illustrate the results of the simulations. Table 3 shows the average minima found by each method, averaged over 100 Monte Carlo runs. Table 4 shows the absolute best minima found by each method over 100 Monte Carlo runs. That is to say, Table 3 shows the average performance of each method, while Table 4 shows the best performance of each method. The best value achieved for each test problem is marked in bold. Note that the normalizations in the tables are based on different scales, so values cannot be compared between the two tables. Each of the functions in this study has 20 independent variables (i.e., $d = 20$).

From Table 3, we see that, on average, LKH is the most effective at finding objective function minimum on twelve of the fourteen benchmarks (F01–F08, F10, and F12–F14). ABC and GA are the second most effective, performing the best on the benchmarks F11 and F09 when multiple runs are made,

TABLE 2: Properties of benchmark functions, lb denotes lower bound, ub denotes upper bound, and opt denotes optimum point.

Number	Function	lb	ub	opt	Continuity	Modality
F01	Ackley	-32.768	32.768	0	Continuous	Multimodal
F02	Fletcher-Powell	$-\pi$	π	0	Continuous	Multimodal
F03	Griewangk	-600	600	0	Continuous	Multimodal
F04	Penalty #1	-50	50	0	Continuous	Multimodal
F05	Penalty #2	-50	50	0	Continuous	Multimodal
F06	Quartic <i>with noise</i>	-1.28	1.28	1	Continuous	Multimodal
F07	Rastrigin	-5.12	5.12	0	Continuous	Multimodal
F08	Rosenbrock	-2.048	2.048	0	Continuous	Unimodal
F09	Schwefel 2.26	-512	512	0	Continuous	Multimodal
F10	Schwefel 1.2	-100	100	0	Continuous	Unimodal
F11	Schwefel 2.22	-10	10	0	Continuous	Unimodal
F12	Schwefel 2.21	-100	100	0	Continuous	Unimodal
F13	Sphere	-5.12	5.12	0	Continuous	Unimodal
F14	Step	-5.12	5.12	0	Discontinuous	Unimodal

TABLE 3: Mean normalized optimization results in fourteen benchmark functions. The values shown are the minimum objective function values found by each algorithm, averaged over 100 Monte Carlo simulations.

	ABC	ACO	BA	CS	DE	ES	GA	HS	KH	LKH	PBIL	PSO
F01	5.26	6.20	7.81	6.84	4.85	7.54	6.70	7.74	1.85	1.00	7.84	6.53
F02	2.63	10.01	14.42	6.82	3.80	9.77	4.25	9.42	3.67	1.00	9.02	8.27
F03	31.49	10.22	182.64	61.09	17.19	78.85	32.57	155.54	4.59	1.00	176.91	64.57
F04	8.5E5	3.3E7	4.5E7	2.6E6	1.1E5	1.9E7	2.7E5	2.9E7	9.2E3	1.00	4.3E7	2.5E6
F05	1.2E6	1.7E7	2.8E7	3.0E6	2.9E5	1.3E7	5.1E5	2.2E7	3.5E4	1.00	2.6E7	3.1E6
F06	3.4E5	3.3E5	5.5E6	7.6E5	1.2E5	4.1E6	3.3E5	3.8E6	3.8E4	1.00	4.6E6	8.8E5
F07	1.22	2.30	3.42	2.64	1.99	3.16	2.04	2.89	1.25	1.00	3.18	2.34
F08	15.83	85.99	89.29	25.57	13.40	110.42	23.00	75.23	5.34	1.00	90.29	26.64
F09	1.77	1.11	3.93	2.86	2.24	2.73	1.00	3.33	2.10	1.93	3.47	3.35
F10	51.56	43.79	123.64	29.15	68.30	72.56	48.30	66.46	33.17	1.00	75.49	51.20
F11	1.00	2.84	4.57	2.79	1.23	4.32	2.19	3.52	1.50	4.22	3.51	2.58
F12	14.65	9.13	15.73	11.05	11.98	14.52	12.31	14.91	2.46	1.00	15.61	12.52
F13	5.6E3	1.5E4	3.2E4	1.2E4	3.1E3	3.3E4	1.1E4	3.0E4	851.62	1.00	3.2E4	1.2E4
F14	205.78	95.69	1.1E3	427.88	103.81	700.63	227.85	1.0E3	29.20	1.00	1.2E3	411.03
Time	2.40	3.22	1.08	2.02	1.95	2.03	2.38	2.77	4.66	4.30	1.00	2.37
Total	1	0	0	0	0	0	1	0	0	12	0	0

*The values are normalized so that the minimum in each row is 1.00. These are not the absolute minima found by each algorithm, but the average minima found by each algorithm.

respectively. Table 4 shows that LKH performs the best on twelve of the fourteen benchmarks which are F01–F04, F06–F08, and F10–F14. ACO and GA are the second most effective, performing the best on the benchmarks F05 and F09 when multiple runs are made, respectively.

Moreover, the computational times of the twelve optimization methods were alike. We collected the average computational time of the optimization methods as applied to the 14 benchmarks considered in this section. The results are given in Table 3. From Table 3, PBIL was the quickest optimization method, and LKH was the eleventh fastest of the twelve algorithms. This is because that the evaluation of step size by Lévy flight is too time consuming. However, we must point out that in the vast majority of real-world engineering

applications, it is the fitness function evaluation that is by far the most expensive part of a population-based optimization algorithm.

In addition, in order to further prove the superiority of the proposed LKH method, convergence plots of ABC, ACO, BA, CS, DE, ES, GA, HS, KH, LKH, PBIL, and PSO are illustrated in Figures 1–14 which mean the process of optimization. The values shown in Figures 1–14 are the average objective function optimum obtained from 100 Monte Carlo simulations, which are the true objective function value, not normalized. Most importantly, note that the best global solutions of the benchmarks (F04, F05, F11, and F14) are illustrated in the form of the semilogarithmic convergence plots. KH is short for KH II in the legends of the figures.

TABLE 4: Best normalized optimization results in fourteen benchmark functions. The values shown are the minimum objective function values found by each algorithm.

	ABC	ACO	BA	CS	DE	ES	GA	HS	KH	LKH	PBIL	PSO
F01	39.13	51.65	64.63	54.80	39.31	66.38	35.21	74.39	6.59	1.00	73.39	56.78
F02	13.81	52.37	68.76	37.85	18.34	52.09	5.64	41.98	16.07	1.00	36.30	40.23
F03	13.52	6.71	91.05	37.41	14.32	53.67	5.95	121.61	1.78	1.00	84.88	46.62
F04	309.00	1.26	3.0E8	9.9E6	7.7E4	4.6E8	282.60	5.5E8	645.76	1.00	1.2E9	1.2E7
F05	2.2E5	1.00	1.7E8	1.8E7	1.9E6	2.0E8	2.1E4	2.0E8	7.3E4	2.70	3.1E8	2.8E7
F06	1.2E6	4.9E6	6.1E7	7.6E6	3.9E6	1.8E8	3.1E6	1.2E8	1.3E6	1.00	1.8E8	2.4E7
F07	2.00	4.53	6.30	4.95	3.68	6.28	3.21	4.75	1.98	1.00	5.90	4.90
F08	10.40	70.89	54.16	15.03	12.74	109.61	17.46	58.83	5.56	1.00	70.98	19.22
F09	4.60	2.18	9.10	6.98	6.28	7.80	1.00	10.10	4.83	4.53	10.01	8.14
F10	560.93	236.20	703.61	265.75	929.67	893.67	280.77	553.77	265.62	1.00	1.1E3	495.02
F11	20.01	32.33	75.00	44.09	29.25	83.22	31.79	88.27	23.70	1.00	86.51	54.41
F12	39.39	18.51	45.36	28.77	34.87	48.27	23.82	48.37	4.08	1.00	45.44	36.44
F13	1.0E4	3.8E4	6.7E4	2.1E4	7.9E3	9.0E4	1.0E4	1.0E5	1.5E3	1.00	7.8E4	3.5E4
F14	595.00	470.00	6.5E3	1.7E3	633.50	4.5E3	592.00	5.8E3	113.00	1.00	7.0E3	1.8E3
Total	0	1	0	0	0	0	1	0	0	12	0	0

*The values are normalized so that the minimum in each row is 1.00. These are the absolute best minima found by each algorithm.

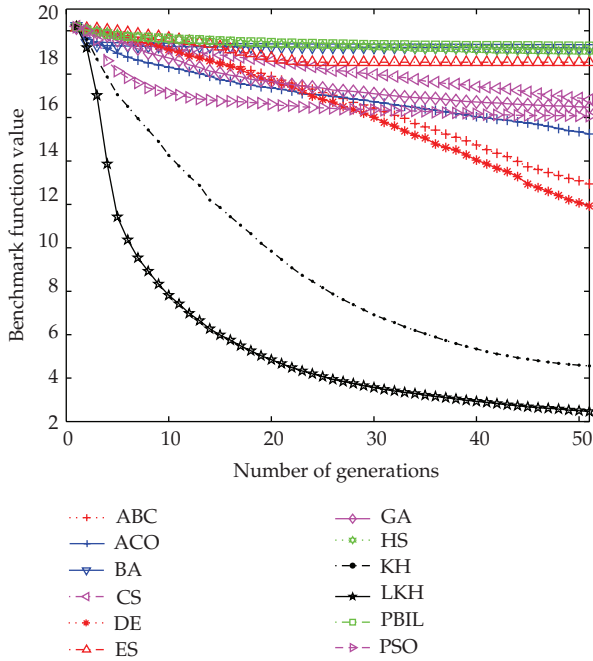


FIGURE 1: Comparison of the performance of the different methods for the F01 Ackley function.

Figure 1 shows the results obtained for the twelve methods when the F01 Ackley function is applied. From Figure 1, clearly, we can draw the conclusion that LKH is significantly superior to all the other algorithms during the process of optimization. For other algorithms, although slower, KH II eventually finds the global minimum close to LKH, while ABC, ACO, BA, CS, DE, ES, GA, HS, PBIL, and PSO fail to search the global minimum within the limited generations. Here, all the algorithms show the almost same starting

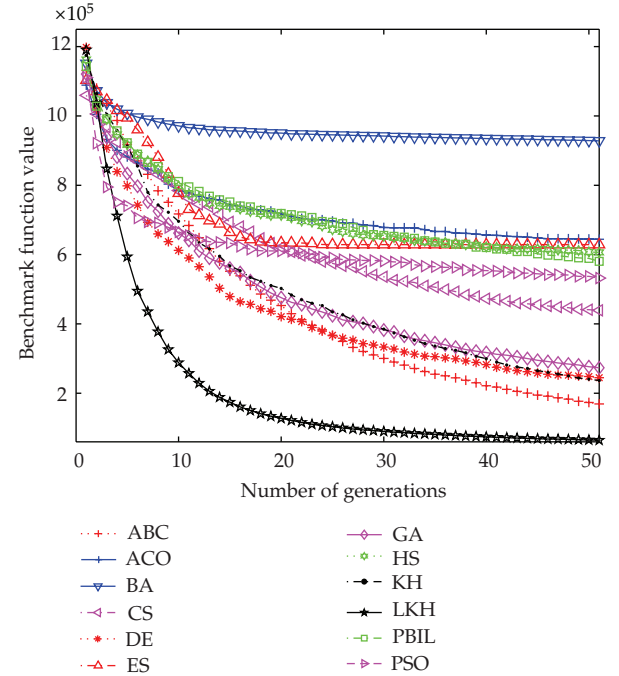


FIGURE 2: Comparison of the performance of the different methods for the F02 Fletcher-Powell function.

point; however, LKH outperforms them with fast and stable convergence rate.

Figure 2 illustrates the optimization results for F02 Fletcher-Powell function. In this multimodal benchmark problem, it is clear that LKH outperforms all other methods during the whole progress of optimization. Other algorithms do not manage to succeed in this benchmark function within maximum number of generations. At last, ABC and KH II converge to the value that is significantly inferior to LKH's.

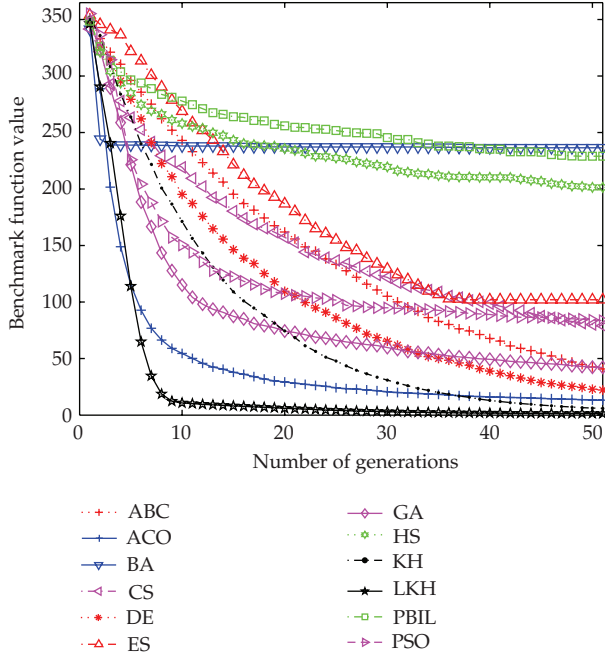


FIGURE 3: Comparison of the performance of the different methods for the F03 Griewank function.

Figure 3 shows the optimization results for F03 Griewank function. From Figure 3, we can see that the figure shows that there is a little difference between the performance of LKH and KH II. However, from Table 3 and Figure 3, we can conclude that, LKH performs better than KH II in this multimodal function. Through carefully looking at Figure 6, ACO has a fast convergence initially towards the known minimum, as the procedure proceeds LKH gets closer and closer to the minimum, while ACO comes into being premature and traps into the local minimum.

Figure 4 shows the results for F04 Penalty #1 function. From Figure 4, clearly, LKH outperforms all other methods during the whole progress of optimization in this multimodal function. Eventually, KH II performs the second best at finding the global minimum. Although slower later, DE performs the third best at finding the global minimum.

Figure 5 shows the performance achieved for F05 Penalty #2 function. For this multimodal function, similar to the F04 Penalty #2 function as shown in Figure 4, LKH is significantly superior to all the other algorithms during the process of optimization. Here, KH II shows a stable convergence rate in the whole optimization process and eventually it performs the second best at finding the global minimum that is significantly superior to the other algorithms.

Figure 6 shows the results achieved for the twelve methods when using the F06 Quartic (*with noise*) function. For this case, the figure shows that there is a little difference among the performance of DE, GA, KH II, and LKH. From Table 3 and Figure 6, we can conclude that LKH performs the best in this multimodal function. KH II, DE, and GA perform as well and have ranks of 2, 3, and 4, respectively. Through carefully looking at Figure 6, PSO has a fast convergence

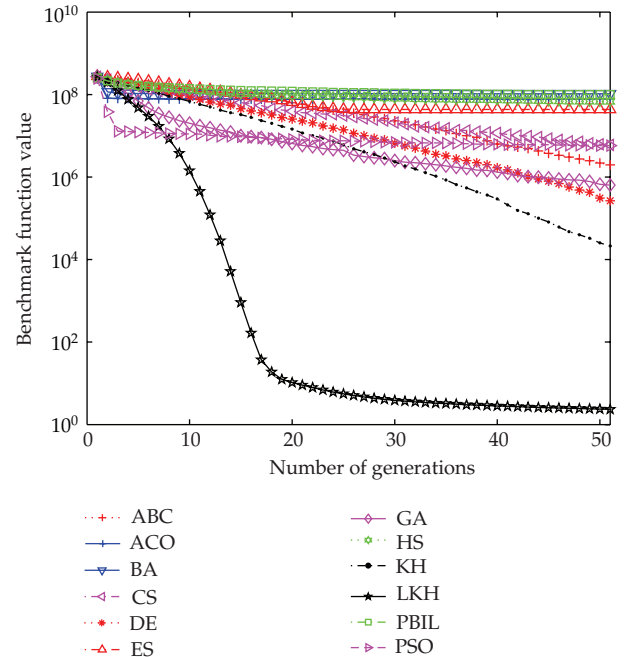


FIGURE 4: Comparison of the performance of the different methods for the F04 Penalty #1 function.

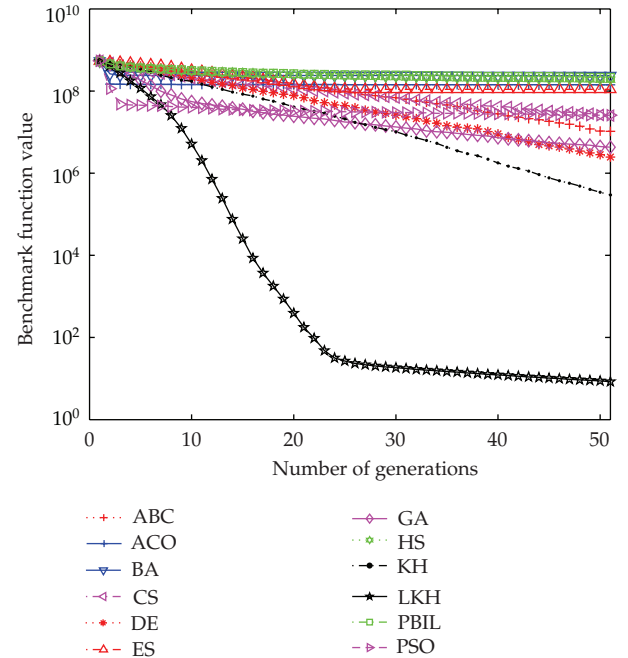


FIGURE 5: Comparison of the performance of the different methods for the F05 Penalty #2 function.

initially towards the known minimum; as the procedure proceeds, LKH gets closer and closer to the minimum, while PSO comes into being premature and traps into the local minimum.

Figure 7 shows the optimization results for the F07 Rastrigin function. In this multimodal benchmark problem,

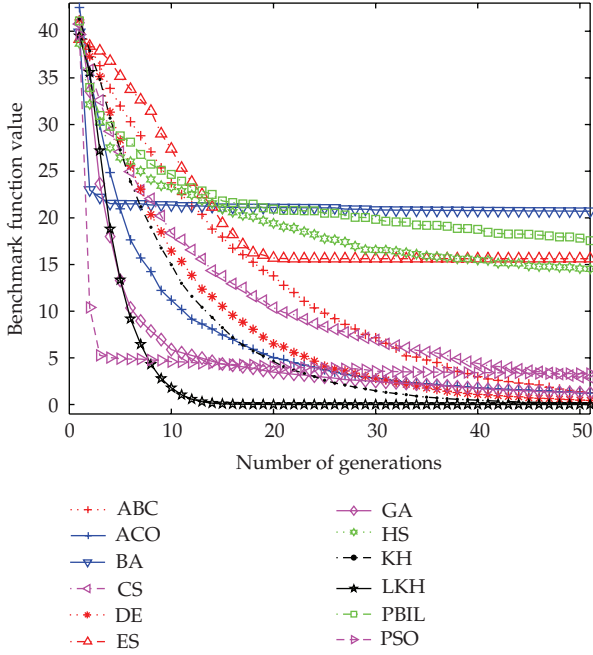


FIGURE 6: Comparison of the performance of the different methods for the F06 Quartic (*with noise*) function.

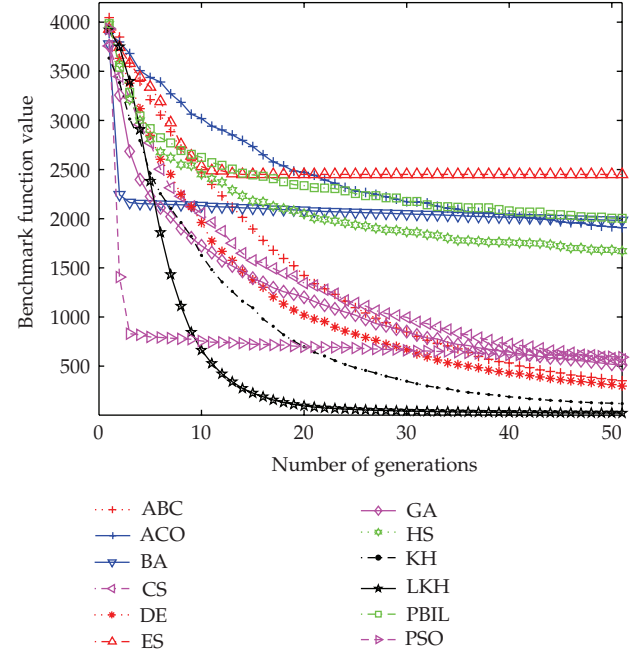


FIGURE 8: Comparison of the performance of the different methods for the F08 Rosenbrock function.

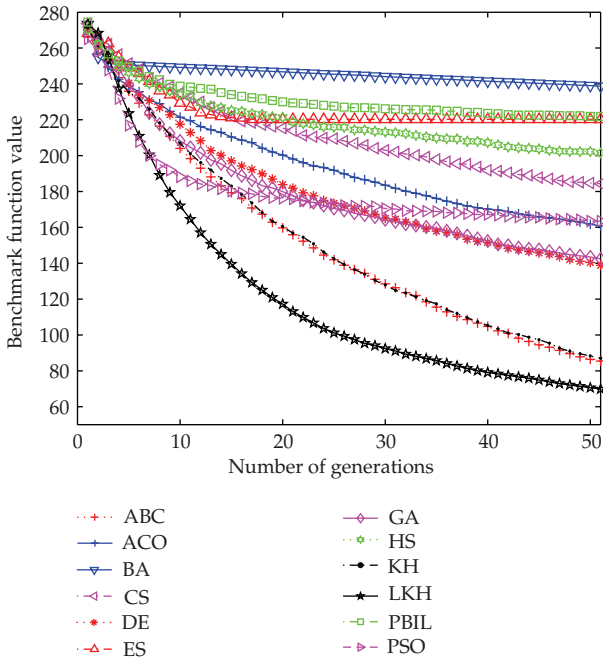


FIGURE 7: Comparison of the performance of the different methods for the F07 Rastrigin function.

it is obvious that LKH outperforms all other methods during the whole progress of optimization. For other algorithms, the figure shows that there is little difference between the performance of ABC and KH II. From Table 3 and Figure 7, we can conclude that, KH II performs slightly better than ABC in this multimodal function. In addition, other algorithms do

not manage to succeed in this benchmark function within the maximum number of generations.

Figure 8 shows the results for F08 Rosenbrock function. From Figure 8, we can conclude that LKH performs the best in this unimodal function. In addition, KH II, DE, and ACO perform very well and have ranks of 2, 3, and 4, respectively. Through carefully looking at Figure 8, PSO has a fast convergence initially towards the known minimum; however, it is outperformed by LKH after 10 generations. For other algorithms, they do not manage to succeed in this benchmark function within the maximum number of generations.

Figure 9 shows the equivalent results for the F09 Schwefel 2.26 function. From Figure 9, clearly, GA is significantly superior to other algorithms including LKH during the process of optimization, while ACO and ABC perform the second and the third best in this multimodal benchmark function, respectively. Unfortunately, LKH only performs the fourth in this multimodal benchmark function.

Figure 10 shows the results for F10 Schwefel 1.2 function. For this case, LKH, CS, KH II, and ACO perform the best and have ranks of 1, 2, 3, and 4, respectively. Looking carefully at Figure 7, LKH has the fastest and stable convergence rate at finding the global minimum and significantly outperforms all other approaches.

Figure 11 shows the results for F11 Schwefel 2.22 function. From Figure 11, similar to the F09 Schwefel 2.26 function as shown in Figure 9, it is clear that ABC is significantly superior to other algorithms including LKH during the process of optimization. For other algorithms, DE and KH II perform very well and have ranks of 2 and 3, respectively. Unfortunately, LKH only performs the tenth best in this unimodal benchmark function among the twelve methods.

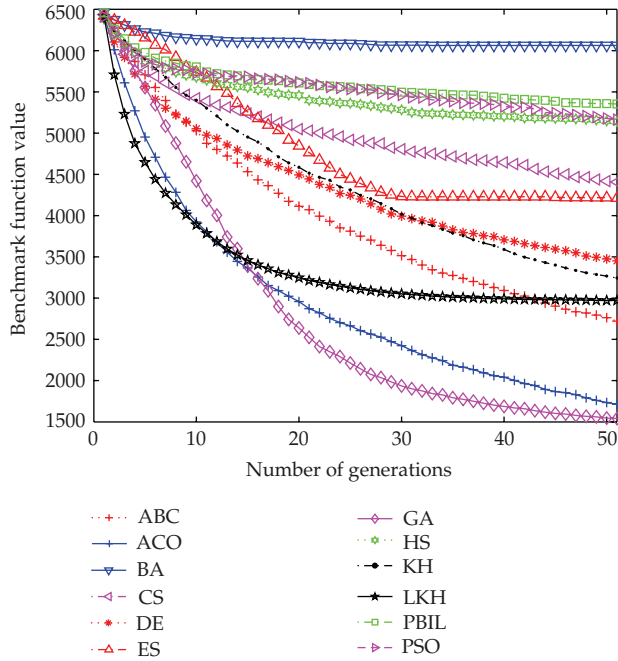


FIGURE 9: Comparison of the performance of the different methods for the F09 Schwefel 2.26 function.

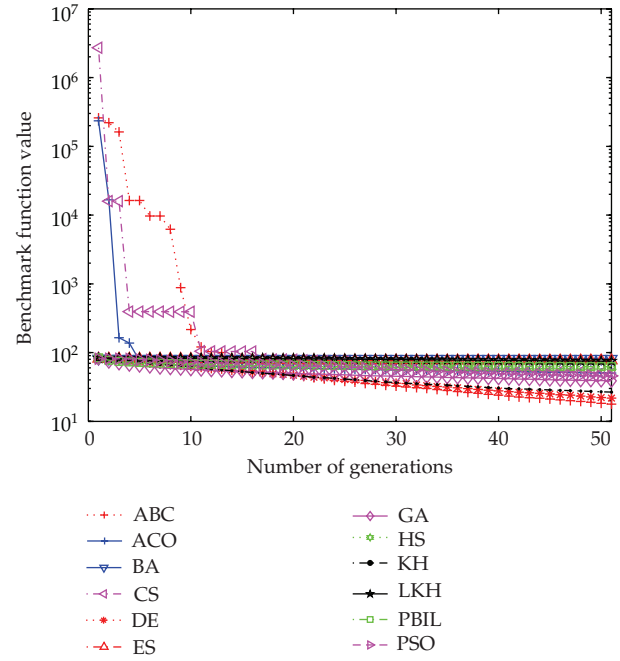


FIGURE 11: Comparison of the performance of the different methods for the F11 Schwefel 2.22 function.

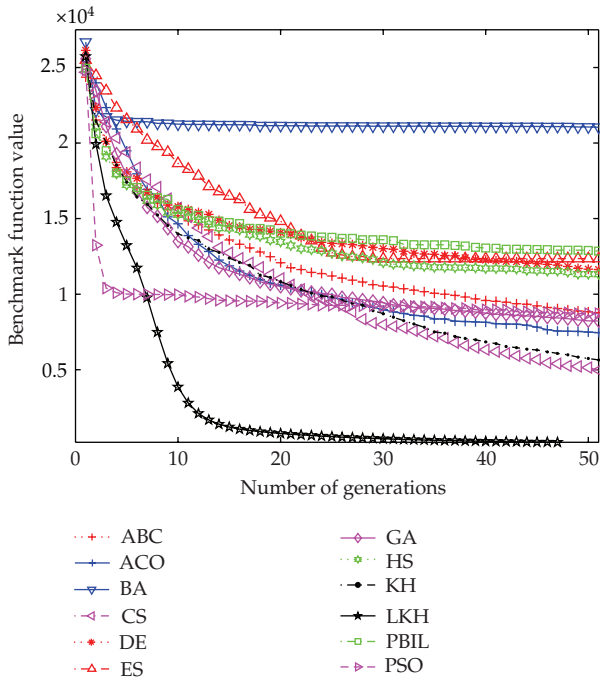


FIGURE 10: Comparison of the performance of the different methods for the F10 Schwefel 1.2 function.

Figure 12 shows the results for F12 Schwefel 2.21 function. Very clearly, LKH has the fastest convergence rate at finding the global minimum and significantly outperforms all other methods. For other algorithms, KH II and ACO that are only inferior to LKH perform very well and have ranks of 2 and 3, respectively.

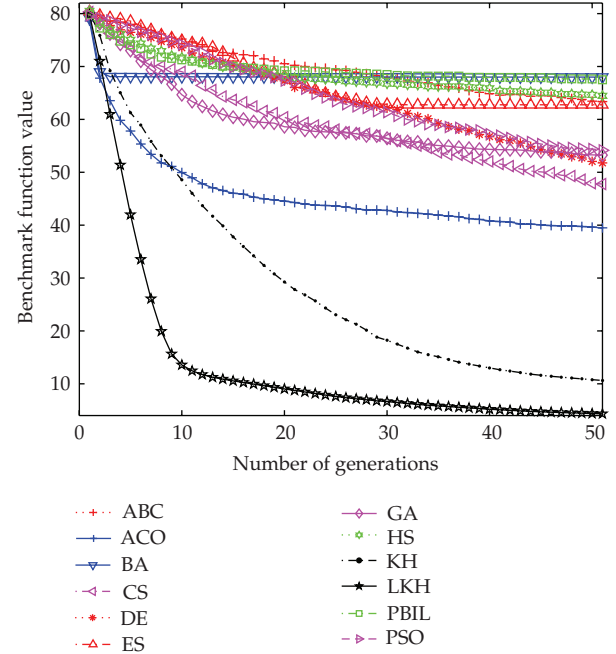


FIGURE 12: Comparison of the performance of the different methods for the F12 Schwefel 2.21 function.

Figure 13 shows the results for F13 Sphere function. From Figure 13, LKH shows the fastest convergence rate at finding the global minimum and significantly outperforms all other methods. In addition, KH II, DE, and ACO perform very well and have ranks of 2, 3, and 4, respectively.

Figure 14 shows the results for F14 Step function. Clearly, LKH shows the fastest convergence rate at finding the

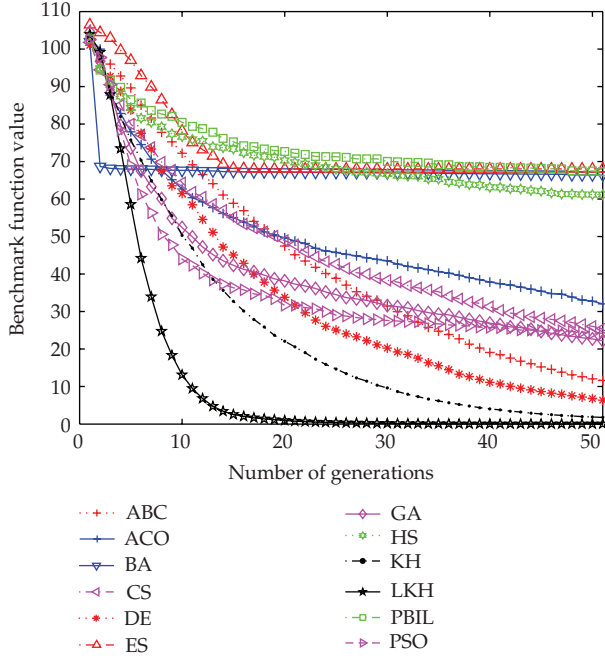


FIGURE 13: Comparison of the performance of the different methods for the F13 Sphere function.

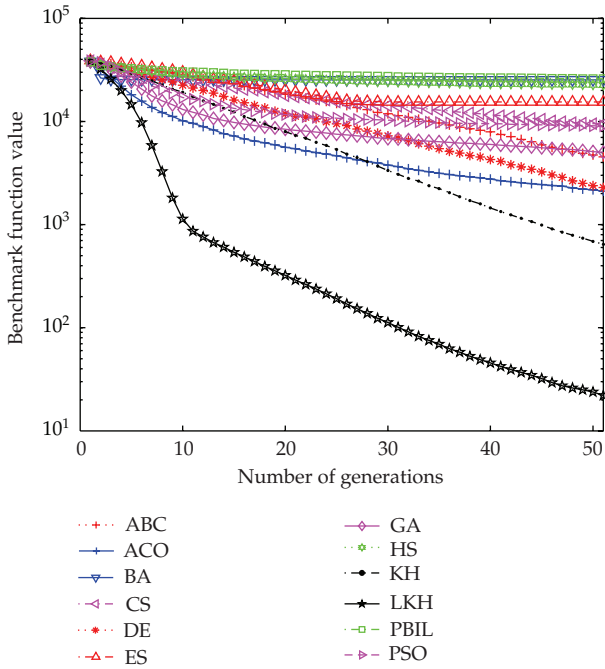


FIGURE 14: Comparison of the performance of the different methods for the F14 Step function.

global minimum and significantly outperforms all other approaches. Though slow, KH II performs the second best at finding the global minimum that is only inferior to the LKH.

From the above analyses about Figures 1–14, we can come to a conclusion that our proposed hybrid metaheuristic LKH algorithm significantly outperforms the other eleven

algorithms. In general, KH II is only inferior to LKH and performs the second best among twelve methods. ABC, ACO, DE, and GA perform the third best only inferior to the LKH and KH II; ABC and GA especially perform better than LKH on benchmark functions F11 and F09, respectively. Furthermore, the illustration of benchmarks F04, F05, F06, F08, and F10 shows that PSO has a faster convergence rate initially, while later, it converges slower and slower to the true objective function value.

4.2. Discussion. For all of the standard benchmark functions considered in this section, the LKH method has been demonstrated to perform better than, or at least highly competitive with, the standard KH and other eleven acclaimed state-of-the-art population-based methods. The advantages of LKH involve performing simply and easily and have few parameters to regulate. The work here proves the LKH to be robust, powerful, and effective over all types of benchmark functions.

Benchmark evaluating is a good way for testing the performance of the metaheuristic methods, but it is also not flawless and has some limitations. First, we did not do much work painstakingly to carefully regulate the optimization methods in this section. In general, different tuning parameter values in the optimization methods might lead to significant differences in their performance. Second, real-world optimization problems may have little of a relationship to benchmark functions. Third, benchmark tests may arrive at fully different conclusions if the grading criteria or problem setup changes. In our present work, we looked into the mean and best values obtained with some population size and after some number of iterations. However, we might reach different conclusions if, for example, we change the population size, or look at how many population size it needs to reach a certain function value, or if we change the iteration. Despite these caveats, the benchmark results represented here are prospective for LKH and show that this novel method might be capable of finding a niche among the plethora of population-based optimization methods.

Note that running time is a bottleneck to the implementation of many population-based optimization algorithms. If an algorithm converges too slowly, it will be impractical and infeasible, since it would take too long to search an optimal or suboptimal solution. LKH seems not to require an unreasonable amount of computational time; of the twelve comparative optimization methods used in this paper, LKH was the eleventh fastest. How to speed up the LKH's convergence is worthy of further study.

In our study, 14 benchmark functions have been applied to evaluate the performance of our LKH method; we will test our proposed method on more optimization problems, such as the high-dimensional ($d \geq 20$) CEC 2010 test suit [44] and the real-world engineering problems. Moreover, we will compare LKH with other optimization algorithms. In addition, we only consider the unconstrained function optimization in this study. Our future work consists of adding the other techniques into LKH for constrained optimization problems, such as constrained real-parameter optimization CEC 2010 test suit [45].

5. Conclusion and Future Work

Due to the limited performance of KH on complex problems, LLF operator has been introduced into the standard KH to develop a novel Lévy-flight krill herd (LKH) algorithm for optimization problems. In LKH, at first, original KH algorithm is applied to shrink the search region to a more promising area. Thereafter, LLF operator is implemented as a critical complement to perform the local search to exploit the limited area intensively to get better solutions. In principle, KH takes full advantage of the three motions in the population and has experimentally demonstrated very good performance on the multimodal problems. In a rugged region of the fitness landscape, KH may fail to proceed to better solutions [27]. Then, LLF operator is adaptively launched to reboost the search. The LKH makes an attempt at taking merits of the KH and Lévy flight in order to avoid all krill getting trapped in inferior local optimal regions. The LKH enables the krill to have more diverse exemplars to learn from as the krill are updated each generation and also form new krill to search in a larger search space. With both techniques combined, LKH can balance exploration and exploitation and effectively solve complex multimodal problems.

Furthermore, this new method can speed up the global convergence rate without losing the strong robustness of the basic KH. From the analysis of the experimental results, we can see that the Lévy-flight KH clearly improves the reliability of the global optimality and they also enhance the quality of the solutions. Based on the results of the twelve methods on the test problems, we can conclude that LKH significantly improves the performances of the KH on most multimodal and unimodal problems. In addition, LKH is simple and implements easily.

In the field of numerical optimization, there are considerable issues that deserve further study, and some more efficient optimization methods should be developed depending on the analysis of specific engineering problem. Our future work will focus on the two issues. On the one hand, we would apply our proposed LKH method to solve real-world civil engineering optimization problems [46], and, obviously, LKH can be a promising method for these optimization problems. On the other hand, we would develop more new metaheuristic methods to solve optimization problems more efficiently and effectively.

Acknowledgments

This work was supported by the State Key Laboratory of Laser Interaction with Material Research Fund under Grant no. SKLLIM0902-01 and Key Research Technology of Electric-discharge Nonchain Pulsed DF Laser under Grant no. LXJJ-11-Q80.

References

- [1] S. Gholizadeh and F. Fattahi, "Design optimization of tall steel buildings by a modified particle swarm algorithm," *The Structural Design of Tall and Special Buildings*. In press.
- [2] S. Talatahari, R. Sheikholeslami, M. Shadfaran, and M. Pourbaba, "Optimum design of gravity retaining walls using charged system search algorithm," *Mathematical Problems in Engineering*, vol. 2012, Article ID 301628, 10 pages, 2012.
- [3] X. S. Yang, A. H. Gandomi, S. Talatahari, and A. H. Alavi, *Metaheuristics in Water, Geotechnical and Transport Engineering*, Elsevier, Waltham, Mass, USA, 2013.
- [4] A. H. Gandomi, X. S. Yang, S. Talatahari, and A. H. Alavi, *Metaheuristic Applications in Structures and Infrastructures*, Elsevier, Waltham, Mass, USA, 2013.
- [5] S. Gholizadeh and A. Barzegar, "Shape optimization of structures for frequency constraints by sequential harmony search algorithm," *Engineering Optimization*. In press.
- [6] S. Chen, Y. Zheng, C. Cattani, and W. Wang, "Modeling of biological intelligence for SCM system optimization," *Computational and Mathematical Methods in Medicine*, vol. 2010, Article ID 769702, 10 pages, 2012.
- [7] X. S. Yang, *Nature-Inspired Metaheuristic Algorithms*, Luniver Press, Frome, UK, 2nd edition, 2010.
- [8] X. S. Yang, *Engineering Optimization: An Introduction with Metaheuristic Applications*, Wiley & Sons, NJ, USA, 2010.
- [9] G. Wang, L. Guo, H. Duan, L. Liu, H. Wang, and M. Shao, "Path planning for uninhabited combat aerial vehicle using hybrid meta-heuristic DE/BBO algorithm," *Advanced Science, Engineering and Medicine*, vol. 4, no. 6, pp. 550–564, 2012.
- [10] G. Wang, L. Guo, H. Duan, L. Liu, and H. Wang, "A bat algorithm with mutation for UCAV path planning," *The Scientific World Journal*, vol. 2012, Article ID 418946, 15 pages, 2012.
- [11] H. Duan, W. Zhao, G. Wang, and X. Feng, "Test-sheet composition using analytic hierarchy process and hybrid metaheuristic algorithm TS/BBO," *Mathematical Problems in Engineering*, vol. 2012, Article ID 712752, 22 pages, 2012.
- [12] W.-H. Ho and A. L.-F. Chan, "Hybrid Taguchi-differential evolution algorithm for parameter estimation of differential equation models with application to HIV dynamics," *Mathematical Problems in Engineering*, vol. 2011, Article ID 514756, 14 pages, 2011.
- [13] D. E. Goldberg, *Genetic Algorithms in Search, Optimization and Machine Learning*, Addison-Wesley, New York, NY, USA, 1998.
- [14] M. Shahsavar, A. A. Najafi, and S. T. A. Niaki, "Statistical design of genetic algorithms for combinatorial optimization problems," *Mathematical Problems in Engineering*, vol. 2011, Article ID 872415, 17 pages, 2011.
- [15] G. Wang and L. Guo, "A novel hybrid bat algorithm with harmony search for global numerical optimization," *Journal of Applied Mathematics*. In press.
- [16] X. S. Yang and A. H. Gandomi, "Bat algorithm: a novel approach for global engineering optimization," *Engineering Computations*, vol. 29, no. 5, pp. 464–483, 2012.
- [17] R. Storn and K. Price, "Differential evolution—a simple and efficient heuristic for global optimization over continuous spaces," *Journal of Global Optimization*, vol. 11, no. 4, pp. 341–359, 1997.
- [18] A. H. Gandomi, X.-S. Yang, S. Talatahari, and S. Deb, "Coupled eagle strategy and differential evolution for unconstrained and constrained global optimization," *Computers & Mathematics with Applications*, vol. 63, no. 1, pp. 191–200, 2012.
- [19] A. H. Gandomi and A. H. Alavi, "Multi-stage genetic programming: a new strategy to nonlinear system modeling," *Information Sciences*, vol. 181, no. 23, pp. 5227–5239, 2011.
- [20] Z. W. Geem, J. H. Kim, and G. V. Loganathan, "A new heuristic optimization algorithm: harmony search," *Simulation*, vol. 76, no. 2, pp. 60–68, 2001.

- [21] G. Wang and L. Guo, "Hybridizing harmony search with biogeography based optimization for global numerical optimization," *Journal of Computational and Theoretical Nanoscience*. In press.
- [22] J. Kennedy and R. Eberhart, "Particle swarm optimization," in *Proceedings of the IEEE International Conference on Neural Networks*, pp. 1942–1948, December 1995.
- [23] S. Talatahari, M. Kheirollahi, C. Farahmandpour, and A. H. Gandomi, "A multi-stage particle swarm for optimum design of truss structures," *Neural Computing & Applications*. In press.
- [24] A. H. Gandomi, G. J. Yun, X. -S. Yang, and S. Talatahari, "Chaos-enhanced accelerated particle swarm optimization," *Communications in Nonlinear Science and Numerical Simulation*, vol. 18, no. 2, pp. 327–340, 2013.
- [25] A. H. Gandomi, X.-S. Yang, and A. H. Alavi, "Cuckoo search algorithm: a metaheuristic approach to solve structural optimization problems," *Engineering with Computers*, vol. 29, no. 1, pp. 1–19, 2013.
- [26] G. Wang, L. Guo, H. Duan, L. Liu, H. Wang, and W. Jianbo, "A hybrid meta-heuristic DE/CS algorithm for UCAV path planning," *Journal of Information and Computational Science*, vol. 9, no. 16, pp. 1–8, 2012.
- [27] A. H. Gandomi and A. H. Alavi, "Krill Herd: a new bio-inspired optimization algorithm," *Communications in Nonlinear Science and Numerical Simulation*, vol. 17, no. 12, pp. 4831–4845, 2012.
- [28] G. Wang, L. Guo, H. Duan, H. Wang, L. Liu, and J. Li, "Incorporating mutation scheme into krill herd algorithm for global numerical optimization," *Neural Computing and Applications*. In press.
- [29] G. Wang, L. Guo, H. Duan, H. Wang, and L. Liu, "A new improved firefly algorithm for global numerical optimization," *Journal of Computational and Theoretical Nanoscience*. In press.
- [30] G. Wang, L. Guo, H. Duan, H. Wang, L. Liu, and M. Shao, "A hybrid meta-heuristic DE/CS algorithm for UCAV three-dimension path planning," *The Scientific World Journal*, vol. 2012, Article ID 583973, 11 pages, 2012.
- [31] G. Wang, L. Guo, A. H. Gandomi et al., "A new improved krill herd algorithm for global numerical optimization," *Neurocomputing*. In press.
- [32] S. Yang and J. Lee, "Multi-basin particle swarm intelligence method for optimal calibration of parametric Lévy models," *Expert Systems with Applications*, vol. 39, no. 1, pp. 482–493, 2012.
- [33] P. Barthelemy, J. Bertolotti, and D. S. Wiersma, "A Lévy flight for light," *Nature*, vol. 453, no. 7194, pp. 495–498, 2008.
- [34] A. Natarajan, S. Subramanian, and K. Premalatha, "A comparative study of cuckoo search and bat algorithm for Bloom filter optimisation in spam filtering," *International Journal of Bio-Inspired Computation*, vol. 4, no. 2, pp. 89–99, 2012.
- [35] X. Yao, Y. Liu, and G. Lin, "Evolutionary programming made faster," *IEEE Transactions on Evolutionary Computation*, vol. 3, no. 2, pp. 82–102, 1999.
- [36] D. Simon, "Biogeography-based optimization," *IEEE Transactions on Evolutionary Computation*, vol. 12, no. 6, pp. 702–713, 2008.
- [37] X. Li, J. Wang, J. Zhou, and M. Yin, "A perturb biogeography based optimization with mutation for global numerical optimization," *Applied Mathematics and Computation*, vol. 218, no. 2, pp. 598–609, 2011.
- [38] D. Karaboga and B. Basturk, "A powerful and efficient algorithm for numerical function optimization: artificial bee colony (ABC) algorithm," *Journal of Global Optimization*, vol. 39, no. 3, pp. 459–471, 2007.
- [39] M. Dorigo and T. Stutzle, *Ant Colony Optimization*, MIT Press, Cambridge, Mass, USA, 2004.
- [40] X. S. Yang and S. Deb, "Engineering optimisation by cuckoo search," *International Journal of Mathematical Modelling and Numerical Optimisation*, vol. 1, no. 4, pp. 330–343, 2010.
- [41] H.-G. Beyer, *The Theory of Evolution Strategies*, Springer, Berlin, Germany, 2001.
- [42] B. Shumeet, "Population-Based Incremental Learning: A Method for Integrating Genetic Search Based Function Optimization and Competitive Learning," Tech. Rep. CMU-CS-94-163, Carnegie Mellon University, Pittsburgh, Pa, USA, 1994.
- [43] G. Wang, L. Guo, H. Duan, L. Liu, and H. Wang, "Dynamic deployment of wireless sensor networks by biogeography based optimization algorithm," *Journal of Sensor and Actuator Networks*, vol. 1, no. 2, pp. 86–96, 2012.
- [44] K. Tang, X. Li, P. N. Suganthan, Z. Yang, and T. Weise, "Benchmark functions for the CEC'2010 special session and competition on large scale global optimization," Inspired Computation and Applications Laboratory, USTC, Hefei, China, 2010.
- [45] R. Mallipeddi and P. Suganthan, "Problem definitions and evaluation criteria for the CEC 2010 Competition on Constrained Real-Parameter Optimization," Nanyang Technological University, Singapore, 2010.
- [46] P. Lu, S. Chen, and Y. Zheng, "Artificial intelligence in civil engineering," *Mathematical Problems in Engineering*, vol. 2012, Article ID 145974, 22 pages, 2012.

Research Article

Simultaneous Topology, Shape, and Sizing Optimisation of Plane Trusses with Adaptive Ground Finite Elements Using MOEAs

Norapat Noilublao¹ and Sujin Bureerat²

¹ Department of Engineering Management, Faculty of Science and Technology, Rajabhat Maha Sarakham University, Maha Sarakham 44000, Thailand

² Department of Mechanical Engineering, Faculty of Engineering, Khon Kaen University, Khon Kaen 40002, Thailand

Correspondence should be addressed to Sujin Bureerat; sujbur@kku.ac.th

Received 4 October 2012; Revised 7 January 2013; Accepted 8 January 2013

Academic Editor: Sheng-yong Chen

Copyright © 2013 N. Noilublao and S. Bureerat. This is an open access article distributed under the Creative Commons Attribution License, which permits unrestricted use, distribution, and reproduction in any medium, provided the original work is properly cited.

This paper proposes a novel integrated design strategy to accomplish simultaneous topology shape and sizing optimisation of a two-dimensional (2D) truss. An optimisation problem is posed to find a structural topology, shape, and element sizes of the truss such that two objective functions, mass and compliance, are minimised. Design constraints include stress, buckling, and compliance. The procedure for an adaptive ground elements approach is proposed and its encoding/decoding process is detailed. Two sets of design variables defining truss layout, shape, and element sizes at the same time are applied. A number of multiobjective evolutionary algorithms (MOEAs) are implemented to solve the design problem. Comparative performance based on a hypervolume indicator shows that multiobjective population-based incremental learning (PBIL) is the best performer. Optimising three design variable types simultaneously is more efficient and effective.

1. Introduction

Nowadays, the use of artificial intelligence techniques in a wide variety of engineering applications has become commonplace as a means of responding to needs to deal with complicated systems which classical mathematical methods cannot solve [1, 2]. Such techniques include, for example, neural networks, fuzzy sets, and evolutionary computation [1]. Applications of evolutionary algorithms (EAs) for tackling engineering design problems have become increasingly popular due to certain advantages. The methods are simple to use, robust, and capable of dealing with almost any kind of design problem, for example, structural design [3–8], supply chain management [9], quay management [10], sensor placement [11], and manufacturing tasks [12, 13]. Design variables can be discrete, continuous, and combinatorial. They can search for global optima effectively. More attractively, the multiobjective versions of evolutionary algorithms can be used to explore a Pareto front within one optimisation run. Nevertheless, EAs have some unavoidable drawbacks as they

have a low convergence rate and a lack of consistency due to randomisation being used in a search process. As a result, there are always needs to improve EAs performance. The hybridisation of existing methods with local search techniques [14] or other EA concepts is a means to achieve such a goal [12, 15]. Also, the use of surrogate models for design problems with expensive function evaluations is an effective way to enhance EAs [16]. When using EAs to solve a new type of design problem, it is always useful to compare the search performance of a number of EAs for such a problem. This is because one particular EA may be efficient for one design problem but it is unlikely to be the best performer for other types of problems [17].

A truss structure is one of the most used structures in engineering applications. Using such a structure is said to be advantageous, since they are simple and inexpensive to construct. It can be employed for many engineering purposes, for example, a billboard structure, a factory roof structure, a bridge structure, and a wind turbine tower. In the past, the design of such a structure was usually carried out in such

a way that an initial structural configuration was formed by an experienced engineering designer for conceptual design. The classical civil engineering design approach is then applied in the preliminary and detailed design stages. In recent years, considerable research work towards design/optimisation of trusses and frames has been conducted. Thousands of research papers have been published (e.g., [18–28]). For truss optimisation, design variables can be classified as topological [23, 29–33], shape, and sizing variables [5, 7, 34–38]. In the past, a designer traditionally performs topology optimisation in the first design phase to obtain an initial structural layout. Shape and sizing optimisation are then conducted to further improve the structure. This can be called a multilevel or multistage optimisation process. Nevertheless, it has been investigated that the better design process is to perform topology, shape, and sizing optimisation simultaneously [28]. Combined topology and sizing [21, 24], shape and sizing [34–38], topology and shape [18, 20, 22], and all three variable types [19, 26, 28, 39–41] have been recently investigated.

One of the most effective design strategies for truss topology optimisation is the use of a ground element approach. The topological design process based upon ground elements can be tackled by both gradient-based [21, 31, 42] and population-based optimisers [28, 29, 33]. The gradient-based methods have advantages in that they have high convergence rate and search consistency (obtaining the same design solution when solving the same problem several times). They are powerful for a large-scale topology design problem. Nevertheless, the population-based or evolutionary approaches have other advantages, since they are more robust and do not require function derivatives for searching. Moreover, for multiobjective design cases, evolutionary algorithms have a special feature: to explore a nondominated front within one optimisation run. This, together with the capability of solving all kinds of design problems, makes the evolutionary algorithms popular among researchers and designers.

This paper presents a novel design strategy to achieve simultaneous topology shape and sizing design of a planar truss structure. A multiobjective design problem with two different sets of design variables is assigned in this work. The problem is minimising structural mass and compliance subject to stress, buckling, and compliance constraints. The first set of design variables is used to design structural topology and truss element sizing while structural shape variables are added to the second set of design variables. These two design variable sets in combination with the adaptive ground element concept result in two multiobjective design problems. MOEAs employed to tackle the problems are second version of strength Pareto evolutionary algorithm (SPEA) [43], population-based incremental learning [44], archived multiobjective simulated annealing (AMOS) [45], multiobjective particle swarm optimisation (MPSO) [46], and unrestricted population size evolutionary multiobjective optimisation algorithm (UPS-EMOA) [47]. The results obtained from using the various optimisers are compared and discussed. It is shown that the second design variables set which includes all types of design variables is superior to the first set.

The rest of the paper is organised as follows. Section 2 briefly details MOEAs. A multiobjective design problem is

expressed in Section 3. Section 4 details the decoding/encoding procedures for simultaneous topology, shape, and sizing design variables with adaptive ground elements. Design results and comparative performance are shown in Section 5 while conclusions are drawn in Section 6.

2. Multiobjective Evolutionary Algorithms

The field of multiobjective evolutionary optimisation is one of the hottest issues in evolutionary computation. The most outstanding ability of MOEAs is that they can explore a Pareto front within one simulation run. This in combination with their simplicity, robustness, and capability of dealing with all kind of variables makes this kind of optimiser more popular and attractive. MOEAs search mechanisms are based on a population of design solutions, which work in such a way that a population is evolved iteration by iteration. A matrix called an external Pareto archive is used to collect nondominated solutions iteratively. The Pareto archive is updated until a termination criterion is fulfilled. The MOEAs used for a comparative performance test in this paper are given below.

2.1. Strength Pareto Evolutionary Algorithm. SPEA was proposed by Zitzler and Thiele [48], and later its improved version SPEA2 [43]. The search procedure starts with an initial population and an external Pareto set. Fitness values are assigned to the population based upon the levels of domination and crowding. A set of solutions are then selected to a mating pool by means of a binary tournament selection operator. A new population is produced using crossover and mutation on those selected individuals. The updated external Pareto solutions are the nondominated solutions of the union set of the previous external Pareto set and the new population. In cases that the Pareto archive is full, the nearest neighbourhood technique is invoked to remove some design solutions from the archive. The Pareto archive is updated repeatedly until the termination criterion is met.

2.2. Population-Based Incremental Learning. The algorithm of multiobjective PBIL [44] starts with an external Pareto archive and initial probability matrix having all elements set to be 0.5. A set of binary design solutions are then created corresponding to the probability matrix while their function values are evaluated. The Pareto archive is updated with the nondominated solutions of the new population and the members of the previous Pareto archive. In cases that the number of nondominated solutions exceeds the predefined archive size, the normal line method is activated to remove some members from the archive. The probability matrix and the Pareto archive are iteratively updated until the termination criteria are fulfilled.

2.3. Archived Multiobjective Simulated Annealing. Simulated Annealing (SA) is one of the most popular random-directed optimisers. It has long been used in a wide variety of design applications [49, 50]. The method is based upon mimicking the random behaviour of molecules during the annealing

process, which involves slow cooling from a high temperature. For AMOSA [45], the method starts with initial temperature, a population, and a Pareto archive. A simple downhill technique is then applied to improve the population and update the archive for a few iterations. Then, a parent design solution is randomly chosen from the archive and it is used to generate a child or candidate solution by means of mutation. The parent is replaced by its offspring if the offspring dominates it. In cases that the parent is nondominated by the offspring, the parent still has a probability of being replaced. Such a probability is based on Boltzmann probability and the amount of domination between them. As the children are created, the Pareto archive is updated while the annealing temperature is reduced iteratively until a termination condition is met. An archiving technique for this algorithm is called a clustering technique.

2.4. Multiobjective Particle Swarm Optimisation. The particle swarm optimisation method uses real codes and searches for an optimum by mimicking the movement of a flock of birds, which aim to find food [46]. The search procedure herein is based on the particle swarm concepts combined with the use of an external Pareto archiving scheme. Starting with an initial set of design solutions (viewed as particles) as well as their initial velocities and objective function values, an initial Pareto archive is filled with the nondominated solutions obtained from sorting the initial population. A new population is then created by using the particle swarm updating strategy where the global best solution is randomly selected from the external Pareto archive. Afterwards, the external archive is updated by the nondominated solutions of the union set of the new population and the previous nondominated solutions. In cases that the number of nondominated solutions is too large, the adaptive grid algorithm [51] is employed to properly remove some solutions from the archive. The Pareto archive is repeatedly improved until fulfilling the termination criteria.

2.5. Unrestricted Population Size Evolutionary Multiobjective Optimisation Algorithm. The unrestricted population-size EMO algorithm was proposed by Aittokoski and Miettinen [47]. Similarly to the nondominated sorting genetic algorithm (NSGAII) [52], this optimiser uses a population to contain nondominated solutions, but its population size is unlimited. Some solutions from an initial population are randomly selected to produce some offspring by using a differential evolution operator. A new population contains nondominated solutions sorted from the combination of the offspring and the current population. The method has an unrestricted population size, therefore this somewhat provides population diversity. The optimiser is usually terminated with the maximum number of function evaluations.

3. Topological Design

Structural topology optimisation of trusses using the ground element approach can be performed in such a way that

ground finite elements, all possible combinations of predefined nodes in the given design domain, are created in the initial stage. Topological design variables determine elements' cross-sectional areas. After an optimisation run, elements with very small sizes will be removed from the structure while other elements are retained as truss members. With such a concept, an initial structural configuration is achieved. In this work, the biobjective design problem for a 2D truss with simultaneous topology shape and sizing design variables can be expressed as follows:

$$\begin{aligned} \min \quad & \{\text{mass}, c\}, \\ \text{subject to} \quad & \sigma_{\max} \leq \sigma_{\text{al}}, \\ & \lambda_i \leq 1, \\ & c \leq c_{\text{al}}, \\ & \mathbf{x} \in \Omega, \end{aligned} \tag{1}$$

$$\tag{2}$$

where mass is structural mass, c is structural compliance, c_{al} is allowable compliance, and σ_{\max} is the maximum stress on truss elements. $\sigma_{\text{al}} = \sigma_{yt}/N_F$ is an allowable stress, λ_i is a buckling factor for each element (defined as the ratio of applied load to critical load), σ_{yt} is yield strength, N_F is the factor for safety, \mathbf{x} is a vector of design variables, and Ω is a design domain of \mathbf{x} .

The first design objective, structural mass, is set to minimise cost while minimising the second objective, which is equivalent to structural stiffness maximisation. The stress and buckling constraints are assigned for safety requirements while the compliance constraint is imposed so as to obtain reasonable structural layouts. For one evaluation, with the input design variables, a finite element (FE) model of a truss is obtained and the FE analysis is performed. Having obtained nodal displacement and axial stresses of truss elements, the local buckling factor for each element can then be computed.

4. Adaptive Ground Elements

Two design variables sets are assigned in this paper. The first set is created for simultaneous topology and sizing optimisation. Figure 1 shows a rectangular design domain sized $W \times H$ for a 2D truss structure used in this study. The structure is subjected to point load $F = 500$ N at the top right-hand corner of the domain [33]. The width was set to be constant at 2 meters while the domain height could be varied in the range of $[H_{\min}, H_{\max}] = [0.25, 1]$ meter. Fixed boundary conditions were assigned at the left edge of the domain as shown.

Given that an array of predefined nodes is defined, ground elements as the combinations between the nodes are formed as shown in Figure 2. With the parameters n_x and n_y being the numbers of equispaced nodes in the x and y directions, respectively, $n_x \times n_y$ nodal positions were then generated where, in this study, $n_x \in \{3, 4, 5\}$ and $n_y \in \{2, 3, 4\}$. The parameters n_x and n_y are the numbers of rows and columns of an input node array, respectively. The total number of ground elements as $N_e = (n_x - 1)n_y + 3(n_x - 1)(n_y - 1)$ node combinations could be obtained as shown in Figure 2.

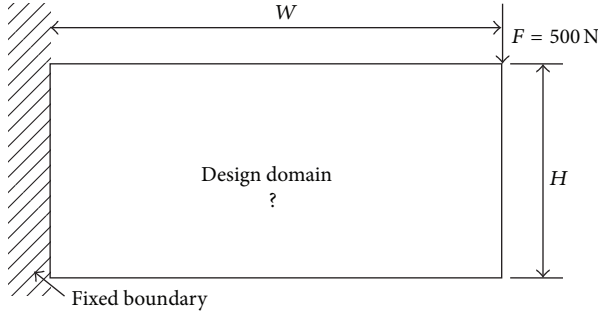


FIGURE 1: Design domain.

The design variables include the parameters H , n_x , and n_y and the diameters of the ground elements. Given that $n_{x,\max}$ and $n_{y,\max}$ are the maximum values for n_x and n_y , respectively, the possible maximum number of design variables is set as $N_{e,\max} + 3$ where $N_{e,\max} = (n_{x,\max} - 1)n_{y,\max} + 3(n_{x,\max} - 1)(n_{y,\max} - 1)$. The computational steps for design variables decoding were as follows.

Input. \mathbf{x} , sized $(N_{e,\max} + 3) \times 1$; $x_i \in [0, 1]$.

- (1) Set $H = H_{\min} + x_1(H_{\max} - H_{\min})$, $n_x = \text{round}(n_{x,\min} + x_2(n_{x,\max} - n_{x,\min}))$, and $n_y = \text{round}(n_{y,\min} + x_3(n_{y,\max} - n_{y,\min}))$.
- (2) Compute $N_e = (n_x - 1)n_y + 3(n_x - 1)(n_y - 1)$.
- (3) Generate $n_x \times n_y$ structural nodes, and N_e ground elements.
- (4) Assign element diameters. Set $y_j = 4x_i$ for $i = 4, \dots, N_e + 3$ and $j = 1, \dots, N_e$, which means $y_j \in [0, 4]$.
- (5) For $j = 1$ to N_e

- (5.1) If $\text{round}(y_j) = 0$, set $d_j = 0.000001$ m
- (5.2) If $\text{round}(y_j) = 1$, set $d_j = 0.01$ m
- (5.3) If $\text{round}(y_j) = 2$, set $d_j = 0.02$ m
- (5.4) If $\text{round}(y_j) = 3$, set $d_j = 0.03$ m
- (5.5) If $\text{round}(y_j) = 4$, set $d_j = 0.04$ m

End

- (6) Assign fixed boundary conditions for all nodes at $x = 0$.
- (7) Apply the y -direction point load at the last node number.

Output. Nodal positions, ground element connections, boundary conditions, force vector, and elements' diameters.

The function $\text{round}(x)$ gives the nearest integer to x . Although the design vector is sized $(N_{e,\max} + 3) \times 1$, only $N_e + 3$ elements were used for each evaluation. The design variables are said to be mixed integer/continuous, which are simpler to deal with by using MOEAs. After having the nondominated solutions, elements with 0.000001 m diameter (or the case of

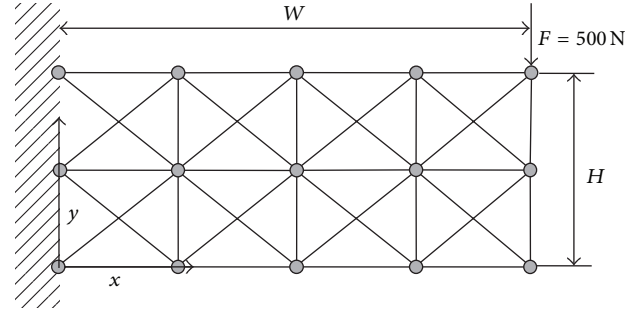


FIGURE 2: Adaptive ground elements.

round(y_j) = 0) were deleted from the ground structure to form a structural layout. A small element diameter is assigned in order to prevent singularity in a global stiffness matrix of a finite element model.

The second design variables set is an extension of the first set where parameters for nodal positions are added. For this study, initial positions of the truss joint are set as an array as the first design variables set shown in Figure 2. Additional shape design parameters determine the position changes of those nodes in x - and y -directions. All truss nodal positions except the fixed joints and the top row nodes are assigned to be varied in both x - and y -directions during an optimisation process. The top row nodal positions are allowed to be changed in the x direction in order to keep all top row nodes at the same level. As a result, the number of additional shape variables is $N_{sh} = (n_x - 1)(2n_y - 1)$. Therefore, the possible maximum number of design variables for this case is $N_{e,\max} + N_{sh,\max} + 3$ where $N_{sh,\max} = (n_{x,\max} - 1)(2n_{y,\max} - 1)$. The computational steps for design vector encoding can be given as follows.

Input. \mathbf{x} , sized $(N_{e,\max} + N_{sh,\max} + 3) \times 1$; $x_i \in [0, 1]$.

- (1) Set $H = H_{\min} + x_1(H_{\max} - H_{\min})$, $n_x = \text{round}(n_{x,\min} + x_2(n_{x,\max} - n_{x,\min}))$, and $n_y = \text{round}(n_{y,\min} + x_3(n_{y,\max} - n_{y,\min}))$.
- (2) Compute $N_e = (n_x - 1)n_y + 3(n_x - 1)(n_y - 1)$.
- (3) Compute $N_{sh,x} = n_y(n_x - 1)$ and $N_{sh,y} = (n_x - 1)(n_y - 1)$.
- (4) Compute the move limit for x -direction nodal position as $\Delta x_{\min} = -(W/2/n_{x,\max} - 0.01)$, and $\Delta x_{\max} = W/2/n_{x,\max} - 0.01$ meter.
- (5) Compute the move limit for y -direction nodal position as $\Delta y_{\min} = -(H_{\min}/2/n_{y,\max} - 0.01)$, and $\Delta y_{\max} = H_{\min}/2/n_{y,\max} - 0.01$ meter.
- (6) Generate $n_x \times n_y$ initial structural nodes \mathbf{X} , \mathbf{Y} , and N_e ground elements where \mathbf{X} and \mathbf{Y} are nodal coordinates in x - and y -directions, respectively.
- (7) Assign element diameters. Set $y_j = 4x_i$ for $i = 4, \dots, N_e + 3$ and $j = 1, \dots, N_e$.
- (8) For $j = 1$ to N_e

- (8.1) If round $(y_j) = 0$, set $d_j = 0.000001$ m
 (8.2) If round $(y_j) = 1$, set $d_j = 0.01$ m
 (8.3) If round $(y_j) = 2$, set $d_j = 0.02$ m
 (8.4) If round $(y_j) = 3$, set $d_j = 0.03$ m
 (8.5) If round $(y_j) = 4$, set $d_j = 0.04$ m
 End
 (9) Set $\Delta x_j = \Delta x_{\min} + (\Delta x_{\max} - \Delta x_{\min})x_i$ for $i = (N_e + 4), \dots, (N_e + N_{sh,x} + 3)$ and $j = 1, \dots, N_{sh,x}$. Update x -direction nodal positions $X_j = X_j + \Delta x_j$ for all node positions allowed to be changed.
 (10) Set $\Delta y_j = \Delta y_{\min} + (\Delta y_{\max} - \Delta y_{\min})x_i$ for $i = (N_e + N_{sh,x} + 4), \dots, (N_e + N_{sh,x} + N_{sh,y} + 3)$ and $j = 1, \dots, N_{sh,y}$. Update y -direction nodal positions $Y_j = Y_j + \Delta y_j$ for all node positions allowed to be changed.
 (11) Assign fixed boundary condition for all nodes at $x = 0$.
 (12) Apply the y -direction point load at the last node number.

Output. Nodal positions, ground element connections, boundary conditions, force vector, and elements' diameters.

The design vector is sized $(N_{e,\max} + N_{sh,\max} + 3) \times 1$; however, only $N_e + N_{sh} + 3$ elements were used for each finite element model. The design problem (1) using the first set of design variables is termed OPT1 whereas the problem using the second set of design variables is named OPT2. The structure is made up of a material with Young modulus, yield strength, and density of 214×10^9 Pa, 360×10^6 Pa, and 7850 kg/m^3 , respectively. The factor for safety was set to be 1.5 while the parameter c_{al} was set to be 0.04 N-m. Seven multiobjective evolutionary strategies are employed in this study where the optimisation settings are detailed as follows.

SPEA1: version two of SPEA using real codes with crossover and mutation rates of 1.0 and 0.05, respectively.

SPEA2: version two of SPEA using real codes with crossover and mutation rates of 1.0 and 0.5, respectively.

SPEA3: version two of SPEA using real codes with crossover and mutation rates of 1.0 and 0.75, respectively.

PBIL using binary codes with 0.05 mutation rate: and 0.2 mutation shift.

AMOSa: performs a simple downhill operator for the first 3 generations before entering the main procedure. In this paper, the method uses real codes where a candidate is obtained by means of mutation.

MPSO: using real codes with a starting inertia weight, an ending inertia weight, a cognitive learning factor, and a social learning factor of 0.75, 0.1, 0.75, and 0.75, respectively.

TABLE 1: Hypervolume comparison of OPT1 and OPT2.

Optimiser	OPT1		OPT2	
	Mean	Std	Mean	Std
SPEA1	0.7098	0.0998	0.8619	0.0267
SPEA2	0.8161	0.0343	0.9274	0.0184
SPEA3	0.8400	0.0564	0.9236	0.0219
PBIL	0.9330	0.0647	0.9519	0.0527
AMOSa	0.6619	0.1143	0.7997	0.0277
MPSO	0.3043	0.1371	0.6699	0.0582
UPSEMOA	0.4334	0.2808	0.6136	0.3885

UPSEMOA: using crossover probability, scaling factor, probability of choosing element from offspring in crossover, minimum population size, and burst size of 0.7, 0.8, 0.5, 10, and 25, respectively.

SPEA and PBIL are the best optimisers in the previous studies [28] while AMOSA is selected instead of the usual NSGAII. MPSO is an optimiser with a different concept from the aforementioned MOEAs while UPSEMOA is used as it is a newly developed algorithm. For OPT1, the number of generations of MOEAs is set to be 250 while both the population and archive size are set as 150. For the second test problem, the number of generations of MOEAs is set to be 300 while both the population and archive size are set as 200. Each optimiser is applied to solve each design problem for 10 optimisation runs starting with the same initial population. The last updated Pareto archive is considered a Pareto optimal set. The nondominated sorting scheme presented in [53] is used to cope with design constraints.

5. Design Results

Having performed each multiobjective evolutionary strategy solving each design problem for ten simulation runs, the performance comparison of the various MOEAs is investigated based on a hypervolume indicator. The hypervolume indicator is one of the most reliable performance indicators used to examine the quality of approximate Pareto fronts obtained from using MOEAs. The parameter determines the area for biobjective or volume for more than two objectives covered by a particular nondominated front with respect to a given reference point. Since there are ten fronts for each method and for each design problem, the average of ten hypervolume values is employed to measure the convergence rate of the optimiser whereas the standard deviation is used to indicate search consistency.

The comparative hypervolumes of the various MOEAs for solving OPT1 and OPT2 are given in Table 1. Note that the hypervolumes in the table are normalised for ease in comparing. It is shown that PBIL is the best optimiser for both design cases based upon the convergence rate while SPEA2 is the most consistent method. However, as the standard deviation of SPEA2 does not approach to zero, the convergence rate is the most important indicator for this study.

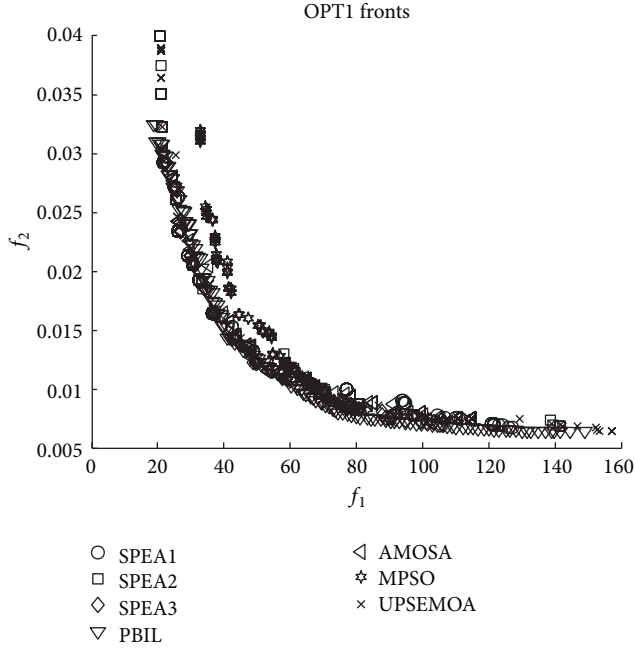


FIGURE 3: OPT1 best Pareto fronts from MOEAs.

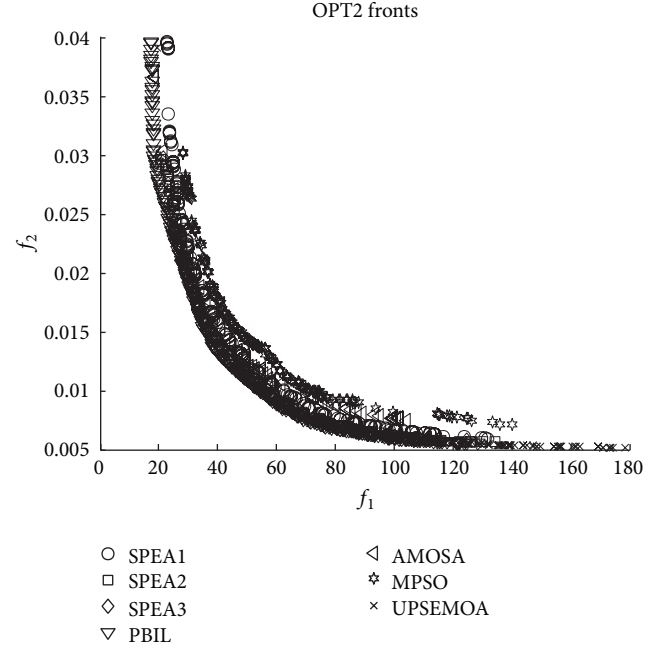


FIGURE 5: OPT2 best Pareto fronts from MOEAs.

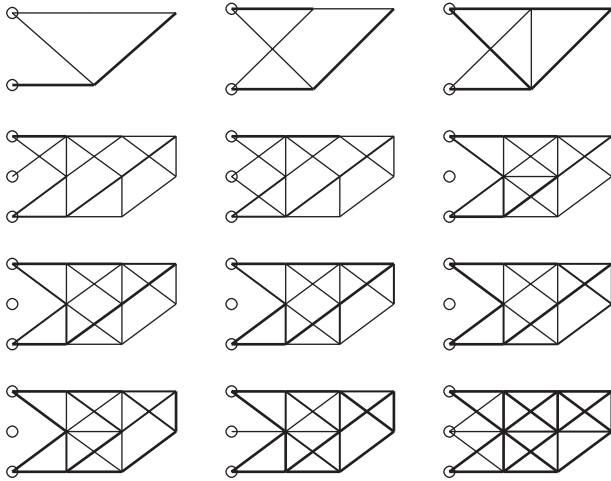


FIGURE 4: Some structures from the best front of PBIL in Figure 3.

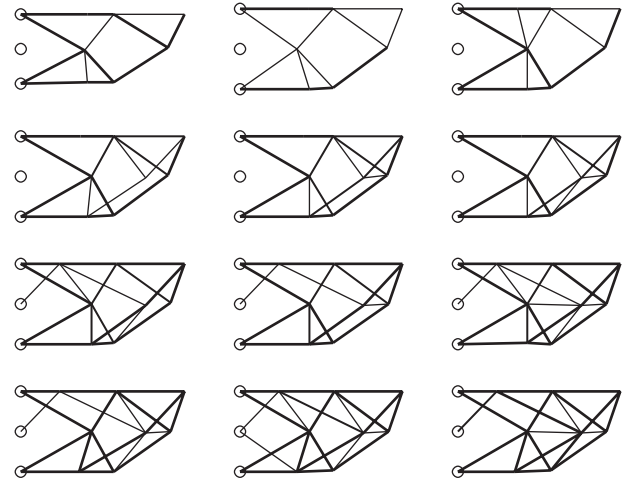


FIGURE 6: Some structures from the best front of PBIL in Figure 5.

Among the SPEA versions, it can be said that SPEA with higher mutation rate is superior to the low mutation rate version. SPEA3 is the second best optimiser for OPT1 while the worst performer for this problem is MPSO. For OPT2, the second best is SPEA2 closely followed by SPEA3 as the third best. The worst for this design case is UPSEMOA.

For the OPT1 design problem, the best fronts obtained from the best run of each multiobjective optimiser are plotted in Figure 3. It can be seen that the fronts are close together although the PBIL front has slightly more advancement and extension. This implies that MOEAs are efficient for this design problem. Some trusses selected from the PBIL front are displayed in Figure 4. The structures have a variety of structural layouts and elements' sizes; however, there are only two sets of node number, that is, 2×1 and 4×2 .

Figure 5 shows Pareto fronts obtained from the best runs of the various optimisers for the OPT2 case. Similarly to the first design case, all seven fronts are somewhat close together with the front obtained from using PBIL having slightly more advancement and extension. Some selected solutions from the PBIL front are displayed in Figure 6. The structures for this case have various topologies, and element dimensions, but tend to have fairly similar shapes. Changing nodal position has significant impact on the resulting structures. There is only one set of nodes array for the ground elements, which is 4×2 . The best fronts obtained from solving OPT1 and OPT2 are plotted together for comparison in Figure 7. It is shown that the best front of OPT2 totally dominates that of OPT1. This implies that the second set of design variables is more efficient and effective.

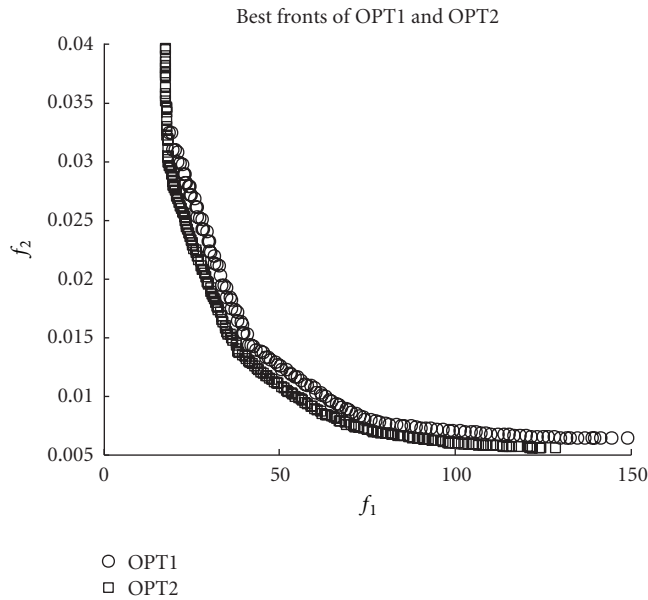


FIGURE 7: OPT1 front versus OPT2 front.

6. Conclusions and Discussion

The design results show that the proposed design strategies are efficient and effective as a variety of reasonable structural configurations could be obtained within one optimisation run. The obtained structures are said to be ready to use as they satisfy all the constraints for safety requirements. The multiobjective topological, shape, and sizing design with an adaptive ground element approach proposed herein can be tackled by an efficient multiobjective evolutionary algorithm. Among the MOEAs employed in this paper, PBIL is the most powerful method for solving both design problems based on the hypervolume indicator. For SPEA as the second best optimiser, using a higher mutation rate is more efficient. The second set of design variables which combines all types of design variables at the same time is superior to the first set which uses only topology and sizing variables. The proposed design approach can be a powerful engineering design tool in the future since, with one optimisation run, various feasible truss structures are obtained for decision making.

Future work could be the application of this design concept to a large-scale truss design problem. Alternative adaptive ground element formations can be created. The application to three-dimensional practical trusses and frames is challenging. Also, performance enhancement of multiobjective optimisers for solving this design problem is to be conducted.

Acknowledgments

The authors are grateful for the support from the Thailand Research Fund (TRF), BRG5580017, and the Graduate School, Rajabhat Maha Sarakham University, Thailand.

References

- [1] P. Lu, S. Chen, and Y. Zheng, "Artificial intelligence in civil engineering," *Mathematical Problems in Engineering*, vol. 2012, Article ID 145974, 22 pages, 2012.
- [2] C. Cattani, S. Chen, and G. Aldashev, "Information and modeling in complexity," *Mathematical Problems in Engineering*, vol. 2012, Article ID 868413, 3 pages, 2012.
- [3] A. R. Yildiz, "Comparison of evolutionary-based optimization algorithms for structural design optimization," *Engineering Applications of Artificial Intelligence*, vol. 26, no. 1, pp. 327–333, 2013.
- [4] A. R. Yildiz and K. N. Solanki, "Multi-objective optimization of vehicle crashworthiness using a new particle swarm based approach," *International Journal of Advanced Manufacturing Technology*, vol. 59, pp. 367–376, 2012.
- [5] A. F. Ulusoy and F. Erbatur, "Discrete and continuous structural optimisation using evolution strategies," in *Proceedings of the 3rd International Conference on Engineering Computational Technology (ICECT '03)*, B. H. V. Topping and Z. Bittnar, Eds., pp. 163–164, Civil-Comp press, Edinburgh, UK, 2002.
- [6] A. R. Yildiz and K. Saitou, "Topology synthesis of multicomponent structural assemblies in continuum domains," *Journal of Mechanical Design*, vol. 133, no. 1, Article ID 011008, 2011.
- [7] N. Pholdee and S. Bureerat, "Performance enhancement of multiobjective evolutionary optimizers for truss design using an approximate gradient," *Computers and Structures*, vol. 106–107, pp. 115–124, 2012.
- [8] I. Durgun and A. R. Yildiz, "Structural design optimization of vehicle components using Cuckoo search algorithm," *Materials Testing*, vol. 54, no. 3, pp. 185–188, 2012.
- [9] S. Chen, Y. Zheng, C. Cattani, and W. Wang, "Modeling of biological intelligence for SCM system optimization," *Computational and Mathematical Methods in Medicine*, vol. 2012, Article ID 769702, 10 pages, 2012.
- [10] M. Zirour, C. Y. Liong, and W. R. Ismail, "Genetic algorithm for a quay management problem," *Australian Journal of Basic and Applied Sciences*, vol. 5, no. 9, pp. 2257–2263, 2011.
- [11] S. Y. Chen and Y. F. Li, "Automatic sensor placement for model-based robot vision," *IEEE Transactions on Systems, Man, and Cybernetics B*, vol. 34, no. 1, pp. 393–408, 2004.
- [12] A. R. Yildiz, "A novel hybrid immune algorithm for global optimization in design and manufacturing," *Robotics and Computer-Integrated Manufacturing*, vol. 25, no. 2, pp. 261–270, 2009.
- [13] A. R. Yildiz, "A new hybrid bee colony optimization approach for robust optimal design and manufacturing," *Applied Soft Computing*. In press.
- [14] V. Kelner, F. Capitanescu, O. Léonard, and L. Wehenkel, "A hybrid optimization technique coupling an evolutionary and a local search algorithm," *Journal of Computational and Applied Mathematics*, vol. 215, no. 2, pp. 448–456, 2008.
- [15] A. R. Yildiz, "A new design optimization framework based on immune algorithm and Taguchi's method," *Computers in Industry*, vol. 60, no. 8, pp. 613–620, 2009.
- [16] S. Kanyakam and S. Bureerat, "Comparative performance of surrogate-assisted MOEAs for geometrical design of pin-fin heat sinks," *Applied Mathematics*, vol. 2012, Article ID 534783, 14 pages, 2012.
- [17] T. Kunakote and S. Bureerat, "Multi-objective topology optimization using evolutionary algorithms," *Engineering Optimization*, vol. 43, no. 5, pp. 541–557, 2011.

- [18] W. Achziger, "On simultaneous optimization of truss geometry and topology," *Structural and Multidisciplinary Optimization*, vol. 33, no. 4-5, pp. 285-304, 2007.
- [19] W. Tang, L. Tong, and Y. Gu, "Improved genetic algorithm for design optimization of truss structures with sizing, shape and topology variables," *International Journal for Numerical Methods in Engineering*, vol. 62, no. 13, pp. 1737-1762, 2005.
- [20] K. Shea and I. F. C. Smith, "Improving full-scale transmission tower design through topology and shape optimization," *Journal of Structural Engineering*, vol. 132, no. 5, pp. 781-790, 2006.
- [21] C. M. Chan and K. M. Wong, "Structural topology and element sizing design optimisation of tall steel frameworks using a hybrid OC-GA method," *Structural and Multidisciplinary Optimization*, vol. 35, no. 5, pp. 473-488, 2008.
- [22] J. Zhu, W. Zhang, P. Beckers, Y. Chen, and Z. Guo, "Simultaneous design of components layout and supporting structures using coupled shape and topology optimization technique," *Structural and Multidisciplinary Optimization*, vol. 36, no. 1, pp. 29-41, 2008.
- [23] M. Giger and P. Ermanni, "Evolutionary truss topology optimization using a graph-based parameterization concept," *Structural and Multidisciplinary Optimization*, vol. 32, no. 4, pp. 313-326, 2006.
- [24] R. Su, X. Wang, L. Gui, and Z. Fan, "Multi-objective topology and sizing optimization of truss structures based on adaptive multi-island search strategy," *Structural and Multidisciplinary Optimization*, vol. 43, no. 2, pp. 275-286, 2011.
- [25] V. Togan and A. Daloglu, "Optimization of 3d trusses with adaptive approach in genetic algorithms," *Engineering Structures*, vol. 28, pp. 1019-1027, 2006.
- [26] H. Rahami, A. Kaveh, and Y. Gholipour, "Sizing, geometry and topology optimization of trusses via force method and genetic algorithm," *Engineering Structures*, vol. 30, no. 9, pp. 2360-2369, 2008.
- [27] O. Hasanc and F. Erbatur, "Layout optimization of trusses using simulated annealing," *Advances in Engineering Software*, vol. 33, pp. 681-696, 2002.
- [28] C. Noilublao and S. Bureerat, "Simultaneous topology shape and sizing optimisation of skeletal structures using multiobjective evolutionary algorithms," in *Evolutionary Computation*, pp. 487-580, 2009.
- [29] T. Hagishita and M. Ohsaki, "Topology optimization of trusses by growing ground structure method," *Structural and Multidisciplinary Optimization*, vol. 37, no. 4, pp. 377-393, 2009.
- [30] A. Asadpoure, M. Tootkaboni, and J. K. Guest, "Robust topology optimization of structures with uncertainties in stiffness—application to truss structures," *Computers and Structures*, vol. 89, no. 11-12, pp. 1131-1141, 2011.
- [31] M. Beckers and C. Fleury, "A primal-dual approach in truss topology optimization," *Computers and Structures*, vol. 64, no. 1-4, pp. 77-88, 1997.
- [32] I. Hajirasouliha, K. Pilakoutas, and H. Moghaddam, "Topology optimization for the seismic design of truss-like structures," *Computers and Structures*, vol. 89, no. 7-8, pp. 702-711, 2011.
- [33] C. Noilublao and S. Bureerat, "Topology and sizing optimization of trusses with adaptive ground finite elements using multi-objective PBIL," *Advanced Materials Research*, vol. 308-310, pp. 1116-1121, 2011.
- [34] S. Silih, M. Premrov, and S. Kravanja, "Optimum design of plane timber trusses considering joint flexibility," *Engineering Structures*, vol. 27, no. 1, pp. 145-154, 2005.
- [35] L. Gil and A. Andreu, "Shape and cross-section optimization of a truss structure," *Computers and Structures*, vol. 79, no. 7, pp. 681-689, 2001.
- [36] R. Karkauskas and A. Norkus, "Truss optimization under stiffness, stability constraints and random loading," *Mechanics Research Communications*, vol. 33, no. 2, pp. 177-189, 2006.
- [37] A. Kaveh and S. Talatahari, "Particle swarm optimizer, ant colony strategy and harmony search scheme hybridized for optimization of truss structures," *Computers and Structures*, vol. 87, no. 5-6, pp. 267-283, 2009.
- [38] A. C. C. Lemonge, H. J. C. Barbosa, A. L. G. A. Coutinho, and C. C. H. Borges, "Multiple cardinality constraints and automatic member grouping in the optimal design of steel framed structures," *Engineering Structures*, vol. 33, no. 2, pp. 433-444, 2011.
- [39] C. Noiluplao and S. Bureerat, "Simultaneous topology and shape optimisation of a 3D framework structure using simulated annealing," in *Proceedings of the Technology and Innovation for Sustainable Development Conference (TISD '08)*, Faculty of Engineering, Khon Kaen University, January 2008.
- [40] P. Martínez, P. Martí, and O. M. Querin, "Growth method for size, topology, and geometry optimization of truss structures," *Structural and Multidisciplinary Optimization*, vol. 33, no. 1, pp. 13-26, 2007.
- [41] M. Zhou, N. Pagaldipti, H. L. Thomas, and Y. K. Shyy, "An integrated approach to topology, sizing, and shape optimization," *Structural and Multidisciplinary Optimization*, vol. 26, no. 5, pp. 308-317, 2004.
- [42] T. Sokol, "A 99 line code for discretized Michell truss optimization written in Mathematica," *Structural and Multidisciplinary Optimization*, vol. 43, no. 2, pp. 181-190, 2011.
- [43] E. Zitzler, M. Laumanns, and L. Thiele, "SPEA2: improving the strength Pareto evolutionary algorithm for multiobjective optimization," in *Evolutionary Methods for Design, Optimization and Control*, Barcelona, Spain, 2002.
- [44] S. Bureerat and S. Srisomporn, "Optimum plate-fin heat sinks by using a multi-objective evolutionary algorithm," *Engineering Optimization*, vol. 42, no. 4, pp. 305-323, 2010.
- [45] S. Bandyopadhyay, S. Saha, U. Maulik, and K. Deb, "A simulated annealing-based multiobjective optimization algorithm: AMOSA," *IEEE Transactions on Evolutionary Computation*, vol. 12, no. 3, pp. 269-283, 2008.
- [46] M. Reyes-Sierra and C. A. C. Coello, "Multi-objective particle swarm optimizers: a survey of the state-of-the-art," *International Journal of Computational Intelligence Research*, vol. 2, pp. 287-308, 2006.
- [47] T. Aittokoski and K. Miettinen, "Efficient evolutionary approach to approximate the Pareto-optimal set in multiobjective optimization, UPS-EMOA," *Optimization Methods and Software*, vol. 25, no. 6, pp. 841-858, 2010.
- [48] E. Zitzler and L. Thiele, "Multiobjective evolutionary algorithms: a comparative case study and the strength Pareto approach," *IEEE Transactions on Evolutionary Computation*, vol. 3, no. 4, pp. 257-271, 1999.
- [49] W. A. Bennage and A. K. Dhingra, "Single and multiobjective structural optimization in discrete-continuous variables using simulated annealing," *International Journal for Numerical Methods in Engineering*, vol. 38, no. 16, pp. 2753-2773, 1995.
- [50] S. Bureerat and J. Limtragool, "Performance enhancement of evolutionary search for structural topology optimisation," *Finite Elements in Analysis and Design*, vol. 42, no. 6, pp. 547-566, 2006.

- [51] J. D. Knowles and D. W. Corne, "Approximating the non-dominated front using the Pareto archived evolution strategy," *Evolutionary computation*, vol. 8, no. 2, pp. 149–172, 2000.
- [52] K. Deb, A. Pratap, S. Agarwal, and T. Meyarivan, "A fast and elitist multiobjective genetic algorithm: NSGA-II," *IEEE Transactions on Evolutionary Computation*, vol. 6, no. 2, pp. 182–197, 2002.
- [53] K. Deb, A. Pratap, and T. Meyarivan, "Constrained test problems for multi-objective evolutionary optimization," KanGAL Report No. 200002, Kanpur Genetic Algorithms Laboratory (KanGAL), Indian Institute of Technology, Kanpur, India, 2000.

Research Article

A Simple Generation Technique of Complex Geotechnical Computational Model

Hang Lin,^{1,2} Taoying Liu,¹ Jiangteng Li,¹ and Ping Cao¹

¹ School of Resources and Safety Engineering, Central South University, Changsha, Hunan 410083, China

² State Key Laboratory of Coal Resources and Safe Mining, China University of Mining and Technology, Xuzhou, Jiangsu 221116, China

Correspondence should be addressed to Hang Lin; linhangabc@126.com

Received 27 November 2012; Accepted 7 January 2013

Academic Editor: Fei Kang

Copyright © 2013 Hang Lin et al. This is an open access article distributed under the Creative Commons Attribution License, which permits unrestricted use, distribution, and reproduction in any medium, provided the original work is properly cited.

Given that FLAC3D (a geotechnical calculation software) is difficult to use for building large, complex, and three-dimensional mining models, the current study proposes a fast and a convenient modeling technique that combines the unique advantages of FLAC3D in numerical calculation and those of SURPAC (a mine design software) in three-dimensional modeling, and the interface program was compiled. First, the relationship between the FLAC3D and the SURPAC unit data was examined, and the transformation technique between the data was given. Then, the interface program that transforms the mine design model to calculate the model was compiled using FORTRAN, and the specific steps of the program implementation were described using a large iron and copper mine modeling example. The results show that the proposed transformation technique and its corresponding interface program transformed the SURPAC model into the FLAC3D model, which expedited FLAC3D modeling, verified the validity and feasibility of the transformation technique, and expanded the application spaces of FLAC3D and SURPAC.

1. Introduction

Along with the rapid development of computer technology in recent years, the numerical method along with artificial intelligence technique has become an important mean of analyzing and calculating modern engineering technologies [1–6] and forecasting engineering stability and reliability [5, 7–9]. FLAC3D (numerical calculation software) has been extensively recognized and applied for analyzing geotechnical issues [10–12]. FLAC3D could be used to examine the changing rules of the field effect of rock mass from the macrotrend and it is suitable for most engineering mechanics issues, particularly for analyzing material elastoplasticity, large deformation, rheology prediction, and for geotechnical numerical simulation of construction processes [13–16]. However, FLAC3D is quite difficult to use for pretreatment modeling, particularly in the geological body of complicated multimedia and multiboundaries [17, 18]. Thus, engineers often use models by simplifications to approximately describe geotechnical models to solve this problem above. But different lithologies have different mechanical features excessive simplification of the model would reduce the reliability

of the numerical simulation results. On the other hand, the geology or mine design platform demonstrates good three-dimensional modeling, and it could accurately express the spatial distribution of the stratum and the geological structure with different lithologies [19–22]. A great progress has been made on simulation methods of complex geological interfaces and features, for instance, Xu et al. [17] suggested a 3D geological modeling technique (SGM) as a tool for constructing complex geological models in rock engineering, Wu and Xu [23] used a simple plane to simulate the fault or multiple combined planes to approximate the fault, for modeling geological faults in 3D, and Zhong et al. [24] presented an integrated 3D geological modeling methodology for modeling and visualization of large 3D geoengineering applications. But mine design is relatively independent of numerical calculation and analysis, and its function is generally limited to visualization and qualitative judgments. Thus, combining the advantages of the mine design platform in modeling and that of FLAC3D in numerical calculation and analysis is necessary. Recently, only few studies have been conducted on this combination.

The numerical calculation of a large mining project often involves complicated three-dimensional geological models. The current study takes the mine design software SURPAC with its powerful modeling function as the platform, builds complex three-dimensional models of mines, and automatically generates a FLAC3D model through data transformation to expand the application of FLAC3D into the numerical simulation of mine projects to solve the difficulties of FLAC3D modeling and to build accurate three-dimensional mining models that can improve the reliability of simulation results and give play to the computational power of FLAC3D. Moreover, SURPAC could also expand its mechanical analytical ability based on its inherent functions such as data collection, storage, management, and inquiry to meet the requirements of an engineering model in prediction and decision support.

2. Development of the Model Transformation Procedure

2.1. SURPAC Modeling. The SURPAC serial software is a set of megadigitized mining engineering software with domestic leading level in minefields, and it is extensively applied to resource appraisal, geological measurement, mine design plan, production plan management, and reclamation design after pit closure [25–27]. Moreover, SURPAC could help metal mines to effectively achieve digitization and informatization of mine design, planning, and management. SURPAC has a complete set of three-dimensional modeling tools, and it could achieve complete imaging of mine exploration, three-dimensional geological modeling, the establishment of engineering database, open gallery and underground mine design, production and mining progress plans, tailing, and reclamation designs. Moreover, SURPAC has a powerful three-dimensional graphic system, and its core is composed of a totally integrated graphic module that has a complete set of visualization means and of data editing tools that visually generates and displays the three-dimensional structures of underground geology or mining areas, ground and terrain models, and other graphics. Moreover, it is an effective, convenient, and fast platform for building complex computational models.

SURPAC adopts a polygon mesh to describe the physical borders of an orebody that forms during extraction, and block modeling is performed after the solid model is built. The solid model is a three-dimensional geometric model based on computer geometric shaping technologies, and it completely describes the spatial structure, geometric configuration, and spatial borderline of the lithology. A block model includes a three-dimensional model consisting of common hexahedral blocks and it is the foundation for lithologic assignment and the subsequent numerical calculation. The basic idea is to divide the spatial geometric model of the orebody into a multitude of unit blocks and then to assign lithology values to the unit blocks that fill the entire orebody.

2.2. Brief Description of FLAC3D. FLAC3D is a numerical modeling code for advanced geotechnical analysis of

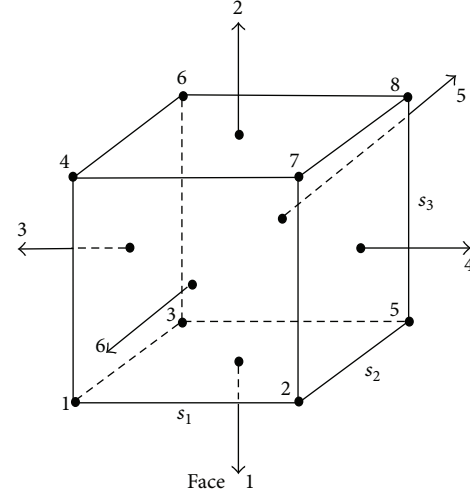


FIGURE 1: Data relationship between FLAC3D and SURPAC unit data.

soil, rock, and structural support in three dimensions [28]. FLAC3D is used in analysis, testing, and design by geotechnical, civil, and mining engineers. It is designed to accommodate any kind of geotechnical engineering project, where continuum analysis is necessary.

FLAC3D utilizes an explicit finite difference formulation that can model complex behaviors not readily suited to FEM codes, such as problems that consist of several stages, large displacements and strains, and nonlinear material behavior and unstable systems (even the cases of yield/failure over large areas or total collapse).

2.3. Transformation of SURPAC and FLAC3D Data. SURPAC provides hexahedral unit shapes for treating units of simulated objects and it changes the sizes of the hexahedral units based on the features of the geological body, precision requirements of calculation, and spatial layout features of the unit shapes. Compared with the unit shapes in FLAC3D, the hexahedra units in SURPAC are known to correspond to block units. The information in a FLAC3D unit includes the three-dimensional coordinates of eight nodes ($p_1 \sim p_8$) in the unit and in the unit group. The information in the SURPAC unit includes a unit centroid (x_0 , y_0 , and z_0), sizes s_1 , s_2 , and s_3 , and unit attributes. Figure 1 shows the mapping relationship between two types of unit nodes. The transformation technique of the unit node coordinates could easily be obtained through the geometric relationship,

$$\begin{aligned} x_{p1} &= \frac{x_0 - s_1}{2}, \\ y_{p1} &= \frac{y_0 - s_2}{2}, \\ z_{p1} &= \frac{z_0 - s_3}{2}, \end{aligned} \quad (1)$$

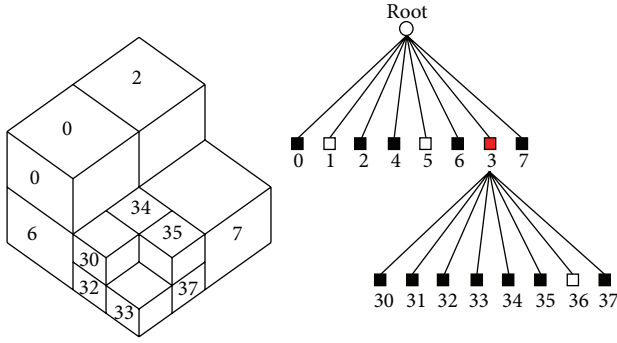


FIGURE 2: Unit subdivision.

where, x_{p_1} , y_{p_1} , and z_{p_1} represent the x , y , and z coordinates of point p_1 , respectively.

The three-dimensional coordinates of points $p_2 \sim p_8$ could be obtained using the same theory.

Parts in the model that need special treatment are grouped together during FLAC3D calculation. Thus, the attributes of each unit is determined along with SURPAC modeling to transform the units with different attributes into different groups in the FLAC3D model. The specific implementation process is as follows: SURPAC builds a block model of the three-dimensional orebody during modeling, that is, three-dimensional dissection of the entity model of the orebody with squares or cuboids.

The blocks are assigned with different attributes. SURPAC adopts a series of three-dimensional arrays to store information, such as grade and lithology, among others. The subscripts of an array correspond to the row, line, and layer number of blocks to save storage space and calculation time. However, SURPAC is inflexible to use because its coordinates rotate quite often during modeling. SURPAC has sharp contradictions in accurately fitting the borderline and the division grain size (storage) of a mine. Thus, the octree method was introduced to solve this problem, that is, continuously dividing the three-dimensional entity space into eight three-dimensional networks of the same size, with one or several attributes, as shown in Figure 2. The unit is continuously subdivided if the mesh is too big until the same area has a single attribute to meet the border of an orebody with different attributes. The border of a geological body could be simulated in form using continuous subdivision, and the mesh will have the attributes of a rock in such spatial position. Thus, the current study builds a three-dimensional geological model to reflect completely the geological structure, the spatial distribution of the lithology, and accurate geological information using continuous subdivision under multimedia complex conditions. Finally, the SURPAC block model generates STR files, which could be opened in text format. The data file has the following format.

- (1) Header message.
- (2) Centroid coordinates, sizes, and attributes of the units.

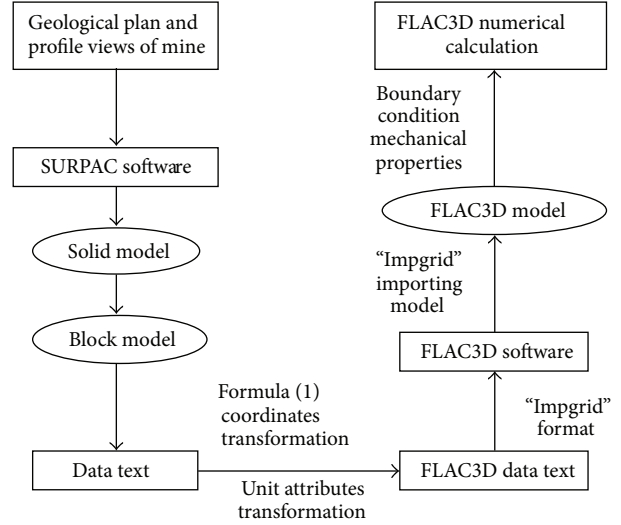


FIGURE 3: Model transformation flowchart.

The geometric parameters and attributes of the SURPAC units are read during data transformation. Then, the three-dimensional coordinates of the FLAC3D unit are transformed in accordance with formulas (1) and are then grouped together. The group name is the attribute of the corresponding SURPAC unit.

The numerical model could be rebuilt through the “call” command in FLAC3D to transform the data, but it will consume many computer hours in building the model because it faces a large amount of unit data. However, the “impgrid” command embedded into FLAC3D could import all the data at one time, which omits the remodeling process of FLAC3D and shortens the computer hours; for instance, the “call” command needs about three hours to build a three-dimensional model with 10,000 units, whereas the “impgrid” command only needs less than a minute at the same computer. However, the “call” and “impgrid” commands have different call formats.

The format of the “impgrid” command is as follows.

- (1) Node information.
 - (a) *GRIDPOINTS.
 - (b) G Node No., Node Coordinate X, Coordinate Y, and Coordinate Z.
- (2) Unit information.
 - (a) Z Unit Type, Unit Number, and Node Number contained by the unit.
- (3) Grouping information.
 - (a) Z Group No., Unit Number contained by this group.

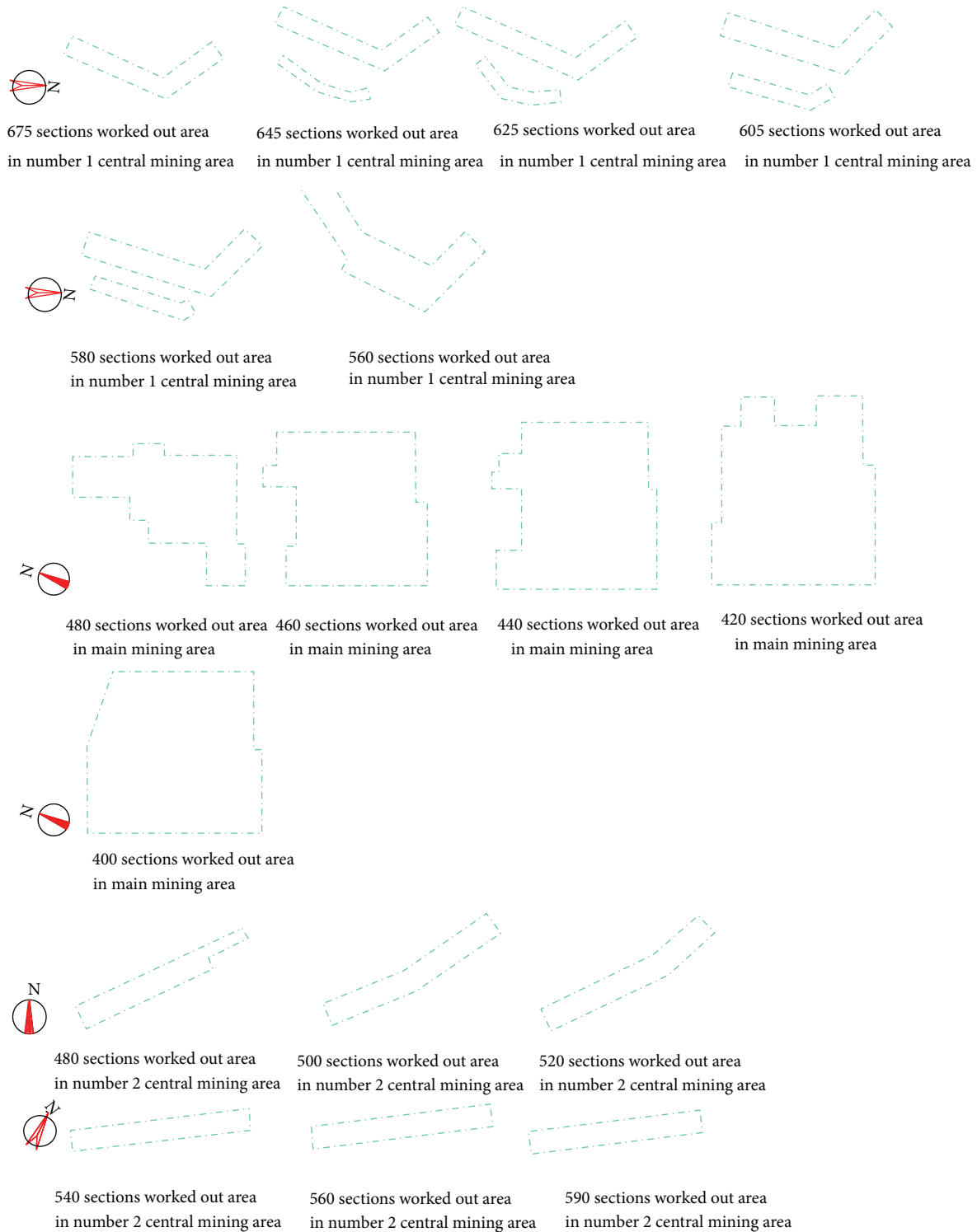


FIGURE 4: AUTOCAD plan view.

Based on the analysis of unit data relationship above, the current study uses FORTRAN to compile the interface program. First, the program transforms the data into the required data format. Then, the program calls in the data using the “impgrid” command of FLAC3D, and then

it sums the boundary condition, initial condition, and dynamic parameters of the soil body for calculations. Refer to Figure 3 for specific procedures. However, the model transferred from SURPAC can not make sure the grid of element meets each other, then the command “attach

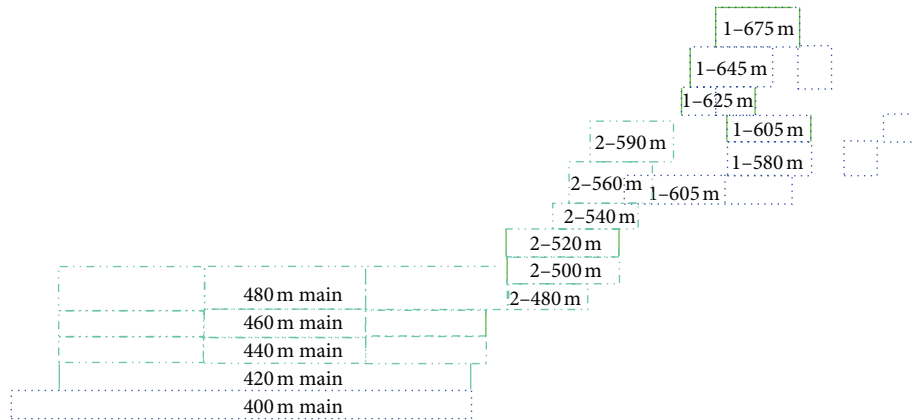
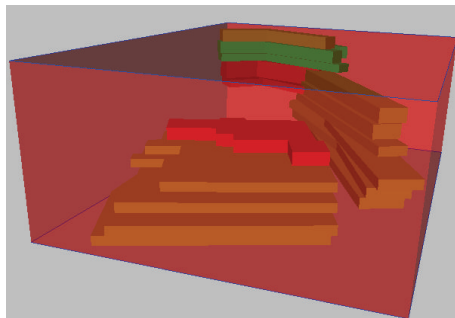
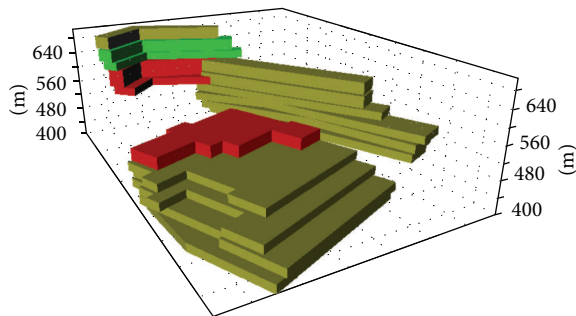


FIGURE 5: AUTOCAD vertical view.



(a) The whole model



(b) The model of stope

FIGURE 6: Solid model of SURPAC.

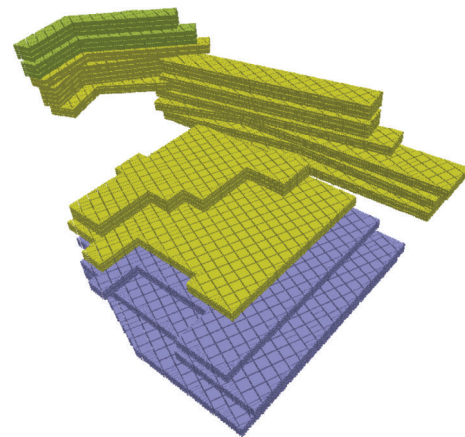


FIGURE 7: Block model of SURPAC.

vertical view of the mine, as shown in Figure 5, and the north direction of each view is inconsistent. If other software, such as ANSYS, is used to build the model, it needs to determine the three-dimensional coordinates of each border of the mine. Moreover, mistakes could easily occur because of the huge work volume. In contrast, SURPAC only needs to read the corresponding DXF files of the AUTOCAD drawings and rotate them into the consistent northern direction, which allows convenient and fast modeling and omits the work of choosing points and determining coordinates.

A three-dimensional model was then constructed using FLAC3D with the transformation technique proposed in this paper and the modeling of the worked out section as an example. The specific procedures are as follows.

- (i) *Building of the solid model.* The AUTOCAD drawings are loaded first, and then the coordinates of each point in the graph are transformed into actual geographical coordinates based on the planar distribution of the prospecting line, the angle between the prospecting line and the east-west axis, and the scale of the

face" in FLAC3D is needed to eliminate the errors of calculation.

3. Application of Model Transformation Procedure

Given a large iron/copper mine and the complicated properties distribution of rock mass the owner provides AUTOCAD plan view of the mine, as shown in Figure 4 and AUTOCAD

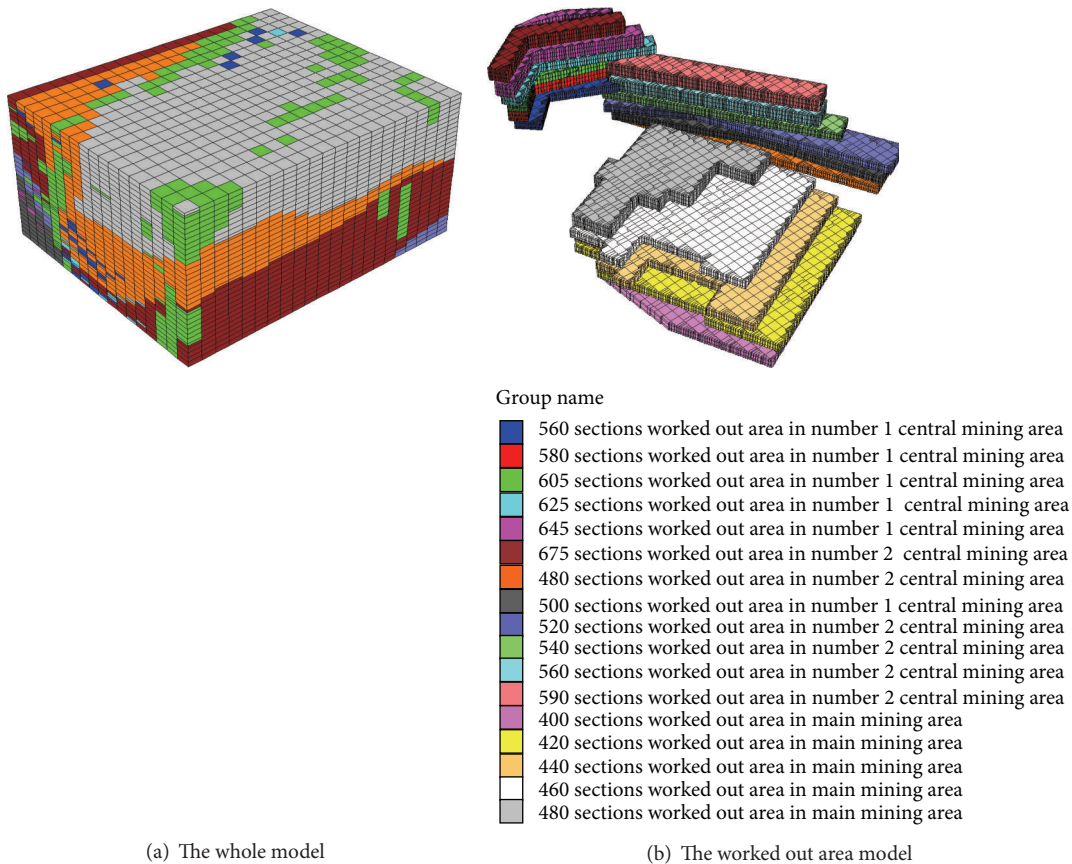


FIGURE 8: FLAC3D model.

profile map. The specific scope of the lithology on each geological prospecting profile is sealed, and then it is linked up in sequence on different profiles. The outermost profile is then sealed to form an encapsulated three-dimensional entity [19], as shown in Figure 6.

- (ii) *Building the block model.* The spatial geometric model of the orebody is divided into a multitude of unit blocks as per the certain sizes of the blocks. Then, values are assigned to the unit blocks that fill the entire scope or orebody, and then the unit blocks of the block model are subdivided automatically at the physical border through the unit subdivision technologies to ensure that the block model simulates the geometric shape of the actual orebody, as shown in Figure 7.
- (iii) *Generation of the FLAC3D model.* The data file generated by SURPAC and the FLAC3D file generated by the interface program developed in the current study, that is, FLAC3D, are used, and the information of the entire model is imported through “impgrid,” as shown in Figure 8. Moreover, the unit subdivision resulted in the misalignment of the meshes in some regions, but the subdivision units and raw units have

integral multiple relationships, as shown in Figure 2. Thus, information transfer in misaligned areas of the meshes could be achieved through the attach face command in FLAC3D.

After calculation by FLAC3D, the displacement and state contours are shown in Figure 9, which is in consistence with the real situation.

4. Conclusion

(1) Considering the difficulty of using FLAC3D (geotechnical calculation software) for pretreatment modeling, the current study combined SURPAC (mine design software) and FLAC3D to utilize the advantage of SURPAC in simulating geological features and to provide a calculation model that conforms to the geological reality of FLAC3D.

(2) The differences between the information from the two types of unit information, that is, SURPAC and FLAC3D, were analyzed, the data relationship between units was built, the data transformation technique was proposed, and the FORTRAN was adopted to compile relevant transformation procedures.

(3) When the transformation technique proposed in the current paper was applied to the modeling of a given large

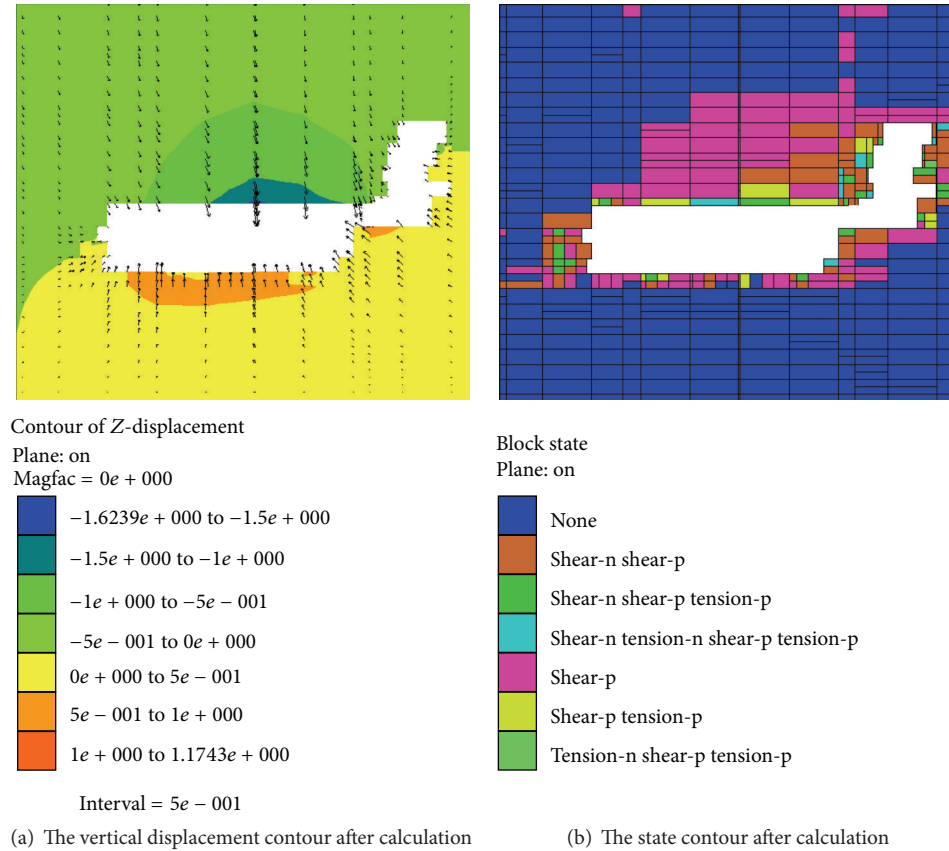


FIGURE 9: The results calculated by FLAC3D.

iron/copper mine, it indicated that the proposed transformation technique and its corresponding interface program transformed the SURPAC model into the FLAC3D model, speeding up the FLAC3D modeling and verifying the feasibility and validity of the proposed transformation technique.

Acknowledgments

This paper gets its funding from Project no. 20120162120014 supported by the Specialized Research Fund for the Doctoral Program of Higher Education of China; from Project no. 2013CB036004 supported by National Basic Research 973 Program of China; from Project no. 201201 supported by Open Fund of Key Laboratory of Mechanics on Disaster and Environment in Western China (Lanzhou University), Ministry of Education; Project no. 12KF01 funded by the Open Projects of State Key Laboratory of Coal Resources and Safe Mining, CUMT. The authors wish to acknowledge these supports.

References

- [1] S. Y. Chen, Y. J. Zheng, C. Cattani, and W. L. Wang, "Modeling of biological intelligence for SCM system optimization," *Computational and Mathematical Methods in Medicine*, vol. 2012, Article ID 769702, 10 pages, 2012.
- [2] Z. Z. Teng, J. He, A. J. Degnan et al., "Critical mechanical conditions around neovessels in carotid atherosclerotic plaque may promote intraplaque hemorrhage," *Atherosclerosis*, vol. 223, no. 2, pp. 321–326, 2012.
- [3] S. Y. Chen, W. Huang, C. Cattani, and G. Altieri, "Traffic dynamics on complex networks: a survey," *Mathematical Problems in Engineering*, vol. 2012, Article ID 732698, 23 pages, 2012.
- [4] K. M. Hosny and M. A. Hafez, "An algorithm for fast computation of 3D Zernike moments for volumetric images," *Mathematical Problems in Engineering*, vol. 2012, Article ID 353406, 17 pages, 2012.
- [5] X. L. Yang and F. Huang, "Slope stability analysis considering joined influences of nonlinearity and dilation," *Journal of Central South University of Technology*, vol. 16, no. 2, pp. 292–296, 2009.
- [6] X. L. Yang, "Seismic displacement of rock slopes with nonlinear Hoek-Brown failure criterion," *International Journal of Rock Mechanics and Mining Sciences*, vol. 44, no. 6, pp. 948–953, 2007.
- [7] S. Lv, J. Tian, and S. Zhong, "Delay-dependent stability analysis for recurrent neural networks with time-varying delays," *Mathematical Problems in Engineering*, vol. 2012, Article ID 910140, 14 pages, 2012.
- [8] Z. Tian and H. Niu, "Modeling and algorithms of the crew rostering problem with given cycle on high-speed railway lines," *Mathematical Problems in Engineering*, vol. 2012, Article ID 214607, 15 pages, 2012.
- [9] H. Lin, P. Cao, F. Q. Gong, J. T. Li, and Y. L. Gui, "Directly searching method for slip plane and its influential factors based

- on critical state of slope,” *Journal of Central South University of Technology*, vol. 16, no. 1, pp. 131–135, 2009.
- [10] S. Kwon, W. J. Cho, and P. S. Han, “Concept development of an underground research tunnel for validating the Korean reference HLW disposal system,” *Tunnelling and Underground Space Technology*, vol. 21, no. 2, pp. 203–217, 2006.
 - [11] J. Rutqvist, Y. Ijiri, and H. Yamamoto, “Implementation of the Barcelona Basic Model into TOUGH-FLAC for simulations of the geomechanical behavior of unsaturated soils,” *Computers and Geosciences*, vol. 37, no. 6, pp. 751–762, 2011.
 - [12] H. Lin and S. W. Sun, “Influence of pile position and length on stress deformation behaviors of layered rock mass slope,” *Disaster Advances*, vol. 5, no. 4, pp. 422–426, 2012.
 - [13] A. Bhattacharjee and A. M. Krishna, “Development of numerical model of wrap-faced walls subjected to seismic excitation,” *Geosynthetics International*, vol. 19, no. 5, pp. 354–369, 2012.
 - [14] R. Hasanpour, H. Chakeri, Y. Ozelik, and H. Denek, “Evaluation of surface settlements in the Istanbul metro in terms of analytical, numerical and direct measurements,” *Bulletin of Engineering Geology and the Environment*, vol. 71, no. 3, pp. 499–510, 2012.
 - [15] S. T. McColl, T. R. H. Davies, and M. J. McSaveney, “The effect of glaciation on the intensity of seismic ground motion,” *Earth Surface Processes and Landforms*, vol. 37, no. 12, pp. 1290–1301, 2012.
 - [16] R. Rai, M. Khandelwal, and A. Jaiswal, “Application of geogrids in waste dump stability: a numerical modeling approach,” *Environmental Earth Sciences*, vol. 66, no. 5, pp. 1459–1465, 2012.
 - [17] N. X. Xu, H. Tian, P. Kulatilake, and Q. W. Duan, “Building a three dimensional sealed geological model to use in numerical stress analysis software: a case study for a dam site,” *Computers and Geotechnics*, vol. 38, no. 8, pp. 1022–1030, 2011.
 - [18] N. X. Xu, X. Wu, X. G. Wang, Z. X. Jia, and Q. W. Duan, “Approach to automatic hexahedron mesh generation for rock-mass with complex structure based on 3D geological modeling,” *Chinese Journal of Geotechnical Engineering*, vol. 28, no. 8, pp. 957–961, 2006.
 - [19] M. Grenon and A.-J. Laflamme, “Slope orientation assessment for open-pit mines, using GIS-based algorithms,” *Computers and Geosciences*, vol. 37, no. 9, pp. 1413–1424, 2011.
 - [20] N. M. Sirakov and F. H. Muge, “A system for reconstructing and visualising three-dimensional objects,” *Computers and Geosciences*, vol. 27, no. 1, pp. 59–69, 2001.
 - [21] M. Grenon and J. Hadjigeorgiou, “Integrated structural stability analysis for preliminary open pit design,” *International Journal of Rock Mechanics and Mining Sciences*, vol. 47, no. 3, pp. 450–460, 2010.
 - [22] N. M. Sirakov, I. Granado, and F. H. Muge, “Interpolation approach for 3D smooth reconstruction of subsurface objects,” *Computers and Geosciences*, vol. 28, no. 8, pp. 877–885, 2002.
 - [23] Q. Wu and H. Xu, “An approach to computer modeling and visualization of geological faults in 3D,” *Computers and Geosciences*, vol. 29, no. 4, pp. 503–509, 2003.
 - [24] D. H. Zhong, M. C. Li, L. G. Song, and G. Wang, “Enhanced NURBS modeling and visualization for large 3D geoen지니어링 applications: an example from the Jinping first-level hydropower engineering project, China,” *Computers and Geosciences*, vol. 32, no. 9, pp. 1270–1282, 2006.
 - [25] B. A. Flores and I. E. Cabral, “Analysis of sensitivity of the pit economic optimization,” *Revista Escola de Minas*, vol. 61, no. 4, pp. 449–454, 2008.
 - [26] Z. Q. Luo, L. Xiao-Ming, S. Jia-Hong, W. Ya-Bin, and L. Wang-Ping, “Deposit 3D modeling and application,” *Journal of Central South University of Technology*, vol. 14, no. 2, pp. 225–229, 2007.
 - [27] Z. Q. Luo, X. M. Liu, B. Zhang, H. Lu, and C. Li, “Cavity 3D modeling and correlative techniques based on cavity monitoring,” *Journal of Central South University of Technology*, vol. 15, no. 5, pp. 639–644, 2008.
 - [28] Itasca Consulting Group, “Fast lagrangian analysis of continua in 3 dimensions,” User Manual Version 3.1, 2004.

Review Article

Mathematical and Metaheuristic Applications in Design Optimization of Steel Frame Structures: An Extensive Review

Mehmet Polat Saka¹ and Zong Woo Geem²

¹ Department of Civil Engineering, University of Bahrain, P.O. Box 32038, Isa Town, Bahrain

² Department of Energy and Information Technology, Gachon University, Seongnam 461-701, Republic of Korea

Correspondence should be addressed to Zong Woo Geem; zwgeem@gmail.com

Received 28 September 2012; Accepted 4 December 2012

Academic Editor: Sheng-yong Chen

Copyright © 2013 M. P. Saka and Z. W. Geem. This is an open access article distributed under the Creative Commons Attribution License, which permits unrestricted use, distribution, and reproduction in any medium, provided the original work is properly cited.

The type of mathematical modeling selected for the optimum design problems of steel skeletal frames affects the size and mathematical complexity of the programming problem obtained. Survey on the structural optimization literature reveals that there are basically two types of design optimization formulation. In the first type only cross sectional properties of frame members are taken as design variables. In such formulation when the values of design variables change during design cycles, it becomes necessary to analyze the structure and update the response of steel frame to the external loading. Structural analysis in this type is a complementary part of the design process. In the second type joint coordinates are also treated as design variables in addition to the cross sectional properties of members. Such formulation eliminates the necessity of carrying out structural analysis in every design cycle. The values of the joint displacements are determined by the optimization techniques in addition to cross sectional properties. The structural optimization literature contains structural design algorithms that make use of both type of formulation. In this study a review is carried out on mathematical and metaheuristic algorithms where the effect of the mathematical modeling on the efficiency of these algorithms is discussed.

1. Introduction

Structural analysis and structural design are two inseparable tools of a structural designer. Design process necessitates finding out the cross-sectional properties of the members of a steel frame such that the frame with these members has the required strength to withstand the external loadings, and its deflected shape is within the limitations specified by design codes. Structural designer can determine the cross-sectional properties of steel frame members in one step if the frame is statically determinate, if there are no restraints on joint displacements. In such frames computation of member forces does not require the prior information of cross-sectional properties, and the design can be completed within one step of structural analysis. Despite the design of statically indeterminate frames, structural analysis cannot be carried out without knowing the values of cross-sectional properties which makes the design process iterative. Designer has to first assume certain values for the cross-sectional properties

or select certain steel profiles from the available list of steel sections for the frame members before the analysis of the frame can be carried out in order to find out internal forces and moments in the members. With these assumed or preselected values of member cross-sectional properties, the structural response of the frame may not be within the limitations imposed by the design codes or the response might be far away from the bounds which are an indication of an overdesign. In this case, the designer has to change the values of the originally adopted cross sectional properties in order to satisfy the conditions that the values of joint displacements and strength of its members are within the limitations imposed by design codes. It is not difficult to envisage that designer has to carry out several trials before the desired set of cross-sectional properties is obtained. Although some engineering experience and intuition can be used in assigning the cross-sectional properties of members, it is needless to mention that finding the best combination of these cross-sectional properties is quite time consuming and

a complex task. It requires tremendous computational time to try all the possible combinations such that the strength and displacement constraints imposed by the design codes are satisfied, and the amount of steel which is required to build the frame is the minimum. However, the emergence of computational methods of mathematical programming and improvements that took place in computers in early 1960's has provided another approach for handling the structural design problems. In this new approach, the design problem is formulated as a decision-making problem where an objective function is to be minimized or maximized, while number of constraint functions is satisfied. The formulation of structural design problems as decision-making problems has yielded a new branch in structural engineering called structural optimization [1–12].

The mathematical model of a decision-making problem has the following form:

$$\text{Minimize } W = f(x_i), \quad i = 1, \dots, n, \quad (1a)$$

$$\text{Subject to } h_j(x_i) = 0, \quad j = 1, \dots, ne, \quad (1b)$$

$$g_j(x_i) \leq 0, \quad j = ne + 1, \dots, m, \quad (1c)$$

$$x_i^l \leq x_i \leq x_i^u, \quad (1d)$$

where x_i represents decision variable i . Decision variables may take continuous or discrete values. Continuous decision variable can take any real value within the range shown in (1d). The decision variables in structural optimization are called design variables which are the parameters that control the geometry or material properties of a steel frame. For example, the moment of inertias of beams and columns in a frame can be considered as continuous design variable if these elements are to be manufactured locally for that particular frame. However, if they are to be selected from commercially available set of steel sections, design variables can only take isolated values which make them discrete variables.

$f(x_i)$ in (1a) represent the objective function which can be used as a measure of effectiveness of the decision. In structural optimization problems generally minimum weight or cost of the structure is taken as objective function. The equalities $h_j(x_i)$ and inequalities $g_j(x_i)$ in (1b) and (1c), respectively, represent the limitations imposed on the behavior of the structure by the design codes. These may be serviceability limitations or ultimate strength requirements if the design code considered is based on limit state design. However, if the design code is based on allowable stress design then the constraints given in (1b) and (1c) become the stiffness equalities, displacement, and/or allowable stress limitations.

The review of the mathematical formulation of design optimization of steel frames is carried out according to the historical developments that took place in the design methods. Earlier steel design codes were based on allowable stress design concept, while the later design codes use limit state design perception.

2. Formulation of Steel Frame Design Optimization Problem

Survey on the structural optimization literature reveals that there are basically two types of design optimization formulation for the optimum design of elastic steel skeletal framed structures although some variations of each type do exist. In the first type of formulation which is also called conventional formulation or coupled analysis and design (CAND) only cross-sectional properties of steel frame members are taken as design variables. Joint displacements are not treated as design variables. In such formulation the stiffness equations are excluded from the mathematical model. Consequently, when the values of cross-sectional properties change during design cycles, it becomes necessary to analyze the structure and update the joint displacements and members forces. Hence structural analysis is a complementary part of the design process. In the second type of formulation joint displacements are also treated as design variables in addition to the cross-sectional properties of frame members. In such formulation the stiffness equations are included as design constraints in addition to other limitations in the mathematical model. This eliminates the necessity of carrying out structural analysis in every design cycle. The values of the joint displacements are determined by the optimization techniques similar to those of cross-sectional properties. It is apparent that in this type of formulation the total number of design variables is much more than the first type of formulation. This type of formulation is called simultaneous analysis and design (SAND). It should be pointed out that both ways of formulation yield the same optimum result. However, depending on the type of formulation adopted in the design problem the size and mathematical complexity of the model acquired differ.

2.1. Coupled Analysis and Design (CAND). In this type of formulation design phase is separated from the analysis phase. This is achieved by only treating the cross-sectional properties such as areas or moment of inertias of members as design variables. The general outlook of the mathematical model of this type of formulation is given in the following if allowable stress design method is considered for the frame:

$$\text{Minimize } W = \rho \sum_{i=1}^{ng} \ell_i A_i, \quad i = 1, \dots, ng, \quad (2a)$$

$$\text{Subject to } \delta_j(A_i) \leq \delta_{ju}, \quad j = 1, \dots, rd, \quad (2b)$$

$$\sigma_k(A_i) \leq \sigma_{all}, \quad k = 1, \dots, nm, \quad (2c)$$

$$A_{il} \leq A_i \leq A_{iu}, \quad (2d)$$

where ρ is the density of steel, A_i represents cross-sectional area for group, and i and ℓ_i is the total length of the members in group i in the steel frame. $\delta_j(A_i)$ is the restricted j th displacement, δ_{ju} is its upper bound, and rd is the total number of such restricted displacements. $\sigma_k(A_i)$ is the maximum stress in member k , and σ_{all} is the allowable stress for steel. nm is the total number of members in the structure.

TABLE 1: a_i and b_i values for W sections.

i	a_i	b_i
1	1.3162	2.1650
2	0.5971	1.8220
3	1.0160	1.5710

In the previously mentioned model joint displacements and stresses that develop in a frame due to external loading are expressed as function of cross-sectional areas of members. It is apparent that determination of the response of the frame under the applied loads requires the values of not only areas of members groups but the other cross-sectional properties such as moment of inertia and sectional modulus. Therefore in order not to increase the number of design variables in the programming problem, it becomes necessary to relate the other cross-sectional properties to sectional areas. This is achieved by applying the least square approximation to sectional properties of practically available steel profiles. These relationships can be expressed in the following form:

$$I_x = a_1 A^{b_1}, \quad I_y = a_2 A^{b_2}, \quad Z = a_3 A^{b_3}, \quad (3)$$

where A is the area, I_x and I_y are the moments of inertia about x - x and y - y , axis and Z is the sectional modulus of the cross-section. $a_1, a_2, a_3, b_1, b_2, b_3$ are constants. The values of these constants are obtained for the W sections of AISC [13] by making use of the least square approximation in [14]. The values of these constants are given in Table 1. It should be noted that in their computation the unit of centimeter (1 cm = 10 mm) was used.

It is apparent from (2b) that restricted displacements are required to be computed to find out whether they satisfy the displacement limitations. The joint displacements in framed structures are related to external loads through stiffness equations; $[K]\{D\} = \{P\}$ where $[K]$ is the overall stiffness matrix, $\{D\}$ is the vector of joint displacements, and $\{P\}$ is the vector of joint loads. The joint displacements can be computed from the stiffness equations as $\{D\} = [K]^{-1}\{P\}$. Although here the inverse of overall stiffness matrix is required to be calculated in order to obtain the joint displacements, this is avoided due to its high computational cost in the application of the optimization techniques used in the solution of the problem. Instead derivatives of the overall stiffness matrix with respect to design variables are calculated depending on the optimization technique selected.

2.2. Simultaneous Analysis and Design (SAND). In this type of formulation joint displacements are also treated as design variables in addition to cross-sectional properties. Since the cross-sectional properties and joint displacements are implicitly related through stiffness equations, it becomes necessary to include the stiffness equations as design constraints in the mathematical model. The general outlook of

the mathematical model of such formulation is given in the following:

$$\text{Minimize } W = \rho \sum_{i=1}^{ng} \ell_i A_i, \quad i = 1, \dots, ng, \quad (4a)$$

$$\text{Subject to } K(A_i)\{D\} = \{P\}, \quad (4b)$$

$$\delta_j \leq \delta_{ju}, \quad j = 1, \dots, rd, \quad (4c)$$

$$\sigma_k(A_i, \delta_j) \leq \sigma_{all}, \quad k = 1, \dots, nm, \quad (4d)$$

$$A_{il} \leq A_i \leq A_{iu}, \quad (4e)$$

where ρ is the density of steel, A_i represents the cross-sectional area selected for group i , and ℓ_i is the total length of the members in group i in the frame. ng is the total number of groups in the steel frame. A_{il} and A_{iu} are the lower and upper bounds imposed on the cross-sectional area i . Equality constraint (4b) represents stiffness equations. $\{D\}$ is the vector of joint displacements, which are treated as design variables. δ_j is the restricted joint displacement, and δ_{ju} is its bound. rd is the total number of restricted displacements. $\sigma_k(A_i, \delta_j)$ represents stress constraint which is a function of area and end joint displacements of member k . σ_{all} is the allowable stress for steel. nm is the total number of the members in the structure.

This way of formulation of the design problem is an integrated formulation which combines design and analysis phases in the same step that eliminates the need of separate structural analysis in each design cycle. Furthermore in this formulation the displacement constraints becomes very simple. Because they are treated as design variables they turn out to be just upper bound constraints. However, the number of design variables and constraints become very large compared to the previous type of formulation which necessitates use of powerful optimization techniques that are efficient for large-scale problems. It should be noticed that further variable transformation is necessary for joint displacement variables in this type of formulation, if mathematical programming techniques are used for the solution of the design problem due to the fact that while joint displacements can be positive or negative, mathematical programming techniques operate with only positive variables. This brings further mathematical burden to a designer. Furthermore, the difference in magnitude between the cross-sectional properties and joint displacements causes numerical difficulties in the solution of the design problem which makes it necessary to normalize the design variables.

Saka [15, 16] carried out reviews of the mathematical modeling and solution algorithms presented in recent years for the optimum design of skeletal structures. The review first introduces the general formulation of the general structural optimization problem based on linear elastic behavior without referencing to a particular design code. Later implementation of the design requirements defined in design codes is also covered. The techniques developed for the solution of optimum design problems are reviewed in a historical order.

Arora and Wang [17] also presented the review of mathematical modeling for structural and mechanical system optimization. In their review it is stated that the formulations are classified into three broad categories. The first type of formulation is known as the conventional formulation where only structural design variables are treated as optimization variables. In the second type of formulation state variables such as node displacements and/or element stresses are treated as design variables in addition to the cross-sectional properties. This type of formulation is called as simultaneous analysis and design (SAND). The third type of formulation is known as a displacement-based two-phase approach where displacements are treated as unknowns in the outer loop and the cross-sectional properties are treated as the unknowns in the inner loop. The review also covers more general formulations that are applicable to economics, optimal control, multidisciplinary problems, and other engineering fields. Altogether 254 references are included in the review.

Optimum design problem of steel frames turns out to be a nonlinear programming problem if allowable stress design is adopted whichever formulation method explained previously is used. The numerical optimization techniques available in the literature for obtaining the solution of nonlinear programming problems can be broadly classified into two groups such as deterministic and stochastic algorithms. Deterministic optimization techniques make use of derivatives of the objective function and constraints in the search of the optimum solution and involve no randomness in the development of solution techniques. The other groups of techniques that are also called metaheuristic optimization techniques do not require the derivatives of the objective function and the constraints. They rely on random search paradigms based on simulation of natural phenomena. These methods are nontraditional search and optimization methods, and they are very suitable and efficient in finding the solution of combinatorial optimization problems.

3. Deterministic Solution Techniques for Elastic Steel Frame Design Optimization Problems

Historically mathematical programming techniques were first to be used to obtain the solution of optimum design problem [1–12]. The developments took place in computers and in the methods of mathematical programming, and they have initiated a new era in designing engineering structures. The need to design aircraft components to have minimum weight and later the requirements of space programs has provided the necessary funds and motivation to engineers to develop effective design tools. As a result of a large number of research works, numerous numerical techniques were developed for the solution of nonlinear programming problems [1–12]. However, when these techniques were applied to the design of real-size practical steel frames numerical difficulties were encountered. It is found out that mathematical programming-based structural optimization methods were

only capable of designing steel frames with few dozen of design variables.

Optimality criteria approach was introduced in late 1960 with the purpose of overcoming the previously mentioned discrepancies of mathematical programming techniques. It was shown that the optimality criteria method was not dependent on the size of design problem and obtained the near-optimum solution with few structural analyses. It was this feature that made the optimality criteria techniques attractive over the mathematical programming methods. Optimality criteria approaches were widely utilized in the design of large-size practical structures.

One of the common features of the both methods is that they consider continuous design variables. In reality, variables in most of the steel frame design problems are to be selected from a set of discrete values that are available in practice. This fact made it necessary to extend the mathematical programming techniques to be capable of handling discrete programming problems. This necessity has brought further difficulties, and the capability of the methods developed to solve such programming problems was found to be limited. Arora [18] recently presented comprehensive review of the methods available for discrete variable structural optimization. In spite of the fact that the number of algorithms has been developed for obtaining the solution of discrete variables steel frame design optimization problems, they have not found widespread application owing to their complexity and inefficiency in dealing with large size structures.

3.1. Mathematical Programming Based Steel Frame Design Optimization Techniques. Mathematical programming techniques start the search for the optimum solution at a preselected initial point and compute the gradients of the objective function and constraints at this point. They take a step in the negative direction of the gradient of the objective function in the case of minimization problems to determine the next point. They continue this process of finding a new point until there is no significant change in the values of design variables within two consecutive iterations. There are several mathematical programming techniques available in the literature. In this paper only those that are used in developing structural optimization algorithms for the optimum design of steel frames are considered. These can be collected in three broad groups. Each group uses different concept. In the first group of algorithms approximation is carried out through the use of linearization concept. The second group converts the constrained problem into unconstrained one, and the third group handles the mathematical programming problem as it is without transforming it into another form.

3.1.1. Sequential Linear Programs. The first group of algorithms employs sequential linear programming method developed by Griffith and Stewart [19]. This method makes use of Taylor expansions to transfer the nonlinear programming problem into a linear programming one. This is achieved by taking first two terms after applying Taylor's expansion to nonlinear functions in the programming problem. The design problems (2a), (2b), (2c), (2d), (4a), (4b),

(4c), (4d), and (4e) can be rewritten in a general form as in the following:

$$\text{Minimize } W = \sum_{k=1}^m w_k(x_i), \quad i = 1, \dots, n, \quad (5a)$$

$$\text{Subject to } h_j(x_i) = 0, \quad j = 1, \dots, ne, \quad (5b)$$

$$g_j(x_i) \leq 0, \quad j = ne + 1, \dots, nc, \quad (5c)$$

where x_i represents the design variable i regardless of the type of the mathematical formulation followed, and n is the total number of design variables the problem. $h_j(x_i)$ represents nonlinear equality constraints, and ne is the total number of such constraints. $g_j(x_i)$ represents a nonlinear inequality constraint j . nc is the total number of constraints in the design problem. The objective function and constraints functions need not be convex. It is assumed that the region defined by (5a), (5b), and (5c) is bounded. This nonlinear programming problem is locally approximated into a linear programming problem by taking two terms of Taylor expansion of every nonlinear function in (5a), (5b), and (5c) about the current design point x^k . To assure that the approximation is adequate, the region of permissible solutions must be kept small. This is accomplished by applying move limits to the design variables.

Assuming that all the constraints are nonlinear, the programming problem (5a), (5b), and (5c) can be linearized about x^k which is the vector of design variables $x^k = \{x_1^k, x_2^k, \dots, x_n^k\}$ as

$$\begin{aligned} \text{Min } W &= w(x^k) + \nabla w(x^k)(x^{k+1} - x^k), \\ \text{subject to } h_j(x^k) + \nabla h_j(x^k)(x^{k+1} - x^k) &= 0, \\ j &= 1, \dots, ne, \\ g_j(x^k) + \nabla g_j(x^k)(x^{k+1} - x^k) &\leq 0, \\ j &= ne + 1, \dots, nc, \\ (1 - m)x^k &\leq x^{k+1} \leq (1 + m)x^k, \end{aligned} \quad (6)$$

where the value of every function is known at the design point x^k , and $\nabla w(x^k)$, $\nabla h_j(x^k)$, and $\nabla g_j(x^k)$ are $(1 \times n)$ gradient vectors of the functions at x^k . The last constraint in (6) defines the region of permissible solutions that is constructed by using some preselected percentage of the current design point. m is known as move limit which is $0 \leq m \leq 1$. The gradient vector $\nabla w(x^k)$ consists of the first derivatives of function $w(x^k)$:

$$\nabla w(x_k) = \left[\frac{\partial w}{\partial x_1^k}, \frac{\partial w}{\partial x_2^k}, \dots, \frac{\partial w}{\partial x_n^k} \right]. \quad (7)$$

The linear programming problem (6) can be arranged in the following form:

$$\begin{aligned} \text{Min. } W &= Cx^{k+1} - C_0, \\ \text{subject to } Ax^{k+1} &\begin{pmatrix} = \\ \leq \end{pmatrix} B, \end{aligned} \quad (8)$$

where C_0 is a constant, C is a vector of order $(1 \times n)$, coefficient matrix A is $[(nc + 2n) \times n]$, and the right-hand side vector is of order of $[(nc + 2n) \times 1]$. They have the following form:

$$\begin{aligned} C_0 &= w(x^k) - \nabla w(x^k)x^k, \\ C &= \nabla w(x^k), \\ [A] &= \begin{bmatrix} \nabla h_j(x^k) \\ \nabla g_j(x^k) \\ I \\ I \end{bmatrix}, \quad [B] = \begin{bmatrix} \nabla h_j(x^k)x^k - h_j(x^k) \\ \nabla g_j(x^k)x^k - g_j(x^k) \\ (1 + m)x^k \\ (1 + m)x^k \end{bmatrix}, \end{aligned} \quad (9)$$

which are constructed at current design point x^k .

The problem (8) is the linear approximation of the original nonlinear programming problem of (5a), (5b), and (5c). The simplex method can now be employed for the solution of this problem to obtain x^{k+1} . The previous design vector x^k is replaced by x^{k+1} , and the linearization is carried out about this new point. This process is repeated with gradually decreasing move limits until no significant improvement occurs in the value of the objective function. It was found reasonable to start with $m = 1$ and reduce to 0.1 each cycle until it reaches 0.1 [3, 5, 20]. Reinschmidt et al. [21], Pope [22] and Johnson, and Brotton [23] are some of the studies which were based on this linearization technique. In all these works, the cross-sectional properties of members were the only design variables. Saka [3, 5] used the linearization technique and treated joint displacements as design variables in addition to cross-sectional areas. Such formulation has also been used by Arora and Haug [24].

Sequential linear-programming-based design algorithms are attractive due to the availability of reliable linear programming packages to most of the computer users. Initial design point required to be selected by user prior to employing the algorithm can be feasible or infeasible. However, the method has a number of disadvantages. Firstly, it requires several optimization cycles to reach the optimum solution which makes it computationally costly. Secondly, choice of move limits is important because it affects the total number of iterations to find the optimum solution. Unfortunately the selection of these limits is problem dependent. Thirdly, when the starting point is infeasible, linearized problem may not have a feasible solution which means that intermediate solutions are practically useless. Furthermore, the convergence difficulties arise in the design of steel frames with large numbers of design variables. In such problems, linearization errors become large, and the linearized problem may not have a feasible solution. In both cases, it becomes necessary to relax the move limits and restart of the application of the method [7, 10].

Sequential quadratic programming also uses the concept of linearization, and it is one of the most effective mathematical programming techniques for nonlinearly constrained optimization problems [12, 25, 26]. The method consists of approximating the original nonlinearly constrained problem

with a quadratic subproblem and solving the subproblem successively until convergence has been achieved on the original problem [27]. It is shown in [28] that sequential quadratic programming is quite efficient in obtaining the solution of large-scale structural optimization problems.

Wang and Arora [29] have presented two alternative formulations based on the concept of simultaneous analysis and design (SAND) for optimum design of framed structures. Nodal displacements and member forces are treated as design variables in addition to member cross-sectional properties. This leads to having stiffness equations as equality constraints in the mathematical model. The objective function and other constraints are expressed as explicit functions of the optimization variables. A sequential quadratic programming method is used to obtain the solution of the design problem. It is concluded that the SAND formulation works quite well for optimization of framed structures.

Wang and Arora [30] studied the sparsity features of simultaneous analysis and design (SAND) type of mathematical modeling for large-scale structures. It is stated that although SAND formulation has a large number of design variables gradients of the functions, and Hessian of the Lagrangian are quite sparsely populated. This property of the formulation is exploited with optimization algorithms with sparse matrix capability such as sequential quadratic programming (SQP) for solving large-scale problems. It is concluded that in terms of the wall-clock time or the CPU time/iteration, the SAND formulations are more efficient than the conventional formulation due to the fact that the number of call-to-analysis routine was much smaller.

3.1.2. Penalty Function Methods. The second group of algorithms uses sequential unconstrained minimization techniques of nonlinear programming methods to obtain the solution of the design problem. These methods replace the constrained nonlinear programming problem by a new unconstrained one so that one of the unconstrained minimization algorithms can be utilized for its solution. Unconstrained minimization methods are quite general and efficient compared to constrained minimization algorithms. Thus, the basic idea is to place a penalty on constraint violation so that the solution is forced to satisfy the constraint functions. Most of the work in this area is based on the development introduced by Carroll [31] and Fiacco and McCormack [32]. These methods are widely used in structural design and have some practical advantages. There are two types of penalty function methods: exterior and interior penalty functions.

Exterior penalty function method transforms the constrained programming problem (5a), (5b), and (5c) into an unconstrained one by the following function:

$$\begin{aligned} \text{Min } \phi(x, r) = & W(x) + r \sum_{j=1}^{nc} h_j^2(x) \\ & + \frac{1}{r} \sum_{j=nc+1}^{nc} \left\{ \min [0, g_j(x)] \right\}^2, \end{aligned} \quad (10)$$

for $r = 1, 0.1, 0.01, 0.001, r_i \rightarrow 0, r_i > 0$, and so forth. Each penalty is directly associated with the corresponding

constraint violation. The inequality terms are treated differently from the equality terms because the penalty applies only for constrained violation. The positive multiplier r controls the magnitude of the penalty terms. The problem is solved by decreasing r in successive steps. In exterior penalty function methods all intermediate solutions lie in the feasible region. The solution may be started from an infeasible point, which provides flexibility for the designer eliminating the need for finding the initial feasible design point. However, the algorithm cannot find a feasible solution before reaching the optimum. All intermediate solutions are infeasible and do not provide a usable design.

Interior penalty function method is employed when only inequality constraint is present in the problem. It has the following form:

$$\phi(x, r) = W(x) + r \sum_{j=1}^{nc} \frac{1}{g_j(x)} \quad (11)$$

or in a logarithmic form

$$\phi(x, r) = W(x) - r \sum_{j=1}^{nc} \log_e [g_j(x)], \quad (12)$$

$$r = 1, 0.1, 0.01, \dots \rightarrow 0, r_i > 0.$$

The interior penalty function method requires feasible initial design point to start with. This provides an advantage over exterior penalty method such that all intermediate solutions are feasible hence provide usable designs. Furthermore, the constraints become critical only near the end of the solution process. This provides advantage to the designers in selecting the near optimal solution, which is a less critical design instead of optimal design.

The structural optimization algorithms based on the penalty function methods are numerically reliable for problems of moderate complexity. They are general and suitable for various optimum structural design formulations. However, they have the drawback of requiring large number of structural analysis which is computationally expensive. Numerical difficulties may also arise in the case of ill-conditioned minimization problems. In the field of optimum structural design these methods have been used by Kavlie and Moe [33, 34], Griswold and Moe [35], and De Silva and Grant [36].

3.1.3. Gradient Method. The third group of techniques approach to the solution of a nonlinear programming problem in a direct manner. Instead of transforming the problem into another form, they deal with the constrained one as it is. These methods approach to the optimum solution step by step. At each step solution moves from current values of design variables to the next values along a suitable direction. This direction is determined by making use of the gradient vectors of the objective and constraint functions. This is why they are called gradient methods. The gradient-projection method proposed by Rosen [37] for linear constraints is based on a projecting search into the subspace defined by the active constraints. This method has been modified by

Haug and Arora [38] for nonlinear constraints and used to develop a structural optimization algorithm. The method of feasible direction proposed by Zoutendijk [39] is employed by Vanderplaats [40, 41] in the popular CONMIN program. The feasible direction method starts with some design point x^0 at the boundary of the feasible region and then searches for the best direction and step size to move within the feasible region, to a new point x^1 such that the objective function values are improved:

$$x^1 = x^0 + \alpha S^0, \quad (13)$$

where α is a step size and S^0 is the direction vector. In determining the direction vector, two conditions must be satisfied. The first is that the direction must be feasible. This is achieved in problems where the constraints at a point curve inward, if $S^T \nabla g_j < 0$. If a constraint is linear or outward curved, it may require $S^T \Delta g_j \geq 0$. The second condition is that the direction must be usable, and the value of objective function is improved. This is satisfied if $S^T \nabla f < 0$.

Despite not being very widely used in structural optimization, there are other nonlinear programming techniques that are employed in solving the steel frame design problem. Among these geometric programming [42] is applied to obtain optimum design of a number of different structural problems [43]. On the other hand, dynamic programming [44] was used in the optimum design of continuous beams and multistory frames by Palmer [45, 46]. Both methods are applicable to problems with specialized form. This is why these techniques have not been used extensively in the field of steel frame design.

It can be concluded that mathematical programming techniques are general. It is possible to include displacement stress, stiffness, and instability constraints in the optimum design formulation of the framed structures. Inclusion of stability constraints results in highly nonlinear programming problem. Among the large number of available methods [47, 48] the techniques used in the structural optimization can be collected in three groups. The literature survey shows that the optimum design algorithms developed are good only in designing structures with few members. Unfortunately, there is no single general nonlinear programming algorithm that can effectively be used in solving all types of structural optimization problems. Those that perform well in small- or moderate-size structures run into numerical difficulties in large-size structures. Except few, computer implementation of these algorithms mostly is cumbersome. They require several structural analyses to be carried out in each design cycle to update the response of the structure. This makes them computationally expensive. Overall, it is reasonable to state that among the existing mathematical programming methods, the ones that make use of approximation techniques such as sequential quadratic programming result in an efficient structural optimization algorithms even for large-scale optimum design problems if the design variables are continuously not discrete.

3.2. Optimality Criteria Methods Based on Steel Frame Design Optimization Techniques. Optimality criteria methods differ

from the mathematical programming methods in the way they solve the optimum design problem. While mathematical programming techniques attempt to minimize the objective function directly considering the constraint functions, the optimality criteria methods derive a criterion based on intuition such as fully stressed design or based on a mathematical statement such as Kuhn-Tucker conditions. They then establish an iterative procedure to achieve this criterion. It is expected that when this is accomplished, the optimum solution will be obtained. Optimality criteria methods are not as general as the mathematical programming techniques. However, they are computationally more efficient. Their performance does not depend on the size of the design problem, and they are easier to implement for computers. Number of structural analysis required to reach the final design is much less than mathematical programming methods. However, in certain cases, they may not converge to the optimum solution.

Optimality criteria methods were originated by Prager and his coworkers [49] for continuous systems using uniform energy distribution criteria. Venkayya et al. [50–52], Berke [53, 54], and Khot et al. [55–57] have later applied this idea to discrete systems. Ragsdell has reviewed these techniques in [58]. In these methods, a prior criterion is derived using Kuhn-Tucker conditions. This criterion that is required to be satisfied in the optimum solution provides a basis in producing a recursive relationship for design variables. This relationship is used to resize the structural elements during the optimum design cycles. The design process is terminated when convergence is attained in the value of objective function. The optimality criteria method is applied to optimum design of pin-jointed structures by Feury and Geradin [59], Fleury [60], and Saka [61]. It is applied to optimum design of steel framed structures by Tabak and Wright [62], Cheng and Truman [63], Khan [64], and Sadek [65]. Khot et al. [55] have carried out the comparison of different optimality criteria methods. In all these algorithms, displacement, stress, and minimum-size constraints on the design variables were all considered. It is shown in these works that the design methods based on the optimality criteria approach are straightforward and easy to program. Their behavior in obtaining the optimum solution does not change depending on the number of design variables. Number of structural analysis required to reach to optimum design is relatively small compared to mathematical programming based techniques which makes optimality criteria based structural optimization algorithms efficient and attractive for practicing engineers.

However, none of the previously mentioned methods have considered the code specifications in the formulation of the design problem. Saka [66] has presented optimality criteria based minimum weight design algorithm for pin jointed steel structures where the design requirements were the same as the ones specified in AISC [13]. In this work, an algorithm is developed for the optimum design of pin-jointed structures under the number of multiple loading cases while considering displacements, stress, buckling, and minimum-size constraints. In contrast to the previous work, fixed-value allowable compressive stresses were not utilized for the compression members; instead they are left to the algorithm

to be decided. The values of critical stresses are computed in every design step by making use of the current values of the design variables. In order to achieve this, the critical stresses are first expressed in terms of design variables as nonlinear linear equations by making use of the relationships given in design codes. These equations are then solved by the Newton-Raphson method to obtain the value of the design variable that satisfies the buckling constraint.

3.2.1. Linear Elastic Steel Frames. The optimum design problem of a rigidly jointed plane frame formulated according to ASD-AISC (Allowable Stress Design, American Institute of Steel Construction) [13] can be expressed as follows:

$$\begin{aligned} \text{Min} \quad & W = \sum_{k=1}^{\text{ng}} A_k \sum_{i=1}^{mk} \rho_i \ell_i, \\ \text{Subject to} \quad & \delta_{j\ell} \leq \delta_{j\ell u}, \quad j = 1, \dots, p, \\ & \ell = 1, \dots, \text{n}\ell\text{c}, \\ & \frac{f_{\text{anl}}}{F_{\text{anl}}} + \frac{m_1}{m_2} \frac{f_{\text{bxnl}}}{F_{\text{bxnl}}} \leq 1, \quad n = 1, \dots, \text{nm}, \\ & A_k \geq A_{k\ell}, \quad k = 1, \dots, \text{ng}, \end{aligned} \quad (14)$$

where A_k is the area of members belonging to group k ; mk is the total number of members in group k ; ρ_i and ℓ_i are the density of the material and the length of members in group i ; ng is the total number of member groups in the structure. $\delta_{j\ell}$ is the displacement of joint j under the load case ℓ , and $\delta_{j\ell u}$ is its upper bound; p is the total number of restricted displacements. $\text{n}\ell\text{c}$ is the total number of load cases that the frame is subjected to. f_{anl} and f_{bxnl} are the computed axial stress and compressive bending stress in member n under load case ℓ . F_{anl} is the allowable axial compressive stress considering that the member is loaded by axial compression only, F_{bxnl} is the allowable compressive bending stress considering that the member i is loaded in bending only. m_1 is a constant and m_2 is an expression given in [13]. nm is the total number of members in the frame. $A_{k\ell}$ is the lower bound on the design variable A_k . This bound is required to prevent member areas being reduced to zero in the optimum solution.

In the optimum design problem (14) only the cross-sectional areas of different groups in the frame are treated as design variables. It is apparent that determination of the response of the frame under the applied loads necessitates the values of the other cross-sectional properties such as moment of inertia and sectional modulus. Therefore it becomes necessary to use the relationship (3) to relate the other cross-sectional properties to sectional areas in order not to increase the number of design variables in the programming problem.

The solution of the design problem (14) is obtained in an iterative manner. The area variables are changed during iterations with the aim of obtaining a better design. It is apparent that the new values of design variables are decided by the most severe design constraint in every design cycle. This necessitates obtaining an expression for updating these

variables depending upon whether the displacement, stress, or the buckling constraints are dominant in the design problem. If neither of these constraints is dominant, then the area variable is decided by the minimum-size limitation.

Dominance of Displacement Constraints. In the case where the displacement constraints are dominant in the design problem, the new values of the design variables are decided by these constraints. If the design problem (14) is rewritten by only considering the displacement constraints, the following mathematical model is obtained:

$$\begin{aligned} \text{Min} \quad & W = \sum_{K=1}^{\text{ng}} A_k \sum_{i=1}^{mk} \rho_i \ell_i, \\ \text{subject to} \quad & g_{i\ell}(A_k) = \delta_{j\ell} - \delta_{j\ell u} \leq 0, \quad j = 1, \dots, p, \\ & \ell = 1, \dots, \text{n}\ell\text{c}. \end{aligned} \quad (15)$$

Employing language multipliers, this constrained problem can be transformed into unconstrained form as

$$\phi(A_k, \lambda_{j\ell}) = \sum_{k=1}^{\text{ng}} A_k \sum_{i=1}^{mk} \rho_i \ell_i + \sum_{\ell=1}^{\text{n}\ell\text{c}} \sum_{j=1}^P \lambda_{j\ell} g_{j\ell}(A_k), \quad (16)$$

where $\lambda_{j\ell}$ is the Lagrangian parameter for the j th constraint under the ℓ th load case. The necessary conditions for the local constrained optimum are obtained by differentiating (16) with respect to the design variable A_k as

$$\frac{\partial \phi(A_k, \lambda_{j\ell})}{\partial A_k} = \sum_{i=1}^{mk} \rho_i \ell_i + \sum_{\ell=1}^{\text{n}\ell\text{c}} \sum_{j=1}^P \lambda_{j\ell} \frac{\partial g_{j\ell}(A_k)}{\partial A_k} = 0. \quad (17)$$

By using the virtual work method δ_{jl} , the j th displacement of the frame under the load case ℓ can be expressed as

$$\delta_{j\ell} = X_{\ell}^T K X_j, \quad (18)$$

where X_j is the virtual displacement vector due to virtual loading corresponding to the j th constraint. This loading case is setup by applying a unit load in the direction of the restricted displacement j . K is the overall stiffness matrix of the frame, and X_{ℓ} is the displacement vector due to the applied load case ℓ . Equation (18) can be decomposed as sum of the contributions of each member in the frame as

$$\delta_{jl} = \sum_{i=1}^{\text{nm}} X_{il}^T K_i X_{ij} = \sum_{i=1}^{\text{nm}} \frac{f_{ijl}}{A_i}, \quad (19)$$

where f_{ijl} is known as the flexibility coefficient

$$f_{ijl} = X_{il}^T K_i X_{ij} A_i, \quad (20)$$

where K_i is the contribution of member i to the overall stiffness matrix. Substituting (20) into the derivative of the displacement constraint leads to the following:

$$\frac{\partial g_{j\ell}(A_k)}{\partial A_k} = -\frac{1}{A_k^2} \sum_{i=1}^{mk} f_{ij\ell}, \quad (21)$$

which only involves with the members in group k . Hence (17) becomes

$$\sum_{i=1}^{mk} \rho_i \ell_i - \sum_{\ell=1}^{n\ell c} \sum_{j=1}^p \lambda_{j\ell} \frac{1}{A_k^2} \sum_{j=1}^{mk} f_{ij\ell} = 0. \quad (22)$$

Rearranging (22), considering constant ρ throughout the frame, and multiplying both sides by A_k^r and then taking the r th root leads to

$$A_k^{v+1} = A_k^v \left[\frac{1}{\rho \sum_{i=1}^{mk} \ell_i} \sum_{\ell=1}^{n\ell c} \sum_{j=1}^p \lambda_{j\ell} \frac{1}{A_k^2} \sum_{j=1}^{mk} f_{ij\ell} \right]^{1/r}, \quad (23)$$

$$k = 1, \dots, ng,$$

where v is the iteration number. This is known as the optimality criterion. It can be used to obtain the new values of design variables in each iteration provided that Lagrange parameters are known. There are several suggestions for the computation of Lagrange parameters. They are summarized in [55]. Among them, the one suggested by Khot [56] is simple and easy to apply:

$$\lambda_{j\ell}^{v+1} = \lambda_{j\ell}^v \left(\frac{\delta_{j\ell}}{\delta_{j\ell u}} \right)^{1/c}, \quad j = 1, \dots, p, \quad (24)$$

where v is the current and $v+1$ is the next iteration number. c is a preselected constant known as a step size. The value of 0.5 provides steady convergence. It is apparent that in order to use (24), it is necessary to select some initial values for Lagrange multipliers.

Dominance of Strength Constraints. In the case where the strength constraints are dominant in the design problem it becomes necessary to derive an expression from which the new values of area variables can be computed. In this study this expression is based on ASD-AISC [13] inequalities which are repeated below for only considering in-plane bending:

$$\frac{f_a}{F_a} + \frac{C_m f_{bx}}{(1 - f_a/F'_{ex}) F_{bx}} \leq 1, \quad (25)$$

$$\frac{f_a}{0.6F_y} + \frac{f_{bx}}{F_{bx}} \leq 1, \quad (26)$$

where x with subscripts b , m , and e is the axis of bending which a particular stress or design property applies, F_y is the yield stress, and f_a and f_b are the computed axial stress and bending stress at the point under consideration. F_a is the allowable axial compressive stress considering that the member is only axially loaded, F_b is the allowable compressive bending stress considering that the member is only under bending loading. C_m is a factor and is given as 0.85 for compression members in frames subject to joint translation. F'_{ex} is Euler stress divided by a factor:

$$F'_{ex} = \frac{12\pi^2 E}{23S^2}, \quad (27)$$

where $S = \eta l_b / r_b$ is the slenderness ratio of member, l_b is the actual unbraced length in the plane of bending, r_b is the corresponding radius of gyration, η is the effective length factor in plane of bending, and E is the modulus of elasticity.

The inequalities (25) and (26) are required to be satisfied for those frame members subjected to both axial compression and bending; the others that are subjected to axial tension and bending require satisfying the inequality (26). In these inequalities the allowable stresses F_a , F_b , and F_e are related to the instability of the member. They are function of various cross-sectional properties that are to be expressed in terms of area variables.

Axial Stability Constraints. The allowable critical stress F_a for a compression member i under load case ℓ is given in ASD-AISC as the following.

If $S_i \geq C$ elastic buckling is

$$F_a = \frac{12\pi^2 E}{23S_i^2}. \quad (28)$$

If $S_i \leq C$ plastic buckling is

$$F_a = \frac{F_y (1 - S_i^2 / 2C^2)}{n}, \quad (29)$$

$$n = \frac{5}{3} + \frac{3 S_i}{8 C} - \frac{S_i^3}{8 C^3},$$

where S_i is the slenderness ratio of the member i and C is given as $\sqrt{(2\pi^2 E / F_y)}$. It is apparent from (28) and (29) that critical stress of a compression member is function of its slenderness ratio which in turn is related to the radius of gyration of the cross section of a member. The cross-sectional areas change from one design step to another as well as from one member to another during the design process. This results in having varying critical stress limits in the design optimization problem of the steel frame. Consequently it becomes necessary to express the allowable critical stress of a compression member in terms of area variables so that its value can be calculated whenever the cross-sectional area of a member changes. This is achieved by employing the approximate relationship given in (3). Computation of allowable critical stress of a compression member differs depending on its slenderness ratio as given in (28) and (29). It is found more suitable here to identify whether a compression member buckles in elastic region or in plastic region through the value of the critical load P_{cr} . This load is obtained by using the fact that for the value of $S_i = C$ (28) and (29) give the same value. That is

$$S_i = C; \quad P_{cr} = F_a A_{cr}; \quad P_{cr} = \frac{12\pi^2 E A_{cr}}{23C}, \quad (30)$$

where A_{cr} is the critical area value for member i . Since a compression member can buckle about its x - x or y - y axis depending on whichever slenderness ratio is critical, it is then necessary to express both radii of gyration in terms of area variables by using the relationship

$$r_x = a_1^{0.5} A^{c_1}, \quad r_y = a_2^{0.5} A^{c_2}, \quad (31)$$

where $c_1 = 0.5(b_1 - 1)$ and $c_2 = 0.5(b_2 - 1)$. It follows from $s_{xi} = l_{xi}/r_{xi}$ and $S_{yi} = l_{yi}/r_{yi}$ where l_{xi} and l_{yi} are the effective length of member i about x - x and y - y axis, respectively. The critical area value is then easily obtained from

$$S_i = \frac{l_k}{(a_k^{0.5} A_{cr})^{c_k}}; \quad A_{cr} = \left[\frac{l_k}{(a_k^{0.5} C)^{c_k}} \right]^{c_k}, \quad (32)$$

where the subscript k of l_k is either x or y and subscript k of a_k and c_k is either 1 or 2, whichever applies.

After the computation of P_{cr} from (37), the check for the elastic or plastic buckling can proceed as the following.

If $P_a \leq P_{cr}$ elastic buckling is

$$F_a = \frac{12\pi^2 E}{23S_i^2}. \quad (33)$$

If $P_a \geq P_{cr}$ plastic buckling is

$$F_a = \frac{F_y (24C^3 - 12CS_i^2)}{40C^3 + 9S_i C^2 - 3S_i^3}, \quad (34)$$

where P_a is the compression force in member i under the load case ℓ .

Finally the previously mentioned allowable stresses can be related to area variables by substituting $S_i = l_k/(a_k^{0.5} A^{c_k})$ which yields to the following expressions.

If $P_a \leq P_{cr}$ elastic buckling is

$$F_a = t_6 A^{2c_k}. \quad (35)$$

If $P_a \geq P_{cr}$ plastic buckling is

$$F_a = \frac{e_1 A^{3c_k} - e_2 A^{c_k}}{e_3 A^{3c_k} + e_4 A^{2c_k} - e_5}, \quad (36)$$

where the constants are

$$t_6 = \frac{12\pi^2 E a_k}{(23l_k^2)}, \quad e_1 = 24F_y C^3 a_k^{1.5}, \quad e_2 = 12F_y l_k^2 C a_k^{0.5}, \quad (37)$$

$$e_3 = 40C^3 a_k^{1.5}, \quad e_4 = 9C^2 l_k a_k, \quad e_5 = 3l_k^3. \quad (38)$$

In the previously mentioned expressions

$$\begin{aligned} \text{if } S_{xi} \leq S_{yi} \text{ then } l_k &= l_{yi}, \quad a_k = a_2, \quad c_k = c_2, \\ \text{if } S_{xi} > S_{yi} \text{ then } l_k &= l_{xi}, \quad a_k = a_1, \quad c_k = c_1. \end{aligned} \quad (39)$$

Consequently, the allowable axial compressive stress F_a of inequality (25) is replaced by either (35) or (36), whichever applies.

Lateral Stability Constraints. The allowable compressive stress F_b of (25) and (26) is given by the following formulae in ASD-AISC:

$$\text{when } \sqrt{\frac{70830C_b}{F_y}} \leq \frac{l_e}{r_t} \leq \sqrt{\frac{354200C_b}{F_y}} \quad (40)$$

$$\text{then } F_b = \left[\frac{2}{3} - \frac{F_y (l_e/r_t)^2}{1.055 \times 10^6 C_b} \right] F_y,$$

$$\text{when } \frac{l_e}{r_t} > \sqrt{\frac{354200C_b}{F_y}} \text{ then } F_b = \frac{1.17 \times 10^5 C_b}{(l_e/r_t)^2}, \quad (41)$$

where the units of the yield stress F_y and the allowable compressive bending stress F_b are kN/cm^2 .

In (40) and (41) the value of F_b cannot be more than 0.6. F_y and r_t are the radii of gyration of I section comprising the flange plus one-third of the compression web area taken about minor axis. l_e is the lateral effective length of the beam. The coefficient C_b is given a

$$C_b = 1.75 + 1.5\beta + 0.3\beta^2 \leq 2.3, \quad (42)$$

in which β is the ratio of the small moment M_1 to the larger moment M_2 acting at the ends of the member. β has positive sign if the member is in single curvature, has negative sign otherwise. Since the end moments of the frame members are available at every design step from the analysis of frame which is carried out at every design step, C_b becomes a constant which makes F_b only a function of r_t . In I shaped sections r_t may be approximated as $1.2r_y$ as given in [67]. r_t can be expressed in terms of area variable by employing the relationship (3) as

$$r_t = 1.2r_y = 1.2a_2^{0.5} A^{c_2}. \quad (43)$$

Substitution of (43) into (44) yields

$$F_b = (t_1 - t_2 A^{-2c_2}), \quad (44)$$

where

$$t_1 = \frac{2F_y}{3}, \quad t_2 = \frac{F_y^2 l_e^2}{(1.519 \times 10^6 a_2 C_b)}. \quad (45)$$

And substituting in (41) gives

$$F_b = t_4 A^{2c_2}, \quad (46)$$

where

$$t_4 = 1.6848 \times 10^5 a_2 C_b l_e^{-2}. \quad (47)$$

Depending on the lateral slenderness ratio of the beam either (44) or (46) is substituted in (25) and (26).

Combined Stress Constraints. The Euler stress given in (27) can also be expressed in terms of area variables by substituting $S_i = I_x / (a_1^{0.5} A^{c_1})$ which yields to the following expression:

$$F'_{ex} = t_5 A^{2c_1}, \quad (48)$$

where

$$t_5 = \frac{12\pi^2 E a_1}{(23I_x^2)}. \quad (49)$$

The axial and bending stresses in the member due to the applied loads are

$$f_a = \frac{P_a}{A}, \quad f_b = \frac{M_x}{(a_3 A^{b_3})}, \quad (50)$$

where P_a and M_x are the axial force and the maximum bending moment in the member.

Substituting (48) and (50) into (25) with $C_m = 0.85$ and carrying out simplifications the combined stress constraint can be reduced to the following nonlinear equation:

$$\begin{aligned} \alpha_1 F_b A^{b_3} - \alpha_2 F_b A^{c_3} + \alpha_3 F_a A - \alpha_4 F_b F_a A^{b_3+1} \\ + \alpha_5 F_b F_a A^{c_3+1} = 0, \end{aligned} \quad (51)$$

where $c_3 = b_3 - 2c_1 - 1$ and the constants are

$$\begin{aligned} \alpha_1 = a_3 t_5 P_a, \quad \alpha_2 = a_3 P_a^2, \quad \alpha_3 = 0.85 M_x t_5, \\ \alpha_4 = a_3 t_5, \quad \alpha_5 = a_3 P_a. \end{aligned} \quad (52)$$

It is apparent from (35), (36), (44), and (46) that F_a and F_b are also nonlinear expressions of area variables. Substitution of these into (51) increases the nonlinearity of the equation even further. Similarly substitution of (50) into the combined stress constraint of (26) reduces this equation into a nonlinear equation of area variable:

$$u_1 F_b A^{b_3} + u_2 A - u_3 F_b A^{b_3+1} = 0, \quad (53)$$

where the constants are

$$u_1 = a_3 P_a, \quad u_2 = 0.6 F_y M_x, \quad u_3 = 0.6 F_y a_3. \quad (54)$$

The equations (51) and (53) are solved using Newton-Raphson method to obtain the value of area variables that satisfy the combined stress constraints. The solution of these equations does not introduce any difficulty although they are highly nonlinear. The derivatives with respect to area variables that are required by Newton-Raphson method are evaluated analytically since F_a and F_b are already expressed in terms of area variables. Numerical experiments have shown that it takes not more than 5 to 6 iterations to obtain the roots of these nonlinear equations. The larger value obtained from these equations is adopted as the member area for the next

design step for the case where the combined stress constraints are dominant in the design problem.

Optimum Design Algorithm. The steps of the design procedure described previously are given in the following.

- (1) Select the initial values of area variables and Lagrange multipliers.
- (2) Analyze the frame with these values of area variables and obtain the joint displacements as well as member end forces under the external loads and unit loads applied in the direction of the restricted displacements.
- (3) Compute the Lagrange multipliers from (24).
- (4) Take each area group in the frame respectively and compute the new value of the area variable which is in the cycle from (23).
- (5) Compute the lower bound on the same area variable for the combined stress constraints from (51) and (53). Select the largest.
- (6) Compare the three area values obtained from dominant displacement constraints, the combined stress constraints, and the minimum size restrictions. Take the largest among three as the new value of the area variable for the next design cycle.
- (7) Carry out the steps 4, 5, and 6 for all the area groups in the frame.
- (8) Check the convergence on the weight of the frame. If it is satisfied go to step 9; else go to step 2.
- (9) Check whether the displacement and combined stress constraints are satisfied. If not then go to step 2; else stop.

The initial design point required to initiate the design procedure can be selected in any way desired. It can be feasible or even be infeasible. The area variables in the initial design point can be selected as all are equal to each other for simplicity or can be decided using engineering judgment. The numerical experimentation carried out has shown that the design algorithm works equally well with all these different initial points.

SODA developed by Grieson and Cameron [68] was the first commercial structural optimization software for practical buildings design. This software considered the design requirements from Canadian Code of Standard Practice for Structural Steel Design (CAN/CSA-S16-01 Limit States Design of Steel Structures) and obtained optimum steel sections for the members of a steel frame from an available set of steel sections. However, the software was limited to relatively small skeleton framework.

Optimality criteria based structural optimization method is presented in [69] for the optimum designs of multi-story reinforced concrete structures with shear walls. The algorithm considers displacement, ultimate axial load, and bending moment and minimum size constraints. Member depths are treated as design variables. The values of design

variables are evaluated from recursive relationships in every design cycle depending on the dominance of design constraints. The largest value of the design variable among those computed from the displacement limitations, ultimate, axial, and bending moment constraints, and minimum size restrictions defines the new value of the design variable in the next optimum design cycle. This process is repeated until convergence is obtained on the objection function.

It is shown in [70] that optimality criteria approach can also be utilized in the optimum geometry design of roof trusses. In this work the slope of upper chord of a truss is treated as a design variable in addition to area variables. Additional optimality criteria were developed for slope variables under the displacement constraints; the algorithm determines the optimum values of the cross-sectional areas in the roof truss as well as optimum height of the apex.

In another application [71], the optimality criteria based structural optimization algorithm is developed for the optimum design of steel frames with tapered members. The algorithm considers the width of an I section as constant together with web and flange thickness, while the depth is assumed to be varying linearly between joints. The depth at each joint in the frame where the lateral restraints are assumed to be provided is treated as a design variable. The objective function taken as the weight of the frame is expressed in terms of the depth at each joint. The displacement and combined axial and flexural strength constraints are considered in the formulation of the design problem in accordance with Load and Resistance Factor Design (LRFD) of AISC code [72]. The strength constraints that take into account the lateral torsional buckling resistance of the members between the adjacent lateral restraints are expressed as a nonlinear function of the depth variables. The optimality criteria method is then used to obtain a recursive relationship for the depth variables under the displacement and strength constraints. The algorithm basically consists of two steps. In the first one, the frame is analyzed under the external and unit loadings for the current values of the design variables. In the second, this response is utilized together with the values of Lagrange multipliers to compute the new values of the depth variables. This process is continued until convergence obtained in the objective function. The optimum design of number of practical pitched roof frames is presented to demonstrate the application of the algorithm.

Al-Mosawi and Saka [73] employed optimality criteria approach to develop an algorithm for the optimum design of single-core shear walls subjected to combined loading of axial force, biaxial bending moment, and torsional moment. The algorithm is based on the limit state theory and considers displacement limitations in addition to strain constraints in concrete and yielding constraints in rebars. It takes into account the effect of warping which can be considerable in the computation of normal stresses when the thin-walled section is subjected to a torsional moment. The design algorithm makes use of sectional properties of section, which is quite useful in describing deformations and stresses when the plane cross-section no longer remains plane. A numerical procedure is developed to calculate the shear center of reinforced concrete thin-walled section in addition to the

sectional and sectional properties. Furthermore, an iterative procedure is presented for finding the location of the neutral axis in reinforced concrete thin-walled sections subjected to axial force, biaxial, moments and torsional moment. It is shown that optimality criteria method can effectively be used in obtaining the optimum solution of highly nonlinear and complex design problem.

Al-Mosawi and Saka [74] presented an algorithm that obtains the optimum cross-sectional dimensions of cold-formed thin-walled steel beams subjected to axial force, biaxial moments, and torsional loadings. The algorithm treats the cross-sectional dimensions such as width, depth and wall thickness as design variables and considers the displacement as well as stress limitations. The presence of torsional moments causes wrapping of thin-walled sections. The effect of warping in the calculations of normal stresses is included using Vlasov [75] theorems. The design problem turns out to be highly nonlinear problem. It is shown that the optimality criteria method can effectively be used to obtain the solution.

Chan and Grierson [76] and Chan [77] presented a practical optimization technique based on the optimality criteria approach for the design of tall steel building frameworks where cross-sectional areas are selected from the standard steel section tables. This computer based method considers the multiple interstory drift, strength, and sizing constraints in accordance with building code and fabrications requirements. The optimality criteria approach and section properties' regression relationship are used to solve the design problem. To achieve a final optimum design using standard steels section a pseudo-discrete optimality criteria technique is applied to assign standard steel sections to the members of the structure while maintaining the least change in structure weight. A full-scale 50 story three-dimensional steel frame is designed to demonstrate the application of the automatic optimal design method.

Soegiarso and Adeli [78] presented an algorithm for the minimum weight design of steel moment resisting space frame structures with or without bracing based on LRFD specifications of AISC. The algorithm is based on the optimality criteria method. The LRFD constraints for moment resisting frames are highly nonlinear and implicit functions of design variables. The structure is subjected to wind loading according to the Uniform Building Code in addition to the dead and live loads. The algorithm is applied to the optimum design of four large high-rise steel building structures ranging up in height from 20 to 81 stories.

3.2.2. Nonlinear Elastic Steel Frames. Optimality criteria approach has been effectively employed in the optimum design of nonlinear skeleton structures. Khot [79] was one of the early researchers who presented an optimization algorithm based on an optimality criteria approach to design a minimum weight space truss with different constraint requirements on system stability. In order to reduce the imperfection sensitivity of a structure, the Eigen values associated with the system buckling modes are separated by a specified interval. This requirement is included as a constraint in the design

problem. This design obtained for the various constraint conditions was analyzed with and without specified geometric imperfections using nonlinear finite element program that accounts geometric nonlinearity. The results obtained for various designs were compared for their imperfection sensitivity. Later, Khot and Kamat [80] presented optimality criteria based algorithm for the minimum weight design of geometrically nonlinear pin-jointed space trusses. The nonlinear critical load is determined by finding the load level at which the Hessian of the potential energy becomes negative. A recurrence relationship is based on the criteria that at the optimum structure the nonlinear strain energy density must be equal in all members. This relationship is used to resize the space truss members. The number of examples is considered to demonstrate the application of the algorithm.

Saka [81] also presented an optimum design algorithm that takes into account the response of space trusses beyond the elastic behavior. The algorithm is developed by coupling a nonlinear analysis technique with an optimality criteria approach. The nonlinear analysis method used determines the changes in the axial stiffness of space truss members from the nonlinear load-deformation curves. These curves are obtained from the tensile stress-strain curve for the tension members and from the stress-strain curve under compression that varies as the slenderness ratio of the member changes. These nonlinear curves are approximated by straight lines. The intersection points of these lines are called as critical points. As the load increases, the slope of linear segments changes. This implies the variation in the axial stiffness of the member. Once the axial stiffness values of all members are specified up to the failure, the nonlinear analysis is easily carried out by allowing these changes in the stiffness of members during the increase of the external loads. The optimality criteria approach is employed to obtain a recurrence relationship for area variables. Consideration of postbuckling and postyielding behavior of truss members makes the stress and buckling constraints redundant. The number of space trusses is designed by the algorithm, and it is shown that optimum designs are obtained after relatively fewer members of iterations.

Saka and Ulker [82] developed a structural optimization algorithm for geometrically nonlinear space trusses subjected to displacement and stress and size constraints. Tangent stiffness method is used to obtain the nonlinear response of the space truss. This response is used by the optimality criteria method to determine the values of area variables in the next design cycle. During the nonlinear analysis, tension members are loaded up to yield stress, and compression members are stressed until their critical limits. The overall loss of elastic stability is checked throughout the steps of the algorithm. It is shown that the consideration of geometric nonlinearity in the optimum design of space trusses makes it possible to achieve further reduction in its overall weight. It is shown that inclusion of the geometric nonlinearity caused 11% reduction in the overall weight in the optimum design of 120-bar laminar dome compared to minimum weight design considering linear behavior. Furthermore, by

considering the geometrical nonlinearity in the optimum design the algorithm takes into account the realistic behavior of space trusses. Geometric nonlinearity becomes important in shallow-framed domes.

Saka and Hayalioglu [83] present a structural optimization algorithm for geometrically nonlinear elastic-plastic frames. The algorithm is developed by coupling the optimality criteria approach with large deformation analysis method for elastic-plastic frames. The optimality criteria method is used to obtain a recursive relationship for the design variables considering the displacement constraints. The nonlinear response of the frame used by the recursive relationship is based on a Euclidian formulation which includes elastic-plastic effects. Local member force-deformation relationships are extended to cover the geometric nonlinearities. An incremental load approach with Newton-Raphson iterations is adopted for the computational procedure. These iterations are terminated when the prescribed load factor reached. It is shown in the optimum design of number of rigid frames considered in the study that inclusion of geometric and material nonlinearity in the optimum design does not only lead to a more realistic approach but also yields to lighter frames. The reduction in the overall weight of the frames varied from 20% to 30% when compared to the linear-elastic optimum frame designs. Later, the algorithm is extended to geometrically nonlinear elastic-plastic steel frames with tapered members [84]. It is shown that consideration of nonlinear behavior in the minimum weight design of pitched roof frame with tapered members yields almost 40% reduction in the weight compared to the optimum design with linear-elastic behavior. It is stated in both works that the optimality criteria approach was quite effective in handling the displacement constraints in such complex design problems. It was noticed that most of the computational time was consumed by the large deformation analysis of elastic-plastic frame.

Saka and Kameshki [85] employed optimality criteria approach to develop an algorithm for the optimum design of unbraced rigid large frames that takes into account the nonlinear response of $P-\delta$ effect. The algorithm considers sway constraints and combined stress limitations in the design problem. A recursive relationship is developed for using optimality criteria approach for the sway limitations and the combined strength constraints are reduced to nonlinear equations of the design variables. The algorithm initiates the design process by carrying out nonlinear analyses of the frame in which in each analysis cycle the overall stability is checked. When the nonlinear response of the frame is obtained without loss of stability, the new values of design variables are computed from the recursive relationships. This process of reanalyses and resizing is repeated until the convergence is obtained in the objection function. It was noticed that the nonlinear value of the top storey sway of 24-story 3-bay unbraced frame due to $P-\delta$ effect was 10% more than its linear value. This clearly indicates the importance of including the geometric nonlinearity in the optimum design of unbraced tall steel frames.

This algorithm is later extended to the optimum design of three-dimensional rigid frames by Saka and Kameshki [86]. The algorithm considers the displacement limitations

and restricts the combined stresses not to be more than yield stress. The stability functions for three-dimensional beam-columns are used to obtain the P- δ effect in the frame. These functions are derived by considering the effect of axial force on flexural stiffness and effect of flexure on axial stiffness. The algorithm employs the optimality criteria approach together with nonlinear overall stiffness matrix to develop a recursive relationship for design variables in the case of dominant displacement constraints. The combined stress constraints are reduced to nonlinear equations of design variables. The algorithm initiates the optimum design at the selected load factor and carries out elastic instability analysis until the ultimate load factor is reached. During these iterations checks of the overall stability of the space rigid frame are conducted. If the nonlinear response is obtained without loss of stability, the algorithm proceeds to the next design cycle. It is shown in the design examples considered that P- δ effect plays important role in the optimum design of framed domes, and its consideration does not only provide more economy in the weight, but also produces more realistic results.

The research work reviewed previously clearly shows that the optimality criteria approach is quite effective in obtaining the optimum design of skeleton structures. The number of design cycles required to reach to the optimum frame is relatively low and it is independent of the size of frame. The optimality criteria approach made it possible to obtain the optimum design of large size, realistic structures. It is also shown that these methods are general and can be employed in the optimum design of linear elastic, nonlinear elastic, and elastic-plastic frames. Furthermore it is shown that they can even be used in the shape optimization of skeleton structures. Thus, it is apparent that in structural engineering problems where the design variables can have continuous values, the optimality criteria based structural optimization algorithm effectively provides solutions. However, the optimum design of steel frames necessitates selection of steel profiles for its members from available list of steel sections which contains discrete values not continuous. Altering optimality criteria algorithms to cater this necessity is cumbersome and do not yield techniques that can be efficiently used in the optimum design of large-size steel frames. This discrepancy of mathematical programming and optimality criteria based design optimization algorithms forced researchers to come up with new ideas which caused the emergence of stochastic search techniques.

4. Discrete Optimum Design Problem of Steel Frames to LRFD-AISC

The design of steel frames requires the selection of steel sections for its columns and beams from a standard steel section tables such that the frame satisfies the serviceability and strength requirements specified by LRFD-AISC (Load and Resistance Factor Design-American Institute of Steel Constitution) [72], while the economy is observed in the overall or material cost of the frame. When formulated as a

programming problem it turns out to be a discrete optimum design problem which has the following mathematical form:

$$\text{Minimize} = \sum_{r=1}^{ng} m_r \sum_{s=1}^{t_r} \ell_s, \quad (55a)$$

$$\text{Subject to} \quad \frac{(\delta_j - \delta_{j-1})}{h_j} \leq \delta_{ju}, \quad j = 1, \dots, ns, \quad (55b)$$

$$\delta_i \leq \delta_{iu}, \quad i = 1, \dots, nd, \quad (55c)$$

$$\frac{P_{uk}}{\phi P_{nk}} + \frac{8}{9} \left(\frac{M_{uxk}}{\phi_b M_{nxxk}} + \frac{M_{uyk}}{\phi_b M_{nyk}} \right) \leq 1, \quad \text{for } \frac{P_{uk}}{\phi P_{nk}} \geq 0.2, \quad (55d)$$

$$\frac{P_{uk}}{2\phi P_{nk}} + \frac{8}{9} \left(\frac{M_{uxk}}{\phi_b M_{nxxk}} + \frac{M_{uyk}}{\phi_b M_{nyk}} \right) \leq 1, \quad \text{for } \frac{P_{uk}}{\phi P_{nk}} < 0.2, \quad (55e)$$

$$M_{uxt} \leq \phi_b M_{nxt}, \quad t = 1, \dots, nb, \quad (55f)$$

$$B_{sc} \leq B_{sb}, \quad s = 1, \dots, nu, \quad (55g)$$

$$D_s \leq D_{s-1}, \quad (55h)$$

$$m_s \leq m_{s-1}, \quad (55i)$$

where (55a) defines the weight of the frame, m_r is the unit weight of the steel section selected from the standard steel sections table that is to be adopted for group r , t_r is the total number of members in group r , and ng is the total number of groups in the frame. ℓ_s is the length of the member s which belongs to the group r .

Inequality (55b) represents the interstorey drift of the multistorey frame. δ_j and δ_{j-1} are lateral deflections of two adjacent storey levels and h_j is the storey height. ns is the total number of storeys in the frame. Equation (55c) defines the displacement restrictions that may be required to include other-than-drift constraints such as deflections in beams. nd is the total number of restricted displacements in the frame. δ_{ju} is the allowable lateral displacement. LRFD-AISC limits the horizontal deflection of columns due to unfactored imposed load and wind loads to height of column/400 in each storey of a building with more than one storey. δ_{iu} is the upper bound on the deflection of beams which is given as span/360 if they carry plaster or other brittle finish.

Inequalities (55d) and (55e) represent strength constraints for doubly and singly symmetric steel members subjected to axial force and bending. If the axial force in member k is tensile force the terms in these equations are given as the following: P_{uk} is the required axial tensile strength, P_{nk} is the nominal tensile strength, ϕ becomes ϕ_t in the case of tension and called strength reduction factor which is given as 0.90 for yielding in the gross section and 0.75 for fracture in the net section, ϕ_b is the strength reduction

factor for flexure given as 0.90, M_{uxk} and M_{uyk} are the required flexural strength, M_{nxx} and M_{nyk} are the nominal flexural strength about major and minor axis of member k , respectively. It should be pointed out that required flexural bending moment should include second-order effects. LRFD suggests an approximate procedure for computation of such effects which is explained in C1 of LRFD. In this case the axial force in member k is a compressive force, and the terms in inequalities (55d) and (55e) are defined as the following: P_{uk} is the required compressive strength, P_{nk} is the nominal compressive strength, and ϕ becomes ϕ_c which is the resistance factor for compression given as 0.85. The remaining notations in inequalities (55d) and (55e) are the same as the definition given previously.

The nominal tensile strength of member k for yielding in the gross section is computed as $P_{nk} = F_y A_{gk}$ where F_y is the specified yield stress and A_{gk} is the gross area of member k . The nominal compressive strength of member k is computed as $P_{nk} = A_{gk} F_{cr}$ where $F_{cr} = (0.658^{\lambda_c^2}) F_y$ for $\lambda_c \leq 1.5$ and $F_{cr} = (0.877/\lambda_c^2) F_y$ for $\lambda_c > 1.5$ and $\lambda_c = (Kl/r\pi)\sqrt{F_y/E}$. In these expressions E is the modulus of elasticity, and K and l are the effective length factor and the laterally unbraced length of member, k respectively.

Inequality (55f) represents the strength requirements for beams in load and resistance factor design according to LRFD-F2. M_{uxb} and M_{nyb} are the required and the nominal moments about major axis in beam b , respectively. ϕ_b is the resistance factor for flexure given as 0.90. M_{nxb} is equal to M_p , plastic moment strength of beam b which is computed as ZF_y where Z is the plastic modulus and F_y is the specified minimum yield stress for laterally supported beams with compact sections. The computation of M_{nxb} for noncompact and partially compact sections is given in Appendix F of LRFD. Inequality (55f) is required to be imposed for each beam in the frame to ensure that each beam has the adequate moment capacity to resist the applied moment. It is assumed that slabs in the building provide sufficient lateral restraint for the beams.

Inequality (55g) is included in the design problem to ensure that the flange width of the beam section at each beam-column connection of storey s should be less than or equal to the flange width of column section.

Inequalities (55h) and (55i) are required to be included to make sure that the depth and the mass per meter of column section at storey s at each beam-column connection are less than or equal to width and mass of the column section at the lower storey $s - 1$. nu is the total number of these constraints.

The solution of the optimum design problems described previously requires the selection of appropriate steel sections from a standard list such that the weight of the frame becomes the minimum while the constraints are satisfied. This turns the design problem into a discrete programming problem. As mentioned earlier the solution techniques available among the mathematical programming methods for obtaining the solution of such problems are somewhat cumbersome and not very efficient for practical use. Consequently structural optimization has not enjoyed the same popularity among the practicing engineers as the one it has enjoyed among the

researchers. On the other hand, the emergence of new computational techniques called as stochastic search techniques or metaheuristic optimization algorithms that are based on the simulation of paradigms found in nature has changed this situation altogether. These techniques are inspired by analogies with physics, with biology, or with ethology.

5. Stochastic Solution Techniques for Steel Frame Design Optimization Problems

The stochastic search techniques make use of ideas inspired from nature, and they are equally efficient for obtaining the solution of both continuous and discrete optimization problems. The basic idea behind these techniques is to simulate the natural phenomena such as survival of the fittest, immune system, swarm intelligence, and the cooling process of molten metals through annealing to a numerical algorithm [87–107]. These methods are nontraditional stochastic search and optimization methods, and they are very suitable and effective in finding the solution of combinatorial optimization problems. They do not require the gradient information or the convexity of the objective function and constraints, and they use probabilistic transition rules not deterministic rules. Furthermore, they do not even require an explicit relationship between the objective function and the constraints. Instead they are based stochastic search techniques that make them quite effective and versatile to counter the combinatorial explosion of the possibilities. An extensive and detailed review of the stochastic search techniques employed in developing optimum design algorithms for steel frames is given in [16]. This review covers the articles published in the literature until 2007. In this paper firstly the summary of stochastic search algorithms is given, and the relevant publications after 2007 are reviewed in detail.

5.1. Evolutionary Algorithms. Evolutionary algorithms are based on the Darwinian theory of evolution and the survival of the fittest. They set up an artificial population that consists of candidate solutions to optimum design problem which are called individuals. These individuals are obtained by collecting the randomly selected values from the discrete set for each design variable. For example in a design problem of a steel frame with three design variables, the 11th, 23rd, and 41st steel sections in the standard section list that contains 64 sections can randomly be selected for each design variable. First these sequence numbers are expressed in binary form as 001011, 010111, and 101001. This is called *encoding*. There are different types of encodings such as binary, real-number, integer, and literal permutation encodings. When these binary numbers are combined together an *individual* consisting of zeros and ones such as 00101101011101001 is obtained. This individual is inserted to the population as a candidate solution. The reason 6 digits are used in the binary representation is to allow the possibility of covering total 64 sections available in the standard section list. The number of individuals can be generated same way and collected together to set up an artificial population. The binary representation of the individual is called its *genome* or *chromosome*. Each

genome consists of a sequence of genes. A value of a gene is called an *allele* or *string*. It is apparent that all these terms are taken from cellular biology. It can be noticed that a new individual can be obtained by just changing one allele. Evolutionary algorithms do exactly this. They modify the genomes in the population to obtain a new individual which are called offspring or a child. Each individual is then checked for its quality which indicates its fitness as a solution for the design problem under consideration. A new population which is called a new generation is then obtained by keeping many of those offsprings with high fitness value and letting the ones with low fitness value to die off. Populations are generated one after another until one individual dominates either certain percentage of the population or after a predetermined number of generations. The individual with the highest fitness value is considered the optimum solution in both approaches. An extensive surveys of evolutionary computation and structural design are carried out in [90, 108–111].

There are varieties of evolutionary algorithms though in general they all are population-based stochastic search algorithms. They differ in the production of the new generations. However, those that are used in steel frame optimization can be collected under two main titles. These are genetic algorithms developed by Holland [87] and evolution strategies developed by Goldberg and Santani [112], Gen and Chang [113], and Chambers [98].

5.1.1. Genetic Algorithms. Genetic algorithm makes use of three basic operators to generate a new population from the current one [16, 90, 114]. The first one is known as *selection*, which involves selection of the individuals from the current population for mating depending on their fitness value. For each individuals a fitness value is calculated which represents the suitability of the individual's potential to be selected as a solution for the design. More highly fit designs send more copies to the mating pool. The fitness of individuals is calculated from the fitness criteria. In order to establish fitness criteria it is necessary to transform the constrained design problem into an unconstrained one. This is achieved by using a penalty function that generates a penalty to the objective function, whenever the constraints are violated. There are various forms of penalty functions used in conjunction with genetic algorithms. The details of these transformations are given in [98, 113, 115].

The second operator is called *crossover* in which the strings of parents selected from the mating pool are broken into segments, and some of these segments are exchanged with corresponding segments of the other parent's string. The crossover operator swaps the genetic information between the mating pair of individuals. There are many different strategies to implement crossover operator such as fixed, flexible, and uniform crossovers [108, 115].

After the application of crossover new individuals are generated with different strings. These constitute the new population. Before repeating the reproduction and crossover once more to obtain another population the third operator called *mutation* is used. Mutation safeguards the process

from a complete premature loss of valuable genetic material during reproduction and crossover. To apply mutation, few individuals of the population are randomly selected, and the string of each individual at a random location if 0 is switched to 1 or vice versa. The mutation operation can be beneficial in reintroducing diversity in a population.

Although initially genetic algorithms used the binary alphabet to code the search space solutions, there are also applications where other types of coding are utilized. Real coding seems particularly natural when tackling optimization problems of parameters with variables in continuous domains [116]. Leite and Topping [117] proposed modifications to one-point crossover by defining effective crossover site and using multiple off-spring tournaments. Modifications also covered to improve the efficiency of genetic operators to allow reduction in computation time and improve the results. Genetic algorithm has been extensively used in discrete optimization design of steel-framed structures [118–133].

Camp et al. [124, 125] developed a method for the optimum design of rigid plane skeleton structures subjected to multiple loading cases using genetic algorithm. The design constraints were implemented according to Allowable Stress Design specifications of American Institutes of Steels Construction (AISC-ASD). The steel sections were selected from AISC database of available structural steel members. Several strategies for reproduction and crossover were investigated. Different penalty functions and fitness policies were used to determine their suitability to ASD design formulation. Saka and Kameshki [126] presented genetic algorithm based algorithm design of multistory steel frames with sideway subjected to multiple loading cases. The design constraints that include serviceability as well as the combined strength constraints were implemented from British Standards BS5950. Saka [127] used genetic algorithm in the minimum design of grillage systems subjected to deflection limitations and allowable stress constraints. Wadali and Saka [128] applied the genetic algorithm to the optimum geometry and spacing design of roof trusses subjected to multiple loading cases. The algorithm obtains a roof truss that has the minimum weight by selecting appropriate steel sections from the standard British Steel Sections tables while satisfying the design limitations specified by BS5950. Saka et al. [129] presented genetic algorithm based optimum design method that find the optimum spacing in addition to optimum sections for the grillage systems. Deflection limitations and allowable stress constraints were considered in the formulation of the design problem. Pezeshk et al. [130] also presented a genetic algorithm based optimization procedure for the design of plane frames including geometric nonlinearity. The design constraints are accounted for AISC-LRFD specifications. Hasançebi and Erbatur [131] carried out evaluation of crossover techniques in genetic algorithm. For this purpose commonly used single-point, 2-point, multi-point, variable-to-variables and uniform crossover are used in the optimum design of steel pin jointed frames. They have concluded that two-point crossover performed better than other crossover types. Erbatur et al. [132] developed GAOS program which implements the constraints from the design code and determines the optimum readymade hot-rolled

sections for the steel trusses and frames. Kameshki and Saka [133] used genetic algorithm to compare the optimum design of multistory nonswaying steel frames with different types of bracing. Kameshki and Saka [134] presented an application of the genetic algorithm to optimum design of semirigid steel frames. The design algorithm considers the service ability and strength constraints as specified in BS5950. Andre et al. [135] discussed the trade-off between accuracy, reliability, and computing time in the binary-encoded genetic algorithm used for global optimization over continuous variables. Large set of analytical test functions are considered to test the effectiveness of the genetic algorithm. Some improvements such as Gray coding and double crossover are suggested for a better performance. Toropov and Mahfouz [136] presented genetic algorithm based structural optimization technique for the optimum design of steel frames. Certain modifications are suggested which improved the performance of the genetic algorithm. The algorithm implements the design constraints from BS5950 and considers the wind loading from BS6399. The steel sections are selected from BS4. Hayalioglu [137] developed a genetic algorithm based optimum design algorithm for three-dimensional steel frames which implements the design constraints from LRFD-AISC. The wind loading is taken from Uniform Building Code (UBC). The algorithm is also extended to include the design constraints according to Allowable Stress Design (ASD) of AISC for comparison. Jenkins [138] used decimal coding instead of binary coding in genetic algorithm. The performance of the decimal coded genetic algorithm is assessed in the optimum design of 640-bar space deck. It is concluded that decimal coding avoids the inevitable large shifts in decoded values of variables when mutation operates at the significant end of binary string. Kameshki and Saka [139] extended the work of [134] to frames with various semirigid beam-to-column connections such as end plate without column stiffeners, top and seat angle with double web angle, top and seat angle without double web angle. Yun and Kim [140] presented optimum design method for inelastic steel frames. Kaveh and Shahrrouzi [141] utilized a direct index coding within the genetic algorithm, such a way that the optimization algorithm can simultaneously integrate topology and size in a minimal length chromosome. Balling et al. [142] also presented a genetic algorithm based optimum design approach for steel frames that can simultaneously optimize size, shape, and topology. It finds multiple optimums and near optimum topologies in a single run. Toğan and Daloğlu [143] suggested the adaptive approach in genetic algorithm which eliminates the necessity of specifying values for penalty parameter and probabilities of crossover and mutation. Kameshki and Saka [144] presented an algorithm for the optimum geometry design of geometrically nonlinear geodesic domes that uses genetic algorithm and elastic instability analysis.

Degertekin [145] compared the performance of the genetic algorithm with simulated annealing in the optimum design of geometrically nonlinear steel space frames where the design formulation is carried out considering both LRFD and ASD specifications of AISC. It is concluded that simulated annealing yielded better designs. Later in [146] the performance of genetic algorithm is compared with that of

tabu search in finding the optimum design of steel space frames and found that tabu search resulted in lighter frames. Issa and Mohammad [147] attempted to modify a distributed genetic algorithm to minimize the weight of steel frames. They have used twin analogy and a number of mutation schemes and reported improved performance for genetic algorithm. Safari et al. [148] have proposed new crossover and mutation operators to improve the performance of the genetic algorithm for the optimum design of steel frames. Significant improvements in the optimum solutions of the design examples considered are reported.

5.1.2. Evolution Strategies. Evolution strategies were originally developed for continuous structural optimization problems [149]. These algorithms are extended to cover discrete design problems by Cai and Thierauf [150]. The basic differences between discrete and continuous evolution strategies are in the mutation and recombination operators. Evolution strategies algorithm randomly generates an initial population consisting of μ parent individuals. It then uses recombination, mutation, and selection operators to attain a new population. The steps of the method are as follows [16, 149].

- (1) *Recombination.* The population of μ parents is recombined to produce λ off springs in i th generation in order to allow the exchange of design characteristics on both levels of design variables and strategy parameters. For every offspring vector a temporary parent vector $s = \{s_1, s_2, \dots, s_n\}$ is first built by means of recombination. The following operators can be used to obtain the recombined s' :

$$s'_i = \begin{cases} s_{a,i} & \text{no recombination,} \\ s_{a,i} \text{ or } s_{b,i} & \text{discrete,} \\ s_{a,i} \text{ or } s_{b,i} & \text{global discrete,} \\ s_{a,i} + \frac{(s_{b,i} - s_{a,i})}{2} & \text{intermediate,} \\ s_{a,i} + \frac{(s_{b,i} - s_{a,i})}{2} & \text{global intermediate,} \end{cases} \quad (56)$$

where s_a and s_b refer to the s component of two parent individuals which are randomly chosen from the parent population. First case corresponds to no recombination case in which s' is directly formed by copying each element of first parent $s_{a,i}$. In the second, s' is chosen from one of the parents under equal probability. In the third, the first parent is kept unchanged, while a new second parent $s_{b,i}$ is chosen randomly from the parent population. The fourth and fifth cases are similar to second and third cases, respectively; however, arithmetic means of the elements are calculated.

- (2) *Mutation.* This operator is not only applied to design variables but also strategy parameters. Carrying out the mutation of strategy parameters first and the design variables later increases the effectiveness of the algorithm. It is suggested in [149] that not all of the components of the parent individuals but only a

few of them should randomly be changed in every generation.

- (3) *Selection.* There are two types of selection application. In the first the best μ individuals are selected from a temporary population of $(\mu + \lambda)$, individuals to form the parents of the next generation. In the second the μ individuals produce λ off springs ($\mu \leq \lambda$) and the selection process defines a new population of μ individuals from the set of λ off springs only.
- (4) *Termination.* The discrete optimization procedure is terminated either when the best value of the objective function in the last $4n\mu/\lambda$ or when the mean value of the objective values from all parent individuals in the last $4n\mu/\lambda$ generations has not been improved by less than a predetermined value ϵ .

There are different types of constraint handling in evolution strategies method. An excellent review of these is given in [151]. In nonadaptive evolution strategies constraint handling is such that if the individual represents an infeasible design point it is discarded from the design space. Hence only the feasible individuals are kept in the population. For this reason many potential designs that are close to acceptable design space are rejected that results in a loss of valuable information. The adaptive evolution strategies suggested in [152] use soft constraints during the initial stages of the search; the constraints become severe as the search approaches the global optimum. The detailed steps of this algorithm are given in [149] where the procedure is explained in a simple example of three-bar steel truss structure. Later, two steel space frames are designed with evolution strategies in which the effect of different selection schemes and constraint handling is studied.

Rajasekaran et al. [153] applied the evolutionary strategies method to the optimum design of large-size steel space structures such as a double-layer grid with 700 degrees of freedom. It is reported that evolutionary strategies method worked effectively to obtain the optimum solutions of these large-size structures. Later Rajasekaran [154] used the same method to obtain the optimum design of laminated nonprismatic thin-walled composite spatial members that are subjected to deflection, buckling, and frequency constraints. Evolutionary strategies technique is applied to determine the optimal fibre orientation of composite laminates.

Ebenau et al. [155] combined evolutionary strategies technique with an adaptive penalty function and a special selection scheme. The algorithm developed is applied to determine the optimum design of three-dimensional geometrically nonlinear steel structures where the design variables were mixed, discrete, or topological.

Hasançebi [156] has compared three different reformulations of evolution strategies for solving discrete optimum design of steel frames. Extensive numerical experimentation is performed in the design examples to facilitate a statistical analysis of their convergence characteristics. The results obtained are presented in the histograms demonstrating the distribution of the best designs located by each approach. Further in [157], the same author investigated the application of evolution strategies to optimize the design of a truss bridge.

The design problem involved identifying the optimum topology, shape, and member sizes of the bridge. The design problem consisted of mixed continuous and discrete design variables. It is shown that evolutionary strategies efficiently found the optimum topology configuration of a bridge in a large and flexible design space.

Hasançebi [158] has improved the computational performance of evolution strategies algorithm by suggesting self-adaptive scheme for continuous and discrete steel frame design problems. A numerical example taken from the literature is studied in depth to verify the enhanced performance of the algorithm, as well as to scrutinize the role and significance of this self-adaptation scheme. It is shown that adaptive evolution strategies algorithms are reliable and powerful tools and well-suited for optimum design of complex structural systems, including large-scale structural optimization.

5.2. Simulated Annealing. Simulated annealing is an iterative search technique inspired by annealing process of metals. During the annealing process a metal first is heated up to high temperatures until it melts which imparts high energy to it. In this stage all molecules of the molten metal can move freely with respect to each other. The metal is then cooled slowly in a controlled manner such that at each stage a temperature is kept of sufficient duration. The atoms then arrange themselves in a low-energy state and leads to a crystallized state which is a stable state that corresponds to an absolute minimum of energy. On the other hand if the cooling is carried out quickly the metal forms polycrystalline state which corresponds to a local minimum energy. The metal reaches thermal equilibrium at each temperature level T described by a probability of being in a state i with energy E_i given by the Boltzman distribution:

$$P_r = \frac{1}{Z(T)} \exp\left(\frac{-E_i}{k_B T}\right), \quad (57)$$

where $Z(T)$ is a normalization factor and k_B is Boltzmann constant. The Boltzmann distribution focuses on the states with the lowest energy as the temperature decreases. An analogy between the annealing and the optimization can be established by considering the energy of the metal as the objective function, while the different states during the cooling represent the different optimum solutions (designs) throughout the optimization process. In the application of the method first the constrained design problem is transferred into an unconstrained problem by using penalty function. If the value of the unconstrained objective function of the randomly selected design is less than the one in the current design, then the current design is replaced by the new design. Otherwise the fate of the new design is decided according to the Metropolis algorithm as explained in the following:

$$p_{ij}(T_k) = \begin{cases} 1 & \text{if } \Delta W_{ij} \leq 0, \\ \exp\left(\frac{-\Delta W_{ij}}{\Delta W T_k}\right) & \text{if } \Delta W_{ij} > 0, \end{cases} \quad (58)$$

where p_{ij} is the acceptance probability of selected design. $\Delta W_{ij} = W_j - W_i$ in which W_j and W_i are the objective

function values of the selected and current designs, ΔW is a normalization constant which is the running average of ΔW_{ij} , and T_k is the strategy temperature. ΔW is updated when $\Delta W_{ij} > 0$ as explained in [88].

The strategy temperature T_k is gradually decreased, while the annealing process proceeds according to a cooling schedule. For this the initial and the final values of the temperature T_s and T_f are to be known. Once the starting acceptance probability P_s is decided the starting temperature is calculated from $T_s = -1/\ln(P_s)$. The strategy temperature is then reduced using $T_{k+1} = \alpha T_k$ where α is the cooling factor and is less than one. While T approaches zero, p_{ij} also approaches zero. For a given final acceptance probability, the final temperature is calculated from $T_f = -1/\ln(P_f)$. After N cycles the final temperature value T_f can be expressed as $T_f = T_s \alpha^{N-1}$.

Simulated annealing is originated by Kirkpatrick et al. [88] and Černý [159] independently at the same time which is based on the previously mentioned phenomenon. The steps of the optimum design algorithm for steel frames using simulated annealing method are given in the following. The method is based on the work of Bennage and Dhingra [160], and the normalization constant in the Metropolis algorithm [161] is taken from the work of Balling [162]. The details of these steps are given in [16, 145].

- (1) Select the values for P_s , P_f , and N and calculate the cooling schedule parameters T_s , T_f , and α as explained previously. Initialize the cycle counter $ic = 1$.
- (2) Generate an initial design randomly where each design variable represents the sequence number of the steel section randomly selected from the list. The initial design is assigned as current design. Carry out the analysis of the frame with steel section selected in the current design and obtain its response under the applied loads. Calculate the value of objective function W .
- (3) Determine the number of iterations required per cycle from the equation mentioned later.

$$i = i_f + (i_s - i_s) \left(\frac{T - T_f}{T_s - T_f} \right), \quad (59)$$

where i_s and i_f are the number of iterations per cycle required at the initial and final temperatures T_s and T_f .

- (4) Select a variable randomly. Apply a random perturbation to this variable, and generate a candidate design in the neighbourhood of the current design. Compute ΔW_{ij} .
- (5) Accept this candidate design as the current design if $\Delta W_{ij} \leq 0$.
- (6) If $\Delta W_{ij} > 0$ then update ΔW . Calculate the acceptance probability p_{ij} from (11). Generate a uniformly distributed random number r over interval $[0, 1]$. If $r < p_{ij}$ go to next step otherwise go to step 4.

- (7) Accept the candidate design as the current design. If the current design is feasible and is better than the previous optimum design, assign it temporarily as the optimum design.
- (8) Update the temperature T_k using $T_{k+1} = \alpha T_k$. Increase the cycle counter by one; $ic = ic + 1$. If $ic > N$ terminate the algorithm and take the last temporary optimum as the final optimum design. Otherwise return to step 3.

Balling [162] adapted simulated annealing strategy for the discrete optimum design of three-dimensional steel frames. The total frame weight is minimized subject to design-code-specified constraints on stress, buckling, and deflection. Three loading cases are considered. In the first loading case a uniform live load was placed on all floors and the roof. In the second and third loading cases horizontal seismic loads in the global X and Z directions were placed at various nodes, respectively, according to Uniform Building Code. Members in the frame were selected from among the discrete standardized shapes. Some approximation techniques were used to reduce the computation time. Later in [163] a filter is suggested through which each design candidate must pass before it is accepted for computationally intensive structural analysis is set-up. A scheme is devised whereby even less feasible candidates can pass through the filter in a probabilistic manner. It is shown that the filter size can speed up convergence to global optimum.

Simulated annealing is applied to optimum design of large tetrahedral truss for minimum surface distortion in [164, 165]. In [166], the simulated annealing is applied to large truss structures where the standard cooling schedule is modified such that the best solution found so far is used as a starting configuration each time the temperature is reduced.

Topping et al. [167] used simulated annealing in simultaneous optimum design for topology and size. The algorithm developed is applied to truss examples from the literature for which the optimum solutions were known. The effects of control parameters are discussed. Later in [168] implementation of parallel simulated annealing models is evaluated by the same authors. It is stated in this work that efficiency of parallel simulated annealing is problem dependant and some engineering problems solution spaces may be very complex and highly constrained. Study provides guidelines for the selection of appropriate schemes in such problems. Tzan and Pantelides [169] developed an annealing method for optimal structural design with sensitivity analysis and automatic reduction of the search range.

Hasançebi and Erbatur [170] presented simulated annealing based structural optimization algorithm for large and complex steel frames. Two general and complementary approaches with alternative methodologies to reformulate the working mechanism of the Boltzmann parameter are introduced to accelerate the convergence reliability of simulated annealing. Later in [171] they have developed simulated annealing based algorithm for the simultaneous optimum design of pin-jointed structures where the size, shape, and topology are taken as design variables. In the examples considered while the weight of trusses is minimized the design

constraints such as nodal displacements, member stress, and stability are implemented from design code specifications.

Degertekin [172] proposed a hybrid tabu-simulated annealing algorithm for the optimum design of steel frames. The algorithm exploits both tabu search and simulated annealing algorithms simultaneously to obtain near optimum solution. The design constraints are implemented from LRD-AISC specification. It is reported that hybrid algorithm yielded lighter optimum structures than those algorithms considered in the study.

Hasancebi et al. [173] have suggested novel approaches to improve the performance of simulated annealing search technique in the optimum design of real-size steel frames to eliminate its drawbacks mentioned in the literature. It is reported that the suggested improvements eliminated the drawbacks in the design examples considered in the study. In [174] the same author has used simulated annealing based optimum design method to evaluate the topological forms for single span steel truss bridge. The optimum design algorithm attains optimum steel profiles for the members and the truss as well as optimum coordinates of top chord joints so that the bridge has the minimum weight. The design constraints and limitations are imposed according to serviceability and strength provisions of ASD-AISC (Allowable Stress Design Code of American Institute of Steel Institution) specification.

5.3. Particle Swarm Optimizer. Particle swarm optimizer is based on the social behavior of animals such as fish schooling, insect swarming, and birds flocking. This behavior is concerned with grouping by social forces that depend on both the memory of each individual as well as the knowledge gained by the swarm [175, 176]. The procedure involves a number of particles which represent the swarm and are initialized randomly in the search space of an objective function. Each particle in the swarm represents a candidate solution of the optimum design problem. The particles fly through the search space, and their positions are updated using the current position, a velocity vector, and a time increment. The steps of the algorithm are outlined in the following as given in [177, 178].

- (1) Initialize swarm of particles with positions x_0^i and initial velocities v_0^i randomly distributed throughout the design space. These are obtained from the following expressions:

$$\begin{aligned} x_0^i &= x_{\min} + r(x_{\max} - x_{\min}), \\ v_0^i &= \left[\frac{(x_{\min} + r(x_{\max} - x_{\min}))}{\Delta t} \right], \end{aligned} \quad (60)$$

where the term r represents a random number between 0 and 1, and x_{\min} and x_{\max} represent the design variables of upper and lower bounds, respectively.

- (2) Evaluate the objective function values $f(x_k^i)$ using the design space positions x_k^i .

- (3) Update the optimum particle position p_k^i at the current iteration k and the global optimum particle position p_k^g .
- (4) Update the position of each particle from $x_{k+1}^i = x_k^i + v_{k+1}^i \Delta t$ where x_{k+1}^i is the position of particle i at iteration $k + 1$, v_{k+1}^i is the corresponding velocity vector, and Δt is the time step value.
- (5) Update the velocity vector of each particle. There are several formulas for this depending on the particular particle swarm optimizer under consideration. The one given in [176, 177] has the following form:

$$v_{k+1}^i = wv_k^i + c_1 r_1 \frac{(p_k^i - x_k^i)}{\Delta t} + c_2 r_2 \frac{(p_k^g - x_k^i)}{\Delta t}, \quad (61)$$

where r_1 and r_2 are random numbers between 0 and 1, p_k^i is the best position found by particle i so far, and p_k^g is the best position in the swarm at time k . w is the inertia of the particle which controls the exploration properties of the algorithm. c_1 and c_2 are trust parameters that indicate how much confidence the particle has in itself and in the swarm, respectively.

- (6) Repeat steps 2–5 until stopping criteria are met.

Fourie and Groenwold [178] applied particle swarm optimizer algorithm to optimal design of structures with sizing and shape variables. Standard size and shape design problems selected from the literature are used to evaluate the performance of the algorithm developed. The performance of particle swarm optimizer is compared with three-gradient based methods and genetic algorithm. It is reported that particle swarm optimizer performed better than genetic algorithm.

Perez and Behdinan [179] presented particle swarm based optimum design algorithm for pin jointed steel frames. Effect of different setting parameters and further improvements are studied. Effectiveness of the approach is tested by considering three benchmark trusses from the literature. It is reported that the proposed algorithm found better optimal solutions than other optimum design techniques considered in these design problems.

In [180] particle swarm optimizer is improved by introducing fly-back mechanism in order to maintain a feasible population. Furthermore, the proposed algorithm is extended to handle mixed variables using a simple scheme and used to determine the solution of five benchmark problems from the literature that are solved with different optimization techniques. It is reported that the proposed algorithm performed better than other techniques. In [181] particle swarm optimizer is improved by considering a passive congregation which is an important biological force preserving swarm integrity. Passive congregation is an attraction of an individual to other group members, but where there is no display of social behavior. Numerical experimentation of the algorithm is carried out on 10 benchmark problems taken from the literature, and it is stated that this improvement enhances the search performance of the algorithm significantly.

Li et al. [182] presented a heuristic particle swarm optimizer for the optimum design of pin jointed steel frames. The algorithm is based on the particle swarm optimizer with passive congregation and harmony search scheme. The method is applied to optimum design of five-planar and spatial truss structures. The results show that proposed improvements accelerate the convergence rate and reach to optimum design quicker than other methods considered in the study.

Doğan and Saka [183] presented particle swarm based optimum design algorithm for unbraced steel frames. The design constraints imposed are in accordance with LRFD-AISC code. The design algorithm selects optimum W sections for beams and columns of unbraced steel frames such that the design constraints are satisfied and the minimum frame weight is obtained.

5.4. Ant Colony Optimization. Ant colony optimization technique is inspired from the way that ant colonies find the shortest route between the food source and their nest. The biologists studied extensively for a long time how ants manage collectively to solve difficult problems in a natural way which is too complex for a single individual. Ants being completely blind individuals can successfully discover as a colony the shortest path between their nest and the food source. They manage this through their typical characteristic of employing volatile substance called pheromones. They perceive these substances through very sensitive receivers located in their antennas. The ants deposit pheromones on the ground when they travel which is used as a trail by other ants in the colony. When there is a choice of selection for an ant between two paths it selects the one where the concentration of pheromone is more. Since the shorter trail will be reinforced more than the long one after a while a great majority of ants in the colony will travel on this route. Ant colony optimization algorithm is developed by Colormi et al. [184] and Dorigo [185, 186] and used in the solution of travelling salesman. The steps of optimum design algorithm for steel frames based on ant colony optimization are as follows [187, 188].

- (1) Calculate an initial trail value as $\tau_0 = 1/w_{\min}$ where w_{\min} is the weight of the frame from assigning the smallest steel sections from the database to each member group of the frame.
- (2) Assign a member group to each ant in the colony randomly, and then select a steel section from the database so that the ant can start its tour. This selection is carried out according to the following decision process:

$$a_{ij}(t) = \frac{[\tau_{ij}(t)] [v_{ij}]^\beta}{\sum_{k=1}^{ns_i} [\tau_{ik}(t)] [v_{ik}]^\beta}, \quad (62)$$

where j is the steel section assigned to member group i , and ns_i is the total number of steel sections in the database. β is a constant. The probability $p_{ij}^\ell(t)$ that

the ant ℓ assigns a steel section j to member group i at time t is given as

$$p_{ij}^\ell(t) = \frac{a_{ij}(t)}{\sum_{k=1}^{ns_i} a_{ik}(t)}. \quad (63)$$

- (3) After the steel section is selected by the first ant as explained in step 2, the intensity of trail on this path is lowered using local update rule $\tau_{ij}(t) = \xi \tau_{ij}(t)$ where ξ is an adjustable parameter between 0 and 1.
- (4) The second ant selects a steel section from the database for its member group i and a local update rule is applied. This procedure is continued until all the ants in the colony select a steel section for the starting member group in their position on the frame. After completing the first iteration of the tour, each ant selects another steel section to its next member group $i + 1$. This procedure is repeated until each ant in the colony has selected a steel section from the database for each member group in the frame. Hence when the selection process is completed the ant colony has m different designs for the frame where m represents the total number of ants selected initially.
- (5) Frame is analyzed for these designs and the violations of constraints corresponding to each ant are calculated and substituted into the penalty function of $F = W(1 + C)^\alpha$ where W is the weight of the frame, C is the total constraint violation, and α is the penalty function exponent. All designs are in a cycle and are ranked by their penalized weights, and the elitist ant that selected the frame with the smallest penalized weight in all cycles is determined. The amount of trail $\Delta\tau_{ij}^e = 1/W_e$ is added to each path chosen by this elitist ant where W_e is the penalized frame weight selected by the elitist ant.
- (6) Carry out the global update of trails from $\tau_{ij}(t + 1) = \rho\tau_{ij}(t) + (1 - \rho)\Delta\tau_{ij}$ where ρ is a constant having value between 0 and 1 that represents the evaporation rate and $\Delta\tau_{ij} = \sum_{k=1}^m \Delta\tau_{ij}^k$ in which m is the total number of ants selected initially.

Camp and Bichon [187] developed discrete optimum design procedure for space trusses based on ant colony optimization technique. The total weight of the structure is minimized, while stress and deflection limitations are considered. The design problem is transformed into modified travelling salesman problem where the network of travelling salesman is taken as the structural topology and the length of the tour is the weight of the structure. The number of trusses is designed using the algorithm developed and results obtained are compared with genetic algorithm and gradient based optimization methods. Later in [188] the work is extended to rigid steel frames. The serviceability and strength constraints are implemented from LRFD-AISC-2001 code. A comparison is presented between ant colony optimization frame design and designs obtained using genetic algorithm.

Kaveh and Shojaei [189] also used ant colony optimization algorithm to develop an approach for the discrete

optimum design of steel frames. The design constraints considered consist of combined bending and compression, combined bending and tension, and deflection limitations which are specified according to ASD-AISC design code. The detailed explanation of ant colony optimization operators is given. Optimum designs of six plane steel structures are obtained using the algorithm developed. Some of the results are compared to those that are achieved by genetic algorithms which are taken from the literature. Bland [190] also used ant colony optimization to obtain the minimum weight of transmission tower which has over 200 members. Kaveh and Talatahari [191] presented an improved ant colony optimization algorithm for the design of steel frames. The algorithm employs suboptimization mechanism based on the principals of finite element method to reduce the search domain, the size of trail matrix, and the number of structural analyses in the global phase, and the optimum design is obtained by considering W sections list in the neighborhood of the result attained in the previous phase. Wang et al. [192] presented an algorithm for a partial topology and member size optimization for wing configuration. Ant colony optimization is used to determine the optimum topology of the wing structure, and gradient based optimization method is used for component size optimization problem. It is stated that this combined procedure was effective in solving wing structure optimization problem. In [193] ant colony algorithm is used to develop design optimization technique for three-dimensional steel frames where the effect of elemental warping is taken into account.

5.5. Harmony Search Method. One other recent addition to metaheuristic algorithms is the harmony search method originated by Geem et al. [194–206]. Harmony search algorithm is based on natural musical performance processes that occur when a musician searches for a better state of harmony. The resemblance for an example between jazz improvisation that seeks to find musically pleasing harmony and the optimization is that the optimum design process seeks to find the optimum solution as determined by the objective function. The pitch of each musical instrument determines the aesthetic quality just as the objective function value is determined by the set of values assigned to each decision variable.

Harmony search algorithm consists of five basic steps. The detailed explanation of these steps can be found in [196] which are summarized in the following.

- (1) Initialize the harmony search parameters. A possible value range for each design variable of the optimum design problem is specified. A pool is constructed by collecting these values together from which the algorithm selects values for the design variables. Furthermore the number of solution vectors in harmony memory (HMS) that is the size of the harmony memory matrix, harmony considering rate (HMCR), pitch adjusting rate (PAR), and the maximum number of searches is also selected in this step.
- (2) Initialize the harmony memory matrix (HM). Each row of harmony memory matrix contains the values

of design variables which randomly selected feasible solutions from the design pool for that particular design variable. Hence, this matrix has n columns where n is the total number of design variables and HMS rows which is selected in the first step. HMS is similar to the total number of individuals in the population matrix of the genetic algorithm.

- (3) Improvise a new harmony memory matrix. In generating a new harmony matrix the new value of the i th design variable can be chosen from any discrete value within the range of i th column of the harmony memory matrix with the probability of HMCR which varies between 0 and 1. In other words, the new value of x_i can be one of the discrete values of the vector $\{x_{i,1}, x_{i,2}, \dots, x_{i,hms}\}^T$ with the probability of HMCR. The same is applied to all other design variables. In the random selection, the new value of the i th design variable can also be chosen randomly from the entire pool with the probability of $1 - \text{HMCR}$. That is

$$x_i^{\text{new}} = \begin{cases} x_i \in \{x_{i,1}, x_{i,2}, \dots, x_{i,hms}\}^T & \text{with probability HMCR} \\ x_i \in \{x_1, x_2, \dots, x_{ns}\}^T & \text{with probability } (1 - \text{HMCR}), \end{cases} \quad (64)$$

where ns is the total number of values for the design variables in the pool. If the new value of the design variable is selected among those of harmony memory matrix, this value is then checked for whether it should be pitch-adjusted. This operation uses pitch adjustment parameter PAR that sets the rate of adjustment for the pitch chosen from the harmony memory matrix as follows:

$$\text{Is } x_i^{\text{new}} \text{ to be pitch-adjusted?} \quad \left\{ \begin{array}{l} \text{Yes with probability of PAR} \\ \text{No with probability of } (1 - \text{PAR}) \end{array} \right\}. \quad (65)$$

Supposing that the new pitch adjustment decision for x_i^{new} came out to be yes from the test and if the value selected for x_i^{new} from the harmony memory is the k th element in the general discrete set, then the neighboring value $k + 1$ or $k - 1$ is taken for new x_i^{new} . This operation prevents stagnation and improves the harmony memory for diversity with a greater change of reaching the global optimum.

- (4) Update the harmony memory matrix. After selecting the new values for each design variable the objective function value is calculated for the new harmony vector. If this value is better than the worst harmony vector in the harmony matrix, it is then included in the matrix, while the worst one is taken out of the matrix. The harmony memory matrix is then sorted in descending order by the objective function value.
- (5) Repeat steps 3 and 4 until the termination criteria is satisfied.

Lee and Geem [196] presented harmony search algorithm based discrete optimum design technique for plane trusses. Eight different plane trusses are selected from the literature and optimized using the approach developed to demonstrate the efficiency and robustness of the harmony search algorithm. In all these examples the proposed algorithm has found the minimum weight that is lighter than those determined by other techniques. In [197], authors have extended the harmony search algorithm to deal with continuous engineering optimization problems. Various engineering design examples including mathematical function minimization and structural engineering optimization problems are considered to demonstrate the effectiveness of the algorithm. It is concluded that the results obtained indicated that the proposed approach is a powerful search and optimization technique that may yield better solutions to engineering problems than those obtained using current algorithms.

Saka [207] presented harmony search algorithm based optimum geometry design technique for single-layer geodesic domes. It treats the height of the crown as design variable in addition to the cross-sectional designations of members. A procedure is developed that calculates the joint coordinates automatically for a given height of the crown. The serviceability and strength requirements are considered in the design problem as specified in BS5950-2000. This code makes use of limit state design concept in which structures are designed by considering the limit states beyond which they would become unfit for their intended use. The design examples considered have shown that harmony search algorithm obtains the optimum height and sectional designations for members in relatively less number of searches. Later this technique is extended to cover the optimum topology design of nonlinear lamella and network domes [208–210] where geometric nonlinearity is also taken into account.

Saka and Erdal [211] used harmony search algorithm to develop a discrete optimum design method for grillage systems. The displacement and strength specifications are implemented from LRFD-AISC. The algorithm selects the appropriate W sections from the database for transverse and longitudinal beams of the grillage system. The number of design examples is considered to demonstrate the efficiency of the proposed algorithm.

Saka [212] presented harmony search algorithm based discrete optimum design method for rigid steel frames. The objective is taken as the minimum weight of the frame and the behavioral and performance limitations are imposed from BS5950. The list of Universal Beam and Universal Column sections of The British Code is considered for the frame members to be selected from. The combined strength constraints that are considered for beam columns take into account the effect of lateral torsional buckling. The effective length computations for columns are automated and decided by the algorithm itself depending upon the steel sections adopted for beams and columns within that design cycle. It is demonstrated that harmony search algorithm is quite effective and robust in finding the solution of minimum weight steel frame design. Degertekin [213] also presented harmony search method based discrete optimum design

method for steel frame where the design constraints are implemented according to LRFD-AISC specifications. The effectiveness and robustness of harmony search algorithm, in comparison with genetic algorithm, simulated annealing and colony optimization based methods and were verified using three planar and two-space steel frames. The comparisons showed that the harmony search algorithm yielded lighter designs for the presented examples. Degertekin et al. [214] used harmony search method to develop an optimum design algorithm for geometrically nonlinear semirigid steel frames where the steel sections are selected from European wide flange steel sections (HE sections). It is stated that harmony search method efficiently obtained the optimum solution of complex design problem requiring relatively less computational time.

Hasançebi et al. [215, 216] developed adaptive harmony search method for optimum design of steel frames where two of the three main operators of classical harmony search methods, namely, harmony memory considering rate and pitch adjusting rate are adjusted automatically by the algorithm itself during the design iterations. The initial values selected for these parameters directly affect the performance of the algorithm. This novel technique eliminates problem-dependent value selection of these parameters. It is shown that adaptive harmony search technique performs much better than the standard harmony search method in obtaining the optimum designs of real-size steel frames.

Erdal et al. [217] formulated design problem of cellular beams as an optimum design problem by treating the depth, the diameter, and the total number of holes as design variables. The design problem is formulated considering the limitations specified in The Steel Construction Institute Publication Number 100 which is consisted BS5950 parts 1 and 3. The solution of the design problem is determined by using the harmony search algorithm and particle swarm optimizers. In the design examples considered it is shown that both methods efficiently obtained the optimum Universal beam section to be selected in the production of the cellular beam subjected to general loading, the optimum hole diameters, and the optimum number of holes in the cellular beam such that the design limitations are all satisfied.

Saka et al. [218] have evaluated the recent enhancements suggested by several authors in order to improve the performance of the standard harmony search method. Among these are the improved harmony search method and global harmony search method by Mahdavi et al. [219, 220], adaptive harmony search method [215], improved harmony search method by Santos Coelho and de Andrade Bernert [221], and dynamic harmony search method by Saka et al. [218]. The optimum design problem of steel space frames is formulated according to the provisions of LRFD-AISC (Load and Resistance Factor Design-American Institute of Steel Corporation). Seven different structural optimization algorithms are developed, each of which is based on one of the previously mentioned versions of harmony search method. Three real-size space steel frames, one of which has 1860 members, are designed using each of these algorithms. The optimum designs obtained by these techniques are compared, and performance of each version is evaluated. It is stated

that, among all, the adaptive and dynamic harmony search methods outperformed the others.

5.6. Big Bang Big Crunch Algorithm. Big Bang-Big Crunch algorithm is developed by Erol and Eksin [222] which is a population based algorithm similar to the genetic algorithm and the particle swarm optimizer. It consists of two phases as its name implies. First phase is the big bang in which the randomly generated candidate solutions are randomly distributed in the search space. In the second phase these points are contracted to a single representative point that is the weighted average of randomly distributed candidate solutions. First application of the algorithm in the optimum design of steel frames is carried out by Camp [223]. The steps of the method are listed later as it is given in [223].

- (1) Decide an initial population size and generate initial population randomly. These candidate solutions are scattered in the design domain. This is called the big bang phase.
- (2) Apply contraction operation. This operation takes the current position of each candidate solution in the population and its associated penalized fitness function value and computes a center of mass. The center of mass is the weighted average of the candidate solution positions with respect to the inverse of the penalized fitness function values:

$$x_{cm} = \left[\sum_{i=1}^{np} \frac{x_i}{f_i} \right] \div \left[\sum_{i=1}^n \frac{1}{f_i} \right], \quad (66)$$

where x_{cm} is the position of the center of mass, x_i is the position of candidate solution i in n dimensional search space, f_i is the penalized fitness function value of candidate solution i , and np is the size of the initial population.

- (3) Compute the position of the candidate solutions in the next iteration using the following expression considering that they are normally distributed around the center of mass x_{cm} :

$$x_i^{next} = x_{cm} + \frac{r\alpha (x_{max} - x_{min})}{s}, \quad (67)$$

where x_i^{next} is the position of the new candidate solution i , r is the random number from a standard normal distribution, α is the parameter that limits the size of the search space, x_{max} and x_{min} are the upper and lower bounds on the design variables, and s is the number of big bang iterations. In the case where steel sections are to be selected from the available steel sections list then it becomes necessary to work with integer numbers. In this case x_i^{next} of (67) is rounded to the nearest integer number as $I_i^{next} = \text{ROUND}(x_i^{next})$ where I_i^{next} represents index number the steel profile from the tabular discrete list.

- (4) Repeat steps 2 and 3 until termination criteria are satisfied.

Camp [223] developed optimum design algorithm for space trusses based on big bang-big crunch optimizer. The number of benchmark design examples having design variables continuous as well discrete is taken from the literature and designed with the developed algorithm. The results are compared with those algorithms of quadratic programming, general geometric programming, genetic algorithm, particle swarm optimizer, and ant colony optimization. It is reported that big bang-big crunch optimizer has relatively small number of parameters to define which provides the algorithm with better performance over the other techniques considered in the study. It is also concluded that the algorithm showed significant improvements in the consistency and computational efficiency when compared to genetic algorithm, particle swarm optimizer, and ant colony technique.

Kaveh and Talatahari [224] also presented big bang-big crunch-based optimum design algorithm for size optimization of space trusses. In this study large size space trusses are designed by the algorithm developed as well as those stochastic search techniques of genetic algorithm, ant colony optimization, particle swarm optimizer, and standard harmony search method. It is stated that big bang-big crunch algorithm performs well in the optimum design of large-size space trusses contrary to other metaheuristic techniques which presents convergence difficulty or get trapped at a local optimum.

Kaveh and Talatahari [225] developed optimum topology design algorithm based on hybrid big bang-big crunch optimization method for schwedler and ribbed domes. The algorithm determines the optimum configuration as well as optimum member sizes of these domes. It is reported that big bang-big crunch optimization method efficiently determined the optimum solution of large dome structures.

Kaveh and Abbasgholiha [226] presented the optimum design algorithm for steel frames based on big bang-big crunch optimizer. The design problem is formulated according to BS5950, ASD-AISC, and LRFD-AISC design codes, and the optimum results obtained by each code are compared. It is stated that LRFD design codes yield to the lightest steel frame as expected among other codes.

5.7. Hybrid and Other Stochastic Search Techniques. Stochastic search techniques have two drawbacks although they are capable of determining the optimum solution of discrete structural optimization problems. First one is that there is no guarantee that the solution found at the end of predetermined number of iterations is the global optimum. There is no mathematical proof available in these techniques due to the fact that they use heuristics not mathematically derived expression. The optimum solution obtained may very well be a local optimum or near optimum solution. Second drawback is that they need large amount of structural analysis to reach the near optimum solution. Some work is carried out to improve the performance of the metaheuristic optimization techniques by hybridizing them. Some of these algorithms are reviewed below.

Kaveh and Talatahari [227, 228] developed hybrid particle swarm and ant colony optimization algorithm for the discrete

optimum design of steel frames. The algorithm uses particle swarm optimizer for global search and ant colony optimization for local search. It is reported that the hybrid algorithm is quite effective in finding the optimum solutions.

Kaveh and Talatahari [229, 230] have also combined the search strategies of the harmony search method, particle swarm optimizer, and ant colony optimization to obtain efficient metaheuristic technique called HPSACO for the optimum design of steel frames. In this technique particle swarm optimization with passive congregation is used for global search, and the ant colony optimization is employed for local search. The harmony search based mechanism is utilized to handle the variable constraints. It is demonstrated in the design examples considered that proposed hybrid technique finds lighter optimum designs than each standard particle swarm optimizer and ant colony optimization as well as harmony search method. Further improvements are suggested for the algorithm in [231].

Kaveh and Rad [232] presented another hybrid genetic algorithm and particle swarm optimization technique for the optimum design of steel frames. They have introduced the maturing phenomenon which is mimicked by particle swarm optimizer where individuals enhance themselves based on social interactions and their private cognition. Crossover is applied to this society. Hence evolution of individuals is no longer restricted to the same generation. The results obtained from the design examples have shown that the hybrid algorithm shows superiority in optimum design of large-size steel frames.

Kaveh and Talatahari [233] presented a structural optimization method based on sociopolitically motivated strategy called imperialist competitive algorithm. Imperialist competitive algorithm initiates the search by considering multiagents where each agent is considered to be a country which is either a colony or an imperialist. Countries form colonies in the search space, and they move towards their related empires. During this movement, weak empires collapses and strong ones get stronger. Such movements direct the algorithm to optimum point. Presented algorithm is used in the optimum design of skeletal steel frames.

Kaveh and Talatahari [234] also introduced a novel heuristic search technique based on some principles of physics and mechanics called charged system search. The method is a multiagent approach where each agent is a charged particle. These particles affect each other based on their fitness values and distances among them. The quantity of the resultant force is determined by using electrostatic laws, and the quality of movement is determined using Newtonian mechanics laws. It is stated that charged system search algorithm is compared with other metaheuristic algorithm on benchmark examples, and it is found that it outperformed the others. The algorithm is applied to optimum design of skeletal structures in [235, 236], to grillage systems in [236], to truss structures in [237], and to geodesic dome in [238]. It is stated in all these works that charged system search algorithm shows better performance than other metaheuristic techniques considered. In [239] an improvement is suggested for the algorithm to enhance its performance even further.

The algorithm is applied to optimum design of steel frames in [240].

Kaveh and Bakhspoori [241] used cuckoo search method to develop optimum design algorithm for steel frames. The design problem is formulated according to Load and Resistance Factor Design code of American Institute of Steel Construction [72]. The optimum designs obtained by cuckoo search algorithm are compared with those attained by other algorithms on benchmark frames. Cuckoo search algorithm is originated by Yang and Deb [242] which simulates reproduction strategy of cuckoo birds. Some species of cuckoo birds lay their eggs in the nests of other birds so that when the eggs are hatched their chicks are fed by the other birds. Sometimes they even remove existing eggs of host nest in order to give more probability of hatching of their own eggs. Some species of cuckoo birds are even specialized to mimic the pattern and color of the eggs of host birds so that host bird could not recognize their eggs which gives more possibility of hatching. In spite of all these efforts to conceal their eggs from the attention of host birds, there is a possibility that host bird may discover that the eggs are not its own. In such cases the host bird either throws these alien eggs away or simply abandons its nest and builds a new nest somewhere else. The engineering design optimization of cuckoo search algorithm is carried out in [243].

5.8. Evaluation of Stochastic Search Techniques. It is apparent that there are a lot of metaheuristic algorithms that can be used in the optimum design of steel frames. The question of which one of these algorithms outperforms the others requires an answer. It should be pointed out that the performance of metaheuristic algorithms is dependent upon the selection of the initial values for their parameters which is quite problem dependent. The following works try to provide an answer to the previously mentioned problem.

Hasançebi et al. [244, 245] evaluated the performance of the stochastic search algorithm used in structural optimization on the large-scale pin jointed and rigidly jointed steel frames. Among these techniques genetic algorithms, simulated annealing, evolution strategies, particle swarm optimizer, tabu search, ant colony optimization, and harmony search method are utilized to develop seven optimum design algorithms for real-size pin and rigidly connected large-scale steel frames. The design problems are formulated according to ASD-AISC (Allowable Stress Design Code of American Institute of Steel Institution). The results reveal that simulated annealing and evolution strategies are the most powerful techniques, and standard harmony search and simple genetic algorithm methods can be characterized by slow convergence rates and unreliable search performance in large-scale problems.

Kaveh and Talatahari [246] used particle swarm optimizer, ant colony optimization, harmony search method, big bang-big crunch, hybrid particle swarm ant colony optimization, and charged system search techniques in the optimum design of single-layer Schwedler and lamella domes. The design problem is formulated according to LRFD-AISC specifications. It is stated that among these algorithm hybrid

particle swarm, ant colony optimization, and charged system search algorithms have illustrated better performance compared to other heuristic algorithms.

6. Conclusions

The review carried out reveals the fact that the mathematical modeling of the optimum design problem of steel frames can be broadly formulated in different ways. In the first way the cross-sectional properties of frame members treated only the optimization variables. In this case joint displacements are not part of optimization model, and their values are required to be obtained through structural analysis in every design cycle. This type of formulation is called coupled analysis and design (CAND). Naturally in this the type of formulation the total number of analysis is large which is computationally inefficient. In the second type of formulation the joint displacements are also treated as optimization variables in addition to cross-sectional properties. This makes it necessary to include the stiffness equations as constraints in the mathematical model as equality constraints. Such formulation is called simultaneous analysis and design (SAND) which eliminates the necessity of carrying out structural analysis in every design cycle. Hence the total number of structural analysis required to reach the optimum solution becomes quite less compared to the first type of modeling. However, in the second type the total number of optimization variables is quite large, and it becomes necessary to utilize powerful optimization techniques that work efficiently in solving large-size optimization problems.

The design code that is to be considered in the modeling of the optimum design problem also affects the complexity of the optimization problem obtained. Formulating the optimum design of steel frames without referencing any design code brings out relatively simple optimization problem if linear elastic structural behavior is assumed. Furthermore, if continuous design variables assumption is also made, then mathematical programming or optimality criteria algorithms efficiently finds the optimum solution of the optimization problem in both ways of modeling. Optimality criteria algorithms also provide optimum solutions without any difficulty even if nonlinear elastic behavior is considered in the optimum design of steel frames. Among the mathematical programming techniques, it seems that sequential quadratic programming method is the most powerful, and it is reported in several works that it can attain the optimum solution without any difficulty in large-size steel frame design optimization. If mathematical modeling of the frame design optimization problem is to be formulated such that the allowable stress design code specifications such as the displacement and stress limitations are required to be satisfied in the optimum design the optimality criteria approaches provide efficient algorithms for that purpose. However, it should be pointed out that in the optimum solution the design variables will have values attained from a continuous variables assumption. On the other hand practicing structural designer needs cross-sectional properties selected from the available steel sections list. This necessitates first finding the continuous optimum solution and then round these to the

nearest available values. Such move may yield loss of what is gained through optimization. Altering the mathematical programming or optimality criteria technique to work with discrete variables makes the algorithms complicated, and they present difficulties in obtaining the optimum solution of real-size steel frames.

Emergence of the stochastic search techniques provides steel frame designers with new capabilities. These new techniques do not need the gradient calculations of objective function and constraints. They do not use mathematical derivation in order to find a way to reach the optimum. Instead they rely on heuristics. These new optimization techniques use nature as a source of inspiration to develop numerical optimization procedures that are capable of solving complex engineering design problems. They are particularly efficient in obtaining the optimum solution where the design variables are to be selected from a tabulated list. As summarized in this paper there are several stochastic search techniques that are successfully used in the optimum design steel frames where the steel sections for the frame members are to be selected from the available steel sections list, while the limit state design code specifications such as serviceability and strength are to be satisfied. These techniques do provide optimum solution that can be directly used by the practicing designers in their projects. However, they also have some drawbacks. The first one is that because they do not use mathematical derivations; it is not possible to prove whether the optimum solution they attain is the global optimum or it is near optimum. The second is that they work with random numbers, and they have a number of parameters which need to be given values by the users prior to their application. Selection of these values affects the performance of algorithms. This requires a sensitivity works with different values of these parameters in order to find the appropriate values for the problem under consideration. Although some techniques are available such as adaptive genetic algorithm and adaptive harmony search method where the values of these parameters are adjusted automatically by the algorithm itself, this is not the case for other techniques. The third drawback is that they need a large number of structural analysis which becomes computationally very expensive for large-size steel frames. Among the existing techniques some of them excel and outperform others. It is apparent that further research is required to reduce the total number of structural analysis required by stochastic search algorithm which is computationally expensive to a reasonable amount. However, the search for finding better stochastic search techniques is continuing. It is difficult at this moment to conclude which one of these techniques will become the standard one that will be used in the design tools of the finite element packages that are used in everyday practice. However, it is not difficult to conclude that metaheuristic techniques are going to be standard design optimization tools in the near future.

Acknowledgments

This work was supported by the Gachon University Research Fund of 2012 (GCU-2012-R259). However, there is no conflict

of interests which exists when professional judgment concerning the validity of research is influenced by a secondary interest, such as financial gain.

References

- [1] L. A. Schmit, "Structural Design by Systematic Synthesis," in *Proceedings of the ASCE 2nd Conference on Electronic Computation*, pp. 105–132, 1960.
- [2] K. I. Majid, *Optimum Design of Structures*, Butterworths, London, UK, 1974.
- [3] M. P. Saka, *Optimum design of structures [Ph.D. thesis]*, University of Aston, Birmingham, UK, 1975.
- [4] L. A. A. Schmit and H. Miura, "Approximating concepts for efficient structural synthesis," Tech. Rep. NASA CR-2552, 1976.
- [5] M. P. Saka, "Optimum design of rigidly jointed frames," *Computers and Structures*, vol. 11, no. 5, pp. 411–419, 1980.
- [6] E. Atrek, R. H. Gallagher, K. M. Ragsdell, and O. C. Zienkewics, Eds., *New Directions in Optimum Structural Design*, John Wiley & Sons, Chichester, UK, 1984.
- [7] R. T. Haftka, "Simultaneous analysis and design," *AIAA Journal*, vol. 23, no. 7, pp. 1099–1103, 1985.
- [8] J. S. Arora, *Introduction to Optimum Design*, McGraw-Hill, 1989.
- [9] R. T. Haftka and Z. Gurdal, *Elements of Structural Optimization*, Kluwer Academic Publishers, The Netherlands, 1992.
- [10] U. Kirsch, *Structural Optimization*, Springer, 1993.
- [11] J. S. Arora, "Guide to structural optimization," ASCE Manuals and Reports on Engineering Practice number 90, ASCE, New York, NY, USA, 1997.
- [12] A. D. Belegundi and T. R. Chandrupath, *Optimization Concepts and Application in Engineering*, Prentice-Hall, 1999.
- [13] American Institutes of Steel Construction, *Manual of Steel Construction, Allowable Stress Design*, American Institutes of Steel Construction, Chicago, Ill, USA, 9th edition, 1989.
- [14] M. P. Saka, "Optimum design of steel frames with stability constraints," *Computers and Structures*, vol. 41, no. 6, pp. 1365–1377, 1991.
- [15] M. P. Saka, "Optimum design of skeletal structures: a review," in *Progress in Civil and Structural Engineering Computing*, H. V. B. Topping, Ed., chapter 10, pp. 237–284, Saxe-Coburg, 2003.
- [16] M. P. Saka, "Optimum design of steel frames using stochastic search techniques based on natural phenomena: a review," in *Civil Engineering Computations: Tools and Techniques*, B. H. V. Topping, Ed., chapter 6, pp. 105–147, Saxe-Coburg, 2007.
- [17] J. S. Arora and Q. Wang, "Review of formulations for structural and mechanical system optimization," *Structural and Multidisciplinary Optimization*, vol. 30, no. 4, pp. 251–272, 2005.
- [18] J. S. Arora, "Methods for discrete variable structural optimization," in *Recent Advances in Optimum Structural Design*, S. A. Burns, Ed., pp. 1–40, ASCE, USA, 2002.
- [19] R. E. Griffith and R. A. Stewart, "A non-linear programming technique for the optimization of continuous processing systems," *Management Science*, vol. 7, no. 4, pp. 379–392, 1961.
- [20] M. P. Saka, "The use of the approximate programming in the optimum structural design," in *Proceedings of International Conference on Mathematics*, Black Sea Technical University, Trabzon, Turkey, September, 1982.
- [21] K. F. Reinschmidt, C. A. Cornell, and J. F. Brotchie, "Iterative design and structural optimization," *Journal of Structural Division*, vol. 92, pp. 319–340, 1966.
- [22] G. Pope, "Application of linear programming technique in the design of optimum structures," in *Proceedings of the AGAR Symposium Structural Optimization*, Istanbul, Turkey, October, 1969.
- [23] D. Johnson and D. M. Brotton, "Optimum elastic design of redundant trusses," *Journal of the Structural Division*, vol. 95, no. 12, pp. 2589–2610, 1969.
- [24] J. S. Arora and E. J. Haug, "Efficient optimal design of structures by generalized steepest descent programming," *International Journal for Numerical Methods in Engineering*, vol. 10, no. 4, pp. 747–766, 1976.
- [25] P. E. Gill, W. Murray, and M. H. Wright, *Practical Optimization*, Academic Press, 1981.
- [26] J. Nocedal and J. S. Wright, *Numerical optimization*, Springer, New York, NY, USA, 1999.
- [27] S. P. Han, "A globally convergent method for nonlinear programming," *Journal of Optimization Theory and Applications*, vol. 22, no. 3, pp. 297–309, 1977.
- [28] M.-W. Huang and J. S. Arora, "A self-scaling implicit SQP method for large scale structural optimization," *International Journal for Numerical Methods in Engineering*, vol. 39, no. 11, pp. 1933–1953, 1996.
- [29] Q. Wang and J. S. Arora, "Alternative formulations for structural optimization: an evaluation using frames," *Journal of Structural Engineering*, vol. 132, no. 12, Article ID 008612QST, pp. 1880–1889, 2006.
- [30] Q. Wang and J. S. Arora, "Optimization of large-scale truss structures using sparse SAND formulations," *International Journal for Numerical Methods in Engineering*, vol. 69, no. 2, pp. 390–407, 2007.
- [31] C. W. Carroll, "The crated response surface technique for optimizing nonlinear restrained systems," *Operations Research*, vol. 9, no. 2, pp. 169–184, 1961.
- [32] A. V. Fiacco and G. P. McCormack, *Nonlinear Programming Sequential Unconstrained Minimization Techniques*, John Wiley & Sons, New York, NY, USA, 1968.
- [33] D. Kavlie and J. Moe, "Automated design of framed structures," *Journal of Structural Division*, vol. 97, no. 1, 33 pages, 62.
- [34] D. Kavlie and J. Moe, "Application of non-linear programming to optimum grillage design with non-convex sets of variables," *International Journal for Numerical Methods in Engineering*, vol. 1, no. 4, pp. 351–378, 1969.
- [35] K. M. Griswold and J. Moe, "A method for non-linear mixed integer programming and its application to design problems," *Journal of Engineering for Industry*, vol. 94, no. 2, 12 pages, 1972.
- [36] B. M. E. de Silva and G. N. C. Grant, "Comparison of some penalty function based optimization procedures for synthesis of a planar truss," *International Journal for Numerical Methods in Engineering*, vol. 7, no. 2, pp. 155–173, 1973.
- [37] J. B. Rosen, "The gradient-projection method for nonlinear programming-Part II," *Journal of the Society for Industrial and Applied Mathematics*, vol. 9, pp. 514–532, 1961.
- [38] E. J. Haug and J. S. Arora, *Applied Optimal Design*, John Wiley, New York, NY, USA, 1979.
- [39] G. Zoutendijk, *Methods of Feasible Directions*, Elsevier Science, Amsterdam, The Netherlands, 1960.
- [40] G.N. Vanderplaats, "CONMIN: a fortran program for constrained function minimization," Tech. Rep. NASA TNX-62282, 1973.
- [41] G. N. Vanderplaats, *Numerical Optimization Techniques for Engineering Design*, McGraw-Hill, New York, NY, USA, 1984.

- [42] C. Zener, *Engineering Design by Geometric Programming*, John Wiley, London, UK, 1971.
- [43] A. J. Morris, "Structural optimization by geometric programming," in *Foundation in Structural Optimization: A Unified Approach*, A. J. Morris, Ed., pp. 573–610, John Wiley & Sons, Chichester, UK, 1982.
- [44] R.E. Bellman, *Dynamic Programming*, Princeton University Press, Princeton, NJ, USA, 1957.
- [45] A.C. Palmer, "Optimum structural design by dynamic programming," *Journal of the Structural Division*, vol. 94, pp. 1887–1906, 1968.
- [46] D. J. Sheppard and A. C. Palmer, "Optimal design of transmission towers by dynamic programming," *Computers and Structures*, vol. 2, no. 4, pp. 455–468, 1972.
- [47] D. M. Himmelblau, *Applied Nonlinear Programming*, McGraw-Hill, New York, NY, USA, 1972.
- [48] E. D. Eason and R. G. Fenton, "Comparison of numerical optimization methods for engineering design," *Journal of Engineering for Industry, Series B*, vol. 96, no. 1, pp. 196–200, 1974.
- [49] W. Prager, "Optimality criteria in structural design," *Proceedings of National Academy for Science*, vol. 61, no. 3, pp. 794–796, 1968.
- [50] V. B. Venkayya, N. S. Khot, and V. S. Reddy, "Energy distribution in optimum structural design," Tech. Rep. AFFDL-TM-68-156, Flight Dynamics laboratory, Wright Patterson, AFB Ohio, USA, 1968.
- [51] V. B. Venkayya, N. S. Khot, and L. Berke, "Application of optimality criteria approaches to automated design of large practical structures," in *Proceedings of the 2nd Symposium on Structural Optimization*, AGARD-CP-123, pp. 3-1–3-19, 1973.
- [52] V. B. Venkayya, "Optimality criteria: a basis for multidisciplinary design optimization," *Computational Mechanics*, vol. 5, no. 1, pp. 1–21, 1989.
- [53] L. Berke, "An efficient approach to the minimum weight design of deflection limited structures," Tech. Rep. AFFDL-TM-70-4-FDTR, 1970.
- [54] L. Berke and N.S. Khot, "Structural optimization using optimality criteria," in *Computer Aided Structural Design*, C. A. M. Soares, Ed., Springer, 1987.
- [55] N. S. Khot, L. Berke, and V. B. Venkayya, "comparison of optimality criteria algorithms for minimum weight design of structures," *AIAA Journal*, vol. 17, no. 2, pp. 182–190, 1979.
- [56] N. S. Khot, "algorithms based on optimality criteria to design minimum weight structures," *Engineering Optimization*, vol. 5, no. 2, pp. 73–90, 1981.
- [57] N. S. Khot, "Optimal design of a structure for system stability for a specified eigenvalue distribution," in *New Directions in Optimum Structural Design*, E. Atrek, R. H. Gallagher, K. M. Ragsdell, and O. C. Zienkiewicz, Eds., pp. 75–87, John Wiley & Sons, New York, NY, USA, 1984.
- [58] K.M. Ragsdell, "Utility of nonlinear programming methods for engineering design," in *New Direction in Optimality Criteria in Structural Design*, E. Atrek et al., Ed., Chapter 18, John Wiley & Sons, 1984.
- [59] C. Feury and M. Geradin, "Optimality criteria and mathematical programming in structural weight optimization," *Journal of Computers and Structures*, vol. 8, no. 1, pp. 7–17, 1978.
- [60] C. Fleury, "An efficient optimality criteria approach to the minimum weight design of elastic structures," *Journal of Computers and Structures*, vol. 11, no. 3, pp. 163–173, 1980.
- [61] M. P. Saka, "Optimum design of space trusses with buckling constraints," in *Proceedings of 3rd International Conference on Space Structures*, University of Surrey, Guildford, U.K., September 1984.
- [62] E. I. Tabak and P. M. Wright, "Optimality criteria method for building frames," *Journal of Structural Division*, vol. 107, no. 7, pp. 1327–1342, 1981.
- [63] F. Y. Cheng and K. Z. Truman, "Optimization algorithm of 3-D building systems for static and seismic loading," in *Modeling and Simulation in Engineering*, W. F. Ames, Ed., pp. 315–326, North-Holland, Amsterdam, The Netherlands, 1983.
- [64] M. R. Khan, "Optimality criterion techniques applied to frames having general cross-sectional relationships," *AIAA Journal*, vol. 22, no. 5, pp. 669–676, 1984.
- [65] E. A. Sadek, "Optimization of structures having general cross-sectional relationships using an optimality criterion method," *Computers and Structures*, vol. 43, no. 5, pp. 959–969, 1992.
- [66] M. P. Saka, "Optimum design of pin-jointed steel structures with practical applications," *Journal of Structural Engineering*, vol. 116, no. 10, pp. 2599–2620, 1990.
- [67] C. G. Salmon, J. E. Johnson, and F. A. Malhas, *Steel Structures: Design and Behavior*, Prentice Hall, New York, NY, USA, 5th edition, 2009.
- [68] D. E. Grieson and G. E. Cameron, *SODA-Structural Optimization Design and Analysis*, Release 3. 1, User manual, Waterloo Engineering Software, Waterloo, Canada, 1990.
- [69] M. P. Saka, "Optimum design of multistorey structures with shear walls," *Computers and Structures*, vol. 44, no. 4, pp. 925–936, 1992.
- [70] M. P. Saka, "Optimum geometry design of roof trusses by optimality criteria method," *Computers and Structures*, vol. 38, no. 1, pp. 83–92, 1991.
- [71] M. P. Saka, "Optimum design of steel frames with tapered members," *Computers and Structures*, vol. 63, no. 4, pp. 797–811, 1997.
- [72] AISC Manual Committee, "Load and resistance factor design," in *Manual of Steel Construction*, AISC, USA, 1999.
- [73] S. S. Al-Mosawi and M. P. Saka, "Optimum design of single core shear walls," *Computers and Structures*, vol. 71, no. 2, pp. 143–162, 1999.
- [74] S. Al-Mosawi and M. P. Saka, "Optimum shape design of cold-formed thin-walled steel sections," *Advances in Engineering Software*, vol. 31, no. 11, pp. 851–862, 2000.
- [75] V. Z. Vlasov, *Thin-Walled Elastic Beams*, National Science Foundation, Wash, USA, 1961.
- [76] C.-M. Chan and G. E. Grierson, "An efficient resizing technique for the design of tall steel buildings subject to multiple drift constraints," in *The Structural Design of Tall Buildings*, vol. 2, no. 1, pp. 17–32, John Wiley & Sons, West Sussex, UK, 1993.
- [77] C.-M. Chan, "How to optimize tall steel building frameworks," in *Guide To Structural Optimization*, ASCE Manuals and Reports on Engineering Practice, J. S. Arora, Ed., no. 90, Chapter 9, pp. 165–196, ASCE, New York, NY, USA, 1997.
- [78] R. Soegiarso and H. Adeli, "Optimum load and resistance factor design of steel space-frame structures," *Journal of Structural Engineering*, vol. 123, no. 2, pp. 184–192, 1997.
- [79] N. S. Khot, "Nonlinear analysis of optimized structure with constraints on system stability," *AIAA Journal*, vol. 21, no. 8, pp. 1181–1186, 1983.
- [80] N. S. Khot and M. P. Kamat, "Minimum weight design of truss structures with geometric nonlinear behavior," *AIAA Journal*, vol. 23, no. 1, pp. 139–144, 1985.

- [81] M. P. Saka, "Optimum design of nonlinear space trusses," *Computers and Structures*, vol. 30, no. 3, pp. 545–551, 1988.
- [82] M. P. Saka and M. Ulker, "Optimum design of geometrically nonlinear space trusses," *Computers and Structures*, vol. 42, no. 3, pp. 289–299, 1992.
- [83] M. P. Saka and M. S. Hayalioglu, "Optimum design of geometrically nonlinear elastic-plastic steel frames," *Computers and Structures*, vol. 38, no. 3, pp. 329–344, 1991.
- [84] M. S. Hayalioglu and M. P. Saka, "Optimum design of geometrically nonlinear elastic-plastic steel frames with tapered members," *Computers and Structures*, vol. 44, no. 4, pp. 915–924, 1992.
- [85] M. P. Saka and E. S. Kameshki, "Optimum design of unbraced rigid frames," *Computers and Structures*, vol. 69, no. 4, pp. 433–442, 1998.
- [86] M. P. Saka and E. S. Kameshki, "Optimum design of nonlinear elastic framed domes," *Advances in Engineering Software*, vol. 29, no. 7-9, pp. 519–528, 1998.
- [87] J. H. Holland, *Adaptation in Natural and Artificial Systems*, The University of Michigan press, Ann Arbor, Minn, USA, 1975.
- [88] S. Kirkpatrick, C. D. Gelatt, and M. P. Vecchi, "Optimization by simulated annealing," *Science*, vol. 220, pp. 671–680, 1983.
- [89] D. E. Goldberg and M. P. Santani, "Engineering optimization via generic algorithm," in *Proceedings of 9th Conference on Electronic Computation*, pp. 471–482, ASCE, New York, NY, USA, 1986.
- [90] D. E. Goldberg, *Genetic Algorithms in Search, Optimization and Machine Learning*, Addison Wesley, 1989.
- [91] R. Paton, *Computing With Biological Metaphors*, Chapman & Hall, New York, NY, USA, 1994.
- [92] R. Horst and P. M. Pardalos, Eds., *Handbook of Global Optimization*, Kluwer Academic Publishers, New York, NY, USA, 1995.
- [93] R. Horst and H. Tuy, *Global Optimization, Deterministic Approaches*, Springer, 1995.
- [94] C. Adami, *An Introduction to Artificial Life*, Springer-Telos, 1998.
- [95] C. Matheck, *Design in Nature: Learning from Trees*, Springer, Berlin, Germany, 1998.
- [96] M. Mitchell, *An Introduction to Genetic Algorithms*, The MIT Press, Boston, Mass, USA, 1998.
- [97] G. W. Flake, *The Computational Beauty of Nature*, MIT Press, Boston, Mass, USA, 2000.
- [98] L. Chambers, *The Practical Handbook of Genetic Algorithms, Applications*, Chapman & Hall, 2nd edition, 2001.
- [99] J. Kennedy, R. Eberhart, and Y. Shi, *Swarm Intelligence*, Morgan Kaufmann, Boston, Mass, USA, 2001.
- [100] G. A. Kochenberger and F. Glover, *Handbook of Meta-Heuristics*, Kluwer Academic Publishers, New York, NY, USA, 2003.
- [101] L. N. De Castro and F. J. Von Zuben, *Recent Developments in Biologically Inspired Computing*, Idea Group Publishing, USA, 2005.
- [102] J. Drezo, A. Petrowski, P. Siarry, and E. Taillard, *Meta-Heuristics for Hard Optimization*, Springer, Berlin, Germany, 2006.
- [103] T. F. Gonzales, *Handbook of Approximation Algorithms and Metaheuristics*, Chapman & Halls/CRC, 2007.
- [104] X.-S. Yang, *Nature-Inspired Metaheuristic Algorithms*, Luniver Press, 2008.
- [105] X. -S. Yang, *Engineering Optimization: An Introduction With Metaheuristic Applications*, John Wiley, New York, NY, USA, 2010.
- [106] S. Luke, "Essentials of Metaheuristics," 2010, <http://cs.gmu.edu/~sean/book/metaheuristics/>.
- [107] P. Lu, S. Chen, and Y. Zheng, "Artificial intelligence in civil engineering," *Mathematical Problems in Engineering*, vol. 2012, Article ID 145974, 22 pages, 2012.
- [108] R. Kicinger, T. Arciszewski, and K. De Jong, "Evolutionary computation and structural design: a survey of the state-of-the-art," *Computers and Structures*, vol. 83, no. 23-24, pp. 1943–1978, 2005.
- [109] I. Rechenberg, "Cybernetic solution path of an experimental problem," in *Royal Aircraft Establishment*, no. 1122, Library Translation, Farnborough, UK, 1965.
- [110] I. Rechenberg, *Evolutionstrategie: optimierung technischer systeme nach prinzipien der biologischen evolution*, Frommann-Holzboog, Stuttgart, Germany, 1973.
- [111] H. -P. Schwefel, "Kybernetische evolution als strategie der experimentellen forschung in der strömungstechnik," in *Diplomarbeit*, Technische Universität, Berlin, Germany, 1965.
- [112] D. E. Goldberg and M. P. Santani, "Engineering optimization via generic algorithm," in *Proceedings of 9th Conference on Electronic Computation*, pp. 471–482, ASCE, New York, NY, USA, 1986.
- [113] M. Gen and R. Chang, *Genetic Algorithm and Engineering Design*, John Wiley & Sons, New York, NY, USA, 2000.
- [114] D. E. Goldberg and M. P. Santani, "Engineering optimization via generic algorithm," in *Proceedings of 9th Conference on Electronic Computation*, pp. 471–482, ASCE, New York, NY, USA, 1986.
- [115] S. Rajev and C. S. Krishnamoorthy, "Discrete optimization of structures using genetic algorithms," *Journal of Structural Engineering*, vol. 118, no. 5, pp. 1233–1250, 1992.
- [116] F. Herrera, M. Lozano, and J. L. Verdegay, "Tackling real-coded genetic algorithms: operators and tools for behavioural analysis," *Artificial Intelligence Review*, vol. 12, no. 4, pp. 265–319, 1998.
- [117] J. P. B. Leite and B. H. V. Topping, "Improved genetic operators for structural engineering optimization," *Advances in Engineering Software*, vol. 29, no. 7–9, pp. 529–562, 1998.
- [118] W. M. Jenkins, "Towards structural optimization via the genetic algorithm," *Computers and Structures*, vol. 40, no. 5, pp. 1321–1327, 1991.
- [119] W. M. Jenkins, "Structural optimization via the genetic algorithm," *The Structural Engineer*, vol. 69, no. 24, pp. 418–422, 1991.
- [120] P. Hajela, "Stochastic search in structural optimization: genetic algorithms and simulated annealing," in *Structural Optimization: Status and Promise*, chapter 22, pp. 611–635, American Institute of Aeronautics and Astronautics, 1992.
- [121] H. Adeli and N. T. Cheng, "Augmented lagrange genetic algorithm for structural optimization," *Journal of Structural Engineering*, vol. 7, no. 3, pp. 104–118, 1994.
- [122] H. Adeli and N. T. Cheng, "Concurrent genetic algorithms for optimization of large structures," *Journal of Aerospace Engineering*, vol. 7, no. 3, pp. 276–296, 1994.
- [123] S. D. Rajan, "Sizing, shape, and topology design optimization of trusses using genetic algorithm," *Journal of Structural Engineering*, vol. 121, no. 10, pp. 1480–1487, 1995.
- [124] C. V. Camp, S. Pezeshk, and G. Cao, "Design of framed structures using a genetic algorithm," in *Advances in Structural Optimization*, D. M. Frangopol and F. Y. Cheng, Eds., pp. 19–30, ASCE, NY, USA, 1997.

- [125] C. Camp, S. Pezeshk, and G. Cao, "Optimized design of two-dimensional structures using a genetic algorithm," *Journal of Structural Engineering*, vol. 124, no. 5, pp. 551–559, 1998.
- [126] M. P. Saka and E. Kameshki, "Optimum design of multi-storey sway steel frames to BS5950 using a genetic algorithm," in *Advances in Engineering Computational Technology*, B. H. V. Topping, Ed., pp. 135–141, Civil-Comp Press, Edinburgh, UK, 1998.
- [127] M. P. Saka, "Optimum design of grillage systems using genetic algorithms," *Computer-Aided Civil and Infrastructure Engineering*, vol. 13, no. 4, pp. 297–302, 1998.
- [128] S. H. Weldali and M. P. Saka, "Optimum geometry and spacing design of roof trusses based on BS5990 using genetic algorithm," *Design Optimization*, vol. 1, no. 2, pp. 198–219, 2000.
- [129] M. P. Saka, A. Daloglu, and F. Malhas, "Optimum spacing design of grillage systems using a genetic algorithm," *Advances in Engineering Software*, vol. 31, no. 11, pp. 863–873, 2000.
- [130] S. Pezeshk, C. V. Camp, and D. Chen, "Design of nonlinear framed structures using genetic optimization," *Journal of Structural Engineering*, vol. 126, no. 3, pp. 387–388, 2000.
- [131] O. Hasançebi and F. Erbatur, "Evaluation of crossover techniques in genetic algorithm based optimum structural design," *Computers and Structures*, vol. 78, no. 1, pp. 435–448, 2000.
- [132] F. Erbatur, O. Hasançebi, İ. Tütüncü, and H. Kılıç, "Optimal design of planar and space structures with genetic algorithms," *Computers and Structures*, vol. 75, pp. 209–224, 2000.
- [133] E. S. Kameshki and M. P. Saka, "Genetic algorithm based optimum bracing design of non-swaying tall plane frames," *Journal of Constructional Steel Research*, vol. 57, no. 10, pp. 1081–1097, 2001.
- [134] E. S. Kameshki and M. P. Saka, "Optimum design of nonlinear steel frames with semi-rigid connections using a genetic algorithm," *Computers and Structures*, vol. 79, no. 17, pp. 1593–1604, 2001.
- [135] J. Andre, P. Siarry, and T. Dognon, "An improvement of the standard genetic algorithm fighting premature convergence in continuous optimization," *Advances in Engineering Software*, vol. 32, no. 1, pp. 49–60, 2001.
- [136] V. V. Toropov and S. Y. Mahfouz, "Design optimization of structural steelwork using a genetic algorithm, FEM and a system of design rules," *Engineering Computations*, vol. 18, no. 3–4, pp. 437–459, 2001.
- [137] M. S. Hayalioglu, "Optimum load and resistance factor design of steel space frames using genetic algorithm," *Structural and Multidisciplinary Optimization*, vol. 21, no. 4, pp. 292–299, 2001.
- [138] W. M. Jenkins, "A decimal-coded evolutionary algorithm for constrained optimization," *Computers and Structures*, vol. 80, no. 5–6, pp. 471–480, 2002.
- [139] E. S. Kameshki and M. P. Saka, "Genetic algorithm based optimum design of nonlinear planar steel frames with various semi-rigid connections," *Journal of Constructional Steel Research*, vol. 59, no. 1, pp. 109–134, 2003.
- [140] Y. M. Yun and B. H. Kim, "Optimum design of plane steel frame structures using second-order inelastic analysis and a genetic algorithm," *Journal of Structural Engineering*, vol. 131, no. 12, pp. 1820–1831, 2005.
- [141] A. Kaveh and M. Shahrouzi, "Simultaneous topology and size optimization of structures by genetic algorithm using minimal length chromosome," *Engineering Computations*, vol. 23, no. 6, pp. 644–674, 2006.
- [142] R. J. Balling, R. R. Briggs, and K. Gillman, "Multiple optimum size/shape/topology designs for skeletal structures using a genetic algorithm," *Journal of Structural Engineering*, vol. 132, no. 7, Article ID 015607QST, pp. 1158–1165, 2006.
- [143] V. Toğan and A. T. Daloglu, "Optimization of 3D trusses with adaptive approach in genetic algorithms," *Engineering Structures*, vol. 28, pp. 1019–1027, 2006.
- [144] E. S. Kameshki and M. P. Saka, "Optimum geometry design of nonlinear braced domes using genetic algorithm," *Computers and Structures*, vol. 85, no. 1–2, pp. 71–79, 2007.
- [145] S. O. Degertekin, "A comparison of simulated annealing and genetic algorithm for optimum design of nonlinear steel space frames," *Structural and Multidisciplinary Optimization*, vol. 34, no. 4, pp. 347–359, 2007.
- [146] S. O. Degertekin, M. P. Saka, and M. S. Hayalioglu, "Optimal load and resistance factor design of geometrically nonlinear steel space frames via tabu search and genetic algorithm," *Engineering Structures*, vol. 30, no. 1, pp. 197–205, 2008.
- [147] H. K. Issa and F. A. Mohammad, "Effect of mutation schemes on convergence to optimum design of steel frames," *Journal of Constructional Steel Research*, vol. 66, no. 7, pp. 954–961, 2010.
- [148] D. Safari, M. R. Maheri, and A. Maheri, "Optimum design of steel frames using a multiple-deme GA with improved reproduction operators," *Journal of Constructional Steel Research*, vol. 67, no. 8, pp. 1232–1243, 2011.
- [149] N. D. Lagaros, M. Papadrakakis, and G. Kokossalakis, "Structural optimization using evolutionary algorithms," *Computers and Structures*, vol. 80, no. 7–8, pp. 571–589, 2002.
- [150] J. Cai and G. Thierauf, "Discrete structural optimization using evolution strategies," in *Neural Networks and Combinatorial Optimization in Civil and Structural Engineering*, B. H. V. Topping and A. I. Khan, Eds., pp. 95–100, Civil-Comp, Edinburgh, UK, 1993.
- [151] C. A. C. Coello, "Theoretical and numerical constraint-handling techniques used with evolutionary algorithms: a survey of the state of the art," *Computer Methods in Applied Mechanics and Engineering*, vol. 191, no. 11–12, pp. 1245–1287, 2002.
- [152] T. Back and M. Schütz, "Evolutionary strategies for mixed-integer optimization of optical multilayer systems," in *Proceedings of the 4th Annual Conference on Evolutionary Programming*, R. J. McDonnell, R. G. Reynolds, and D. B. Fogel, Eds., pp. 33–51, MIT Press, Cambridge, Mass, USA.
- [153] S. Rajasekaran, V. S. Mohan, and O. Khamis, "The optimisation of space structures using evolution strategies with functional networks," *Engineering with Computers*, vol. 20, no. 1, pp. 75–87, 2004.
- [154] S. Rajasekaran, "Optimal laminate sequence of non-prismatic thin-walled composite spatial members of generic section," *Composite Structures*, vol. 70, no. 2, pp. 200–211, 2005.
- [155] G. Ebenau, J. Rottschäfer, and G. Thierauf, "An advanced evolutionary strategy with an adaptive penalty function for mixed-discrete structural optimisation," *Advances in Engineering Software*, vol. 36, no. 1, pp. 29–38, 2005.
- [156] O. Hasançebi, "Discrete approaches in evolution strategies based optimum design of steel frames," *Structural Engineering and Mechanics*, vol. 26, no. 2, pp. 191–210, 2007.
- [157] O. Hasançebi, "Optimization of truss bridges within a specified design domain using evolution strategies," *Engineering Optimization*, vol. 39, no. 6, pp. 737–756, 2007.

- [158] O. Hasançebi, "Adaptive evolution strategies in structural optimization: Enhancing their computational performance with applications to large-scale structures," *Computers and Structures*, vol. 86, no. 1-2, pp. 119–132, 2008.
- [159] V. Černý, "Thermodynamical approach to the traveling salesman problem: An efficient simulation algorithm," *Journal of Optimization Theory and Applications*, vol. 45, no. 1, pp. 41–51, 1985.
- [160] W. A. Bennage and A. K. Dhingra, "Single and multiobjective structural optimization in discrete-continuous variables using simulated annealing," *International Journal for Numerical Methods in Engineering*, vol. 38, no. 16, pp. 2753–2773, 1995.
- [161] N. Metropolis, A. W. Rosenbluth, M. N. Rosenbluth, A. H. Teller, and E. Teller, "Equation of state calculations by fast computing machines," *The Journal of Chemical Physics*, vol. 21, no. 6, pp. 1087–1092, 1953.
- [162] R. J. Balling, "Optimal steel frame design by simulated annealing," *Journal of Structural Engineering*, vol. 117, no. 6, pp. 1780–1795, 1991.
- [163] S. A. May and R. J. Balling, "A filtered simulated annealing strategy for discrete optimization of 3D steel frameworks," *Structural Optimization*, vol. 4, no. 3-4, pp. 142–148, 1992.
- [164] R. K. Kincaid, "Minimizing distortion and internal forces in truss structures by simulated annealing," in *Proceedings of 31st AIAA/ASME/ASCE/AHS/ASC Structural Materials and Dynamics Conference*, pp. 327–333, Long Beach, Calif, USA, April 1990.
- [165] R. K. Kincaid, "Minimizing distortion and internal forces in truss structures by simulated annealing," in *Proceedings of 32nd AIAA/ASME/ASCE/AHS/ASC Structural Materials and Dynamics Conference*, pp. 327–333, Baltimore, Md, USA, April 1990.
- [166] G. S. Chen, R. J. Bruno, and M. Salama, "Optimal placement of active/passive members in truss structures using simulated annealing," *AIAA Journal*, vol. 29, no. 8, pp. 1327–1334, 1991.
- [167] B. H. V. Topping, A. I. Khan, and J. P. B. Leite, "Topological design of truss structures using simulated annealing," in *Neural Networks and Combinatorial Optimization in Civil and Structural Engineering*, B. H. V. Topping and A. I. Khan, Eds., pp. 151–165, Civil-Comp Press, UK, 1993.
- [168] J. P. B. Leite and B. H. V. Topping, "Parallel simulated annealing for structural optimization," *Computers and Structures*, vol. 73, no. 1-5, pp. 545–564, 1999.
- [169] S. R. Tzan and C. P. Pantelides, "Annealing strategy for optimal structural design," *Journal of Structural Engineering*, vol. 122, no. 7, pp. 815–827, 1996.
- [170] O. Hasançebi and F. Erbatur, "On efficient use of simulated annealing in complex structural optimization problems," *Acta Mechanica*, vol. 157, no. 1-4, pp. 27–50, 2002.
- [171] O. Hasançebi and F. Erbatur, "Layout optimisation of trusses using simulated annealing," *Advances in Engineering Software*, vol. 33, no. 7-10, pp. 681–696, 2002.
- [172] S. O. Degertekin, M. S. Hayalioglu, and M. Ulker, "A hybrid tabu-simulated annealing heuristic algorithm for optimum design of steel frames," *Steel and Composite Structures*, vol. 8, no. 6, pp. 475–490, 2008.
- [173] O. Hasançebi, S. Carbas, and M. P. Saka, "Improving the performance of simulated annealing in structural optimization," *Structural and Multidisciplinary Optimization*, vol. 41, no. 2, pp. 189–203, 2010.
- [174] O. Hasançebi and E. Doğan, "Evaluation of topological forms for weight-effective optimum design of single-span steel truss bridges," *Asian Journal of Civil Engineering*, vol. 12, no. 4, pp. 431–448, 2011.
- [175] J. Kennedy and R. Eberhart, "Particle swarm optimization," in *Proceedings of the IEEE International Conference on Neural Networks*, vol. 4, pp. 1942–1948, December 1995.
- [176] J. Kennedy and R. Eberhart, *Swarm Intelligence*, Morgan Kaufman, 2001.
- [177] G. Venter and J. Sobieszczanski-Sobieski, "Multidisciplinary optimization of a transport aircraft wing using particle swarm optimization," *Structural and Multidisciplinary Optimization*, vol. 26, no. 1-2, pp. 121–131, 2004.
- [178] P. C. Fourie and A. A. Groenwold, "The particle swarm optimization algorithm in size and shape optimization," *Structural and Multidisciplinary Optimization*, vol. 23, no. 4, pp. 259–267, 2002.
- [179] R. E. Perez and K. Behdinan, "Particle swarm approach for structural design optimization," *Computers and Structures*, vol. 85, no. 19-20, pp. 1579–1588, 2007.
- [180] S. He, E. Prempan, and Q. H. Wu, "An improved particle swarm optimizer for mechanical design optimization problems," *Engineering Optimization*, vol. 36, no. 5, pp. 585–605, 2004.
- [181] S. He, Q. H. Wu, J. Y. Wen, J. R. Saunders, and R. C. Paton, "A particle swarm optimizer with passive congregation," *BioSystems*, vol. 78, no. 1-3, pp. 135–147, 2004.
- [182] L. J. Li, Z. B. Huang, F. Liu, and Q. H. Wu, "A heuristic particle swarm optimizer for optimization of pin connected structures," *Computers and Structures*, vol. 85, no. 7-8, pp. 340–349, 2007.
- [183] E. Doğan and M. P. Saka, "Optimum design of unbraced steel frames to LRFD-AISC using particle swarm optimization," *Advances in Engineering Software*, vol. 46, pp. 27–34, 2012.
- [184] A. Colnari, M. Dorigo, and V. Maniezzo, "Distributed optimization by ant colony," in *Proceedings of 1st European Conference on Artificial Life*, pp. 134–142, USA, 1991.
- [185] M. Dorigo, *Optimization, learning and natural algorithms [Ph.D. thesis]*, Dipartimento Elettronica e Informazione, Politecnico di Milano, Italy, 1992.
- [186] M. Dorigo and T. Stützle, *Ant Colony Optimization*, A Bradford Book, MIT, USA, 2004.
- [187] C. V. Camp and B. J. Bichon, "Design of space trusses using ant colony optimization," *Journal of Structural Engineering*, vol. 130, no. 5, pp. 741–751, 2004.
- [188] C. V. Camp, B. J. Bichon, and S. P. Stovall, "Design of steel frames using ant colony optimization," *Journal of Structural Engineering*, vol. 131, no. 3, pp. 369–379, 2005.
- [189] A. Kaveh and S. Shojaei, "Optimal design of skeletal structures using ant colony optimization," *International Journal for Numerical Methods in Engineering*, vol. 70, no. 5, pp. 563–581, 2007.
- [190] J. A. Bland, "Automatic optimal design of structures using swarm intelligence," in *Proceedings of the Annual Conference of the Canadian Society for Civil Engineering*, pp. 1945–1954, Canada, June 2008.
- [191] A. Kaveh and S. Talatahari, "An improved ant colony optimization for the design of planar steel frames," *Engineering Structures*, vol. 32, no. 3, pp. 864–873, 2010.
- [192] W. Wang, S. Guo, and W. Yang, "Simultaneous partial topology and size optimization of a wing structure using ant colony and gradient based methods," *Engineering Optimization*, vol. 43, no. 4, pp. 433–446, 2011.

- [193] İ. Aydoğdu and M. P. Saka, "Ant colony optimization of irregular steel frames including elemental warping effect," *Advances in Engineering Software*, vol. 44, no. 1, pp. 150–169, 2012.
- [194] Z. W. Geem, J. H. Kim, and G. V. Loganathan, "A new heuristic optimization algorithm: harmony search," *Simulation*, vol. 76, no. 2, pp. 60–68, 2001.
- [195] Z. W. Geem, J. H. Kim, and G. V. Loganathan, "Harmony search optimization: application to pipe network design," *International Journal of Modelling and Simulation*, vol. 22, no. 2, pp. 125–133, 2002.
- [196] K. S. Lee and Z. W. Geem, "A new structural optimization method based on the harmony search algorithm," *Computers and Structures*, vol. 82, no. 9-10, pp. 781–798, 2004.
- [197] K. S. Lee and Z. W. Geem, "A new meta-heuristic algorithm for continuous engineering optimization: harmony search theory and practice," *Computer Methods in Applied Mechanics and Engineering*, vol. 194, no. 36-38, pp. 3902–3933, 2005.
- [198] Z. W. Geem, K. S. Lee, and C. L. Tseng, "Harmony search for structural design," in *Proceedings of the Genetic and Evolutionary Computation Conference (GECCO '05)*, pp. 651–652, Washington, DC, USA, June 2005.
- [199] Z. W. Geem, "Optimal cost design of water distribution networks using harmony search," *Engineering Optimization*, vol. 38, no. 3, pp. 259–280, 2006.
- [200] Z. W. Geem, "Novel derivative of harmony search algorithm for discrete design variables," *Applied Mathematics and Computation*, vol. 199, no. 1, pp. 223–230, 2008.
- [201] Z. W. Geem, Ed., *Music-Inspired Harmony Search Algorithm*, Springer, 2009.
- [202] Z. W. Geem, "Particle-swarm harmony search for water network design," *Engineering Optimization*, vol. 41, no. 4, pp. 297–311, 2009.
- [203] Z. W. Geem, Ed., *Recent Advances in Harmony Search Algorithm*, Springer, 2010.
- [204] Z. W. Geem, Ed., *Harmony Search Algorithms for Structural Design Optimization*, Springer, 2010.
- [205] Z. W. Geem, "Harmony search algorithm," 2011, <http://www.harmonysearch.info/>.
- [206] Z. W. Geem and W. E. Roper, "Various continuous harmony search algorithms for web-based hydrologic parameter optimization," *International Journal of Mathematical Modelling and Numerical Optimisation*, vol. 1, no. 3, pp. 231–226, 2010.
- [207] M. P. Saka, "Optimum geometry design of geodesic domes using harmony search algorithm," *Advances in Structural Engineering*, vol. 10, no. 6, pp. 595–606, 2007.
- [208] S. Carbas and M. P. Saka, "A harmony search algorithm for optimum topology design of single layer lamella domes," in *Proceedings of The 9th International Conference on Computational Structures Technology*, B. H. V. Topping and M. Papadrakakis, Eds., no. 50, Civil-Comp Press, Scotland, UK, 2008.
- [209] S. Çarbaş and M. P. Saka, "Optimum design of single layer network domes using harmony search method," *Asian Journal of Civil Engineering*, vol. 10, no. 1, pp. 97–112, 2009.
- [210] S. Çarbaş and M. P. Saka, "Optimum topology design of various geometrically nonlinear latticed domes using improved harmony search method," *Structural and Multidisciplinary Optimization*, vol. 45, no. 3, pp. 377–399, 2011.
- [211] M. P. Saka and F. Erdal, "Harmony search based algorithm for the optimum design of grillage systems to LRFD-AISC," *Structural and Multidisciplinary Optimization*, vol. 38, no. 1, pp. 25–41, 2009.
- [212] M. P. Saka, "Optimum design of steel sway frames to BS5950 using harmony search algorithm," *Journal of Constructional Steel Research*, vol. 65, no. 1, pp. 36–43, 2009.
- [213] S. O. Degertekin, "Optimum design of steel frames via harmony search algorithm," *Studies in Computational Intelligence*, vol. 239, pp. 51–78, 2009.
- [214] S. O. Degertekin, M. S. Hayalioglu, and H. Gorgun, "Optimum design of geometrically non-linear steel frames with semi-rigid connections using a harmony search algorithm," *Steel and Composite Structures*, vol. 9, no. 6, pp. 535–555, 2009.
- [215] M. P. Saka and O. Hasancebi, "Adaptive harmony search algorithm for design code optimization of steel structures," in *Harmony Search Algorithms for Structural Design Optimization*, Z. W. Geem, Ed., chapter 3, SCI 239, pp. 79–120, Springer, Berlin, Germany, 2009.
- [216] O. Hasancebi, F. Erdal, and M. P. Saka, "An adaptive harmony search method for structural optimization," *Journal of Structural Engineering*, vol. 136, no. 4, pp. 419–431, 2010.
- [217] F. Erdal, E. Doan, and M. P. Saka, "Optimum design of cellular beams using harmony search and particle swarm optimizers," *Journal of Constructional Steel Research*, vol. 67, no. 2, pp. 237–247, 2011.
- [218] M. P. Saka, I. Aydogdu, O. Hasancebi, and Z. W. Geem, "Harmony search algorithms in structural engineering," in *Computational Optimization and Applications in Engineering and Industry*, X.-S. Yang and S. Koziel, Eds., Chapter 6, Springer, Berlin, Germany, 2011.
- [219] M. Mahdavi, M. Fesanghary, and E. Damangir, "An improved harmony search algorithm for solving optimization problems," *Applied Mathematics and Computation*, vol. 188, no. 2, pp. 1567–1579, 2007.
- [220] M. G. H. Omran and M. Mahdavi, "Global-best harmony search," *Applied Mathematics and Computation*, vol. 198, no. 2, pp. 643–656, 2008.
- [221] L. D. Santos Coelho and D. L. de Andrade Bernert, "An improved harmony search algorithm for synchronization of discrete-time chaotic systems," *Chaos, Solitons and Fractals*, vol. 41, no. 5, pp. 2526–2532, 2009.
- [222] O. K. Erol and I. Eksin, "A new optimization method: Big Bang-Big Crunch," *Advances in Engineering Software*, vol. 37, no. 2, pp. 106–111, 2006.
- [223] C. V. Camp, "Design of space trusses using big bang-big crunch optimization," *Journal of Structural Engineering*, vol. 133, no. 7, pp. 999–1008, 2007.
- [224] A. Kaveh and S. Talatahari, "Size optimization of space trusses using Big Bang-Big Crunch algorithm," *Computers and Structures*, vol. 87, no. 17-18, pp. 1129–1140, 2009.
- [225] A. Kaveh and S. Talatahari, "Optimal design of Schwedler and ribbed domes via hybrid Big Bang-Big Crunch algorithm," *Journal of Constructional Steel Research*, vol. 66, no. 3, pp. 412–419, 2010.
- [226] A. Kaveh and H. Abbasgholiha, "Optimum design of steel sway frames using Big Bang-Big Crunch algorithm," *Asian Journal of Civil Engineering*, vol. 12, no. 3, pp. 293–317, 2011.
- [227] A. Kaveh and S. Talatahari, "A discrete particle swarm ant colony optimization for design of steel frames," *Asian Journal of Civil Engineering*, vol. 9, no. 6, pp. 563–575, 2008.
- [228] A. Kaveh and S. Talatahari, "A particle swarm ant colony optimization for truss structures with discrete variables," *Journal of Constructional Steel Research*, vol. 65, no. 8-9, pp. 1558–1568, 2009.

- [229] A. Kaveh and S. Talatahari, "Hybrid algorithm of harmony search, particle swarm and ant colony for structural design optimization," *Studies in Computational Intelligence*, vol. 239, pp. 159–198, 2009.
- [230] A. Kaveh and S. Talatahari, "Particle swarm optimizer, ant colony strategy and harmony search scheme hybridized for optimization of truss structures," *Computers and Structures*, vol. 87, no. 5-6, pp. 267–283, 2009.
- [231] A. Kaveh, S. Talatahari, and B. Farahmand Azar, "An improved hpsaco for engineering optimum design problems," *Asian Journal of Civil Engineering*, vol. 12, no. 2, pp. 133–141, 2010.
- [232] A. Kaveh and S. M. Rad, "Hybrid genetic algorithm and particle swarm optimization for the force method-based simultaneous analysis and design," *Iranian Journal of Science and Technology, Transaction B*, vol. 34, no. 1, pp. 15–34, 2010.
- [233] A. Kaveh and S. Talatahari, "Optimum design of skeletal structures using imperialist competitive algorithm," *Computers and Structures*, vol. 88, no. 21-22, pp. 1220–1229, 2010.
- [234] A. Kaveh and S. Talatahari, "A novel heuristic optimization method: charged system search," *Acta Mechanica*, vol. 213, pp. 267–289, 2010.
- [235] A. Kaveh and S. Talatahari, "Optimal design of skeletal structures via the charged system search algorithm," *Structural and Multidisciplinary Optimization*, vol. 41, no. 6, pp. 893–911, 2010.
- [236] A. Kaveh and S. Talatahari, "Charged system search for optimum grillage system design using the LRFD-AISC code," *Journal of Constructional Steel Research*, vol. 66, no. 6, pp. 767–771, 2010.
- [237] A. Kaveh and S. Talatahari, "A charged system search with a fly to boundary method for discrete optimum design of truss structures," *Asian Journal of Civil Engineering*, vol. 11, no. 3, pp. 277–293, 2010.
- [238] A. Kaveh and S. Talatahari, "Geometry and topology optimization of geodesic domes using charged system search," *Structural and Multidisciplinary Optimization*, vol. 43, no. 2, pp. 215–229, 2011.
- [239] A. Kaveh and A. Zolghadr, "Shape and size optimization of truss structures with frequency constraints using enhanced charged system search algorithm," *Asian Journal of Civil Engineering*, vol. 12, no. 4, pp. 487–509, 2011.
- [240] A. Kaveh and S. Talatahari, "Charged system search for optimal design of frame structures," *Applied Soft Computing*, vol. 12, pp. 382–393, 2012.
- [241] A. Kaveh and T. Bakhspoori, "Optimum design of steel frames using cuckoo search algorithm with levy flights," *The Structural Design of Tall and Special Buildings*. In press.
- [242] X. -S Yang and S. Deb, "Engineering Optimization by Cuckoo Search," *International Journal of Mathematical Modelling and Numerical Optimisation*, vol. 1, no. 4, pp. 330–343, 2010.
- [243] A. H. Gandomi, X.-S. Yang, and A. H. Alavi, "Cuckoo search algorithm: a metaheuristic approach to solve structural optimization problems," *Engineering with Computers*. In press.
- [244] O. Hasançebi, S. Çarbaş, E. Doğan, F. Erdal, and M. P. Saka, "Performance evaluation of metaheuristic search techniques in the optimum design of real size pin jointed structures," *Computers and Structures*, vol. 87, no. 5-6, pp. 284–302, 2009.
- [245] O. Hasançebi, S. Çarbaş, E. Doğan, F. Erdal, and M. P. Saka, "Comparison of non-deterministic search techniques in the optimum design of real size steel frames," *Computers and Structures*, vol. 88, no. 17-18, pp. 1033–1048, 2010.
- [246] A. Kaveh and S. Talatahari, "Optimal design of single layer domes using meta-heuristic algorithms; a comparative study," *International Journal of Space Structures*, vol. 25, no. 4, pp. 217–227, 2010.

Research Article

Accelerated Particle Swarm for Optimum Design of Frame Structures

S. Talatahari,¹ E. Khalili,² and S. M. Alavizadeh³

¹ Marand Faculty of Engineering, University of Tabriz, Tabriz 51666-14766, Iran

² Department of Engineering, Islamic Azad University, Ahar Branch, Ahar 54516, Iran

³ Department of Structural Engineering, Islamic Azad University, Shabestar Branch, Shabestar 57168-14758, Iran

Correspondence should be addressed to S. Talatahari; talatahari@tabrizu.ac.ir

Received 29 November 2012; Revised 29 December 2012; Accepted 30 December 2012

Academic Editor: Fei Kang

Copyright © 2013 S. Talatahari et al. This is an open access article distributed under the Creative Commons Attribution License, which permits unrestricted use, distribution, and reproduction in any medium, provided the original work is properly cited.

Accelerated particle swarm optimization (APSO) is developed for finding optimum design of frame structures. APSO shows some extra advantages in convergence for global search. The modifications on standard PSO effectively accelerate the convergence rate of the algorithm and improve the performance of the algorithm in finding better optimum solutions. The performance of the APSO algorithm is also validated by solving two frame structure problems.

1. Introduction

Optimum design of frame structures are inclined to determine suitable sections for elements that fulfill all design requirements while having the lowest possible cost. In this issue, optimization provides engineers with a variety of techniques to deal with these problems [1]. These techniques can be categorized as two general groups: classical methods and metaheuristic approaches [2]. Classical methods are often based on mathematical programming, and many of metaheuristic methods make use of the ideas from nature and do not suffer the discrepancies of mathematical programming [3–8].

Particle swarm optimization (PSO), one of meta-heuristic algorithms, is based on the simulation of the social behavior of bird flocking and fish schooling. PSO is the most successful swarm intelligence inspired optimization algorithms. However, the local search capability of PSO is poor [9], since premature convergence occurs often. In order to overcome these disadvantages of PSO, many improvements have been proposed. Shi and Eberhart [10] introduced a fuzzy system to adapt the inertia weight for three benchmark test functions. Liu et al. [11] proposed center particle swarm optimization

by adding a center particle into PSO to improve the performance. An improved quantum-behaved PSO was proposed by Xi et al. [12]. Jiao et al. [13] proposed the dynamic inertia weight PSO, by defining a dynamic inertia weight to decrease the inertia factor in the velocity update equation of the original PSO. Yang et al. [14] proposed another dynamic inertia weight to modify the velocity update formula in a method called modified particle swarm optimization with dynamic adaptation.

A number of studies have applied the PSO and improved it to be used in the field of structural engineering [15–21]. In this study, we developed an improved PSO, so-called accelerated particle swarm optimization (APSO) [22], to find optimum design of frame structures. The resulted method is then tested by some numerical examples to estimate its potential for solving structural optimization problems.

2. Statement of Structural Optimization Problem

Optimum design of structures includes finding optimum sections for members that minimizes the structural weight W .

This minimum design should also satisfy inequality constraints that limit design variables and structural responses. Thus, the optimal design of a structure is formulated as [23]

$$\begin{aligned} \text{minimize } W(\{x\}) &= \sum_{i=1}^n \gamma_i \cdot A_i \cdot l_i, \\ \text{subject to : } g_{\min} &\leq g_i(\{x\}) \leq g_{\max}, \quad i = 1, 2, 3, \dots, m, \end{aligned} \quad (1)$$

where $W(\{x\})$ is the weight of the structure; n and m are the number of members making up the structure and the number of total constraints, respectively; max and min denote upper and lower bounds, respectively; $g(\{x\})$ denotes the constraints considered for the structure containing interaction constraints as well as the lateral and interstory displacements, as follows.

The maximum lateral displacement:

$$g^\Delta = \frac{\Delta_T}{H} - R \geq 0. \quad (2)$$

The interstory displacements:

$$g_j^d = \frac{d_j}{h_j} - R_I \geq 0, \quad j = 1, 2, \dots, ns, \quad (3)$$

where Δ_T is the maximum lateral displacement; H is the height of the frame structure; R is the maximum drift index; d_j is the inter-story drift; h_j is the story height of the j th floor; ns is the total number of stories; R_I is the inter-story drift index permitted by the code of the practice.

LRFD interaction formula constraints (AISC 2001 [24, Equation H1-1a,b]):

$$\begin{aligned} g_i^I &= \frac{P_u}{2\phi_c P_n} + \left(\frac{M_{ux}}{\phi_b M_{nx}} + \frac{M_{uy}}{\phi_b M_{ny}} \right) - 1 \geq 0 \quad \text{for } \frac{P_u}{\phi_c P_n} < 0.2, \\ g_i^I &= \frac{P_u}{\phi_c P_n} + \frac{8}{9} \left(\frac{M_{ux}}{\phi_b M_{nx}} + \frac{M_{uy}}{\phi_b M_{ny}} \right) - 1 \geq 0 \quad \text{for } \frac{P_u}{\phi_c P_n} \geq 0.2, \end{aligned} \quad (4)$$

where P_u is the required strength (tension or compression); P_n is the nominal axial strength (tension or compression); ϕ_c is the resistance factor ($\phi_c = 0.9$ for tension, $\phi_c = 0.85$ for compression); M_{ux} and M_{uy} are the required flexural strengths in the x and y directions, respectively; M_{nx} and M_{ny} are the nominal flexural strengths in the x and y directions (for two-dimensional structures, $M_{ny} = 0$); ϕ_b is the flexural resistance reduction factor ($\phi_b = 0.90$).

For the proposed method, it is essential to transform the constrained optimization problem to an unconstrained one. A detailed review of some constraint-handling approaches is presented in [25]. In this study, a modified penalty function method is utilized for handling the design constraints which is calculated using the following formulas [2]:

$$\begin{aligned} g_i \leq 0 &\implies \Phi_g^{(i)} = 0, \\ g_i > 0 &\implies \Phi_g^{(i)} = g_i. \end{aligned} \quad (5)$$

The objective function that determines the fitness of each particle is defined as

$$\text{Mer}^k = \varepsilon_1 \cdot W^k + \varepsilon_2 \cdot \left(\sum \Phi_g^{(i)} \right)^{\varepsilon_3}, \quad (6)$$

where Mer is the merit function to be minimized; ε_1 , ε_2 , and ε_3 are the coefficients of merit function; $\Phi_g^{(i)}$ denotes the summation of penalties. In this study, ε_1 and ε_2 are set to 1 and W (the weight of structure), respectively, while the value of ε_3 is taken as 0.85 in order to achieve a feasible solution [26]. Before calculating $\Phi_g^{(i)}$, we first determine the weight of the structures generated by the particles, and if it becomes smaller than the so far best solution, then $\Phi_g^{(i)}$ will be calculated; otherwise the structural analysis does not perform. This methodology will decrease the required computational costs, considerably.

3. Canonical Particle Swarm Optimization (PSO)

The PSO algorithm, inspired by social behavior simulation [27, 28], is a population-based optimization algorithm which involves a number of particles that move through the search space, and their positions are updated based on the best positions of individual particles (called x_i^*) and the best of the swarm (called g^*) in each iteration. This matter is shown mathematically as the following equations:

$$v_i^{t+1} = w \cdot v_i^t + \alpha \cdot \text{rand}_1 (x_i^* - x_i^t) + \beta \cdot \text{rand}_2 (g_i^* - x_i^t), \quad (7)$$

$$x_i^{t+1} = x_i^t + v_i^{t+1}, \quad (8)$$

where x_i and v_i represent the current position and the velocity of the i th particle, respectively; rand_1 and rand_2 represent random numbers between 0 and 1; x_i^* is the best position visited by each particle itself; g^* corresponds to the global best position in the swarm up to iteration k ; α and β represent cognitive and social parameters, respectively. According to Kennedy and Eberhart [27], these two constants are set to 2 in order to make the average velocity change coefficient close to one. W is a weighting factor (inertia weight) which controls the trade-off between the global exploration and the local exploitation abilities of the flying particles. A larger inertia weight makes the global exploration easier, while a smaller inertia weight tends to facilitate local exploitation. The inertia weight can be reduced linearly from 0.9 to 0.4 during the optimization process [29].

4. Accelerated Particle Swarm Optimization

The standard PSO uses both the current global best g^* and the individual best x^* . The reason of using the individual best is primarily to increase the diversity in the quality solutions; however, this diversity can be simulated using some randomness. Subsequently, there is no compelling reason for using the individual best, unless the optimization problem of interest is highly nonlinear and multimodal [22].

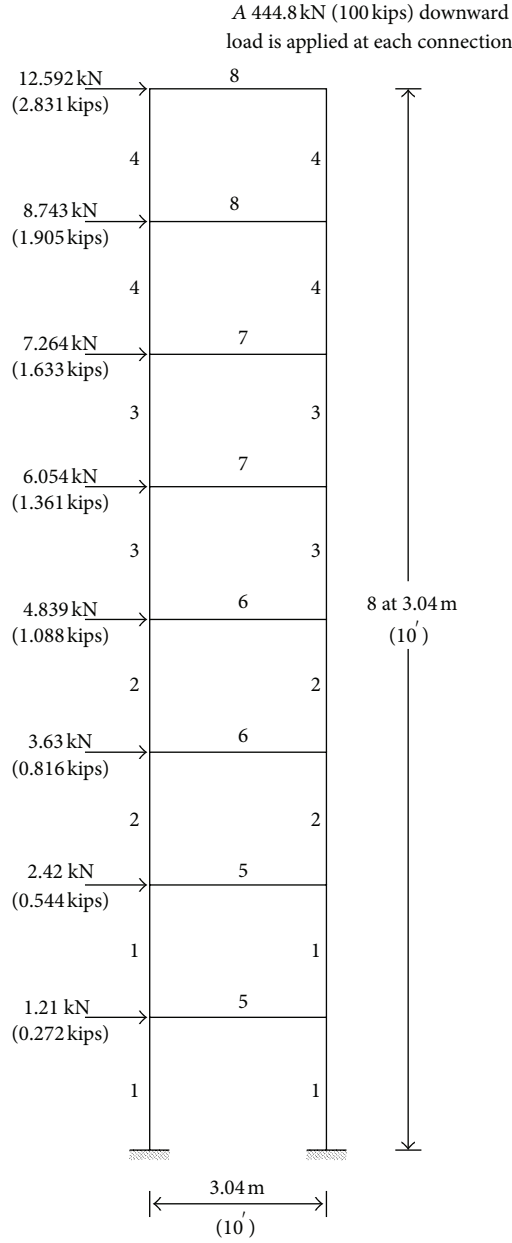


FIGURE 1: Topology of the 1-bay 8-story frame.

A simplified version which could accelerate the convergence of the algorithm is to use the global best only. Thus, in the APSO [22], the velocity vector is generated by a simpler formula as

$$v_i^{t+1} = v_i^t + \alpha \cdot \text{randn}(t) + \beta \cdot (g^* - x_i^t), \quad (9)$$

where randn is drawn from $N(0, 1)$ to replace the second term. The update of the position is simply like (8). In order to increase the convergence even further, we can also write the update of the location in a single step, as

$$x_i^{t+1} = (1 - \beta) x_i^t + \beta g^* + \alpha r. \quad (10)$$

TABLE 1: Optimal design comparison for the 1-bay 8-story frame.

Element group	Optimal W-shaped sections			This study
	GA [31]	ACO [32]	IACO [26]	
1	W18 × 35	W16 × 26	W21 × 44	W21 × 44
2	W18 × 35	W18 × 40	W18 × 35	W16 × 26
3	W18 × 35	W18 × 35	W18 × 35	W14 × 22
4	W18 × 26	W14 × 22	W12 × 22	W12 × 16
5	W18 × 46	W21 × 50	W18 × 40	W18 × 35
6	W16 × 31	W16 × 26	W16 × 26	W18 × 35
7	W16 × 26	W16 × 26	W16 × 26	W18 × 35
8	W12 × 16	W12 × 14	W12 × 14	W16 × 26
Weight (kN)	32.83	31.68	31.05	30.91

TABLE 2: Optimal design comparison for the 3-bay 15-story frame.

Element group	Optimal W-shaped sections			This study
	PSO [18]	HBB-BC [33]	ICA [34]	
1	W33 × 118	W24 × 117	W24 × 117	W27 × 129
2	W33 × 263	W21 × 132	W21 × 147	W21 × 147
3	W24 × 76	W12 × 95	W27 × 84	W16 × 77
4	W36 × 256	W18 × 119	W27 × 114	W27 × 114
5	W21 × 73	W21 × 93	W14 × 74	W14 × 74
6	W18 × 86	W18 × 97	W18 × 86	W30 × 99
7	W18 × 65	W18 × 76	W12 × 96	W12 × 72
8	W21 × 68	W18 × 65	W24 × 68	W12 × 79
9	W18 × 60	W18 × 60	W10 × 39	W8 × 24
10	W18 × 65	W10 × 39	W12 × 40	W14 × 43
11	W21 × 44	W21 × 48	W21 × 44	W21 × 44
Weight (kN)	496.68	434.54	417.46	411.50

This simpler version will give the same order of convergence [30]. Typically, $\alpha = 0.1L-0.5L$, where L is the scale of each variable, while $\beta = 0.2-0.7$ is sufficient for most applications. It is worth pointing out that the velocity does not appear in (10), and there is no need to deal with initialization of velocity vectors. Therefore, the APSO is much simpler. Comparing with many PSO variants, the APSO uses only two parameters, and the mechanism is simple to understand. A further improvement to the accelerated PSO is to reduce the randomness as iterations proceed. This means that we can use a monotonically decreasing function. In our implementation, we use [30]

$$\alpha = 0.7^t, \quad (11)$$

where $t \in [0, t_{\max}]$ and t_{\max} is the maximum number of iterations.

5. Numerical Examples

This section presents the numerical examples to evaluate the capability of the new algorithm in finding the optimal design of the steel structures. The final results are compared to the solutions of other methods to show the efficiency of the present approach. The proposed algorithm is coded in Matlab, and structures are analyzed using the direct stiffness

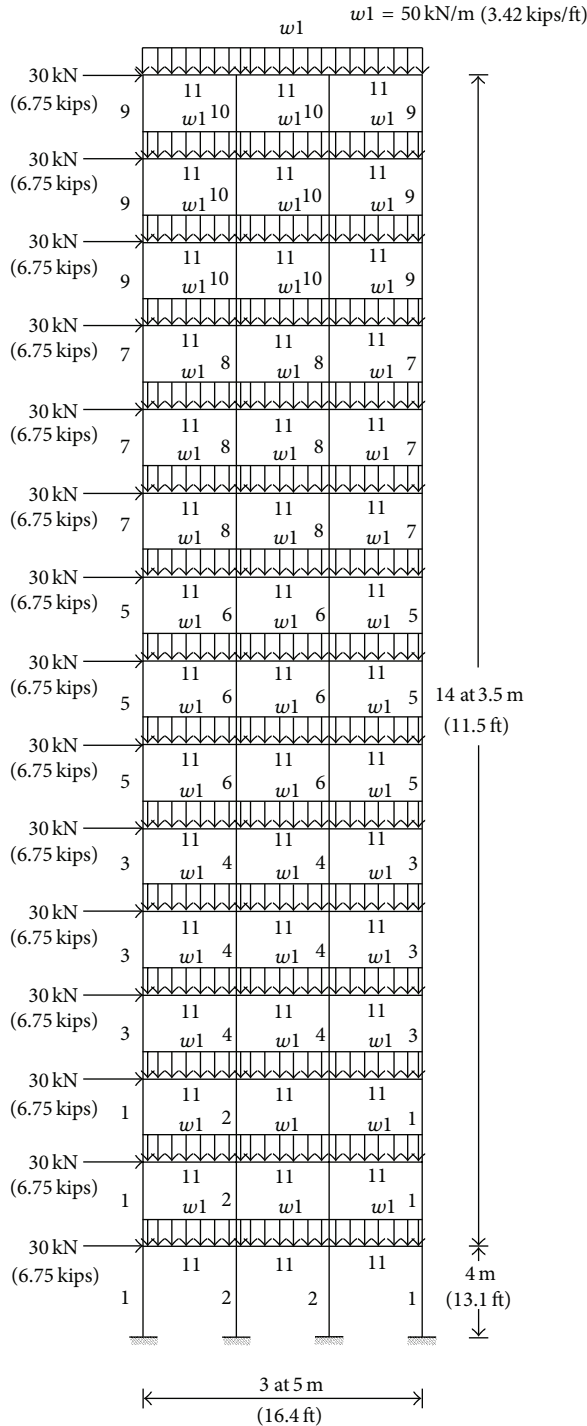


FIGURE 2: Topology of the 3-bay 15-story frame.

method. The steel members used for the design consist of 267 W-shaped sections from the AISC database.

5.1. 1-Bay 8-Story Frame. Figure 1 shows the configuration of the 1-bay 8-story framed structure and applied loads. Several researchers have developed design procedures for this frame; Camp et al. [31] used a genetic algorithm, Kaveh and Shojaei

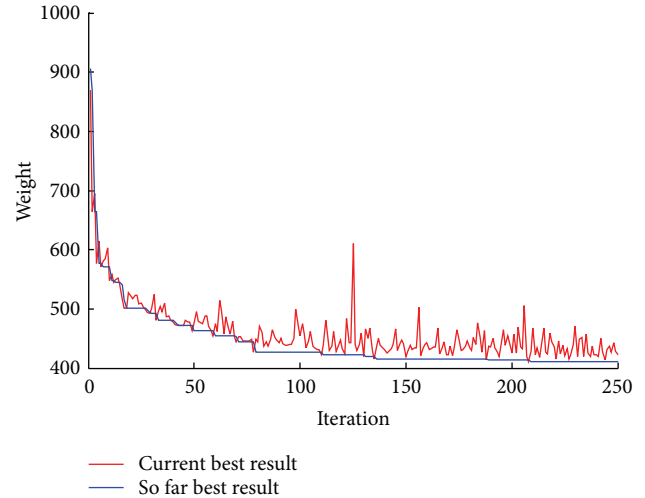


FIGURE 3: The convergence history for the 3-bay 15-story frame.

[32] utilized ACO, and Kaveh and Talatahari [26] applied an improved ACO to solve this problem.

The APSO algorithm found the optimal weight of the one-bay eight-story frame to be 30.91 kN which is the best one compared to the other method. Table 1 lists the optimal values of the eight design variables obtained by this research and compares them with other results.

5.2. Design of a 3-Bay 15-Story Frame. The configuration and applied loads of a 3-bay 15-story frame structure is shown in Figure 2. The sway of the top story is limited to 23.5 cm (9.25 in). The material has a modulus of elasticity equal to $E = 200 \text{ GPa}$ and a yield stress of $F_y = 248.2 \text{ MPa}$.

The effective length factors of the members are calculated as $K_x \geq 0$ for a sway-permitted frame, and the out-of-plane effective length factor is specified as $K_y = 1.0$. Each column is considered as non-braced along its length, and the non-braced length for each beam member is specified as one-fifth of the span length.

The optimum design of the frame obtained by using APSO has the minimum weight of 411.50 kN. The optimum designs for PSO [18], HBB-BC [33], and ICA [34] had the weights of 496.68 kN, 434.54 kN, and 417.46 kN, respectively. Table 2 summarizes the optimal results for these different algorithms. Clearly, it can be seen that the present algorithm can find the better design. Figure 3 provides the convergence history for this example obtained by the APSO.

6. Conclusions

The APSO algorithm, as an improved meta-heuristic algorithm, is developed to solve frame structural optimization problems. Optimization software based on the APSO algorithm was coded in the Matlab using object-oriented technology. A methodology to handle the constraints is also developed in a way that we first determine the weight of the structures generated by the particles, and if they become smaller than the so far best solution, then the structural

analyses are performed. Two test problems were studied using the optimization program to show the efficiency of the algorithm. The comparison of the results of the new algorithm with those of other algorithms shows that the APSO algorithm provides results as good as or better than other algorithms and can be used effectively for solving engineering problems.

References

- [1] A. Kaveh and S. Talatahari, "Optimal design of skeletal structures via the charged system search algorithm," *Structural and Multidisciplinary Optimization*, vol. 41, no. 6, pp. 893–911, 2010.
- [2] A. Kaveh, B. F. Azar, and S. Talatahari, "Ant colony optimization for design of space trusses," *International Journal of Space Structures*, vol. 23, no. 3, pp. 167–181, 2008.
- [3] S. Talatahari, M. Kheirollahi, C. Farahmandpour, and A. H. Gandomi, "Optimum design of truss structures using multi stage particle swarm optimization," *Neural Computing & Applications*, 2012.
- [4] S. Chen, Y. Zheng, C. Cattani, and W. Wang, "Modeling of biological intelligence for SCM system optimization," *Computational and Mathematical Methods in Medicine*, vol. 2012, Article ID 769702, 10 pages, 2012.
- [5] S. Chen, Y. Wang, and C. Cattani, "Key issues in modeling of complex 3D structures from video sequences," *Mathematical Problems in Engineering*, vol. 2012, Article ID 856523, 17 pages, 2012.
- [6] S. Chen, W. Huang, C. Cattani, and G. Altieri, "Traffic dynamics on complex networks: a survey," *Mathematical Problems in Engineering*, vol. 2012, Article ID 732698, 23 pages, 2012.
- [7] F. Kang, J. Li, and Z. Ma, "Rosenbrock artificial bee colony algorithm for accurate global optimization of numerical functions," *Information Sciences*, vol. 181, no. 16, pp. 3508–3531, 2011.
- [8] F. Kang, J. Li, and Z. Ma, "An artificial bee colony algorithm for locating the critical slip surface in slope stability analysis," *Engineering Optimization*, vol. 45, no. 2, pp. 207–223, 2013.
- [9] P. Angeline, "Evolutionary optimization versus particle swarm optimization: philosophy and performance difference," in *Proceedings of the Evolutionary Programming Conference*, San Diego, Calif, USA, 1998.
- [10] Y. Shi and R. C. Eberhart, "Fuzzy adaptive particle swarm optimization," in *Proceedings of the Congress on Evolutionary Computation*, pp. 101–106, May 2001.
- [11] Y. Liu, Z. Qin, Z. Shi, and J. Lu, "Center particle swarm optimization," *Neurocomputing*, vol. 70, no. 4–6, pp. 672–679, 2007.
- [12] M. Xi, J. Sun, and W. Xu, "An improved quantum-behaved particle swarm optimization algorithm with weighted mean best position," *Applied Mathematics and Computation*, vol. 205, no. 2, pp. 751–759, 2008.
- [13] B. Jiao, Z. Lian, and X. S. Gu, "A dynamic inertia weight particle swarm optimization algorithm," *Chaos, Solitons and Fractals*, vol. 37, no. 3, pp. 698–705, 2008.
- [14] X. Yang, J. Yuan, J. Yuan, and H. Mao, "A modified particle swarm optimizer with dynamic adaptation," *Applied Mathematics and Computation*, vol. 189, no. 2, pp. 1205–1213, 2007.
- [15] A. Kaveh and S. Talatahari, "A particle swarm ant colony optimization for truss structures with discrete variables," *Journal of Constructional Steel Research*, vol. 65, no. 8–9, pp. 1558–1568, 2009.
- [16] A. Kaveh and S. Talatahari, "Particle swarm optimizer, ant colony strategy and harmony search scheme hybridized for optimization of truss structures," *Computers and Structures*, vol. 87, no. 5–6, pp. 267–283, 2009.
- [17] P. C. Fourie and A. A. Groenwold, "The particle swarm optimization algorithm in size and shape optimization," *Structural and Multidisciplinary Optimization*, vol. 23, no. 4, pp. 259–267, 2002.
- [18] A. Kaveh and S. Talatahari, "Hybrid algorithm of harmony search, particle swarm and ant colony for structural design optimization," in *Studies in Computational Intelligence*, vol. 239, pp. 159–198, Springer, Berlin, Heidelberg, 2009.
- [19] A. Hadidi, A. Kaveh, B. Farahnadazar, S. Talatahari, and C. Farahmandpour, "An efficient hybrid algorithm based on particle swarm and simulated annealing for optimal design of space trusses," *International Journal of Optimization in Civil Engineering*, vol. 1, no. 3, pp. 377–395, 2011.
- [20] J. F. Schutte and A. A. Groenwold, "Sizing design of truss structures using particle swarms," *Structural and Multidisciplinary Optimization*, vol. 25, no. 4, pp. 261–269, 2003.
- [21] F. Kang, J. Li, and Q. Xu, "Damage detection based on improved particle swarm optimization using vibration data," *Applied Soft Computing*, vol. 12, no. 8, pp. 2329–2335, 2012.
- [22] X. S. Yang, *Nature-Inspired Metaheuristic Algorithms*, Luniver Press, 2nd edition, 2010.
- [23] A. Kaveh and S. Talatahari, "Charged system search for optimal design of frame structures," *Applied Soft Computing*, vol. 12, no. 1, pp. 382–393, 2012.
- [24] American Institute of Steel Construction (AISC), *Manual of Steel Construction Load Resistance Factor Design*, AISC, Chicago, Ill, USA, 3rd edition, 2001.
- [25] C. A. C. Coello, "Theoretical and numerical constraint-handling techniques used with evolutionary algorithms: a survey of the state of the art," *Computer Methods in Applied Mechanics and Engineering*, vol. 191, no. 11–12, pp. 1245–1287, 2002.
- [26] A. Kaveh and S. Talatahari, "An improved ant colony optimization for the design of planar steel frames," *Engineering Structures*, vol. 32, no. 3, pp. 864–873, 2010.
- [27] J. Kennedy and R. C. Eberhart, "Particle swarm optimization," in *Proceedings of the IEEE International Conference on Neural Networks*, vol. 4, pp. 1942–1948, December 1995.
- [28] R. C. Eberhart and J. Kennedy, "A new optimizer using particle swarm theory," in *Proceedings of the 6th International Symposium on Micro Machine and Human Science*, pp. 39–43, Nagoya, Japan, October 1995.
- [29] R. C. Eberhart and Y. Shi, "Comparing inertia weights and constriction factors in particle swarm optimization," in *Proceedings of the Congress on Evolutionary Computation (CEC '00)*, pp. 84–88, July 2000.
- [30] A. H. Gandomi, G. J. Yun, X. S. Yang, and S. Talatahari, "Combination of chaos and accelerated particle swarm optimization," *Communications in Nonlinear Science and Numerical Simulations*, vol. 18, pp. 327–340, 2013.
- [31] C. V. Camp, S. Pezeshk, and G. Cao, "Optimized design of two-dimensional structures using a genetic algorithm," *Journal of Structural Engineering*, vol. 124, no. 5, pp. 551–559, 1998.
- [32] A. Kaveh and S. Shojaei, "Optimal design of skeletal structures using ant colony optimization," *International Journal for Numerical Methods in Engineering*, vol. 70, no. 5, pp. 563–581, 2007.
- [33] A. Kaveh and S. Talatahari, "A discrete Big Bang—Big Crunch algorithm for optimal design of skeletal structures," *Asian Journal of Civil Engineering*, vol. 11, no. 1, pp. 103–122, 2010.

- [34] A. Kaveh and S. Talatahari, "Optimum design of skeletal structures using imperialist competitive algorithm," *Computers and Structures*, vol. 88, no. 21-22, pp. 1220–1229, 2010.

Research Article

E-Block: A Tangible Programming Tool with Graphical Blocks

Danli Wang,¹ Yang Zhang,¹ and Shengyong Chen²

¹ Institute of Software, Chinese Academy of Sciences, Beijing 100190, China

² College of Computer Science, Zhejiang University of Technology, Hangzhou 310023, China

Correspondence should be addressed to Danli Wang; danli@iscas.ac.cn

Received 27 November 2012; Accepted 5 January 2013

Academic Editor: Fei Kang

Copyright © 2013 Danli Wang et al. This is an open access article distributed under the Creative Commons Attribution License, which permits unrestricted use, distribution, and reproduction in any medium, provided the original work is properly cited.

This paper designs a tangible programming tool, E-Block, for children aged 5 to 9 to experience the preliminary understanding of programming by building blocks. With embedded artificial intelligence, the tool defines the programming blocks with the sensors as the input and enables children to write programs to complete the tasks in the computer. The symbol on the programming block's surface is used to help children understanding the function of each block. The sequence information is transferred to computer by microcomputers and then translated into semantic information. The system applies wireless and infrared technologies and provides user with feedbacks on both screen and programming blocks. Preliminary user studies using observation and user interview methods are shown for E-Block's prototype. The test results prove that E-Block is attractive to children and easy to learn and use. The project also highlights potential advantages of using single chip microcomputer (SCM) technology to develop tangible programming tools for children.

1. Introduction

Papert and Resnick et al. mentioned in their contributions that learning how to program may result in changes to the ways people think [1, 2]. Early studies with Logo also showed that when introduced in a structured way, computer programming can help children improve visual memories and basic numbers senses as well as develop problem-solving techniques and language skills [3]. However, most of the existing programming languages are designed for professionals and are based on texts and symbols which are difficult for children to understand [4, 5]. Hence, previous research works are conducted aiming at lowering the barrier of programming for children [6].

Graphical programming has some significant advantages over textual programming especially in providing visual cues for young programmers [7, 8]. However, the usage of keyboard and mouse which are major input methods in GUI may be difficult for children [9, 10]. What is more is GUI's nature drawback that it falls short of embracing the richness of human's interaction with physical world [11]. This kind of activities contribute to children's learning [12].

Artificial intelligence with tangible programming is kind of feasible programming method for children [13]. Tangible interaction can stimulate multiple senses of children and develop their cognitive abilities [14]. In addition, compared with directly operating computers, using physical objects to interact with computer is much easier to involve children in the process [15]. Instead of using lines of dull codes, the program becomes a collection of physical objects. Children can write programs by assembling the physical objects without keystrokes [16]. Thus, the programming could be more intuitive to children.

Based on our previous work—T-maze [17], this paper proposes a tangible programming tool: E-Block, which is designed for children aged 5 to 9. It defines the programming blocks and the sensors as the input and enables children to write programs to complete the tasks in the computer as Figure 1 shows. The symbol on the programming block's surface is used to help children understand the function of each block. The sequence information is transferred to computer by microcomputers and then translated into semantic information. In E-Block, children need first to find a path for the character to escape the maze in programming stage and



FIGURE 1: Children with E-Block.

then run the program and trigger sensors when necessary in running stage. In programming stage, when children add a new block into sequence, feedbacks on the screen and block itself will show whether it is placed correctly. Only when it's right, the children can continue programming. After finishing the programming, children could run the program by pressing the start button and enter the running stage. In running stage the character will stop if hits the sensor cells. Children should trigger relative sensors to keep the character going.

2. Related Work

One of the earliest tangible programming projects is AlgoBlock [18]. It adopts several blocks as the interaction medium. Every block has special semantics. Children could write their own program to play a marine game by connecting the objects. RoboTable2 [19] connects tangible programming and graphical programming together on an interactive table which combines several technologies such as camera, projector, computer vision, and blue tooth. It supports the novice to manipulate robots by gestures [17], TUI, and GUI. The whole system is based on the event model by which user needs to define events to trigger certain behavior on the robot. Though the concept of programming in the above works is easy to understand, there still exist some improvements that could be done to the manipulations. The wires between blocks might limit children's activities. Moreover, some complicated scenarios are not suitable for young children.

Tangible programming bricks [20] proposed by MIT with PIC microprocessor built in each physical programming brick communicate with the computer by using a card slot. Children put the bricks into the card slot in different sequences to control the game objects like toy trains and household appliances. This work is highly functional, containing a lot of different programming concepts. TurTan [21] is a desktop tangible programming system designed for Turtle Geometry, which is based on Logo. It adds multitouch and gesture recognition into the system. It uses a camera to capture and recognize the real-time position of fingers and objects on the desktop. Then the projector outputs the real-time feedback of the system. Users can control the entire drawing process by manipulating predefined commands in

a tangible user interface on the table. The above works require scientific knowledge or contain other concept in the defined commands which might be hard for young children to understand.

Electronic Block [22, 23] uses building blocks to program. It consists of three types of building blocks: sensor block as input, logic block to conduct logic computation, and behavior block as output. It is designed for the preschoolers so that the syntax is simple, easy to manipulate, and free from spatial limitation [24, 25]. Schweikardt and Gross [26] proposes a tangible programming language named roBlock. A processor is installed in each block. The blocks are divided into 4 categories according to their functions: sensor, actuator, logic, and utility. Users can build their own robots by connecting different blocks. Its working principle is quite similar to Electronic Block, so they are all highly functional. Tern [27, 28] is another tangible programming language given by Horn and Jacob and so forth. The programming blocks are made of wooden blocks and every block has specific semantics. Children assemble the blocks to express certain meanings. After writing program with the blocks, children need to manually use camera to capture the block sequence's image that is transferred to computer to identify the information and control virtual roles or real walking robot. Though, the above programming tools are easy to manipulate; however, they fail to support real-time debug and thus offer little help on the programming debug. Once errors are detected, the systems depend on children's own understanding about the task to correct them, which makes programming difficult for beginners.

Based on these previous contributions, we want to develop a system which has the following characteristics. When a child is programming, the system is highly synchronous to the child's latest manipulation. Children are able to place the program blocks with no space limitation. Different kinds of feedbacks will appear on both the computer screen and the tangible programming tools, making benefits for children to position and analyze accurately.

3. Implementation

E-Block was proposed to solve problems in our previous system T-Maze which is based on computer vision technology [29]. In our user study, children were asked to use two systems in order to find the potential advantages of using single chip microcomputer (SCM) technology to develop tangible programming tools of children. Therefore it is needed to briefly describe how T-Maze functions.

3.1. T-Maze System. T-Maze is composed of maze game, programming wooden blocks, camera, and sensor input devices. The maze escaping game, which is the same with the one of E-Block, requires children to control the virtual character in maze to go through relative sensor cells and finally reach the exit of the maze. Children manipulate different wooden blocks to write their own program, which can control the character's moving in the maze. The tool uses a camera to catch the image of the wooden blocks which can be used to

analyze the semantics of children's program. Several problems were found in the T-Maze. First, children are required to program within an area of 25 cm * 30 cm. The programs out of this identification area of cameras could not be captured, which results in children's confusion. Second, the system is based on computer vision which has its inborn drawbacks—camera occlusion. During the test of T-Maze, children could not help raising their hands, blocking between cameras and programs. This caused the delay problem of feedback. Third, feedback is totally shown on screen. Children have to switch attentions between screen and blocks in order to debug. Figure 2 shows T-Maze system.

3.2. E-Block System. E-Block is composed of four parts: the maze game, the programming blocks, the wireless box, and the sensors (see Figure 3). We will introduce each part next.

3.2.1. Maze Game. The virtual maze is composed of four kinds of cells (see Figure 4): start cell, end cell, normal cell, and sensor cell. There is a face on the top left corner of screen to show the real-time feedback. In the programming stage, the character starts from the start cell and children can place the direction block and the sensor block to indicate a path from start cell to end cell. In the running process, the character starts to walk and children have to trigger the relative sensor when the character is stopped by the sensor cell. The rules of this game are listed as follows.

- R1: If input is Direction Top Right and the upper right cell of the current location of character is feasible, then give smiley face, green arrow on the screen and blue LED on block.
- R2: If input is Direction Top Right and the upper right cell of the current location of character is not feasible, then give sad face on screen and red LED on blocks.
- R3: If input is Direction Top Left and the upper left cell of the current location of character is feasible, then give smiley face, green arrow on the screen and blue LED on blocks.
- R4: If input is Direction Top Left and the upper left cell of the current location of character is not feasible, then give sad face on screen and red LED on blocks.
- R5: If input is Direction Bottom Right and the lower right cell of the current location of character is feasible, then give smiley face, green arrow on the screen and blue LED on blocks.
- R6: If input is Direction Bottom Right and the lower right cell of the current location of character is not feasible, then give sad face on screen and red LED on blocks.
- R7: If input is Direction Bottom Left and the lower left cell of the current location of character is feasible, then give smiley face, green arrow on the screen and blue LED on blocks.
- R8: If input is Direction Bottom Left and the lower left cell of the current location of character is not feasible, then give sad face on screen and red LED on blocks.



FIGURE 2: T-Maze system.

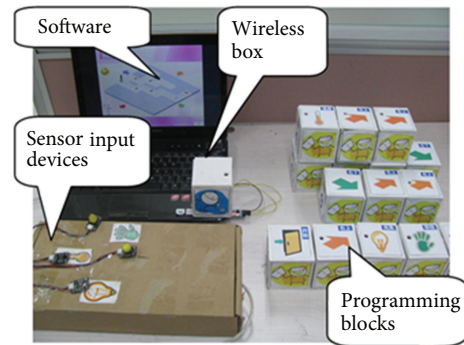


FIGURE 3: E-Block tool.

- R9: If input is Tangible Button and there exist Tangible Button cell nearby, then give smiley face, green arrow on the screen and blue LED on blocks.
- R10: If input is Tangible Button and there is no Tangible Button cell nearby, then give sad face on screen and red LED on blocks.
- R11: If input is Light Sensor and there exist Light Sensor cell nearby, then give smiley face, green arrow on the screen and blue LED on blocks.
- R12: If input is Light Sensor and there is no Light Sensor cell nearby, then give sad face on screen and red LED on blocks.
- R13: If input is Temperature Sensor and there exist Temperature Sensor cell nearby, then give smiley face, green arrow on the screen and blue LED on blocks.
- R14: If input is Temperature Sensor and there is no Temperature Sensor cell nearby, then give sad face on screen and red LED on blocks.

3.2.2. Programming Blocks. Programming blocks send computer their physical information which is then translated into the program semantics. In E-Blocks, there are four kinds of

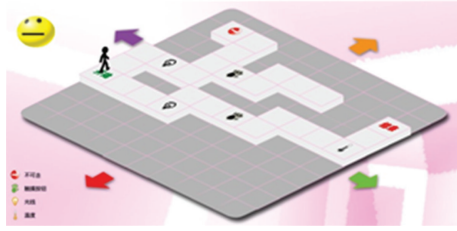


FIGURE 4: Maze game.

programming blocks: start block, end block, direction block, and sensor block (see Figure 5). As Figure 6 shows, each block has a single chip microcomputer, an infrared transmitter and receiver module, a cell battery module, a wireless module, and an LED. When a new block is added to the array, the former block's infrared signal will activate the new added one. The new added block will send its identity code to wireless box which is connected to PC through USB port. At the same time, it will open its own infrared transmitter. Wireless box will get the physical information from the content and the order of the identity codes received and will then send this information to PC.

(1) *Infrared Transmitter and Receiver Module.* The adjacent programming blocks transmit data through infrared transmitter and receiver module (VS0038). The former block's infrared signal activates the latter one. After activated, a block will send its identity code to computer by wireless module; at the same time, it will open its infrared transmitter and wait to activate next added block. Computer will get the sequence information from the identity code received. We use Pulse Width Modulation (PWM) to encode the identity code. Similar technology is used in the television remote control.

(2) *Wireless Module.* The computer communicates with the programming blocks through wireless module. After activated, a block will send identity code to computer by wireless module. Computer will get the sequence of blocks by adding the new identity code to the end of sequence. In the same way, computer will remove the identity code from sequence if the block is removed. If the new added block is not correct, the wireless module will receive a signal from computer and notice the red LED to flash.

(3) *LED Module.* In the maze map, the gray cells are not reachable. If the child manipulates the character to the unreachable cell, or if the child places a direction block in the sensor cell instead of a sensor block, it will generate an error. If the new added block fits the cell, the blue LED of the block will start to light to distinguish it from the unattached blocks. If the computer finds errors in the programming sequence, the smile face on the screen will turn sad. After that, the computer will find the location of the problematic block and then send a signal to the wireless module of the problematic programming block. As a result, the red LED of the block starts to light to indicate potential error. In this case, children can find the problematic block easily and then try to solve the

problem. LED module is on the upper surface of the block so that users can notice it easily as soon as it starts to flash.

(4) *Wireless Box.* Wireless box is connected to PC through USB port. It will send a request to the programming blocks in turn and wait for their responses. If the wireless box does not receive anything, it means that the programming block is not in the sequence. On the contrary, if the block is added to the sequence, it will send to wireless box its own code. The wireless box will then send the information to PC via USB port. When PC finds some errors in the programming block sequence, it will send a signal to the relative block which will cause the LED to flash.

3.2.3. *Sensor Input Devices.* Sensor input devices have two functions. Firstly, when children finish programming, they need to press the start button on the sensor input devices to change the programming stage into the running stage. Secondly, in running stage, when the character meets the sensor cell, children need to trigger the relative sensor to keep it going. There are three kinds of sensors as Figure 7 shows: Temperature Sensor, Light Sensor, and Tangible Button Sensor. Each sensor has its own way of being triggered: Temperature Sensor needs to be warmed, Light Sensor shaded, and Tangible Button Sensor pressed. We provide sensor input part because it corresponds to the input part of the program's operation, and at the same time, increases the interests of children and adds more elements to the system.

3.2.4. System Advantages

(1) *Fast-Real Time Presentation on PC.* Fast real time presentation indicates that it needs about 0.1-0.2 s to change one or more program blocks (produce one or a group of new orders) to PC recognition and finally to the disposal of this group of orders. With the questionnaire, we found that when finishing the placement of a new program block, children would pay attention to the change in the computer screen. In the previous T-Maze experiment, a large number of children responded that the computer processing speed on the program block change was too slow, which resulted in their confusions about the feedback of their manipulations. E-Block solved the problem by the adoption of infrared and wireless technologies.

(2) *Fixable and Free Placed Position of Program Block.* The effective identification area of E-Block program block is very large. In a range of 4-5 meters, it can effectively and rapidly recognize the program block. When placing the program block, it does not need to be operated in the fixed range of the camera. Children can randomly place blocks in their own favorite positions. At the same time, as long as they are not changing the order, they could move the well-placed blocks to anywhere.

(3) *Feedback Appeared in Both Blocks and PC Screen.* This function contributes to children's debug of program and leads the children to focus on the task and operation, rather than staring at the smiling face in the upper-left corner of the

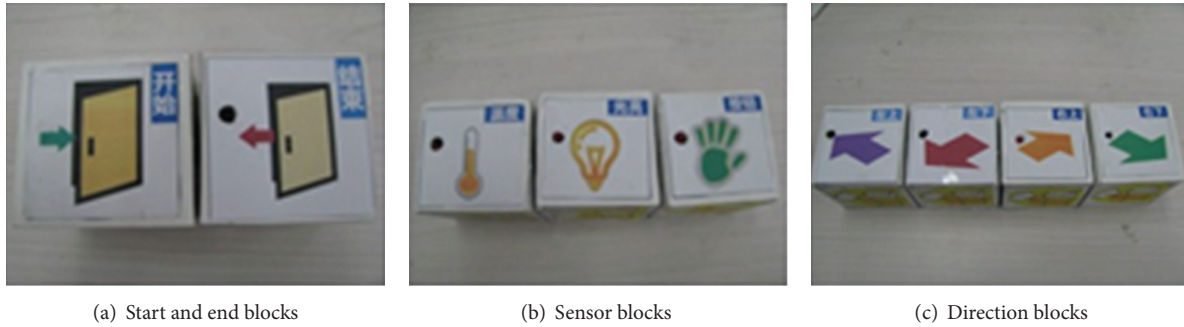


FIGURE 5: Tangible Blocks.

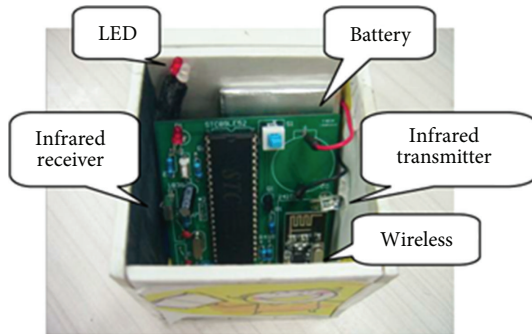


FIGURE 6: Single chip microcomputer in E-Block.



FIGURE 7: Sensor input devices.

screen. This feedback mechanism can also act as a trial to the manipulation of information mutualization. Children can place the manipulation to programming, and at the same time the operation result of the program will be shown in the tangibles.

(4) *The Role of Sensor.* The sensor has the following several effects: correspond to the input part of the operation section in the actual programming, while increasing the interest of children, adding more abundant element for the system. In our tradition programming method, there will be some statements (such as “printf” function in C language) to receive some orders from the keyboard or mouse in the program operation. After the program is operated, we can input the orders or data with these external devices to keep the program operating. So is the role of sensor. At the same time, the sensors can make the system more attractive for children. In the test process, many children showed great

interest in the Pressure Sensor and Temperature Sensor devices. The sensors raised children’s degree of participation in the running stage of their programs.

4. Use Case

In E-Block, children need first to find a path for the character to escape the maze in programming stage and then run the program and trigger sensors when necessary in running stage. In this part, a simple use case will be described.

4.1. Programming Stage. After successfully choosing a mission, children will start the programming stage. Children must place the start block as the start of the block sequence. Then they need to put the proper direction block into the block sequence which indicates the direction user wants the character to go. When programming the path of the character, children need to place the right sensor block to go on the path when the path hits any sensor cells. If children place wrong programming block in the sequence the smile face on the screen will turn sad. In the meanwhile, the LED in the problematic block turns red so that user can easily find which block is wrong (see Figure 8).

4.2. Running Stage. When children finish the task in programming stage, they need to press the start button on the sensor input devices to turn the E-Block into running stage. And the character will start walking according to the path programmed before. When the character encounters a sensor cell, it will stop until children trigger the relative sensor (see Figure 9).

5. User Study

The user study is a comparison test between E-Block with the former work, T-Maze, which uses computer vision technology to realize the recognition of blocks. It talks about the advantages and disadvantages of SCM-version tangible programming tool, E-Block, compared with the camera-version tool T-Maze.

5.1. Procedure. We ran the user study with a total of 11 children (3 boys and 8 girls) aged 5 to 9. They were asked



FIGURE 8: A simple case of usage.



FIGURE 9: Trigger the relative sensor.

to complete three levels of tasks that need 7, 11, and 12 programming blocks, respectively. The maze-escaping tasks in T-Maze and E-Block were basically the same. The only difference was the blocks they used in the test; T-Maze used computer vision technology and the block was smaller (about 3 cm * 3 cm * 3 cm) with no feedback providing function itself, while blocks of E-Block had LED as feedback and were bigger (about 7 cm * 7 cm * 7 cm). One researcher was available to support children. The study included three stages: explanation and demonstration stage, test stage, and interview stage.

The first stage: explanation and demonstration. We first introduced the composition of T-Maze and E-Block and how to use them. After that, a detailed demonstration video was played together with a real demonstration.

The second stage: test. Children were randomly divided into two groups: 5 children played T-Maze first and then played E-Block. The rest played in the adverse way. We videotaped the whole test process.

The third stage: interview. Once the children completed both T-Maze and E-Block tasks, they were asked to finish a questionnaire and then interviewed individually to gauge their perception on their play experience.

5.2. Coding. Based on the information that we got from interview and tapes, we focused our research on the following aspects: first, whether the tool is easy for children in learning and manipulation; second, what merits are brought by the SCM-version tangible programming tool, E-Block, compared with the camera-version tool, T-Maze, and how these merits influence children's learning and manipulations. For the

TABLE 1: Coding scheme for behaviors.

Behavior type	Example
Space-related behavior	Move the out-of-boundary programming blocks back to the recognition region
Feedback-related behavior	Look at screen/LED immediately after an addition of a block
Occlusion-related behavior	Put hand between camera and blocks
Programming operation	Add/remove a block to/from sequence of programming blocks

TABLE 2: Coding scheme for utterances.

Utterance type	Example
Space-related talk	You should keep unused blocks out of the recognition region
Feedback-related talk	Look, the smiling face turns sad; do you notice, the LED is flashing?
Occlusion-related talk	Remember, you should add a block like this; don't put your hand over blocks
Other talk	That's so cool!; I need a green block

11 children being videotaped, we transfer their manipulations together with researcher's guidance manipulations into behaviors and transfer their conversations into utterances.

Because the running state of T-Maze and E-Block is exactly the same, we only use codes to analyze programming state in order to find the differences between them. A total of 300 minutes (132 minutes of T-Maze and 168 minutes of E-Block) were reviewed and annotated by two researchers. Codes were used for analysis if they occurred or not within every five-second interval. Videos were coded into one of four categories: *space-related behavior*, *occlusion-related behavior*, *feedback-related behavior*, or *programming operation*, the numbers of which are shown in Figure 10. Accordingly, we also coded all the utterances consisting of continuous talk without long pauses into one of four categories: *space-related talk*, *occlusion-related talk*, *feedback-related talk*, or *other talk*, the numbers of which are shown in Figure 11. The full set of codes is shown in Tables 1 and 2. In total, we coded 1106 behaviors and 151 utterances in T-Maze: an average of 33.5 behaviors (SD = 11.24) and 4.58 utterances (SD = 2.08) per task. In E-Block, the numbers are 773 behaviors and 98 utterances in total. 23.4 behaviors (SD = 4.36) and 2.97 utterances (SD = 1.08) per task. We obtained almost perfect

agreements for data of behaviors and 90% agreements for data of utterances based on 100% of the data ($Kappa = 1$ and 0.87 resp.). We defined space-related and occlusion-related behaviors and utterances to have negative influence on programming because they were to solve the problem caused by hardware and did not contribute to program. We hope E-Block can better focus children on programming by reducing such behaviors and utterances. The questionnaire in interview section was a Likert-type scale composed of four questions with punctuation from one to five, one being the minimum and five the maximum score. We analyze the results of video and interview in the following section.

5.3. Results. In this section, we first prove E-Block to be easy for children in learning and manipulation and then start to compare E-Block with T-Maze. The major difference between E-Block and T-Maze is that E-Block enables children to place the block without considering the camera's view scope and occlusion problem. Spatial constraints, occlusion problem, feedback, and programming operation are used as comparison points. They are represented by behaviors and utterances, respectively. We discuss the totals, averages, and proportions for all behaviors and utterances in the programming stage, which leads to a preliminary comparison between tangible programming tools using computer vision technology and single chip microcomputer. We hope this comparison may provide references for future design.

5.3.1. General Results. According to the observation and the questionnaires we collected in the test, we find that every child in our test showed great interest in E-Block. Many children were interested in the sensor and asked us "what is this? How to use it?" Once they saw the character escaping the maze, some said: "Well done!" In the questionnaire, when asked how much they like the game (like very much, like, normal, dislike, dislike very much), 6 children said they liked it very much, 3 selected "like" and 2 selected "normal". When being asked which part they liked most, some children said that they liked triggering the sensor and some said that they are fond of placing the block and manipulating the character to escape the maze. According to the observation, we found that all the children could master the tangible programming block tool quickly. Although some younger children could not place all the blocks in the right order for the first time, we find they were able to adjust the blocks according to the real-time feedback on the screen or the feedback on the block.

5.3.2. Spatial Constraints. In E-Block, children would not need to worry about whether the block is within the range of the camera because they can place them anywhere as long as wireless box can receive wireless signal from wireless module in each block. This distance is about 15 meters from a limit test of E-Block while the programming space of T-Maze is only $25\text{ cm} \times 30\text{ cm}$. As defined in Table 1, the average number of space-related behaviors is 3.33 ($SD = 1.05$) per task in T-Maze and 2 ($SD = 0.94$) in E-Block. As defined in Table 2 the average number of space-related utterances is 1.67 ($SD = 0.58$) per task in T-Maze and 0.27 ($SD = 0.46$) in

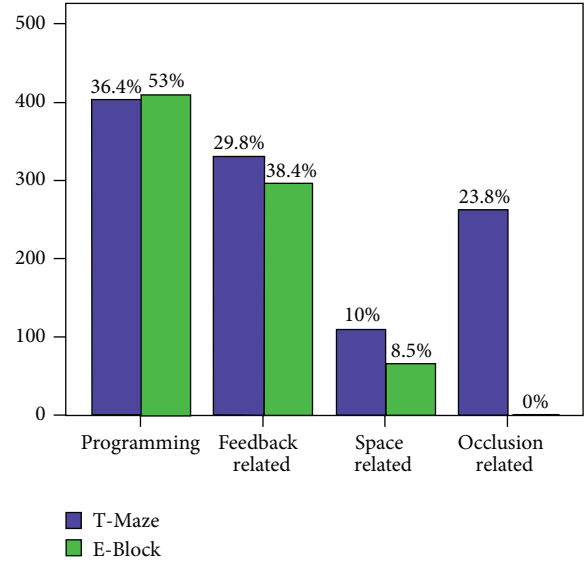


FIGURE 10: Number of behaviors by category type.

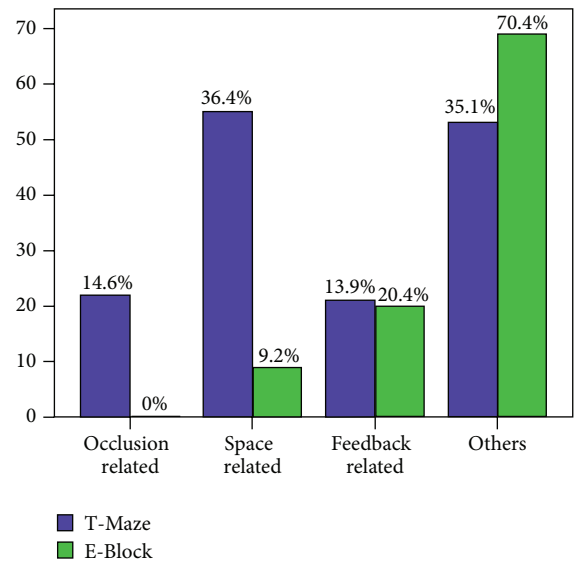


FIGURE 11: Number of utterances by category type.

E-Block. Figures 10 and 11 demonstrate that such behaviors and utterances reduced significantly in E-Block; however, large size of the programming block also caused some space-related behaviors and utterances. Children had to push the existing block sequence to keep it from going out of desktop. Therefore, we deduce that if the programming blocks in E-Block had had the same size of those in T-Maze, space-related behaviors and utterances would have appeared even fewer. The recognition area of camera-version programming tool is influenced by the performance of camera to a great extent; however, the wireless technology of SCM enables children to manipulate in much larger area.

5.3.3. Occlusion Problem. In E-Block, children had no needs to worry about whether they may block the camera. The

average number of occlusion-related behavior is 7.97 ($SD = 2.33$) per task in T-Maze and 0 ($SD = 0$) in E-Block. The average number of occlusion-related utterance is 0.67 ($SD = 0.58$) per task in T-Maze and 0 ($SD = 0$) in E-Block. When playing T-Maze, even being told that they shall not put their hands on the block, children still did it unconsciously. Such occlusion-related behaviors might cause the inaccurate feedback. When children saw the result on the screen being different from what they expected, they were confused and even changed the right program. Some of them asked in T-Maze: "Why cannot I just tell the computer what I have placed?" Such problem disappeared in test of E-Block for the different way of block recognition. In this case, the occlusion problem of camera-version programming tool is solved by SCM technology [25].

5.3.4. Feedback. In T-Maze the only feedback is the smiling/sad face on the top left corner of screen. While in E-Block, besides that feedback, the LED on wrong programming block in the sequence will also start to flash if a programming error is detected. The total number of feedback-related behaviors and utterances is close to the number of programming operations. We found that in most cases, children would look for feedback after a programming operation unless they were very confident. The average number of feedback-related behaviors is 10 ($SD = 1.27$) per task in T-Maze and 9 ($SD = 1.03$) in E-Block. The average number of feedback-related utterances is 0.64 ($SD = 0.58$) per task in T-Maze and 0.61 ($SD = 0.55$) in E-Block. The numbers of such behavior and utterance in E-Block differed slightly from that of T-Maze; however, from the collected questionnaire, 9 children said that the feedback on block helped them to find the wrong block much more quickly and accurately compared with that in T-Maze. Only 2 boys did not pay much attention to the block's feedback, because they learned E-Block in the shortest time and always placed the right block. This feedback mechanism can also act as a trial to realize information mutualization between children and the physical objects they manipulate. It can be easily realized by SCM-version programming tool thanks to the inner circuit of each block.

6. Discussion

Figure 10 shows that children devoted a much larger portion of their total behaviors to programming in E-Block (53.0% compared with 36.4%). In addition, Figure 11 shows that the utterances concerning spatial constraint and occlusion problem in E-Block were much fewer than those in T-Maze (9.2% compared with 51.0%). In E-Block, children had fewer behaviors and utterances irrelevant to programming, by which we conclude that E-Block enables children to better focus on programming rather than solving the problem caused by camera. The questionnaires further support our conclusion that 5 out of 11 children said that spatial constraint made it difficult for them to program and 9 out of 11 children said T-Maze is unstable which we attribute to the occlusion

problem. After the user study, we found two problems: (a) recognition speed has a crucial influence on children's learning of E-Block, and (b) feedback should be properly designed for children's attentions.

6.1. Recognition Speed. In the user study, a large number of tested children responded that T-Maze is too slow (about 3 seconds to react). They doubted whether their programs are right and can function because of the delay. Such problem, though few, also appeared in the first version of E-Block. The improved E-Block better solved the delay problem by reprogramming each block and changing the communication method between master SCM (in wireless box) and servant SCM (in each programming block). The limit test showed the improved E-Block reacted to the change of block sequence within 0.3 second.

6.2. Feedback. Flashing of LED was inconspicuous based on our user study. Therefore, we reprogrammed and added blue and red LEDs to each block. After the user study, we invited 5 children playing the same tasks as in the user study. We focused on how the improved E-Block solved the problems above and how the improvement influenced children's programming performances.

We video-recorded the programming stage and counted the number of each kind of behaviors and utterances just like the user study. The feedback-related behaviors and utterances were further divided into *feedback on block related* and *feedback on screen related*. The data shows that when playing with improved E-Block, children had a higher proportion of behaviors and utterances related to the feedbacks on block rather than on screen (64% and 72% compared with 43% and 47%, resp.). The user study demonstrated that the improved E-Block reacted faster and provided conspicuous feedback.

7. Conclusion and Future Work

This paper's contribution could be summarized into the following points. Firstly, it presents a programming tool which enables children to write programs by placing wooden blocks. Secondly, it provides a new map method between the block's function and the program semantics. Thirdly, the system offers help on debug by giving feedbacks on both screen and the programming blocks, which effectively helps children to learn programming. We conducted the user experiments on this programming tool. The user study is designed to compare E-Block with the former work: T-Maze. The comparison leads to a further discussion between SCM-version programming tool and camera-version tool. The result shows that E-Block is not only interesting to children but also easy to learn and use. Compared with T-Maze, E-Block better focuses children on programming because of the high proportion of programming operations and low proportion of space-related and occlusion-related utterances. The conclusion is also supported by the result of the interview.

In the future, we intend to design more programming blocks and add more scenarios into this tool to introduce more programming concepts. Feedback on physical object

itself is a great source of inspiration for future work. Future work will mainly focus on getting rid of the computer screen. Children can place the blocks to programming and the operation's result of the program will be shown on the blocks themselves.

Acknowledgments

This research is supported by the National Natural Science Foundation of China under Grants nos. 60970090 and 61272325, the Major State Basic Research Development Program of China (973 Program) under Grant no. 2013CB328805, the Frontier Project of the Knowledge Innovation of Chinese Academy of Sciences under Grant no. ISCAS 2009-QY03, the Cooperation Projects of Guangdong Province and Chinese Academy of Sciences under Grant no. 2011B090300086, and the Cooperation Projects of Chinese Academy of Sciences and Foshan city under Grant No. 2012YS04. The authors would like to acknowledge the support of Tianyuan Gu, Cheng Zhang, Liang He, Tingting Wang, Li Shen, and Muyan Li. We thank the teachers and students in Kindergarten of Chinese Academy of Sciences for their cooperation.

References

- [1] S. Papert, *Mindstorms: Children, Computers, and Powerful Ideas*, Basic Books, New York, NY, USA, 1993.
- [2] M. Resnick, F. Martin, R. Sargent, and B. Silverman, "Programmable bricks: toys to think with," *IBM Systems Journal*, vol. 35, no. 3-4, pp. 443-452, 1996.
- [3] D. Clements, "The future of educational computing research: the case of computer programming," *Information Technology in Childhood Education Annual*, no. 1, pp. 147-179, 1999.
- [4] G. Revelle, O. Zuckerman, A. Druin, and M. Bolas, "Tangible user interfaces for children," in *Proceedings of the Conference on Human Factors in Computing Systems (CHI '05)*, pp. 2051-2052, ACM Press.
- [5] S. Y. Chen, "Active vision for robotic manipulation," *Industrial Robot*, vol. 39, no. 2, pp. 111-112, 2012.
- [6] M. Eisenberg, N. Elumeze, M. MacFerrin, and L. Buechley, "Children's programming, reconsidered: settings, stuff, and surfaces," in *Proceedings of the 8th International Conference on Interaction Design and Children (IDC '09)*, pp. 1-8, June 2009.
- [7] A. Begel, *LogoBlocks: A Graphical Programming Language for Interacting With the World*, MIT Press, Boston, Mass, USA, 1996.
- [8] J. Maloney, M. Resnick, N. Rusk, B. Silverman, and E. Eastmond, "The scratch programming language and environment," *ACM Transactions on Computing Education*, vol. 10, no. 4, p. 16, 2010.
- [9] J. A. Fails, A. Druin, M. L. Guha, G. Chipman, S. Simms, and W. Churaman, "Child's play: a comparison of desktop and physical interactive environments," in *Proceedings of the Conference on Interaction Design and Children (IDC '05)*, pp. 48-55, ACM Press, 2005.
- [10] P. H. Juan, B. B. Benjamin, D. Allison, and Guimbreti re, "Differences in pointing task performance between preschool children and adults using mice," *ACM Transactions on Computer-Human Interaction*, vol. 11, no. 4, pp. 357-368, 2004.
- [11] H. Ishii and B. Ullmer, "Tangible bits: towards seamless interfaces between people, bits and atoms," in *Proceedings of the Conference on Human Factors in Computing Systems (CHI '97)*, pp. 234-241, March 1997.
- [12] M. Andrew and O. M. Claire, "Tangibles for learning: a representational analysis of physical manipulation," *Personal and Ubiquitous Computing*, vol. 16, no. 4, pp. 405-419, 2012.
- [13] P. Lu, S. Chen, and Y. Zheng, "Artificial intelligence in civil engineering," *Mathematical Problems in Engineering*, vol. 2013, Article ID 145974, 22 pages, 2013.
- [14] E. Hornecker and A. D nser, "Of pages and paddles: children's expectations and mistaken interactions with physical-digital tools," *Interacting with Computers*, vol. 21, no. 1-2, pp. 95-107, 2009.
- [15] T. S. McNerney, *Tangible programming bricks: an approach to making programming accessible to everyone [M.S. thesis]*, MIT Press, Boston, Mass, USA, 2000.
- [16] T. McNerney, "From turtles to tangible programming bricks: explorations in physical language design," *Personal and Ubiquitous Computing*, vol. 8, no. 5, pp. 326-337, 2004.
- [17] D. L. Wang, C. Zhang, and H. A. Wang, "T-Maze: A tangible programming tool for children," in *Proceedings of the 10th International Conference on Interaction Design and Children (IDC '11)*, pp. 127-135, June 2011.
- [18] H. Suzuki and H. Kato, "Interaction-level support for collaborative learning: AlgoBlock-an open programming language," in *Proceedings of the 1st International Conference on Computer Support for Collaborative Learning (CSCL '95)*, pp. 349-355, ACM Press, 1995.
- [19] M. Sugimoto, T. Fujita, H. Mi, and A. Krzywinski, "RoboTable2 a novel programming environment using physical robots on a tabletop platform," in *Proceedings of the 8th International Conference on Advances in Computer Entertainment Technology (ACE '11)*, ACM Press, 2011.
- [20] T. S. McNerney, *Tangible programming bricks: an approach to making programming accessible to everyone [M.S. thesis]*, MIT Press, Boston, Mass, USA, 2000.
- [21] D. Gallardo, C. F. Juli a, and S. Jord a, "TurTan: a Tangible programming language for creative exploration," in *Proceedings of the 3rd annual IEEE international workshop on horizontal human-computer systems (TABLETOP '08)*, pp. 412-420, IEEE Press, 2008.
- [22] P. Wyeth and H. C. Purchase, "Tangible programming elements for young children," in *Proceedings of the Extended Abstracts on Human Factors in Computing Systems (CHI '02)*, pp. 774-775, ACM Press, 2002.
- [23] P. Wyeth and G. Wyeth, "Electronic blocks: tangible programming elements for preschoolers," in *Proceedings of the International Conference on Human-Computer Interaction (INTERACT '01)*, pp. 496-503, 2001.
- [24] H. Shi, W. Wang, N. M. Kwok, and S. Y. Chen, "Game theory for wireless sensor networks: a survey," *Sensors*, vol. 12, no. 7, pp. 9055-9097, 2012.
- [25] C. Cattani, S. Chen, and G. Aldashev, "Information and modeling in complexity," *Mathematical Problems in Engineering*, vol. 2012, Article ID 868413, 4 pages, 2012.
- [26] E. Schweikardt and M. D. Gross, "RoBlocks: a robotic construction kit for mathematics and science education," in *Proceedings of the 8th International Conference on Multimodal Interfaces (ICMI '06)*, pp. 72-75, November 2006.

- [27] M. S. Horn and R. J. K. Jacob, "Tangible programming in the classroom with tern," in *Proceedings of the 25th SIGCHI Conference on Human Factors in Computing Systems (CHI '07)*, pp. 1965–1970, May 2007.
- [28] M. S. Horn and R. J. K. Jacob, "Designing tangible programming languages for classroom use," in *Proceedings of the 1st International Conference on Tangible and Embedded Interaction*, pp. 159–162, February 2007.
- [29] D. L. Wang, Y. Zhang, T. Y. Gu, L. He, and H. A. Wang, "E-Block: a tangible programming tool for children," in *Proceedings of the 25th Annual ACM Symposium on User Interface Software and Technology (UIST '12)*, pp. 71–72, ACM Press, 2012.

Research Article

Factors Influencing Quasistatic Modeling of Deformation and Failure in Rock-Like Solids by the Smoothed Particle Hydrodynamics Method

X. W. Tang,¹ Y. D. Zhou,² and Y. L. Liu²

¹ State Key Laboratory of Subtropical Building Science, School of Civil Engineering and Transportation, South China University of Technology, Guangzhou 510640, China

² State Key Laboratory of Hydrosience and Engineering, Department of Hydraulic Engineering, Tsinghua University, Beijing 100084, China

Correspondence should be addressed to Y. D. Zhou; zhouyd@mail.tsinghua.edu.cn

Received 26 November 2012; Accepted 25 December 2012

Academic Editor: Fei Kang

Copyright © 2013 X. W. Tang et al. This is an open access article distributed under the Creative Commons Attribution License, which permits unrestricted use, distribution, and reproduction in any medium, provided the original work is properly cited.

As a Lagrangian mesh-free numerical method, the Smoothed Particle Hydrodynamics (SPH) method has been traditionally applied for modeling astrophysics, fluid flows and thermal problems, and there has been a growing interest in applying SPH to solid deformation problems. However, the potential of this method for quasistatic analysis of rock-like brittle materials has not been clearly explored. The major aim of this paper is to investigate the effects of key factors in SPH on the load-deformation response of rock-like solids, including variations in the particle approximation theory, the magnitude of the smoothing length and its variable method. Simple uniaxial compression (UC) loading conditions were chosen, and a series of numerical studies were carried out sequentially on an idealized elastic case and an actual test of marble material. Typical results of the axial stress-strain response from infinitesimal to finite deformation as well as the progressive failure process for the marble tests are given and the influences of various factors are discussed. It is found that only provided proper choices of particle momentum equation and the smoothing length parameter, the SPH method is capable for favorably reproducing the deformation and progressive failure evolution in rock-like materials under quasistatic compression loads.

1. Introduction

SPH is a mesh-free, adaptive, Lagrangian particle method that can be used to obtain solutions to systems of partial differential equations. In contrast to the concept of discretization methods which discretize a continuum into a finite set of nodal points, SPH consolidates a set of discrete particles into a quasicontinuum, and each particle represents specific material volumes. Since there is no mesh to distort, the method can handle large deformations in a pure Lagrangian frame [1], hence presenting extraordinary power for easy treatment of void regions, material interfaces, and multifracturing in materials. The technique was initially formulated to solve astrophysical problems [2, 3] and has been widely adopted in fluid dynamics related areas [4–6].

Material strength can be considered in a fairly straight forward manner, and Libersky and Petschek [7] were the first to incorporate an elastic-perfectly plastic material strength model into the SPH framework and they applied it to the simulation of the impact of an iron rod with a rigid surface. In recent years, there has been a growing interest in applying SPH for modeling solid deformation problems in a broad range of applications. However, most of these studies were focused on the high velocity impact, blasting, and granular flow types of problems, such as the study of the deformation of a metal cylinder resulting from the normal impact against a rigid surface [8, 9], modeling of impact induced fractures in brittle solids [10, 11], and the simulation of broken-ice fields floating on the water surface and moving under the effect of wind forces [12]. Rather limited publications can be found

to date with regard to the application of the SPH method in quasistatic analysis of deformation and possible failure response of solid materials.

Given the extraordinary potential of SPH in dealing with large deformation, the method has also obtained a number of applications in the field of geotechnical engineering. Previous applications of the SPH method in geotechnics mostly dealt with fluid-like flow problems, in particular, those involved in analyses of dam-break flood hazard [13, 14], water-structure interaction [15, 16], and pore-scale flow phenomena in soil-like porous media [17, 18]. More recently, Bui et al. [19] also developed SPH to solve the large deformation and postfailure flow of noncohesive and cohesive soils. Ma et al. [20, 21] applied SPH to investigate the static or dynamic failure of brittle heterogeneous materials by tracing the propagation of the microscopic cracks as well as the macromechanical behaviors, in which the material heterogeneity was modeled by a statistical approach.

Furthermore, with the fast development of SPH theory, quite a number of extensions using different particle approximation theories, varied choices of the smoothing length and correction techniques have been proposed. To the best of our knowledge, no discussion of various options in SPH and their effects on the modeling of progressive deformation and in turn failure process of rock-like materials under quasistatic loads has been reported in literature. The primary aims of this paper are to study the suitability of the SPH method for quasistatic modeling of rock-like materials and to study the effects of influencing factors on the load-deformation response and the associated failure progress. The paper is organized as follows: firstly, a brief introduction to the fundamentals of SPH is provided, forming the basis of following parametric numerical studies and discussions; secondly, the main part of this paper presents a series of numerical investigation into the effects of varied options in SPH on the uniaxial compression response, in which two typical cases are chosen, an idealized elastic case of a cubic specimen and an inelastic case considering possible damage and failure of marble materials; in the final part, a summary of the parametric studies and some conclusive discussions are provided.

2. Fundamentals of SPH Method

2.1. Basic Formulations. The theoretical fundamentals of SPH can be described in two main steps. The first is the integral representation or kernel approximation of the field functions. The second step is the approximation of particle variables, that is, the modeling domain is discretized into a finite number of particles which carry field variables such as mass, density, stress, and so forth and move along the particle velocity. As in the framework of continuum mechanics, the governing equations for constructing SPH formulations are mainly composed of mass, momentum, and energy conservation laws.

The material properties of each particle, such as velocity, density, stress, and so forth, are calculated through the use of an interpolation process over its neighboring particles, which

is based on the integral representation of a field function $f(\mathbf{x})$ as follows:

$$\langle f(\mathbf{x}) \rangle = \int_{\Omega} f(\mathbf{x}') W(\mathbf{x} - \mathbf{x}', h) d\mathbf{x}', \quad (1)$$

where W denotes the kernel or smoothing function, and h is the smoothing length, which defines the influence domain of W . Generally, the chosen kernel function W should satisfy three conditions: the normalization condition, the delta function property, and the compact support condition as follows:

$$\begin{aligned} \int_{\Omega} W(\mathbf{x} - \mathbf{x}', h) d\mathbf{x}' &= 1, \\ \lim_{h \rightarrow 0} W(\mathbf{x} - \mathbf{x}', h) &= \delta(\mathbf{x} - \mathbf{x}') \\ W(\mathbf{x} - \mathbf{x}', h) &= 0 \quad \text{when } \|\mathbf{x} - \mathbf{x}'\| > kh \end{aligned} \quad (2)$$

in which k is a constant that specifies the nonzero region of the smoothing function for a point at a position vector \mathbf{x} . This implies that the integration over the entire domain Ω is localized to an integration over the support domain of the smoothing function.

The integral representation (1) can be then discretized as a summation over the particles within the support domain as follows:

$$\langle f(\mathbf{x}) \rangle = \sum_{j=1}^N \frac{m_j}{\rho_j} f(\mathbf{x}_j) W(\mathbf{x} - \mathbf{x}_j, h), \quad (3)$$

where $j = 1, 2, \dots, N$ denote particles within the support domain of the particle at \mathbf{x} , m_j , and ρ_j are the mass and density of particle j , respectively. In a similar manner, the approximation for the spatial derivatives $\partial f(\mathbf{x})/\partial \mathbf{x}$ can be obtained.

Using the above particle approximations for a function and its gradient at a particle, the conservation laws in the form of partial differential equations can be then converted into equations of motion of discrete particles and then solved by an updated Lagrangian numerical scheme. However, different transformations or operations may result in different discretized forms of SPH equations [19, 22]. In the coming section, some typical and commonly used SPH formulations shall be presented, forming the basis of subsequent discussions on the numerical results of the chosen cases. More details on the SPH method and technical treatments can be found in the textbook by G. R. Liu and M. B. Liu [23] and a recent review of SPH development by Monaghan [24].

2.2. Choices of Particle Approximation Theory. A large variety of SPH formulations have been proposed by many researchers, which originate from the application of different forms of kernel functions and variable transformation options. Obviously the choice of the kernel function W in (1) will directly influence the accuracy, efficiency, and stability of the numerical analysis [22, 23]. Several types of kernel functions have been proposed in literature, such as bell-shaped function, Gaussian function, quadratic function, and

spline functions of cubic or higher order. By far the most widely used kernel function in SPH is the one devised by Monaghan and Lattanzio [25] based on the cubic B-spline function, which is given as

$$W(q) = \frac{1}{\pi h^3} \begin{cases} \left(1 - \frac{3}{2}q^2 + \frac{3}{4}q^3\right) & 0 \leq q \leq 1 \\ \frac{1}{4}(2-q)^3 & 1 < q < 2 \\ 0 & \text{otherwise} \end{cases} \quad (4)$$

for three dimensions where $q = |\mathbf{x}_i - \mathbf{x}_j|/h$ is the normalized distance, and the coefficients assure proper normalization. This function has the advantage of having compact support and a continuous second derivative and was chosen for the following numerical analyses.

As the main focus of this paper is on quasistatic deformation and progressive failure analysis of rock-like solids using the SPH method, obviously the equation of motion plays a dominant role during this type of analysis. Hence, our attention is given to the variable choices of discrete interpolations for the linear momentum equation. Four types of typical formulations are chosen in this study and outlined as follows. It should be noted that the formulations given in this section are all constructed assuming no body force, no mass, and no heat sources involved.

Formula I:

$$\frac{d\mathbf{V}_i}{dt} = -\sum_{j=1}^N m_j \left(\frac{\boldsymbol{\sigma}_i}{\rho_i^2} A_{ij} - \frac{\boldsymbol{\sigma}_j}{\rho_j^2} A_{ji} \right). \quad (5)$$

Formula II:

$$\frac{d\mathbf{V}_i}{dt} = -\sum_{j=1}^N m_j \left(\frac{\boldsymbol{\sigma}_i}{\rho_i^2} + \frac{\boldsymbol{\sigma}_j}{\rho_j^2} \right) \cdot \nabla_i W_{ij}. \quad (6)$$

Formula III:

$$\frac{d\mathbf{V}_i}{dt} = - \left[\sum_{j=1}^N m_j \left(\frac{\boldsymbol{\sigma}_i}{\rho_i^2} A_{ij} - \frac{\boldsymbol{\sigma}_j}{\rho_j^2} A_{ji} \right) \right] : B_{ij}. \quad (7)$$

Formula IV:

$$\frac{d\mathbf{V}_i}{dt} = - \left[\sum_{j=1}^N m_j \left(\frac{\boldsymbol{\sigma}_i}{\rho_i^2} + \frac{\boldsymbol{\sigma}_j}{\rho_j^2} \right) \cdot \nabla_i W_{ij} \right] : B_{ij}, \quad (8)$$

where \mathbf{V} denotes the velocity of each SPH particle, and the indices i and j denote the particle number; $\boldsymbol{\sigma}$ is the stress tensor; $\nabla_i W_{ij}$ denotes the gradient of kernel function $W_{ij} = W(|\mathbf{x}_i - \mathbf{x}_j|/h)$, which is taken with respect to the \mathbf{x}_i as $\partial W_{ij}/\partial \mathbf{x}_i = (\partial W_{ij}/\partial |\mathbf{x}_i - \mathbf{x}_j|)(\mathbf{x}_i - \mathbf{x}_j)/|\mathbf{x}_i - \mathbf{x}_j|$. A_{ij} and A_{ji} , respectively, denote the gradient of kernel function with respect to the \mathbf{x}_i and \mathbf{x}_j . One can easily note that Formulas III and IV are established through a renormalization correction on the former two equations, respectively, as denoted by a second rank tensor B_{ij} in (7) and (8). The purpose of the correction treatment is to impose general boundary conditions as well as to diminish the effect of particle

deficiency at boundaries due to inaccurate sum estimates. Detailed formulation and technical treatments of the tensor B_{ij} can be found in [1], which extended the “ghost particles” approach by Libersky and Petschek [7].

The above Formula I represents a general summation interpolant for the linear momentum equation. Specifically with an assumption that the smoothing function is symmetric and the smoothing length h at each particle remains the same constant, the equation will be equivalent to Formula II. Also some other summation interpolants can be found in literature using different approximation rules.

Commonly the continuity equation and the energy equation are also transformed into summation interpolants as parts of fundamental SPH equations in continuum mechanics. Using the same approximation rules as in the derivation of the above momentum equation, the SPH continuity and energy equations can be given as follows:

$$\begin{aligned} \frac{d\rho_i}{dt} &= \rho_i \sum_{j=1}^N \frac{m_j}{\rho_j} (\mathbf{V}_i - \mathbf{V}_j) \cdot \nabla_i W_{ij}, \\ \frac{dE_i}{dt} &= \frac{P_i}{\rho_i^2} \sum_{j=1}^N m_j (\mathbf{V}_i - \mathbf{V}_j) \cdot \nabla_i W_{ij}, \end{aligned} \quad (9)$$

where E is specific internal energy, P denotes the hydrostatic pressure for the stress tensor at a particle. It should be noted that the use of continuity and energy equation may be optional in the current SPH application to quasistatic deformation and failure analysis of rock-like materials.

2.3. Choices of Smoothing Length. The smoothing length h represents the influence width of the kernel and its magnitude determines the number of particles with which a given SPH particle interacts. Hence it is straightforward to raise a problem about the influence of the h value on quasistatic modeling of deformation and failure process of rock-like materials. During the explicit integration of the above governing equations, routinely the initial value of the smoothing length for each particle is determined as the maximum of the minimum distance between every particle. Moreover, a scaling factor denoted by k is commonly introduced for the adjustment of h value, which means that the actual influence width of the kernel will be scaled to kh . Obviously a choice of k value should be not less than 1.

Another important aspect in the choice of h is about its evolution during the entire simulation. Early SPH simulations used a fixed smoothing length for all particles, which indicates that the number of particles within the influence zone significantly depends on the type of loading. For instance, for compressive loading condition the number of particles increases, whilst for tensile loading less particles would be inside the influence zone. However, the above summation interpolants imply that the accuracy of an SPH simulation depends on having a sufficient number of particles within the smoothing length. Allowing each particle to have its own variable smoothing length which changes with time and space according to local conditions may increase the spatial resolution substantially [26, 27]. Different ways for

the evaluation of the variable smoothing length have been proposed by many researchers. Two types of frequently used definitions of the variable h are given as follows.

h method I:

$$\frac{dh}{dt} = \frac{1}{3}h \operatorname{div}(\mathbf{V}). \quad (10)$$

h method II:

$$\frac{dh}{dt} = \frac{1}{3}h(\operatorname{div}(\mathbf{V}))^{1/3}, \quad (11)$$

where $\operatorname{div}(\mathbf{V})$ means the divergence of velocity \mathbf{V} . The smoothing length h increases when particles separate from each other and reduces when the concentration of particles is important, aiming to keep the same number of particles in the neighborhood.

3. Numerical Experiments of UC Test

In this section a simple unconfined compression test was chosen and parametric studies were conducted. The numerical investigation was comprised of two parts as follows: in the first part, a series of elastic analyses were conducted on an idealized cubic sample as a benchmark case, through which the influences of various SPH options on the load-deformation response from infinitesimal to large axial strain conditions, were analyzed and discussed; in the second part, inelastic analyses of typical UC tests of Georgia Cherokee marble material by Hudson et al. [28] were carried out considering possible damage and failure behavior. Three-dimensional numerical studies were chosen for these two types of analyses using the commercial software LS-DYNA ver971 [29, 30], in which the above-described particle approximation formulations and the control of h magnitude as well as its variable methods have been well implemented.

3.1. Idealized Elastic Case

3.1.1. Model Description. For the idealized elastic case, a cubic specimen of 100 mm in side length was chosen as a threefold symmetric distribution of SPH particle can be obtained along three orthogonal directions. As shown in Figure 1, the numerical models consist of three major components, namely, (1) the upper rigid platen, (2) the lower rigid platen, and (3) the specimen in between. The dimensions of the two platens were defined to be a bit larger in section (120 mm × 120 mm) and 10 mm in thickness, such that a full contact between the platen and the specimen end surfaces can be maintained even at the stage of large lateral deformation induced by top compression.

In the numerical model, the upper and lower steel platens were modeled by linear hexahedron solid finite elements (FEs). The Young's modulus of the platen was taken as 2.0×10^5 MPa, and Poisson's ratio equal to 0.28 as commonly applied values for steel material. For the cubic specimen modeled by SPH particles, the elastic constants were chosen as: Young's modulus = 2.0×10^4 MPa, and Poisson's ratio = 0.2, similar to those of common types of rock material. Regarding

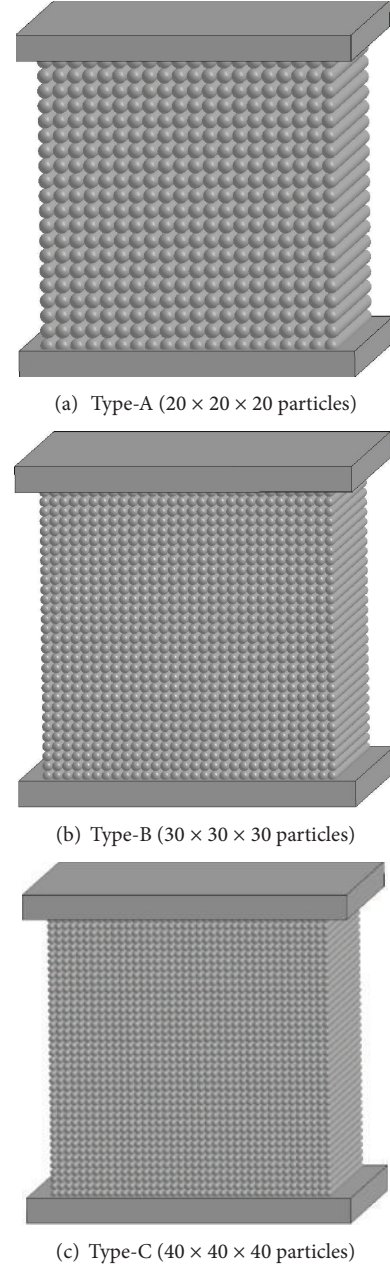


FIGURE 1: Three types of SPH based numerical model for the cubic UC test (each SPH particle is shown by a sphere of a radius h).

the mass properties of the platens and the specimen, the magnitude of density parameter would not influence the load-deformation response for such a quasistatic analysis. However, the choice can greatly affect the allowable time increment and in turn the computational cost. Herein the density of the platens was defined as 7.8×10^3 kg/m³, a common value for steel material. For the specimen, the density was taken as 2.7×10^3 kg/m³ as common types of rock material, and a mass scaling of 1.0×10^6 was applied. The Courant-Friedrichs-Lewy (CFL) condition is necessary for convergence in the explicit integrations of the above system equations, which requires the time step to be negatively

TABLE 1: Elastic UC analysis programme.

Series	Particle distribution	Particle momentum equation	k value	h variable
1	Type-A, Type-B, Type-C	Formula III	1.0	Equation (10)
2	Type-B	Formulas I–IV	1.0	Equation (10)
3	Type-B	Formula III	1.0, 1.1, 1.2	Equation (10)
4	Type-B	Formula III	1.0	Equations (10) and (11)

proportional to the sound of speed. Obviously the above mass scaling can enlarge the allowable time increment by about 1000 during the explicit integration analysis.

Regarding the load and boundary conditions, the bottom platen was specified as a fixed support. The compression was defined by a vertical displacement control on the top platen. A final magnitude of 10 mm was chosen for obtaining a large axial strain level of about 10% finally, such that the suitability of the SPH method for modeling elastic solids from infinitesimal to large strain can be examined. The top compression was initiated from zero and increased linearly to 10 mm in a time period of 30 seconds, which was sufficiently slow for the requirement of a quasistatic analysis through a posterior check. For the interaction between the SPH particles and the FE domain, a master-slave contact algorithm was applied to couple the two techniques. In this study, a penalty based “nodes to surface” contact [29] is adopted. The SPH particle elements are defined as the slave side and the finite elements are defined as the master side. Zero friction contact interaction was defined between the specimen and the two platens, simulating an ideal unconfined compression case.

3.1.2. Analysis Programme. Four series of analyses have been conducted and the details of each series are listed in Table 1. Series 1 aims to examine the effect of particle density, using three types of particle distribution models as given in Figure 1. The effect of different particle momentum equations, as given in the above section, is examined in Series 2 using the Type-B particle distribution model. Series 3 investigates the influence of the variation in h magnitude by adjusting the k parameter, and three k values falling in a range of 1.0 ~ 1.2, as commonly adopted in literature, are considered. The analyses in Series 4 aim to study the effects of the two h variable methods during the integration process, which are, respectively, shown in (10) and (11).

3.1.3. Results. A summary of the axial load-displacement results from the series of SPH analyses is given in Figure 2, and the individual effect of the above factors on the UC response for the cubic specimen is demonstrated. Moreover, a three-dimensional single element FE analysis for the UC test has been conducted and the modeling result is also shown in Figure 2 for comparison. It can be observed that generally all the predictions using SPH method with varied options in Table 1 compare favorably with the one-element FE solution at an early stage with relatively small top compression, lower than 1 mm for the studied model, whilst more noticeable discrepancy is shown at a later stage with greater compressions applied.

The effect of SPH particle density is shown in Figure 2(a). It is found that at the early stage with low value of top compression, approximately at a level of axial strain lower than 1%, the predictions by the three types of models are close to the analytical solution, all showing a linear increase of axial load with respect to the top compression. A comparison of the slope of the curves at this stage shows that amongst the three models, the Type-C model using the finest particle distribution gives the best prediction with a minor difference (~4.7%) with respect to the one-element FE solution, and the predictions by the other two models using coarser particle distribution give a slope difference of 8.6% (Type-A) and 6.1% (Type-B), respectively, relative to the FE solution. One can also note that with a greater than twofold increase of SPH particles from 27000 (Type-B) to 64000 (Type-C), only a small improvement in the accuracy of load-displacement response is shown by the SPH method.

With a larger top compression applied at the later stage, geometric nonlinearity plays a more significant role and the stiffening effect induces a slightly concave-downward curve. It can be seen that all the modeling results in Figure 2(a) reproduce this essential behavior, also one can note that comparatively more prominent discrepancy is shown between the simulation results and the FE solution with the axial deformation increased, particularly at an axial strain level greater than 2.5%. Again, it is shown that the Type-C model with the finest particle distribution gives the best prediction at a larger top compression, except at an intermediate stage with the top compression falling in the range of 1 mm to 2.5 mm due to the occurrence of a nearly horizontal plateau in the curve. The underlying mechanism of this phenomenon is addressed in the Discussions section.

Figure 2(b) illustrates the influence of varied choices of the particle momentum equation. It is shown by the comparison that a better prediction can be obtained by Formulas III and IV in which the renormalization technique was applied, and the two choices basically gave the same results. For the other two choices using Formulas I and II, the simulation results are basically the same and compare less favorably with the one-element FE solution. Also it can be observed that an occurrence of nearly horizontal plateau is shown by all the SPH modeling curves at a compression level of around 1 mm.

The effect of variation in h by adjusting the k parameter is shown in Figure 2(c). It is found that with the k parameter increased from a standard value 1.0 to 1.2, the predicted load-displacement curves were significantly influenced at the later stage with a larger top compression. In particular, for the case with $k = 1.2$, a top compression greater than 4.5 mm could trigger a significant deviation from the exact solution,

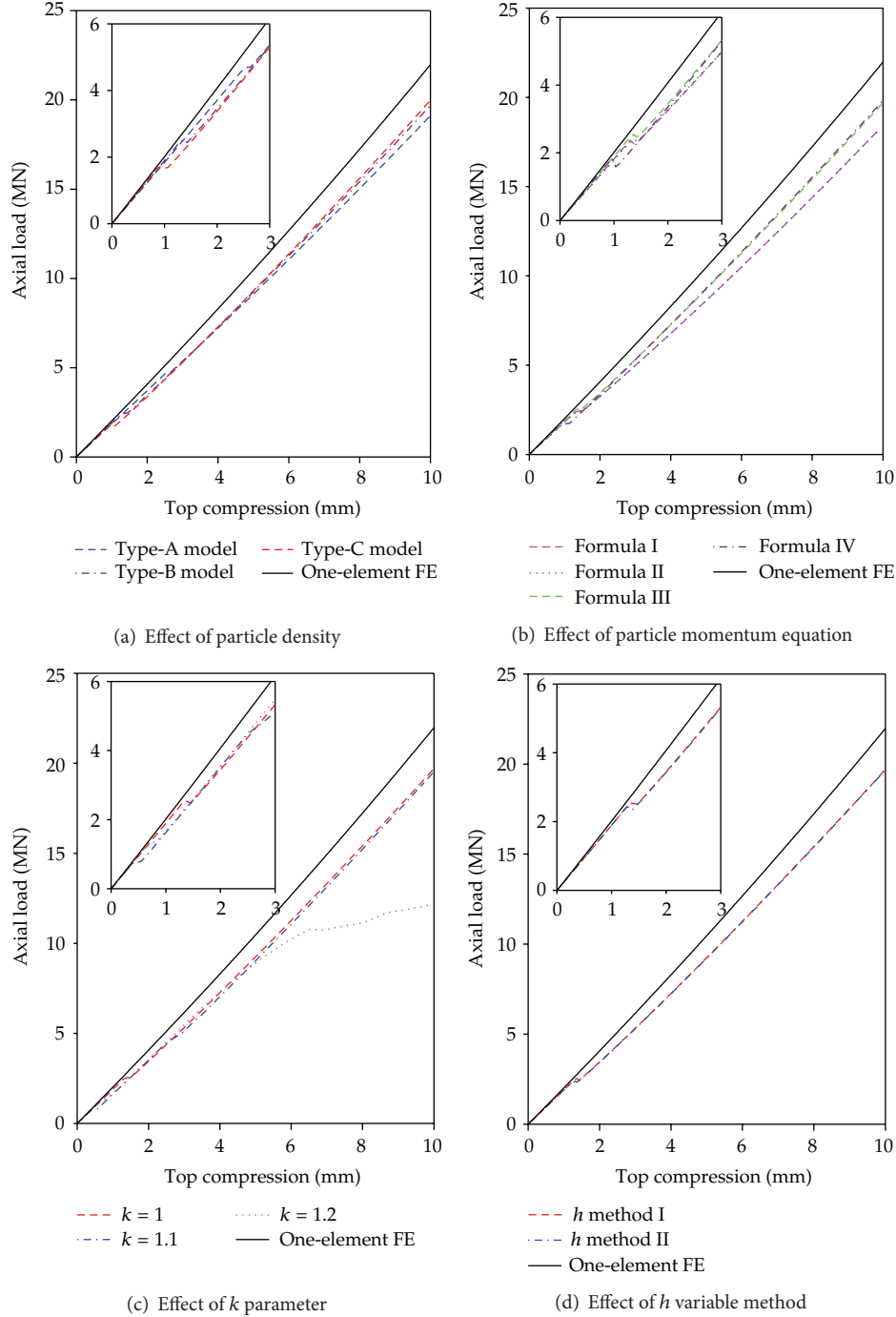


FIGURE 2: Comparison of axial load-deformation response from the series of elastic UC analysis (each inset figure shows detailed response at early stage of top compression).

which seems unfavorable and the mechanism behind this is addressed in the Discussions section.

A comparison of the results using the two types of h variable methods during the integration process is shown in Figure 2(d). The two curves are approximately the same from the initial infinitesimal compression to the final large deformation, which illustrates that the two types of h variable methods in (10) and (11) may induce only negligible influence

on the load-displacement response for the UC problem in this study.

3.2. Inelastic Case of Marble UC Tests

3.2.1. Model Description. To further investigate the capability of the SPH method as well as the effects of the above factors on deformation and failure analyses of rock-like materials,

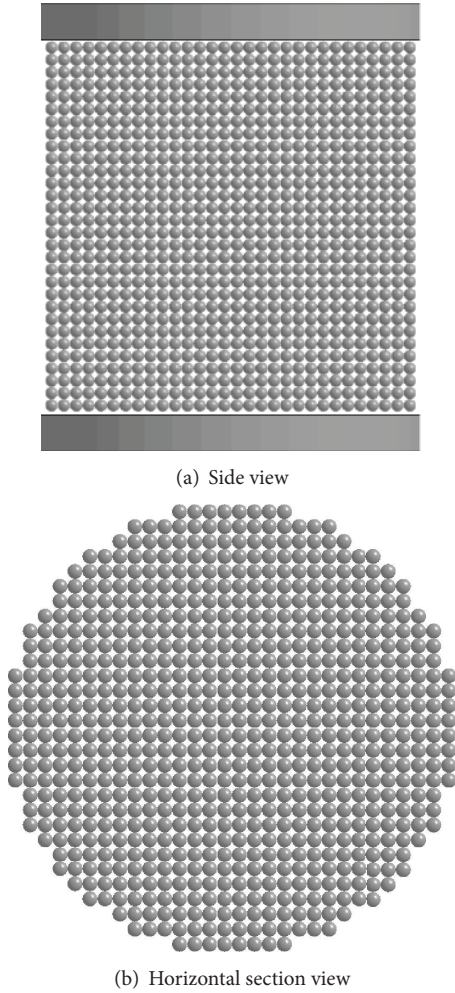


FIGURE 3: SPH model for the marble UC tests.

parametric studies were conducted in this section for typical UC tests of Georgia Cherokee marble material by Hudson et al. [28]. In their study, quite a number of UC tests considering a wide variety of size and shape have been conducted for the specified marble material. The cylindrical test samples with a diameter of 101.6 mm (4 inches) and a height/diameter (H/D) ratio equal to one were chosen in this study. Referring to the above elastic analyses, a particle discretization of 30 lines of particles along the three orthogonal directions, the same as that in Type-B model in Figure 1, was considered fine enough for the following analyses. The established numerical model was shown in Figure 3. A total of 21480 SPH particles were defined to approximate the cylinder specimen. Also one can note a regular distribution along the horizontal section was adopted rather than a circumferentially equally spaced distribution, which was applied to minimize the inter-particle distance discrepancy and better approximation can be expected [29]. The upper and lower steel platens were modeled by finite elements and their diameters were defined the same as that of the specimen in accordance with the actual test conditions [28]. A constant friction coefficient $f = 0.6$ was applied for the definition of the contact interaction

between the platens and the marble specimen, as no special measure for diminishing the frictional restraint effect was applied during the tests.

A coupled damage-plastic material model by Malvar et al. [31] was adopted to simulate the marble behavior. The model supports nonlinear elasticity and uses a three-invariant formulation for the failure surface. It is characterized by the employment of three failure surfaces, including the maximum, residual, and initial yield surfaces, for a proper representation of material behavior along multiple stress paths, including uniaxial, biaxial, and triaxial tension and compression. Although the model was originally developed for modeling the deformation and damage behavior of concrete materials, it was chosen in this study based on the presumption that the constitutive response characteristics of most types of rock and concrete materials are relatively similar. More details about the constitutive model can be found in [31].

Regarding the inputs of relevant parameters for the Georgia marble, as limited test data of the UC axial stress versus strain curves were provided in [28], only the deformation modulus and the UC strength parameters could be calibrated from the test results. Even though a variety of numerical approaches have been proposed by many researchers for the parameter calibration based on incomplete test data, such as those based on artificial intelligence [32], the calibration process in this study was simply based on trial analyses. The initial values of most parameters for the above model were determined using the internal parameter generation capability by Malvar et al. [33], during which only the unconfined compressive strength is needed and typical concrete test data are taken as a solid basis. Some minor adjustments were further made on the autogenerated parameter values as follows: a uniaxial tensile strength of 4.6 MPa for the same type of marble given by Schwartz [34] was adopted; and a slight adjustment of the compressive scaling exponent (b_1 parameter) from the autogenerated value of 1.6 to 1.0 was applied for a better match of the observed UC softening response. A list of the input parameter values for the above material model was given in Table 2. Note that for the definition of nonlinear elasticity, the internally generated relation curve of loading and unload/reload bulk modulus with respect to volumetric strain was directly used as given in Figure 4. The corresponding shear modulus can be calculated by the bulk modulus curve and the specified Poisson's ratio according to the prescribed procedure in [31].

3.2.2. Analysis Programme. With the analysis results of the above elastic case forming a basis, two series of analyses have been conducted for this inelastic case: firstly, the effect of the two types of particle momentum equations with renormalization technique (Formulas III and IV) on the inelastic load-deformation response was examined, as either choice gave more favorable predictions and present only slight difference on the load-deformation response in the above elastic case; secondly, the influence of the two h variable methods during the integration process, as shown in (10) and (11), was investigated. Regarding the h magnitude, a constant k value of 1.0 was deemed most appropriate from the above

TABLE 2: Input material properties for marble.

Property	Parameter	Input value
Physical	Mass density	2691 kg/m ³
Uniaxial strength	Compressive	70.7 MPa
	Tensile	4.6 MPa
Elastic behavior	Pressure-volumetric strain relation	As given in Figure 4
	Poisson's ratio	0.2
Maximum failure surface	a_0	20.9 MPa
	a_1	0.446
	a_2	1.143 GPa ⁻¹
Residual failure surface	a_{1f}	0.442
	a_{2f}	1.674 GPa ⁻¹
Initial yield surface	a_{0y}	15.77 MPa
	a_{1y}	0.625
	a_{2y}	3.644 GPa ⁻¹
Damage accumulation	Compressive scaling exponent b_1	1.0
	Tensile scaling exponent b_2	1.35
	Triaxial tensile scaling coefficient b_3	1.15

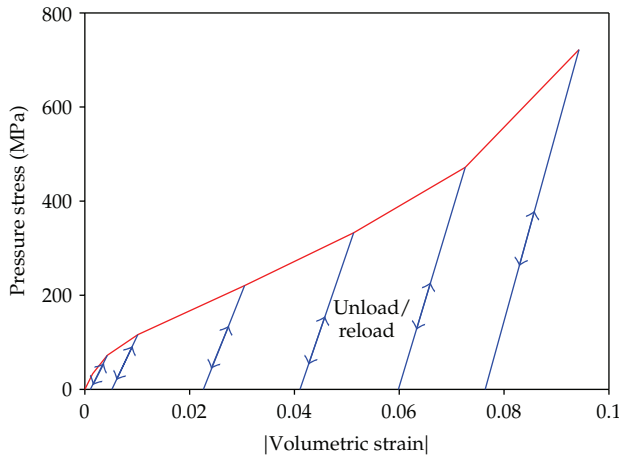


FIGURE 4: Input pressure stress versus volumetric strain curve for the marble UC model (the slope of each unload/reload curve denotes the bulk unload/reload modulus at the historically reached peak volumetric strain level).

elastic analysis results and was chosen in all the simulations of this section.

3.2.3. Results. A comparison of the nominal axial stress versus strain response from the numerical results is given in Figure 5, and the effects of the above two factors are separately illustrated. The corresponding test results from different sized specimens but with the same H/D ratio equal to unity are shown in the figure. The experiments exhibit an initial nonlinearity due to the closure of microcracking within the specimens that has not been included in the models, and removed in the comparison shown in Figure 5. It is shown that generally the SPH based modeling can adequately reproduce the complete axial stress versus strain response.

The alternative choice of the prescribed particle momentum equations and the h variable methods would not essentially change the modeling results, and only small difference was shown at the postpeak stage.

All the four simulation cases gave approximately the same peak stresses, 84.4 MPa, which closely match the test results (90.7 MPa) of cubic specimens with a diameter of 101.6 mm. However, one may note the difference between the predicted peak stress and the input value of unconfined compressive strength for the marble material, 70.7 MPa given in Table 2. It should be pointed out that the input UC strength was chosen from the test data of samples with a largest H/D ratio of 3:1 and a largest diameter of 101.6 mm, as routinely recommended in the suggested methods for the measurement of UC strength of rock materials [35]. It is also found that the test data by Hudson et al. [28] present an obvious trend of increase of the UC strength with the decrease of the H/D ratio from 3 to 1. Hence the observed difference between the predicted maximum stress and the input UC strength parameter can be attributed to the specimen shape effect on the compressive strength, which was caused by severely nonuniform stress distribution in the specimens with small H/D ratios [28].

The softening response is highly affected by the mechanism of progressive structural breakdown of the test specimen [28], and the development of damage and failure within the specimen is worthy of discussion. As the modeling results of the postpeak softening response in Figure 5 for all the cases compare favorably with the test records, the case using Formula III and h variable method I was taken as an instance. The progressive damage and failure evolution at typical stages along a vertical diametrical section of the specimen is given in Figure 6, as indicated by the distribution of a scaled damage measure $d \in [0, 2]$. For the chosen coupled damage-plasticity model [31], a d value increasing from 1 to 2 means the current failure surface is contracting from the maximum to

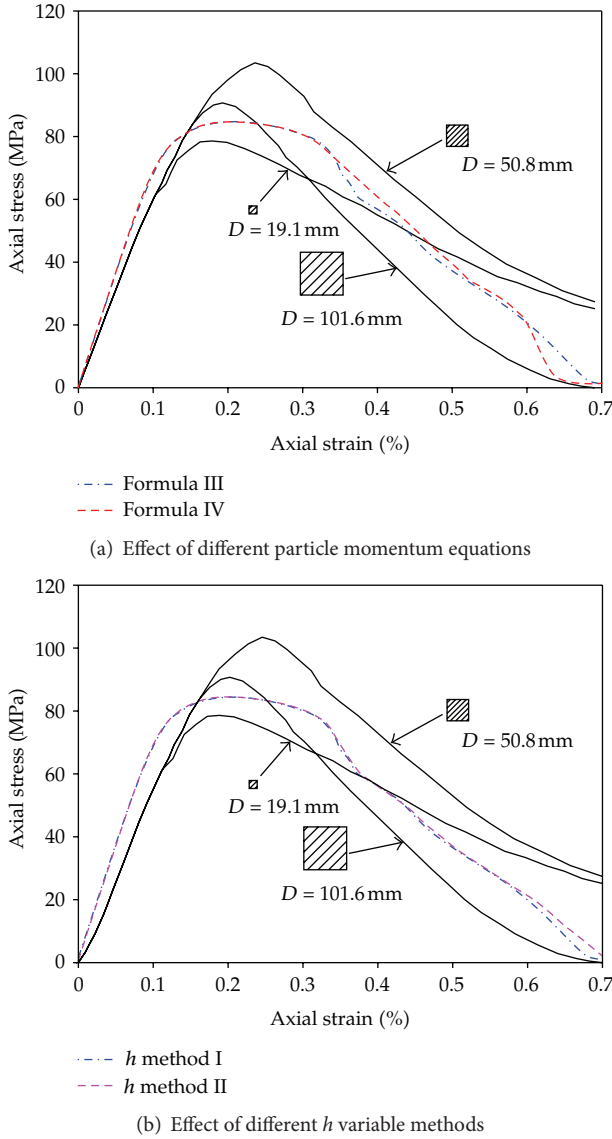


FIGURE 5: Comparison of the simulation and test results of axial stress-strain response for the marble UC tests (the solid lines denote the test results from different sized specimens [28]).

the residual failure surface (softening). As the aim of this investigation is to identify the evolution of specimen failure, a range of d from 1.8 to 2.0 is selected and its distribution is shown in Figure 6. For surficial parts with approximately zero confining pressure stress, a d value close to 2 would indicate the region is nearly completely damaged since the residual strength for rock material in tension is zero.

It is shown that for the marble specimen under unconfined compression, the damage initiated circumferentially from the surficial parts (Figures 6(a) and 6(b)), including the portions near the edge corner and the middle region, where less lateral confinement would come from the upper and lower platens. With the top compression progressively applied, the surficial damage zones coalesced into one circumferential part and a type of slabbing failure was formed

as expected (Figures 6(c) and 6(d)). At later softening stages, the compression induced damage propagated towards the internal central portion (Figures 6(e) and 6(f)) and connected at the center of the specimen at a top compression of 0.31 mm. Also it is found that the undamaged zones close to the upper and lower platens at this stage are of similar shapes as those of the horizontally confined zone for a cubic UC specimen due to frictional constraint given by van Vliet and van Mier [36]. Further top compression induced the vertical extension of severe damage zone (Figure 6(g)), and the load capacity of the specimen dropped to nearly zero at a top compression of about 0.71 mm for the interconnected fully damaged zone caused the structural collapse of the test specimen (Figure 6(h)). Moreover, a typical distribution of damage and cracking at an advanced state of failure from the marble test results is given in Figure 7. A comparison of the simulation and test results demonstrates that the apparent slabbing failure pattern and the behind mechanism of progressive structural breakdown process for the marble UC tests can be adequately and favorably reproduced by the SPH method.

4. Discussions

4.1. Mechanism of Plateaus in Load-Deformation Curves. From the above UC modeling results of idealized elastic case, it has already been noticed that each load-displacement curve in Figure 2 presents a nearly horizontal small plateau at a varied deformation level, and the plateau would be mobilized earlier at a lower magnitude of axial deformation when a relatively denser particle distribution was applied. Also the results using a variable k parameter in Figure 2(c) shows that when the k factor is enlarged to a certain extent, herein $k = 1.2$ as an instance, the simulated load-deformation curve deviates from the analytical solution to a remarkable extent at a top compression greater than 4.5 mm. An investigation into the particle approximation process during the UC analysis has been conducted for the cause of the mentioned discrepancies. Taking the cases in Figure 2(c) as an instance, Figure 8 presents the variation of the smoothing length h for typical particles with respect to the top compression during the UC analysis. As noted by the inset figure, five particles at typical positions on the top surface of the specimen, which are in direct contact with the loading platen, were chosen considering its double symmetry.

Generally the results in Figure 8 for the three cases reveal that there exists a good correlation between the abrupt change of h value and the occurrences of horizontal plateaus or noticeable deviation from the accurate solution in the load-compression response. With a relatively small input of k value, 1.0 and 1.1 in this study, a general decreasing trend is shown by the variation of h with the top compression (Figures 8(a) and 8(b)), which is reasonably attributed to the UC induced contractive response as a whole. Differently, the results for the case with $k = 1.2$ (Figure 8(c)) indicate that an opposite increasing trend of h value is mobilized at two particles near the centre of top surface, exactly at the same stage of compression as that of the deviation point in the load-compression response. The observation can be explained by

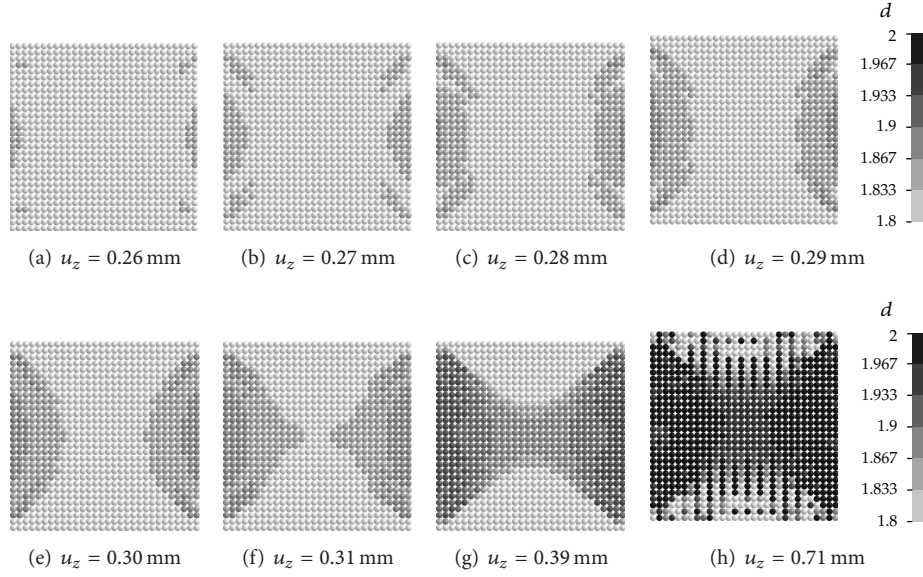


FIGURE 6: Numerical results of progressive damage distribution at typical levels of top compression (u_z) along the diametrical section of the marble UC test model (the case using Formula III and h variable I was chosen).

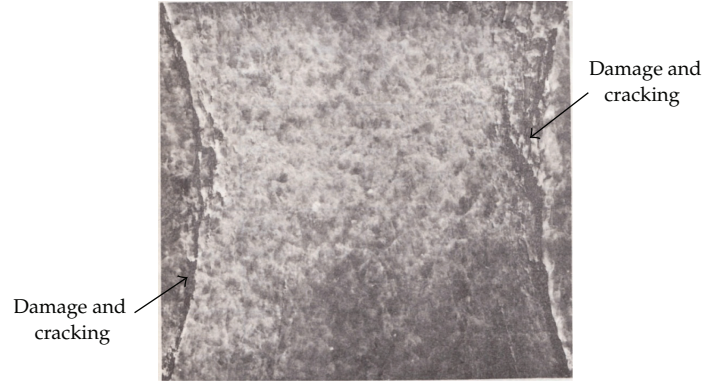


FIGURE 7: A sample of damage and cracking pattern of the marble specimens ($H/D = 1$, $D = 101.6$ mm) along the diametrical cross-section at an advanced state of failure [28].

the relatively more disordered distribution of particles at this stage as compared to the other two cases, which also implied the adverse effect of enlarging the influence domain by a larger k value on the accuracy of particle approximation of the SPH method (3) for the compression analysis of rock-like solids. It is also found that the modeling results of the h development using the alternative choice of the h variable method are basically the same as described above (Figure 8).

Overall, it is found that the occurrences of the small plateaus or even significant deviation from the accurate response were mainly attributed to the abrupt change of h at the corresponding compression stage, which in turn greatly affected the number of particles within the support domain and the approximation accuracy.

4.2. Factors Influencing Load Capacity and Failure Patterns. It can be observed that the predictions of axial load versus displacement response in the idealized elastic UC test

(Figure 2), even with noticeable improvement when considering the renormalization technique for the kernel function, still underestimate the load capacity, particularly when a larger axial compression is applied. The observation can be attributed to the particle approximations in SPH (3), which, as already noted by many researchers, do not have the property of strict interpolants such that in general they are not precisely equal to the particle value of the dependent variable. Hence the essential boundary conditions cannot be treated in a rigorous way. Moreover, when the particles get relatively more disordered due to large top compression, comparatively more prominent error or discrepancy from the actual value would be expected for the simulation results.

When the possible damage in UC specimens is considered, the above simulation results for the marble tests present basically the same damage evolution processes, and the correspondence of the numerical response to the physical response by Hudson et al. [28] is good. The observations

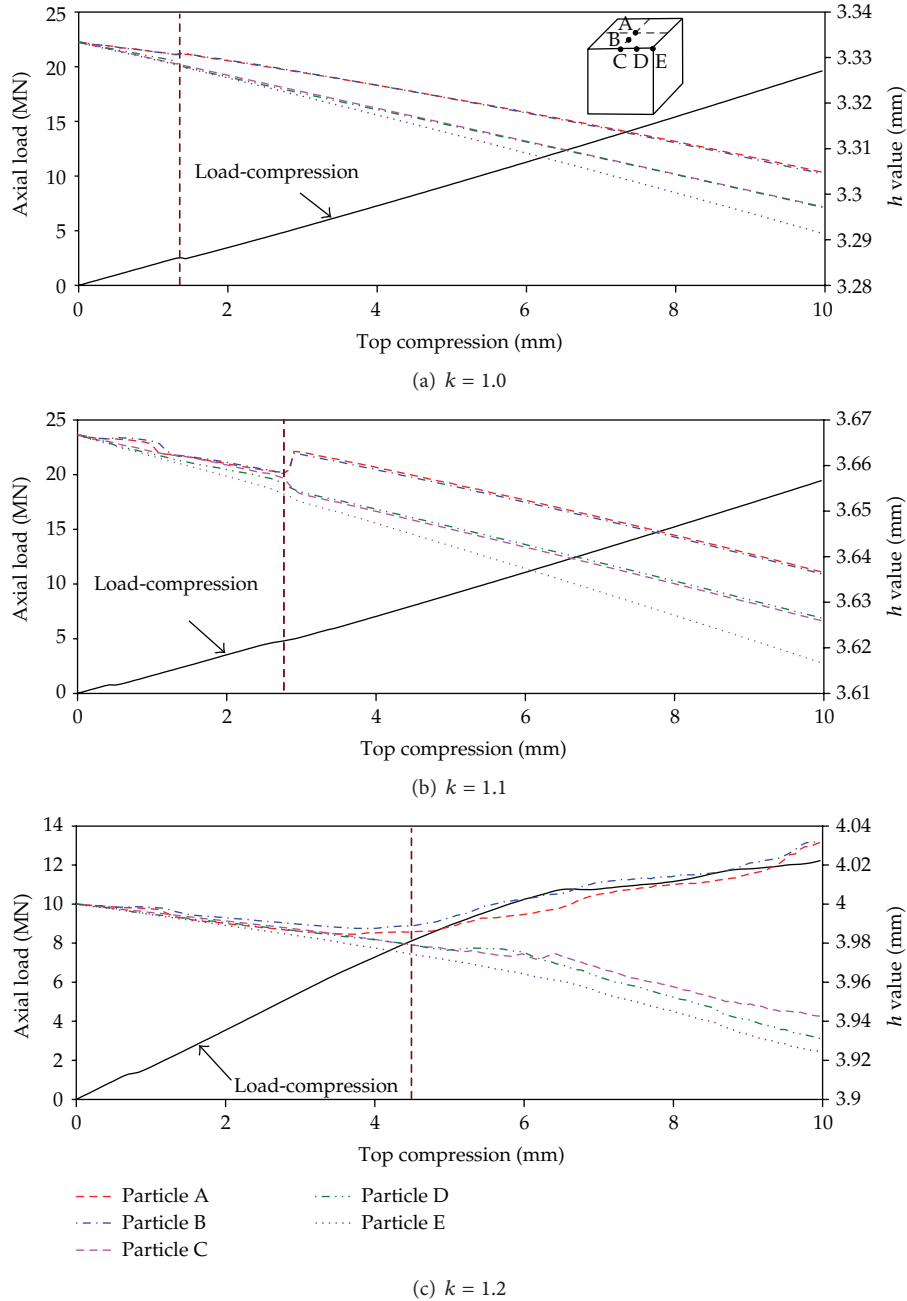


FIGURE 8: Development of h value at typical points during the idealized elastic UC test (the inset figure shows the positions of five typical particles on the top surface of the cubic specimen, and the solid line shows the corresponding axial load-compression response).

indicate that the two types of momentum equations are capable of predicting the progressive structural breakdown of the UC specimen when the renormalization technique is applied. However, through additional analyses considering the varieties in the k value, it is found that the damage and failure evolution can be strongly dependent on the input k value. Figure 9 shows the damage distribution at a typical postpeak stage predicted by an enlarged k value of 1.1 and 1.2, respectively. By comparing with the result using a k value of 1.0 shown in Figure 6(f), it is clearly demonstrated that significant difference in the damage pattern can be

induced by increasing the k value, and the case using the original influence width of the kernel ($k = 1.0$) seems more capable of reproducing the test response. The observation can be attributed to the nonlocal characters in the kernel approximation (3).

Even though the SPH method suffers from reduced accuracy when large axial strain is considered in the modeling of idealized elastic UC tests, the above simulation results for the marble UC tests demonstrate the capability of this method for common compression test conditions of rock-like materials. Herein with the marble UC test as an instance, it seems that

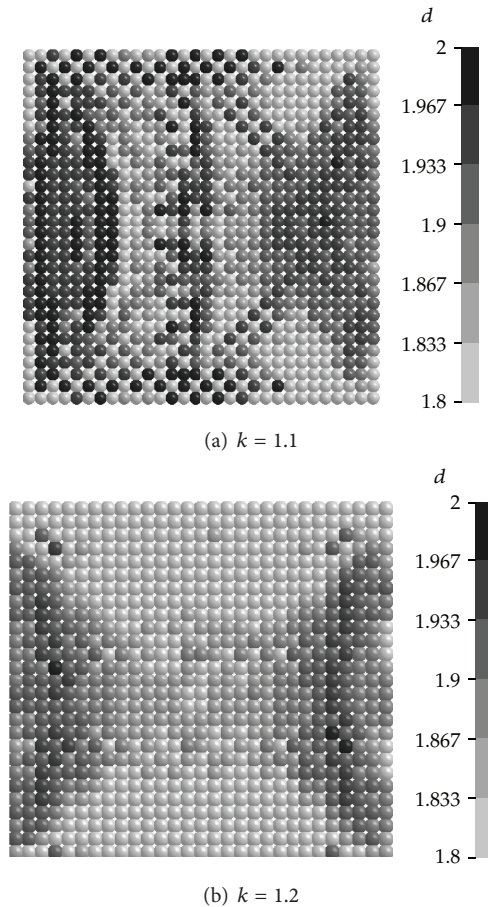


FIGURE 9: Comparison of predicted damage distribution at $u_z = 0.31$ mm along the diametrical section of the marble UC test model using different k values (Formula III is adopted).

a maximum strain level lower than 0.01 may be acceptable for a good estimate of the deformation and progressive failure process using the two types of momentum equations with renormalization technique incorporated, and the two types of h variable methods are both appropriate for simulating such a type of quasistatic UC problem. It is also worthy to note that a proper definition of the postpeak softening properties of rock materials is of great significance in this type of analysis and should be considered appropriately according to the particle distribution.

5. Conclusions

A series of parametric numerical studies have been carried out in this study to shed some light on the applicability of the SPH method for quasistatic deformation and progressive failure analysis of rock-like materials. The numerical experiments, including an idealized elastic case and an inelastic modeling of marble UC tests, reveal that the SPH method can be a reliable tool for adequately accurate and stable simulation of quasistatic load-deformation response, provided that suitable particle approximation rule and choice of the smoothing length are defined in the SPH model. From

the analysis results using the cubic B-spline kernel function, it is recommended to adopt the particle momentum equation with renormalization technique incorporated, and a radius of influence equal to $2h$, that is, $k = 1.0$, for simulating the deformation and failure process of rock-like solids under quasistatic loads. Either choice of the two variable methods for the smoothing length h aforementioned in this paper can lead to acceptable results for the UC analysis. Also it is found that the occurrences of small horizontal plateaus in the load-deformation response or even prominent deviation from the accurate solution is caused by the abrupt change of h value during the explicit integration process. The optional increase of the influence width of the kernel function by raising the k value can lead to an inappropriate prediction of the failure evolution in rock-like solids. It is also worthy to note that the effects of these factors on the quasistatic analysis of other types of solid problems, such as tension or shear dominant cases, are still open and need to be investigated.

Conflict of Interests

This statement is to declare that, X. W. Tang, Y. D. Zhou, and Y. L. Liu, the authors of this paper do not possess any financial relationships that might bias their work. They hereby declare that no conflict of interests exists in this work.

Acknowledgments

The authors acknowledge the support by the National Natural Science Foundation of China under Grant no. 11172321 and 51109083, as well as partial support from Fundamental Research Funds for the Central Universities under Grant no. 2012ZM0091.

References

- [1] P. W. Randles and L. D. Libersky, "Smoothed particle hydrodynamics: some recent improvements and applications," *Computer Methods in Applied Mechanics and Engineering*, vol. 139, no. 1-4, pp. 375-408, 1996.
- [2] L. B. Lucy, "A numerical approach to the testing of the fission hypothesis," *Astronomical Journal*, vol. 82, pp. 1013-1024, 1977.
- [3] R. A. Gingold and J. J. Monaghan, "Smoothed particle hydrodynamics—theory and application to non-spherical stars," *Monthly Notices of the Royal Astronomical Society*, vol. 181, pp. 375-389, 1977.
- [4] J. W. Swegle, Report at Sandia National Laboratories, 1992.
- [5] J. J. Monaghan, "Simulating free surface flows with SPH," *Journal of Computational Physics*, vol. 110, no. 2, pp. 399-406, 1994.
- [6] J. P. Morris, P. J. Fox, and Y. Zhu, "Modeling low Reynolds number incompressible flows using SPH," *Journal of Computational Physics*, vol. 136, no. 1, pp. 214-226, 1997.
- [7] L. D. Libersky and A. G. Petschek, "Smooth particle hydrodynamics with strength of materials," in *Advances in the Free-Lagrange Method*, H. E. Trease and W. P. Crowley, Eds., p. 248, Springer, Berlin, Germany, 1990.

- [8] L. D. Libersky, A. G. Petschek, T. C. Carney, J. R. Hipp, and F. A. Allahdadi, "High strain lagrangian hydrodynamics: a three-dimensional SPH code for dynamic material response," *Journal of Computational Physics*, vol. 109, no. 1, pp. 67–75, 1993.
- [9] A. G. Petschek and L. D. Libersky, "Cylindrical smoothed particle hydrodynamics," *Journal of Computational Physics*, vol. 109, no. 1, pp. 76–83, 1993.
- [10] W. Benz and E. Asphaug, "Impact simulations with fracture. I. Method and tests," *Icarus*, vol. 107, no. 1, pp. 98–116, 1994.
- [11] R. Das and P. W. Cleary, "Effect of rock shapes on brittle fracture using Smoothed Particle Hydrodynamics," *Theoretical and Applied Fracture Mechanics*, vol. 53, no. 1, pp. 47–60, 2010.
- [12] L. Oger and S. B. Savage, "Smoothed particle hydrodynamics for cohesive grains," *Computer Methods in Applied Mechanics and Engineering*, vol. 180, no. 1-2, pp. 169–183, 1999.
- [13] J. Bonet, S. Kulasegaram, M. X. Rodriguez-Paz, and M. Profit, "Variational formulation for the smooth particle hydrodynamics (SPH) simulation of fluid and solid problems," *Computer Methods in Applied Mechanics and Engineering*, vol. 193, no. 12–14, pp. 1245–1256, 2004.
- [14] V. Roubtsova and R. Kahawita, "The SPH technique applied to free surface flows," *Computers and Fluids*, vol. 35, no. 10, pp. 1359–1371, 2006.
- [15] H. Mutsuda and Y. Doi, "Numerical simulation of interaction between wave breaking and coastal structure using SPH," in *Proceedings of the 19th Conference on Numerical Simulation of Fluid Mechanics*, vol. 12, pp. 1–7, Tokyo, Japan, 2005.
- [16] M. Gómez-Gesteira, D. Cerqueiro, C. Crespo, and R. A. Dalrymple, "Green water overtopping analyzed with a SPH model," *Ocean Engineering*, vol. 32, no. 2, pp. 223–238, 2005.
- [17] Y. I. Zhu, P. J. Fox, and J. P. Morris, "A pore-scale numerical model for flow through porous media," *International Journal for Numerical and Analytical Methods in Geomechanics*, vol. 23, no. 9, pp. 881–904, 1999.
- [18] H. H. Bui, R. Fukagawa, and K. Sako, "Smoothed particle hydrodynamics for soil mechanics," in *Proceedings of the 6th European Conference on Numerical Methods in Geotechnical Engineering*, pp. 278–281, Taylor & Francis Group, Graz, Austria, September 2006.
- [19] H. H. Bui, R. Fukagawa, K. Sako, and S. Ohno, "Lagrangian meshfree particles method (SPH) for large deformation and failure flows of geomaterial using elastic-plastic soil constitutive model," *International Journal for Numerical and Analytical Methods in Geomechanics*, vol. 32, no. 12, pp. 1537–1570, 2008.
- [20] G. W. Ma, X. J. Wang, and Q. M. Li, "Modeling strain rate effect of heterogeneous materials using SPH method," *Rock Mechanics and Rock Engineering*, vol. 43, no. 6, pp. 763–776, 2010.
- [21] G. W. Ma, X. J. Wang, and F. Ren, "Numerical simulation of compressive failure of heterogeneous rock-like materials using SPH method," *International Journal of Rock Mechanics and Mining Sciences*, vol. 48, no. 3, pp. 353–363, 2011.
- [22] S. Li and W. K. Liu, *Meshfree Particle Methods*, Springer, 2007.
- [23] G. R. Liu and M. B. Liu, *Smoothed Particle Hydrodynamics: A Meshfree Particle Method*, World Scientific, Singapore, 2003.
- [24] J. J. Monaghan, "Smoothed particle hydrodynamics," *Reports on Progress in Physics*, vol. 68, no. 8, pp. 1703–1759, 2005.
- [25] J. J. Monaghan and J. C. Lattanzio, "A refined particle method for astrophysical problems," *Astronomy & Astrophysics*, vol. 149, no. 1, pp. 135–143, 1985.
- [26] L. Hernquist and N. Katz, "TREESPH—a unification of SPH with the hierarchical tree method," *Astrophysical Journal Supplement Series*, vol. 70, no. 2, pp. 419–446, 1989.
- [27] W. Benz, "Smooth particle hydrodynamics: a review," in *The Numerical Modelling of Nonlinear Stellar Pulsations, Problems and Prospects*, pp. 269–288, Kluwer Academic, Boston, Mass, USA, 1990.
- [28] J. A. Hudson, E. T. Brown, and C. Fairhurst, "Shape of the complete stress-strain curve for rock," in *Stability of Rock Slopes: Proceedings of the 13th Symposium on Rock Mechanics*, E. J. Cording, Ed., pp. 773–795, ASCE, New York, NY, USA, 1971.
- [29] Livermore Software Technology Corporation (LSTC), *LS-DYNA Theory Manual*, 2006.
- [30] Livermore Software Technology Corporation (LSTC), *LS-DYNA Keyword Users Manual, Version 971*, 2007.
- [31] L. J. Malvar, J. E. Crawford, J. W. Wesevich, and D. Simons, "A plasticity concrete material model for DYNA3D," *International Journal of Impact Engineering*, vol. 19, no. 9-10, pp. 847–873, 1997.
- [32] P. Lu, S. Chen, and Y. Zheng, "Artificial intelligence in civil engineering," *Mathematical Problems in Engineering*, vol. 2013, Article ID 145974, 20 pages, 2013.
- [33] L. J. Malvar, J. E. Crawford, and K. B. Morrill, "K&C concrete material model release III—automated generation of material model input," Tech. Rep. TR-99-24-B1, K&C, 2000.
- [34] A. E. Schwartz, "Failure of rock in the triaxial test," in *Proceedings of the 6th Symposium on Rock Mechanics*, pp. 109–151, Rolla, Mo, USA, 1964.
- [35] R. Ulusay and J. A. Hudson, "Determining uniaxial compressive strength and deformability of rock materials," in *The Complete ISRM Suggested Methods for Rock Characterization, Testing and Monitoring: 1974–2006*, pp. 153–156, 1979.
- [36] M. R. A. van Vliet and J. G. M. van Mier, "Experimental investigation of concrete fracture under uniaxial compression," *Mechanics of Cohesive-Frictional Materials*, no. 1, pp. 115–127, 1996.

Research Article

Combined Data with Particle Swarm Optimization for Structural Damage Detection

Fei Kang,¹ Junjie Li,¹ and Sheng Liu²

¹ Faculty of Infrastructure Engineering, Dalian University of Technology, Dalian 116024, China

² College of Computer Science and Technology, Zhejiang University of Technology, Hangzhou 310023, China

Correspondence should be addressed to Fei Kang; kangfei@dlut.edu.cn

Received 23 October 2012; Accepted 11 December 2012

Academic Editor: Sheng-yong Chen

Copyright © 2013 Fei Kang et al. This is an open access article distributed under the Creative Commons Attribution License, which permits unrestricted use, distribution, and reproduction in any medium, provided the original work is properly cited.

This paper proposes a damage detection method based on combined data of static and modal tests using particle swarm optimization (PSO). To improve the performance of PSO, some immune properties such as selection, receptor editing, and vaccination are introduced into the basic PSO and an improved PSO algorithm is formed. Simulations on three benchmark functions show that the new algorithm performs better than PSO. The efficiency of the proposed damage detection method is tested on a clamped beam, and the results demonstrate that it is more efficient than PSO, differential evolution, and an adaptive real-parameter simulated annealing genetic algorithm.

1. Introduction

A structural system or mechanical component continuously accumulates damage during their service life. The presence of damages may reduce the performance of a structure, such as decreasing the service life, or even progressing to catastrophic failure. In recent years, the damage assessment of structures has drawn wide attention from various engineering fields. Structural damage usually causes a decrease in structural stiffness, which produces changes in the vibration characteristics and static displacements of the structure. Major damage detection approaches can be clarified into three major categories, the static identification methods using static test data [1, 2], the dynamic identification methods using vibration test data [3, 4], and the combination methods adopt both vibration data and static data [5]. The vibration data of a structure include natural frequencies, mode shapes, frequency response functions, and modal curvatures. Static responses generally include static displacements and static strain.

The usual damage detection methods minimize an objective function, which is defined in terms of the discrepancies between the vibration data or static data identified by testing and those which are computed from the analytical model.

Traditional damage detection methods have some disadvantages such as the damage position and damage extent cannot be detected simultaneously and are not so efficient in detecting the damage extent and adopt local optimization methods which usually lead to a local minimum only.

In recent years, evolutionary algorithms have been extensively applied to damage detection and the related optimal sensor placement problems [6–8]. For example, genetic algorithm (GA) as a stochastic search algorithm using static data [1, 2] or vibration data [3, 4] has been applied to damage detection. Some combination methods using both dynamic data and static data can be seen in [5, 9]. Damage detection methods of GA combining with simulated annealing [10] and artificial neural networks [11] were also proposed. In order to get more accurate structural parameters and structural responses for damage detection, parthenogenetic algorithm approach was proposed for optimal sensor placement [12, 13]. However, the disadvantage of GA is it exhibits a distinguished drop in efficiency as the number of unknown parameters to be identified is more than two [14] and premature convergence is likely to happen [15–19].

Addition to GA, some new techniques are proposed for engineering optimization problems, such as particle swarm optimization (PSO) [20–22], differential evolution [23, 24],

artificial bee colony (ABC) [25–28], and so on. Among these optimization algorithms, PSO has obtained the most extensive attention and applications. Although PSO shares many similarities with genetic algorithms, the standard PSO does not use genetic operators such as crossover and mutation. PSO is applied to structural damage detection problems. Meanwhile, to improve the convergence speed and accuracy, some immune mechanisms, such as selection, receptor editing, and vaccination, are incorporated into PSO and propose an immunity enhanced particle swarm optimization (IEPSO). The algorithm is applied to the benchmark function optimization and damage detection problems using combined data. Results show that the performance of PSO is improved, because the convergence speed is accelerated and the default, which is easily getting entrapped in a local optimum when solving complex multimodal problems, is meliorated. Compared with PSO, DE and an adaptive real-parameter simulated annealing genetic algorithm (ARSAGA), IEPSO is the most efficient optimization method for damage identification.

This paper is organized as follows. Section 2 presents the mathematical model for structural damage detection. Section 3 introduces the original PSO, several immune mechanisms and then IEPSO is proposed. Sections 4 and 5 shows the performance of IEPSO on function optimization and damage detection, respectively. Finally, conclusions are given in Section 6.

2. Mathematical Model for Structural Damage Detection Using Combined Data

The analytical static model for an intact structure in the finite-element formulation is

$$\mathbf{K}\mathbf{u} = \mathbf{p}. \quad (1)$$

The characteristic evaluation of a dynamic undamaged structure can be expressed as

$$\mathbf{K}\phi_i - \omega_i^2 \mathbf{M}\phi_i = 0. \quad (2)$$

In (1), \mathbf{K} is the structural stiffness matrix, \mathbf{u} is the displacement vector, and \mathbf{p} is the load vector. In (2), \mathbf{M} is the mass matrix, ω_i is the i th natural frequency, and ϕ_i is the corresponding mode shape.

In the context of discretized finite elements, structural damage can be represented by a decrease in the stiffness of the individual elements as

$$\mathbf{k}_d^e = \alpha_e \mathbf{k}^e, \quad (3)$$

where \mathbf{k}_d^e is the e th element stiffness matrix of the damaged structure, α_e is the stiffness damage factor (SDF) [13] of the e th element and is a value between 0 and 1. α_e is 1 with no damage and zero with complete damage in the e th element, respectively.

A uniform damage for the whole element has been assumed in (3). The SDF allows estimating not only the damage severity but also the damage location since the damage identification is carried out at the element level.

In general, a small number of sensors will result in nonunique solutions. The sparsity of measurement can be overcome by increasing the number of loading conditions instead of increasing the number of sensors [29]; So we adopt several load cases which have been used in [2, 10]. To combine the static responses (displacements) and dynamic responses (natural frequencies), the final objective function can be written as

$$f = \sum_{i=1}^{NL} \sum_{j=1}^{NP} \left(w_{ij} \left(\frac{u_{m,ij} - u_{th,ij}}{u_{m,ij}} \right) \right)^2 + \sum_{k=1}^{NF} \left(w_k \left(\frac{\omega_{m,k} - \omega_{th,k}}{\omega_{th,k}} \right) \right)^2, \quad (4)$$

where w_{ij} is a weight factor of the output error at the j th point due to the i th load case. NP is the number of displacement points considered and NL is the number of load cases. $u_{m,ij}$ is the measured displacement of the j th point due to the i th load case, and $u_{th,ij}$ is the theoretically computed counterpart. $\omega_{m,k}$ is the k th measured natural frequency, and $\omega_{th,k}$ is the k th theoretically computed natural frequency. w_k is a weighting factor for the output error of the k th natural frequency. NF is the number of natural frequencies considered.

The first part is defined by the normalized difference between the measured and theoretical computed displacements. The second part is defined by the normalized difference between the measured and theoretically computed natural frequencies. Differences between displacements and natural frequencies are normalized to get a better representation of the relative change in response.

To include the uncertainty in the measured data and to study the sensitivity of IEPSO to noise, uniformly distributed random noise [2] is added to measurements in the simulated tests as

$$\begin{aligned} u'_{m,ij} &= u_{m,ij} (1 + \beta e) \\ \omega'_{m,k} &= \omega_{m,k} (1 + \gamma e), \end{aligned} \quad (5)$$

where $u'_{m,ij}$ is the measured displacement of the j th point due to the i th load case with noise; $\omega'_{m,k}$ is the k th measured natural frequency with noise; β and γ are the noise amplitudes; e is a uniformly distributed random variable in the range $[-1, 1]$.

3. Immunity-Enhanced Particle Swarm Optimization

3.1. Particle Swarm Optimization. Inspired by a model of social interactions between independent animals seeking for food, PSO utilizes swarm intelligence to achieve the goal of optimization. Instead of using genetic operators to manipulate the individuals, each individual in PSO flies in the search space with a velocity which is dynamically adjusted according to its own flying experience and flying experience of its companions [20, 21]. Each individual is treated as a volumeless particle (a point) in the D -dimensional search space. The i th particle is represented as $\mathbf{x}_i = (x_{i1}, x_{i2}, \dots, x_{iD})$ in the D -dimensional space, where $x_{id} \in [l_d, u_d]$, $d \in [1, D]$. The best previous position of the i th particle is recorded

as $\mathbf{p}_i = (p_{i1}, p_{i2}, \dots, p_{iD})$. The index of the best particle among all the particles in the population is represented by the symbol g . The velocity for particle i is represented as $\mathbf{v}_i = (v_{i1}, v_{i2}, \dots, v_{iD})$, which is clamped to a maximum velocity V_{\max} . In each time step t , the particles are manipulated according to the following equations:

$$v_{id} = v_{id} + r_1 c_1 (p_{id} - x_{id}) + r_2 c_2 (p_{gd} - x_{id}) \quad (6)$$

$$x_{id} = x_{id} + v_{id}, \quad (7)$$

where c_1 and c_2 are two positive constants, which control how far a particle will move in a single iteration. r_1 and r_2 are random values in the range $[0, 1]$.

Shi and Eberhart [21] later introduced inertia term w term by modifying (6) to

$$v_{id} = w v_{id} + r_1 c_1 (p_{id} - x_{id}) + r_2 c_2 (p_{gd} - x_{id}). \quad (8)$$

They proposed that suitable selection of w will provide a balance between global and local explorations, thus requiring fewer iterations on average to find a sufficiently optimal solution. As originally developed, w often decrease linearly from about 0.9 to 0.4 according to the following equation:

$$w = w_{\max} - \frac{w_{\max} - w_{\min}}{t_{\max}} \times t, \quad (9)$$

where w_{\max} and w_{\min} are the initial weight and final weight, respectively, t_{\max} is the maximum number of allowable generations, and t the current generation number.

An explicit maximum velocity or a constriction factor is usually utilized in PSO algorithms to control the exploration abilities of particles; however, it cannot prevent them from going outside the allowable solution space and hence produce invalid solutions. Four types of boundary conditions, namely, absorbing, reflecting, invisible, and damping, have been reported in the literature [30]. The optimization of a 2D array antenna [31] shows that the damping boundary condition offers more robust and consistent performance.

As for damage detection problem, generally only few elements are damaged and most elements are still intact. The parameter values of these intact elements are always in the upper bound [9]. In order to avoid oscillating around the upper boundary and to quickly return to the feasible region around the lower boundary, a combined boundary condition is used. This boundary is also convenient to the comparison of different algorithms. The upper bound adopts damping bound [30] and the low bound adopts the bound described in [24], which can be described as follows:

$$x_{id} = \begin{cases} l_d + (l_d - x_{id}) & x_{id} < l_d \\ u_d & x_{id} > u_d \end{cases} \quad (10)$$

$$v_{id} = -\text{rand}() \cdot v_{id} \quad x_{id} < l_d \text{ or } x_{id} > u_d,$$

where l_d and u_d are the lower and upper bounds of dimension d , respectively, $\text{rand}()$ is a random number in the range $[0, 1]$.

3.2. Artificial Immune System. AIS can be defined as abstract computational systems inspired by theoretical immunology and observed immune functions, principles, and models, applied to solve problems [32]. In AIS, an antigen is used to represent the programming problem to be addressed. An antibody is set (a repertoire), wherein each member represents a candidate solution. Affinity is used to represent the fit of an antibody (a solution candidate) to the antigen (the problem) [33]. Several immune properties, selection, receptor editing, and vaccination, can be adopted to improve the performance of PSO.

3.2.1. Selection. The antibodies present in a population set contain much information regarding the solution of the problem. Based on their affinity, the antibodies are selected to proliferate and produce clones. Traditionally, deterministic selection rule is adopted to select better antibodies for proliferation. However, deterministic selection rule selects only the best antibodies for proliferation, and that may lead to the premature convergence of the algorithm [34].

To overcome this difficulty, rank-based fitness assignment and roulette wheel selection rule is adopted. The fitness of an individual can be calculated as

$$\text{fitpos} = 2 - \text{sp} + \frac{2(\text{sp} - 1)(\text{pos} - 1)}{(N - 1)}, \quad (11)$$

where N is the population size, pos is the order number of the individual in the whole population, sp is the selection pressure, $\text{sp} \in [1.0, 2.0]$, fitpos is the rank-based fitness of the individual.

3.2.2. Receptor Editing. In AIS, receptor editing allows an antibody to take large steps, landing in a locale where the affinity might be lower. However, occasionally the leap will lead to an antibody on the side where the region is more promising. From this locale, point mutations followed by selection can drive the antibody to reach the global optimum. Receptor editing offers the ability to escape from local optima [32]. In order to simulate receptor editing, we introduce non-uniform mutation [35] into PSO.

For each individual $\mathbf{x}_i(t)$ in a population of generation t , create an offspring $\mathbf{x}_i(t+1)$ through a non-uniform mutation as follows: if $\mathbf{x}_i(t) = \{x_{i1}, \dots, x_{id}, \dots, x_{iD}\}$ is a solution and the element x_{id} is selected for this mutation, the result is a vector $\mathbf{x}_i(t+1) = \{x_{i1}, \dots, x'_{id}, \dots, x_{iD}\}$, where

$$x'_{id} = \begin{cases} x_{id} + \Delta(t, u_d - x_{id}) & \text{if a random } \xi \text{ is } 0 \\ x_{id} - \Delta(t, x_{id} - l_d) & \text{if a random } \xi \text{ is } 1, \end{cases} \quad (12)$$

where l_d and u_d are the lower and upper bounds of the variable x_{id} , respectively. The function $\Delta(t, y)$ returns a value in the range $[0, y]$ such that $\Delta(t, y)$ approaches to zero as t increases. This property allows this operator to search the space uniformly at early stages, and very locally at later stages. We use the following function:

$$\Delta(t, y) = y \cdot \left(1 - r^{(1-t/T)^b}\right), \quad (13)$$


```

Algorithm IEPSO
Begin;
Initialize the population (generate a random population of  $N$  solutions);
For  $i = 1$  to the maximum number of generations;
  For each individual  $j \in N$ ;
    Evolving individual  $j$  according to (7) and (8);
    If (rand () <  $p_r$ ) receptor editing;
    If (rand () <  $p_v$ ) vaccination;
    Evaluate individual  $j$ ;
    If (fit ( $j$ ) <  $\mathbf{p}_j$ ) Update the best position of individual  $j$ ;
    If (fit ( $j$ ) <  $\mathbf{p}_g$ ) Update the best position of the whole population;
  End;
  Selection;
  Calculate  $w$  of each individual according to (9);
Next  $i$ ;
End;

```

ALGORITHM 1: Pseudocodes for IEPSO algorithm.

where r is a uniform random number in the range $[0, 1]$, and b is a system parameter determining the degree of nonuniformity.

3.2.3. Vaccination. Given an individual \mathbf{x} , vaccination means modifying the genes on some bits in accordance with a priori knowledge so as to gain a better solution with greater probability [36]. As for real-parameter optimization problems, a vaccination means modifying the elements of some individuals. A vaccine is abstracted from the prior knowledge of the problem. During the actual operation, a detailed analysis is firstly carried out on the problem, simultaneously, as many basic characteristics of the problem as possible ought to be found. Then, the characteristics are abstracted to be a vaccine. A vaccine can also be regarded as estimation on some elements of the optimal individual.

Two types of vaccines are adopted for function optimization and damage detection. For the function optimization problem, the vaccine can be abstracted from the best individuals of the population. If $\mathbf{x}_i(t) = \{x_{i1}, \dots, x_{id}, \dots, x_{iD}\}$ is an individual and the element x_k is selected for vaccination, the result is a vector $\mathbf{x}_i(t+1) = \{x_{i1}, \dots, x_{id\text{best}}, \dots, x_{iD}\}$, where $x_{id\text{best}}$ means the d th element of the best individual. For the damage detection problem, generally only few elements are damaged and most elements are still intact. The parameter values of these intact elements are always in the upper bound. So boundary mutation is adopted as a vaccine for damage detection problem. If $\mathbf{x}_i(t) = \{x_{i1}, \dots, x_{id}, \dots, x_{iD}\}$ is an individual and the element x_{id} is selected for vaccination, the result is a vector: $\mathbf{x}_i(t+1) = \{x_{i1}, \dots, u_d, \dots, x_{iD}\}$.

3.3. Immunity-Enhanced Particle Swarm Optimization. In IEPSO, a population of particles is sampled randomly in the feasible space. Then the population executes PSO or its variants, including the update of position and velocity. After that, it executes receptor editing operator (non-uniform mutation) according to a certain probability p_r , and vaccination operator according to probability p_v . The

new generation is obtained by the selection operator after the flying of particles and two immune operators (receptor editing and vaccination). Pseudocodes for IEPSO are shown in Algorithm 1.

In Algorithm 1, p_r is the receptor editing probability; p_v is the vaccination probability; \mathbf{p}_j is the best position of individual j ; \mathbf{p}_g is the best position of the whole population; $\text{fit}(j)$ is the fitness of individual j .

In the new algorithm, selection and vaccination can improve the convergence speed and receptor editing, helping the algorithm to avoid premature convergence.

4. Tests on Benchmark Functions

Three nonlinear benchmark functions that are commonly used in literatures are adopted. Their formulas and variable ranges are shown in Table 1.

To evaluate the performance of the proposed IEPSO, the basic PSO and DE are used for comparisons. The version of DE used in this paper is known as DE/rand/1/bin, or “classic DE” [23].

The parameters used for IEPSO and PSO are recommended in [21, 22]. The parameter w used is recommended by Shi and Eberhart [21] with a linearly decreasing, which changes from 0.9 to 0.4 according to (9). The maximum velocity V_{\max} and minimum velocity V_{\min} are set at half value of the upper bound and lower bound, respectively. The acceleration constants c_1 and c_2 are both 2.0. For DE algorithm, the parameters are recommended in [23, 24]. The control parameters are $F = 0.9$ or 0.5 and $\text{Cr} = 0.9$. The other parameters for IEPSO are listed in Table 2. The generation number and population size of PSO and DE are the same as IEPSO.

The three algorithms are executed in 50 independent runs. The mean fitness values of the best individual found during the 50 runs for the three functions are listed in Table 3. Evolutionary processes for three functions are shown in Figure 1. From Table 3 and Figure 1, it can be seen that IEPSO outperforms PSO and DE in most cases. By introducing

TABLE 1: Benchmark test functions.

Name	Formula	n	Range
Sphere	$f_1(x) = \sum_{i=1}^n x_i^2$	30	$[-100, 100]^n$
Rosenbrock	$f_2(x) = \sum_{i=1}^{n-1} (100(x_{i+1} - x_i^2)^2 + (x_i - 1)^2)$	30	$[-30, 30]^n$
Rastrigin	$f_3(x) = \sum_{i=1}^n (x_i^2 - 10 \cos(2\pi x_i) + 10)$	30	$[-5.12, 5.12]^n$

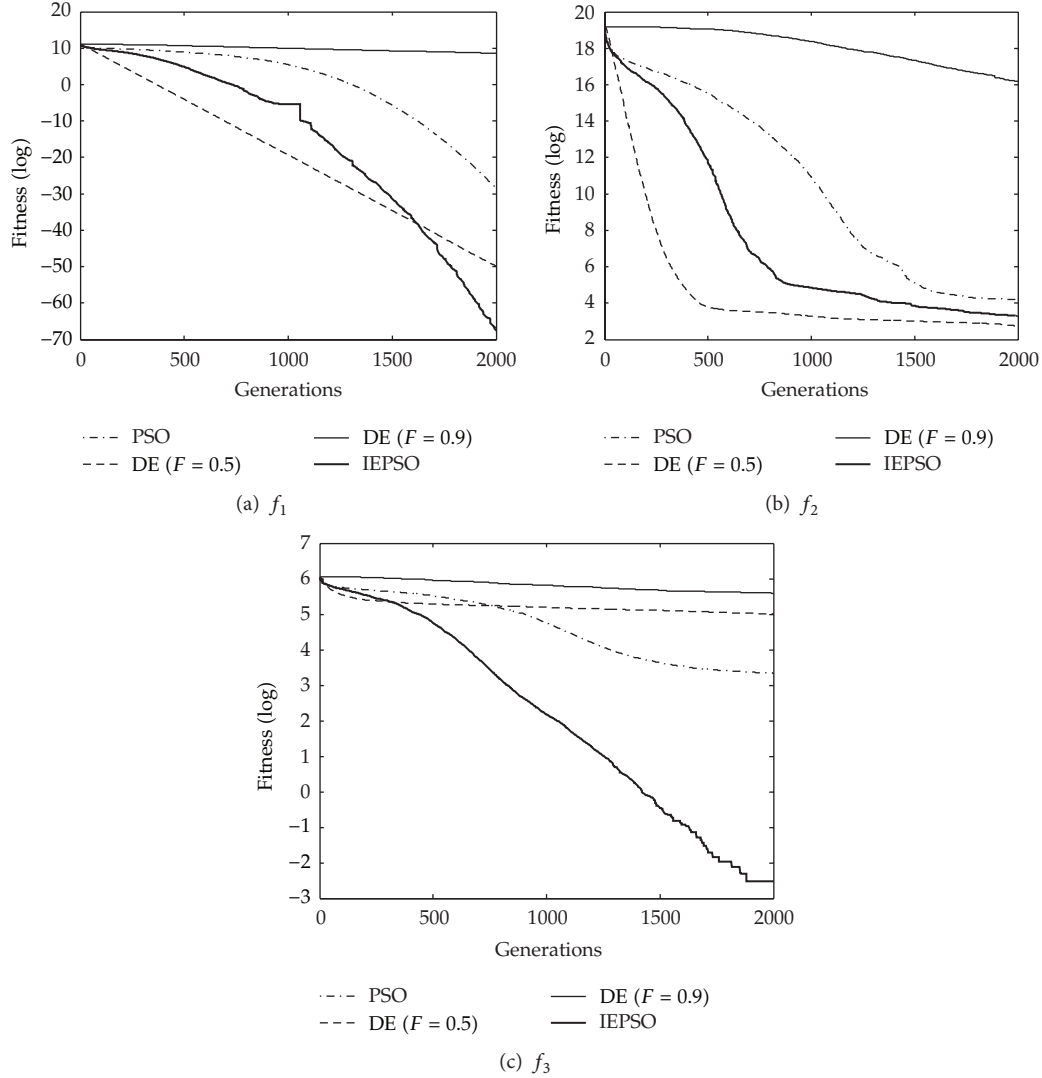


FIGURE 1: Convergence processes of mean best fitness for three benchmark functions.

selection operator and vaccination operator, the convergence speed is accelerated and by introducing receptor editing operator, the ability of escaping from a local optimum is enhanced.

5. Damage Detection Examples

A clamped beam adopted from Wang et al. [9] is used to verify the efficiency of IEPso on damage identification. The initial geometry of the beam is shown in Figure 2. The total

numbers of elements and nodes are 20 and 21, respectively. There are two applied load cases. The first load case $P_1 = 50$ N and acts at node 11, and the second load case $P_2 = 50$ N and acts at node six. The material properties are $E = 70.0$ GPa, $\rho = 2.70 \times 10^3$ kg/m³. In the following tests the objective functions include nineteen node displacements in each load case and the first 10 natural frequencies. The weight factor in (13) is chosen as $w_{ij} = w_k = 1000$.

Statistical analysis is a good way to compare different stochastic algorithms. But the damage detection of a structure

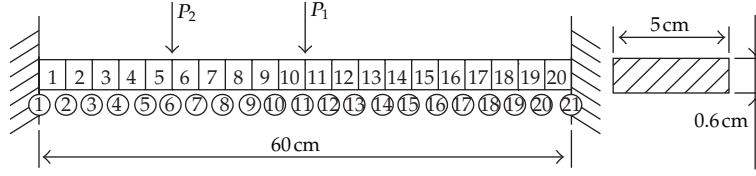


FIGURE 2: A clamped beam and its cross-section.

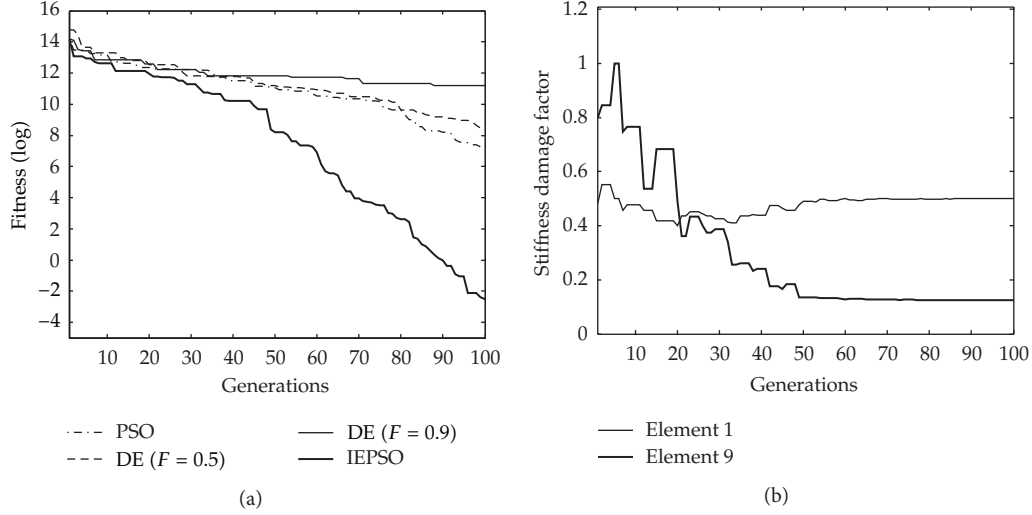


FIGURE 3: Convergence processes in case 1: (a) best fitness; (b) SDFs of damaged elements.

TABLE 2: Parameter values used in IEPSO.

Parameter	Function optimization	Damage detection
Generation number	2000	100
Population size	80	40
P_r	0.1	0.05
P_v	0.1	0.25
SP	1.8	1.8
b	5	5

TABLE 3: Mean best fitness values of three functions.

Function	DE	PSO	IEPSO
f_1	$2.06e - 22$	$4.42e - 13$	$4.61e - 30$
f_2	$1.56e + 01$	$6.73e + 01$	$2.69e + 01$
f_3	$1.49e + 02$	$2.82e + 01$	$7.96e - 02$

needs a long time. To compare different stochastic algorithms on these time-consuming problems, usually adopt the best results obtained from several runs, and this can avoid chance in some extent [37, 38]. In this paper each stochastic algorithm performs three independent runs [14, 26], and the best results obtained from each algorithm are presented as

representative ones to yield more clear conclusions because values obtained are not much different.

5.1. Double Damage Occurrence. The first case (case 1) has two damages in which element 1 has 50% reduction in Young's modulus and element 9 has a severe 87.5% reduction in Young's modulus. That means $\alpha_1 = 0.5$ and $\alpha_9 = 0.125$ in this case.

The comparison of logarithmic best fitness values of three algorithms is shown in Figure 3(a). From this figure, we can see that IEPSO converges the fastest and PSO converges faster than DE. The convergence processes of SDF of damaged elements are shown in Figure 3(b). It can be seen that the SDF of element 1 and element 9 quickly converges to 0.49998 and 0.12504 which are quite close to the theoretical values. The comparison of SDF of each element between theoretical values and IEPSO detected values is shown in Figure 4(a). It can be seen that the detected values are quite close to the theoretical values and no extra damage is detected. The comparison of damage detection results using three algorithms after 100 generations is shown in Figure 4(b). It can be seen that IEPSO outperforms PSO and DE.

5.2. Triple Tiny Damage Occurrence. A triple damage occurrence with different damage extents (case 2) is considered. In this example, element 2 has 10% reduction in Young's

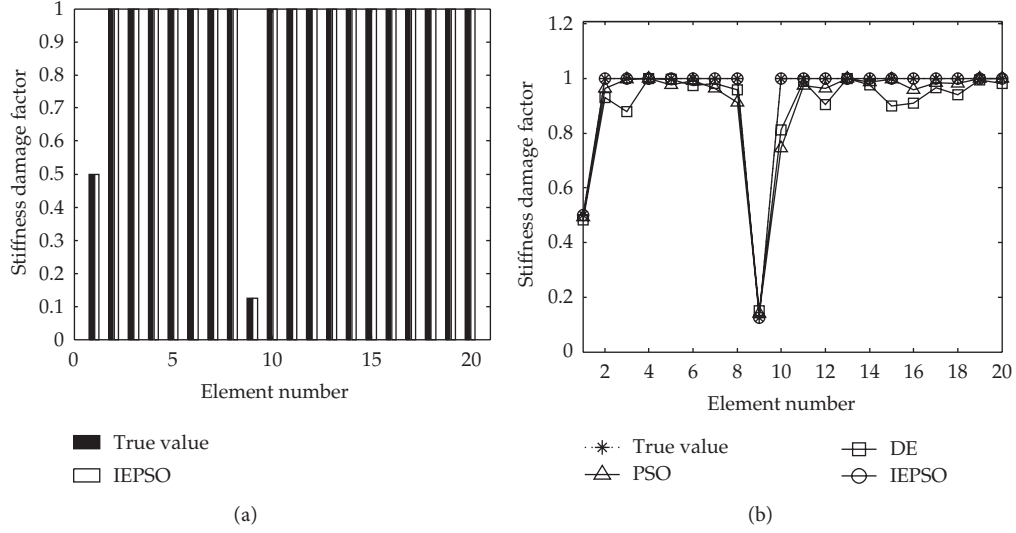


FIGURE 4: Comparison of damage detection results in case 1: (a) between theoretical value and IEPSO detected value; (b) between different algorithms.

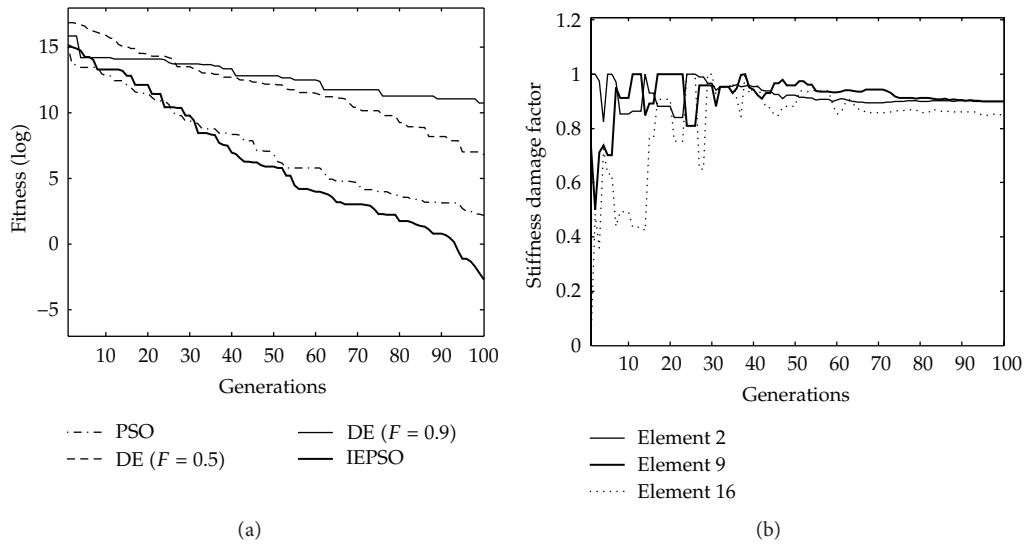


FIGURE 5: Convergence processes in case 3: (a) best fitness; (b) SDFs of damaged elements.

modulus, element 9 has 10% reduction in Young's modulus, and element 16 has 15% reduction in Young's modulus. This means that $\alpha_2 = 0.9$, $\alpha_9 = 0.9$, and $\alpha_{16} = 0.85$. It is noted that all the three damage extents are very tiny, and the difficulty in damage detection is increased.

The comparison of logarithmic best fitness values of three algorithms is shown in Figure 5(a). From this figure, we can see that IEPSO still converge the fastest and PSO converges faster than DE. The convergence processes of SDF of damaged elements are shown in Figure 5(b). It can be seen that the SDF of element 2, element 9, and element 16 quickly converges to 0.90015, 0.90101, and 0.85091 which are quite close to the theoretical values. The comparison of SDF of each element between theoretical values and IEPSO detected values is shown in Figure 6(a). It can be seen that the detected

values are quite close to the theoretical values and no extra damage is detected. The comparison of damage detection results using three algorithms after 100 generations is shown in Figure 6(b). It can be seen that IEPSO still performs better than PSO and DE.

Damage detection performance of IEPSO is also compared with ARSAGA [10] in this case and the result is shown in Table 4. The value in the parenthesis represents the relative error. The damaged elements and the maximum errors of different algorithms are shown in bold. It can be seen that damage detection accuracy of IEPSO is higher than ARSAGA.

5.3. The Effect of Noise. To include the uncertainty in the measured data and to study the sensitivity of IEPSO to

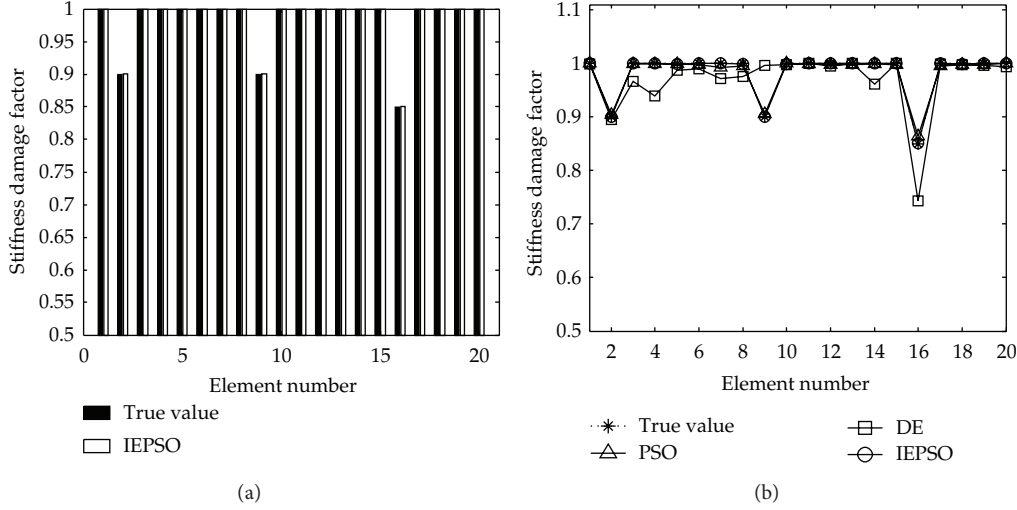


FIGURE 6: Comparison of damage detection results in case 3: (a) between theoretical value and IEPSO detected value; (b) between different algorithms.

TABLE 4: Comparison of damage detection results of case one by ARSAGA and IEPSO.

Element no.	Stiffness damage factors		
	Exact	ARSAGA	IEPSO
1	1.0	0.963 (−3.7%)	1.0
2	0.9	0.914	0.9
3	1.0	1.0	1.0
4	1.0	0.984	0.999
5	1.0	0.992	1.0
6	1.0	1.0	1.0
7	1.0	1.0	1.0
8	1.0	0.978	0.999
9	0.9	0.905	0.901
10	1.0	1.0	1.0
11	1.0	1.0	1.0
12	1.0	0.987	1.0
13	1.0	1.0	1.0
14	1.0	0.991	1.0
15	1.0	1.0	1.0
16	0.85	0.852	0.851 (0.12%)
17	1.0	1.0	1.0
18	1.0	1.0	0.999
19	1.0	1.0	1.0
20	1.0	1.0	1.0

noise, different uniformly distributed random noise is added to measured data in the simulation as described (5). It is commonly believed that the relative measurement error of frequency is about 1% [3]. Take case 1 as an example, in the first test 1% noise is added to both static displacements and natural frequencies. In the second test 5% noise is added to static displacements and 2% noise is added to natural frequencies.

The comparison of SDF of each element between theoretical values and IEPSO detected values under the condition 1% noise is shown in Figure 7(a). It can be seen that the detected values are still quite close to the true values and a tiny extra damage is detected in element 19. The comparison of SDF of each element between theoretical values and IEPSO detected values under the condition with 5% noise is shown in Figure 7(b). It can be seen that the two damages can still be detected under this condition, but several tiny extra damages are also detected.

It can be seen from these figures that noise decreases the accuracy of the algorithm. When noise increases, the misidentifications also increase. This may be because that large noise increases the uncertainty in theoretical response data and noise may be taken as damage by the procedure. From this point, the results detected by the procedure are still reasonable.

6. Conclusions

In this paper, a new IEPSO algorithm for structural damage identification is presented. It bases on a particle swarm optimization algorithm and introduces immune properties selection, receptor editing, and vaccination into it. Selection and vaccination can improve the convergence speed and receptor editing helps the algorithm to avoid premature convergence.

Boundary conditions for PSO are also discussed in the paper, and a combined boundary is adopted for damage detection problems. This boundary condition can avoid oscillating around the upper boundary and can quickly return to the feasible region around the lower boundary.

The feasibility of the methodology is first demonstrated through several numerical examples. Three benchmark functions are used to test the performance of IEPSO in complex function optimization problems. Numerical results show that IEPSO performs better than PSO and DE in most cases

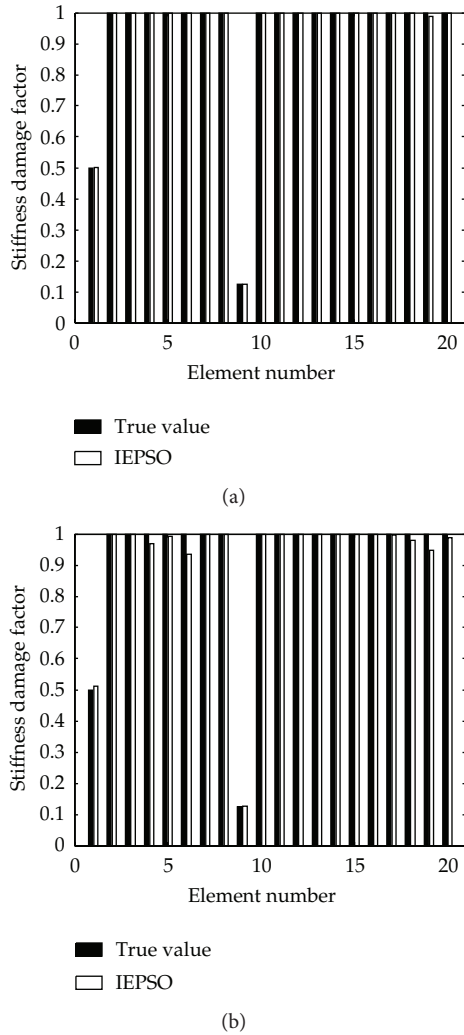


FIGURE 7: Comparison of damage detection results in case 1 with noise: (a) 1% noise is added to both static displacements and natural frequencies; (b) 5% noise is added to static displacements and 2% noise is added to natural frequencies.

because its convergence speed is the fastest and converges to the best fitness value.

The proposed algorithm is then tested on damage detection problems of a clamped beam. Two damage cases can be detected quickly and accurately by the proposed algorithm when noise is free. Comparing with PSO and DE, IEP SO is more efficient in damage detection problems. The accuracy of IEP SO is also higher than ARSAGA in case 2. When different levels of noise are added, the accuracy of the algorithm is decreased. However, this is still reasonable because noise may be taken as damages in the beam during the damage detection process.

Acknowledgments

This work was supported by the National Natural Science Foundation of China (51109028, 90815024) and the

Fundamental Research Funds for the Central Universities (DUT11RC(3)38).

References

- [1] F. Bakhtiari-Nejad, A. Rahai, and A. Esfandiari, "A structural damage detection method using static noisy data," *Engineering Structures*, vol. 27, no. 12, pp. 1784–1793, 2005.
- [2] B. Kouchmeshky, W. Aquino, J. C. Bongard, and H. Lipson, "Co-evolutionary algorithm for structural damage identification using minimal physical testing," *International Journal for Numerical Methods in Engineering*, vol. 69, no. 5, pp. 1085–1107, 2007.
- [3] B. H. Koh and S. J. Dyke, "Structural health monitoring for flexible bridge structures using correlation and sensitivity of modal data," *Computers and Structures*, vol. 85, no. 3–4, pp. 117–130, 2007.
- [4] F. Kang, J. J. Li, and Q. Xu, "Damage detection based on improved particle swarm optimization using vibration data," *Applied Soft Computing*, vol. 12, no. 8, pp. 2329–2335, 2012.
- [5] B. H. Oh and B. S. Jung, "Structural damage assessment with combined data of static and modal tests," *Journal of Structural Engineering*, vol. 124, no. 8, pp. 956–965, 1998.
- [6] S. Y. Chen, Y. J. Zheng, C. Cattani, and W. L. Wang, "Modeling of biological intelligence for SCM system optimization," *Computational and Mathematical Methods in Medicine*, vol. 2012, Article ID 769702, 10 pages, 2012.
- [7] P. Z. Lu, S. Y. Chen, and Y. J. Zheng, "Artificial intelligence in civil engineering," *Mathematical Problems in Engineering*, vol. 2012, Article ID 145974, 22 pages, 2012.
- [8] S. Y. Chen and Y. F. Li, "Automatic sensor placement for model-based robot vision," *IEEE Transactions on Systems, Man, and Cybernetics B*, vol. 34, no. 1, pp. 393–408, 2004.
- [9] X. Wang, N. Hu, H. Fukunaga, and Z. H. Yao, "Structural damage identification using static test data and changes in frequencies," *Engineering Structures*, vol. 23, no. 6, pp. 610–621, 2001.
- [10] R. S. He and S. F. Hwang, "Damage detection by an adaptive real-parameter simulated annealing genetic algorithm," *Computers and Structures*, vol. 84, no. 31–32, pp. 2231–2243, 2006.
- [11] B. Sahoo and D. Maity, "Damage assessment of structures using hybrid neuro-genetic algorithm," *Applied Soft Computing Journal*, vol. 7, no. 1, pp. 89–104, 2007.
- [12] F. Kang, J. J. Li, and Q. Xu, "Strategy for optimizing sensor placement related to structural health monitoring," in *Proceeding of International Conference on Health Monitoring of Structure, Material and Environment*, pp. 474–478, Southeast University Press, Nanjing, China, 2007.
- [13] F. Kang, J. J. Li, and Q. Xu, "Virus coevolution partheno-genetic algorithms for optimal sensor placement," *Advanced Engineering Informatics*, vol. 22, no. 3, pp. 362–370, 2008.
- [14] K. H. Lee, S. W. Baek, and K. W. Kim, "Inverse radiation analysis using repulsive particle swarm optimization algorithm," *International Journal of Heat and Mass Transfer*, vol. 51, no. 11–12, pp. 2772–2783, 2008.
- [15] S. Y. Chen, C. Y. Yao, G. Xiao, Y. S. Ying, and W. L. Wang, "Fault detection and prediction of clocks and timers based on computer audition and probabilistic neural networks," in *Computational Intelligence and Bioinspired Systems*, vol. 3512 of *Lecture Notes on Computer Science*, pp. 952–959, 2005.
- [16] M. Li, S. C. Lim, and S. Chen, "Exact solution of impulse response to a class of fractional oscillators and its stability,"

- Mathematical Problems in Engineering*, vol. 2011, Article ID 657839, 9 pages, 2011.
- [17] S. C. Lim, C. H. Eab, K. H. Mak, M. Li, and S. Y. Chen, "Solving linear coupled fractional differential equations by direct operational method and some applications," *Mathematical Problems in Engineering*, vol. 2012, Article ID 653939, 28 pages, 2012.
 - [18] S. Y. Chen, Y. H. Wang, and C. Cattani, "Key issues in modeling of complex 3D structures from video sequences," *Mathematical Problems in Engineering*, vol. 2012, Article ID 856523, 17 pages, 2012.
 - [19] Z. Teng, J. He, A. J. Degnan et al., "Critical mechanical conditions around neovessels in carotid atherosclerotic plaque may promote intraplaque hemorrhage," *Atherosclerosis*, vol. 223, no. 2, pp. 321–326, 2012.
 - [20] J. Kennedy and R. C. Eberhart, "Particle swarm optimization," in *Proceedings of the IEEE International Conference on Neural Networks*, pp. 1942–1948, December 1995.
 - [21] Y. Shi and R. C. Eberhart, "A modified particle swarm optimizer," in *Proceedings of the IEEE International Conference on Evolutionary Computation (ICEC '98)*, pp. 69–73, May 1998.
 - [22] Y. Shi and R. C. Eberhart, "Empirical study of particle swarm optimization," in *Proceeding of the IEEE Congress on Evolutionary Computation (CEC '99)*, pp. 1945–1950, July 1999.
 - [23] R. Storn and K. Price, "Differential evolution—a simple and efficient heuristic for global optimization over continuous spaces," *Journal of Global Optimization*, vol. 11, no. 4, pp. 341–359, 1997.
 - [24] J. Rönkkönen, S. Kukkonen, and K. V. Price, "Real-parameter optimization with differential evolution," in *Proceedings of the IEEE Congress on Evolutionary Computation (CEC '05)*, pp. 506–513, Edinburgh, Scotland, September 2005.
 - [25] D. Karaboga and B. Basturk, "A powerful and efficient algorithm for numerical function optimization: artificial bee colony (ABC) algorithm," *Journal of Global Optimization*, vol. 39, no. 3, pp. 459–471, 2007.
 - [26] F. Kang, J. J. Li, and Q. Xu, "Structural inverse analysis by hybrid simplex artificial bee colony algorithms," *Computers and Structures*, vol. 87, no. 13–14, pp. 861–870, 2009.
 - [27] F. Kang, J. Li, and Z. Ma, "Rosenbrock artificial bee colony algorithm for accurate global optimization of numerical functions," *Information Sciences*, vol. 181, no. 16, pp. 3508–3531, 2011.
 - [28] F. Kang, J. Li, and Z. Ma, "An artificial bee colony algorithm for locating the criticalslip surface in slope stability analysis," *Engineering Optimization*. In press.
 - [29] I. Y. Choi, J. S. Lee, E. Choi, and H. N. Cho, "Development of elastic damage load theorem for damage detection in a statically determinate beam," *Computers and Structures*, vol. 82, no. 29–30, pp. 2483–2492, 2004.
 - [30] T. Huang and A. S. Mohan, "A hybrid boundary condition for robust particle swarm optimization," *IEEE Antennas and Wireless Propagation Letters*, vol. 4, no. 1, pp. 112–117, 2005.
 - [31] S. H. Xu and Y. Rahmat-Samii, "Boundary conditions in particle swarm optimization revisited," *IEEE Transactions on Antennas and Propagation*, vol. 55, no. 3, pp. 760–765, 2007.
 - [32] L. N. de Castro and J. I. Timmis, *Artificial Immune Systems: A New Computational Intelligence Paradigm*, Springer, New York, NY, USA, 2002.
 - [33] P. Musilek, A. Lau, M. Reformat, and L. Wyard-Scott, "Immune programming," *Information Sciences*, vol. 176, no. 8, pp. 972–1002, 2006.
 - [34] N. Khilwani, A. Prakash, R. Shankar, and M. K. Tiwari, "Fast clonal algorithm," *Engineering Applications of Artificial Intelligence*, vol. 21, no. 1, pp. 106–128, 2008.
 - [35] X. C. Zhao, X. S. Gao, and Z. C. Hu, "Evolutionary programming based on non-uniform mutation," *Applied Mathematics and Computation*, vol. 192, no. 1, pp. 1–11, 2007.
 - [36] L. C. Jiao and L. Wang, "A novel genetic algorithm based on immunity," *IEEE Transactions on Systems, Man, and Cybernetics A*, vol. 30, no. 5, pp. 552–561, 2000.
 - [37] T. Yi, H. Li, and X. Zhang, "Sensor placement on Canton Tower for health monitoring using asynchronous-climbing monkey algorithm," *Smart Materials and Structures*, vol. 21, no. 12, pp. 1–12, 2012.
 - [38] T. Yi, H. Li, and M. Gu, "Optimal sensor placement for structural health monitoring based on multiple optimization strategies," *The Structural Design of Tall and Special Buildings*, vol. 20, no. 7, pp. 881–900, 2011.

Research Article

Inverse Parametric Analysis of Seismic Permanent Deformation for Earth-Rockfill Dams Using Artificial Neural Networks

Xu Wang,¹ Fei Kang,¹ Junjie Li,¹ and Xin Wang²

¹ Faculty of Infrastructure Engineering, Dalian University of Technology, Dalian, Liaoning 116024, China

² College of Computer Science and Technology, Zhejiang University of Technology, Hangzhou, Zhejiang 310023, China

Correspondence should be addressed to Fei Kang, kangfei@dlut.edu.cn

Received 27 October 2012; Accepted 3 December 2012

Academic Editor: Sheng-yong Chen

Copyright © 2012 Xu Wang et al. This is an open access article distributed under the Creative Commons Attribution License, which permits unrestricted use, distribution, and reproduction in any medium, provided the original work is properly cited.

This paper investigates the potential application of artificial neural networks in permanent deformation parameter identification for rockfill dams. Two kinds of neural network models, multilayer feedforward network (BP) and radial basis function (RBF) networks, are adopted to identify the parameters of seismic permanent deformation for Zipingpu Dam in China. The dynamic analysis is carried out by three-dimensional finite element method, and earthquake-induced permanent deformation is calculated by an equivalent nodal force method. Based on the sensitivity analysis of permanent deformation parameters, an objective function for network training is established by considering parameter sensitivity, which can improve the accuracy of parameter identification. By comparison, it is found that RBF outperforms the BP network in this problem. The proposed inverse analysis model for earth-rockfill dams can identify the seismic deformation parameters with just a small amount of sample designs, and much calculation time can be saved by this method.

1. Introduction

The dynamic response of rockfill dams under earthquake actions, mainly including absolute acceleration and permanent deformation, attracts more and more attention from engineers. The former is used to assess the dynamical load and seismic resistance of the dam. The latter is adopted to provide a basis for the dam height reserved during the design phase. So the prediction of permanent deformation is an essential problem in the seismic design for rockfill dams. As a result, it is important to select model parameters of rockfill dams reasonably, which makes for improving the accuracy of the numerical calculation.

However, it is not easy to carry out. Because of the difference of construction technology and construction quality and so on, the spatial distribution of material properties

is considerably random in each project. Along with the development of construction technology, the maximum particle size of materials of rockfill dams may be bigger and bigger, but the model parameters are usually measured in the laboratory by using samples with much smaller size. The prepared experimental samples in the laboratory are different from the construction conditions. Therefore, the mechanical properties of samples determined in the laboratory may be more or less differing from those in situ. And then the stress and deformation acquired with laboratory parameters deviate far from the actual values inevitably. As a consequence, it is necessary to take measures to get model parameters in accord with the results of dam observation and make an accurate evaluation of dam safety and stability after that. Displacement backanalysis is an effective method to check and modify the parameters of soils.

In recent years, reverse analysis is mainly based on two methodologies: optimization algorithms and neural networks [1–5]. There are three types of optimization algorithms that have been frequently used in inverse analysis. The first type is gradient-based direct search algorithms, such as Levenberg-Marquardt method. The second type is the relatively simple direct search methods making no use of gradient, such as the simplex search method. The last type is kinds of intelligent global search algorithms, such as genetic algorithms, differential evolution, particle swarm optimization, and ant colony optimization. The first and the second type algorithms both have an advantage of estimating the solutions in relatively short computational time, but the results are affected by the initial values, and premature convergence is likely to happen. As an alternative to the direct search algorithms, intelligent global search algorithms are being widely adopted in reverse analysis, but they have a disadvantage of being time consuming.

In the geotechnical engineering field, intelligent backanalysis methods based on artificial neural networks (ANNs) and genetic algorithms [6, 7] are often adopted. As for generic algorithms, the range and trial values of the undetermined parameters should be given before the analysis, and then the time-consuming finite element method (FEM) calculation is performed repeatedly, so it is hard to ideally solve complicated nonlinear problems with a lot of finite elements. That is why it has been primarily used for seeking answers to static problems and two-dimensional problems so far. They need relatively few iterations and finite elements. Comparatively speaking, the strong nonlinear relationship between the known and unknown quantity in geotechnical engineering can be mapped well by using ANNs. And neural network approach can obtain inversion parameters quickly with just a small amount of sample designs.

The aim of this paper is to present an inverse analysis model for seismic permanent deformation parameters of earth-rockfill dams based on artificial neural networks. Section 2 presents the theories of forward computational models for static analysis, dynamic response analysis, permanent deformation analysis, and sensitivity analysis of design parameters. Section 3 introduces backpropagation neural networks (BPNNs) and radial basis function neural networks (RBFNNs). Section 4 shows the performance of both ANNs. Finally, conclusions are made in Section 5.

2. The Mathematical Model

2.1. Static Analysis

Duncan and Chang's E-B model [8] is used to simulate the mechanical behavior of the rockfill materials. It is a nonlinear elastic model with wide application and is characterized by seven

parameters: cohesion c , friction φ (or $\varphi_0, \Delta\varphi$), failure ration R_f , modulus number K , modulus exponent n , bulk modulus number K_b , and bulk modulus exponent m . The nonlinear stress-strain relation of rockfill is represented by a hyperbola, whose instantaneous slope is the tangent modulus E_t . According to the conventional triaxial tests, E_t can be expressed as follows:

$$E_t = \left[1 - \frac{R_f(1 - \sin \varphi)}{2c \times \cos \varphi + 2\sigma_3 \sin \varphi} (\sigma_1 - \sigma_3) \right]^2 \times K \times P_a \left(\frac{\sigma_3}{P_a} \right)^n. \quad (2.1)$$

The E-B model follows the Mohr-Coulomb criterion, and the wider the range of pressure involved the greater the curvature of the Mohr-Coulomb envelopes, since friction φ becomes smaller with the increase of minor principal stress σ_3 . So as to coarse-grained soil, friction φ is not constant everywhere in dams. This variation in property may be represented by an equation of the form:

$$\varphi = \varphi_0 - \Delta\varphi \lg \left(\frac{\sigma_3}{P_a} \right), \quad (2.2)$$

where φ_0 is the value of φ for $\sigma_3 = P_a$ and $\Delta\varphi$ is the reduction of φ for a 10-fold increase in σ_3 . And the bulk modulus can be expressed as

$$B = K_b P_a \left(\frac{\sigma_3}{P_a} \right)^m. \quad (2.3)$$

2.2. Dynamic Analysis

Equivalent linear elastic model [9] is used to simulate the dynamic properties of the earth-rock mixtures with two basic characteristics: nonlinearity and hysteresis. Soils have been deemed to be viscoelasticity in the model, and the dynamic stress-strain relationship is reflected with equivalent shear modulus G and equivalent damping ratio λ . The key of the model is to determine the relation between maximum dynamic shear modulus G_{\max} and mean effective principal stress σ_0 , as well as the variation of G and λ along with the amplitude of dynamic shear strain. Based on a large number of experiments conducted by China Institute of Water Resources and Hydropower Research (IWHR), maximum dynamic shear modulus G_{\max} can be expressed as

$$G_{\max} = K \times P_a \times \left(\frac{\sigma_0}{P_a} \right)^n, \quad (2.4)$$

where K, n are modulus and exponent usually determined by experiments. P_a is the atmospheric pressure. In the experiments, the three-axis instrument and wave velocity test device were used. In regard to G and λ , a relation curve is achieved firstly through experiments, which describes the variation of the dynamic shear modulus ratio G/G_{\max} and damping ratio λ with dynamic shear strain γ . Then γ is normalized by reference shear strain γ_r to make instantaneous G and λ easy to get through interpolation.

The effects of hydrodynamic pressure have to be considered when analyzing the dynamic interaction between dam and water in reservoir, since reservoirs may not always operate at a low water level during an earthquake. An ideal way to consider the effects is to divide finite element grids regarding the water and dam body as a whole, and interface element is utilized between contacting surfaces. However, it requires the computer with sufficient memory for the process and is very time consuming. Besides, stiffness coefficient of the interface element is hard to determine. So the additional mass method has been widely used so far. The effects of dynamic water pressure on seismic response of the dam are taken into account with the equivalent additional mass, and the dynamic analysis is done by adding the equivalent mass and the mass of the dam itself.

In this paper, equivalent additional mass is calculated by the lumped-mass method. The equivalent additional mass focusing on node i is calculated by simplified Westergaard formula [10]:

$$m_{wi} = \frac{\psi}{90} \frac{7}{8} \rho \sqrt{H_0 y_i} A_i, \quad (2.5)$$

where ψ is the angle between the upstream slop and the horizontal plane H_0 is depth of water from the surface to the bottom of reservoirs. y_i is depth of water from the surface to node i , and A_i is the corresponding control area of node i .

2.3. Permanent Deformation Analysis

2.3.1. The Model of Permanent Deformation

There have been several models for permanent deformation calculation at present, such as IWHR model [11], Debouchure model, Shen Zhujiang model [12], and improved models about them [13, 14], among which Shen Zhujiang model owns the broadest application so that the model is expressed in an incremental form, and permanent deformations in various conditions including different vibrations, dynamic shear strain, and stress levels can be calculated with only a set of parameters. Compared with the other models, Shen Zhujiang model not only has a consideration on both shearing deformation and volume deformation, but also is easier to use. Residual volumetric strain ε_{vr} and residual shear strain γ_r can be written as

$$\begin{aligned} \varepsilon_{vr} &= c_{vr} \lg(1 + N), \\ \gamma_r &= c_{dr} \lg(1 + N), \\ c_{vr} &= c_1 (\gamma_d)^{c_2} \exp(-c_3 S_l^2), \\ c_{dr} &= c_4 (\gamma_d)^{c_5} S_l^2, \end{aligned} \quad (2.6)$$

where γ_d is dynamic shear strain amplitude, S_l is stress level, N is the number of vibrations, and c_1 , c_2 , c_3 , c_4 , and c_5 are experimental parameters. The parameter c_3 is assumed to have nothing to do with c_{vy} , that is, $c_3 = 0$.

However, studies in recent years have suggested that the deformations calculated by Shen Zhujiang model are larger than actual performance, and it is adverse to an accurate

evaluation of the seismic behavior of faced rockfill dams. So it is necessary to appropriately improve the model. Zou Degao focused on the influence of stress level on the residual shear deformation and presented an improved model based on a large number of cycle triaxial experiments [13]. When the earthquake-induced permanent deformations are calculated with FEM, the improved model can be expressed as an incremental form as follows:

$$\begin{aligned}\Delta\varepsilon_{vr} &= c_1(\gamma_d)^{c_2} \exp\left(-c_3 S_l^2\right) \frac{\Delta N}{1+N}, \\ \Delta\gamma_r &= c_4(\gamma_d)^{c_5} S_l \frac{\Delta N}{1+N},\end{aligned}\quad (2.7)$$

where $\Delta\varepsilon_{vr}$, $\Delta\gamma_r$ are increments of residual volumetric strain and residual shear strain, respectively.

2.3.2. The Method of Permanent Deformation Analysis

The major ways of overall seismic deformation analysis are based on the method of equivalent nodal force and modulus soften model [15] now. The calculation process of modulus soften model is relatively complicated, so the method of equivalent nodal force is a better choice for the permanent deformation analysis; the ideal about it is that the residual strain during an earthquake is determined firstly by an empirical formula, then the residual strain is converted to equivalent node force of finite elements, and the contributions of residual strain to the dam are replaced by the displacement calculated with the equivalent nodal force. The procedure comprises the following three steps.

- (1) Perform static calculation for the dam with midpoint incremental method, to get the initial static stress σ_0 and stress level S_l .
- (2) Perform dynamical calculation through the approach on the basis of equivalent linear viscoelastic model, to get the dynamic stress of soil, then convert the dynamic stress to stress state in laboratory, and get residual strain potential ε_v^p , $\Delta\gamma_r^p$ according to (2.7). And strain potential of finite elements is obtained according to the following formula:

$$\{\Delta\xi_p\} = \begin{Bmatrix} \Delta\xi_x \\ \Delta\xi_y \\ \Delta\xi_z \\ \Delta\gamma_{xy} \\ \Delta\gamma_{yz} \\ \Delta\gamma_{zx} \end{Bmatrix} = \frac{1}{3}\Delta\varepsilon_v^p \begin{Bmatrix} 1 \\ 1 \\ 1 \\ 0 \\ 0 \\ 0 \end{Bmatrix} + \frac{\Delta\gamma_{r\max}^p}{q} \begin{Bmatrix} \sigma_x - p \\ \sigma_y - p \\ \sigma_z - p \\ 2\tau_{xy} \\ 2\tau_{yz} \\ 2\tau_{zx} \end{Bmatrix}, \quad (2.8)$$

where q is generalized shear stress, p is average principal stress, and $\{\Delta\xi_p\}$ is increment of residual strain in Cartesian coordinates.

- (3) Calculate the equivalent nodal force with the converted strain potential according to the formula that

$$\{\Delta F\} = \iiint_v [B]^T [D] \{\Delta\xi_p\} dV, \quad (2.9)$$

where $[B]$ is the conversion matrix of strain $[D]$ is the elastic matrix. Then permanent deformations are calculated with the equivalent nodal force applied on finite elements.

3. Permanent Deformation Parameters Inversion Using Artificial Neural Networks

3.1. BP Neural Networks

For a BPNN with a structure $m-k-p$, that is, a vector input $x(x_1, x_2, \dots, x_m)$, k hidden units, and an output vector $y(y_1, y_2, \dots, y_p)$ as in Figure 1, the equation that expresses the relationship between the input and output can be written as

$$y_j = f_{\text{output}} \left[\sum_{h=1}^k w_{jh} f_{\text{hidden}} \left(\sum_{i=1}^m w_{hi} x_i + \text{bias}_{1h} \right) \right] + \text{bias}_{2j}, \quad (3.1)$$

where m is the number of input units, k is the number of neurons in the hidden layer, x_i is the i th input unit, w_{hi} is the weight parameter between input i and hidden neuron h , w_{jh} is the weight parameter between hidden neuron h and output neuron j , f_{hidden} is the activation function of the hidden layer, and f_{output} is the transfer function of output layer.

The weights were estimated and adjusted in the learning process with an aim of minimizing an error function E_d as follows:

$$E_D = \sum_{i=1}^n (y_i - t_i)^2 = \sum_{i=1}^n e_i^2, \quad (3.2)$$

where n is the number of input and output examples of the training dataset and t is the target value. The errors were fed backward through the network to adjust the weights until the error E_D was acceptable for the network model. Once the ANN is satisfied in the training process, the synaptic weights will be saved and then used to predict the outcome for the new data. To minimize E_D , optimal parameters of weights and biases have to be determined. One of the algorithms for solving this problem is the Levenberg-Marquardt (LM) algorithm. This algorithm is a modification of the Newton algorithm for finding optimal solutions to a minimization problem. The weights of an LMNN are calculated using the following equation:

$$w_{i+1} = w_i - \left(J_i^T J_i + \mu_i I \right)^{-1} J_i^T e_i, \quad (3.3)$$

where J is the Jacobian matrix of output errors, I is the identity matrix, and μ is an adaptive parameter. When $\mu = 0$, it becomes the Gauss-Newton method using the approximate Hessian matrix. If μ is large enough, the LM algorithm becomes a gradient descent with a small step size (the same as in the standard backpropagation algorithm).

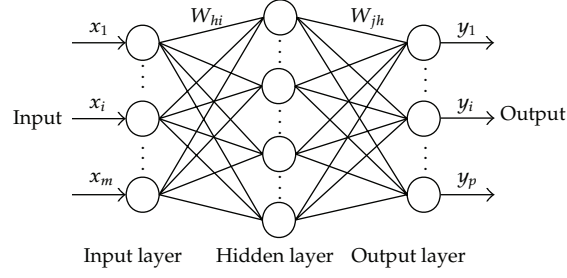


Figure 1: Structure of BP neural network.

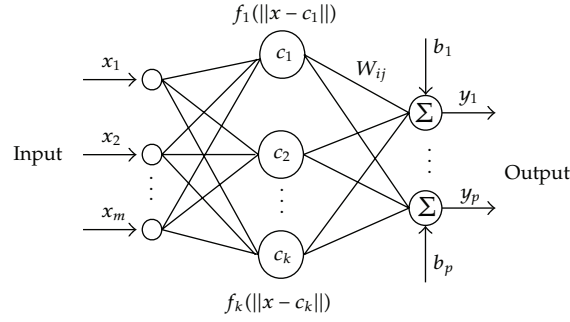


Figure 2: Structure of RBF neural network.

3.2. RBF Neural Networks

RBFNN is a kind of feedforward neural network and generally consists of three components: input layer, hidden layer, and output layer. Figure 2 displays an RBF network with a structure $m-k-p$ that there are m inputs, k hidden units and p outputs. $x = (x_1, x_2, \dots, x_m)^T \in R^m$ is the input vector. W is the weight matrix of inputs and $W \in R^{k \times p}$, b_1, \dots, b_p are offset of output units. $y = (y_1, \dots, y_p)^T \in R^p$ is the output vector of the network, and $f_i(\|x - c_i\|)$ is the activation function of the hidden unit i ; one common function is the Gaussian function:

$$\varphi(x) = \exp\left(-\frac{x^2}{2\sigma^2}\right), \quad (3.4)$$

where σ is spread constant, the role of which is to adjust sensitivity of the Gaussian function.

The final output of unit i can be expressed as

$$y_i = \sum_{j=1}^k w_{ij} \exp\left(-\frac{\|x - c_j\|^2}{2\sigma_j^2}\right) + b_i, \quad (3.5)$$

where w_{ij} is the weight of output layer and σ_j is spread constant of the base function.

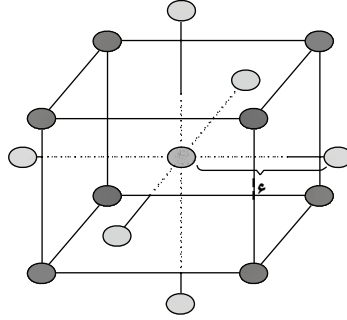


Figure 3: Central composite design schemes for three factors.

3.3. Sample Set Designs

The prediction accuracy of neural networks is determined by sample quality to some extent, the samples used for inversion have to be accurate and balanced, so as to be representative enough, and it is better to reflect inner characters of the model system. In this paper, the methods of central composite design [16] and orthogonal design are utilized to design samples. The central composite design was presented by Box and Wilson. It consists of the following three parts: a full factorial or fractional factorial design, a central point, and an additional design, often a star design in which experimental points are at a distance α from its center. Figure 3 illustrates the full central composite design for optimization of three variables. Full uniformly rotatable central composite designs present the following characteristics:

- (1) require an experiment number according to $N = k^2 + 2k + c_p$, where k is the factor number and c_p is the replicate number of the central point.
- (2) α -values depend on the number of variables and can be calculated by $\alpha = 2^{(k-p)/4}$. For two, three, and four variables, it equals 1.41, 1.68, and 2.00, respectively.
- (3) All factors are studied in five levels $(-\alpha, -1, 0, +1, +\alpha)$.

As a result, samples designed by both methods embody not only inner but also outer conditions of the cube within certain realms, and they have good density distribution and representativeness.

3.4. Parameter Sensitivity Analysis

Sensitivity analysis can estimate the influence of parameter variation on outputs and make us have a more intuitive understanding about the parameters to be considered. Morris method [17] was more applied in sensitivity analysis. It figured out the influence of arguments on the dependent variable through disturbing a parameter and keeping the others the same. The corrected Morris method changed arguments at a fixed step size, calculated the value of influence in each condition, and then took the average like this:

$$S = \sum_{i=1}^{q-1} \frac{((Y_{i+1} - Y_i)/Y_0)/((P_{i+1} - P_i)/100)}{(q-1)}, \quad (3.6)$$

Table 1: The principal parameters for static calculation.

Material zoning	ρ (kg/m ³)	φ (°)	$\Delta\varphi$ (°)	R_f	K	n	K_b	m
Cushion layer	2300	57.51	10.65	0.84	1274	0.44	1260	-0.026
Transition layer	2250	57.63	11.44	0.75	1153	0.38	1085	-0.089
Main rockfill	2160	55.39	10.60	0.75	1120	0.32	490	0.12
Secondary rockfill	2150	55.39	10.60	0.71	1033	0.38	338	0.03
Covering layer	2150	49.00	10.00	0.80	820	0.40	430	0.25

where S is the sensitivity factor, Y_i is the output of condition i , Y_0 is the output derived from the initial parameters, p_i is the percentage of parameter variations in condition i compared to the initial parameters, and q is the number of conditions.

4. Example Analysis

4.1. Brief Introduction to the Project

The Zipingpu dam is located in a valley, 9 km away in northwest from the Chengdu City, Sichuan province. It is one of the high CFRDs more than 150 m in China, with a maximum height of 156 m and the crest length 663.77 m. It encountered the Sichuan 8.0-magnitude earthquake which was higher than its actual design level. The dam body emerged obvious damage, and it provided rich and precious materials [18, 19] for earthquake engineering research on CFRDs.

4.2. Results of Static Calculation

Static parameters were directly selected from the experimental results coming from the IWHR, considering as well the results from Professor Zhu Cheng who partly backanalyzed the parameters of the project by immune genetic algorithm. Integrating both results, the parameters of rockfill were determined in Table 1. Besides, the linear elastic model was adopted for the calculation of concrete panels, concrete strength grade was C25, and the corresponding material parameters were density $\rho = 2400$ kg/m³, $E = 2.8 \times 10^4$ MPa, Poisson's ratio $\mu = 0.167$.

To simulate the process of construction and impoundment of the CFRD, midpoint incremental method and multistage loading process were used in the calculations. The dam was meshed into 6772 finite elements with total 6846 nodes, as shown in Figure 4. And the main results of a typical cross-section in rockfill zone were shown as in Figures 5 and 6, which were at operational water level before the earthquake.

4.3. Results of Dynamic Calculation

Due to influence of all kinds of factors, Zipingpu dam had no acceleration recordings of the actual principle shock of base rock. According to analysis [20, 21] of many scholars, the actual input ground motion was likely to be more than 0.5 g. Referring to the attenuation relationship [22] given by Yu et al., and considering the hanging wall and footwall effects, Professor Zhu Cheng deduced that the peak accelerations of dam site in three directions,

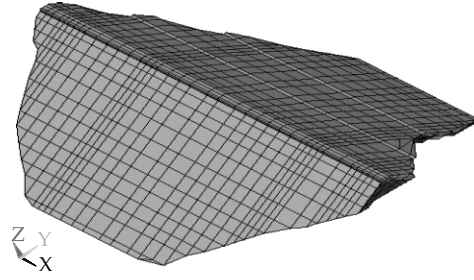


Figure 4: 3D mesh of the dam for calculation.

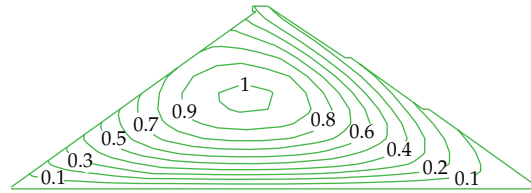


Figure 5: Continuous contours of vertical displacement of the dam before earthquake (m).

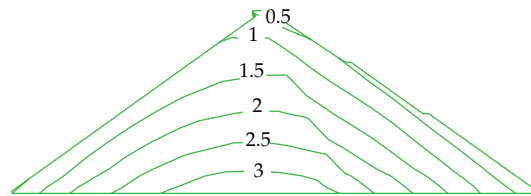


Figure 6: Continuous contours of major stress of the dam before earthquake (MPa).

respectively, were 0.52 g in east-west, 0.46 g in north-south, and 0.43 g in vertical. And based on the materials concerned in [22], the relative position of seismometer stations and dam site was shown in Figure 7. Finally, the seismograms of Wolong Station (051WCW) closer to the dam site were selected as the ground motion input; meanwhile the acceleration time histories were scaled in accordance with the peak accelerations as aforementioned, as shown in Figure 8.

According to the calculation results, the basic frequency of dam vibration was about 1.65 Hz and the maximum acceleration responses at dam crest were 0.86 g along the river, 0.74 g in vertical, and 1.36 g along the dam axial, which were consistent with the analysis results obtained by Kong et al. [21]. Under the three-dimensional earthquake, the maximum acceleration response lay in the downstream dam crest, and rockfill slid when its acceleration response exceeded yield acceleration, which qualitatively explained the phenomenon on Zipingpu dam that some grains in the downstream dam crest loosened and tumbled.

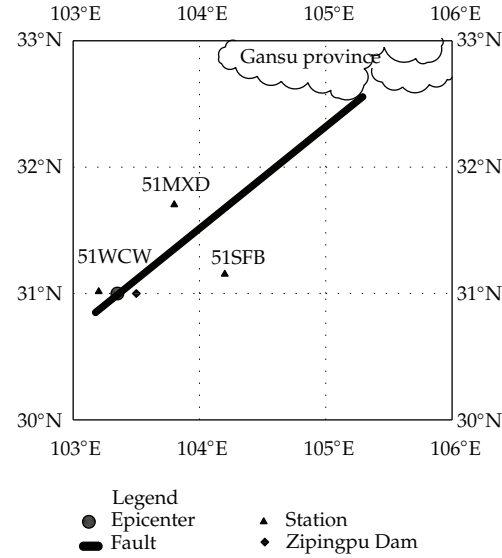


Figure 7: Epicenter of “5.12” Wenchuan Earthquake and observation stations.

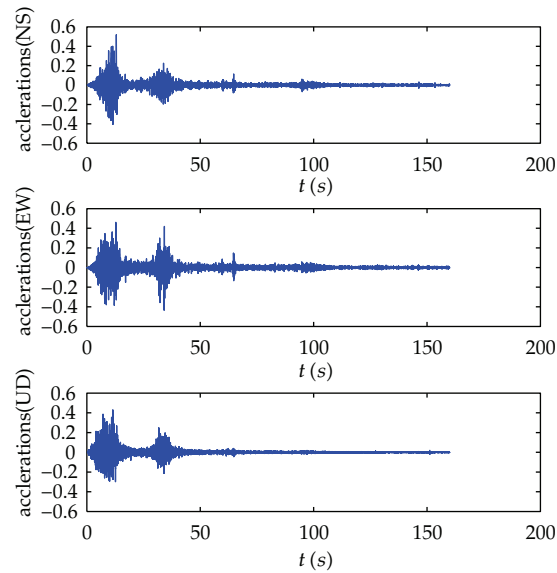


Figure 8: Acceleration time histories of dam site (a/g).

4.4. Backanalysis of the Project

Though the dam has different material zoning, material sources are same the and the construction control indexes are very near; therefore dynamic properties of different zones will not vary much. To reduce the workload, all rockfills were thought to have the same set of permanent deformation parameters, they were c_1, c_2, c_4, c_5 but c_3 was out of the inversion range for that it was a constant as mentioned in (2.6). Reference [23] listed several project cases at home and abroad and gave the test values of corresponding permanent deformation parameters [24–27]. However, parameters of different projects varied entirely; as a result, a

Table 2: Ranges of parameters to be inversed and initial values.

Parameter variation	c_1	c_2	c_4	c_5
Inversion range of parameters	0.005 ~0.01	0.5 ~1.0	0.1 ~0.2	0.75 ~1.50
Initial parameters	0.0064	0.75	0.18	1.33

set of initial parameters were determined firstly referring to the similar engineering and the inversion range of parameter was preliminarily determined as Table 2.

4.4.1. Parameter Sensitivity Analysis

Disturb a parameter with a fixed step size 10% and keep the other parameters the same. And then sensitivity analysis of the dam on maximum subsidence was performed, and the result was shown in Figures 9 and 10.

According to the classification results in [17], parameter sensitivity was graded into four levels: $|S_i| \geq 1$ highly sensitive, $0.2 \leq |S_i| < 1$ sensitive, $0.05 \leq |S_i| < 0.2$ moderately sensitive, and $0 \leq |S_i| < 0.05$ insensitive. Figure 10 shows that c_1 is a moderately sensitive parameter, c_2 , c_4 are sensitive ones, and c_5 is highly sensitive. Besides, Figure 9 shows that the subsidence under earthquake increases with the increase of c_1 , c_4 and decreases with the increase of c_2 , c_5 .

4.4.2. Comparison of RBF and BP Networks in Inversion

In order to improve the generalization ability of neural network, a training method [28] was taken that samples were partitioned into several subsets, and then the network was trained and appraisal was done at the same time with the change of spread constant. Samples were partitioned into three subsets here for training, validation, and testing. The training and validation datasets were used to determine synoptic weights of the network model whereas the testing dataset is used to evaluate the prediction results. If the performance index (generally mean square error, (MSE)) of errors of training dataset was satisfied, then determine the optimal network according to that of verification dataset.

There were 90 training samples in all generated by the methods of central composite design and orthogonal design, and 9 samples generated at random among which 6 ones were used for verification, and the others were for testing. With observation displacement as input vector and permanent deformation parameter as an output vector, the neural network could be trained. One of the common ways to evaluate performance of the network was by error of mean square root (RMSE). However, backanalysis of permanent deformation parameters by neural network was a problem of multi-input-output, if the network performance was still evaluated like that:

$$\text{RMSE} = \sqrt{\frac{\sum_{i=1}^n \sum_{j=1}^p (y_{ij} - t_{ij})^2}{n}}. \quad (4.1)$$

Then it could not reflect the error influence of different parameters; that is to say, the results calculated by inversion parameters might deviate considerably from the actual value since

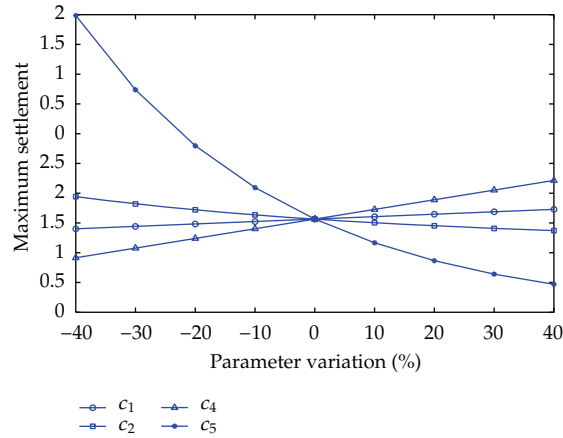


Figure 9: Trend of vertical subsidence change.

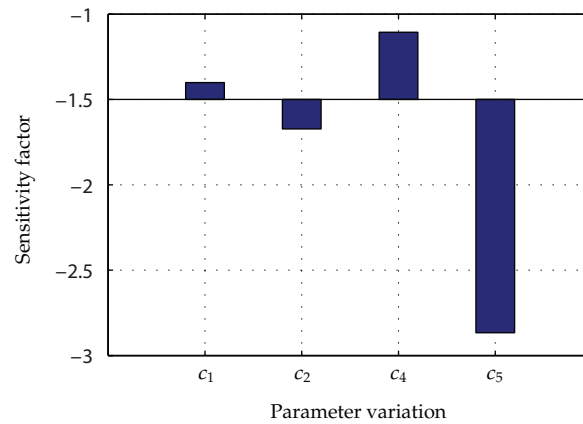


Figure 10: Result of parameter sensitivity analysis.

the forecasting error of highly sensitive parameter was relatively big, though the total error was small. So in this paper, an objective function for evaluating network performance was put forward to improve fitting accuracy of high sensitive parameter, where sensitivity factors were taken as weights of error, as follows:

$$\text{RMSE} = \sqrt{\sum_{i=1}^n \sum_{j=1}^p \frac{[(y_{ij} - t_{ij}) * S_j]^2}{n}}, \quad (4.2)$$

where n is the sample number of validation dataset, p is the dimension of the output vector, and y_{ij} and t_{ij} are final parameter output and the actual parameter value, respectively.

The key of RBF network training is to determine the neural number of hidden layer. It has been a common method at present to gradually increase the neural number

automatically by checking the output error, starting from zero. So the process of establishing a network is also the one of training. Spread constant σ was adjusted until the prediction accuracy of testing samples met the engineering requirements, and then the trained network can be practically used for parameter inversion. It is beneficial for the generalization of neural network to adjust spread constant, the higher the σ , the more smooth the fitting, but not the higher the better, if σ is too high, all outputs are likely to become common and the base functions tend to overlap completely. Its value generally depends on the distance between the input vectors. To analyze the effectiveness of the training, the transition of the RMSE was traced with the change of σ as shown in Figure 11. It can be seen that the RMSE decreases rapidly in the initial stages and almost remains the same after $\sigma = 1.6$.

The process of BP network training was similar to the RBF network; after MSE of training dataset was satisfied, then determine the optimal network according to RMSE of verification dataset. The maximum number of training epochs was set to 3000. The MSE goal was set to 0.001. The initial value of adaptive parameter μ was set to 0.001. μ increased by 10 and decreased by 0.1 until performance value reduced, and its maximum value is set to $1e10$. During the training phase, the data were processed several times to see whether any changes occurred due to the assignment of random initial weights. Figure 12 describes the results that the value of RMSE decreases from the largest value of 0.98 with one hidden neuron to the value of 0.18 with 11 hidden neurons. RMSE was then stable at this value with an increasing number of hidden neurons.

To test the prediction accuracy of the networks, the outputs of the testing samples were listed in Table 3. For the three samples, the prediction accuracy of all parameters by RBFNN is around 5% whereas not all the results by BPNN are satisfactory. However, for both networks, the forecasting error of parameter c_5 is generally smaller, which indicates that it has a pronounced effect on improvement of highly sensitive parameters with the function of error evaluation, in the problem of multiple parameter inversion.

To further check the error precision of influence on subsidence, the predictive parameters by RBFNN were used for finite element calculations. Owing to space reasons, for the second sample only, the results were compared with the actual value as in Figure 13, and the observation points were on central axis of the typical section. It can be seen that the computation values are very close, which indicates that the prediction effect by the RBF network can basically meet engineering accuracy.

With actual observation displacement of Zipingpu dam as input vector, permanent deformation parameters of rockfill were backanalyzed by the trained RBF network, and the results are shown in Table 4.

The permanent displacement calculated by the inversion parameters is shown in Figure 14, and the marked values are actual displacements of the dam. It can be seen that the vertical displacements increase with the increment of dam height, which accords with the law of the measured settlement, and both values are also very close. Figure 15 shows the deformed mesh for finite element calculations, where deformation has already been enlarged to see clearly. Besides, the dam section becomes smaller and the slopes of both upstream and downstream shrink inward, which embodies the macroscopic character of rockfill under earthquake action. Due to the upstream water load, the maximum of the horizontal permanent deformation points to the downstream of the dam but the earthquake-induced permanent deformation is predominantly vertical settlement. In summary, the results are qualitatively rational, which indicates that it is feasible to calculate the earthquake-induced

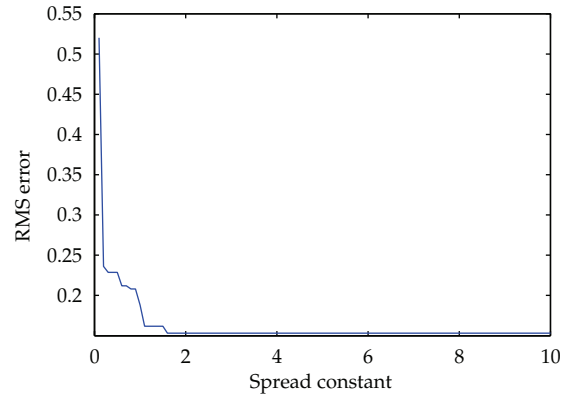


Figure 11: History of RMSE along with expand constant.

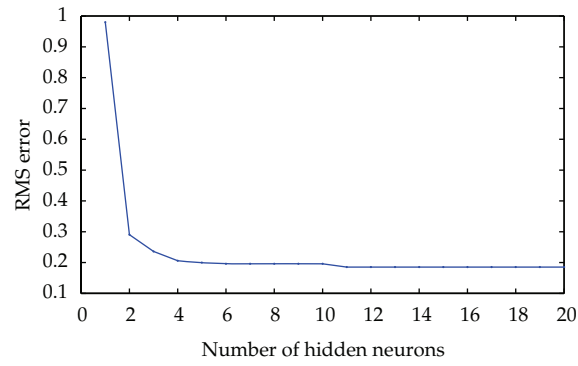


Figure 12: History of RMSE along with the number of hidden neurons.

Table 3: Comparison of predicted results and actual values of the test samples' parameters.

Testing samples		RBF				BP			
		c_1	c_2	c_4	c_5	c_1	c_2	c_4	c_5
1	Actual value	0.0064	0.7500	0.1850	1.3300	0.0064	0.7500	0.1850	1.3300
	Predictive value	0.0064	0.7658	0.1894	1.3263	0.0073	0.8075	0.1851	1.3250
	Error/%	0.0000	2.1067	2.3784	-0.2782	14.5467	7.6702	0.0876	0.3763
2	Actual value	0.0058	0.6750	0.1665	1.1970	0.0058	0.6750	0.1665	1.1970
	Predictive value	0.0062	0.7226	0.1753	1.1950	0.0070	0.7525	0.1675	1.1895
	Error/%	6.8966	7.05185	5.2853	-0.1671	20.7000	11.4833	0.6283	0.6293
3	Actual value	0.0070	0.8250	0.2035	1.4630	0.0070	0.8250	0.2035	1.4630
	Predictive value	0.0068	0.8127	0.1954	1.4354	0.0077	0.8645	0.1982	1.4496
	Error/%	-2.8571	-1.4909	-3.9803	-1.8865	9.7816	4.7920	2.5910	0.9153

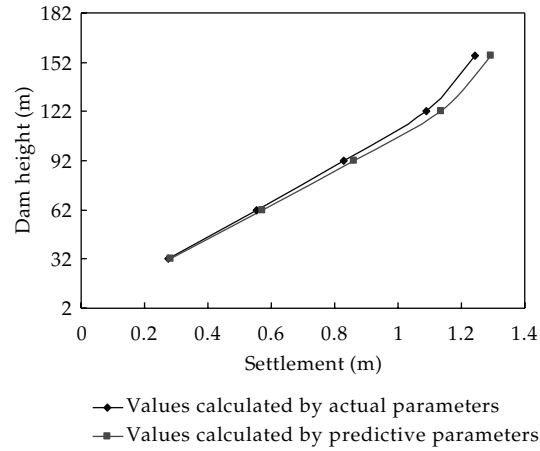


Figure 13: Comparison of dam subsidence.

Table 4: Backanalysis results of rockfill deformation parameters.

Material	c_1	c_2	c_4	c_5
Rockfill	0.0072	0.8000	0.1342	1.4477

permanent deformation by the method of equivalent nodal force on the basis of improved Shen Zhujiang model.

5. Conclusions

In the process of conventional back/inverse analysis, it is necessary to perform FEM analysis frequently. For a large-scale multiple parameter and nonlinear problem such as backanalysis of displacement of an earth-rockfill dam, the workload is so daunting that sometimes the backanalysis cannot be carried out. In this paper, ANNs were introduced in the field of dynamic parameter inversion of earth-rockfill dam, BP and RBF networks were compared, then on the basis of RBFNN, a backanalysis model for earthquake-induced permanent deformation parameters was proposed, and it was used for backanalysis of parameters for Zipingpu CFRD. The results indicate the following:

- (1) The RBFNN model appears more robust and efficient than BPNN model for backanalysis of earthquake-induced permanent deformation parameters of the earth-rockfill dam. Due to the assignment of random initial weights, the structure of BPNN is difficult to determine, network training results are unstable, and it can easily be trap in a local optimum; all of the problems are still to be resolved, and so RBFNN is a better choice.
- (2) It is an easy and effective way to backanalysis of earthquake-induced permanent deformation parameters of the earth-rockfill dam with RBF network model. In this way, the inversion range of parameters is determined according to the similar engineering, and several samples are generated through the experimental design methods; then after the neural network is trained, the residual deformation

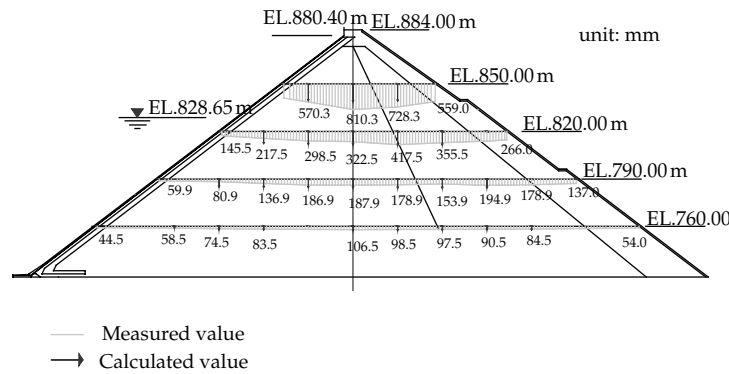


Figure 14: Comparison of dam subsidence.

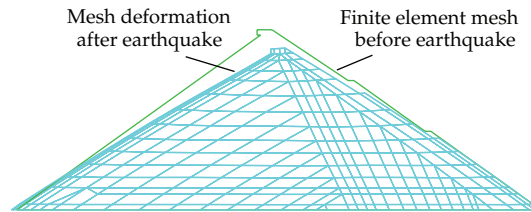


Figure 15: The deformation of the dam grid figure.

parameters can be acquired quickly by putting in actual permanent deformations of the dam.

- (3) The existing theory and method of dynamic calculation can basically reflect the earthquake-resistant behavior of earth-rockfill dam, but it is still an extremely complex subject to research; many factors such as seismic input and calculation model may lead to great gap between calculated value and actual value. Thereby, further study on dynamic analysis method will make the inversion of permanent deformation parameters more meaningful.

Acknowledgments

This work was supported by National Natural Science Foundation of China (51109028 and 90815024) and the Fundamental Research Funds for the Central Universities (DUT11RC(3)38).

References

- [1] F. Kang, J. Li, and Q. Xu, "Structural inverse analysis by hybrid simplex artificial bee colony algorithms," *Computers and Structures*, vol. 87, no. 13-14, pp. 861-870, 2009.
- [2] P. Z. Lu, S. Y. Chen, and Y. J. Zheng, "Artificial intelligence in civil engineering," *Mathematical Problems in Engineering*, vol. 2012, Article ID 145974, 22 pages, 2012.
- [3] S. Chen, Y. Zheng, C. Cattani, and W. Wang, "Modeling of biological intelligence for SCM system optimization," *Computational and Mathematical Methods in Medicine*, vol. 2012, Article ID 769702, 10 pages, 2012.

- [4] X.-H. Yang, F.-L. Jiang, S.-Y. Chen, and W.-L. Wang, "Modeling evolution of weighted clique networks," *Communications in Theoretical Physics*, vol. 56, no. 5, pp. 952–956, 2011.
- [5] S. Y. Chen, C. Y. Yao, G. Xiao, Y. S. Ying, and W. L. Wang, "Fault detection and prediction of clocks and timers based on computer audition and probabilistic neural networks," *Lecture Notes on Computer Science*, vol. 3512, pp. 952–959, 2005.
- [6] Y. Yu, B. Zhang, and H. Yuan, "An intelligent displacement back-analysis method for earth-rockfill dams," *Computers and Geotechnics*, vol. 34, no. 6, pp. 423–434, 2007.
- [7] S. Zhu, G. Yang, J. P. Zhou, and Y. G. Song, "Back analysis on static and dynamic characteristics of Zipingpu CFRD under "5.12" Wenchuan Earthquake," *Journal of Sichuan University*, vol. 42, no. 5, pp. 113–119, 2010.
- [8] J. M. Duncan and C. Y. Chang, "Nonlinear analysis of stress and strain in soils," *Journal of the Soil Mechanics and Foundations Division ASCE*, vol. 96, no. SM5, pp. 1629–1653, 1970.
- [9] X. S. Liu, Z. N. Wang, X. G. Wang et al., *Large-Scale Shaking Table Model Test and Dynamic Analysis for CFRD*, China Waterpower Press, Beijing, China, 2010.
- [10] H. Chen, S. Hou, and D. Yang, "Study on arch dam reservoir interaction under earthquake condition," *Journal of Hydraulic Engineering*, vol. 10, no. 7, pp. 29–39, 1989.
- [11] K. Y. Wang, Y. P. Chang, and N. Chen, "Residual deformation characteristics of coarse-grained soils under cyclic loading," *China Civil Engineering Journal*, vol. 33, no. 3, pp. 48–53, 2000.
- [12] Z. J. Shen and G. Xu, "Deformation behavior of rock material under cyclic loading," *Hydro-Science and Engineering*, vol. 6, no. 2, pp. 143–150, 1996.
- [13] D. G. Zou, F. W. Meng, X. J. Kong et al., "Residual deformation behavior of rock-fill materials," *Chinese Journal of Geotechnical Engineering*, vol. 30, no. 6, pp. 807–812, 2008.
- [14] S. Zhu and J. B. Zhou, "Deformation behavior of coarse grained materials under cyclic loading," *Rock and Soil Mechanics*, vol. 31, no. 5, pp. 1375–1380, 2010.
- [15] H. L. Liu, Z. Z. Lu, and J. H. Qian, "Earthquake-induced permanent deformation of earth-rock dams," *Journal of Hohai University*, vol. 24, no. 1, pp. 91–96, 1996.
- [16] M. A. Bezerra, R. E. Santelli, E. P. Oliveira, L. S. Villar, and L. A. Escalera, "Response surface methodology (RSM) as a tool for optimization in analytical chemistry," *Talanta*, vol. 76, no. 5, pp. 965–977, 2008.
- [17] J. L. Huang, P. F. Du, W. Q. He, Z. D. Ou, H. C. Wang, and Z. S. Wang, "Local sensitivity analysis for urban rainfall runoff modelling," *China Environmental Science*, vol. 27, no. 4, pp. 549–553, 2007.
- [18] S. S. Chen, J. P. Huo, and W. M. Zhang, "Analysis of effects of "5.12" Wenchuan Earthquake on Zipingpu Concrete Face Rock-fill Dam," *Chinese Journal of Geotechnical Engineering*, vol. 30, no. 6, pp. 795–801, 2008.
- [19] Z. Y. Yang, J. M. Zhang, and X. Z. Gao, "A primary analysis of seismic behavior and damage for Zipingpu CFRD during Wenchuan Earthquake," *Water Power*, vol. 35, no. 7, pp. 30–33, 2009.
- [20] H. Q. Chen, Z. P. Xu, and M. Lee, "Wenchuan Earthquake and seismic safety of large dams," *Journal of Hydraulic Engineering*, vol. 39, no. 10, pp. 1158–1167, 2008.
- [21] X. J. Kong, D. G. Zou, Y. Zhou, and B. Xu, "Earthquake damage analysis of Zipingpu concrete face rock-fill dam during Wenchuan earthquake," *Journal of Dalian University of Technology*, vol. 49, no. 5, pp. 667–674, 2009.
- [22] H. Yu, D. Wang, Y. Yang, Q. Xie, W. Jiang, and B. Zhou, "The preliminary analysis of strong ground motion records from the M s 8.0 Wenchuan Earthquake," *Journal of Earthquake Engineering and Engineering Vibration*, vol. 29, no. 1, pp. 1–13, 2009.
- [23] G. C. Gu, C. S. Shen, and W. J. Cen, *Earthquake Engineering for Earthrock Dams*, China Waterpower Press, Beijing, China, 2009.
- [24] S. Y. Chen and Q. Guan, "Parametric shape representation by a deformable NURBS model for cardiac functional measurements," *IEEE Transactions on Biomedical Engineering*, vol. 58, no. 3, pp. 480–487, 2011.
- [25] M. Li, S. C. Lim, and S. Chen, "Exact solution of impulse response to a class of fractional oscillators and its stability," *Mathematical Problems in Engineering*, vol. 2011, Article ID 657839, 9 pages, 2011.
- [26] S. Chen, Y. Wang, and C. Cattani, "Key issues in modeling of complex 3D structures from video sequences," *Mathematical Problems in Engineering*, vol. 2012, Article ID 856523, 17 pages, 2012.
- [27] M. Carlini, S. Castellucci, M. Guerrieri, and T. Honorati, "Stability and control for energy production parametric dependence," *Mathematical Problems in Engineering*, vol. 2010, Article ID 842380, 21 pages, 2010.

- [28] S. Duan, C. He, L. Xu, and D. Ma, "A training method for improving the generalization performance of radial basis function networks," in *Proceedings of the 3th World Congress on Intelligent Control and Automation*, pp. 859–863, July 2000.

Research Article

Intelligent Risk Assessment for Dewatering of Metro-Tunnel Deep Excavations

X. W. Ye,¹ L. Ran,² T. H. Yi,³ and X. B. Dong²

¹ *Institute of Transportation Engineering, College of Civil Engineering and Architecture, Zhejiang University, Hangzhou 310058, China*

² *Hangzhou Metro Group Co., Ltd., Hangzhou 310020, China*

³ *Research Center for Structural Health Monitoring and Control, School of Civil Engineering, Dalian University of Technology, Dalian 116023, China*

Correspondence should be addressed to T. H. Yi, yth@dlut.edu.cn

Received 14 October 2012; Accepted 4 November 2012

Academic Editor: Sheng-yong Chen

Copyright © 2012 X. W. Ye et al. This is an open access article distributed under the Creative Commons Attribution License, which permits unrestricted use, distribution, and reproduction in any medium, provided the original work is properly cited.

In recent years, China has been undergoing a metro railway construction boom in order to alleviate the urban traffic congestion problem resulting from the rapid urbanization and population growth in many metropolises. In the construction of metro systems, deep excavations and continuous dewatering for construction of the metro tunnels and stations remain a challenging and high risk task in densely populated urban areas. Intelligent computational methods and techniques have exhibited the exceptional talent in dealing with the complicated problems inherent in the deep excavation and dewatering practice. In this paper, an intelligent risk assessment system for deep excavation dewatering is developed and has been applied in the project of Hangzhou Metro Line 1 which is the first metro line of the urban rapid rail transit system in Hangzhou, China. The specific characteristics and great challenges in deep excavation dewatering of the metro-tunnel airshaft of Hangzhou Metro Line 1 are addressed. A novel design method based on the coupled three-dimensional flow theory for dewatering of the deep excavation is introduced. The modularly designed system for excavation dewatering risk assessment is described, and the field observations in dewatering risk assessment of the airshaft excavation of Hangzhou Metro Line 1 are also presented.

1. Introduction

With the rapid expansion of industrialization and urbanization, traffic congestion has become a serious social problem in most of the large cities in China. Establishment of a large-scale metro network has been recognized to be a most effective way in alleviating the urban traffic congestion problem [1, 2]. In recent years, a large amount of metro railway construction

accompanied by deep excavations in densely populated areas has been undergone in the metropolises of China. For the metro-tunnel excavation to be opened below the groundwater level, a reasonable and robust dewatering system is always desired to obtain the required working condition during the excavation construction period. An effective and efficient dewatering system can be achieved through the integration of groundwater flow modeling, inverse simulation analysis, and optimization formulation to minimize the total amount of water pumpage or implementation cost while satisfying the design criteria [3–5].

It has been well known that the dewatering of the confined aquifer for deep excavations may bring adverse impacts on the surrounding buildings and environments, such as consolidation and compression of the soil layers, settlement and deformation of the piles, cracking and inclination of the buildings, and so forth [6]. Therefore, it becomes essential and desirable to investigate the hydraulic characteristics of deep excavation dewatering as well as the interactions of the underground continuous wall, the seepage well, and the soil layers, which have attracted a great deal of academic and industrial attention from numerous investigators and practitioners worldwide [7–11].

Chen and Xiang [12] proposed a procedure for estimation of dewatering-induced pile settlement through four steps including a pumping model, a simplified consolidation evaluation, a pile-soil interaction model, and a semitheoretical pile settlement prediction. Schroeder et al. [13] presented the practice of planning and execution of dewatering for a deep excavation in coarse alluvium containing cobbles and boulders. Wang et al. [14] developed a decision support system for dewatering systems selection (DSSDSS) for determination of the most appropriate dewatering system for a project. Forth [15] reported the groundwater control for deep excavations and geotechnical aspects in Hong Kong.

Up to now, a set of nature-inspired computational methodologies and approaches, such as artificial neural networks, fuzzy logic systems, genetic algorithms, and so forth, have been developed and are being powerful tools for quantitatively identifying the constitutive parameters and solving the optimization problems in various engineering fields [16–23]. In this study, an intelligent risk assessment system for deep excavation dewatering construction is developed with integration of the novel computational intelligence and has been exemplified to implement dewatering risk assessment of the airshaft excavation of Hangzhou Metro Line 1.

2. Deep Excavation Dewatering of Metro-Tunnel Airshaft

2.1. Metro-Tunnel Airshaft

Hangzhou Metro Line 1 is the first metro line of the urban rapid rail transit system in Hangzhou, China, which is one of the largest municipal projects of Hangzhou and is being constructed starting from 28 March 2007 and will be officially put into operation in the end of October 2012. This metro line has a total length of 48 km and 34 stations, connecting Hangzhou downtown with suburban area of the city. It starts from the south at the Xianghu Station in Xiaoshan District, stretches northwards to the Binjiang Station adjacent to the Qiantang River, crosses beneath the Qiantang River to the Fuchun Road Station, passes through Hangzhou downtown, and ends in the Linping Station, with a branch line ending in Xiasha District which diverges from the main line at the Jiubao Station. The 2nd construction segment of Hangzhou Metro Line 1 covers from the Binjiang Station to the Jiubao Station with a length of 25 km. In this construction section, a two-lane single-bore shield tunnel has

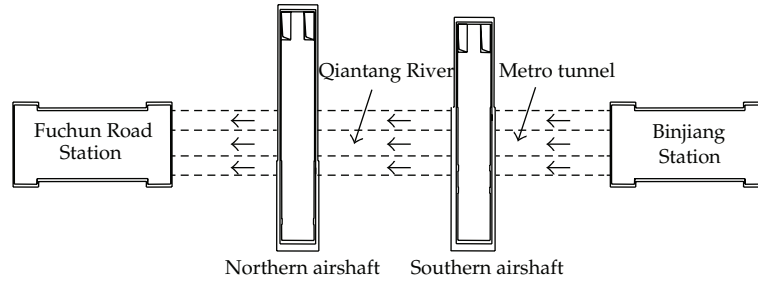


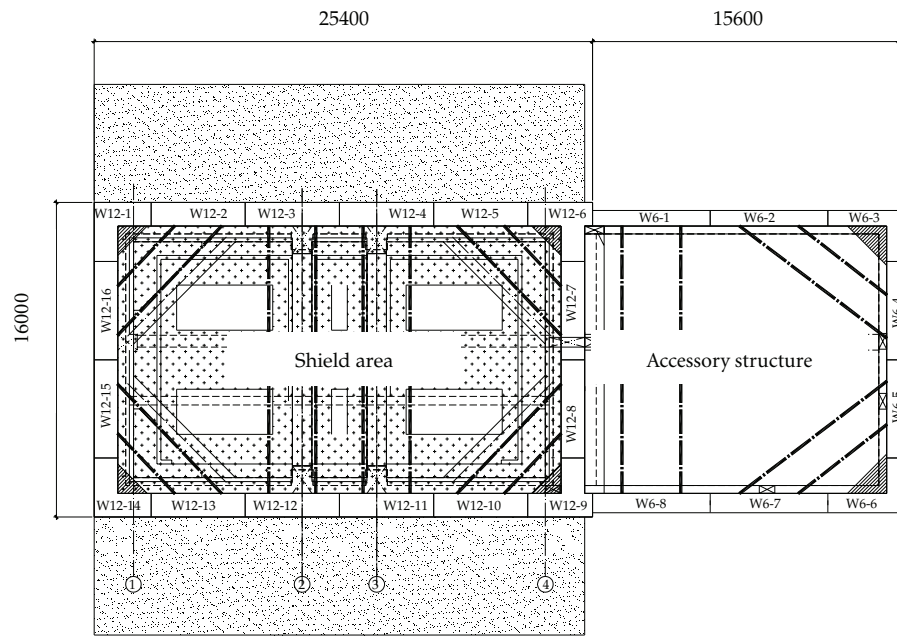
Figure 1: River-crossing metro tunnel and airshafts.

been constructed under the Qiantang River to link the Binjiang Station and the Fuchun Road Station, with two airshafts (the southern airshaft and the northern airshaft) being settled at both sides of the Qiantang River, as illustrated in Figure 1.

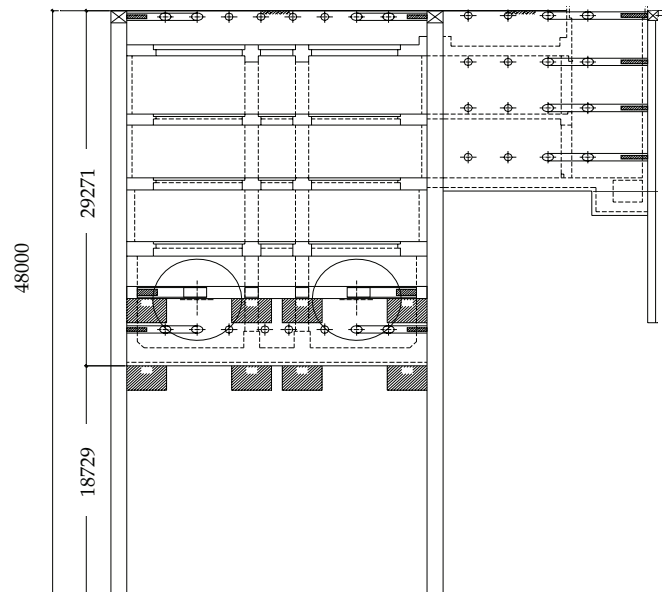
2.2. Dewatering of Airshaft Excavation

In this study, the deep excavation and dewatering strategy for the southern airshaft will be addressed. As illustrated in Figure 2, the excavation depth of the southern airshaft is 29.271 m with a planar dimension of 25.4 m \times 16.0 m, and the maintenance depth of the southern airshaft excavation is 48.0 m. The deep excavation construction of the southern airshaft excavation contains 15 construction steps, that is, step 1—excavation of the fourth soil layer, step 2—construction of the fourth concrete ring-shape purlin, step 3—construction of the lining wall on the second floor underground, step 4—excavation of the fifth soil layer, step 5—construction of the fifth concrete ring-shape purlin and supporting structures, step 6—construction of the lining wall on the third floor underground, step 7—concrete curing, step 8—excavation of the sixth soil layer, step 9—construction of the sixth concrete ring-shape purlin, step 10—concrete curing, step 11—excavation of the last soil layer, step 12—base-plate pouring, step 13—base-plate curing, step 14—lining pouring, and step 15—capping operation.

With the aid of the static cone penetration tests, the foundation of the southern airshaft can be divided into 20 soil layers in the depth direction. Table 1 lists the hydraulic and mechanical properties of different soil layers of the southern airshaft foundation. Two confined aquifers are distributed in the soil layer ⑥₃ and the soil layers (14)₁ and (14)₂, and the groundwater level will be greatly affected by the seasonal variation and the water level of the Qiantang River. The complicated engineering geological and hydrogeological conditions of the southern airshaft foundation bring great challenges in excavation dewatering works. The complexity and high risks in the dewatering process for deep excavation of the southern airshaft are reflected in the following issues: (i) the excavation depth of the southern airshaft excavation is large; (ii) the round gravel layer with a high coefficient of permeability is not deeply buried; (iii) the underground water level is anticipated to be largely descended to meet the designed drawdown requirement; (iv) the southern airshaft excavation is adjacent to the Qiantang River and the hydraulic relationship between the surface water and the underground water is inexplicit; (v) the hydraulic connection between different soil layers of the southern airshaft foundation is not clear.



(a) Plan view



(b) Cross-sectional view

Figure 2: Schematic of southern airshaft excavation (unit: mm).

Table 1: Hydraulic and mechanical properties of soil layers of southern airshaft foundation.

No.	Soil layer	Thickness of soil layer (m)	Coefficient of permeability (cm/s)	Modulus of compressibility (MPa)
① ₁	Miscellaneous fill soil	0.70 ~ 3.10	5.0E - 03	—
① ₂	Plain fill soil	0.30 ~ 6.00	8.0E - 04	6.5
③ ₁	Sandy silt	3.4	4.0E - 04	7.0
③ ₂	Sandy silt	3.50 ~ 9.70	7.0E - 04	8.5
③ ₄	Sandy silt	1.00 ~ 5.90	6.5E - 04	5.5
③ ₅	Silty sand and sandy silt	1.60 ~ 7.00	3.0E - 03	7.0
③ ₆	Silt	4.20 ~ 10.95	4.0E - 03	10.0
③ ₇	Sandy silt	0.80 ~ 6.20	2.0E - 04	5.5
③ ₈	Silt	—	4.5E - 03	10.5
④ ₃	Silty soft clay	2.60 ~ 6.70	3.0E - 06	2.6
⑥ ₁	Silty soft clay	1.50 ~ 3.70	2.0E - 06	2.7
⑥ ₂	Silty soft clay	1.00 ~ 8.30	5.0E - 06	2.8
⑥ ₃	Silt	0.50 ~ 3.85	3.0E - 03	8.0
⑧ ₂	Silty soft clay	0.80 ~ 8.20	4.0E - 05	3.0
⑧ ₃	Silty-fine sand	1.80 ~ 8.50	5.0E - 03	8.5
⑩ ₁	Silty clay	1.90 ~ 4.30	8.0E - 06	3.2
⑩ ₂	Silty clay	2.80 ~ 4.60	4.0E - 06	4.5
(14) ₁	Medium sand	—	6.0E - 03	11.0
(14) ₂	Rounded pebble	—	3.5E - 01	—

3. Intelligent Dewatering Risk Assessment System

3.1. Novel Design Method of Deep Excavation Dewatering

During the dewatering process of the deep excavation, one of the key problems is how to handle the issue of confined water decompression which is the most critical risk sources in the deep excavation practices. Currently existent design methods for dewatering of the deep excavation are primarily based on the theory of groundwater dynamics and have the following limitations: (i) the existing design methods for dewatering of the deep excavation are originated from the water supply theory and have not sufficiently taken into account the function of the waterproof curtain of the supporting structure; (ii) the empirical equations or the analytical methods are mainly adopted in the existing design methods for dewatering of the deep excavation with the fact of ignoring the detouring flow effect of the underground wall; (iii) both the anisotropic property of the soil layer and the three-dimensional flow effect of the partially penetrating well near the underground wall are neglected in the existing design methods for dewatering of the deep excavation.

For deep excavation construction of the southern airshaft of Hangzhou Metro Line 1, the traditional dewatering method is lack of robustness in fulfilling the targeted drawdown requirement. In this connection, a novel design method based on the coupled three-dimensional flow theory for dewatering of the airshaft excavation is developed in recognition that the implementation of the full waterproof curtain is highly difficult and costly. In the proposed method, the coupling effects amongst the underground continuous wall, the seepage

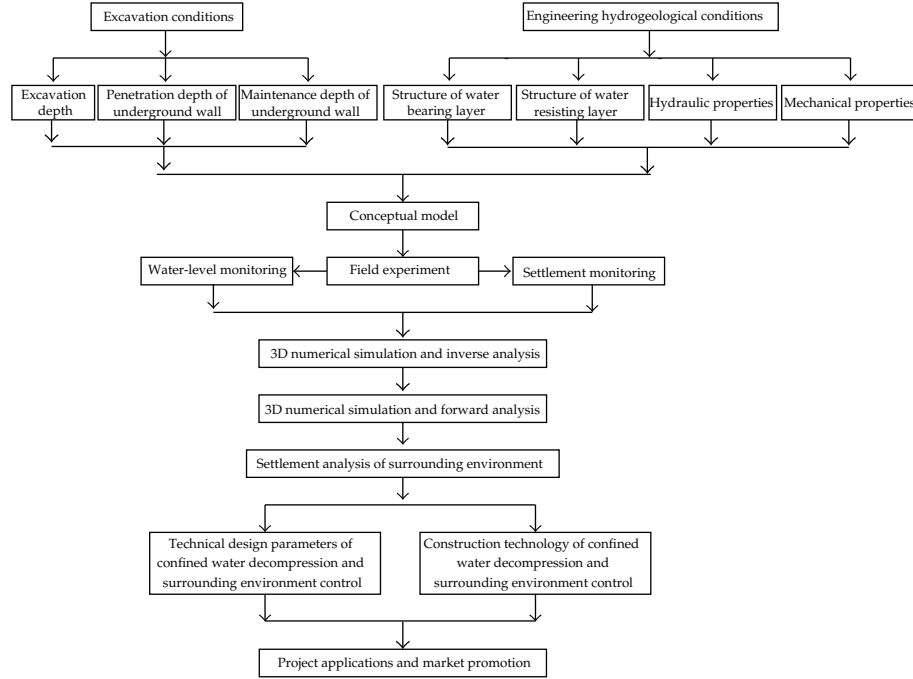


Figure 3: Design and implementation procedure for dewatering of airshaft excavation.

well, and the soil layers are fully taken into account to reach the targets of maximizing the water-level drawdown inside the airshaft excavation and minimizing both the pump output inside the airshaft excavation and the water-level drawdown outside the airshaft excavation. Figure 3 illustrates the basic design and implementation procedure of the proposed method for dewatering of the airshaft excavation.

3.2. Framework of Intelligent Risk Assessment

In recognizing the complexity of dewatering for the confined water in the round gravel layer, an intelligent risk assessment system has been developed to ensure the construction safety during the dewatering process for the southern airshaft excavation. This system is modularly designed and consists of four independent modules: Module 1—Water-level Automatic Collection and Surveillance System (WL-ACSS), Module 2—Water-level Remote Transmission and Assessment System (WL-RTAS), Module 3—Water-level Automated Alarming System (WL-AAS), and Module 4—Auxiliary and Inspection System (AIS). The integration of these four modules is shown in Figure 4.

The WL-ACSS system employs advanced water-level automatic instruments and high-precision vibrating-wire water-level sensors to automatically monitor the underground water-level of the airshaft excavation. It is devised to continuously collect and record the kinetic water-level data for both the observation wells and the pumping wells within a designated time interval. Incorporated with the customized software, the WL-ACSS system is capable of graphically displaying the monitored water-level data and intuitively reflecting the present operational condition of depressurization dewatering. By so doing, the abnormal

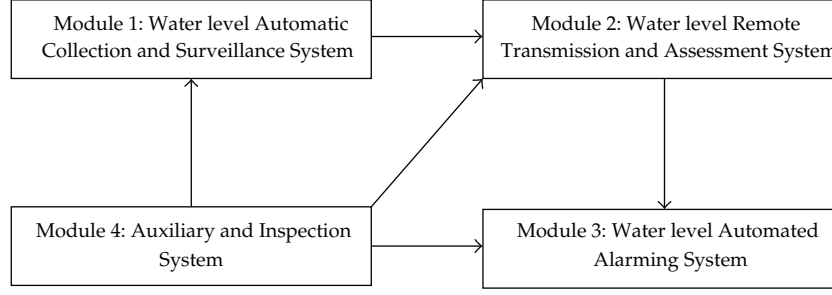


Figure 4: Modular architecture of intelligent risk assessment system.

phenomenon during the dewatering for the airshaft excavation could be readily seized and surveilled in real time to facilitate decision making on timely actions in the event of an emergency.

The WL-RTAS system compiles the monitored water-level data acquired by the WL-ACSS system and generates the specified files suitable for remote transmission through tethered and/or wireless networks. Once the client computers receive the transmitted files, the real-time water-level data will be evaluated with the aid of the coupled three-dimensional flow model which can be expressed by

$$\begin{aligned}
 \frac{\partial}{\partial x} \left(k_{xx} \frac{\partial h}{\partial x} \right) + \frac{\partial}{\partial y} \left(k_{yy} \frac{\partial h}{\partial y} \right) + \frac{\partial}{\partial z} \left(k_{zz} \frac{\partial h}{\partial z} \right) - W &= S_s \frac{\partial h}{\partial t}, \\
 k_{xx} \frac{\partial h}{\partial n_x} + k_{yy} \frac{\partial h}{\partial n_y} + k_{zz} \frac{\partial h}{\partial n_z} \Big|_{\Gamma_2} &= q(x, y, z, t), \\
 h(x, y, z, t) \Big|_{t=t_0} &= h_0(x, y, z),
 \end{aligned} \tag{3.1}$$

where k_{xx} , k_{yy} , and k_{zz} represent the coefficients of permeability in x , y , and z direction, respectively; h is the water head in time t ; W is the source/sink term; S_s is the water storage rate; Γ_2 is the boundary condition; n_x , n_y , and n_z denote the unit vectors of the external normal lines along x , y , and z directions, respectively; q is the water recharge per unit area.

The WL-AAS system includes the water-level anomaly alarming system and the power-supply interruption alarming system. For the water-level anomaly alarming system, the warning facilities are allocated at the wellheads and the control room for generating the alarm buming with light signals. The dynamic variation of the water-level of the airshaft excavation will be tracked and the alarm trigger will be activated once the abnormal water-level is identified by use of a novel threshold detection algorithm. The power-supply interruption alarming system will promptly notify the site managers to inspect or switch the electric circuits when the power goes out.

The AIS system provides the accessory equipment for the intelligent risk assessment system and a laptop-computer-aided portable system for inspecting and maintaining sensors, data acquisition units, and cable networks.

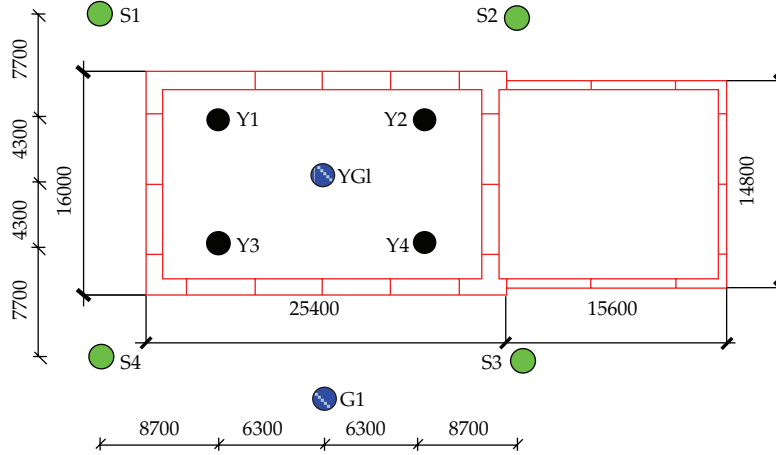


Figure 5: Dewatering wells distributed around southern airshaft excavation (unit: mm).

4. Dewatering Risk Assessment of Airshaft Excavation

4.1. Field Pumping Experiments

After rationally disposing the pumping wells and the observation wells around the region of airshaft excavation, field pumping experiments have been conducted with the purpose of providing sufficient data samples for numerical simulation study of the coupling effect amongst the underground wall, the seepage well, and the soil layers, inferring the hydro-geological parameters of the soil layers and the single-well water flow rate, and validating the hydraulic relationships between different soil layers and the feasibility of confined aquifer dewatering. Figure 5 shows the plan view of the dewatering wells distributed around the excavation area of the southern airshaft. Four pumping wells with a depth of 50 m, that is, Y1, Y2, Y3, and Y4, were allocated inside the southern airshaft excavation; while four pumping wells, that is, S1, S2, S3, and S4 with a depth of 54 m, were deployed outside the southern airshaft excavation. Additionally, two observation wells, that is, YG1 with a depth of 50 m and G1 with a depth of 48 m, were arranged inside the southern airshaft excavation and outside the southern airshaft excavation, respectively.

Multiwell pumping experiments have been carried out for efficiency assessment of the dewatering wells inside the southern airshaft excavation (Y1~Y4) and outside the southern airshaft excavation (S1~S4), respectively. The water-level drawdown of the observation wells (YG1 and G1) has been continuously recorded by the water-level automatic collection system and remotely transmitted to the control room in real time. For the pumping experiments inside the southern airshaft excavation, four pumping wells will be activated in sequence at a time interval of 2 hours and then ceased sequentially at the same time interval; while for the four pumping experiments outside the southern airshaft excavation, the time interval for turn-on and shut-down of the pumping wells is 10 hours.

Figure 6 illustrates the measured water-level drawdown of the two observation wells (YG1 and G1) during multiwell pumping experiments inside the southern airshaft excavation. It is seen from Figure 6 that the water-level of the observation well YG1 which is located inside the southern airshaft excavation declines dramatically when the four pumping wells (Y1~Y4) are enabled gradually. The maximum water-level drawdown of the observation well

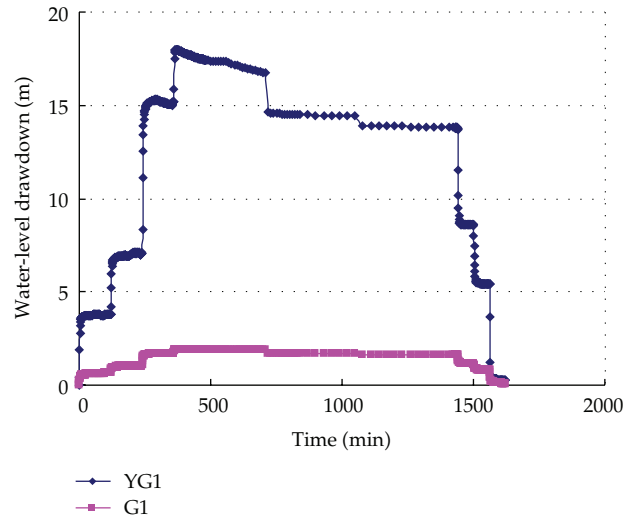


Figure 6: Water-level drawdown of observation wells during multiwell pumping experiments inside southern airshaft excavation.

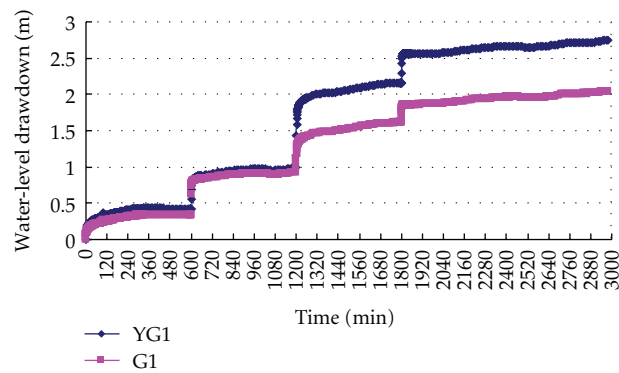


Figure 7: Water-level drawdown of observation wells during multiwell pumping experiments outside southern airshaft excavation.

YG1 reaches 18.00 m which is larger than the targeted water-level drawdown of 11.72 m. On the other hand, the water-level of the observation well G1 outside the southern airshaft excavation declines slowly and the maximum water-level drawdown of the observation well G1 is only 1.92 m. The main reason for the great difference of water-level drawdown between the two observation wells is because the underground continuous wall obstructs the hydraulic connection between the confined aquifers inside and outside the southern airshaft excavation.

Figure 7 shows the measured water-level drawdown of the two observation wells (YG1 and G1) during multiwell pumping experiments outside the southern airshaft excavation. It is observed from Figure 7 that the water-levels of the two observation wells decline almost synchronously. The maximum water-level drawdown of the two observation wells is 2.75 m which is much less than the targeted water-level drawdown of 11.72 m. Therefore,

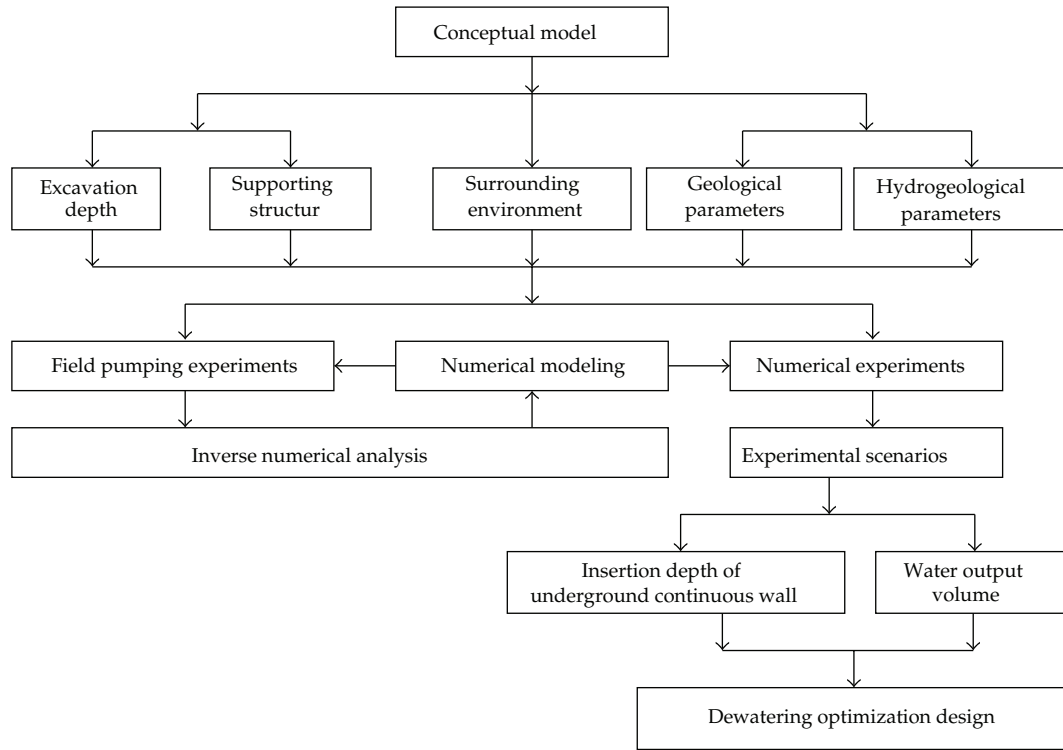


Figure 8: Flowchart of inverse simulation analysis for deep excavation dewatering.

the dewatering scheme by pumping the wells outside the southern airshaft excavation will not be adopted in this project.

4.2. Inverse Simulation and Extrapolation Analysis

Based on the measurement data from the field pumping experiments, the hydraulic parameters of different soil layers are derived by inverse simulation analysis, and then the conceptual model of excavation dewatering will be improved to be a quantitative analytical model for further dewatering efficiency analysis and risk assessment of various scenarios. Meanwhile, with such an updated analytical model, the interaction analysis between the underground continuous wall and the dewatering wall can be executed to facilitate the dewatering optimization design, dewatering mechanism analysis, and dewatering method extrapolation. Figure 8 shows the flowchart of the inverse simulation analysis for dewatering of the airshaft excavation.

Figure 9 shows the calculated water-level drawdown at three different locations, that is, the top of the confined aquifer (YG1-A), the middle of the confined aquifer (YG1-B), and the bottom of the confined aquifer (YG1-C) with the variation of the insertion depth of the underground continuous wall. It is revealed from Figure 9 that with the increasing of the insertion depth of the underground continuous wall, the water-level drawdown will increase gradually for all the three measurement locations. Figure 10 illustrates the predicted water output volume with the variation of the insertion depth of the underground continuous wall

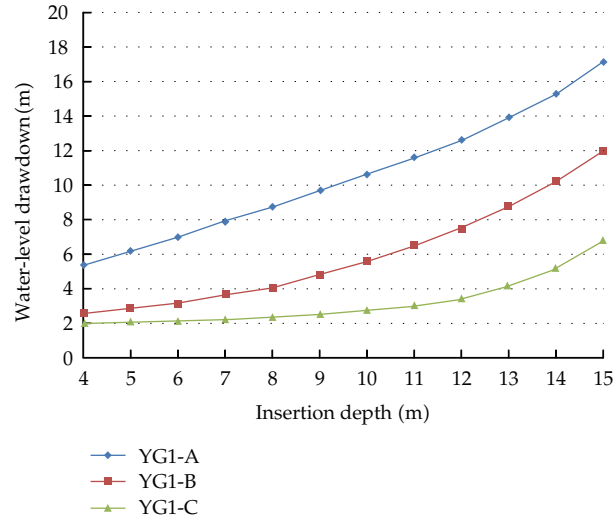


Figure 9: Water-level drawdown versus insertion depth of underground continuous wall.

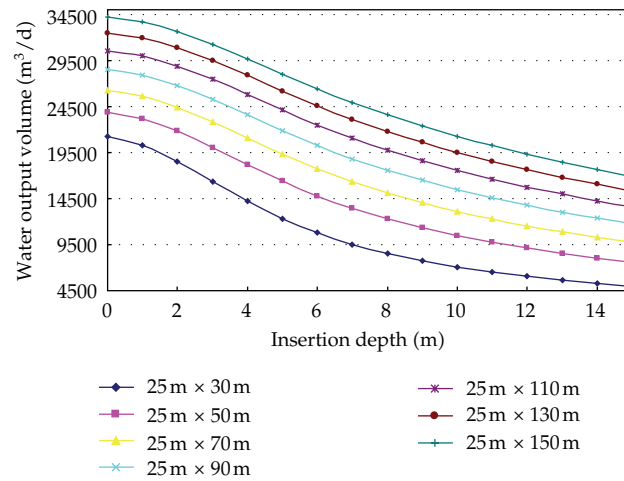


Figure 10: Water output volume versus insertion depth of underground continuous wall.

for different geometrical dimensions of the deep excavation. From Figure 10, it is indicated that the predicted water output volume will decrease gradually with the increasing of the insertion depth of the underground continuous wall. A further observation into Figure 10 reveals that with the increasing of the geometrical dimensions of the deep excavation, the predicted water output volume will increase.

5. Conclusions

The safety of deep excavation dewatering for the metro tunnels and stations has gained great concerns which will bring geological disasters and pose threat to the public safety in metropolitan regions. In recognition of the limitations existent in the traditional dewatering

method, a novel design method for excavation dewatering has been developed on the basis of the coupled three-dimensional flow theory. An intelligent risk assessment system has been developed in modular architecture and applied to evaluate the safety of excavation dewatering for the metro-tunnel airshaft of Hangzhou Metro Line 1.

In this study, the following specific conclusions are drawn: (i) there is a great difference of water-level drawdown between the observation well inside the airshaft excavation and that outside the airshaft excavation during multiwell pumping experiments inside the airshaft excavation; this is because the underground continuous wall obstructs the hydraulic connection between the confined aquifers inside and outside the airshaft excavation; (ii) the water-level drawdown results of the observation wells during multiwell pumping experiments outside the airshaft excavation reveal that the dewatering scheme by pumping the wells outside the airshaft excavation is inappropriate; (iii) with the increasing of the insertion depth of the underground continuous wall, the water-level drawdown will increase gradually while the predicted water output volume will decrease.

Acknowledgments

This research work was jointly supported by the Science Fund for Creative Research Groups of the NSFC (Grant no. 51121005), the National Natural Science Foundation of China (Grant no. 51178083, 51222806), and the Program for New Century Excellent Talents in University (Grant no. NCET-10-0287). The authors also wish to express their thanks to the Hangzhou Metro Group Co., Ltd., for permission to publish this paper.

References

- [1] Y. Y. Kim and K. K. Lee, "Disturbance of groundwater table by subway construction in the Seoul area, Korea," *Geosciences Journal*, vol. 7, no. 1, pp. 37–46, 2003.
- [2] J. C. Ni and W. C. Cheng, "Shield machine disassembly in grouted soils outside the ventilation shaft: a case history in Taipei Rapid Transit System (TRTS)," *Tunnelling and Underground Space Technology*, vol. 26, no. 2, pp. 435–443, 2011.
- [3] M. Tokgoz, K. K. Yilmaz, and H. Yazicigil, "Optimal aquifer dewatering schemes for excavation of collector line," *Journal of Water Resources Planning and Management*, vol. 128, no. 4, pp. 248–261, 2002.
- [4] D. Roy and K. E. Robinson, "Surface settlements at a soft soil site due to bedrock dewatering," *Engineering Geology*, vol. 107, no. 3–4, pp. 109–117, 2009.
- [5] K. Demirbas, A. B. Altan-Sakarya, and H. Onder, "Optimal dewatering of an excavation site," *Proceedings of the Institution of Civil Engineers. Water Management*, vol. 165, no. 6, pp. 327–337, 2012.
- [6] N. Zhou, P. A. Vermeer, R. Lou, Y. Tang, and S. Jiang, "Numerical simulation of deep foundation pit dewatering and optimization of controlling land subsidence," *Engineering Geology*, vol. 114, no. 3–4, pp. 251–260, 2010.
- [7] M. Preece and W. Powrie, "Steady-state performance of construction dewatering systems in fine soils," *Geotechnique*, vol. 43, no. 2, pp. 191–205, 1993.
- [8] W. Powrie and T. O. L. Roberts, "Case history of a dewatering and recharge system in chalk," *Geotechnique*, vol. 45, no. 4, pp. 599–609, 1995.
- [9] C. I. Mansur and S. G. Durrett, "Dewatering cofferdam for construction of Olmsted Locks," *Journal of Geotechnical and Geoenvironmental Engineering*, vol. 128, no. 6, pp. 496–510, 2002.
- [10] A. Aryafar and F. D. Ardejani, "Anisotropy and bedding effects on the hydro geological regime in a confined aquifer to design an appropriate dewatering system," *International Journal of Environmental Science and Technology*, vol. 6, no. 4, pp. 563–570, 2009.
- [11] M. A. Bevan, W. Powrie, and T. O. L. Roberts, "Influence of large-scale inhomogeneities on a construction dewatering system in chalk," *Geotechnique*, vol. 60, no. 8, pp. 635–649, 2010.
- [12] S. Chen and Y. Xiang, "A procedure for theoretical estimation of dewatering-induced pile settlement," *Computers and Geotechnics*, vol. 33, no. 4–5, pp. 278–282, 2006.

- [13] W. L. Schroeder, V. W. Rybel, and L. Cochran, "Dewatering for Opal Springs Powerhouse excavation," *Journal of Construction Engineering and Management*, vol. 112, no. 3, pp. 440–451, 1986.
- [14] S. Q. Wang, Y. P. Wee, and G. Ofori, "DSSDSS: a decision support system for dewatering systems selection," *Building and Environment*, vol. 37, no. 6, pp. 625–645, 2002.
- [15] R. A. Forth, "Groundwater and geotechnical aspects of deep excavations in Hong Kong," *Engineering Geology*, vol. 72, no. 3-4, pp. 253–260, 2004.
- [16] C. Rechea, S. Levasseur, and R. Finno, "Inverse analysis techniques for parameter identification in simulation of excavation support systems," *Computers and Geotechnics*, vol. 35, no. 3, pp. 331–345, 2008.
- [17] S. Y. Chen and Y. F. Li, "Vision sensor planning for 3-D model acquisition," *IEEE Transactions on Systems, Man, and Cybernetics, Part B*, vol. 35, no. 5, pp. 894–904, 2005.
- [18] S. Y. Chen, Y. F. Li, and J. Zhang, "Vision processing for realtime 3-D data acquisition based on coded structured light," *IEEE Transactions on Image Processing*, vol. 17, no. 2, pp. 167–176, 2008.
- [19] F. Kang, J. Li, and Q. Xu, "Structural inverse analysis by hybrid simplex artificial bee colony algorithms," *Computers and Structures*, vol. 87, no. 13-14, pp. 861–870, 2009.
- [20] Y. Q. Ni, X. W. Ye, and J. M. Ko, "Monitoring-based fatigue reliability assessment of steel bridges: analytical model and application," *Journal of Structural Engineering*, vol. 136, no. 12, pp. 1563–1573, 2010.
- [21] S. Y. Chen, "Kalman filter for robot vision: a survey," *IEEE Transactions on Industrial Electronics*, vol. 59, no. 11, pp. 4409–4420, 2012.
- [22] S. Y. Chen, H. Tong, and C. Cattani, "Markov models for image labeling," *Mathematical Problems in Engineering*, vol. 2012, Article ID 814356, 18 pages, 2012.
- [23] Y. Q. Ni, X. W. Ye, and J. M. Ko, "Modeling of stress spectrum using long-term monitoring data and finite mixture distributions," *Journal of Engineering Mechanics*, vol. 138, no. 2, pp. 175–183, 2012.

Research Article

Prediction of Optimal Design and Deflection of Space Structures Using Neural Networks

**Reza Kamyab Moghadas,^{1,2} Kok Keong Choong,²
and Sabarudin Bin Mohd³**

¹ *The Iranian Academic Center for Education, Culture and Research, Kerman 7616914111, Iran*

² *School of Civil Engineering, Universiti Sains Malaysia, Nibong Tebal, Penang, Malaysia*

³ *City University College, Petaling Jaya, Selangor, Malaysia*

Correspondence should be addressed to Reza Kamyab Moghadas, r_kamyab_m@yahoo.com

Received 8 October 2012; Accepted 18 November 2012

Academic Editor: Siamak Talatahari

Copyright © 2012 Reza Kamyab Moghadas et al. This is an open access article distributed under the Creative Commons Attribution License, which permits unrestricted use, distribution, and reproduction in any medium, provided the original work is properly cited.

The main aim of the present work is to determine the optimal design and maximum deflection of double layer grids spending low computational cost using neural networks. The design variables of the optimization problem are cross-sectional area of the elements as well as the length of the span and height of the structures. In this paper, a number of double layer grids with various random values of length and height are selected and optimized by simultaneous perturbation stochastic approximation algorithm. Then, radial basis function (RBF) and generalized regression (GR) neural networks are trained to predict the optimal design and maximum deflection of the structures. The numerical results demonstrate the efficiency of the proposed methodology.

1. Introduction

The history of the applications of Artificial Intelligence to civil and structural engineering is simultaneously brief and long. It is brief if compared to the history of civil and structural engineering, whose definition as a discipline can be fixed a very long time ago. It makes sense to consider civil and structural engineering as the most ancient applicative discipline, being founded in preclassical world by Egyptians and Babylonians. It is long, instead, if compared to the history of Artificial Intelligence, whose name first appeared in science at the end of the sixties of the twentieth century. The earliest applications to civil and structural engineering are very likely [1], where authors review tools and techniques for knowledge-based expert system for engineering design. An even earlier paper whose scope was indeed wider, but introduced some fundamental themes, is [2]. We can definitely settle a start date in 1986 when

the first International Symposium on this theme took place [3]. In statistical terms, since we can fix Artificial Intelligence engineering applications start date in 1950 when the first attempt to provide a true intelligent program was carried out [4], this means that, nowadays, we are experiencing 18 years of history of the applications of Artificial Intelligence techniques to civil and structural engineering.

As in this study our main aim is to employ neural networks to predict the optimal design and maximum deflection of the double layer grids, the next paragraph is devoted to review the literature about the optimal design of space structures by soft computing techniques.

Erbatur et al. [5] reported the development of a computer-based systematic approach for discrete optimal design of planar and space structures composed of one-dimensional elements. Rajasekaran [6] created the input for large space structures using Formian. In this paper, a new optimization technique called cellular automata (CA) has been combined with genetic algorithm (GA) to develop different search and optimization known as cellular genetic algorithm (CGA), which considers the areas of the space structures as discrete variables. Krishnamoorthy et al. [7] proposed GA with objective-oriented framework which was used in space truss optimization. Tashakori and Adeli [8] adopted the patented robust neural dynamics model for optimum design of space trusses made of commercially available cold-formed shapes in accordance with AISC specification. E. Salajegheh and J. Salajegheh [9] achieved the optimal design of space structures while the design variables are continuous and discrete. To reduce the computational work involved in the optimization process they employed a semiquadratic function; also they use a hybrid form of the approximation. Kaveh and Dehkordi [10] trained neural networks for the analysis, design, and prediction of the displacements of domes using the backpropagation and radial basis Functions neural networks. The performance of these networks is compared when applied to domes. Kaveh et al. [11] combined the energy method and the force method in the context of transmission tower optimization in order to form a holistic design and optimization approach, eliminating the need for time-intensive matrix inversion. The addition of a neural network as an analysis tool reduces the overall computational load. Kaveh and Servati [12] trained neural networks for design of square diagonal-on-diagonal double layer grids. They employed backpropagation algorithm for training the networks for evaluation of the maximum deflection, weight, and design of the double layer grids. Salajegheh and Gholizadeh [13] employed a modified genetic algorithm (GA) and radial basis function (RBF) neural networks to optimize space structures. Kaveh et al. [14] employed ant colony optimization (ACO) algorithm for optimal design of space structures with fixed geometry. Gholizadeh et al. [15] employed a combination of GA and wavelet radial basis function (WRBF) neural networks to find the optimal weight of structures subject to multiple natural frequency constraints.

Much more other applications of neural networks in the field of civil engineering can be found in the literature [16–20].

In this investigation, an innovative methodology is proposed to predict the optimal design and maximum deflection of the square-on-square double layer grids. This methodology consists of three stages. In the first stage, a number of the double layer grids with random spans and heights are generated. In the second stage the generated double layer grids are optimized by an optimization algorithm. Although, in the recent years many new structural optimization algorithms have been proposed by the researchers [21–25], in this paper, simultaneous perturbation stochastic approximation (SPSA) [26] algorithm is used due to its computational merits. Also, the maximum deflections of the optimal structures are

saved. In the third stage, radial basis function (RBF) [27] and generalized regression (GR) [27] neural networks are trained to predict the optimal design and maximum deflection of the double layer grids. To design neural networks MATLAB [28] is employed.

2. Formulation of Optimization Problem

In optimal design problem of space trusses the aim is to minimize the weight of the truss under constraints on stresses and displacements. This optimization problem can be expressed as follows:

$$\text{minimize: } w(x_1, \dots, x_n, \dots, x_{ng}) = \sum_{n=1}^{ng} x_n \sum_{m=1}^{nm} \gamma_m l_m, \quad (2.1)$$

$$\begin{aligned} \text{subject to: } \sigma_i &\leq \sigma_{\text{all},i}, \quad i = 1, 2, \dots, ne, \\ \delta_j &\leq \delta_{\text{all},j}, \quad j = 1, 2, \dots, nj, \end{aligned} \quad (2.2)$$

where x_n , γ_m , and l_m are cross-sectional area of members belonging to group n , weight density, and length of m th element in this group, respectively; ng and nm are the total number of groups in the structure and the number of members in group n , respectively; ne and nj are the total number of the elements and nodes in truss, respectively; σ_i and δ_j are stress in the i th element and displacement of the j th node, respectively. Also, $\sigma_{\text{all},i}$ and $\delta_{\text{all},j}$ are allowable stress in the i th member and allowable deflection of the j th node, respectively.

In this study, besides cross-sectional areas (x_n) the geometry dependent parameters of the double layer grid, L and h , are also variables. In other words, the aim is to find optimal cross-sectional areas for each set of L and h . Thus, (2.1) can be reexpressed as follows:

$$\text{For each set of } L \text{ and } h \text{ minimize } w(x_1, \dots, x_n, \dots, x_{ng}) = \sum_{n=1}^{ng} x_n \sum_{m=1}^{nm} \gamma_m l_m. \quad (2.3)$$

It is obvious that the computational burden of the above optimization problem is very high due to the fact that L and h are variables. Employing the neural network technique can substantially reduce the computational costs.

As the SPSA requires less number of function evaluations (structural analyses) than the other type of gradient-based methods, it is selected as the optimizer in this study. The basic concepts of the SPSA are explained in the next section.

3. SPSA Optimization Algorithm

SPSA has recently attracted considerable international attention in areas such as statistical parameter estimation, feedback control, simulation-based optimization, signal and image processing, and experimental design. The essential feature of SPSA is the underlying gradient approximation that requires only two measurements of the objective function regardless of the dimension of the optimization problem. This feature allows for a significant reduction in computational effort of optimization, especially in problems with a large number of variables

to be optimized. The basic unconstrained SPSA optimization algorithm is in the general recursive stochastic approximation (SA) form [26]:

$$\hat{X}_{k+1} = \hat{X}_k - a_k \hat{G}_k(\hat{X}_k), \quad (3.1)$$

where \hat{X}_k represents the estimate of X at k th iteration, $a_k > 0$ represent a scalar gain coefficient, and $\hat{G}(\hat{X}_k)$ represent an approximate gradient at \hat{X}_k . Under appropriate condition, (3.1) will converge to optimum design X^* in some stochastic sense. The essential part of (3.1) is the gradient approximation that is obtained using the simultaneous perturbation (SP) method. Let $w(\cdot)$ denote a measurement of objective function at a design level represented by the dot and let c_k be some positive number. The SP approximation has all elements of \hat{X}_k randomly perturbed together to obtain two measurements of $w(\cdot)$, but each component is formed from a ratio involving the individual components in the perturbation vector and the difference in the two corresponding measurement. For two sided simultaneous perturbation, we have

$$G_{ki}(\hat{X}_k) = \frac{w(\hat{X}_k + c_k \Delta_{ki}) - w(\hat{X}_k - c_k \Delta_{ki})}{2c_k \Delta_{ki}}, \quad (3.2)$$

where the distribution of the user-specified n_v dimensional random perturbation vector $\Delta_k = \{\Delta_{k1}, \Delta_{k2}, \dots, \Delta_{kn_v}\}^T$ satisfies condition discussed in [26].

It is observed that each iteration of SPSA needs only two objective function measurements independent of n_v because the numerator is the same in all n_v components. This circumstance provides the potential for SPSA to achieve a large savings in the total number of measurements required to estimate X^* when n_v is large.

3.1. Implementation of SPSA

The following step-by-step summary shows how SPSA iteratively produces a sequence of estimates [26].

Step 1 (initialization and coefficient selection). Set counter index $k = 0$. Pick initial guess and nonnegative coefficients a, c, A, α , and γ in the SPSA gain sequences $a_k = a/(A + k + 1)^\alpha$ and $c_k = c/(k + 1)^\gamma$. The choice of gain sequences (a_k and c_k) is critical to the performance of SPSA. Spall provides some guidance on picking these coefficients in a practically manner.

Step 2 (generation of the simultaneous perturbation vector). Generate by Monte Carlo an n_v -dimensional random perturbation vector Δ_k , where each of the n_v components of Δ_k is independently generated from a zero mean probability distribution satisfying some conditions. A simple choice for each component of Δ_k is to use a Bernoulli ± 1 distribution with probability of 1/2 for each ± 1 outcome. Note that uniform and normal random variables are not allowed for the elements of Δ_k by the SPSA regularity conditions.

Step 3 (objective function evaluations). Obtain two measurements of the objective function $w(\cdot)$ based on simultaneous perturbation around the current \hat{X}_k : $w(\hat{X}_k + c_k \Delta_k)$ and $w(\hat{X}_k - c_k \Delta_k)$ with the c_k and Δ_k from Steps 1 and 2.

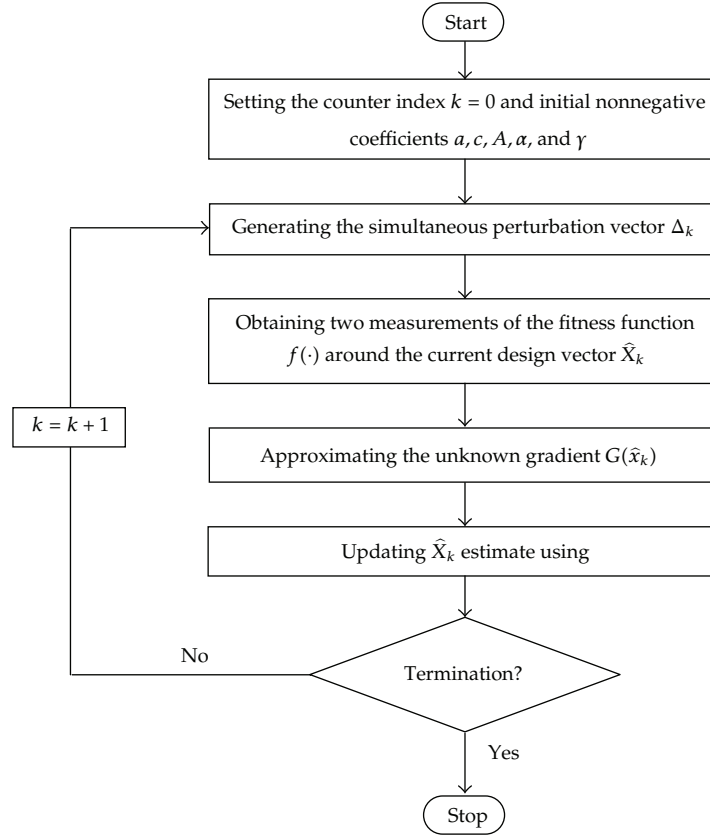


Figure 1: Flowchart of the SPSA.

Step 4 (gradient approximation). Generate the simultaneous perturbation approximation to the unknown gradient $G(\hat{X}_k)$:

$$\hat{G}_k(\hat{X}_k) = \frac{w(\hat{X}_k + c_k \Delta_k) - w(\hat{X}_k - c_k \Delta_k)}{2c_k} \begin{bmatrix} \Delta_{k1}^{-1} \\ \Delta_{k2}^{-1} \\ \vdots \\ \Delta_{kn_v}^{-1} \end{bmatrix}, \quad (3.3)$$

where Δ_{ki} is the i th component of Δ_k vector.

Step 5 (updating X estimate). Use the standard SA to update \hat{X}_k to new value \hat{X}_{k+1} .

Step 6 (iteration or termination). Return to Step 2 with $k + 1$ replacing k . Terminate the algorithm if there is little change in several successive iterates or the maximum allowable number of iterations has been reached. Figure 1 shows the flowchart of the SPSA.

In the present work, we suppose that the length and height of the double layer grids are varied in specific ranges. Our aim is to optimize all of the possible structures defined in the

ranges. Therefore it can be observed that the additional difficulty is the huge computational burden of the optimization process. In order to mitigate the difficulty, RBF and GR neural networks are employed to predict the optimal design of the double layer grids with various length and height.

4. Neural Networks

In the recent years, neural networks are considered as more appropriate techniques for simplification of complex and time consuming problems. The interest shown to neural networks is mainly due to their ability to process and map external data and information based on past experiences. Neural networks are not programmed to solve specific problems. Indeed, neural networks never use rules or physic equations related to the specific problem in which they are employed. Neural networks use the knowledge gained from past experiences to adapt themselves to solve the new problems.

4.1. Radial Basis Function

The use of RBF in the design of neural networks was first introduced by Wasserman in 1993 [27]. The RBF network basically involves three entirely different layers: an input layer, a hidden layer of high enough dimension, and an output layer. The transformation from the hidden unit to the output space is *linear*. Each output node is the weighted sums of the outputs of the hidden layer. However, the transformation from the input layer to the hidden layer is *nonlinear*. Each neuron or node in the hidden layer forming a linear combination of the basis (or kernel) functions which produces a localized response with respect to the input signals. This is to say that RBF produce a significant nonzero response only when the input falls within a small localized region of the input space. The most common basis of the RBF is a Gaussian kernel function of the form:

$$\varphi_l(Z) = \exp \left[-\frac{(Z - C_l)^T (Z - C_l)}{2\sigma_l} \right], \quad l = 1, 2, \dots, q, \quad (4.1)$$

where φ_l is the output of the l th node in hidden layer; Z is the input pattern; C_l is the weight vector for the l th node in hidden layer, that is, the center of the Gaussian for node l ; σ_l is the normalization parameter (the measure of spread) for the l th node; and q is the number of nodes in the hidden layer. The outputs are in the range from zero to one so that the closer the input is to the center of the Gaussian, the larger the response of the node is. The name RBF comes from the fact that these Gaussian kernels are radially symmetric; that is, each node produces an identical output for inputs that lie a fixed radial distance from the center of the kernel C_l . The network outputs are given by

$$y_i = Q_i^T \varphi_l(Z), \quad i = 1, 2, \dots, M, \quad (4.2)$$

where y_i is the output of the i th node, Q_i is the weight vector for this node, and M is the number of nodes in the output layer.

There are two common ways to calculate the measure of spread σ_l .

- (1) Find the measure of spread from the set of all training patterns grouped with each cluster center C_l ; that is, set them equal to the average distance between the cluster centers and the training patterns:

$$\sigma_l^2 = \frac{1}{N_l} \sum_{k \in C_l} (Z_k - C_l)^T (Z_k - C_l), \quad l = 1, 2, \dots, q, \quad (4.3)$$

where N_l is the number of patterns that belong to the l th cluster and k is the index number of a pattern that belongs to the l th cluster.

- (2) Find the measure of spread from among the centers (p -nearest neighbor heuristic):

$$\sigma_l^2 = \frac{1}{N_l} \sum_{k=1}^q (C_k - C_l)^T (C_k - C_l), \quad l = 1, 2, \dots, q. \quad (4.4)$$

4.2. Generalized Regression

Generalized regression network (GR) subsumes the basis function methods. This network does not require iterative training. The structure of GR is designated such that transpose of input matrix and transpose of desired output (target) matrix are chosen as first layer and second layer weight matrices, respectively. GR algorithm is based on nonlinear regression theory, a well established statistical technique for function estimation. Except the approach of adjusting of second layer weights, the other aspects of GR are identical to RBF neural networks.

5. Proposed Methodology

5.1. Double Layer Grid Model

In this section dimensions of considered double layer grid structure and its corresponding model are described. The model considered here is a double layer grid with bar elements connected by pin joints. The length of the spans, L , is varied between 25 and 75 m with step of 5 m. The height is varied between 0.035 and 0.095 L with steps of 0.2 m. The smallest and biggest structures in this interval are shown in Figure 2. The sum of dead and live loads equal to 250 kg/m² is applied to the nodes of the top layer.

In order to satisfy practical demands, in the optimization of large-scaled structure such as space structures, the structural elements should be divided into some groups. In this study the elements are put into 18 different groups. For this purpose a step-by-step summary defined bellow is employed.

Step 1. A similar cross sectional area is initially assigned to all elements of the structure.

Step 2. The structure is analyzed through FE and axial stresses of all members are obtained.

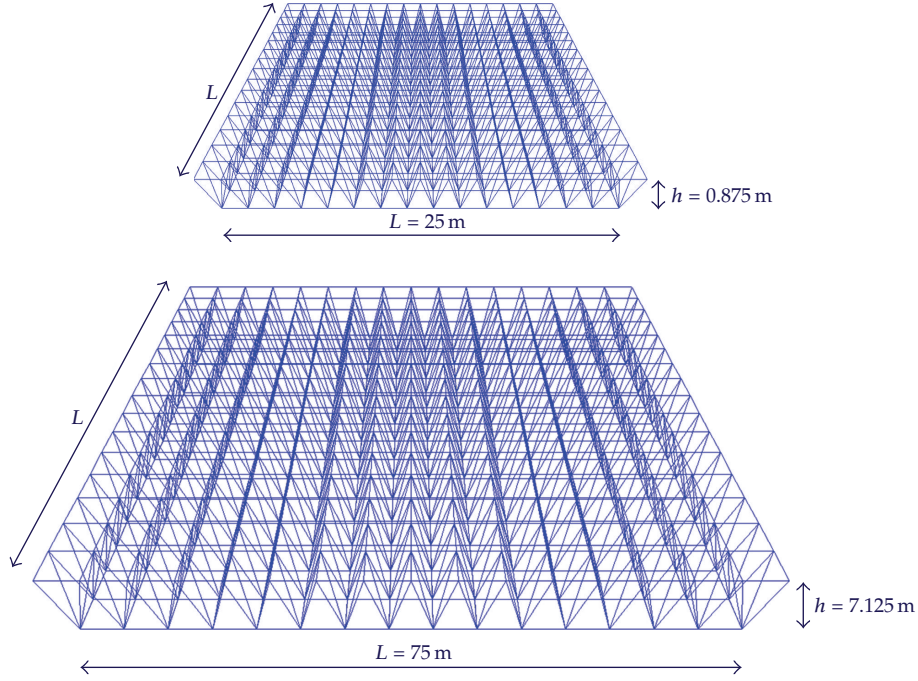


Figure 2: The smallest and biggest structures in the considered interval.

Step 3. All tension members of the structure are put into 6 groups according to their stress states as follows:

$$\begin{aligned}
 0.00 \leq \sigma < 200 \text{ kg/cm}^2 &\Rightarrow \text{group 1,} \\
 200 \leq \sigma < 400 \text{ kg/cm}^2 &\Rightarrow \text{group 2,} \\
 400 \leq \sigma < 600 \text{ kg/cm}^2 &\Rightarrow \text{group 3,} \\
 600 \leq \sigma < 800 \text{ kg/cm}^2 &\Rightarrow \text{group 4,} \\
 800 \leq \sigma < 1000 \text{ kg/cm}^2 &\Rightarrow \text{group 5,} \\
 \sigma \geq 1000 \text{ kg/cm}^2 &\Rightarrow \text{group 6.}
 \end{aligned} \tag{5.1}$$

Step 4. All compressive members of top and bottom layer elements of structure are put into 6 deferent groups according to their stress values as follows:

$$\begin{aligned}
 -200 \leq \sigma < -0.00 \text{ kg/cm}^2 &\Rightarrow \text{group 7,} \\
 -400 \leq \sigma < -200 \text{ kg/cm}^2 &\Rightarrow \text{group 8,} \\
 -600 \leq \sigma < -400 \text{ kg/cm}^2 &\Rightarrow \text{group 9,} \\
 -800 \leq \sigma < -600 \text{ kg/cm}^2 &\Rightarrow \text{group 10,}
 \end{aligned}$$

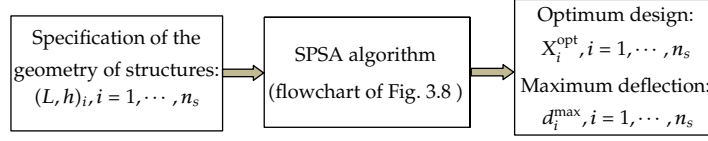


Figure 3: Data generation process.

$$\begin{aligned}
 -1000 \leq \sigma < -800 \text{ kg/cm}^2 &\Rightarrow \text{group 11,} \\
 \sigma < -1000 \text{ kg/cm}^2 &\Rightarrow \text{group 12.}
 \end{aligned} \tag{5.2}$$

Step 5. All compressive members of middle layer elements of structure are also put into 6 deferent groups based on their stresses as follows:

$$\begin{aligned}
 -200 \leq \sigma < -0.00 \text{ kg/cm}^2 &\Rightarrow \text{group 13,} \\
 -400 \leq \sigma < -200 \text{ kg/cm}^2 &\Rightarrow \text{group 14,} \\
 -600 \leq \sigma < -400 \text{ kg/cm}^2 &\Rightarrow \text{group 15,} \\
 -800 \leq \sigma < -600 \text{ kg/cm}^2 &\Rightarrow \text{group 16,} \\
 -1000 \leq \sigma < -800 \text{ kg/cm}^2 &\Rightarrow \text{group 17,} \\
 \sigma < -1000 \text{ kg/cm}^2 &\Rightarrow \text{group 18.}
 \end{aligned} \tag{5.3}$$

Preparing a neural network is achieved in three stages: data generating, training, and testing. In the first stage, a number of input and output pairs are provided and divided into training and testing sets. In the second stage, the training set is used and the modifiable parameters of the neural network are adjusted. In the last stage the performance generality of the trained neural network is examined through the testing set.

In order to provide the required data (data generation), a number of double layer grids according to their L and h are randomly selected. All of the selected structures are optimized using SPSA. Optimal designs of the selected structures and their corresponding maximum deflections are saved. This process is shown in Figure 3.

In order to train neural networks, the generated data should be separated to n_{tr} training data and n_{ts} testing data ($n_{tr} + n_{ts} = n_s$) as follows.

Training data for optimal design predictor networks:

$$\text{Training data : } \left\{ \begin{array}{l} \text{Inputs: } (L, h)_i, \\ \text{Outputs: } X_i^{\text{opt}} = \begin{bmatrix} x_1^{\text{opt}} \\ x_2^{\text{opt}} \\ \vdots \\ x_{18}^{\text{opt}} \end{bmatrix}_i, \quad i = 1, 2, \dots, n_{tr}. \end{array} \right. \tag{5.4}$$

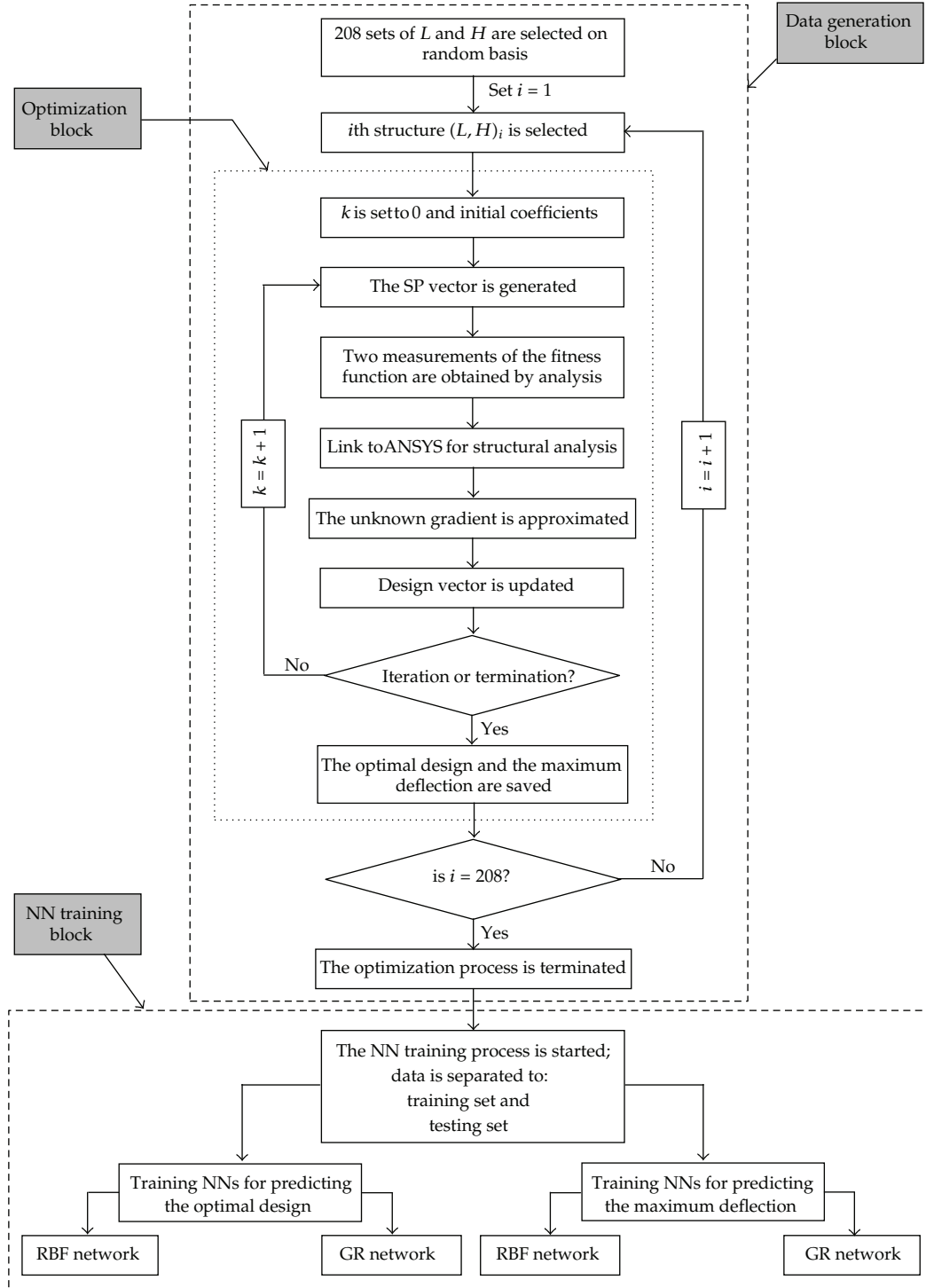


Figure 4: Flowchart of the proposed methodology.

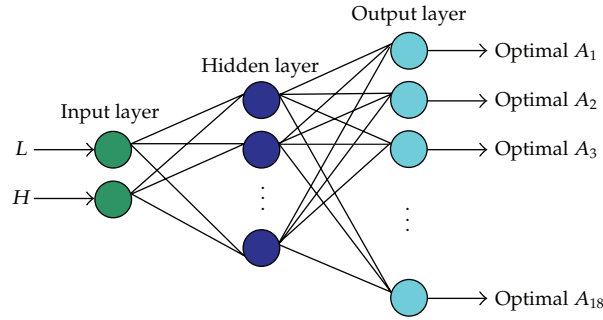


Figure 5: Typical topology of a neural network model to predict the optimal design.

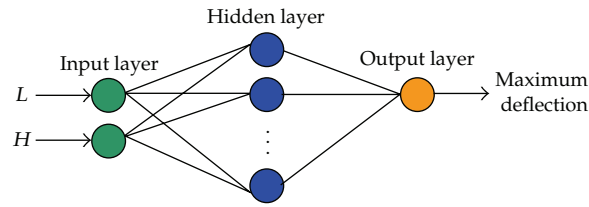


Figure 6: Typical topology of a neural network model to predict the maximum deflection.

Training data for maximum deflection predictor networks:

$$\text{Training data : } \begin{cases} \text{Inputs: } (L, h)_i, \\ \text{Outputs: } d_i^{\max}, \end{cases} \quad i = 1, 2, \dots, n_{\text{tr}}. \quad (5.5)$$

Testing data for optimal design predictor networks:

$$\text{Testing data : } \begin{cases} \text{Inputs: } (L, h)_i, \\ \text{Outputs: } X_i^{\text{opt}} = \begin{bmatrix} x_1^{\text{opt}} \\ x_2^{\text{opt}} \\ \vdots \\ x_{18}^{\text{opt}} \end{bmatrix}_i, \end{cases} \quad i = 1, 2, \dots, n_{\text{ts}}. \quad (5.6)$$

Testing data for maximum deflection predictor networks:

$$\text{Testing data: } \begin{cases} \text{Inputs: } (L, h)_i, \\ \text{Outputs: } d_i^{\max}, \end{cases} \quad i = 1, 2, \dots, n_{\text{ts}}. \quad (5.7)$$

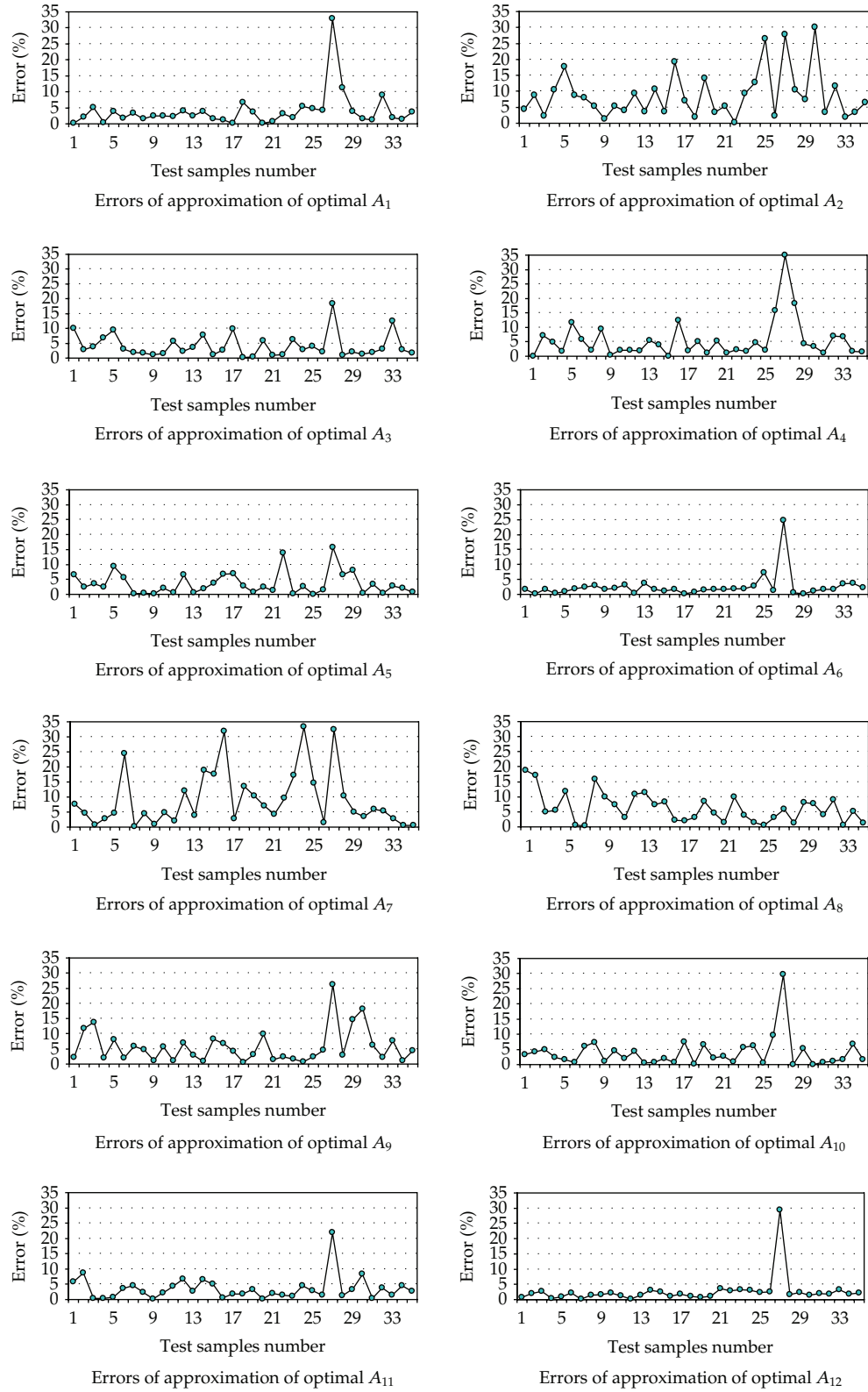


Figure 7: Continued.

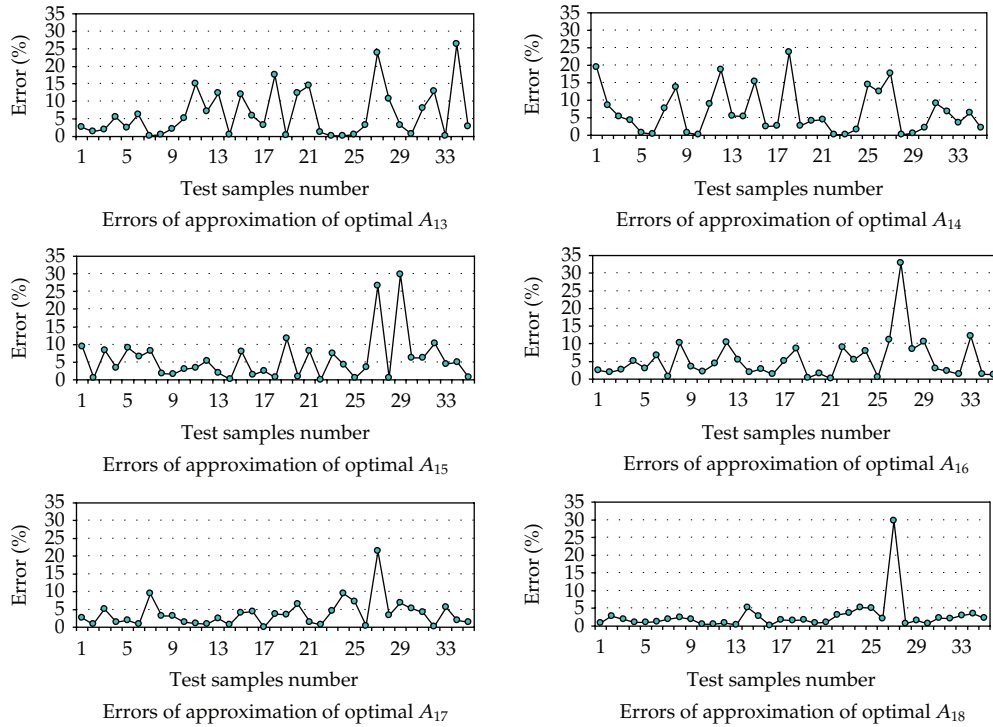


Figure 7: RBF errors in approximation of optimal cross-sectional areas.

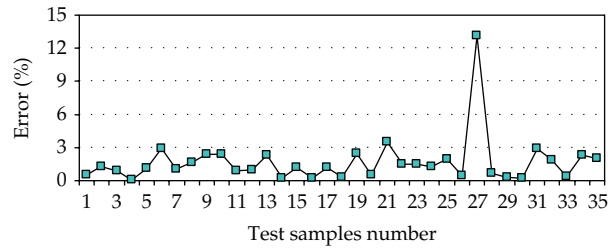


Figure 8: Errors of RBF for predicting the maximum deflections.

5.2. Main Steps in Training Neural Network

As a summary the main steps in training of RBF and GR NNs to predict optimal design and maximum deflection of the structure are as follows:

- (1) configuration processing of the selected space structures employing Formian,
- (2) selection a list of available tube sections from the standard lists,
- (3) implementation member grouping,
- (4) generation of some structures, based on span and height, to produce training set,
- (5) static analysis of the structures,
- (6) designing for optimal weight by SPSA according to AISC-ASD code,

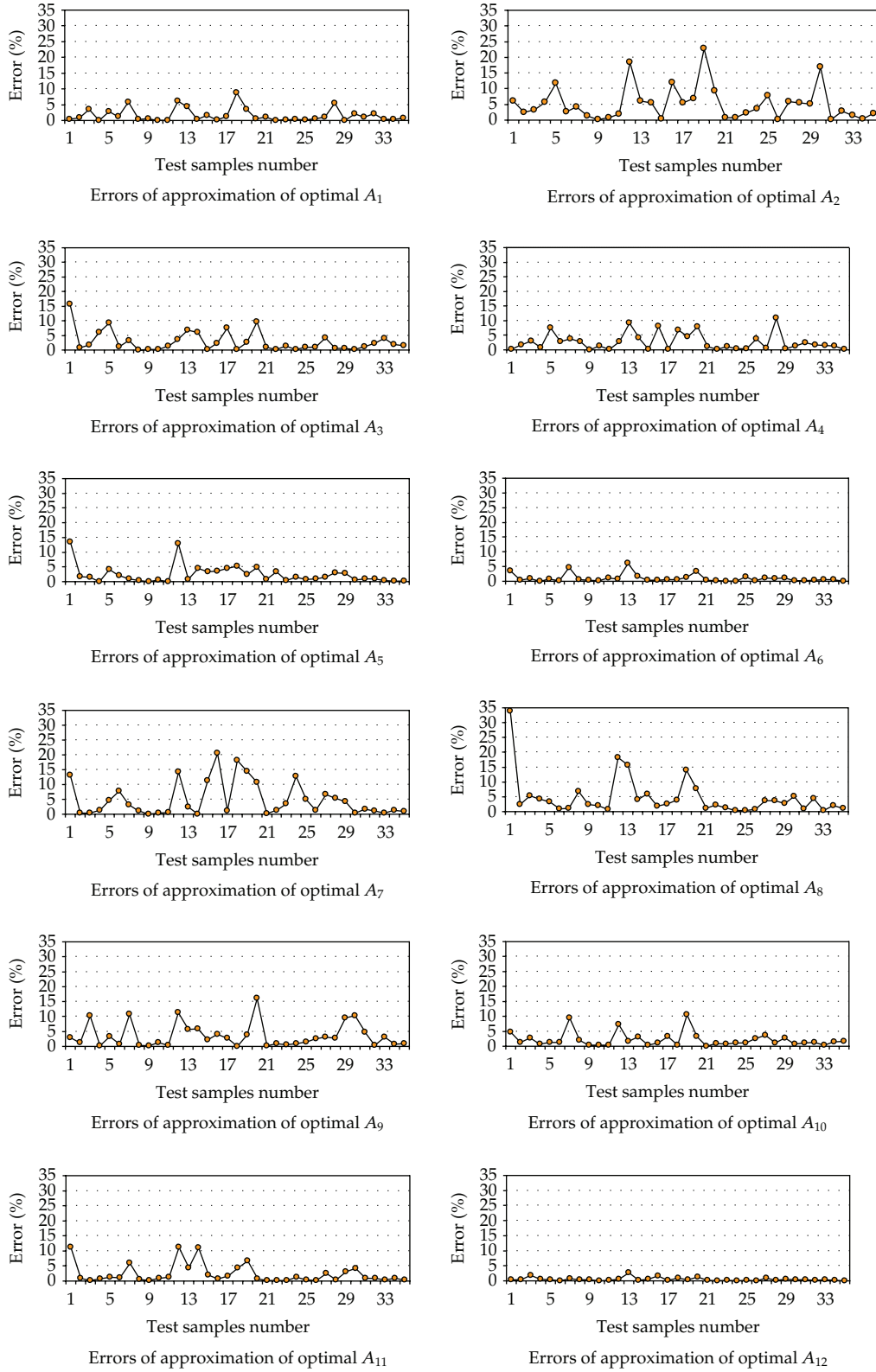


Figure 9: Continued.

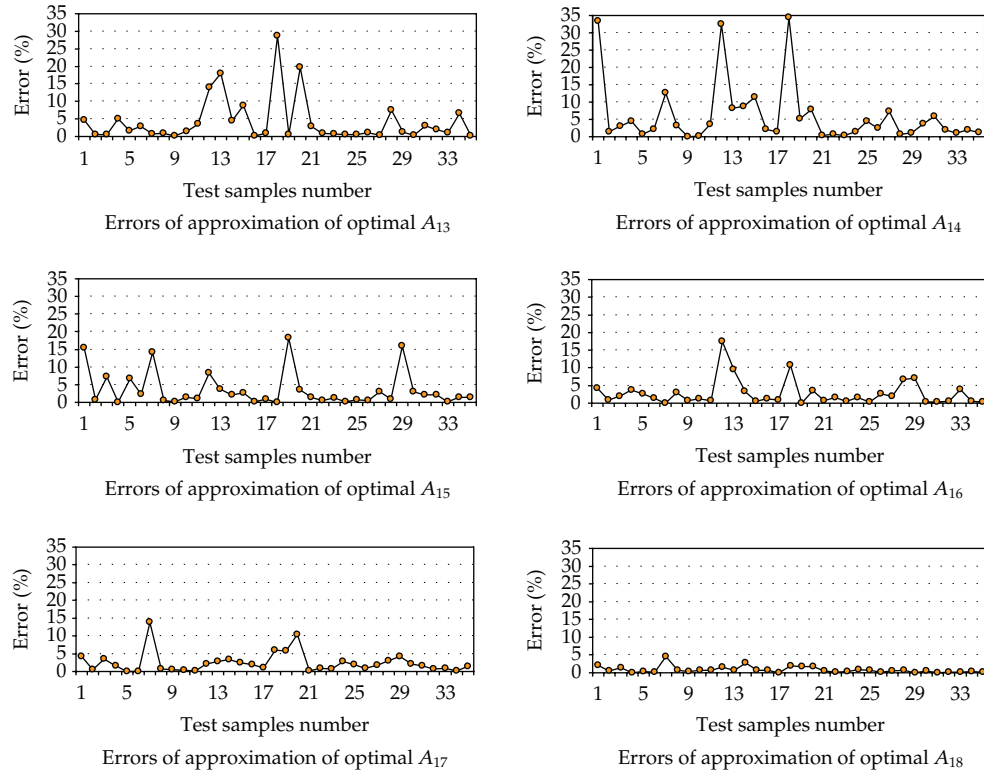


Figure 9: GR errors in approximation of optimal cross-sectional areas.

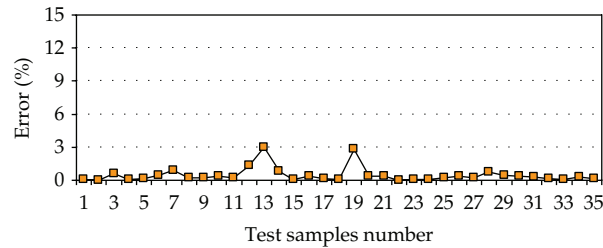


Figure 10: Errors of GR for predicting the maximum deflections.

- (7) training and testing RBF and GR to predict optimal design and maximum deflection,
- (8) improving generalization of the neural networks if it is necessary.

5.3. Flowchart of the Methodology

The flowchart of the proposed methodology is shown in Figure 4. This flowchart includes three main blocks: data generation, optimization, and NN training. The data generation block includes the optimization block. In these two blocks the data needed for neural network training is produced. The mentioned data are stated through (5.4) to (5.7).

Table 1: Summary of errors of RBF and GRNN in approximation of optimal designs.

Cross-sectional area	RBF		GRNN	
	Max. error	Mean of errors	Max. error	Mean of errors
1	32.8501	3.9054	8.8182	1.6575
2	30.0348	8.7955	22.8185	5.2312
3	18.3493	4.1153	15.6306	2.8343
4	36.8009	5.5074	10.8515	2.7220
5	15.6441	3.5933	13.4325	2.4476
6	24.8060	2.4974	6.1103	0.9992
7	33.3249	9.2145	20.4911	4.9154
8	18.7265	6.1936	33.8892	4.7607
9	26.1423	5.6690	16.1963	3.6055
10	29.7808	3.8814	10.6282	2.1702
11	21.9747	3.5231	11.3200	2.3858
12	29.3597	2.6233	2.6899	0.4795
13	26.4572	6.4117	28.6768	4.1939
14	23.7474	6.6549	37.5173	6.1356
15	29.8091	5.7633	18.2707	3.5529
16	32.8732	5.3975	17.5221	2.7931
17	21.5389	3.7532	13.8589	2.4312
18	29.6637	2.7991	4.4832	0.8361
Avr.	26.7714	5.0166	16.2892	3.0185

Table 2: Summary of errors of RBF and GRNN in approximation of maximum deflection.

RBF		GRNN	
Max. error	Mean of errors	Max. error	Mean of errors
13.1166	1.6675	3.0084	0.4641

6. Numerical Results

Typical topology of the RBF and GR neural networks to predict the optimal design and maximum deflection of the double layer grids is shown in Figures 5 and 6, respectively.

To find the optimal spread in the RBF and GR networks the minimum distance between training set and test set errors are employed [29]. The spread values in RBF networks trained to predict the optimal design and maximum deflection are 11.5 and 11.75 and for GR are 12.5 and 10.25, respectively. The results of RBF for predicting the optimal cross-sectional areas are shown in Figure 7.

The errors of RBF for predicting the maximum deflections are shown in Figure 8. The results of GR for predicting the optimal cross-sectional areas are shown in Figure 9. The errors of GR for predicting the maximum deflections are shown in Figure 10. Maximum and mean of errors of RBF and GRNN in approximation of optimal designs and maximum deflection are given in Tables 1 and 2, respectively.

The numerical results demonstrate that the generality of the GR is better than that of the RBF neural network in prediction of optimal design and maximum deflection of the double layer grids.

7. Conclusion

In this investigation, an innovative methodology is proposed to predict the optimal design and maximum deflection of the square-on-square double layer grids. This methodology consists of three stages. In the first stage, a number of the double layer grids with random spans and heights are generated. In the second stage the generated double layer grids are optimized by SPSA algorithm. Also, the maximum deflections of the optimal structures are saved. In the third stage, RBF and GR neural networks are trained to predict the optimal design and maximum deflection of the double layer grids.

By concerning the following points, it can be observed that the proposed methodology is novel and innovative.

- (1) It is the first study based on employing the SPSA optimization algorithm to optimize double layer grids with variable geometry.
- (2) Application of the RBF and GR neural networks to predict the optimal design and maximum deflection of the double layer is achieved for the first time in this study.
- (3) The main advantage of the proposed methodology is to predict the optimal design and maximum deflection of the double layer grids with high speed and trivial errors in comparison with the traditional methods.

References

- [1] M. L. Maher, D. Sriram, and S. J. Fennes, "Tools and techniques for knowledge based expert systems for engineering design," *Advances in Engineering Software*, vol. 6, no. 4, pp. 178–188, 1984.
- [2] R. Davis and J. J. King, "An overview of production systems," in *Machine Intelligence 8: Machine Representations and Knowledge*, E. Elcock and D. Michie, Eds., pp. 300–332, John Wiley & Sons, New York, NY, USA, 1977.
- [3] C. N. Kostem and M. L. Maher, Eds., *First Symposium on Expert Systems in Civil Engineering*, ASCE, Seattle, Wash, USA, 1986.
- [4] C. E. Shannon, "Programming a computer for playing chess," *Philosophical Magazine*, vol. 41, series 7, no. 314, pp. 256–275, 1950.
- [5] F. Erbatır, O. Hasançebi, I. Tütüncü, and H. Kinodotliç, "Optimal design of planar and space structures with genetic algorithms," *Computers and Structures*, vol. 75, no. 2, pp. 209–224, 2000.
- [6] S. Rajasekaran, "Optimization of large scale three dimensional reticulated structures using cellular genetics and neural networks," *International Journal of Space Structures*, vol. 16, no. 4, pp. 315–324, 2001.
- [7] C. S. Krishnamoorthy, V. P. Prasanna, and R. Sudarshan, "Object-oriented framework for genetic algorithms with application to space truss optimization," *Journal of Computing in Civil Engineering*, vol. 16, no. 1, pp. 66–75, 2002.
- [8] A. Tashakori and H. Adeli, "Optimum design of cold-formed steel space structures using neural dynamics model," *Journal of Constructional Steel Research*, vol. 58, no. 12, pp. 1545–1566, 2002.
- [9] E. Salajegheh and J. Salajegheh, "Continuous-discrete variable optimization of space structures with sizing variables using approximation methods," *International Journal of Space Structures*, vol. 16, no. 4, pp. 237–251, 2001.
- [10] A. Kaveh and M. R. Dehkordi, "Neural networks for the analysis and design of domes," *International Journal of Space Structures*, vol. 18, no. 3, pp. 181–193, 2003.
- [11] A. Kaveh, Y. Gholipour, and H. Rahami, "Optimal design of transmission towers using genetic algorithm and neural networks," *International Journal of Space Structures*, vol. 23, no. 1, pp. 1–19, 2008.
- [12] A. Kaveh and H. Servati, "Design of double layer grids using backpropagation neural networks," *Computers and Structures*, vol. 79, no. 17, pp. 1561–1568, 2001.
- [13] E. Salajegheh and S. Gholizadeh, "Optimum design of structures by an improved genetic algorithm using neural networks," *Advances in Engineering Software*, vol. 36, no. 11–12, pp. 757–767, 2005.

- [14] A. Kaveh, B. F. Azar, and S. Talatahari, "Ant colony optimization for design of space trusses," *International Journal of Space Structures*, vol. 23, no. 3, pp. 167–181, 2008.
- [15] S. Gholizadeh, E. Salajegheh, and P. Torkzadeh, "Structural optimization with frequency constraints by genetic algorithm using wavelet radial basis function neural network," *Journal of Sound and Vibration*, vol. 312, no. 1-2, pp. 316–331, 2008.
- [16] S. Gholizadeh and E. Salajegheh, "Optimal design of structures subjected to time history loading by swarm intelligence and an advanced metamodel," *Computer Methods in Applied Mechanics and Engineering*, vol. 198, no. 37–40, pp. 2936–2949, 2009.
- [17] A. H. Alavi and A. H. Gandomi, "Prediction of principal ground-motion parameters using a hybrid method coupling artificial neural networks and simulated annealing," *Computers and Structures*, vol. 89, no. 23-24, pp. 2176–2194, 2011.
- [18] S. Gholizadeh, A. Pirmoz, and R. Attarnejad, "Assessment of load carrying capacity of castellated steel beams by neural networks," *Journal of Constructional Steel Research*, vol. 67, no. 5, pp. 770–779, 2011.
- [19] A. H. Gandomi and A. H. Alavi, "Applications of computational intelligence in behavior simulation of concrete materials," in *Computational Optimization and Applications in Engineering and Industry*, X. S. Yang and S. Koziel, Eds., vol. 359, chapter 9, pp. 221–243, Springer, New York, NY, USA, 2011.
- [20] S. Gholizadeh and S. M. Seyedpoor, "Shape optimization of arch dams by metaheuristics and neural networks for frequency constraints," *Scientia Iranica*, vol. 18, no. 5, pp. 1020–1027, 2011.
- [21] S. Talatahari, A. H. Gandomi, and G. J. Yun, "Optimum design of tower structures using firefly algorithm," *The Structural Design of Tall and Special Buildings*. In press.
- [22] S. Gholizadeh and A. Barzegar, "Shape optimization of structures for frequency constraints by sequential harmony search algorithm," *Engineering Optimization*. In press.
- [23] A. H. Gandomi, S. Talatahari, X. S. Yang, and S. Deb, "Design optimization of truss structures using cuckoo search algorithm," *The Structural Design of Tall and Special Buildings*. In press.
- [24] S. Gholizadeh and F. Fattahi, "Design optimization of tall steel buildings by a modified particle swarm algorithm," *The Structural Design of Tall and Special Buildings*. In press.
- [25] S. Talatahari, M. Kheirollahi, C. Farahmandpour, and A. H. Gandomi, "A multi-stage particleswarm for optimum design of truss structures," *Neural Computing & Applications*. In press.
- [26] J. C. Spall, "An overview of the simultaneous perturbation method for efficient optimization," *Johns Hopkins APL Technical Digest*, vol. 19, no. 4, pp. 482–492, 1998.
- [27] P. D. Wasserman, *Advanced Methods in Neural Computing*, Prentice Hall, D. Van Nostrand, New York, NY, USA, 1993.
- [28] The Language of Technical Computing, *MATLAB*, Math Works, 2006.
- [29] S. S. Sadat Hosseini and A. H. Gandomi, "Short-term load forecasting of power systems by gene expression programming," *Neural Computing and Applications*, vol. 21, no. 2, pp. 377–389, 2012.

Research Article

Adaptive Parameters for a Modified Comprehensive Learning Particle Swarm Optimizer

Yu-Jun Zheng,¹ Hai-Feng Ling,² and Qiu Guan¹

¹ College of Computer Science and Technology, Zhejiang University of Technology, Hangzhou, Zhejiang 310023, China

² Engineering Institute of Engineering Corps, PLA University of Science and Technology, Nanjing, Jiangsu 210007, China

Correspondence should be addressed to Yu-Jun Zheng, yujun.zheng@computer.org

Received 5 October 2012; Accepted 25 November 2012

Academic Editor: Sheng-yong Chen

Copyright © 2012 Yu-Jun Zheng et al. This is an open access article distributed under the Creative Commons Attribution License, which permits unrestricted use, distribution, and reproduction in any medium, provided the original work is properly cited.

Particle swarm optimization (PSO) is a stochastic optimization method sensitive to parameter settings. The paper presents a modification on the comprehensive learning particle swarm optimizer (CLPSO), which is one of the best performing PSO algorithms. The proposed method introduces a self-adaptive mechanism that dynamically changes the values of key parameters including inertia weight and acceleration coefficient based on evolutionary information of individual particles and the swarm during the search. Numerical experiments demonstrate that our approach with adaptive parameters can provide comparable improvement in performance of solving global optimization problems.

1. Introduction

The complexity of many real-world problems has made exact solution methods impractical to solve them within a reasonable amount of time and thus gives rise to various types of nonexact metaheuristic approaches [1–3]. In particular, swarm intelligence methods, which simulate a population of simple individuals evolving their solutions by interacting with one another and with the environment, have shown promising performance on many difficult problems and have become a very active research area in recent years [4–11]. Among these methods, particle swarm optimization (PSO), initially proposed by Kennedy and Eberhart [4], is a population-based global optimization technique that involves algorithmic mechanisms similar to social behavior of bird flocking. The method enables a number of individual solutions, called particles, to move through the solution space and towards

the most promising area for optimal solution(s) by stochastic search. Consider a D -dimensional optimization problem as follows:

$$\begin{aligned} \min \quad & f(\mathbf{x}), \quad \mathbf{x} = [x_1, x_2, \dots, x_D]^T \\ \text{s.t.} \quad & x_{iL} \leq x_i \leq x_{iU}, \quad 0 < i \leq D. \end{aligned} \quad (1.1)$$

In the D -dimensional search space, each particle i of the swarm is associated with a position vector $\mathbf{x}_i = (x_{i1}, x_{i2}, \dots, x_{iD})$ and a velocity vector $\mathbf{v}_i = (v_{i1}, v_{i2}, \dots, v_{iD})$, which are iteratively adjusted by learning from a local best pbest_i found by the particle itself and a current global best gbest found by the whole swarm:

$$\mathbf{v}_i^{(t+1)} = \mathbf{v}_i^{(t)} + c_1 r_1 (\text{pbest}_i^{(t)} - \mathbf{x}_i^{(t)}) + c_2 r_2 (\text{gbest}^{(t)} - \mathbf{x}_i^{(t)}), \quad (1.2)$$

$$\mathbf{x}_i^{(t+1)} = \mathbf{x}_i^{(t)} + \mathbf{v}_i^{(t+1)}, \quad (1.3)$$

where c_1 and c_2 are two acceleration constants reflecting the weighting of “cognitive” and “social” learning, respectively, and r_1 and r_2 are two distinct random numbers in $[0, 1]$. It is recommended that $c_1 = c_2 = 2$ since it on average makes the weights for cognitive and social parts both to be 1.

To achieve a better balance between the exploration (global search) and exploitation (local search), Shi and Eberhart [12] introduce a parameter named inertia weight w to control velocity, which is currently the most widely used form of velocity update equation in PSO algorithms:

$$\mathbf{v}_i^{(t+1)} = w \mathbf{v}_i^{(t)} + c_1 r_1 (\text{pbest}_i^{(t)} - \mathbf{x}_i^{(t)}) + c_2 r_2 (\text{gbest}^{(t)} - \mathbf{x}_i^{(t)}). \quad (1.4)$$

Empirical studies have shown that a large inertia weight facilitates exploration and a small inertia weight one facilitates exploitation and a linear decreasing inertia weight can be effective in improving the algorithm performance:

$$w^{(t)} = w_{\min} + \frac{t_{\max} - t}{t_{\max}} (w_{\max} - w_{\min}), \quad (1.5)$$

where t is the current iteration number, t_{\max} is the maximum number of allowable iterations, and w_{\max} and w_{\min} are the initial value and the final value of inertia weight, respectively. It is suggested that w_{\max} can be set to around 1.2 and w_{\min} around 0.9, which can result in a good algorithm performance and remove the need for velocity limiting.

PSO is conceptually simple and easy to implement, and has been proven to be effective in a wide range of optimization problems [13–20]. Furthermore, It can be easily parallelized by concurrently processing multiple particles while sharing the social information [21, 22]. Kwok et al. [23] present an empirical study on the effect of randomness on the control coefficients of PSO, and the results show that the selective and uniformly distributed random coefficients perform better on complicate functions.

In recent years, PSO has attracted a high level of interest, and a number of variant PSO methods (e.g., [24–32]) have been proposed to accelerate convergence speed and avoid local

optima. In particular, Liang et al. develop a comprehensive learning particle swarm optimizer (CLPSO) [26], which uses all other particles' historical best information (instead of pbest and gbest) to update a particle's velocity:

$$v_{i,d}^{(t)} = w^{(t)} v_{i,d}^{(t-1)} + cr_{i,d} \left(\text{pbest}_{fi(d),d}^{(t)} - x_{i,d}^{(t-1)} \right), \quad (1.6)$$

where $\text{pbest}_{fi(d),d}$ can be the d th dimension of any particle's pbest (including pbest_{*i*} itself), and particle $fi(d)$ is selected based on a learning probability P_{C_i} . The authors suggest a tournament selection procedure that randomly chooses two particles and then select one with the best fitness as the exemplar to learn from for that dimension. Note that CLPSO has only one acceleration coefficient c which is normally set to 1.494, and it limits the inertia weight value in the range of [0.4, 0.9].

According to empirical studies [29, 30, 33], CLPSO has been shown to be one of the best performing PSO algorithms, especially for complex multimodal function optimization. In [34] a self-adaptation technique is introduced to adaptively adjust the learning probability, and the historical information is used in the velocity update equation, which effectively improve the performance of CLPSO on single modal problems.

Wu et al. [35] adapt the CLPSO algorithm by improving the search behavior to optimize the continuous externality for antenna design. In [36] Li and Tan present a hybrid strategy to combine CLPSO with Broyden-Fletcher-Goldfarb-Shanno (BFGS) method, which defines a local diversity index to indicate whether the swarm enters into an optimality region in a high probability. They apply the method to identify multiple local optima of the generalization bounds of support vector machine parameters and obtain satisfying results. However, to the best of our knowledge, modifications of CLPSO based on adaptive inertia weight and acceleration coefficient have not been reported.

In this paper we propose an improved CLPSO algorithm, named CLPSO-AP, by introducing a new adaptive parameter strategy. The algorithm evaluates the evolutionary states of individual particles and the whole swarm, based on which values of inertia weight and acceleration coefficient are dynamically adjusted to search more effectively. Numerical experiments on test functions show that our algorithm can significantly improve the performance of CLPSO.

In the rest of the paper, Section 2 presents our PSO method with adaptive parameters, Section 3 presents the computational experiments, and Section 4 concludes with discussion.

2. The CLPSO-AP Algorithm

2.1. Adaptive Inertia Weight and Acceleration Coefficient

To provide an adaptive parameter strategy, we first need to determine the situation of each particle at each iteration. In this paper, two concepts are used for this purpose. The first one considers whether or not a particle i improves its personal best solution at the t th iteration (in the paper we assume the problem is to minimize the objective function without loss of generality):

$$s_i^{(t)} = \begin{cases} 1 & \text{if } f(\text{pbest}_i^{(t)}) < f(\text{pbest}_i^{(t-1)}) \\ 0 & \text{else.} \end{cases} \quad (2.1)$$

And the second considers the particle's "rate of growth" from the $(t - 1)$ th iteration to the t th iteration:

$$\gamma_i^{(t)} = \frac{f(\mathbf{x}_i^{(t)}) - f(\mathbf{x}_i^{(t-1)})}{|\mathbf{x}_i^{(t)} - \mathbf{x}_i^{(t-1)}|}, \quad (2.2)$$

where $|\mathbf{x}_i^{(t)} - \mathbf{x}_i^{(t-1)}|$ denotes the Euclidean distance between $\mathbf{x}_i^{(t)}$ and $\mathbf{x}_i^{(t-1)}$:

$$|\mathbf{x}_i^{(t)} - \mathbf{x}_i^{(t-1)}| = \sqrt{\sum_{k=1}^D (x_{ik}^{(t)} - x_{ik}^{(t-1)})^2}. \quad (2.3)$$

Based on (2.1), we can calculate the percentage of particles that successfully improve their personal better solutions:

$$\rho^{(t)} = \frac{\sum_{i=1}^p s_i^{(t)}}{p}, \quad (2.4)$$

where p is the number of particles in the swarm. This measure has been utilized in [33] and some other evolutionary algorithms such as [37]. Generally, in PSO a high ρ indicates a high probability that the particles have converged to a nonoptimum point or slowly moving toward the optimum, while a low ρ indicates that the particles are oscillating around the optimum without much improvement. Considering role of inertia weight in the convergence behavior of PSO, in the former case the swarm should have a large inertial weight and in the latter case the swarm should have a small inertial weight. Here we use the following nonlinear function to map the values of ρ to w :

$$w^{(t)} = e^{\rho^{(t)} - 1}. \quad (2.5)$$

It is easy to derive that w ranges from about 0.36 to 1. The nonlinear and non-monotonous change of inertial weight can improve the adaptivity and diversity of the swarm, because the search process of PSO is highly complicated on most problems.

Most PSO algorithms use constant acceleration coefficients in (1.4). But it deserves to note that Ratnaweera et al. [38] introduce a time-varying acceleration coefficient strategy where the cognitive coefficient is linearly decreased and the social coefficient is linearly increased. The basic CLPSO also uses a constant acceleration coefficient in (1.6), where c reflects the weighting of stochastic acceleration term that pulls each particle i towards the personal best position of particle $fi(d)$ at each dimension d . Considering the measure defined in (2.2), a large value of $\gamma_i^{(t)}$ indicates that at t time, particle i falls rapidly in the search space and gets a considerable improvement on the fitness function; thus it is reasonable to anticipate that the particle may also gain much improvement at least at the next iteration. On the contrary, a small value of $\gamma_i^{(t)}$ indicates that particle i progresses slowly and thus needs a large acceleration towards the exemplar.

From the previous analysis, we suggest that the acceleration coefficient should be an increasing function of $\gamma_i^{(t)} / \Gamma^{(t)}$, where $\Gamma^{(t)}$ is the SRSS of the rates of growth of all the particles in the swarm:

$$\Gamma^{(t)} = \sqrt{\sum_{j=1}^p \left(\gamma_j^{(t)}\right)^2}. \quad (2.6)$$

Based on our empirical tests, we use the following function to map the values of γ_i to c_i :

$$c_i^{(t)} = 1.8 \left(1 - \frac{\gamma_i^{(t)}}{\Gamma^{(t)}} \right). \quad (2.7)$$

2.2. The Proposed Algorithm

Using the adaptive parameter strategy described in the previous section, the equation for velocity update for the CLPSO-AP algorithm is

$$v_{i,d}^{(t)} = w^{(t)} v_{i,d}^{(t-1)} + c_i^{(t)} r_{i,d} \left(\text{pbest}_{fi(d),d}^{(t)} - x_{i,d}^{(t-1)} \right), \quad (2.8)$$

where $w^{(t)}$ and $c_i^{(t)}$ are calculated based on (2.5) and (2.7), respectively.

Now we present the flow of CLPSO-AP algorithm as follows.

- (1) Generate a swarm of p particles with random positions and velocities in the range. Let $t = 0$ and initialize $w^{(t)} = 1$ and each $c_i^{(t)} = 1$.
- (2) Generate a learning probability P_{C_i} for each particle based on the following equation suggested in [10]:

$$P_{C_i} = 0.05 + 0.45 \frac{\exp(10(i-1)/(p-1)) - 1}{\exp(10) - 1}. \quad (2.9)$$

- (3) Evaluate the fitness of each particle and update its pbest and then select a particle with the best fitness value as gbest.
- (4) For each particle i in the swarm do the following.
 - (4.1) For $d = 1$ to D do the next.
 - (4.1.1) Generate a random number rand in the range $[0, 1]$.
 - (4.1.2) If $\text{rand} > P_{C_i}$, let $fi(d) = i$.
 - (4.1.3) Else, randomly choose two other distinct particles i_1 and i_2 , and select the one with better fitness value as $fi(d)$.
 - (4.1.4) Update the d th dimension of the particle's velocity according to (2.8).
 - (4.2) Update the particle's position according to (1.3).
 - (4.3) Calculate $s_i^{(t)}$ and $r_i^{(t)}$ for the particle according to (2.1) and (2.2), respectively.

- (5) Calculate $w^{(t)}$ of the swarm based on (2.4) and (2.5).
- (6) Calculate $\Gamma^{(t)}$ based on (2.5), and then calculate $c_i^{(t)}$ for each particle i based on (2.7).
- (7) Let $t = t + 1$. If $t = t_{\max}$ or any other termination condition is satisfied, the algorithm stops and returns gbest.
- (8) Go to step 3.

In Step (7), other termination conditions can be that a required function value is obtained, or all the particles converge to a stable point.

3. Numerical Experiments

In order to evaluate the performance of the proposed algorithm, we choose a set of well-known test functions as benchmark problems, the definitions of which are listed in the Appendix section. The search ranges, optimal points and corresponding fitness values, and required accuracies are shown in Table 1.

We comparatively execute the basic PSO algorithm, CLPSO algorithm, and our CLPSO-AP algorithm on the test functions with 10 and 30 dimensions, where each experiment is run for 40 times. The parameter settings for the algorithms are given in Table 2.

We use the mean best fitness value and the success rate (with respect to the required accuracy shown in Table 1) as two criteria for measuring the performance of the algorithms. The experimental results (averaged over 40 runs) of which are presented in Tables 3, 4, 5, and 6 respectively.

As we can see from the experimental results, for all 10D and 30D dimensional problems, CLPSO-AP performs better than CLPSO in terms of both mean best values and success rates. Among the seven test functions, Ackley function is the only one on which CLPSO performs no better than the basic PSO. However, CLPSO-AP performs better than basic PSO on both the 10D and 30D Ackley functions, and thus CLPSO-AP also outperforms basic PSO on all benchmark problems. It also deserves to note the 10D Rosenbrock function, for which CLPSO and most of the other PSO variants hardly succeed [26, 39, 40] while our CLPSO-AP algorithm gains a 10% success rate. Except for the 30D Rosenbrock function, CLPSO-AP successfully obtains the global optimum for all the other functions. In summary, our algorithm performs very well and overwhelms the other two algorithms on all of the test problems.

4. Conclusion

CLPSO has been shown to be one of the best performing PSO algorithms. The paper proposes a new improved CLPSO algorithm, named CLPSO-AP, which uses evolutionary information of individual particles to dynamically adapt the inertia weight and acceleration coefficient at each iteration. Experimental results on seven test functions show that our algorithm can significantly improve the performance of CLPSO. Ongoing work includes applying our algorithm to intelligent feature selection and lighting control in robotics [41–43] and extending the adaptive strategy to other PSO variants, including those for fuzzy and/or multiobjective problems [44, 45].

Table 1: Detailed information of the test functions used in the paper.

No.	Function	Search range	\mathbf{x}^*	$f(\mathbf{x}^*)$	Required accuracy
f_1	Sphere	$[-100, 100]^D$	$[0, 0, \dots, 0]$	0	0.000001
f_2	Rosenbrock	$[-2.048, 2.048]^D$	$[1, 1, \dots, 1]$	0	0.01
f_3	Schwefel	$[-500, 500]^D$	$[420.96, 420.96, \dots, 420.96]$	0	0.01
f_4	Rastrigin	$[-5.12, 5.12]^D$	$[0, 0, \dots, 0]$	0	0.01
f_5	Griewank	$[-600, 600]^D$	$[0, 0, \dots, 0]$	0	0.000001
f_6	Ackley	$[-32.768, 32.768]^D$	$[0, 0, \dots, 0]$	0	0.000001
f_7	Weierstrass	$[-0.5, 0.5]^D$	$[0, 0, \dots, 0]$	0	0.000001

Table 2: Parameter settings of the algorithms.

Algorithm	Inertial weight	Acceleration coefficient(s)	10D functions		30D functions	
			p	t_{\max}	p	t_{\max}
PSO	$[0.4, 1.2]$	$c_1 = c_2 = 1.49445$	10	5000	30	10000
CLPSO	$[0.4, 0.9]$	$c = 1.49445$	10	5000	30	10000
CLPSO-AP	N/A	N/A	10	5000	30	10000

Table 3: The mean best values obtained by the algorithms for 10D problems.

Function	PSO	CLPSO	CLPSO-AP
Sphere	$3.239E - 27$	$8.138E - 79$	$5.479E - 96$
Rosenbrock	$2.172E + 00$	$2.005E + 00$	$1.106E + 00$
Schwefel	$1.048E + 03$	0	0
Rastrigin	$5.774E - 01$	0	0
Griewank	$8.132E - 02$	$1.313E - 02$	$6.467E - 03$
Ackley	$5.951E - 15$	$2.181E - 13$	$4.707E - 15$
Weierstrass	0	0	0

Table 4: The success rates obtained by the algorithms for 10D problems.

Function	PSO	CLPSO	CLPSO-AP
Sphere	100%	100%	100%
Rosenbrock	0	0	10%
Schwefel	5%	100%	100%
Rastrigin	12.5%	100%	100%
Griewank	0	1.75%	75%
Ackley	100%	100%	100%
Weierstrass	100%	100%	100%

Table 5: The mean best values obtained by the algorithms for 30-D problems.

Function	PSO	CLPSO	CLPSO-AP
Sphere	$4.900E - 14$	$1.077E - 57$	$3.852E - 75$
Rosenbrock	$5.164E + 01$	$2.158E + 01$	$1.954E + 01$
Schwefel	$1.425E + 02$	$7.913E + 01$	$6.883E + 01$
Rastrigin	$4.726E + 00$	$4.974E - 02$	0
Griewank	$2.745E - 02$	$1.616E - 10$	$1.167E - 12$
Ackley	$1.106E - 13$	$6.594E - 12$	$3.242E - 14$
Weierstrass	$1.155E - 14$	$1.155E - 14$	$1.155E - 14$

Table 6: The success rates obtained by the algorithms for 30-D problems.

Function	PSO	CLPSO	CLPSO-AP
Sphere	100%	100%	100%
Rosenbrock	0	0	0
Schwefel	0	50%	55%
Rastrigin	0	95%	100%
Griewank	37.5%	100%	100%
Ackley	100%	100%	100%
Weierstrass	100%	100%	100%

Appendix

Definitions of the Test Functions

(1) Sphere function:

$$f_1(x) = \sum_{i=1}^D x_i^2. \quad (\text{A.1})$$

(2) Rosenbrock's function:

$$f_2(x) = \sum_{i=2}^{D-1} \left(100(x_i^2 - x_{i-1})^2 + (x_i - 1)^2 \right). \quad (\text{A.2})$$

(3) Schwefel's function:

$$f_3(x) = 418.9829 \times D - \sum_{i=1}^D x_i \sin(|x_i|^{1/2}). \quad (\text{A.3})$$

(4) Rastrigin's function:

$$f_4(x) = \sum_{i=1}^D \left(x_i^2 - 10 \cos(2\pi x_i) + 10 \right). \quad (\text{A.4})$$

(5) Griewank's function:

$$f_5(x) = \sum_{i=1}^D \frac{x_i^2}{4000} - \prod_{i=1}^D \cos\left(\frac{x_i}{\sqrt{i}}\right) + 1. \quad (\text{A.5})$$

(6) Ackley's function:

$$f_6(x) = -20 \exp\left(-0.2 \sqrt{\frac{1}{D} \sum_{i=1}^D x_i^2}\right) - \exp\left(\frac{1}{D} \sum_{i=1}^D \cos(2\pi x_i)\right) + 20 + e. \quad (\text{A.6})$$

(7) Weierstrass function:

$$f_7(x) = \sum_{i=1}^D \left(\sum_{k=0}^{k_{\max}} \left[a^k \cos(2\pi b^k (x_i + 0.5)) \right] \right) - D \sum_{k=0}^{k_{\max}} \left[a^k \cos(2\pi b^k \cdot 0.5) \right]. \quad (\text{A.7})$$

Acknowledgment

This work was supported in part by grants from National Natural Science Foundation (Grant no. 61020106009, 61105073, 61103140, and 61173096) of China.

References

- [1] R. Chiong and T. Weise, "Special issue on modern search heuristics and applications," *Evolutionary Intelligence*, vol. 4, no. 1, pp. 1–2, 2011.
- [2] S. Chen, W. Huang, C. Cattani, and G. Altieri, "Traffic dynamics on complex networks: a survey," *Mathematical Problems in Engineering*, vol. 2012, Article ID 732698, 23 pages, 2012.
- [3] M. Li, W. Zhao, and S. Chen, "mBm-based scalings of traffic propagated in internet," *Mathematical Problems in Engineering*, vol. 2011, Article ID 389803, 21 pages, 2011.
- [4] J. Kennedy and R. Eberhart, "Particle swarm optimization," in *Proceedings of the IEEE International Conference on Neural Networks*, pp. 1942–1948, Perth, Australia, 1995.
- [5] M. Dorigo, V. Maniezzo, and A. Colnari, "Ant system: optimization by a colony of cooperating agents," *IEEE Transactions on Systems, Man, and Cybernetics B*, vol. 26, no. 1, pp. 29–41, 1996.
- [6] X. Li, *A new intelligent optimization artificial fish school algorithm [doctor thesis]*, Zhejiang University, Hangzhou, China, 2003.
- [7] D. Karaboga and B. Basturk, "A powerful and efficient algorithm for numerical function optimization: artificial bee colony (ABC) algorithm," *Journal of Global Optimization*, vol. 39, no. 3, pp. 459–471, 2007.
- [8] Y. Tan and Y. Zhu, "Fireworks algorithm for optimization," in *Advances in Swarm Intelligence*, vol. 6145 of *Lecture Notes in Computer Science*, pp. 355–364, 2010.
- [9] S. Chen, Y. Zheng, C. Cattani, and W. Wang, "Modeling of biological intelligence for SCM system optimization," *Computational and Mathematical Methods in Medicine*, vol. 2012, Article ID 769702, 10 pages, 2012.
- [10] X. Wen, Y. Zhao, Y. Xu, and D. Sheng, "Quasiparticle swarm optimization for cross-section linear profile error evaluation of variation elliptical piston skirt," *Mathematical Problems in Engineering*, vol. 2012, Article ID 761978, 15 pages, 2012.
- [11] Y. J. Zheng, X. L. Xu, H. F. Ling, and S. Y. Chen, "A hybrid fireworks optimization method with differential evolution operators," *Neurocomputing*. In press.
- [12] Y. Shi and R. Eberhart, "Modified particle swarm optimizer," in *Proceedings of the IEEE International Conference on Evolutionary Computation (ICEC '98)*, pp. 69–73, Anchorage, Alaska, USA, May 1998.
- [13] X. D. Li and A. P. Engelbrecht, "Particle swarm optimization: an introduction and its recent developments," in *Proceedings of the Genetic and Evolutionary Computation Conference*, pp. 3391–3414, London, UK, 2007.
- [14] W. N. Chen, J. Zhang, H. S. H. Chung, W. L. Zhong, W. G. Wu, and Y. H. Shi, "A novel set-based particle swarm optimization method for discrete optimization problems," *IEEE Transactions on Evolutionary Computation*, vol. 14, no. 2, pp. 278–300, 2010.
- [15] R. C. Eberhart and Y. H. Shi, "Tracking and optimizing dynamic systems with particle swarms," in *Proceedings of the IEEE Congress on Evolutionary Computation*, pp. 94–97, Seoul, Korea, 2001.
- [16] M. Thidaa, H. L. Eng, D. N. Monekosso, and P. Remagnino, "A particle swarm optimisation algorithm with interactive swarms for tracking multiple targets," *Applied Soft Computing*. In press.
- [17] S. Y. Chen, H. Tong, Z. Wang, S. Liu, M. Li, and B. Zhang, "Improved generalized belief propagation for vision processing," *Mathematical Problems in Engineering*, vol. 2011, Article ID 416963, 12 pages, 2011.
- [18] M. Li, S. C. Lim, and S. Chen, "Exact solution of impulse response to a class of fractional oscillators and its stability," *Mathematical Problems in Engineering*, vol. 2011, Article ID 657839, 9 pages, 2011.

- [19] C. Cattani, "Fractals and hidden symmetries in DNA," *Mathematical Problems in Engineering*, vol. 2012, Article ID 507056, 31 pages, 2010.
- [20] Y. J. Zheng and S. Y. Chen, "Cooperative particle swarm optimization for multiobjective transportation planning," *Applied Intelligence*. In press.
- [21] B. I. Koh, A. D. George, R. T. Haftka, and B. J. Fregly, "Parallel asynchronous particle swarm optimization," *International Journal for Numerical Methods in Engineering*, vol. 67, no. 4, pp. 578–595, 2006.
- [22] K. E. Parsopoulos, "Parallel cooperative micro-particle swarm optimization: a master-slave model," *Applied Soft Computing*, vol. 12, pp. 3552–3579, 2012.
- [23] N. M. Kwok, D. K. Liu, K. C. Tan, and Q. P. Ha, "An empirical study on the settings of control coefficients in particle swarm optimization," in *Proceedings of the IEEE Congress on Evolutionary Computation*, pp. 3165–3172, Vancouver, Canada, 2006.
- [24] R. Mendes, J. Kennedy, and J. Neves, "The fully informed particle swarm: simpler, maybe better," *IEEE Transactions on Evolutionary Computation*, vol. 8, no. 3, pp. 204–210, 2004.
- [25] K. E. Parsopoulos and M. N. Vrahatis, "UPSO: a unified particle swarm optimization scheme," in *Proceedings of the International Conference of Computational Methods in Sciences and Engineering (ICCMSE '04)*, vol. 1 of *Lecture Series on Computer and Computational Sciences*, pp. 868–873, VSP International Science Publishers, 2004.
- [26] J. J. Liang, A. K. Qin, P. N. Suganthan, and S. Baskar, "Comprehensive learning particle swarm optimizer for global optimization of multimodal functions," *IEEE Transactions on Evolutionary Computation*, vol. 10, no. 3, pp. 281–295, 2006.
- [27] N. M. Kwok, Q. P. Ha, D. K. Liu, G. Fang, and K. C. Tan, "Efficient particle swarm optimization: a termination condition based on the decision-making approach," in *Proceedings of the IEEE Congress on Evolutionary Computation (CEC '07)*, pp. 3353–3360, September 2007.
- [28] N. M. Kwok, G. Fang, Q. R. Ha, and D. K. Liu, "An enhanced particle swarm optimization algorithm for multi-modal functions," in *Proceedings of the IEEE International Conference on Mechatronics and Automation (ICMA '07)*, pp. 457–462, Harbin, China, August 2007.
- [29] Z. H. Zhan, J. Zhang, Y. Li, and H. S. H. Chung, "Adaptive particle swarm optimization," *IEEE Transactions on Systems, Man, and Cybernetics B*, vol. 39, pp. 1362–1381, 2009.
- [30] Y. Shi, H. Liu, L. Gao, and G. Zhang, "Cellular particle swarm optimization," *Information Sciences*, vol. 181, no. 20, pp. 4460–4493, 2011.
- [31] M. S. Leu and M. F. Yeh, "Grey particle swarm optimization," *Applied Soft Computing*, vol. 12, no. 9, pp. 2985–2996, 2012.
- [32] M. M. Noel, "A new gradient based particle swarm optimization algorithm for accurate computation of global minimum," *Applied Soft Computing*, vol. 12, no. 1, pp. 353–359, 2012.
- [33] A. Nickabadi, M. M. Ebadzadeh, and R. Safabakhsh, "A novel particle swarm optimization algorithm with adaptive inertia weight," *Applied Soft Computing Journal*, vol. 11, no. 4, pp. 3658–3670, 2011.
- [34] J. J. Liang and P. N. Suganthan, "Adaptive comprehensive learning particle swarm optimizer with history learning," in *Simulated Evolution and Learning*, vol. 4247 of *Lecture Notes in Computer Science*, pp. 213–220, 2006.
- [35] H. Wu, J. Geng, R. Jin et al., "An improved comprehensive learning particle swarm optimization and its application to the semiautomatic design of antennas," *IEEE Transactions on Antennas and Propagation*, vol. 57, no. 10, pp. 3018–3028, 2009.
- [36] S. Li and M. Tan, "Tuning SVM parameters by using a hybrid CLPSO-BFGS algorithm," *Neurocomputing*, vol. 73, pp. 2089–2096, 2010.
- [37] H.-G. Beyer and H.-P. Schwefel, "Evolution strategies—a comprehensive introduction," *Natural Computing*, vol. 1, no. 1, pp. 3–52, 2002.
- [38] A. Ratnaweera, S. K. Halgamuge, and H. C. Watson, "Self-organizing hierarchical particle swarm optimizer with time-varying acceleration coefficients," *IEEE Transactions on Evolutionary Computation*, vol. 8, no. 3, pp. 240–255, 2004.
- [39] M. Pant, R. Thangaraj, and A. Abraham, "Particle swarm optimization using adaptive mutation," in *Proceedings of the 19th International Conference on Database and Expert Systems Applications (DEXA '08)*, pp. 519–523, Turin, Italy, September 2008.
- [40] J. Vesterstrøm and R. Thomsen, "A comparative study of differential evolution, particle swarm optimization, and evolutionary algorithms on numerical benchmark problems," in *Proceedings of the Congress on Evolutionary Computation (CEC '04)*, pp. 1980–1987, June 2004.
- [41] S. Y. Chen, Y. F. Li, and N. M. Kwok, "Active vision in robotic systems: a survey of recent developments," *The International Journal of Robotics Research*, vol. 30, no. 11, pp. 1343–1377, 2011.

- [42] S. Y. Chen, J. W. Zhang, H. X. Zhang, N. M. Kwok, and Y. F. Li, "Intelligent lighting control for vision-based robotic manipulation," *IEEE Transactions on Industrial Electronics*, vol. 59, pp. 3254–3263, 2012.
- [43] S. Wen, W. Zheng, J. Zhu, X. Li, and S. Chen, "Elman fuzzy adaptive control for obstacle avoidance of mobile robots using hybrid force/position incorporation," *IEEE Transactions on Systems, Man and Cybernetics C*, vol. 42, no. 4, pp. 603–608, 2012.
- [44] Y. J. Zheng, H. H. Shi, and S. Y. Chen, "Fuzzy combinatorial optimization with multiple ranking criteria: a staged tabu search framework," *Pacific Journal of Optimization*, vol. 8, pp. 457–472, 2012.
- [45] K. Wang and Y. J. Zheng, "A new particle swarm optimization algorithm for fuzzy optimization of armored vehicle scheme design," *Applied Intelligence*, vol. 37, pp. 520–526, 2012.

Research Article

Combination of Interacting Multiple Models with the Particle Filter for Three-Dimensional Target Tracking in Underwater Wireless Sensor Networks

Xin Wang,¹ Mengxi Xu,² Huibin Wang,¹ Yan Wu,¹ and Haiyan Shi³

¹ College of Computer and Information, Hohai University, Nanjing, Jiangsu 211100, China

² School of Computer Engineering, Nanjing Institute of Technology, Jiangsu 210000, China

³ College of Computer Science and Technology, Zhejiang University of Technology, Zhejiang 310023, China

Correspondence should be addressed to Xin Wang, wang.xin@hhu.edu.cn

Received 4 October 2012; Accepted 13 November 2012

Academic Editor: Sheng-yong Chen

Copyright © 2012 Xin Wang et al. This is an open access article distributed under the Creative Commons Attribution License, which permits unrestricted use, distribution, and reproduction in any medium, provided the original work is properly cited.

Tracking underwater targets is a focused application area in modern underwater defence systems. Using traditional techniques based on imaging or sensor arrays may be difficult and impractical in some mission-critical systems. Alternatively, the underwater wireless sensor network (UWSN) is able to offer a promising solution. This paper tackles the problem of accurately tracking underwater targets moving through the UWSN environment. This problem is considered nonlinear and non-Gaussian where the present solution methods based on the particle filter technique are powerful and simple to implement. For three-dimensional underwater maneuvering target tracking, the traditional particle filter tracking algorithm may fail to track the targets robustly and accurately. Thus, the interacting multiple model method is combined with the particle filter to cope with uncertainties in target maneuvers. Simulation results show that the proposed method is a promising substitute for the traditional imaging-based or sensor-based approaches.

1. Introduction

Nowadays, tracking targets in the underwater environment is an indispensable part in many military or civil fields, such as modern underwater defense systems, navigation and control of mobile robots, and traffic monitoring in intelligent transportation systems. Much attention has been paid to it and various techniques have been developed based on imaging [1] or sensor arrays [2, 3]. Thereinto, imaging-based methods utilize underwater optical imaging or underwater sonar imaging for underwater target tracking. However, for the imaging process is always disturbed by water turbidity, underwater illumination intensity, or underwater

noise, such techniques usually cannot get satisfactory tracking results. Other underwater target tracking techniques use underwater sensor arrays to measure azimuth, elevation angle, and distance of the underwater targets and then track them by classical filtering techniques, such as Kalman's filter (KF), extended Kalman filter (EKF), and unscented Kalman filter (UKF) [4]. Nevertheless, these sensor arrays are generally mounted on or towed by a ship or a submersible or deployed prior to the application, which makes the tracking range limited or makes them unsuitable for on-demand tracking missions [5].

In terms of surveillance and reconnaissance, the wireless sensor network (WSN) stands as a promising technology [6–8]. The main advantages of WSN include its low cost, rapid deployment, self-organization, and fault tolerance [9]. As a specific case of WSN, the underwater wireless sensor network (UWSN) is developed to enable applications for assisted navigation, oceanographic data collection, obstacle avoidance, and tactical surveillance [10]. Some effort has been made for underwater target tracking with UWSN [11–13]. For example, in [11], Yu et al. present a distributed tracking algorithm for a single moving target through UWSN as well as the issues of estimating the state of target and improving energy efficiency by applying a Kalman filter in a distributed architecture. In [12], Isbitiren and Akan design a three-dimensional (3D) underwater target tracking algorithm for underwater acoustic sensor networks. Based on the time of arrival of the echoes from the target after transmitting acoustic pulses from the sensors, the ranges of the nodes to the target are determined, and trilateration is used to obtain the location of the target. The location and the calculated velocity of the target are then exploited to achieve tracking. Kim et al. [13] propose a bearings-only tracking scheme based on distributed floating beacons in UWSN. It adopts a multidimensional assignment for rejecting clutters and unscented Kalman filter for tracking a target.

To achieve three-dimensional (3D) underwater target tracking, the following challenges must be considered. For example, the measurement value of the sensor usually has a nonlinear relationship with the estimated value in UWSN. However, most of the existing algorithms for underwater target tracking do not consider the nonlinear problem, which results in poor tracking accuracy. Moreover, in order to avoid underwater obstacles or other moving objects, the trajectory of the underwater target might be very complex. A single motion model is not sufficient to capture its movement.

To solve the aforementioned issues, we present combination of interacting multiple model (IMM) with the particle filter (PF) for three-dimensional target tracking in UWSN. The particle filter [14–17] is a sequential Monte Carlo approach that uses random samples, called particles, to approximate the posterior probability density. It is an efficient way to solve nonlinear and non-Gaussian problems [18–20]. However, the traditional PF algorithm with a single motion model cannot solve the maneuvering problems of underwater target tracking [21]. For maneuvering target tracking, the interacting multiple model (IMM) method is widely used [22, 23]. It can estimate the state of a dynamic system with several behavioral modes that switch from one to another using mode likelihoods and mode transition probabilities. In the beginning, the filter underlying the modes in the IMM framework was KF or EKF. Later, PF was substituted for KF or EKF in the IMM framework (so-called IMMPF) [24]. Subsequently, IMMPF is widely applied to various target tracking problems [25, 26]. For instance, in [25], the IMMPF is applied to the problem of maneuvering target tracking with passive coherent location radar. In [26], it is used for a land vehicle Global Position System/Dead Reckoning navigation system. Although IMMPF has been extensively used, the study of target tracking in UWSN is still in its infancy. Therefore, this paper focuses on the issue of underwater target tracking based on IMMPF.

The rest of the paper is organized as follows. In Section 2, the UWSN architecture and target motion models, as well as the measurement model of the UWSN are given. Section 3 presents the IMMPF 3D underwater target tracking algorithm. Following that, simulation results are presented in Section 4, and conclusions are drawn in Section 5.

2. Problem Formulation

2.1. UWSN Architecture

Figure 1 shows the architecture of the UWSN used for 3D underwater target tracking. It is composed of multiple underwater acoustic sensors. These sensor nodes are deployed by binding to ropes which are docked onto the bed of water or a floater. As a result, all nodes form a three-dimensional network. In this paper, we consider three different types of sensor nodes: surface buoys, anchor nodes, and ordinary nodes. Surface buoys are nodes that drift on the water surface. They are often equipped with common Global Positioning System (GPS) and can get their absolute locations from GPS. Anchor nodes are those who can directly contact the surface buoys to get their absolute positions. Ordinary nodes cannot directly talk to the surface buoys because of cost or other constraints but can communicate with anchor nodes to estimate their own positions. There are extensive studies for the localization of UWSN [27–29]. In this paper, we will not contribute to this part. Instead, we mainly tackle the problem of underwater target tracking with UWSN.

2.2. Underwater Target Motion Models

For underwater target tracking, to precisely predict and estimate the motion information of targets, the exact motion models of targets should be designed [30–33]. In order to capture the movement of the underwater target, three different dynamic models, namely, constant velocity (CV), constant acceleration (CA), and coordinated turn (CT), are studied here.

Underwater target motion can be described by the following discrete dynamic state equation:

$$\mathbf{X}_{k+1} = \mathbf{F}_k \mathbf{X}_k + \mathbf{w}_k, \quad (2.1)$$

where \mathbf{X}_k is the target state vector at the k time step; \mathbf{F}_k is the state transition matrix; \mathbf{w}_k is the process noise.

Considering that the underwater target moves in a three-dimensional physical world, the target state vector \mathbf{X}_k can be defined as

$$\mathbf{X}_k = [x_k \ \dot{x}_k \ \ddot{x}_k \ y_k \ \dot{y}_k \ \ddot{y}_k \ z_k \ \dot{z}_k \ \ddot{z}_k]^T, \quad (2.2)$$

where x_k is the position of the target along x -axis at k ; \dot{x}_k is the x -axis velocity of the target at k ; \ddot{x}_k is the x -axis acceleration of the target at k . y_k , \dot{y}_k , \ddot{y}_k , z_k , \dot{z}_k , and \ddot{z}_k are similarly defined. Notice that the acceleration of the target at each coordinate equals to zero for CV model and the state vector is taken to be $\mathbf{X}_k = [x_k \ \dot{x}_k \ y_k \ \dot{y}_k \ z_k \ \dot{z}_k]^T$.

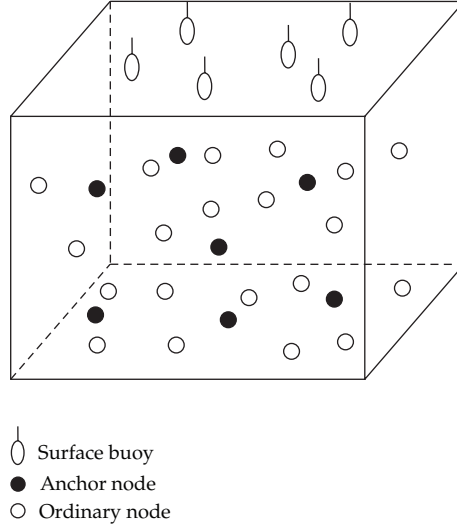


Figure 1: Architecture of UWSN.

2.2.1. CV Model

The constant velocity model is the basic motion manner for underwater targets, such as submarines, torpedoes, and autonomous underwater vehicles. The state transition matrix \mathbf{F}_k of this model is

$$\mathbf{F}_k = \begin{bmatrix} 1 & T & 0 & 0 & 0 & 0 \\ 0 & 1 & 0 & 0 & 0 & 0 \\ 0 & 0 & 1 & T & 0 & 0 \\ 0 & 0 & 0 & 1 & 0 & 0 \\ 0 & 0 & 0 & 0 & 1 & T \\ 0 & 0 & 0 & 0 & 0 & 1 \end{bmatrix}, \quad (2.3)$$

where T is the time interval between samples.

While the underwater target does constant velocity motion, its speed may change slightly due to the effect of wind and water flow, which can be represented by a white noise process \mathbf{w}_k with variance σ_w^2 . The corresponding covariance matrix of the noise is given by

$$\mathbf{Q}_k = \begin{bmatrix} \frac{T^4}{4} & \frac{T^3}{2} & 0 & 0 & 0 & 0 \\ \frac{T^3}{2} & T^2 & 0 & 0 & 0 & 0 \\ 0 & 0 & \frac{T^4}{4} & \frac{T^3}{2} & 0 & 0 \\ 0 & 0 & \frac{T^3}{2} & T^2 & 0 & 0 \\ 0 & 0 & 0 & 0 & \frac{T^4}{4} & \frac{T^3}{2} \\ 0 & 0 & 0 & 0 & \frac{T^3}{2} & T^2 \end{bmatrix} \sigma_w^2. \quad (2.4)$$

2.2.2. CA Model

Beside the nonmaneuvering motion, we need to consider maneuvering motions for underwater targets. To account for the accelerations in the movement, the constant acceleration model is introduced. Its state transition matrix \mathbf{F}_k and the covariance matrix \mathbf{Q}_k of the independent white noise process \mathbf{w}_k are

$$\mathbf{F}_k = \begin{bmatrix} 1 & T & \frac{T^2}{2} & 0 & 0 & 0 & 0 & 0 & 0 \\ 0 & 1 & T & 0 & 0 & 0 & 0 & 0 & 0 \\ 0 & 0 & 1 & 0 & 0 & 0 & 0 & 0 & 0 \\ 0 & 0 & 0 & 1 & T & \frac{T^2}{2} & 0 & 0 & 0 \\ 0 & 0 & 0 & 0 & 1 & T & 0 & 0 & 0 \\ 0 & 0 & 0 & 0 & 0 & 1 & 0 & 0 & 0 \\ 0 & 0 & 0 & 0 & 0 & 0 & 1 & T & \frac{T^2}{2} \\ 0 & 0 & 0 & 0 & 0 & 0 & 0 & 1 & T \\ 0 & 0 & 0 & 0 & 0 & 0 & 0 & 0 & 1 \end{bmatrix},$$

$$\mathbf{Q}_k = \begin{bmatrix} \frac{T^4}{4} & \frac{T^3}{2} & \frac{T^2}{2} & 0 & 0 & 0 & 0 & 0 & 0 \\ \frac{T^3}{2} & \frac{T^2}{2} & T & 0 & 0 & 0 & 0 & 0 & 0 \\ \frac{T^2}{2} & T & 1 & 0 & 0 & 0 & 0 & 0 & 0 \\ 0 & 0 & 0 & \frac{T^4}{4} & \frac{T^3}{2} & \frac{T^2}{2} & 0 & 0 & 0 \\ 0 & 0 & 0 & \frac{T^3}{2} & \frac{T^2}{2} & T & 0 & 0 & 0 \\ 0 & 0 & 0 & \frac{T^2}{2} & T & 1 & 0 & 0 & 0 \\ 0 & 0 & 0 & 0 & 0 & 0 & \frac{T^4}{4} & \frac{T^3}{2} & \frac{T^2}{2} \\ 0 & 0 & 0 & 0 & 0 & 0 & \frac{T^3}{2} & \frac{T^2}{2} & T \\ 0 & 0 & 0 & 0 & 0 & 0 & \frac{T^2}{2} & T & 1 \end{bmatrix} \sigma_w^2. \quad (2.5)$$

2.2.3. CT Model

Sometimes, the underwater target may make a turn. In order to capture this behavior, the coordinated turn model is investigated. This model presumes that the target moves with

constant speed and constant turn rate. Assuming that the underwater target turns only in the XY-plane, the corresponding state transition matrix F_k is

$$F_k = \begin{bmatrix} 1 & \frac{\sin \omega T}{\omega} & 0 & 0 & -\frac{1 - \cos \omega T}{\omega} & 0 & 0 & 0 & 0 \\ 0 & \cos \omega T & 0 & 0 & -\sin \omega T & 0 & 0 & 0 & 0 \\ 0 & 0 & 1 & 0 & 0 & 0 & 0 & 0 & 0 \\ 0 & \frac{1 - \cos \omega T}{\omega} & 0 & 1 & \frac{\sin \omega T}{\omega} & 0 & 0 & 0 & 0 \\ 0 & \sin \omega T & 0 & 0 & \cos \omega T & 0 & 0 & 0 & 0 \\ 0 & 0 & 0 & 0 & 0 & 1 & 0 & 0 & 0 \\ 0 & 0 & 0 & 0 & 0 & 0 & 1 & 0 & 0 \\ 0 & 0 & 0 & 0 & 0 & 0 & 0 & 1 & 0 \\ 0 & 0 & 0 & 0 & 0 & 0 & 0 & 0 & 1 \end{bmatrix}, \quad (2.6)$$

where ω is the turn rate. The zero-mean white noise \mathbf{w}_k in the CA model is used to model the perturbation of the trajectory from the CT motion.

2.3. Measurement Model of UWSN

Sensors used for target tracking provide measurements of a target, such as range r , azimuth α , and elevation angle β [31]. For example, there are $N = 3$ sensor nodes involved in target tracking (see Figure 2). (x_k, y_k, z_k) are the coordinates of the target at time k . (x_i, y_i, z_i) represent the coordinates of the i th sensor node. The measurements $r_{k,i}$, $\alpha_{k,i}$, and $\beta_{k,i}$ represent the distance, azimuth, and elevation angle provided by the i th sensor node, respectively.

From Figure 2, we can see that the measurements can be calculated by the following equations:

$$\begin{aligned} r_{k,i} &= \sqrt{(x_k - x_i)^2 + (y_k - y_i)^2 + (z_k - z_i)^2}, \quad i = 1, 2, \dots, N, \\ \alpha_{k,i} &= \arctan \frac{y_k - y_i}{x_k - x_i}, \quad i = 1, 2, \dots, N, \\ \beta_{k,i} &= \arctan \frac{z_k - z_i}{\sqrt{(x_k - x_i)^2 + (y_k - y_i)^2}}, \quad i = 1, 2, \dots, N. \end{aligned} \quad (2.7)$$

The measurement equation from the i th sensor is given by

$$\begin{aligned} \mathbf{Z}_{k,i} &= \mathbf{h}_{k,i}(\mathbf{X}_k) + \mathbf{v}_{k,i} \\ &= [r_{k,i}, \alpha_{k,i}, \beta_{k,i}]^T + \mathbf{v}_{k,i}, \quad i = 1, 2, \dots, N, \end{aligned} \quad (2.8)$$

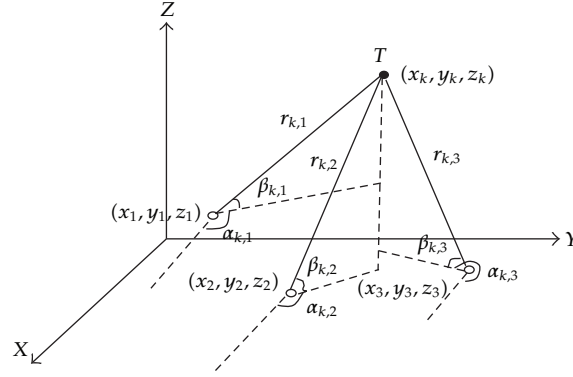


Figure 2: Measurement system of UWSN.

where $\mathbf{Z}_{k,i}$ is the measurement from the i th sensor at time k . $\mathbf{v}_{k,i}$ is the independent zero-mean Gaussian measurement noise with covariance matrix \mathbf{R}_k . At time k , the accumulated measurement of UWSN \mathbf{Z}_k is given by

$$\mathbf{Z}_k = [\mathbf{Z}_{k,1}, \mathbf{Z}_{k,2}, \dots, \mathbf{Z}_{k,N}]^T. \quad (2.9)$$

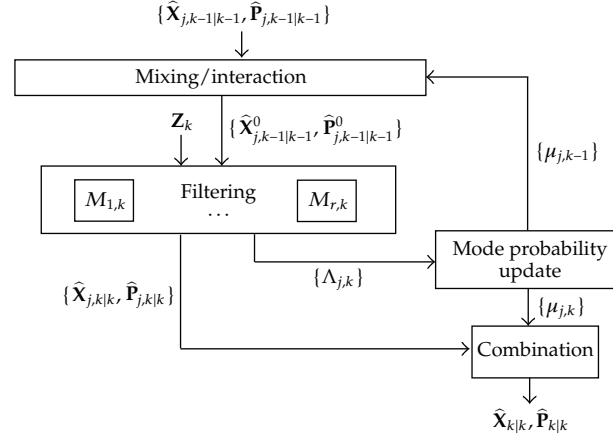
3. IMMPF Underwater Target Tracking Algorithm

3.1. Interacting Multiple Model

The interacting multiple model, as one of the most efficient dynamic multiple model (MM) estimators, was proposed by Blom and Bar-Shalom [34]. Different from many other methods which assume a particular moving pattern of the node, the IMM filter incorporates all the possible moving patterns of the node, by running a bank of filters parallel with each filter corresponding to one particular moving pattern. And the overall state estimate is a certain combination of these model-conditional estimates. A complete cycle of the IMM filter process consists of four essential operations, namely, mixing/interaction, filtering, mode probability update, and combination [35]. The flow diagram of an IMM method is shown in Figure 3.

3.2. IMMPF

Particle filter can solve the nonlinear problem of underwater target tracking. However, it cannot handle the maneuvers of the target for it only uses a single motion model. The interacting multiple model method is suitable for tracking maneuvering motions of the target. Therefore, we combine IMM with PF, namely, IMMPF, for three-dimensional target tracking in UWSN. The flowchart of IMMPF algorithm is shown in Figure 4. It can be noted that IMMPF has four stages: mixing and interaction stage, particle filter stage (emphasized by the dotted box), mode probability update stage, and state update stage (combination).



$M_{j,k}$: model j at time k , $j = 1, \dots, r$
 $\hat{\mathbf{X}}_{j,k-1|k-1}, \hat{\mathbf{P}}_{j,k-1|k-1}$: the prior state estimate and its covariance for $M_{j,k}$
 $\hat{\mathbf{X}}_{j,k-1|k-1}^0, \hat{\mathbf{P}}_{j,k-1|k-1}^0$: the initial state estimate and its covariance for $M_{j,k}$
 \mathbf{Z}_k : the measurement at time k
 $\hat{\mathbf{X}}_{j,k|k}, \hat{\mathbf{P}}_{j,k|k}$: the state estimate and its covariance for $M_{j,k}$
 $\Lambda_{j,k}$: the likelihood function for $M_{j,k}$
 $\mu_{j,k}$: the mode probability of $M_{j,k}$
 $\hat{\mathbf{X}}_{k|k}, \hat{\mathbf{P}}_{k|k}$: the combined state estimate and its covariance

Figure 3: Flow diagram of the IMM method.

The outline of IMMPF algorithm is given below (it assumes that there are r modes).

(1) Interaction. For $M_{j,k}$, compute the initial state estimate and its covariance:

$$\begin{aligned}
 \hat{\mathbf{X}}_{j,k-1|k-1}^0 &= \sum_{i=1}^r \hat{\mathbf{X}}_{i,k-1|k-1} \mu_{i|j, k-1|k-1}, \\
 \hat{\mathbf{P}}_{j,k-1|k-1}^0 &= \sum_{i=1}^r \mu_{i|j, k-1|k-1} \left[\hat{\mathbf{P}}_{i,k-1|k-1} + \left(\hat{\mathbf{X}}_{i, k-1|k-1} - \hat{\mathbf{X}}_{j, k-1|k-1}^0 \right) \right. \\
 &\quad \left. \left(\hat{\mathbf{X}}_{i, k-1|k-1} - \hat{\mathbf{X}}_{j, k-1|k-1}^0 \right)^T \right],
 \end{aligned} \tag{3.1}$$

where $\mu_{i|j,k-1|k-1} = \bar{c}_j^{-1} p_{ij} \mu_{i,k-1}$ is mixing probability; $\bar{c}_j = \sum_{i=1}^r p_{ij} \mu_{i,k-1}$ is the normalization constant; p_{ij} is the transition probability for switching from model i to model j .

(2) Particle filter. Through the use of the initial state estimate and its covariance from the interaction step, as well as the measurement \mathbf{Z}_k , model updates for $M_{j,k}$ are performed by computing the state estimate $\hat{\mathbf{X}}_{j,k|k}$, and its covariance $\hat{\mathbf{P}}_{j,k|k}$. The process of particle filter is described as follows:

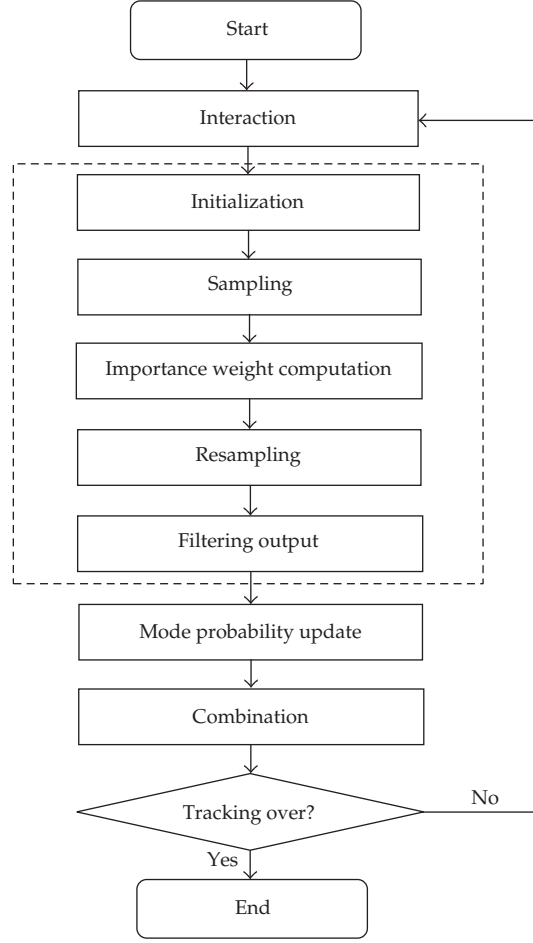


Figure 4: Flowchart of the IMMPPF algorithm.

- (a) Initialization. Generate samples $\{\hat{\mathbf{X}}_{j,k-1|k-1}^{(i)}\}_{i=1}^{Ns}$ from the prior probability density function by $N(\hat{\mathbf{X}}_{j,k-1|k-1}^0, \hat{\mathbf{P}}_{j,k-1|k-1}^0)$. Set initial weights $w_{j,k-1}^{(i)} = 1/Ns$.
- (b) Sampling. Draw sample $\hat{\mathbf{X}}_{j,k|k}^{(i)}$ from the proposal distribution $q(\hat{\mathbf{X}}_{j,k|k} | \hat{\mathbf{X}}_{j,0:k-1}, \mathbf{Z}_{j,1:k})$.
- (c) Importance weights computation. Compute and normalize the importance weights:

$$\tilde{w}_{j,k}^{(i)} = \tilde{w}_{j,k-1}^{(i)} \frac{p(\mathbf{Z}_{j,k} | \hat{\mathbf{X}}_{j,k|k}^{(i)}) p(\hat{\mathbf{X}}_{j,k|k}^{(i)} | \hat{\mathbf{X}}_{j,k-1|k-1}^{(i)})}{q(\hat{\mathbf{X}}_{j,k|k}^{(i)} | \hat{\mathbf{X}}_{j,0:k-1}^{(i)}, \mathbf{Z}_{j,1:k})}, \quad (3.2)$$

$$w_{j,k}^{(i)} = \frac{\tilde{w}_{j,k}^{(i)}}{\sum_{i=1}^{Ns} \tilde{w}_{j,k}^{(i)}}.$$

- (d) Resampling. Calculate $N_{j,\text{eff}} = [\sum_{i=1}^{N_s} (w_{j,k}^{(i)})^2]^{-1}$. If $N_{j,\text{eff}}$ is below a user-defined threshold $N_{j,\text{thres}}$, perform resampling to generate equally weighted particles $\{\hat{\mathbf{X}}_{j,k|k}^{(i)}, w_{j,k}^{(i)}\}_{i=1}^{N_s}$.
- (e) Filtering output. Compute the state estimate and its covariance:

$$\begin{aligned}\hat{\mathbf{X}}_{j,k|k} &= \sum_{i=1}^{N_s} w_{j,k}^{(i)} \hat{\mathbf{X}}_{j,k|k}^{(i)}, \\ \hat{\mathbf{P}}_{j,k|k} &= \sum_{i=1}^{N_s} w_{j,k}^{(i)} (\hat{\mathbf{X}}_{j,k|k}^{(i)} - \hat{\mathbf{X}}_{j,k|k}) (\hat{\mathbf{X}}_{j,k|k}^{(i)} - \hat{\mathbf{X}}_{j,k|k})^T.\end{aligned}\tag{3.3}$$

- (3) Mode probability update. The mode probability of $M_{j,k}$ is computed as

$$\mu_{j,k} = \frac{1}{c} \Lambda_{j,k} \bar{c}_j,\tag{3.4}$$

where $c = \sum_{i=1}^r \Lambda_{i,k} \bar{c}_i$. And the likelihood function is calculated as

$$\Lambda_{j,k} = \mathbb{N}(\tilde{\mathbf{Z}}_{j,k}; 0, \hat{\mathbf{S}}_{j,k}),\tag{3.5}$$

where $\mathbb{N}(\cdot)$ represents Gaussian distribution; $\tilde{\mathbf{Z}}_{j,k}$ is the filter residual; $\hat{\mathbf{S}}_{j,k}$ is the corresponding filter residual covariance.

- (4) Combination. The combined state estimate and its covariance are computed as:

$$\begin{aligned}\hat{\mathbf{X}}_{k|k} &= \sum_{i=1}^r \mu_{i,k} \hat{\mathbf{X}}_{i,k|k}, \\ \hat{\mathbf{P}}_{k|k} &= \sum_{i=1}^r \mu_{i,k} \left[\hat{\mathbf{P}}_{i,k|k} + (\hat{\mathbf{X}}_{i,k|k} - \hat{\mathbf{X}}_{k|k}) (\hat{\mathbf{X}}_{i,k|k} - \hat{\mathbf{X}}_{k|k})^T \right].\end{aligned}\tag{3.6}$$

4. Simulation and Results

To evaluate our proposed method, we design two simulation cases. At first, PF, EKF, and UKF are used to compare the tracking performance for the nonlinear problem of underwater target tracking. Then, the proposed algorithm and PF are applied to a problem on the 3D underwater target tracking, respectively.

4.1. Performance Evaluations

We analyze the performance of the presented algorithm and other filtering methods by state estimation errors. The total number of independent simulation runs is $R = 50$. Let (x_k, y_k, z_k)

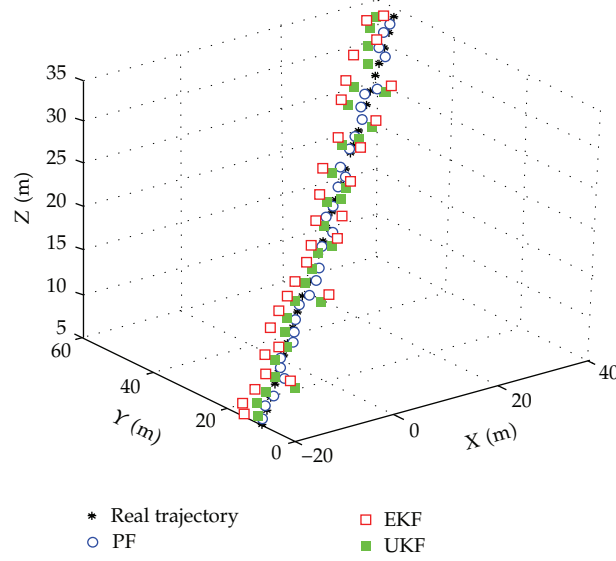


Figure 5: Real and estimated 3D target trajectories obtained with PF, EKF, and UKF.

denote the real position at time k , and the corresponding estimated position is $(\hat{x}_{k|k}, \hat{y}_{k|k}, \hat{z}_{k|k})$. The tracking errors along the x -axis, y -axis, and z -axis are given as

$$\begin{aligned}
 E_x(k) &= \frac{1}{R} \sum_{i=1}^R |x_k - \hat{x}_{i,k|k}|, \\
 E_y(k) &= \frac{1}{R} \sum_{i=1}^R |y_k - \hat{y}_{i,k|k}|, \\
 E_z(k) &= \frac{1}{R} \sum_{i=1}^R |z_k - \hat{z}_{i,k|k}|,
 \end{aligned} \tag{4.1}$$

The root mean square error (RMSE) in the estimation of position is defined as

$$E(k) = \sqrt{\frac{1}{R} \sum_{i=1}^R [(x_k - \hat{x}_{i,k|k})^2 + (y_k - \hat{y}_{i,k|k})^2 + (z_k - \hat{z}_{i,k|k})^2]}. \tag{4.2}$$

4.2. Tracking Performance Comparison between PF, EKF, and UKF

4.2.1. Simulation Conditions

In our first experiment, we assume the initial position of the target is $(-20, 10, 5)$ m, and the initial velocity is $(2, 1.5, 1)$ m/s. From 0 to 30 s, it moves at CV. The process noise or measurement noise is $\mathbb{N}(0, 0.1^2)$ Gaussian distribution. The sampling interval (time interval between successive scans) is $T = 1$ s and the total number of time steps for the duration of tracking a target is $L = 30$.

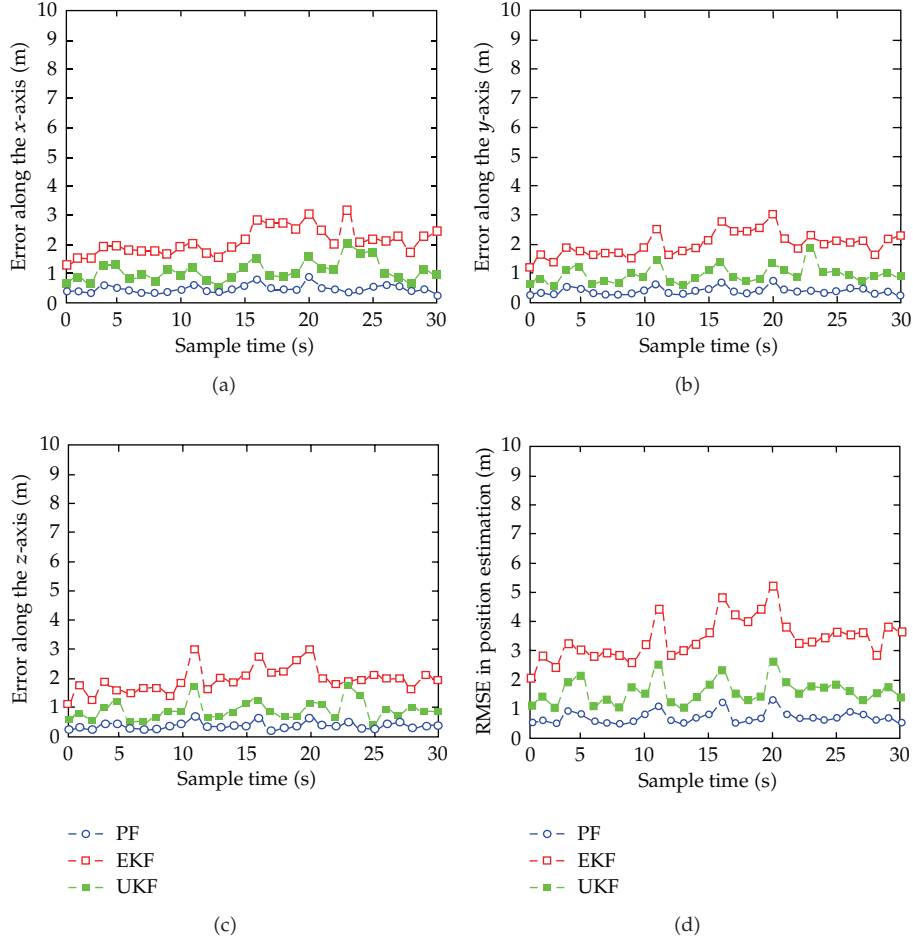


Figure 6: Tracking performance of PF, EKF, and UKF. (a) The estimation error of the x -axis. (b) The estimation error of the y -axis. (c) The estimation error of the z -axis. (d) RMSE of target position estimation.

4.2.2. Simulation Results

Figure 5 shows the real and estimated target trajectories obtained with PF, EKF, and UKF. Figure 6 provides the corresponding target position estimation errors. The comparison results indicate that PF has a better tracking accuracy than EKF and UKF. This is because tracking targets in UWSN is a nonlinear and non-Gaussian problem. EKF uses the first-order Taylor series expansions to approximate nonlinear system functions, and its performance may degrade as the system becomes nonlinear or non-Gaussian. Compared with EKF, UKF transforms the analytic integral operator into an approximate summation operator through a set of deterministic point, so it can improve the tracking precision. Nevertheless, its performance may still be unsatisfactory in multimode and non-Gaussian problems. Moreover, PF is not bounded by linearization models and Gauss assumptions and applies to any nonlinear and non-Gaussian random systems. Therefore, PF is more suitable for underwater target tracking.

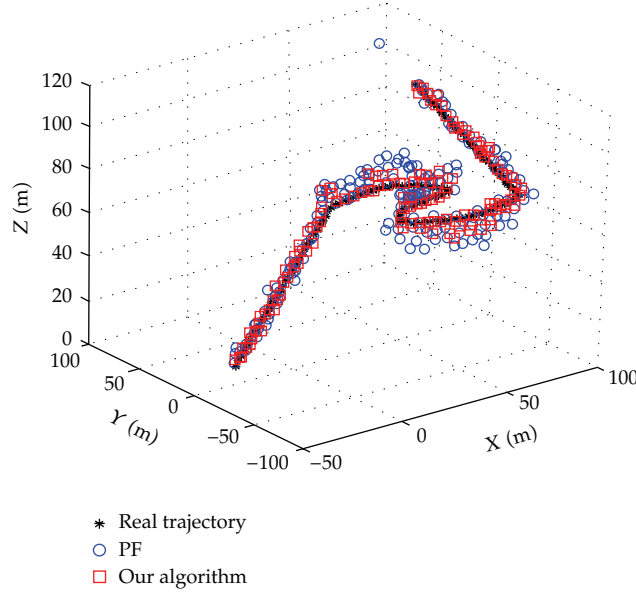


Figure 7: Real and estimated 3D target trajectories obtained with PF and the presented scheme.

4.3. Tracking Performance Comparison between the Presented Algorithm and PF

4.3.1. Simulation Conditions

The initial state vector is $[-20, 2, 0, 10, 1.5, 0, 5, 1, 0]^T$. From 0 to 40 s, it moves at CV. From 41 to 70 s, it makes a CT with turn rate $\omega = -0.1$ rad/s. From 71 to 100 s, it moves at CA. From 101 to 140 s, it makes a CT with turn rate $\omega = 0.1$ rad/s. From 141 to 170 s, it moves at CV. The process noise or measurement noise is $\mathcal{N}(0, 0.1^2)$ Gaussian distribution. The sampling interval is $T = 1$ s and the total number of time steps is $L = 170$.

Let model 1, model 2, model 3, and model 4 denote CV, CA, and CT with turn rate $\omega = -0.1$ rad/s, CT with turn rate $\omega = 0.1$ rad/s, respectively. The transition probability matrix and the initial mode probability are

$$\begin{bmatrix} 0.8 & 0.1 & 0.05 & 0.05 \\ 0.2 & 0.7 & 0.05 & 0.05 \\ 0.15 & 0.05 & 0.75 & 0.05 \\ 0.15 & 0.05 & 0.05 & 0.75 \end{bmatrix}, \quad [0.8 \ 0.1 \ 0.05 \ 0.05]. \quad (4.3)$$

The initial covariance matrixes are $P_{01} = \text{diag}(9, 4, 9, 4, 9, 4)$, $P_{02} = \text{diag}(9, 4, 1, 9, 4, 1, 9, 4, 1)$, $P_{03} = P_{04} = \text{diag}(9, 4, 0.09, 9, 4, 0.09, 9, 4, 0.09)$.

4.3.2. Simulation Results

Figure 7 shows the real and estimated target trajectories of PF and our algorithm, and the corresponding state estimation errors are given in Figure 8. In USWN, the target often does

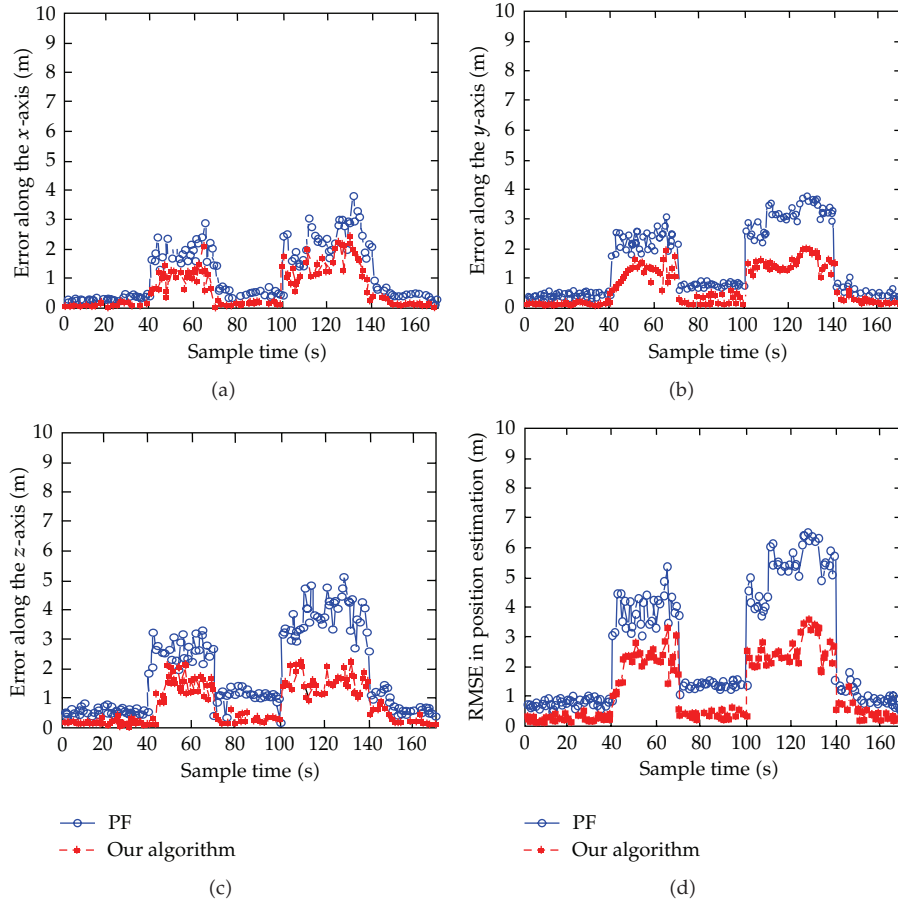


Figure 8: Tracking performance of PF and the presented scheme. (a) The estimation error of the x -axis. (b) The estimation error of the y -axis. (c) The estimation error of the z -axis. (d) RMSE of target position estimation.

maneuvering motions, which makes the tracking problem intractable. Nevertheless, it can be seen from Figures 7 and 8 that compared with PF, the presented method combining IMM with PF can yield higher tracking precision. In addition, the surges in state estimation errors at the onset and at the termination of a maneuver are also significantly smaller than those for PF.

5. Conclusions

This paper focuses on the nonlinear and maneuvering problems for underwater target tracking based on underwater wireless sensor networks. It firstly designs the UWSN architecture for target tracking. Then, to estimate the states of the target, a 3D underwater target tracking algorithm combining interacting multiple model with the particle filter is presented. The simulation results show that compared with PF, EKF, or UKF, the presented method can improve the accuracy and effectiveness of the underwater target tracking.

Acknowledgments

This work is supported by the Special Fund for Basic Scientific Research of Central Colleges, Hohai University (Grant no. 2011B09314), the China Postdoctoral Science Foundation funded project (Grant no. 2012M511185) the Jiangsu Planned Projects for Postdoctoral Research Funds (Grant no. 1102069C), and the National Natural Science Foundation of China (Grant No. 61263029).

References

- [1] K. M. Han and H. T. Choi, "Shape context based object recognition and tracking in structured underwater environment," in *Proceedings of the IEEE International Conference on Geoscience and Remote Sensing Symposium*, pp. 617–620, 2011.
- [2] S. Han and Z. Xu, "Passive tracking of maneuvering target based on bearings-frequency of two sonar sensors," in *Proceedings of the International Conference on Electronics, Communications and Control*, pp. 2174–2177, 2011.
- [3] S. K. Rao, K. S. L. Murthy, and K. R. Rajeswari, "Data fusion for underwater target tracking," *IET Radar, Sonar and Navigation*, vol. 4, no. 4, pp. 576–585, 2010.
- [4] S. Y. Chen, "Kalman filter for robot vision: a survey," *IEEE Transactions on Industrial Electronics*, vol. 59, no. 11, pp. 4409–4420, 2012.
- [5] D. Eickstedt, M. Benjamin, H. Schmidt et al., "Adaptive tracking of underwater targets with autonomous sensor networks," *Journal of Underwater Acoustics*, vol. 56, pp. 465–495, 2006.
- [6] H. Shi, W. Wang, N. M. Kwok, and S. Y. Chen, "Game theory for wireless sensor networks: a survey," *Sensors*, vol. 12, no. 7, pp. 9055–9097, 2012.
- [7] S. Chen, W. Huang, C. Cattani, and G. Altieri, "Traffic dynamics on complex networks: a survey," *Mathematical Problems in Engineering*, vol. 2012, Article ID 732698, 23 pages, 2012.
- [8] J. Xue, M. Li, W. Zhao, and S. Chen, "Bound maxima as a traffic feature under DDOS flood attacks," *Mathematical Problems in Engineering*, vol. 2012, Article ID 419319, 20 pages, 2012.
- [9] L. Z. Xu, X. F. Li, and S. X. Yang, "Wireless network and communication signal processing," *Intelligent Automation & Soft Computing*, vol. 17, no. 8, article 1019, 2011.
- [10] I. F. Akyildiz, D. Pompili, and T. Melodia, "Underwater acoustic sensor networks: research challenges," *Ad Hoc Networks*, vol. 3, no. 3, pp. 257–279, 2005.
- [11] C. H. Yu, K. H. Lee, J. W. Choi, and Y. B. Seo, "Distributed single target tracking in underwater wireless sensor networks," in *Proceedings of the SICE Annual Conference*, pp. 1351–1356, Japan, August 2008.
- [12] G. Isbitiren and O. B. Akan, "Three-dimensional underwater target tracking with acoustic sensor networks," *IEEE Transactions on Vehicular Technology*, vol. 60, no. 8, pp. 3897–3906, 2011.
- [13] E. Kim, S. Lee, C. Kim, and K. Kim, "Bearings-only tracking systems with distributed floating beacons in underwater sensor networks," in *Proceedings of the IEEE/IFIP 8th International Conference on Embedded and Ubiquitous Computing, (EUC '10)*, pp. 311–315, December 2010.
- [14] L. Z. Xu, X. F. Ding, X. Wang, G. F. Lv, and F. C. Huang, "Trust region based sequential quasi-Monte Carlo filter," *Acta Electronica Sinica*, vol. 39, no. 3 A, pp. 24–30, 2011.
- [15] S. Y. Chen and Z. J. Wang, "Acceleration strategies in generalized belief propagation," *IEEE Transactions on Industrial Informatics*, vol. 8, no. 1, pp. 41–48, 2012.
- [16] X. F. Ding, L. Z. Xu, X. Wang et al., "Robust visual object tracking using covariance features in Quasi-Monte Carlo filter," *Intelligent Automation and Soft Computing*, vol. 17, no. 5, pp. 571–582, 2011.
- [17] X. Wang and Z. Tang, "Modified particle filter-based infrared pedestrian tracking," *Infrared Physics and Technology*, vol. 53, no. 4, pp. 280–287, 2010.
- [18] M. Li, S. C. Lim, and S. Chen, "Exact solution of impulse response to a class of fractional oscillators and its stability," *Mathematical Problems in Engineering*, vol. 2011, Article ID 657839, 9 pages, 2011.
- [19] S. Y. Chen, H. Tong, Z. Wang, S. Liu, M. Li, and B. Zhang, "Improved generalized belief propagation for vision processing," *Mathematical Problems in Engineering*, vol. 2011, Article ID 416963, 12 pages, 2011.
- [20] C. Cattani, "Shannon wavelets for the solution of integrodifferential equations," *Mathematical Problems in Engineering*, vol. 2010, Article ID 408418, 22 pages, 2010.

- [21] F. Zhang, X. P. Zhou, X. H. Chen, and R. L. Liu, "Particle filter for underwater bearings-only passive target tracking," in *Proceedings of the Pacific-Asia Workshop on Computational Intelligence and Industrial Application, (PACIIA '08)*, pp. 847–851, December 2008.
- [22] H. Q. Liu, M. Chitre, and R. Gao, "AUV positioning based on interactive multiple model," in *Proceedings of the IEEE Conference on OCEANS*, pp. 1–6, May 2010.
- [23] C. H. Yu, H. P. Moon, J. W. Choi, Y. B. Seo, T. I. Seo, and E. J. Kim, "Interacting multiple model based distributed target tracking algorithm in UWSNs," in *Proceedings of the ICROS-SICE International Joint Conference, (ICCAS-SICE '09)*, pp. 1752–1759, August 2009.
- [24] Y. Boers and J. N. Driessen, "Interacting multiple model particle filter," *Proceedings of the IEEE Proceedings: Radar, Sonar and Navigation*, vol. 150, no. 5, pp. 344–349, 2003.
- [25] H. W. Li and J. Wang, "Particle filter for manoeuvring target tracking via passive radar measurements with glint noise," *IET Radar, Sonar and Navigation*, vol. 6, no. 3, pp. 180–189, 2012.
- [26] N. Yang, P. Li, J. Zhang, and Y. Zhu, "Parameter identification of land vehicle location model based on IMMPE," in *Proceedings of the 3rd International Conference on Computer Research and Development, (ICCRD '11)*, pp. 266–269, March 2011.
- [27] Z. Zhou, J. H. Cui, and S. L. Zhou, "Localization for large-scale underwater sensor networks," in *Proceedings of the 6th international IFIP-TC6 Conference on Ad Hoc and Sensor Networks, Wireless Networks, Next Generation Internet*, pp. 108–119, 2007.
- [28] B. T. Lee and S. Kim, "Scalable DV-Hop localization for wireless sensor networks," in *Proceedings of the 14th Asia-Pacific Conference on Communications, (APCC '08)*, pp. 1–4, October 2008.
- [29] J. Liu, X. Han, M. Al-Bzoor et al., "PADP: prediction assisted dynamic surface gateway placement for mobile underwater networks," in *Proceedings of the IEEE Symposium on Computers and Communications*, pp. 139–144, 2012.
- [30] X. R. Li and V. P. Jilkov, "Survey of maneuvering target tracking. part I: dynamic models," *IEEE Transactions on Aerospace and Electronic Systems*, vol. 39, no. 4, pp. 1333–1364, 2003.
- [31] X. R. Li and V. P. Jilkov, "A survey of maneuvering target tracking—part III: measurement models," in *Signal and Data Processing of Small Targets*, vol. 4473 of *Proceedings of SPIE*, pp. 423–446, August 2001.
- [32] S. Chen, Y. Wang, and C. Cattani, "Key issues in modeling of complex 3D structures from video sequences," *Mathematical Problems in Engineering*, vol. 2012, Article ID 856523, 17 pages, 2012.
- [33] C. Cattani, S. Chen, and G. Aldashev, "Information and modeling in complexity," *Mathematical Problems in Engineering*, vol. 2012, Article ID 868413, 4 pages, 2012.
- [34] H. A. P. Blom and Y. Bar-Shalom, "Interacting multiple model algorithm for systems with Markovian switching coefficients," *IEEE Transactions on Automatic Control*, vol. 33, no. 8, pp. 780–783, 1988.
- [35] P. H. Foo, "Combining the interacting multiple model method with particle filters for manoeuvring target tracking with a multistatic radar system," *IET Radar, Sonar and Navigation*, vol. 5, no. 7, pp. 697–706, 2011.

Research Article

Optimal Placement of Passive Energy Dissipation Devices by Genetic Algorithms

Ji-ting Qu^{1,2} and Hong-nan Li³

¹ Faculty of Infrastructure Engineering, Dalian University of Technology, Dalian, Liaoning 116024, China

² State Key Laboratory of Structural Analysis for Industrial Equipment, Dalian University of Technology, Dalian, Liaoning 116024, China

³ State Key Laboratory of Coastal and Offshore Engineering, Dalian University of Technology, Dalian, Liaoning 116024, China

Correspondence should be addressed to Ji-ting Qu, qjt@dlut.edu.cn

Received 5 October 2012; Accepted 23 November 2012

Academic Editor: Fei Kang

Copyright © 2012 J.-t. Qu and H.-n. Li. This is an open access article distributed under the Creative Commons Attribution License, which permits unrestricted use, distribution, and reproduction in any medium, provided the original work is properly cited.

A mathematical model is proposed in this paper for locating optimal positions for passive energy dissipative dampers. Three control indices of structural responses with the storey-drift angle, storey displacement, and acceleration are taken in this model. Firstly, six combination modes of these indices are presented. On the premise that the number of dampers is fixed, this paper deals with the optimal placement of two types of passive dampers for several building models with different number of storeys and seismic ground motions at four types of sites using genetic algorithm. Secondly, two estimating indices are presented to assess the reasonable combination mode of coefficients under different conditions, which can generally express the best response control. Numerical examples are illustrated to verify the effectiveness and feasibility of the proposed mathematical model. At last, several significant conclusions are given based on numerical results.

1. Introduction

The technique of energy dissipation belongs to a kind of passive structural control. The basic role of passive energy dissipation devices is to absorb or consume a portion of the input energy from earthquake or wind, reduce the structural response, and protect structural members. These devices are classified as displacement-based and velocity-based dampers in the China Seismic Code. Among them, metallic yielding damper (MD) and friction damper are the most widely used displacement-based devices, and their force-deformation responses only depend on the relative displacement between each end of device. They could be

effective on energy dissipation only if slip displacement is reached. Viscoelastic and viscous dampers are the two typically used velocity-based devices. The viscoelastic damper (VED) dissipates vibration energy when viscoelastic material is subjected to shear deformation, thereby reducing the structural response. These devices are applied in seismic control of buildings broadly because they rarely need to be repaired after being installed and have economical and simple conformation performance.

It is well known that the installation of dampers will reduce seismic responses of structures. To design a structure with energy dissipation devices, the optimal locations of devices will have a significant effect on reducing responses and achieving desired design objectives. Commonly, it may be convenient to distribute the devices to every storey or one storey interval. However, such a placement may be uneconomical and not be the most effective means because installation of dampers may increase the stiffness of corresponding storey and enlarge responses of neighboring stories. Therefore, the research of optimal design causes designers' interest.

In the past decades, many researchers have contributed themselves to studies on the optimal location of dampers in structures. Haftka and Adelman [1] had a study on selection of actuator locations in large space structures based on worst out in and exhaustive single-point substitution methods. However, this technique leads to a locally optimal solution near the starting design guess. Ashour and Hanson [2] suggested placing devices on locations that would maximize the damping ratio of the fundamental mode because of its dominance in multistorey buildings' mode. Zhang and Soong [3] used a simplified sequential search algorithm to determine the optimal location of VEDs in an unsymmetrical shear building. Parametric and positioning optimization analyses about VEDs were conducted by Gürgöze and Müller [4] for a linear multi-degree-of-freedom structure. Several other methods were adopted for location optimization, such as topological approach suggested by Natke and Soong [5], simulated annealing optimization used by Milman and Chu [6], and others by Takewaki [7] and Takewaki et al. [8] made use of a gradient-based method to search for optimal locations. According to the capability and characteristic of structures with VEDs, Zhou et al. [9] proposed five different optimum design methods for installation of dampers and analyzed an example of a ten-floor reinforced concrete structure. Zhang et al. [10] suggested a convenient and practical methodology about choosing parameters and locations of VEDs, and effects of controlling of structural vibration for different positions of these devices were compared. In practical applications, the location variables are discrete as the numbers of dampers are fixed. Theoretically, the optimal solution of such a discrete problem can be obtained by an enumerative search of every possible combination of dampers' position. In fact, the number of feasible locations is too large. Thus, a versatile and flexible method called genetic algorithm was suggested especially for problems whose performance index is not a continuous function when the design variable and the variable design space are discrete [11–13]. Singh and Moreschi [14] utilized this approach to study the layout and parametric optimization of viscous and viscoelastic dampers to achieve a desired performance. Moreschi and Singh [15] presented a methodology to determine the optimal design parameters for the yielding metallic and friction devices installed at different locations in a building for a desired performance objective. An optimal installation method of MR dampers using genetic algorithms was put forward in order to reduce the vibration response of high-rise building under wind load [16]. Bei and Li [17] gave a new method of improved genetic algorithm and quadratic performance index. Five optimal methods were used to determine the number and location of the magnetorheological dampers in the structure, and several principles were pointed out.

As displacement-based energy dissipative devices present highly nonlinear characteristics, the installation of such dampers in a structure will render it to behave nonlinearly even if all other structural members are designed to remain linear. Thus, the analysis of structures with these devices must be done by a step-by-step time history analysis. Investigations on optimal placement of displacement-based dampers are not enough and mainly focus on parametrical optimization. Besides, there are two aspects of shortage [18] needed to be improved on location optimization of dampers: on one hand, the objective functions suggested by different scholars are diverse, thus the optimal results are different which can confuse the designers; on the other hand, the investigations all aim at a given structure subjected to one earthquake record. Optimal solutions may change for different structures subjected to various earthquakes. The optimal results derived from one certain earthquake record may be unsatisfied for another record.

The main objective of this research is to study the optimal objective functions of two types of passive energy dissipation devices with fixed numbers. A new mathematic model of location optimization will be established, which is suitable for different kinds of passive dampers. Three seismic response performance indices are taken in this model. To achieve the optimal coefficients of storey-drift angle, acceleration, and storey-displacement indices, this paper deals with the optimal location of two types of passive dampers for several building models with different number of storeys and ground motions at four types of sites. Numerical analyses are illustrated to verify effective and feasibility of the model for optimal locations of dampers and structural control, in which a genetic algorithm is used.

2. Analytical Modeling of Passive Energy Dissipation Devices

2.1. Model of Force-Deformation Relation

The displacement-based devices are installed in series with bracings at the interstorey of structures. The force-deformation model has often been expressed by the bilinear model. The model of yielding metallic dampers is shown in Figure 1(a), and elastic-perfectly-plastic model is used to approximate friction dampers' model. The combination of a damper and the bracings is called as the device-brace assembly, and its force is represented as $g_{db}(x)$. The stiffness of assembly can be expressed as

$$k_{db0} = \frac{k_{d0}k_b}{k_{d0} + k_b}, \quad k_{db1} = \frac{k_{d1}k_b}{k_{d1} + k_b}, \quad (2.1)$$

where k_{db0} and k_{db1} represent the initialized stiffness and the second stiffness of the assembly; k_{d0} and k_{d1} represent the initialized stiffness and the second stiffness of dampers.

The combinational stiffness of assembly for friction dampers can be given by

$$k_{db0} = k_b, \quad k_{db1} = 0. \quad (2.2)$$

A number of models of VED with the force-deformation relation have been brought forward, and they are applicable to different conditions. The equivalent stiffness and damping model [19] are here adopted for its wide and simple application. The hysteretic

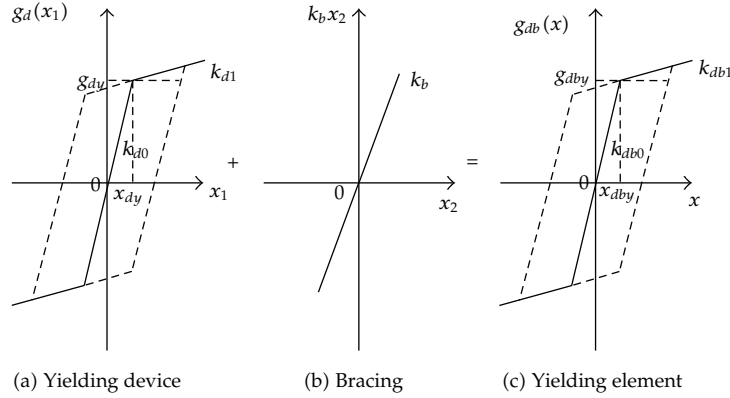


Figure 1: Force-deformation model of yielding metallic dissipation device.

loop of this model is shown in Figure 2. The general formula for the resistance force F_v takes the following form:

$$F_v = c_v(\omega)\dot{u} + k_v(\omega)u, \quad (2.3)$$

where $c_v(\omega)$ and $k_v(\omega)$ represent the frequency-dependent damping and stiffness coefficients for the dampers, and they can be determined by

$$c_v(\omega) = \frac{\eta(\omega)G'(\omega)A}{\omega\delta}, \quad k_v(\omega) = \frac{G'(\omega)A}{\delta}, \quad (2.4)$$

$$\eta(\omega) = \frac{G''(\omega)}{G'(\omega)},$$

where G' and G'' are defined as the shear storage modulus and the shear loss modulus of the VE material, respectively; A represents the area of VE material; δ means the thickness of the VE material; $\eta(\omega)$ is the loss factor that provides a measure of the energy dissipation capability of the VE material; ω corresponds to the frequency at which these properties are determined.

2.2. System Equations of Controlled Structure

The equation of motion for an N -degree-freedom structure with displacement-based energy dissipation devices subjected to earthquake can be written by

$$[M][\ddot{X}] + [C][\dot{X}] + [g(x, \dot{x})] + [g_{db}(x)] = -[M][\ddot{X}_g], \quad (2.5)$$

where $[M]$ and $[C]$ mean the $N \times N$ mass and inherent damping matrices of the structure, $[X]$ is the N -dimensional relative displacement vector with respect to the base, $[\dot{X}]$ and $[\ddot{X}]$ are relative velocity and acceleration vector of N -dimension, $[\ddot{X}_g]$ implies the seismic excitation,

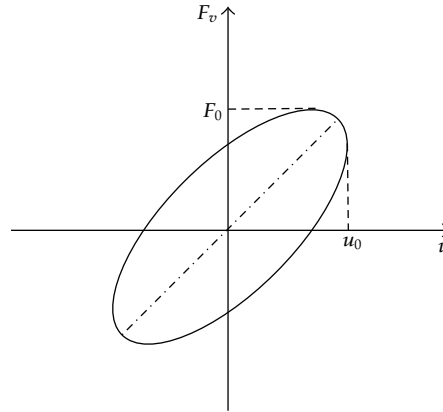


Figure 2: Force-deformation model of VED.

$[g(x, \dot{x})]$ represents force matrix of structure, which depends on the structural force-deformation relationship model; $[g_{db}(x)]$ denotes force matrix of device-bracing assembly, which can be determined by hysteretic model of energy dissipation devices.

The equation of motion for an N degree of freedom structure with VEDs subjected to earthquake motion can be written by

$$[M][\ddot{u}(t)] + ([C_s] + [C_v])[\dot{u}(t)] + ([K_s] + [K_v])[u(t)] = -[M][I][\ddot{u}_g(t)], \quad (2.6)$$

where $[M]$, $[C_s]$, and $[K_s]$ represent the $N \times N$ mass, inherent damping, and stiffness matrices of structure, $[\ddot{u}(t)]$, $[\dot{u}(t)]$ and $[u(t)]$ are the relative acceleration, velocity, and displacement vectors of N -dimension, respectively, $[\ddot{u}_g(t)]$ is the seismic excitation at the base of structure, and $[C_v]$ and $[K_v]$ denote the added damping and stiffness matrices of the VEDs.

3. Optimization Based on Genetic Algorithm

3.1. Genetic Algorithm

The genetic algorithm (GA) was proposed firstly by professor Holland in 1975 and is a globally optimal and self-adaptive searching method of probability, which is based on principles of “survival of the fittest” and adaptation of biology in nature [20]. GA is effective for optimal questions especially for discrete variables and space, whereas traditional math methods are disabled or hard to resolve [21]. An essential characteristic of the GA is the coding of variables that describe the problem. The most common coding method is to transform the variables to a binary string of specific length, and fitness function is provided to measure the fitness of individual. In GA, a generation of population undergoes successive evolution into future generations through the repeated use of genetic operators, containing reproduction operator, crossover operator, and mutation operator [22–25]. As a new population is created, the performance index is evaluated for each new design to determine its fitness with respect to other designs in the population, until no further

improvement is observed in the best individual in the subsequent generations, and the optimal solution is obtained.

3.2. Objective Function

To bring forward an objective function is a core in optimal design. To design a structure with energy dissipation devices, the optimal location of dampers can make the performance indices be restricted within desired objectives as the number of dampers is fixed. The optimal solutions are often diverse when the optimization formulations are different. For example, if the acceleration control is considered as the performance index, the optimal location of dampers can give a better limit for the acceleration. In the literature, several optimization formulations were proposed with different indices as follows [10]: (1) the largest relative displacement of interstorey; (2) storey-displacement and relative displacement of interstorey; (3) relative displacement of interstorey and the displacement of the peak storey.

These indices all focus on the deformation of structures, which should not be regarded as the only index to be reduced especially for high rise. It is a crucial problem to put forward an optimization formulation considering different indices of seismic response and confirm the combination of coefficients for all the indices.

The aim of seismic control of structures is to make structures safe and comfortable in accord with the Codes. Three indices with the storey-drift angle, acceleration, and storey displacement can reflect the two aspects of structural performance. Thus, a new objective function of optimal location is presented in this paper, expressed as a linear combination of three nondimensional items, considering both security and coziness. In order to avoid the optimal solution applicable only to the special earthquake excitation, three seismic records are used for every kind of site in the step-by-step time history analysis. The optimization formulation can be written in the following form:

$$\min Z = \alpha \frac{\theta_{\max}}{\theta_{0,\max}} + \beta \frac{a_{\max}}{a_{0,\max}} + \gamma \frac{u_{\max}}{u_{0,\max}}, \quad (3.1)$$

where θ_{\max} and $\theta_{0,\max}$ mean the largest storey-drift angles of structure with and without additional energy dissipation devices, u_{\max} and $u_{0,\max}$ are the largest displacements of structure with and without devices, a_{\max} and $a_{0,\max}$ represent the largest accelerations of structure with and without devices and, α , β , and γ denote the weight coefficients, respectively, which have different values according to the demand of application in engineering. The combination of the three weight coefficients is given in detail in Section 4.3.

3.3. Optimal Variables

In the context of the problem of optimal location of dampers using GA, optimal variables need to be confirmed. They are expressed as a matrix of position P consisting of 0 and 1, which indicates locating a damper if the number is one. Premising a determinate number of dampers, the optimal variable shows different positions of number 1 and 0. The dimension of the positional matrix is determined by the storey number of a structure. For example, if dampers are located one at the second, third and forth floor of a 6-storey structure, respectively, the matrix of position can be written as follow: $P = [0 \ 1 \ 1 \ 1 \ 0 \ 0]$.

3.4. Estimating Indices for Combination Modes of Coefficients

For different form of buildings with different number of storeys and ground motions at four types of sites, the optimal results about six kinds of combination modes of coefficients may be different. In order to compare these modes with another one to decide which one can generate better control of the structures with optimal location of dampers, two estimating dimensionless indices are proposed, which can be denoted as

$$J_1 = \frac{1}{n} \sum_{i=1}^n \left(\frac{\theta_{i,\max}}{\theta_{0,i,\max}} \right)^2, \quad J_2 = \frac{1}{n} \sum_{i=1}^n \left(\frac{a_{i,\max}}{a_{0,i,\max}} \right)^2, \quad (3.2)$$

where $\theta_{i,\max}$ and $\theta_{0,i,\max}$ imply the mean values of largest storey-drift angle of structures with and without dampers for the i th floor, $a_{i,\max}$ and $a_{0,i,\max}$ represent the mean values of largest accelerations of structures with and without the devices, respectively. J_1 and J_2 all take responses of each floor into consideration, which can reflect the response control in general. For six combination modes of coefficients, the two indices should be calculated, respectively, for different buildings with optimal located dampers. The smaller the values of the indices are, the better the combination mode is.

3.5. Optimal Design Process Based on Genetic Algorithms

- (1) Confirm decision-making variables and conditions of restriction, and create a stochastic initial population P_0 .
- (2) Optimal formulation is established; namely, confirm the type of objective function (determine the maximum or the minimum value of the objective function).
- (3) Design genetic operators, such as select, crossover, and mutation operators.
- (4) Make certain related parameters of GA, containing the number of population (M), the terminate generation of genetic operation (T), probability of crossover (p_c), and probability of mutation (p_m).
- (5) Do step-by-step time history analysis of system by inputting records of earthquakes, and compute the value of the objective function associated with the satisfied solution to get the optimal placement of supplemental dampers.

The system analysis and location optimization procedures are programmed by adopting MATLAB programming language. Figure 3 illustrates the optimal design flow chart.

4. Numerical Analyses

In order to realize the optimal locations to diverse structures at different types of sites, three structures with low, moderate, and high rise height are chosen separately here. The positional optimization of displacement-based energy dissipative devices (MD is considered) and velocity-based devices (VEDs are considered) is processed according to four-site condition. For each type of site, three earthquake records are selected having the close period with the characteristic period of corresponding site. The parameters of GA are taken as follows. The terminate generation of genetic operation is 300. The probabilities of crossover and mutation are 0.8 and 0.2, respectively.

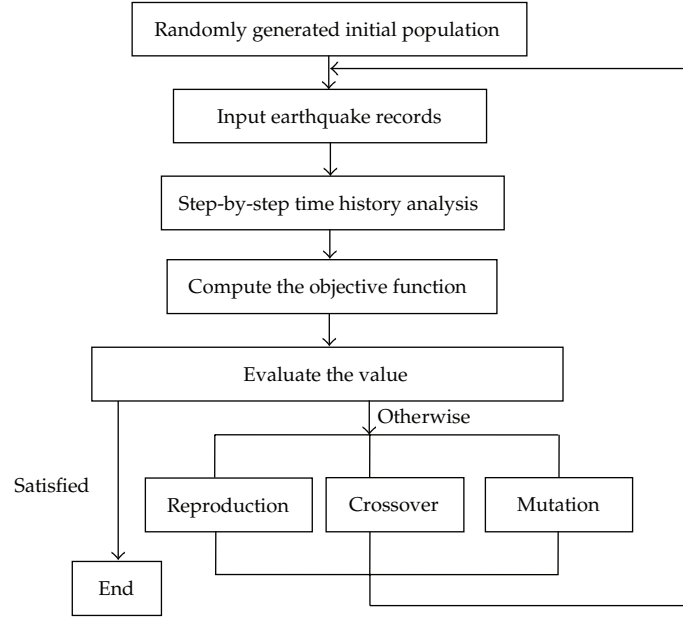


Figure 3: Optimal design flow chart.

4.1. Building Models and Parameters of Dampers

Building 1.

A 5-storey shear building has uniform properties along its height. The mass is 2.0×10^5 kg, the story stiffness is 4.2×10^8 N/m, and the height for each story is 3.3 m. The damping ratio is taken as 5%, and the period of structure is obtained with 0.4817 s. 3 VEDs or MDs will be installed on the structure.

Building 2 (see [9]).

A 10-storey shear building is considered. The mechanical properties of this building are depicted in Table 1. The damping ratio is 5% and period of structure is 1.4583 s. 6 VEDs or MDs are chosen to be placed.

Building 3 (see [26]).

The third structure is a 16-storey shear building. Its mechanical properties are provided in Table 2. The damping ratio is 5%, and period of structure is 2.3848 s. According to the formula of effective damping ratio attached by energy dissipation in China Seismic Code, seventy-two VEDs will provide the same effective damping ratio as nine MDs do. So 9 MDs or 72 VEDs are chosen to be installed.

The typical VED with two viscoelastic layers is designed, where $G' = 1.5 \times 10^7$ N/m², $G'' = 2.01 \times 10^7$ N/m², $A_s = 3 \times 10^{-2}$ m², and $\delta = 1.3 \times 10^{-2}$ m. The working temperature is 25°C. Three initial stiffness of the device-bracing assembly installed on three buildings are

Table 1: Mechanical properties of 10-storey building.

Floor	Mass (kg)	Highness (m)	Stiffness ($\text{N} \times \text{m}^{-1}$)
1	1.52×10^6	3.0	2×10^9
2	1.52×10^6		1×10^9
3	1.349×10^6		1.43×10^9
4	1.349×10^6		1.11×10^9
5	1.349×10^6		1×10^9
6–9	1.349×10^6		0.769×10^9
10	1.187×10^6		0.417×10^9

Table 2: Mechanical properties of 16-storey building.

Floor	Mass (kg)	Highness (m)	Stiffness ($\text{N} \times \text{m}^{-1}$)
1	4.84×10^6	3.6	5.1×10^9
2	4.67×10^6	3.0	3.6×10^9
3	4.35×10^6	3.0	3.8×10^9
4	4.31×10^6	3.0	3.21×10^9
5–9	4.07×10^6	3.0	2.54×10^9
10–13	3.81×10^6	3.0	2.13×10^9
14–16	3.57×10^6	3.0	1.92×10^9

Table 3: Earthquake records.

Site	Group	Records	Component	Interval (s)	Time (s)	Peak value (cm/s^2)
I	F1	1985, La Union, Michoacan Mexico	N00E	0.01	62.71	162.79
	F2	1994, Los Angeles Griffith Observation, Northridge	360	0.005	28.75	163.80
	N1	1988, Zhutang, A, Langcang	S00E	0.01	25.32	541.60
II	F3	1971, Castaic Old bridge Route, San Fernando	N69W	0.02	61.87	265.40
	F4	1979, El Centro, Array no. 10, Imperial valley	N69W	0.01	37.07	168.21
	N2	1988, Gengma Gengma1	S00E	0.02	12.36	140.75
III	F6	1984, Coyote Lake Dam, Morgan Hill	285	0.02	59.98	1137.80
	F7	1940, El Centro-Imp Vall Irr Dist, El Centro	270	0.02	53.47	210.10
	N3	1988, Gengma Gengma 2	S00E	0.02	16.56	90.02
IV	F8	1949, Olympia Hwy Test Lab, Western Washington	356	0.02	89.16	161.63
	F9	1981, Westmor and, Westmoreland	90	0.02	88.43	353.97
	N4	1976, Tianjin Hospital, Tangshan	WE	0.01	19.19	104.18

$2.928 \times 10^8 \text{ N/m}$, $1.64 \times 10^8 \text{ N/m}$, and $8 \times 10^8 \text{ N/m}$. The yield deformation of dampers is taken as 4 mm.

4.2. Earthquake Records

Different earthquake records, even though similar intensities, lead to widely varying responses, and results based on a single record may not be conclusive. Here, twelve earthquake records are chosen [26] and three for each type of site are shown in Table 3. The values of peak ground accelerations are scaled to 400 gal.

Table 4: Combination modes of optimal coefficients.

Mode	α	β	γ	Objective of optimization
1	1	0	0	Considering storey-drift angle only, namely, security
2	0.7	0.1	0.2	Taking storey-drift angle as the main factor, acceleration, and storey displacement as additive factors.
3	0.5	0.3	0.2	Considering the weight of storey-drift angle as half of the importance
4	0.1	0.7	0.2	Considering acceleration as the main factor
5	0	1	0	Considering acceleration only, namely, amenity
6	0.5	0.5	0	Considering only storey drift to reflect deformation of the structure

Table 5: Location optimization of MDs for 5-storey building.

Site	Modes 1 and 2	Mode 3	Modes 4 and 5	Mode 6
I	1 2 3	1 2 3	1 2 4	1 2 4
II	1 2 3	1 2 3	1 2 3	1 2 3
III	1 2 3	1 2 3	1 2 5	1 2 5
IV	1 2 3	1 2 5	1 2 5/1 3 5	1 2 5

Annotation: the numbers in the table represent the floor of optimal location. For example, number 1 and 2 mean that dampers are positioned at the first and the second floor of the building.

Table 6: Location optimization of MDs for 10-storey building.

Site	Modes 1 and 2	Mode 3	Modes 4 and 5	Mode 6
I	2 4 5 6 7 10	2 5 6 7 8 10	2 6 7 8 9 10	1 2 5 6 8 9
II	1 2 5 6 7 9	1 2 5 6 7 10	1 2 6 7 8 10	1 2 5 6 7 10
III	1 2 3 4 6 7	1 2 5 6 7 10	1 2 6 7 9 10	1 2 3 5 6 7
IV	2 3 4 5 6 7	1 2 3 4 5 6	1 2 3 4 5 6	2 5 6 7 8 10

Table 7: Location optimization of VEDs for 10-storey building.

Site	Modes 1 and 2	Mode 3	Modes 4 and 5	Mode 6
I	2 6 7 8 9 10	2 6 7 8 9 10	5 6 7 8 9 10	2 6 7 8 9 10
II	1 2 5 6 7 8	2 5 6 7 8 10	2 6 7 8 9 10	2 6 7 8 9 10
III	2 4 5 6 7 10	2 4 5 6 7 10	2 6 7 8 9 10	2 5 6 7 8 10
IV	2 3 4 5 6 7	2 4 5 6 7 8	2 5 6 7 8 10	2 5 6 7 8 10

4.3. Combination of Coefficients in Optimal Function

In order to confirm the value of weight numbers α , β , and γ preliminarily, the calculation of coefficient values is done. When α values are taken from 0.8~1, 0.6~0.8, and 0.3~0.6, the optimal results are almost the same. Consequently, six kinds of combination modes are proposed considering α as the main factors shown in Table 4.

4.4. Optimal Results

Utilizing the above combination modes of coefficients in the objective function, the location optimizations of two types of dampers for three structures at four types of sites are done.

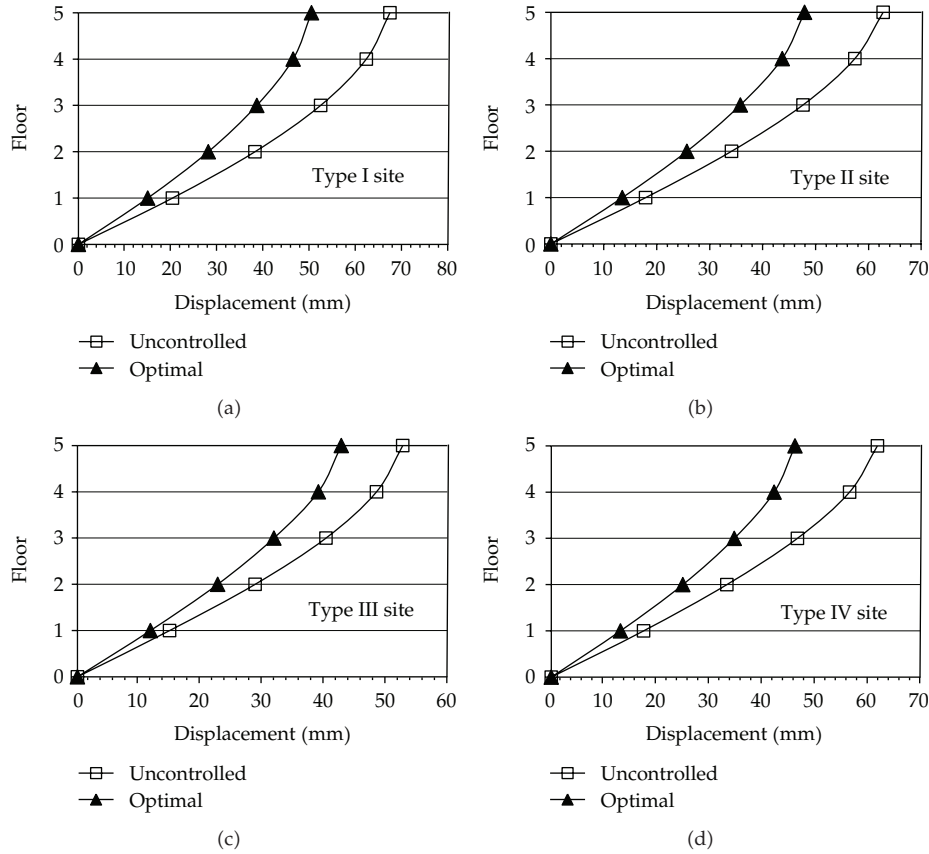


Figure 4: Envelope diagrams of maximal displacement for 5-storey structure with VEDs.

4.4.1. 5-Storey Building

The optimal results of VEDs are all the same for different sites and different combination modes. The dampers are positioned with one in each storey from the first to the third floor. It has no influence on the optimal solution for the low building whether the acceleration factor is taken into account or not as the safety factor is considered. As the force-deformation responses are dependent on the relative velocity and acceleration between each end of these types of devices, the acceleration factor has been considered when the dampers are placed on the structure.

According to the optimal results of MDs shown in Table 5, optimal locations are the same for modes 1, 2, and 3 and same for modes 4, 5, and 6 on sites I and III. For the sites IV, optimal results of modes 1 and 2 are the same and modes 3, 4, and 6 are the same also. The optimal locations are uniform on site II for six combination mode.

4.4.2. 10-Storey Building

The optimal locations of two types of dampers are shown in Tables 6 and 7. The results indicate that optimal solutions are the same for the combination modes 1 and 2. Meanwhile,

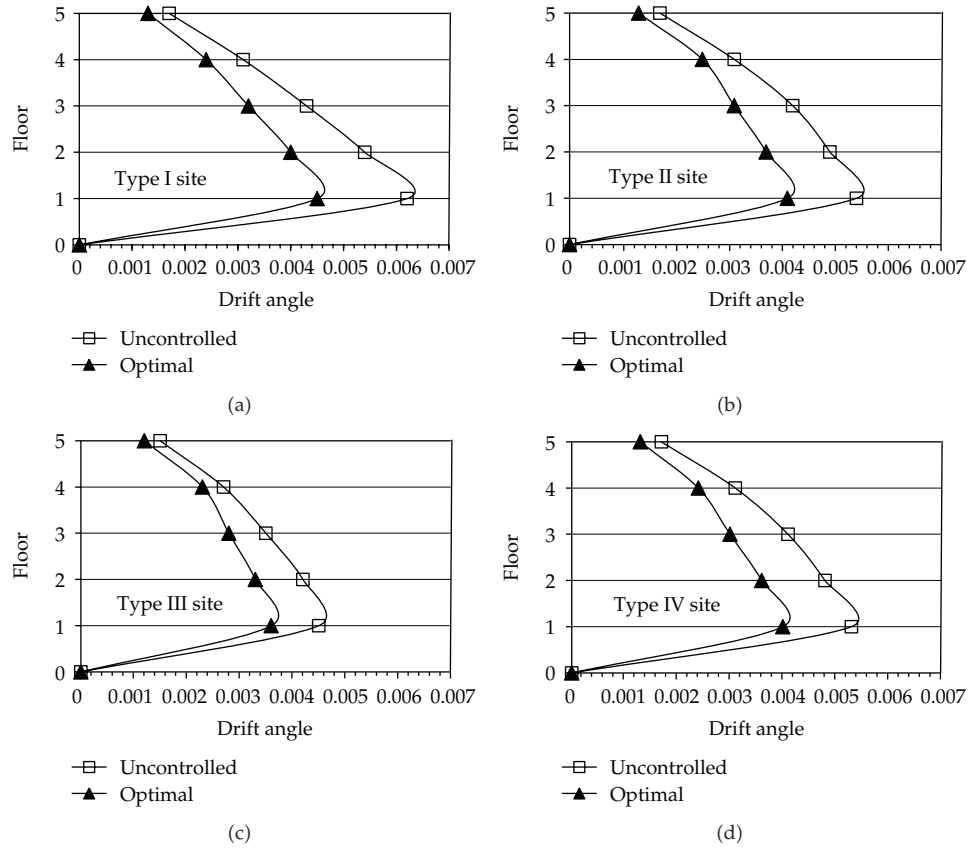


Figure 5: Envelope diagrams of maximal drift angle for 5-storey structure with VEDs.

when the modes 4 and 5 are adopted respectively, the optimal results for dampers are the same. For the site I, the optimal locations of VEDs are uniform for the modes 1, 2, 3, and 6 with dampers mainly located on top part of the building. When the modes 4 and 5 are adopted, the VEDs are placed on average at the top six floors. The MDs are mainly located in the middle and top of the building on the site I. For the sites II and III, the VEDs are positioned in the middle and top part, while the MDs are located on the bottom and middle of the building. For the site IV, the optimal locations of two types of dampers are uniform for the modes 1 and 2. The optimal results of VEDs using modes 4, 5, and 6 are the same as results of MDs using mode 6. These results indicate that the appropriate increase in acceleration weight has less effect on the optimal results of velocity-based dampers.

4.4.3. 16-Storey Building

The optimal locations of two types of dampers on the four soil sites are shown in Tables 8 and 9. The optimal results indicate that optimal locations of VEDs are the same by using the combination modes 1 and 2 for each site condition. For the site I, dampers are mainly located in the middle part of the structure. Considering the sites II and III, dampers are placed on the bottom and middle part. Dampers are positioned in the middle and top part of the building

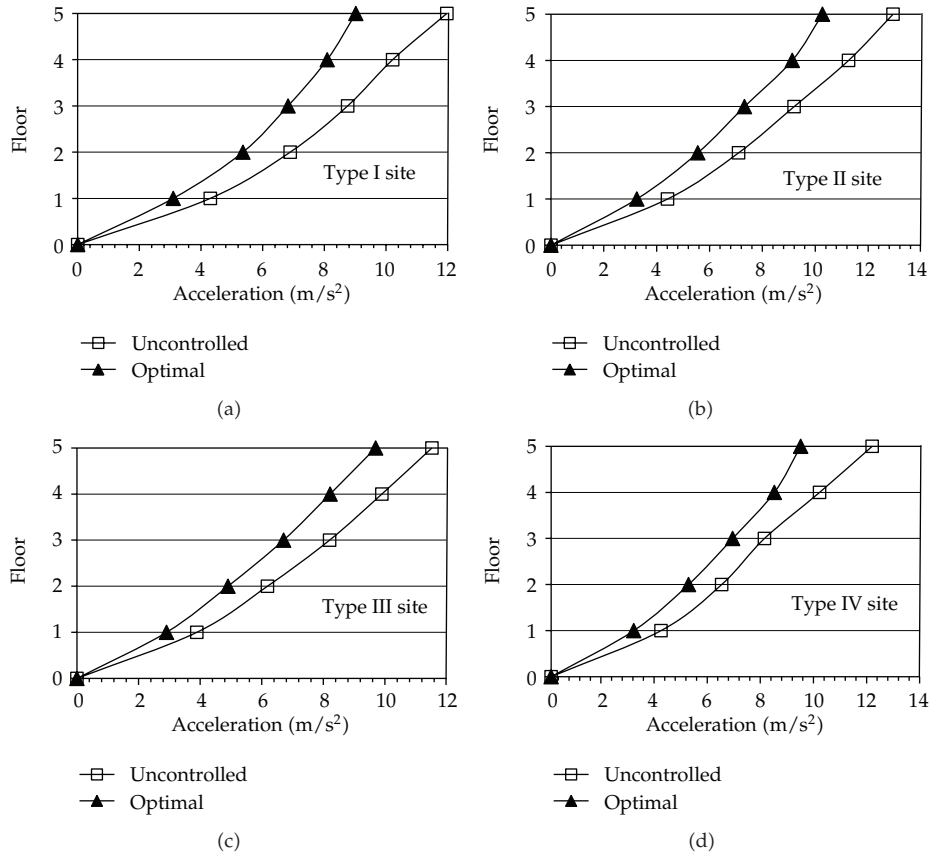


Figure 6: Envelope diagrams of maximal acceleration for 5-storey structure with VEDs.

on the site IV. These results mean that the acceleration factor has an impact upon the optimal locations for high buildings. As far as the MDs are taken, optimal results are the same for the modes 1 and 2 and same for the modes 4 and 5 only on the site I.

When the dampers are located in structures according to the optimal results with six modes of coefficients combination, the step-by-step time history analysis is utilized to obtain the responses of structures with two types of dampers on the four types of sites, respectively. As the space of the paper is limited, some typical envelope diagrams of three buildings on the different sites are displayed from Figures 4, 5, 6, 7, 8, 9, 10, and 11.

4.5. Comparisons between Different Combination Modes

4.5.1. 5-Storey Building

No comparisons are done because the optimal results of VEDs are all the same for 6 combination modes. In order to compare six modes with one another to decide which one can generate better control effectiveness of structures with optimal locations of MDs, two estimating dimensionless indices are calculated according to formula (3.2) as shown in Table 10.

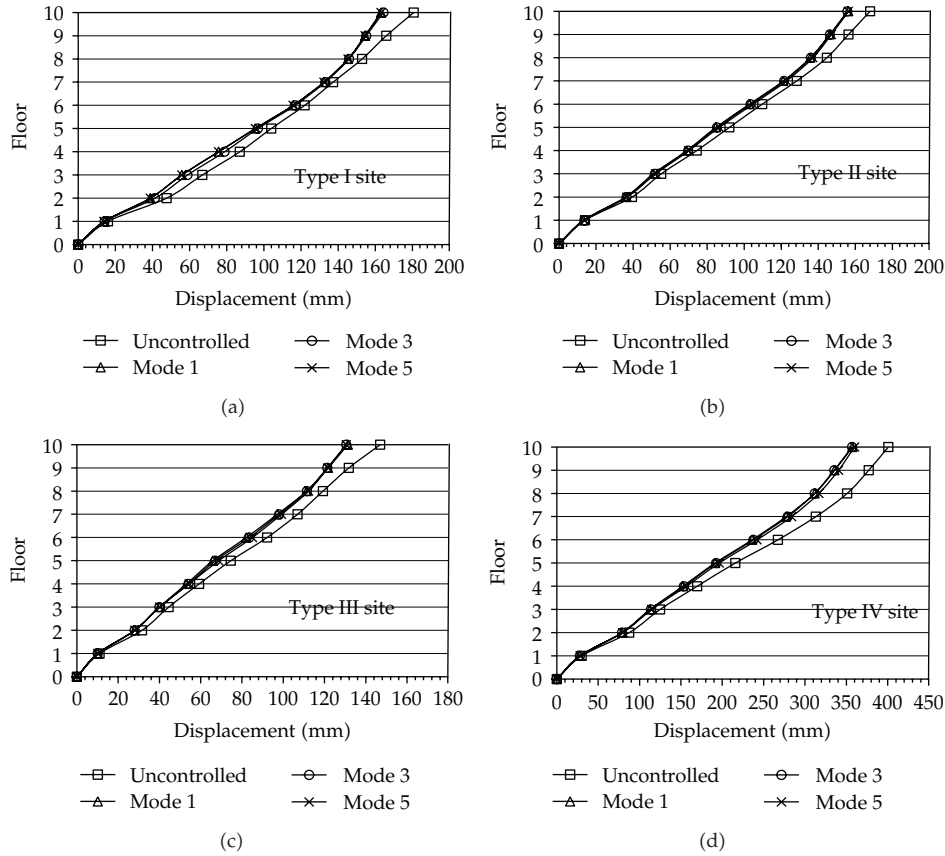


Figure 7: Envelope diagrams of maximal displacement for 10-storey structure with VEDs.

Table 8: Location optimization of VEDs for 16-storey building.

Site	Modes 1 and 2	Modes 3 and 6	Modes 4 and 5
I	2 3 5 6 7 8 10 11 12	1 2 5 6 7 8 10 11 12/ 1 2 3 5 6 7 8 10 11	1 2 3 5 6 7 8 12 14/ 1 2 3 5 6 8 11 12 14
II	1 2 3 4 5 6 7 8 11	1 2 3 4 5 6 7 8 10/ 1 2 3 4 5 6 7 8 9	5 6 7 8 9 10 14 15 16
III	2 3 4 5 6 7 8 10 11	1 2 4 5 6 7 8 10 11/ 1 2 3 5 6 7 8 10 11	1 3 4 5 6 7 10 11 13/ 1 2 4 6 7 10 11 12 13
IV	2 5 6 7 8 9 10 11 13	1 2 3 4 5 10 11 14 16/ 2 5 6 7 8 9 10 11 12	1 2 10 11 12 13 14 15 16/ 1 9 10 11 12 13 14 15 16

As far as drift angle is concerned, the control effect is better for modes 1, 2, and 3 on sites I, II, and III. For the site IV, mode 3 can obtain the best optimal results. When the acceleration is taken into consideration, the values of J_2 are same on site II. For other three sites, the acceleration control is better when modes 5 and 6 are adopted. The acceleration responses of the whole structure may be enlarged when using MDs on sites III and IV.

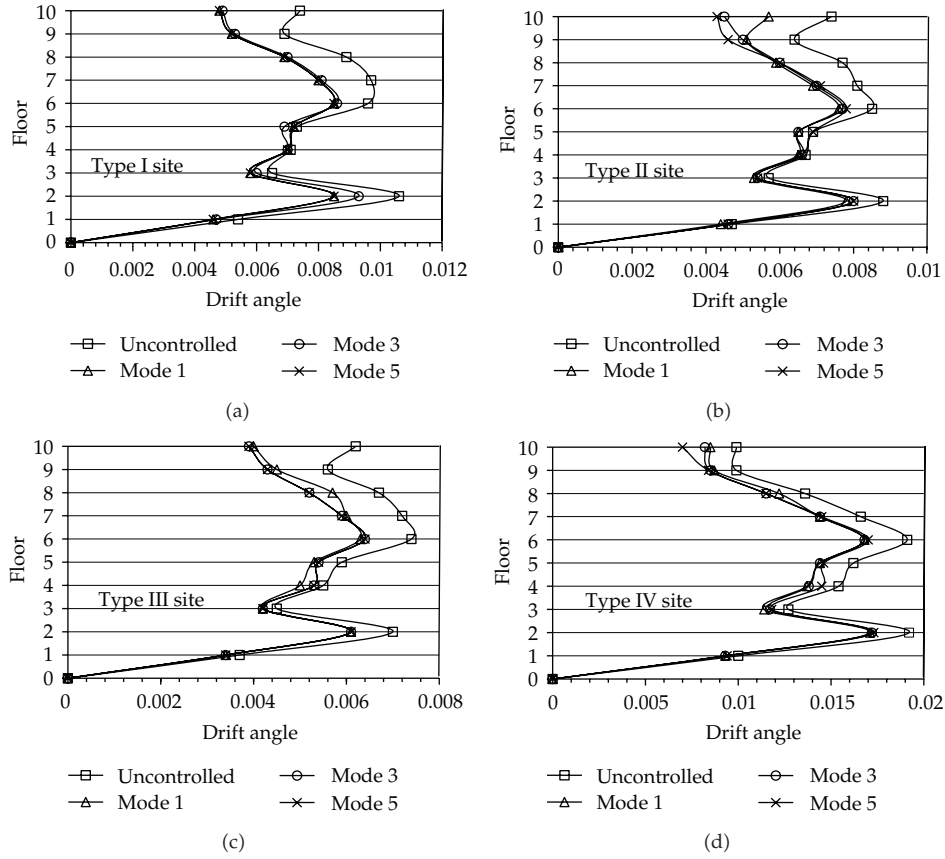


Figure 8: Envelope diagrams of maximal drift angle for 10-storey structure with VEDs.

Table 9: Location optimization of MDs for 16-storey building.

Site	Modes 1 and 2	Modes 3 and 6	Modes 4 and 5
I	1 2 3 5 6 7 9 10 11	2 4 6 7 8 9 10 11 16/ 1 3 6 7 8 9 10 11 16	2 3 4 6 7 8 9 10 16
II	1 5 6 7 8 9 10 11 12/ 1 5 6 7 8 9 10 14 15	1 4 5 6 7 8 9 10 14/ 3 4 5 6 7 8 9 10 15	6 8 9 10 11 12 13 14 16/ 1 2 6 7 8 9 13 14 15
III	1 2 3 4 5 8 9 10 11/ 3 4 5 6 8 9 10 12 15	1 2 5 6 7 8 9 10 11/ 2 3 5 6 7 8 9 10 11	2 3 6 7 8 10 11 14 15/ 1 2 3 6 8 9 11 15 16
IV	1 2 3 4 5 6 7 10 14/ 1 2 3 4 5 6 7 8 10	1 2 3 4 5 6 10 15 16/ 1 2 3 4 6 13 14 15 16	2 3 4 5 6 7 10 11 15/ 3 4 5 7 9 10 12 13 14

Table 10: Evaluation indices of objective function for 5-storey structure with MD.

Index site	J_1			J_2		
	Mode 1	Mode 3	Modes 5 and 6	Mode 1	Mode 3	Modes 5 and 6
I	0.4774	0.4774	0.4978	0.7898	0.7898	0.7666
II	0.4814	0.4814	0.4814	0.7664	0.7664	0.7664
III	0.4945	0.4945	0.5101	1.0782	1.0782	0.9577
IV	0.4790	0.4410	0.4871	1.0449	1.0580	1.0494

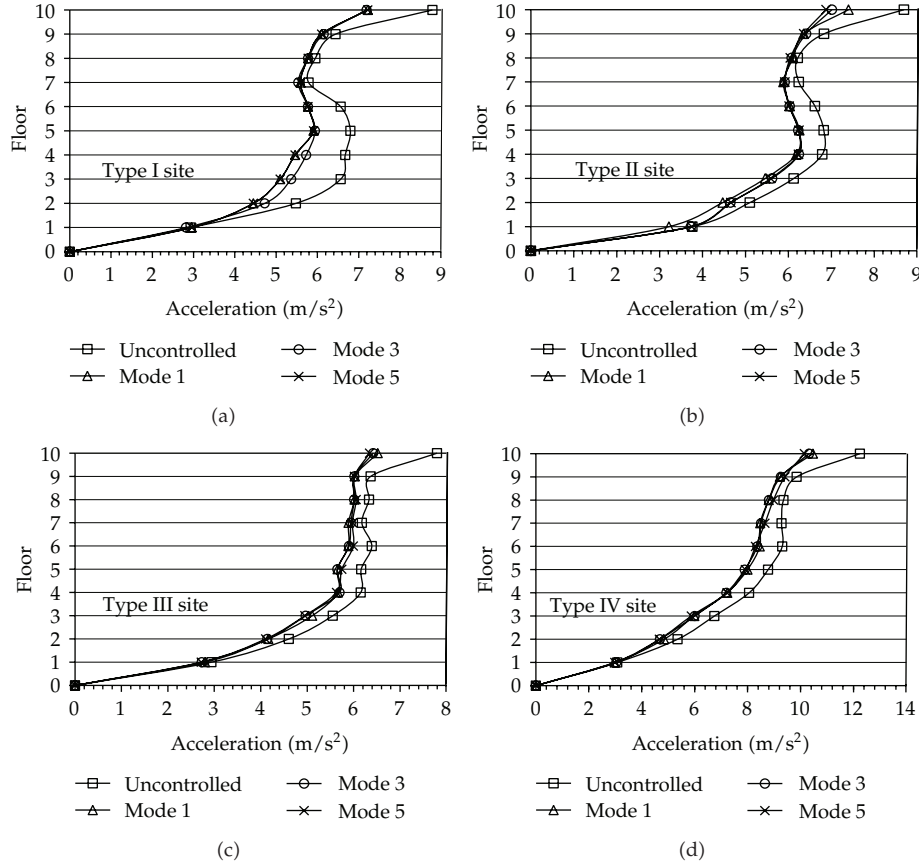


Figure 9: Envelope diagrams of maximal acceleration for 10-storey structure with VEDs.

4.5.2. 10-Storey Building

Two estimating indices are calculated as shown in Table 11 for the structure with MDs. The results in Table 11 indicate that the mode 1 is best for the drift angle control on the site I and the value of mode 3 is better than other modes except for the mode 1. As far as acceleration is taken into account, it is obvious that the mode 6 is the best. For the site II, the control effects of drift angle are the best when using modes 3 and 6 while mode 1 is the best for acceleration control. For the site III, mode 3 can obtain the smallest J_1 value. Meanwhile, the acceleration control effects are better for modes 5 and 3. For the site IV, the results are the same when using modes 3 and 5 which can obtain the best control effects of drift angle and acceleration. According to the above analysis, the optimal objective function should use mode 1 on site I, mode 3 on sites II and III and mode 5 on site IV for intermediate period structure with displacement-based dampers.

Two evaluation indices are calculated as shown in Table 12 for the structure with VEDs. The J_1 and J_2 values of modes 1, 2, 3, and 6 are the same on site I. The results shown in Table 12 indicate that mode 3 is the best one for drift-angle control on sites I, II, and III while modes 5 and 6 are better on site IV. When the acceleration is taken into consideration, the numerical difference of J_2 is not obvious. Considering two indices and simple form of

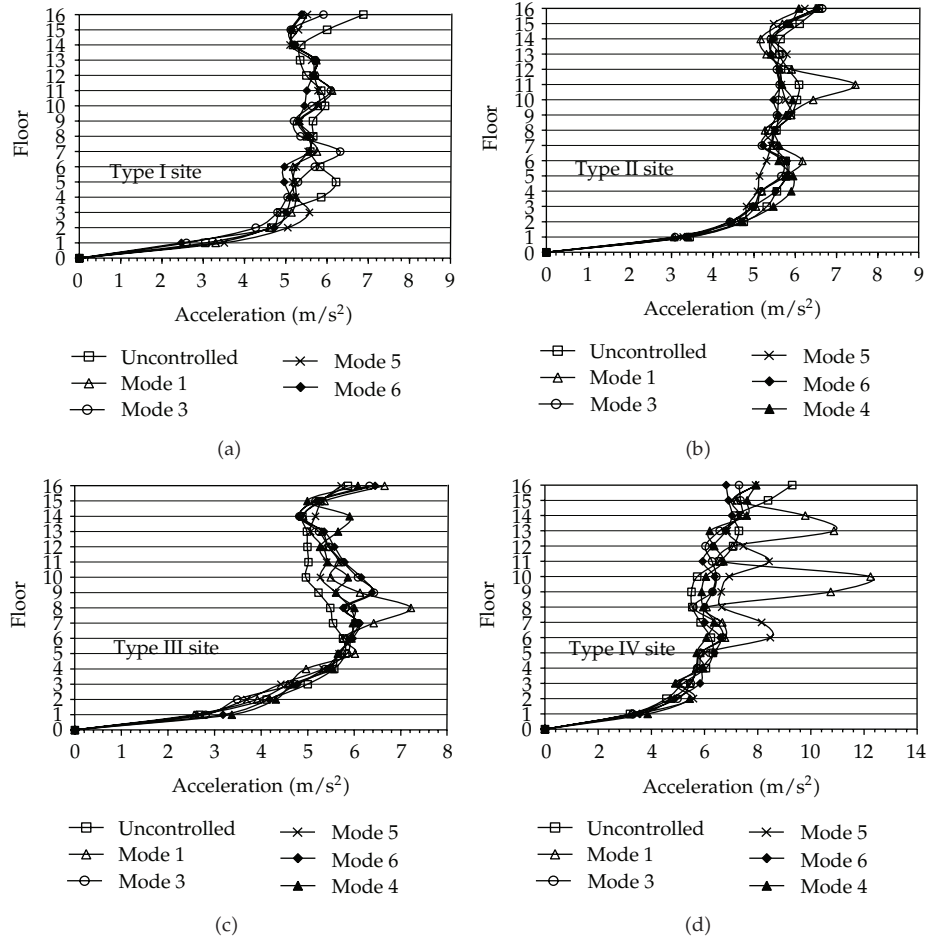


Figure 10: Envelope diagrams of maximal acceleration for 16-storey structure with MDs.

objective functions, the optimal objective function should use mode 1 on sites I and II, mode 5 on sites III and IV for intermediate period structure with velocity-based dampers.

4.5.3. 16-Storey Building

The indices J_1 and J_2 are calculated for the 16-storey building with MDs shown in Table 13. The results in Table 13 show that the mode 3 is the best for drift angle control on the site I. The mode 6 is the best for acceleration control, while modes 1, 2, and 3 are better than other modes except for mode 6 on the site I. For the site II, the control effects of drift angle are the best when using mode 1, while modes 2 and 5 are better for acceleration control. For the sites III and IV, mode 3 can obtain the smallest J_1 values, while the acceleration may be enlarged for the structure with the MDs. According to the above analysis, the optimal objective function should use the mode 3 for a long-period structure with the displacement-based dampers which can obtain better control effectiveness for the drift angle.

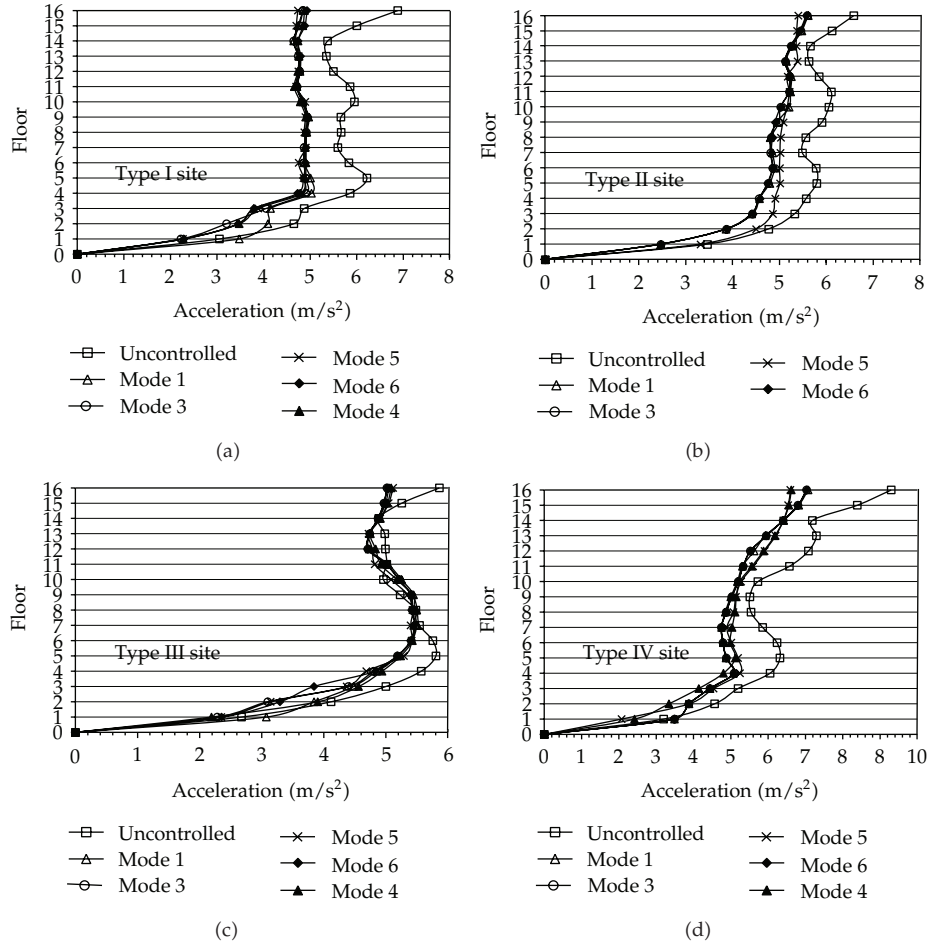


Figure 11: Envelope diagrams of maximal acceleration for 16-storey structure with VEDs.

Table 11: Evaluation indices of objective function for 10-storey structure with MD.

Index site	J_1				J_2			
	Mode 1	Mode 3	Mode 5	Mode 6	Mode 1	Mode 3	Mode 5	Mode 6
I	0.6596	0.6759	0.7028	0.6902	0.9448	0.9333	0.9268	0.8771
II	0.7984	0.7806	0.7928	0.7806	0.9169	0.9287	0.9454	0.9287
III	0.6880	0.6668	0.6709	0.6760	0.9336	0.8905	0.8794	0.9233
IV	0.6469	0.6419	0.6419	0.6454	0.8991	0.8080	0.8080	0.9077

Table 12: Evaluation indices of objective function for 10-storey structure with VED.

Index site	J_1				J_2			
	Mode 1	Mode 3	Mode 5	Mode 6	Mode 1	Mode 3	Mode 5	Mode 6
I	0.7164	0.7164	0.7392	0.7164	0.7927	0.7927	0.8048	0.7927
II	0.7696	0.7694	0.7724	0.7724	0.8242	0.8550	0.8506	0.8506
III	0.7246	0.7246	0.7313	0.7248	0.8519	0.8519	0.8439	0.8418
IV	0.7886	0.7774	0.7748	0.7748	0.8334	0.8269	0.8262	0.8262

Table 13: Evaluation indices of objective function for 16-storey structure with MD.

Index site	J_1						J_2					
	M 1	M 2	M 3	M 4	M 5	M 6	M 1	M 2	M 3	M 4	M 5	M 6
I	0.538	0.538	0.503	0.544	0.544	0.514	0.911	0.911	0.922	0.963	0.963	0.870
II	0.644	0.650	0.647	0.676	0.681	0.648	0.988	0.909	0.920	0.973	0.911	0.928
III	0.637	0.619	0.593	0.607	0.599	0.612	1.133	1.169	1.111	1.154	1.034	1.161
IV	0.525	0.535	0.518	0.546	0.623	0.556	1.535	1.143	0.970	1.021	1.230	1.011

Table 14: Evaluation indices of objective function for 16-storey structure with VED.

Index site	J_1						J_2					
	M 1	M 2	M 3	M 4	M 5	M 6	M 1	M 2	M 3	M 4	M 5	M 6
I	0.4645	0.4645	0.4568	0.4690	0.4680	0.4664	0.7435	0.7435	0.6696	0.6704	0.6671	0.6754
II	0.5606	0.5606	0.5480	0.6063	0.6063	0.5522	0.7287	0.7287	0.7228	0.8009	0.8009	0.7225
III	0.5172	0.5172	0.5130	0.5267	0.5264	0.5189	0.9421	0.9421	0.8773	0.9071	0.8748	0.8724
IV	0.6165	0.6165	0.5950	0.6192	0.6306	0.6185	0.7235	0.7235	0.6665	0.6880	0.7050	0.7236

Two indices are calculated for the 16-storey building with VEDs shown in Table 14. The results reveal that the mode 3 is the best for drift-angle control on all of the four sites. As far as the acceleration control is concerned, mode 5 is best on site I and mode 3 is better than other modes on site I. The values of modes 6 and 3 are better on sites II and III. For the site IV, mode 3 can obtain the smallest J_2 value. When control of deformation and acceleration are both taken into account, the mode 3 is the most ideal one for long-period structure with velocity-based dampers.

5. Conclusions

The optimal objective functions are different for two types of dampers placed on different buildings on different types of sites.

It has no influence on the optimal locations of VEDs for low buildings whether coziness is taken into account or not as the safety factor is considered on four types of sites. As far as displacement-based dampers are taken, the influence of acceleration factor is very small, but acceleration may be enlarged on the sites III and IV. The objective function of velocity-based dampers can be predigested as $\min Z = \theta_{\max}/\theta_{0,\max}$ regardless of the type of site, which has easier form to compute. According to the evaluation indices, the objective function of displacement-based dampers can be taken as $\min Z = \theta_{\max}/\theta_{0,\max}$ on sites I, II, and III while adopting the form $\min Z = 0.5(\theta_{\max}/\theta_{0,\max}) + 0.3(a_{\max}/a_{0,\max}) + 0.2(u_{\max}/u_{0,\max})$ on site IV.

For intermediate period structures, it is suggested to use $\min Z = \theta_{\max}/\theta_{0,\max}$ as the objective function on site I, $\min Z = 0.5(\theta_{\max}/\theta_{0,\max}) + 0.3(a_{\max}/a_{0,\max}) + 0.2(u_{\max}/u_{0,\max})$ on sites II, III and $\min Z = a_{\max}/a_{0,\max}$ on site IV for displacement-based dampers. As far as velocity-based dampers are taken, the objective function should be taken as $\min Z = \theta_{\max}/\theta_{0,\max}$ on sites I, II and $\min Z = a_{\max}/a_{0,\max}$ on sites III and IV.

For long-period structures, both safety and amenity should be taken into consideration to obtain better acceleration control. It is suggested to use $\min Z = 0.5(\theta_{\max}/\theta_{0,\max}) + 0.3(a_{\max}/a_{0,\max}) + 0.2(u_{\max}/u_{0,\max})$ as the objective function of two type dampers regardless of types of sites.

Acknowledgments

This research work was jointly supported by the Science Fund for Creative Research Groups of the NSFC (Grant no. 51121005), the National Science Foundation for Distinguished Young Scholars of China (Grant no. 51108064), and the Fundamental Research Funds for the Central Universities. The authors would like to thank the reviewers for their careful reading of the paper and their constructive criticism.

References

- [1] R. T. Haftka and H. M. Adelman, "Selection of actuator locations for static shape control of large space structures by heuristic integer programming," *Computers and Structures*, vol. 20, no. 1–3, pp. 575–582, 1985.
- [2] S. A. Ashour and R. D. Hanson, "Elastic seismic response of buildings with supplemental damping," Tech. Rep. UMCE 87-01, Department of Civil Engineering, University of Michigan, Ann Arbor, Mich, USA, 1987.
- [3] R. H. Zhang and T. T. Soong, "Seismic design of viscoelastic dampers for structural applications," *Journal of Structural Engineering, ASCE*, vol. 118, no. 5, pp. 1375–1392, 1992.
- [4] M. Gürgöze and P. C. Müller, "Optimal positioning of dampers in multi-body systems," *Journal of Sound and Vibration*, vol. 158, no. 3, pp. 517–530, 1992.
- [5] H. G. Natke and T. T. Soong, "Topological structural optimization under dynamic loads," in *Optimization of Structural systems and Applications*, S. Hernandez and C. A. Brebbia, Eds., Computational Mechanics Publications, Southampton, UK, 1993.
- [6] M. H. Milman and C. C. Chu, "Optimization methods for passive damper replacement and tuning," *Journal of Guidance, Control, and Dynamics*, vol. 17, no. 4, pp. 848–856, 1994.
- [7] I. Takewaki, "Optimal damper placement for minimum transfer functions," *Earthquake Engineering and Structural Dynamics*, vol. 26, no. 11, pp. 1113–1124, 1997.
- [8] I. Takewaki, S. Yoshitomi, K. Uetani, and M. Tsuji, "Non-monotonic optimal damper placement via steepest direction search," *Earthquake Engineering and Structural Dynamics*, vol. 28, pp. 655–670, 1999.
- [9] Y. Zhou, Z. D. Xu, and X. S. Deng, "Optimal installation of the dampers in the viscoelastic structures," *World Information of Earthquake Engineering*, vol. 14, no. 3, pp. 15–20, 1998.
- [10] Q. Zhang, W. J. Lou, and Y. Chen, "The objective function and realization of optimal placement for viscoelastic dampers," *Industrial Construction*, vol. 33, no. 6, pp. 10–13, 2003.
- [11] P. Lu, S. Chen, and Y. Zheng, "Artificial intelligence in civil engineering," *Mathematical Problems in Engineering*, vol. 2013, Article ID 145974, 20 pages, 2013.
- [12] S. Y. Chen and Y. F. Li, "Automatic sensor placement for model-based robot vision," *IEEE Transactions on Systems, Man, and Cybernetics B*, vol. 34, no. 1, pp. 393–408, 2004.
- [13] C. Cattani, S. Chen, and G. Aldashev, "Information and modeling in complexity," *Mathematical Problems in Engineering*, vol. 2012, Article ID 868413, 4 pages, 2012.
- [14] M. P. Singh and L. M. Moreschi, "Optimal placement of dampers for passive response control," *Earthquake Engineering and Structural Dynamics*, vol. 31, no. 4, pp. 955–976, 2002.
- [15] L. M. Moreschi and M. P. Singh, "Design of yielding metallic and friction dampers for optimal seismic performance," *Earthquake Engineering and Structural Dynamics*, vol. 32, no. 8, pp. 1291–1311, 2003.
- [16] W. Zheng, S. Yan, and J. H. Mo, "Optimum installation of the MR dampers for the high-rise structures by genetic algorithm," *Journal of Shenyang Jianzhu University (Natural Science)*, vol. 21, no. 6, pp. 606–611, 2005.
- [17] W. M. Bei and H. N. Li, "Study on the optimal placement of magnetorheological dampers in structural control," *Earthquake Resistant Engineering and Retrofitting*, vol. 28, no. 3, pp. 73–78, 2006.
- [18] K. C. Chang, M. L. Lai, T. T. Soong, D. S. Hao, and Y. C. Yeh, "Seismic behavior and design guidelines for steel frame structures with added viscoelastic damper," NCEER 93-0009, National Center for Earthquake Engineering Research, Buffalo, NY, USA, 1993.
- [19] Z. Ming and S. Shudong, *The Principle and Application of Genetic Algorithms*, National Defense Industry Press, Beijing, China, 1999.

- [20] G. Giardini and T. Kalmár-Nagy, "Genetic algorithm for combinatorial path planning: the subtour problem," *Mathematical Problems in Engineering*, vol. 2011, Article ID 483643, 31 pages, 2011.
- [21] Z. D. Xu, Y. Zhou, and H. T. Zhao, "Optimum design method of the viscoelastic structure," *Journal of Xi'an University of Architecture and Technology (Natural Science Edition)*, vol. 31, no. 3, pp. 246–248, 1999.
- [22] S. Chen, Y. Wang, and C. Cattani, "Key issues in modeling of complex 3D structures from video sequences," *Mathematical Problems in Engineering*, vol. 2012, Article ID 856523, 17 pages, 2012.
- [23] S. Chen, W. Huang, C. Cattani, and G. Altieri, "Traffic dynamics on complex networks: a survey," *Mathematical Problems in Engineering*, vol. 2012, Article ID 732698, 23 pages, 2012.
- [24] S. C. Lim, C. H. Eab, K. H. Mak, M. Li, and S. Y. Chen, "Solving linear coupled fractional differential equations by direct operational method and some applications," *Mathematical Problems in Engineering*, vol. 2012, Article ID 653939, 28 pages, 2012.
- [25] S. Y. Chen, J. Zhang, Q. Guan, and S. Liu, "Detection and amendment of shape distortions based on moment invariants for active shape models," *IET Image Processing*, vol. 5, no. 3, pp. 273–285, 2011.
- [26] L. Xie and C. Zhai, "Study on the severest real ground motion for seismic design and analysis," *Acta Seismologica Sinica*, vol. 25, no. 3, pp. 250–261, 2003.

Research Article

Sludge Bulking Prediction Using Principle Component Regression and Artificial Neural Network

Inchio Lou¹ and Yuchao Zhao²

¹ Department of Civil and Environmental Engineering, Faculty of Science and Technology,
University of Macau, Avenue Padre Tomás Pereira, Taipa 999078, Macau

² State Key Joint Laboratory of Environmental Simulation and Pollution Control, School of Environment,
Beijing Normal University, Beijing 100875, China

Correspondence should be addressed to Inchio Lou, iclou@umac.mo
and Yuchao Zhao, zhaoy@bnu.edu.cn

Received 5 August 2012; Revised 22 October 2012; Accepted 25 October 2012

Academic Editor: Siamak Talatahari

Copyright © 2012 I. Lou and Y. Zhao. This is an open access article distributed under the Creative Commons Attribution License, which permits unrestricted use, distribution, and reproduction in any medium, provided the original work is properly cited.

Sludge bulking is the most common solids settling problem in wastewater treatment plants, which is caused by the excessive growth of filamentous bacteria extending outside the flocs, resulting in decreasing the wastewater treatment efficiency and deteriorating the water quality in the effluent. Previous studies using molecular techniques have been widely used from the microbiological aspects, while the mechanisms have not yet been completely understood to form the deterministic cause-effect relationship. In this study, system identification techniques based on the analysis of the inputs and outputs of the activated sludge system are applied to the data-driven modeling. Principle component regression (PCR) and artificial neural network (ANN) were identified using the data from Chongqing wastewater treatment plant (CQWWTP), including temperature, pH, biochemical oxygen demand (BOD), chemical oxygen demand (COD), suspended solids (SSs), ammonia (NH_4^+), total nitrogen (TN), total phosphorus (TP), and mixed liquor suspended solids (MLSSs). The models were subsequently used to predict the sludge volume index (SVI), the indicator of the bulking occurrence. Comparison of the results obtained by both models is also presented. The results showed that ANN has better prediction power ($R^2 = 0.9$) than PCR ($R^2 = 0.7$) and thus provides a useful guide for practical sludge bulking control.

1. Introduction

Sludge bulking is the most common solid separation problem in activated sludge problem, which is caused by the excessive growth of filamentous bacteria extending outside the flocs, thus interfering with the settling of activated sludge. It has been reported that over 50%

of the wastewater treatments in US experience bulking [1]. Bulking leads to high level of total suspended solids in effluent that exceeds the discharge permit limitation and subsequently loses activated sludge in the aeration basin, resulting in the deterioration of wastewater treatment process [1]. Sludge setting and compaction are often quantified using sludge volume index (SVI). When SVI reaches 150 mL/g, bulking can be considered to happen.

Various theories and factors, such as kinetic selection theory [2–4], filamentous backbone theory [5], substrate diffusion limitation [6], storage phenomena [7, 8], and the difference in the decay rates between filaments and floc formers [9], have been proposed and extensively studied for explaining the competition between filaments and floc formers. However, no single or combined proposed mechanisms can explain completely the sludge bulking problem; for example, the uncertainty about the factors triggering the filaments, growth is still unclear. The current efforts to study sludge bulking problem rely mostly on experimental observation of filamentous bacteria population in the system, while some experimental results could lead to contradictory conclusions. Thus it is difficult to formulate deterministic mathematical models for predicting the filaments population, though some existing models were developed [9, 10].

Developing a model that could predict in real time with reasonable accuracy the potential for bulking is of great practical importance, as it can be used to improve the treatment plant efficiency and cost saving [11]. The complexity of the problem can be overcome by applying data-driven model for the whole system, rather than the breaking down of the system into small components described individually, in which only the inputs and outputs of the system are taken into consideration. One major advantage of the data-driven models over mechanistic models is that they require minimal information of the intrinsic processes of the system.

In PCR, PCA is first used to convert a set of observations of possibly correlated variables by orthogonal transformation into a set of values of uncorrelated variables called PCs, thus reducing the complexity of multidimensional system by maximization of component loadings variance and elimination of invalid components. PCA has been used alone or in combination with other methods, such as MLR, to model aquatic environmental and ecological processes including algal blooms problem in freshwater reservoirs [12–14]. From these studies, only the PCs with eigenvalues greater than 1 were selected for MLR, which can explain the high percentage of total variation of the environmental variables in PCA. It is followed by the MLR to check if the chlorophyll-a, cyanobacteria abundance, or microcystin concentrations could be explained by environmental variables and to be used for further prediction. On the other hand, ANN is regarded as an efficient tool for modeling and forecasting due to its wide range of applicability and capability to treat complicated nonlinear problems. After training, ANN can be used to predict the output with the new independent input parameter; thus, it is appropriate for modeling the water parameters data [15]. It was reported that ANN provided better results than PCR model, particularly in handling collinearity and nonlinear structures of forecast problems [12, 16–18].

In the aspect of wastewater treatment processes, the application of PCR and ANN as popular data-driven approaches has been widely researched in the literature. Belanche et al. [19] used ANN as error predictor to improve the accuracy of an existing mechanistic model of activated sludge process by coupling both techniques. Five key variables including effluent SS, COD, ammonia, mixed liquor oxygen, and volatile SS were simulated and predicted. Two steps were involved: optimization of model parameters was first investigated using

the downhill simplex method to minimize the sum of the square errors between observation and prediction; then ANN models were used to predict the remaining errors of the optimized mechanistic model. This study used over 10 days' 6–9 h measurements from the activated sludge treatment plant located at Norwich, England. Though the study is based on the real data, the models were not used for predicting bulking phenomena.

Côté et al. [20] developed and applied ANN models for the prediction of future bulking episodes. The simple prediction models based on the online data (flow rates), analytical data (COD, BOD), and qualitative data (presence of foam, filamentous bacteria, microfauna, and appearance) were developed for the effluent TSS that is an indicator of plant performance. The data came from the WWTP from Catalonia, Spain, in 609 consecutive days. Through the combined use of the rough set theory and ANN, the reasonable prediction models are found to show the different importance of variables and provide insight into the processes' dynamics. However, compared to SVI, TSS was not a good indicator for bulking, though during bulking episodes, the effluent TSS undoubtedly increases. Besides, the parameters sets used for selecting the significant variables are incomplete. For example, the important variables including temperature, pH, TN, and TP are not included in the selection, resulting in losing the key information for explaining the bulking phenomena.

A recent study [21] utilized a self-organizing radial basis function (SORBF) neural network method to predict the evolution of SVI. The hidden nodes in the SORBF neural network can be grown or pruned based on the node activity and mutuality to achieve the appropriate network complexity and overall computational efficiency. The performance of this method was verified in a real WWTP. This method enhanced the capacity of the RBF model to adapt to nonlinear dynamic system and thus yielded more accurate predictions than the other method. However, in this study only limited input parameters, influent flow rate, DO, pH, BOD, COD, and TN were included, which are not enough to explain sludge bulking mechanisms.

Considering the drawbacks of previous studies using ANN in wastewater treatment system, the purpose of the present study is to analyze bulking problems of CQWWTP that used the A/A/O treatment process that has not been discussed before, based on more complete daily variables including temperature, pH, BOD, COD, SS, NH_4^+ , TN, TP, and MLSS for the whole year. These variables provide more complete data input to explain the bulking mechanisms, in spite of applying only the data-driven models developed in the study. The models can be used to evaluate the relative influence of the operational conditions, influents characteristics, and activated sludge concentrations on the SVI and to predict the SVI values using PCR and ANN. The comparisons of both models in this study and the prediction model developed by Han and Qiao [21] were made to select the best prediction method for wastewater treatment management. The key contributions of this paper not only focus on the mathematical modeling itself, but also take the complete main factors that affect the bulking into consideration, by integrating all of those potential mechanistic bulking causative variables into both models, though only the data-driven models were applied.

The rest of this paper was organized as follows. The study area and data source of CQWWTP were first introduced concisely, followed by modeling approaches (PCR and ANN) formulation and the performance indicators used for evaluation in Section 2. Section 3 presented and discussed the modeling results performed by PCR and ANN, respectively, and made comparisons between both methods. The conclusion was drawn finally in Section 4.

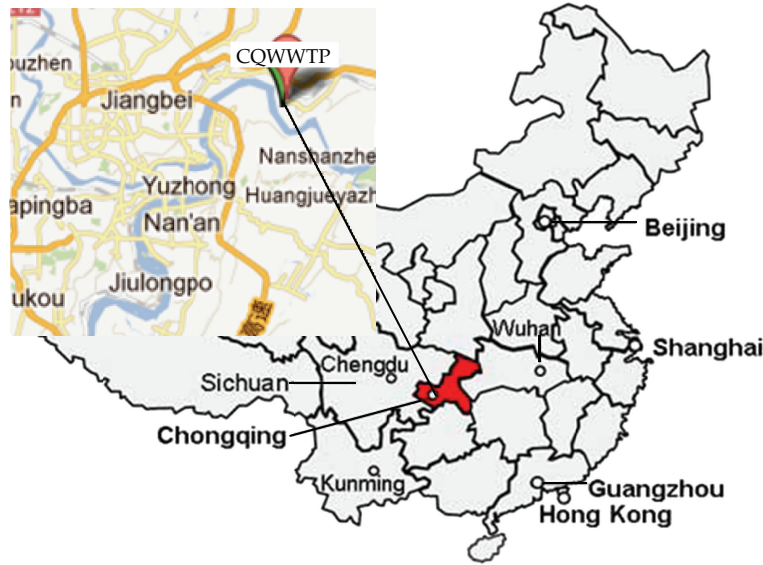


Figure 1: Location of CQWWTP.

2. Materials and Methods

2.1. Study Area

Chongqing is the biggest city in Western China. Like Beijing, Tianjin, and Shanghai, it is directly under the central government of China. The city has grown very quickly during the last 10 years, with the population of 31 millions and the area of 82,400 km². There is now a big effort to collect and treat the wastewater, due to the recent achievement of the three-gorge dam in the downstream. CQWWTP (29.601615 in latitude and 106.634133 E in longitude, Figure 1), one of biggest WWTP in Chongqing, is designed to have a capacity of an average flow rate of 300,000 m³/d and about 750,000 person equivalents (in carbon, nitrogen, and phosphorus). CQWWTP uses conventional A/A/O (anaerobic/anoxic/aerobic) treatment processes (Figure 2) that are susceptible to sludge bulking. It was reported that 36% of sludge experience bulking in the year of 2010, and the situation appeared to be worsening in the recent years, particularly in the springs.

2.2. Data Source

Sludge samples were collected daily in the reaction tank over the year of 2010. The monitored parameters included operational conditions (temperature and pH), influent characteristics (BOD, COD, SS, NH₄⁺, TN, and TP), and activated sludge concentrations (MLSS). Water samples were preserved, delivered, and analyzed using the standard methods of the American Public Health Association [22].

Figure 3 showed the changes of water parameters over the time, with the simple statistical analysis shown in Table 1. It was showed that the pH is maintained stable over the range of 7.6–8.2. The water temperatures matched the atmospheric temperatures that are low in the winter and high in the summer. The BOD and COD concentrations in

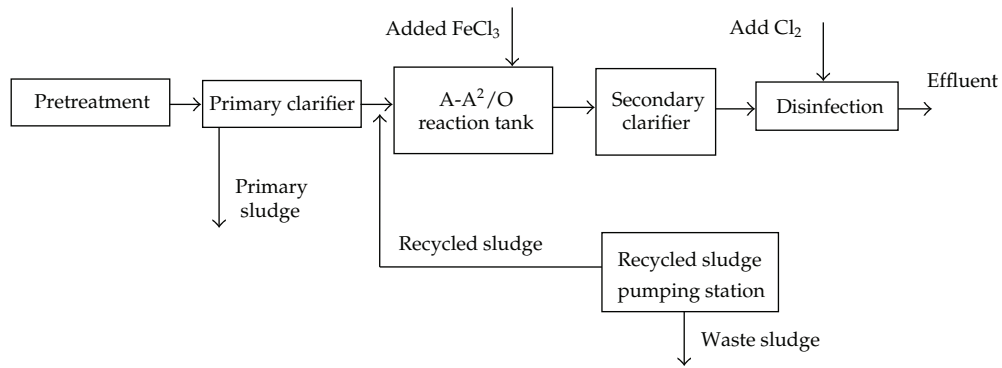


Figure 2: CQWWTP treatment processes.

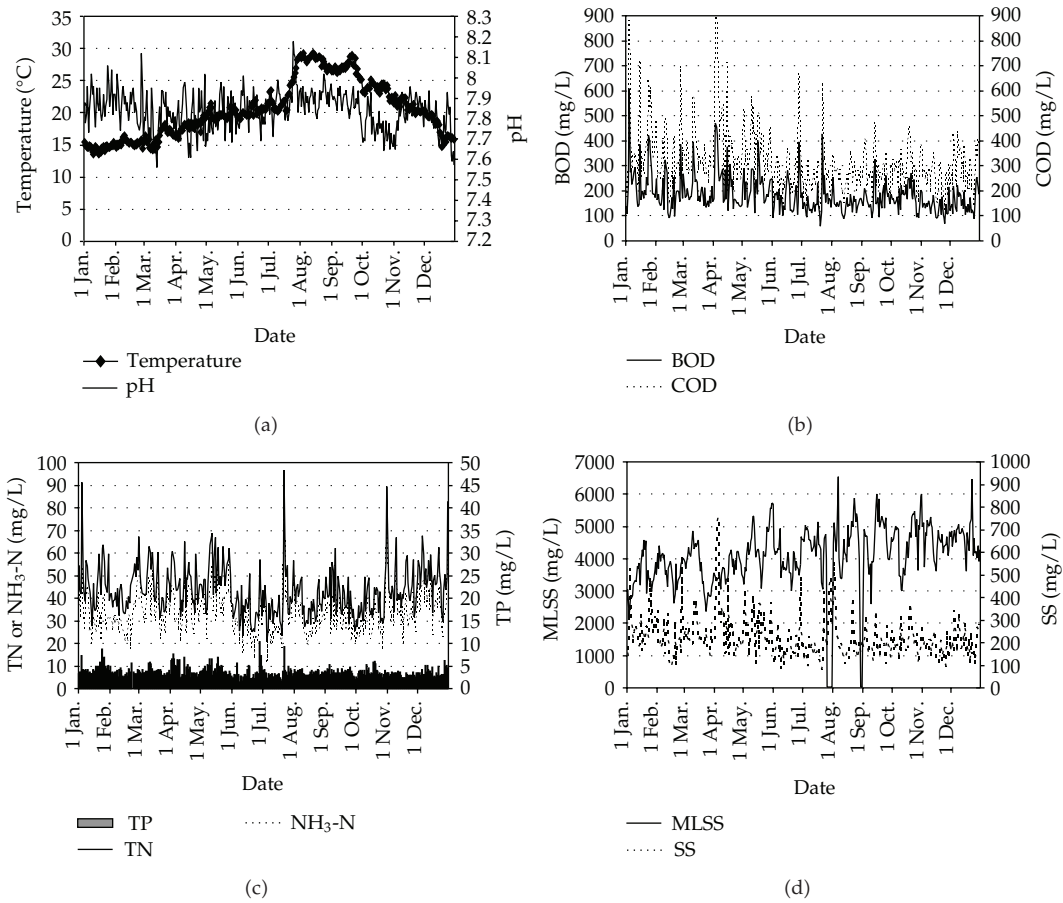
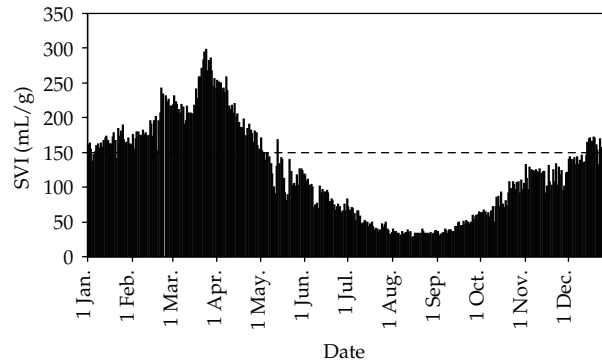
Figure 3: Change of water parameters over time in 2010. (a) Temperature and pH; (b) MLSS and SS; (c) BOD and COD; (d) TN/NH₃-N (lines) and TP (bar chart).

Table 1: Water quality characteristics of CQ from Jan. 1, 2010 to Dec. 31, 2010.

Parameter	Max.	Min.	Mean	Std. dev.
Temp.	29.2	13.5	20.499	4.395
MLSS	6530	14	4088.363	999.860
BOD	609	58	184.975	74.802
COD	899	113	305.094	122.215
SS	755	80	224.798	99.811
pH	8.18	7.56	7.840	0.099
TP	10.4	1.38	3.772	1.220
TN	96.9	20.6	43.460	11.295
NH ₄ ⁺ -N	82	11.2	32.875	9.334
SVI	298	27	123.141	67.893

**Figure 4:** Change of SVIs over time in 2010.

the influents fluctuated from time to time, with high standard deviations of 74.8 mg/L for BOD and 113 mg/L for COD. However the BOD/COD ratios were within 0.53–0.8 for 85% of data, which were within the normal range of municipal wastewater, indicating that it is readily biodegradable wastewater. Similarly, the nitrogen and phosphorus concentrations in the influents fluctuated with 2-3 times higher or lower than the average values, which were believed to be the highly possible reasons that affected the growth of the bulking-causing filamentous bacteria in the reaction tank afterward. Due to the instability of the wastewater characteristics and the occurrence of bulking, the MLSS in the aeration tank cannot keep stable, ranging from 2000 mg/L to more than 6500 mg/L. It was also noted that the closely zero concentrations at the end of July and August were due to the measurement errors.

Figure 4 showed the change of SVIs over time, which clearly indicates that the bulking mostly happened in the springs from Jan. to April, with the SVIs greater than 150 mL/g. On the other hand, bulking levels were low in the summers from July to September, with the SVI around 50 mL/g. When Figure 4 was compared with Figure 3, it was found that there is a correlation between temperature and SVI, showing that bulking in CQWWTP mostly happened in the spring and nonbulking occurred in the summer. This relationship would be further investigated in the following statistical studies.

2.3. Modeling Approaches

Two different modeling techniques, PCR and ANN, were analyzed and applied to model the SVI data from CQWWTP. The measured SVI values in the reaction tank reflected the bulking levels, which in turn depended on the various variables including physical, chemical, and biological water parameters and the interaction among them. They all affect the growth of the filamentous bacteria in the biological WWTP. From the literature review [23, 24], those important parameters include temperature, pH, BOD, COD, SS, NH_4^+ , TN, TP, and MLSS. Temperature and pH are the growth environment for microorganisms. The temperature increases the growth of floc-forming bacteria and filamentous bacteria and strengthen, their interaction and competition. The optimum pH in the reaction tank is 7–7.5, and pH below 6.0 would favor the growth of fungi that induces filamentous bulking. SS and MLSS is the indicator of the amount of activated sludge. The wastewater compositions, BOD/COD, NH_4^+ /TN, and TP are the carbon source, nitrogen source and phosphorus source for microorganisms, respectively. High carbohydrate components and low substrate concentrations with low F/M (food/microorganism) ratios appear to be conducive to sludge bulking [1]. Besides, the deficiency of nitrogen and phosphorus results in the production of nutrient-deficient floc particles and loss of settleability in reaction tanks. Thus all these parameters were taken as the input of the models.

2.3.1. PCR

PCR is divided into two parts, principle component analysis (PCA) and multiple linear regressions (MLRs). PCA is a multivariate statistical method which uses an orthogonal transformation to convert a set of observations of possibly correlated variables into a set of values of uncorrelated variables called principle components (PCs), thus reducing the complexity of multidimensional system by maximization of component loadings variance and elimination of invalid components. MLR attempts to model the relationship between two or more explanatory variables and a response variable by fitting a linear equation to observed data. The eigenvalues of the standardized matrix are calculated from following equation:

$$|C - \lambda I| = 0, \quad (2.1)$$

where C is the correlation matrix of the standardized data, λ is the eigenvalues, and I is the identity matrix. Then the weights of the variables in the PC are calculated by

$$|C - \lambda I|W = 0, \quad (2.2)$$

where W is the matrix of the weights.

Varimax rotation was used to obtain values of rotated factor loadings for evaluating the influence of each variable in the PC. These loadings represent the contribution of each variable in a specific principle component.

In this study, the PCA was performed on the water parameters to rank their relative significance and to describe their interrelation patterns as well as on the phytoplankton population levels. The stepwise option was used to choose the principle components, and the principle component scores of the selected parameters were used as independent variables in the MLR to check if the occurrences of phytoplankton could be explained by environmental

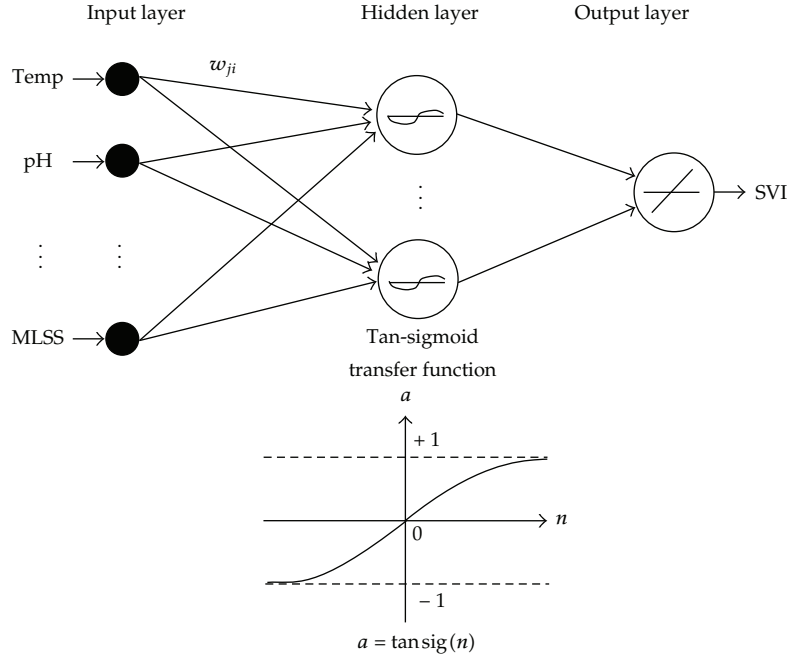


Figure 5: Three-layer feedforward network with Tan-sigmoid function.

variables as well as to predict the phytoplankton abundance. Since phytoplankton abundance did not show normal distribution, logarithmic transformation was applied to phytoplankton data to be used in PCA. Kaiser-Meyer-Olkin (KMO) measure of sample adequacy and Bartlett's test of Sphericity were used to verify the applicability of PCA [25]. PCA and MLR were carried out using PASW 19 software package (SPSS Inc.). The detail procedure of PCR has been described in our previous study [26].

2.3.2. ANN

ANN computing is a new approach to system modeling and identification, with the attractive self-learning system. Different from conventional computational methods to process information, ANN is a system based on the operation of biological neural networks. It has the advantage of being able to assign significance to the input parameters and map the inputs to outputs when the relationships between parameters are unknown.

The ANN model was built with a three-layered feedforward network (Figure 5): an input layer, one or more hidden layers, and an output layer. The nodes in each layer were connected by weights, which will be adjusted through the training process to obtain the optimum model. Tan-sigmoid transfer function was used in the hidden layer to give the nonlinear modeling capability. The neural network architecture consists of two or more layers of neurons connected by weights denoted as w_{ji} . Each neuron is used to calculate its output based on the amount of stimulation it receives from the individual input vector x_i

(where x_i is the input of neuron i). Then the net input of a neuron is calculated as the weighted sum of its inputs, and the output of the neuron are used to estimate the magnitude of this net input via the transfer. The net output u_j from a neuron can be expressed as

$$u_j = \sum_{i=1}^p w_{ji} x_i, \quad (2.3)$$

Sigmoid function was selected as the transfer function in this study, which is represented in the following equation:

$$\begin{aligned} \varphi(v) &= \frac{1}{1 + \exp(-v)}, \\ y_j &= \varphi(u_j), \end{aligned} \quad (2.4)$$

where y_j is the output of the j th neuron in the layers.

The ANN is first to establish a relationship between a set of input variables and a set of output variables from the historical data sets. This is achieved by repeatedly presenting examples of the desired relationship to the network and adjusting the connection weights (i.e., the model coefficients) to reduce the mean-root-square error (RMSE) between the simulated outputs and the observed outputs. The weights of the network continually change until the total error of all the training set is below the acceptable error or other stop mechanism.

Backpropagation is most widely used due to its broad applicability to solve complex nonlinear problems in many domains, such as classification, prediction, and modeling. It works to determine the optimal weights and improve function approximation potential for complex nonlinear data by increasing the number of the hidden layers or the neuron in the hidden layers. Thus the new weights can be calculated by adding a modification to the old weights. The collected data is divided into two sets, one for training and the other for testing.

Determining the size of the hidden layer is a significant task in ANN. Some general rules for selecting the number of hidden nodes N^H in the ANN model suggest that it should be within N^I and $2N^I + 1$ [27], where N^I is the number of input nodes. Moreover, in order to prevent overfitting of the training data, Rogers and Dowla [28] also suggest that the condition $N^H \leq N^{\text{TR}} / (N^I + 1)$ needs to be satisfied, where N^{TR} is the number of training samples. In this study, a trial-and-error approach was carried out to find the optimum number of hidden nodes in the models. In general, a network structure with less hidden nodes is more preferable; this usually gives better generalization capabilities and fewer overfitting problems. To avoid the overfitting problem, which commonly occurs with the application of ANN, cross-validation tests were used. The selection of the network was performed by considering a minimum value of MSE for the cross-validation data set [29].

In this study, ANN development and simulation were conducted using ANN toolbox of Matlab 2011a (Matwork, NA). Batch gradient decent backpropagation training algorithm was adopted; the training stops when it hits one of the several stopping criteria, including

Table 2: Correlation coefficients between SVIs and water parameters in MSR.

Water parameter	Temp	MLSS	BOD	COD	SS	pH	TP	TN	N-NH ₃
SVI	−0.82	−0.18	0.26	0.32	0.21	−0.23	0.18	0.28	0.19

maximum number of iteration, maximum training time, targeted total sum-squared error, and minimum gradient.

2.4. Performance Indicators

The performance of models was evaluated using the following indicators: coefficient of determination (R^2) that provides the variability measure for the data reproduced in the model. Prediction R^2 is a good measure for both comparison and seeing the model's prediction capability. The calculation method is also known as the cross-validation, in which we exclude the first observation, and build the model with the remaining ones, use this model to predict the excluded observation, and repeat for all observations. It is a good measure for out-of-sample accuracy. As this test cannot give the accuracy of the model, other statistical parameters should be reported. Mean absolute error (MAE) and root-mean-square error (RMSE) measure residual errors, providing a global idea of the difference between the observation and modeling. The indicators were defined as follow:

$$R^2 = \frac{\sum_{i=1}^n (Y_i - \bar{Y}_i)^2 - \sum_{i=1}^n (Y_i - \hat{Y}_i)^2}{\sum_{i=1}^n (Y_i - \bar{Y}_i)^2},$$

$$\text{MAE} = \frac{1}{n} \sum_{i=1}^n |\hat{Y}_i - Y_i|, \quad (2.5)$$

$$\text{RMSE} = \sqrt{\frac{1}{n} \sum_{i=1}^n (\hat{Y}_i - Y_i)^2},$$

where n is the number of data; Y_i and \bar{Y}_i are the observation data and the mean of observation data; respectively, and \hat{Y}_i is the modeling results.

3. Results and Discussion

Correlation between SVIs and water parameters were analyzed to evaluate the influence of each parameter on the bulking level, which provides a measure of linear relationship between SVI and each parameter. The results (Table 2) showed that all the coefficients were greater than 0.15, indicating that all these parameters had high correlation with SVIs and thus included in the models as input variables. It is noted that high correlation coefficient (0.82)

Table 3: Eigenvalue and percentage variance of the 9 principle components for the prediction model.

PC	1	2	3	4	5	6	7	8	9
Eigenvalue	4.3	1.3	1.1	0.9	0.7	0.3	0.2	0.1	0.1
% variance	47.8	14.8	12.5	10.3	7.4	3.6	1.9	1.1	0.6

Table 4: Composition of the principle components for the prediction model.

Variables	Component		
	PC1	PC2	PC3
COD	.938	.006	-.131
BOD	.913	-.055	-.100
SS	.897	-.049	.007
TP	.855	.019	.016
TN	.685	.551	-.110
NH3	.582	.653	-.048
MLSS	-.197	.729	-.004
pH	.114	-.265	.767
Temperature	-.246	.210	.762

was found between SVI and temperature, which was consistent with the observation that bulking of CQWWTP mostly occurs in the springs.

3.1. PCA

The values of KMO for both prediction and forecast models were above the criteria value of 0.6, indicating that the PCA was applicable [13]. PCA demonstrates the relative importance of each standardized variable in the PC calculations.

The PCA for the prediction model was performed using the 9 selected parameters from the result of correlation analysis. Table 3 showed that the first 3 principle components can explain 74.1% variation of the data variation. The scree test suggested only 3 components with the eigenvalues greater than 1 to be retained, in which all the 9 parameters were included. The composition of the 3 principle components are shown in Table 4, in which PC1 represented the component of water characteristics in the influent expressed as a function of COD, BOD, SS, TP, TN, and NH₃-N, PC2 represented the component of activated sludge mixed liquor concentration expressed as a function of MLSS, and the PC3 represented the component of environmental condition expressed as a function of temperature and pH.

3.2. MLR

The MLR results for the prediction model were shown in Table 5. Stepwise approach was adopted. A *t*-test (significance level of 0.05) was applied to calculate the statistically valid parameters. MLR result showed that all PCs were significant. Therefore, the prediction model for phytoplankton abundance can be written as $SVI = 468.935 + 0.025(PC1) - 0.007(PC2) - 15.898(PC3)$.

Table 5: MLR result for prediction model.

Included independent variables	Regression coefficient (B)	Std. Error of B	Std. regression coefficient (β)	t	Sig.
(Constant)	468.935	16.782		27.942	.000
PC1	.025	.008	.097	3.238	.001
PC2	-.007	.003	-.070	-2.392	.017
PC3	-15.898	.603	-.794	-26.381	.000

Table 6: Performance indexes of the PCR and ANN prediction models.

Performance index	Accuracy performance (training set)		Generalization performance (testing set)	
	PCR	ANN	PCR	ANN
R^2	0.689	0.901	0.772	0.907
RMSE	37.360	21.141	31.673	20.258
MAE	28.524	16.375	24.490	15.899

3.3. ANN

To apply the ANN model, several network structures were tested to find the most appropriate topology. Using the 9 water parameters as inputs, the best architecture consisted of a three-layer network. Sigmoid and linear functions were used as activation function in the neurons of the hidden layer and output neuron, respectively. 70% of original data were used for training, among which 10% were randomly selected for cross-validation, and the remaining 30% of data were used for testing. The training was performed for a maximum of 30000 iterations. The detailed results were presented in Figures 6–9, and they are discussed in more detail in the next section.

3.4. Modeling Results Comparison

Testing of the models invoked two parts, the accuracy performance and the generalization performance. Accuracy performance is to test the capability of the model to predict the output for the given input set that originally used to train the model, while generalization performance is to test the capability of the model to predict the output for the given input sets that were not in the training set. In order to prevent the overfitting issue of the model, both performance checks need to be considered. In the present research, the performance indexes for ANN's models were averaged with 50 runs.

The performance of prediction models were shown in Table 6. Using the PCR model, the performance indexes for the testing step were generally better than those for the training step, with the R^2 of 0.689 for training and 0.772 for testing. Compared to PCR model, the ANN model has the best performance, with R^2 (0.901, 0.907), RMSE (21.141, 20.258), and MAE (16.375, 15.899) for accuracy and generalization performance, indicating that instead of PCR, ANN can handle well the nonlinear relationship between SVIs and water parameters.

It was noted that the ANN model did not need to perform PCA to obtain the good results. The PCA-ANN results obtained with the R^2 of 0.9 (not shown here) cannot improve the prediction powers for testing and training data sets, confirming that ANN is a powerful tool for dealing with collinearity of data.

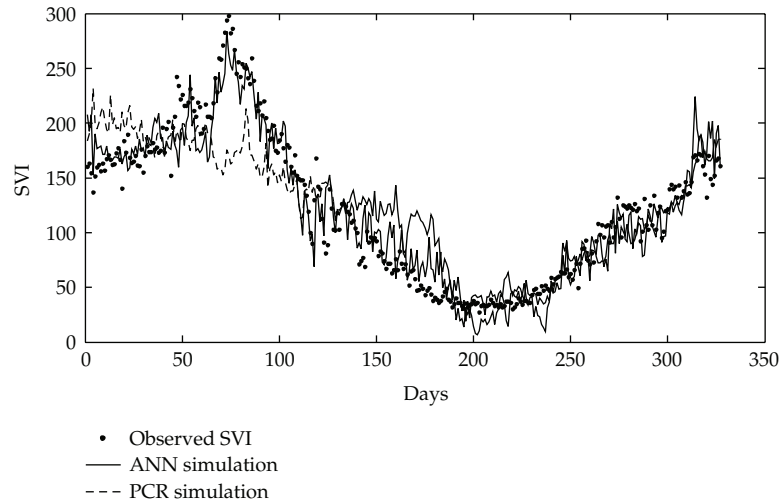


Figure 6: Observed and predicted SVIs for the training data set of the prediction model.

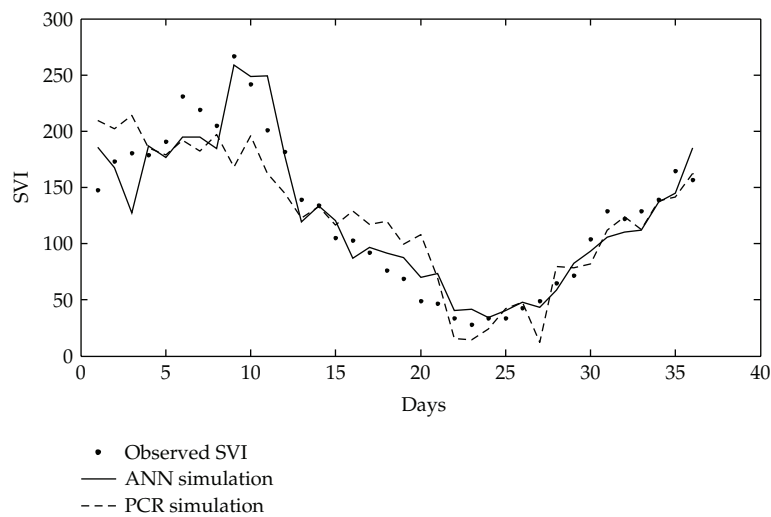


Figure 7: Observed and predicted SVIs for the testing data set of the prediction model.

In the prediction models, no delay was observed for the PCR model in the training set data (Figure 6), but the magnitude is more fluctuate than the ANN models. The prediction of the testing set in Figure 7 for both models exhibit over-estimates in the low SVI level region. In general, ANN was successful to predict the SVIs with a reasonable degree of accuracy for the forecast and the prediction model.

The modeling SVIs versus observed SVIs for PCR and ANN were showed in Figures 8 and 9, respectively. For both training and testing data, both models fitted the measured data well, with the slopes equal to 1 for both fitting curves, that is, the modeling results are equal to the measured data. However, compared to the PCR in which the measured data were distributed more scatter along the fitting curve, ANN models provided better simulation for the measurements, confirming that ANN fits better than PCR when used

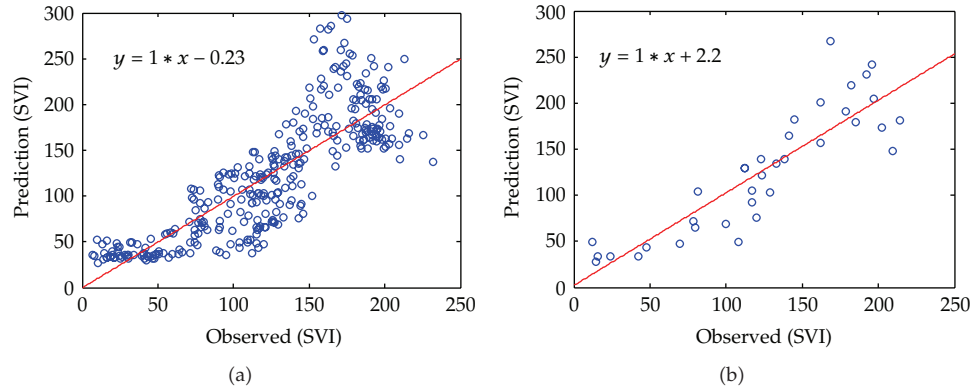


Figure 8: Training (a) and testing (b) results of PCR prediction model.

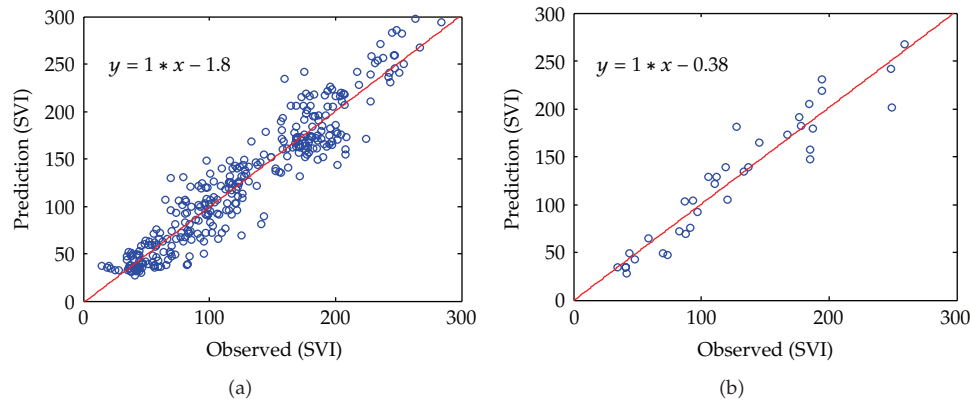


Figure 9: Training (a) and testing (b) results of ANN prediction model.

in predicting the SVIs of CQWWTP. From the modeling point of view, a disadvantage of ANN is that the mechanisms of the inner signal processing are unknown. However, it has provided enough information for CQWWTP to prevent the sludge bulking problems; for controlling the sludge bulking problem occurrence, the engineers can only control the predicted $SVI < 150 \text{ mL/g}$ by adjusting the operational variables, such as MLSS, without understanding the complete mechanisms and the relationships among the variables. ANN was demonstrated to effectively solve the problems where response flexibility and constant tuning of the models are required.

When compared with the SORBF model recently developed by Han and Qiao [21], our ANN models showed similar values of RMSE and R^2 and simpler ANN algorithm, demonstrating that our ANN model is suitable and has more advantages for the SVI prediction. This is highly probably due to the more complete bulking causative variables involved in the ANN model thus providing more information in explaining the sludge bulking phenomena, despite that the complete mechanisms causing bulking and the relationships among variables are still unclear.

In summary, predicting sludge bulking using our ANN model can provide accurate prediction results. The fitting accuracy was found to improve with the increasing number

of bulking causative variables. The model has been tested in the CQWWTP using A/A/O processes, which are different from the traditional aerobic process. Thus, empirical studies will also be conducted in the future for additional data sets to demonstrate that the ANN model is generalizable to extensive data sets under different circumstances.

4. Conclusions

The econometric technique (PCR) and the artificial intelligence technique (ANN) applied in the study are powerful analysis tools that can be used to solve a problem that is poorly understood or difficult to solve with the traditional deterministic relationship. The updated knowledge on sludge bulking is still unclear, and thus the unconventional systematic data-driven modeling approaches could be used to improve the prediction. Prediction models with PCR and ANN were compared for simulating the SVIs in CQWWTP, using nine water parameters including environmental conditions of temperature and pH, wastewater characteristics of BOD, COD, SS, NH_4^+ , TN, and TP, and activated sludge concentration of MLSS. PCA result indicated that only 3 PCs with eigenvalues greater than 1 were obtained, which can explain 74.1% variance of data. The application of PCA in the PCR model was considered better than using the original data, as it would eliminate the collinearity problem and reduce the number of inputs, thus decreasing the model complexity.

PCR showed worse prediction performance than ANN, indicating that the complex nonlinear relationship among the variables in the treatment systems cannot not be simulated using linear model alone. Besides, by using PCR, the highest SVI values were underestimated during the training step. On the other hand, ANN had better prediction power with the R^2 of 0.9 for both accuracy performance and generalization performance, implying that ANN is good to deal with the collinearity problem in the data without performing data pretreatment using PCA. Compared with the recently developed SORBF model, ANN model is suitable and has more advantages for the SVI prediction by using simpler ANN algorithm and including more bulking causative variables in the model. The ANN models established by this research project performed well to address the wastewater quality and sludge bulking problem of CQWWTP. The modeling approach described here for analyzing the bulking problem has yielded useful information for effective wastewater treatment management.

Though the ANN presented here is obtained from the CQWWTP, the technique can also be applied for the other WWTPs, as the input parameters and operational conditions are similar. The method can be used for control of wastewater treatment operation in order to improve the treatment performance.

Acknowledgments

The authors thank Mio Cheng (Alice) Chan, the undergraduate student in the Faculty of Science and Technology at the University of Macau, for assistance in performing ANN and the technical staff in CQWWTP for all water parameters measurement. The financial support from the Fundo para o Desenvolvimento das Ciências e da Tecnologia (FDCT) and the Research Committee at University of Macau under Grant no. MYRG106 (Y1-L3)-FST12-LIC is gratefully acknowledged.

References

- [1] D. Jenkins, M. G. Richard, and G. T. Digger, *Manual on the Caused and Control of Activated Sludge Bulking, Foaming and other Solids Separation Problems*, Lewis Publishers, New York, NY, USA, 2003.
- [2] J. Chudoba, J. Blaha, and V. Madera, "Control of activated sludge filamentous bulking. III. Effect of sludge loading," *Water Research*, vol. 8, no. 4, pp. 231–237, 1974.
- [3] J. Chudoba, P. Grau, and V. Ottova, "Control of activated sludge filamentous bulking. II. Selection of microorganisms by means of a selector," *Water Research*, vol. 7, no. 10, pp. 1389–1406, 1973.
- [4] J. Chudoba, V. Ottova, and V. Madera, "Control of activated sludge filamentous bulking: I. Effect of the hydraulic regime or degree of mixing in an aeration tank," *Water Research*, vol. 7, no. 8, pp. 1163–1182, 1973.
- [5] M. Sezgin, D. Jenkins, and D. S. Parker, "A unified theory of filamentous activated sludge bulking," *Journal of the Water Pollution Control Federation*, vol. 50, no. 2, pp. 362–381, 1978.
- [6] A. M. P. Martins, J. J. Heijnen, and M. C. M. Van Loosdrecht, "Effect of feeding pattern and storage on the sludge settleability under aerobic conditions," *Water Research*, vol. 37, no. 11, pp. 2555–2570, 2003.
- [7] R. Goel, T. Mino, H. Satoh, and T. Matsuo, "Intracellular storage compounds, oxygen uptake rates and biomass yield with readily and slowly degradable substrates," *Water Science and Technology*, vol. 38, no. 8–9, pp. 85–93, 1998.
- [8] M. C. M. Van Loosdrecht, M. A. Pot, and J. J. Heijnen, "Importance of bacterial storage polymers in bioprocesses," *Water Science and Technology*, vol. 35, no. 1, pp. 41–47, 1997.
- [9] C. L. In and F. L. De Los Reyes, "Integrating decay, storage, kinetic selection, and filamentous backbone factors in a bacterial competition model," *Water Environment Research*, vol. 77, no. 3, pp. 287–296, 2005.
- [10] I. Lou and F. L. De Los Reyes III, "Substrate uptake tests and quantitative FISH show differences in kinetic growth of bulking and non-bulking activated sludge," *Biotechnology and Bioengineering*, vol. 92, no. 6, pp. 729–739, 2005.
- [11] A. G. Capodaglio, H. V. Jones, V. Novotny, and X. Feng, "Sludge bulking analysis and forecasting: application of system identification and artificial neural computing technologies," *Water Research*, vol. 25, no. 10, pp. 1217–1224, 1991.
- [12] H. R. Maier, A. Jain, G. C. Dandy, and K. P. Sudheer, "Methods used for the development of neural networks for the prediction of water resource variables in river systems: current status and future directions," *Environmental Modelling and Software*, vol. 25, no. 8, pp. 891–909, 2010.
- [13] H. Çamdevýren, N. Demýr, A. Kanik, and S. Keskýn, "Use of principal component scores in multiple linear regression models for prediction of Chlorophyll-a in reservoirs," *Ecological Modelling*, vol. 181, no. 4, pp. 581–589, 2005.
- [14] S. H. Te and K. Y. H. Gin, "The dynamics of cyanobacteria and microcystin production in a tropical reservoir of Singapore," *Harmful Algae*, vol. 10, no. 3, pp. 319–329, 2011.
- [15] J. T. Kuo, Y. Y. Wang, and W. S. Lung, "A hybrid neural-genetic algorithm for reservoir water quality management," *Water Research*, vol. 40, no. 7, pp. 1367–1376, 2006.
- [16] F. Recknagel, M. French, P. Harkonen, and K. I. Yabunaka, "Artificial neural network approach for modelling and prediction of algal blooms," *Ecological Modelling*, vol. 96, no. 1–3, pp. 11–28, 1997.
- [17] K. I. Yabunaka, M. Hosomi, and A. Murakami, "Novel application of a back-propagation artificial neural network model formulated to predict algal bloom," *Water Science and Technology*, vol. 36, no. 5, pp. 89–97, 1997.
- [18] P. P. Zhang, "Time series forecasting using a hybrid ARIMA and neural network model," *Neuro-computing*, vol. 50, pp. 159–175, 2003.
- [19] L. Belanche, J. J. Valdés, J. Comas, I. R. Roda, and M. Poch, "Prediction of the bulking phenomenon in wastewater treatment plants," *Artificial Intelligence in Engineering*, vol. 14, no. 4, pp. 307–317, 2000.
- [20] M. Côté, B. P. A. Grandjean, P. Lessard, and J. Thibault, "Dynamic modelling of the activated sludge process: improving prediction using neural networks," *Water Research*, vol. 29, no. 4, pp. 995–1004, 1995.
- [21] H. G. Han and J. F. Qiao, "Prediction of activated sludge bulking based on a self-organizing RBF neural network," *Journal of Process Control*, vol. 22, no. 6, pp. 1103–1112, 2012.
- [22] APHA, AWWA, and WEF, *Standard Methods for the Examination of Water and Wastewater*, American Public Health Association, Washington, DC, USA, 2002.
- [23] P. H. Nielsen, C. Kragelund, R. J. Seviour, and J. L. Nielsen, "Identity and ecophysiology of filamentous bacteria in activated sludge," *FEMS Microbiology Reviews*, vol. 33, no. 6, pp. 969–998, 2009.

- [24] A. M. P. Martins, K. Pagilla, J. J. Heijnen, and M. C. M. Van Loosdrecht, "Filamentous bulking sludge—a critical review," *Water Research*, vol. 38, no. 4, pp. 793–817, 2004.
- [25] J. . Pallant, I. Chorus, and J. Bartram, "Toxic cyanobacteria in water," in *SPSS Survival Manual*, McGraw Hill, 2007.
- [26] W. . Zhang, I. Lou, W. K. Ung, Y. Kong, and K. M. Mok, "Eutrophication in Macau main storage reservoir," in *Proceedings of the 12th International Conference on Environmental Science and Technology*, pp. 1114–1121, Rhodes Island, Greece, September 2011.
- [27] R. . Hecht-Nielsen, "Kolmogorov's mapping neural network existence theorem," in *Proceedings of the 1st IEEE International Joint Conference of Neural Networks*, vol. 3, pp. 11–14, New York, NY, USA, 1987.
- [28] L. L. Rogers and F. U. Dowla, "Optimization of groundwater remediation using artificial neural networks with parallel solute transport modeling," *Water Resources Research*, vol. 30, no. 2, pp. 457–481, 1994.
- [29] S. I. V. Sousa, F. G. Martins, M. C. M. Alvim-Ferraz, and M. C. Pereira, "Multiple linear regression and artificial neural networks based on principal components to predict ozone concentrations," *Environmental Modelling and Software*, vol. 22, no. 1, pp. 97–103, 2007.

Research Article

Particle Swarm Optimization Algorithm Coupled with Finite Element Limit Equilibrium Method for Geotechnical Practices

Hongjun Li,¹ Hong Zhong,² Zuwen Yan,¹ and Xuedong Zhang¹

¹ State Key Laboratory of Simulation and Regulation of Water Cycle in River Basin,
China Institute of Water Resources and Hydropower Research, Beijing 100048, China

² Faculty of Infrastructure Engineering, Dalian University of Technology, Dalian 116024, China

Correspondence should be addressed to Hongjun Li, lijunli1995@163.com

Received 5 October 2012; Accepted 10 November 2012

Academic Editor: Fei Kang

Copyright © 2012 Hongjun Li et al. This is an open access article distributed under the Creative Commons Attribution License, which permits unrestricted use, distribution, and reproduction in any medium, provided the original work is properly cited.

This paper proposes a modified particle swarm optimization algorithm coupled with the finite element limit equilibrium method (FELEM) for the minimum factor of safety and the location of associated noncircular critical failure surfaces for various geotechnical practices. During the search process, the stress compatibility constraints coupled with the geometrical and kinematical compatibility constraints are firstly established based on the features of slope geometry and stress distribution to guarantee realistic slip surfaces from being unreasonable. Furthermore, in the FELEM, based on rigorous theoretical analyses and derivation, it is noted that the physical meaning of the factor of safety can be formulated on the basis of strength reserving theory rather than the overloading theory. Consequently, compared with the limit equilibrium method (LEM) and the shear strength reduction method (SSRM) through several numerical examples, the FELEM in conjunction with the improved search strategy is proved to be an effective and efficient approach to routine analysis and design in geotechnical practices with a high level of confidence.

1. Introduction

Slope stability analysis is still a hot issue and complex problem in the field of geotechnical engineering, which has been attracting the attention of many geotechnical researchers. Nowadays, the limit equilibrium method (LEM), the shear strength reduction method (SSRM), and the finite element limit equilibrium method (FELEM) are generally employed in geotechnical practices by engineers and researchers.

The LEM is a conventional and well-defined approach due to its simplicity and applicability. It can handily evaluate the stability of soil slope via the minimum factor of safety and associated critical failure surface. However, the major limitation of the LEM is

that it is established based on some assumptions on the distributions of internal forces or the normal force within the rigid slices. In addition, the LEM requires many trial failure surfaces and great effort to locate the critical failure surface. Recently, many advanced heuristic global optimization methods have been proposed successfully and detailed discussion on these methods for the special N-P type global optimization problem has been provided by Cheng et al. [1–6]. Unfortunately, for a nonhomogeneous soil slope, whose mechanical properties change with time and stress state, the LEM built on rigid plastic theory might be unreasonable.

Since the first application of the Shear strength reduction method (SSRM) in slope stability analysis by Zienkiewicz et al. [7], thorough studies on the approach have been carried out by Griffiths and Lane [8], Cheng et al. [9], and others. Assumptions on the shape and location of the critical slip surface for this technique are unnecessary. In addition, it can depict directly the process of progressive failure through display of strain field or displacement field for soil slopes. However, Cheng et al. [9] have conducted an extensive comparison between the LEM and SSRM and pointed out two major critical limitations of the SSRM, as follows: (i) it is hard to achieve a good evaluation for a soil slope with soft band; (ii) the results obtained from the SSRM are sensitive to the FEM mesh, the choice of the tolerance and the solution of the nonlinear equations, convergence criterion, constitutive model and boundary condition, and so on.

The finite element limit equilibrium method, which effectively couples the limit equilibrium method and finite element stress analysis, can quickly obtain the factor of safety under actual stress field. In the past decades, the FELEM for circular slip surface has been well established and applied successfully into the stability analysis of soil slopes due to its simplicity and practicability by Zou et al. [10], Kim and Lee [11], Pham and Fredlund [12], Yamagami and Ueta [13], and Shao et al. [14]. In addition, the simplex method, dynamic programming, and leap-frog method have been successfully introduced into the search of the critical slip surfaces. However, most of the above-mentioned studies are limited to circular slip surface. Consequently, the two issues, (i) whether the FELEM is suitable for the stability analysis with noncircular slip surface and (ii) whether the modern heuristic optimization techniques which have been employed successfully in the LEM are suitable for the FELEM to search for the critical non-circular failure surface, still puzzle the researchers and geotechnical engineers. Thus, before introducing the FELEM associated with the non-circular slip surface into routine practice and design in geotechnical engineering, the following three key problems must be figured out: (i) the definition and physical meaning of factor of safety for non-circular slip surface in the FELEM; (ii) the effective and efficient optimization algorithm to determine the global minimum factor of safety and associated critical non-circular slip surface; (iii) the relationships of the minimum factor of safety and location of critical non-circular slip surface in the LEM, SSRM, and FELEM in routine geotechnical practices.

In this paper, the factor of safety for non-circular slip surface in the FELEM is derived from the necessary and sufficient conditions making the sliding body reaches the critical limit equilibrium state. The particle swarm optimization algorithm for searching the critical non-circular slip surface which was adopted in the LEM by Cheng et al. [15] is modified to couple with the FELEM. In the modified particle swarm optimization method, the requirements of a kinematically acceptable failure mechanism and stress compatibility mechanism are presented. Finally, the factors of safety and the locations of associated critical non-circular

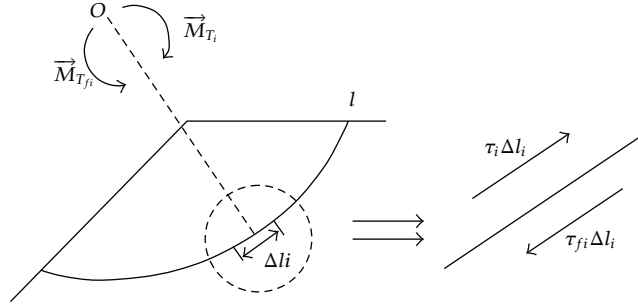


Figure 1: Equilibriums of force and moment in a segment of the slip surface.

failure surfaces obtained by the FELEM, LEM, and SSRM are compared for various soil slopes.

2. Formulation of Necessary and Sufficient Conditions

As represented in Figure 1, given l as a continuous slip surface for arbitrary shape in soil slope, the critical limit equilibrium state for the sliding body implies that the shear force and moment counterpoise the resistant shear force and moment in any segment (Δl_i) of the slip surface. Meanwhile, the integral of the sliding force and moment counterpoises that of the resistant sliding force and moment along the slip surface. The relationships of force and moment equilibrium in one segment of slip surface are depicted in Figure 1. Explicit expressions for the above-defined critical limit equilibrium state are obtained in (2.1a)~(2.3):

$$\vec{T}_i - \vec{T}_{fi} = 0, \quad i = 1, n, \quad (2.1a)$$

$$\vec{M}_{\vec{T}_i} - \vec{M}_{\vec{T}_{fi}} = 0, \quad i = 1, n. \quad (2.1b)$$

Summarizing both sides of (2.1a) and (2.1b) from 1 to n , the following relations are obtained:

$$\sum_{i=1}^n \vec{T}_i - \sum_{i=1}^n \vec{T}_{fi} = 0, \quad (2.2)$$

$$\sum_{i=1}^n \vec{M}_{\vec{T}_i} - \sum_{i=1}^n \vec{M}_{\vec{T}_{fi}} = 0, \quad (2.3)$$

where \vec{T}_i , $\vec{M}_{\vec{T}_i}$, \vec{T}_{fi} , and $\vec{M}_{\vec{T}_{fi}}$ represent the driving force and moment, resistant sliding force, and moment acted on segment i of the slip surface, respectively; τ_i and τ_{fi} are the shear stress and resistant shear strength of the segment i ; Δl_i is the length of segment i ; n represents the number of segments constituting the failure surface l .

It will be proved that the necessary and sufficient condition for the equilibrium between the driving force and the resistant sliding force in any segment of the slip surface

can be expressed by (2.4) as the sliding body reaches the steady state; namely, the integration of shear stress equals to that of resistant shear strength along the slip surface l :

$$\int_l \tau dl = \int_l \tau_f dl. \quad (2.4)$$

Firstly, given that the driving force equals to the resistant sliding force in any segment of failure surface, which validates (2.1a), then (2.2) can be achieved. The derivations are presented as follows.

The force equilibrium of segment i in the tangential direction gives

$$\tau_i \cdot \Delta \vec{l}_i - \tau_{fi} \cdot \Delta \vec{l}_i = 0. \quad (2.5)$$

Then (2.5) can be rewritten into the following form:

$$(\tau_i \cdot \Delta l_i - \tau_{fi} \cdot \Delta l_i) \vec{l}_i = 0, \quad (2.6)$$

where \vec{l}_i is the direction vector of segment i in the tangential direction.

If (2.6) is justified, (2.7) can be achieved by transforming (2.6) into a scalar form:

$$\tau_i \cdot \Delta l_i - \tau_{fi} \cdot \Delta l_i = 0. \quad (2.7)$$

Then by summarizing both sides of (2.7) from 1 to n , (2.4) can be formulated in another form:

$$\sum_{i=1}^n \tau_i \cdot \Delta l_i - \sum_{i=1}^n \tau_{fi} \cdot \Delta l_i = 0. \quad (2.8)$$

Secondly, if (2.4) or (2.8) is tenable, the equation can be rewritten as

$$\sum_{i=1}^n (\tau_i - \tau_{fi}) \cdot \Delta l_i = 0. \quad (2.9)$$

By considering the stress compatibility mechanism for all the segments of the slip surface reaching the critical equilibrium state, the additional stress compatibility restriction of failure surface should be guaranteed as follows:

$$\tau_i \leq \tau_{fi}. \quad (2.10)$$

Considering the restriction condition, if (2.9) can be satisfied, then (2.11) must be justified:

$$\tau_i \cdot \Delta l_i - \tau_{fi} \cdot \Delta l_i = 0. \quad (2.11)$$

Then, (2.1a)~(2.3) are resulted.

It is noted that for the sliding body being in a critical limit equilibrium state along the surface l , (2.1a), (2.1b) and (2.4) must be satisfied. So the necessary and sufficient conditions for the sliding body reaching the critical limit equilibrium state along the surface l can be expressed in

$$\frac{\int_l \tau_f dl}{\int_l \tau dl} = 1. \quad (2.12)$$

3. Factor of Safety in FELEM

Apparently, the definition of factor of safety F_s which can be provided with reasonable physical meaning is the most important issue in the slope stability analysis. So far, there are two commonly used definitions. The first is based on the strength reserving theory, which defines F_s as the coefficient by which the shear strength of the soil would be reduced to drive the slope into the critical limit equilibrium state. The second definition is based on the overloading theory, which obtains the F_s as the ratio of the ultimate limit loading that militates the occurrence of slope failure to the insitu loading acting on the soil slope. In the LEM, the strength reserving theory which is utilized to form the equilibrium equations of slices is formulated to solve the statically indeterminate problem. Likewise, in the SSRM, F_s is also derived through the strength reserving theory, which assumes that while c and φ are reduced simultaneously by an efficient, the slip failure would initially trigger in soil slope.

In the FELEM, given that $F_s(l)$ is the function of strength reduction coefficient for segments along the surface l , that is, (2.1a) and (2.1b) can be achieved by dividing the shear strength by the function in any segment of the sliding surface l , and then the necessary and sufficient conditions for the sliding body along the surface l reaching the critical limit equilibrium state (2.12) can be rewritten as

$$\int_l \frac{\tau_f}{F_s(l)} dl = \int_l \tau dl. \quad (3.1)$$

Based on the mean value theorem, the left side of (3.1) can be transformed into

$$\int_l \frac{\tau_f}{F_s(l)} dl = \frac{\int_l \tau_f dl}{F_s}. \quad (3.2)$$

According to (3.1) and (3.2), the factor of safety in the FELEM can be formulated as

$$F_s = \frac{\int_l \tau_f dl}{\int_l \tau dl}. \quad (3.3)$$

Based on the above derivations, it is proved that the definition of factor of safety in the FELEM is also established on the strength reserving theory as in the LEM and SSRM. Furthermore, the physical meaning of factor of safety in the FELEM is the average strength reduction coefficient for the whole potential sliding body reaching the critical limit equilibrium state along the slip surface.

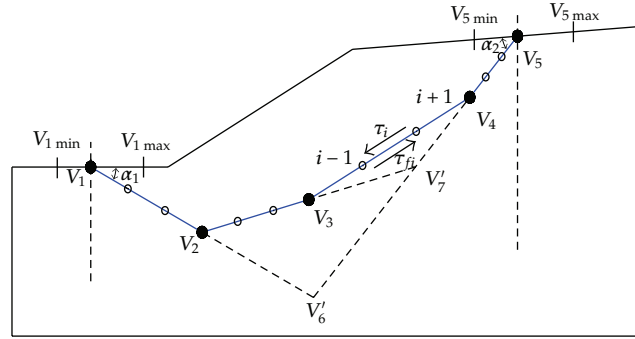


Figure 2: Generation of reasonable failure surface.

4. Modified Particle Swarm Optimization Algorithm in FELEM

In this paper, a modern search procedure based on a modified particle swarm optimization algorithm is proposed. In the modified approach, the method of generating trial failure surfaces which are kinematically acceptable and stress compatibility is similar to that by Cheng et al. [15], Greco [16], and Malkawi et al. [17].

Considering the trial surface with four segments and five vertices (V_1, V_2, V_3, V_4 , and V_5) shown in Figure 2, it can be represented by eight control variables including $x_1, x_5, \alpha_1, \alpha_2, \delta_1, \delta_2, \delta_3$, and δ_4 . Here x_1 and x_5 are the horizontal coordinates of the initial point, and end point respectively; α_1 and α_2 are the initial angle and end angle. $\delta_1, \delta_2, \dots, \delta_4$ are random numbers in the range $(-0.5, 0.5)$. Implementation of the trial slip surface includes the following steps: (i) the initial point and end point are determined based on the given lower bound and upper bound; (ii) the α_1 and α_2 are achieved by the random procedure in the range $(0, \pi/2)$ until the reasonable intersection points of V'_{16} and V'_{56} (Figure 2) are obtained; (iii) the positions of V_2 and V_7 are located according to the random numbers δ_1 and δ_2 ; (iv) the positions of V_3 and V_4 are achieved based on the random numbers δ_3 and δ_4 between the two adjacent segments which have the largest horizontal distance. Herein, according to the above principle, the specified number of vertices or segments can be produced. However, although the trial slip surfaces generated by the above procedure are kinematically admissible, the stress compatibility condition for these trial failure surfaces cannot be guaranteed strictly, which means that (2.10) may not be satisfied. Thus, the segments constituting the slip surface should be subdivided to make sure that the stress constraint condition is met.

Based on the above descriptions, the formulations for a typical slope stability analysis can be written as follows:

$$\min F_S(x), \quad (4.1)$$

$$\text{s.t. } x_l \leq x_1 \leq x_u, \quad x_l \leq x_{n+1} \leq x_u, \quad (4.2)$$

$$\text{s.t.} \quad 0 < \alpha_1 < \frac{\pi}{2}; \quad 0 < \alpha_2 < \frac{\pi}{2}, \quad (4.3)$$

$$\text{s.t.} \quad 0 < \delta_i < 0.5, \quad i = 1, 2n-4, \quad (4.4)$$

$$\text{s.t. } \tau_i \leq \tau_{fi}, \quad i = 1, n \times m, \quad (4.5)$$

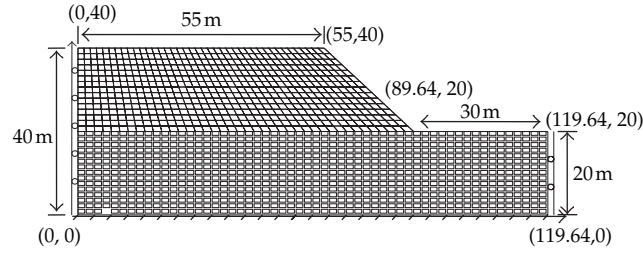


Figure 3: Mesh for a homogeneous soil slope.

where n is the number of segments constituting the slip surface; m is the number of subdivisions of one segment. In fact, the constraint condition (4.5) has little effect on the results, but it can guarantee the stress compatibility of slip surface and achievement of necessary and sufficient conditions.

Recently, the particle swarm optimization (PSO) which is a modern heuristic global optimization algorithm has been broadly used in complex continuous optimization problems [18, 19]. However, it is noted that the accuracy and efficiency for the method cannot be guaranteed as the number of control variables becomes more. To obtain the optimized solution with fewer trials, a new version called Modified PSO (MPSO) was developed by Cheng [1]. In MPSO, only several particles which have better objective function values are allowed to fly. In the flying procedures, several flies are allowed for each particle in the group; that is, one particle can fly more than once according to its objective function value. The better the objective function value of one particle, the more times it is allowed to fly. Herein, the number of speciated flies does not represent the number of speciated particles that can fly. After the specified flies are achieved, the objective function value of these flies is checked. Then new position and velocity are randomly chosen for the particles which have the chance to fly more than once for the next circle and other new positions and velocities will be assigned randomly to those nonflying particles in the current iteration. Other procedures of the applied method not mentioned here are the same as the original particle swarm optimization.

5. Verifications

Based on the above formulations and derivations, the authors have developed a program FELEM-2D and five typical examples are used for the thorough study of the FELEM in geotechnical practices. For the LEM, the Spencer method, which satisfies both moment and force equilibrium, is adopted. The critical failure surfaces in the LEM and FELEM are achieved by the combination of the modified Particle swarm optimization method (MPSO). The inertial weight coefficient is 0.5. The stochastic weighting coefficients are 2.0. The number of iterations is 200. The specified number of segments and flies in one iteration is 30 and 15, respectively. For the SSRM, the plastic strain is used to depict the critical failure surface and the failure to converge is adopted as the failure criterion for a soil slope. In addition, the elastic perfectly plastic model with nonassociated flow law and Mohr-Coulomb failure principle is incorporated into the finite element stress analysis in the FELEM and SSRM.

Example 5.1 (Homogeneous soil slope). Firstly, a homogeneous soil slope (Figure 3) [20] is adopted. The intensity properties and unit weight of the soil are 42 kPa, 17° , and 25 kN/m^3 ,

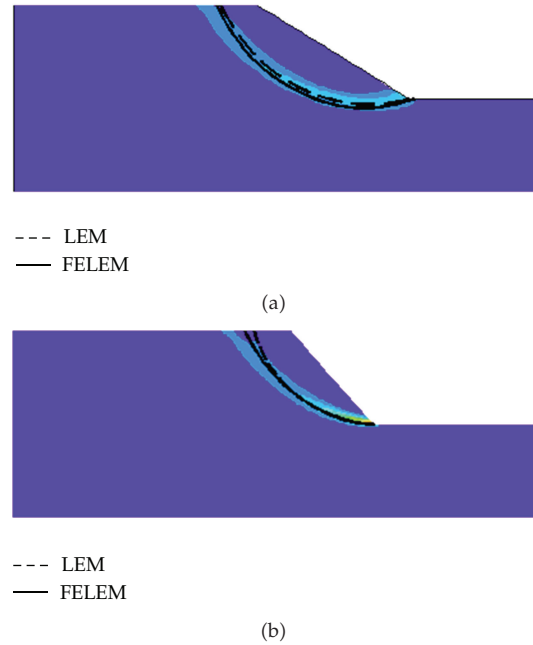


Figure 4: Comparisons of critical slip surfaces for two slope inclinations: (a) 30°; (b) 50°.

Table 1: Factors of safety by the LEM, SSRM and FELEM.

Methods	Slope inclination				
	30°	35°	40°	45°	50°
FELEM	1.408	1.287	1.178	1.075	1.007
SSRM	1.390	1.260	1.150	1.070	1.000
LEM	1.392	1.260	1.152	1.063	0.985

respectively. In the study, the slope with different slope inclinations are considered and the LEM, SSRM, and FELEM analyses are carried out. The slope inclination of 30°, 35°, 40°, 45°, and 50° are studied, respectively. The elastic modulus and Poisson's ratio of the soil are assumed to be 10 MPa and 0.3, respectively, throughout the numerical examples in this paper unless specified. The boundary conditions are depicted in Figure 3. The stress field is obtained by the well-known commercial geotechnical finite element programs Z-SOIL. The results of stability analysis from the LEM and SSRM are obtained through SLIDE5.0 and Z-SOIL, respectively.

In Figure 4, the dashed curves and the solid curves denote the critical slip surface obtained by the LEM and the FELEM, respectively, while the shade zones (plastic strain) denote the potential sliding surface obtained by the SSRM. From Table 1 and Figure 4, it is found that the factor of safety and associated critical failure surface determined by the LEM, SSRM, and FELEM are fairly consistent for different slope inclinations. Based on the same shear strength parameters, all the factors of safety obtained by the LEM and SSRM differ by less than 3% with respect to the FELEM with the increase of slope inclination. Since the results obtained by the LEM, SSRM, and FELEM are in good agreement and only minor

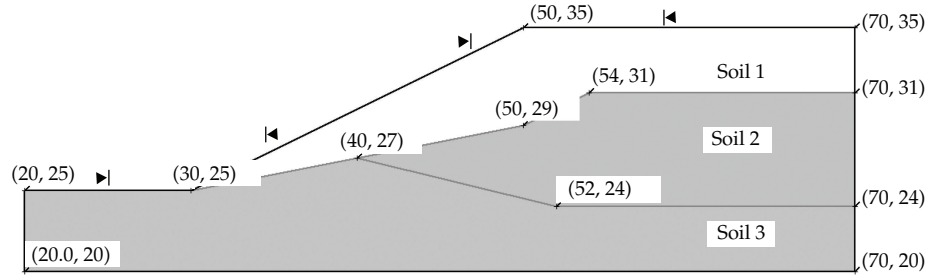


Figure 5: Geometry of a nonhomogeneous soil slope.

Table 2: Parameters of soil material.

Soil	c/kPa	$\phi/(^{\circ})$	$\gamma/(\text{kN}/\text{m}^3)$	$E/(\text{kPa})$	μ	K_0
1	0	38	19.5	10000	0.25	0.65
2	5.3	23	19.5	10000	0.25	0.65
3	7.2	20	19.5	10000	0.25	0.65

differences exist, it can be concluded that the performances of the LEM, SSRM, and FELEM are all satisfactory for the case of homogeneous soil slope.

Example 5.2 (Nonhomogeneous soil slope). In this example, the proposed method in conjunction with the MPSO is employed for analysis of a nonhomogeneous soil slope (Figure 5). Table 2 gives the geotechnical parameters for this example. The stress field is obtained by the Z-SOIL. The results of stability analysis from the LEM and SSRM are obtained through SLIDE5.0 and PLAXIS, respectively.

Figures 6 and 7 show the non-circular critical slip surfaces with 30 segments obtained by the LEM (Spencer) the SSRM and the FELEM, respectively. The factors of safety and associated critical failure surfaces are in good agreement with the LEM, SSRM, and FELEM as can be seen from Table 3 and Figures 6 and 7. It is noted that the right end of slip surface moves closer to the crest of the slope in the LEM and FELEM.

Example 5.3 (Slope with a soft band). A soil slope with a thin soft band (Figure 8) [21] which was considered by Griffiths and Lane [8] is studied. The friction angles of both the soft band and surrounding soil are equal to be zero. The unit weight, elastic modulus, and Poisson's ratio of the two soils are the same, with the value shown in Example 5.1. c_{u2} and c_{u1} are the strengths of the soft band and the surrounding soil, respectively. $c_{u1}/\gamma H = 0.25$ holds for the surrounding soil.

Considering the effect of the ratio c_{u2}/c_{u1} in the LEM, SSRM, and FELEM, the stability analysis is conducted with six strength ratios that range between 0.4 and 1.0. The results are listed in Table 4 and the associated critical sliding surfaces obtained by the SSRM and FELEM for two typical cases are depicted in Figures 9 and 10.

From Table 4 and Figures 9 and 10, it can be found that the minimum factors of safety and associated critical failure surfaces achieved by the FELEM are in good agreement with the SSRM. The locations of the critical failure surfaces from the SSRM and FELEM for the strength ratios from 0.6 to 1.0 are virtually similar. However, it is noted that the critical failure surface is obviously sensitive to the strength parameters of the soft band. The non-circular failure surfaces, as shown in Figures 9 and 10, are almost along the soft band as the strength

Table 3: Factors of safety by the LEM, SSRM, and FELEM.

Method	Factor of safety
FELEM (Mohr-Coulomb principle)	1.382
SSRM (Mohr-Coulomb principle)	1.324
Simplified Bishop	1.394
Spencer	1.373

Table 4: Factors of safety by the SSRM and FELEM.

Methods	c_{u2}/c_{u1}					
	0.4	0.5	0.6	0.7	0.8	1.0
FELEM	—	1.166	1.373	1.409	1.430	1.456
SSRM	0.990	1.215	1.370	1.400	1.420	1.455

ratio is below 0.6. As the ratio of c_{u2} and c_{u1} is above 0.6, the circular failure mechanism governs the stability of slope, and the factor of safety is essentially irrelevant of the strength of soft band. Furthermore, it is noted that the proposed method cannot achieve the factor of safety and the location of failure surface as the given strength ratio is below 0.5, because in the special case the plastic finite element stress analysis cannot obtain a convergent solution, which means that the actual stress field for the soil slope cannot be determined.

Example 5.4 (Soil slope under steady-state seepage). A homogeneous slope with free surface shown in Figure 11 has the same geotechnical parameters and FEM mesh as in Example 5.1.

Regarding the role of the seepage, the SEEP/W is conducted to achieve the distribution of pore pressure in soil slope. In the elastic-plastic FEM analysis, the effective stress of each gauss point can be used in the stability analysis by subtracting the pore pressure from the total stress. The factor of safety of the slope has been determined for several different slope inclinations, which varies from 30° to 50° . The comparisons for the minimum factor of safety are shown in Table 5.

Excellent agreements concerning the minimum factors of safety between the three methods are observed from the above results.

Example 5.5 (Ultimate bearing capacity for soil footing). Formerly, the ultimate bearing capacity of soil footing, which is usually regarded as the external loading which can drive the soil footing into onset of failure, can be obtained by the LEM, limit analysis. For the special example (Figure 12) [21], Griffiths got limit collapse loading for soil footing by elastic-plastic finite element method based on a single failure criterion of misconvergence. In the present paper, the FELEM is performed to determine the ultimate bearing capacity of soil footing, implying that an additional failure criterion that the factor of safety of critical surface should be equal to unity is added into the process of computation of the ultimate bearing capacity. Figure 12 shows a homogeneous soil footing without self-weight under vertical loading. The analytical solution of limit load can be obtained by the Prandtl method as expressed in (5.1).

Table 5: Factors of safety by the LEM, SSRM, and FELEM.

Methods	Slope inclination				
	30°	35°	40°	45°	50°
FELEM	1.350	1.280	1.220	1.155	1.088
SSRM	1.340	1.260	1.210	1.150	1.080
LEM	1.334	1.254	1.181	1.113	1.055

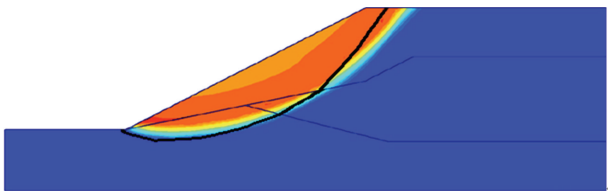


Figure 6: Comparison of critical slip surfaces between the FELEM and SSRM.

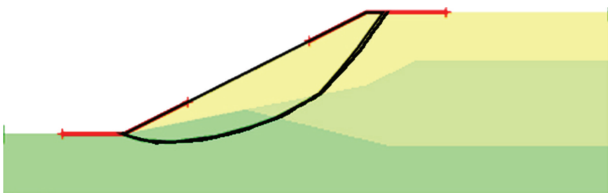


Figure 7: Comparison of critical slip surfaces between the FELEM and LEM.

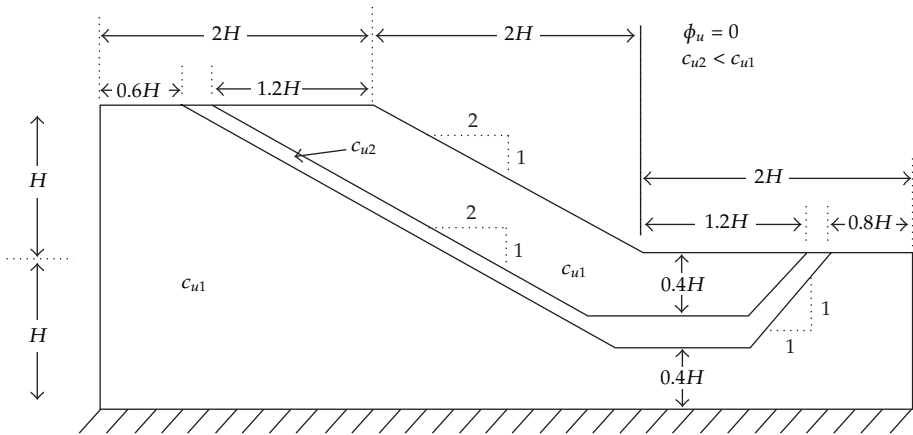


Figure 8: Soil slope with a soft band.

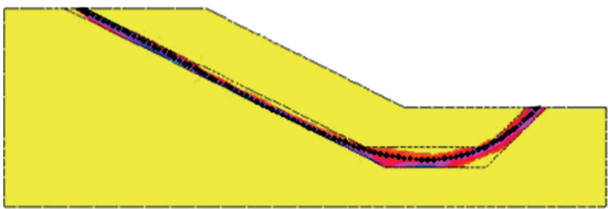


Figure 9: Slip surface comparisons with c_{u2}/c_{u1} equal to 0.5.

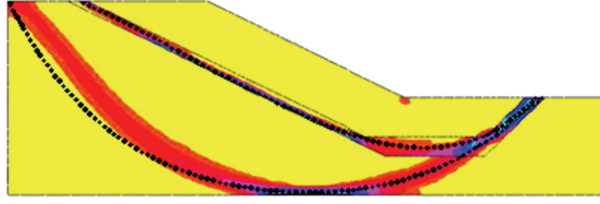


Figure 10: Slip surface comparisons with c_{u2}/c_{u1} equal to 0.6.

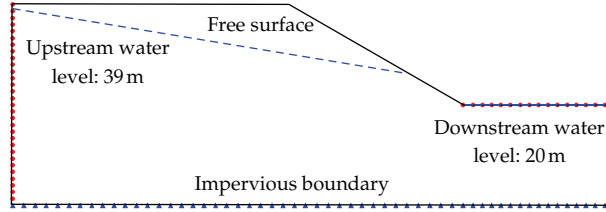


Figure 11: Homogeneous slope under steady-state seepage.

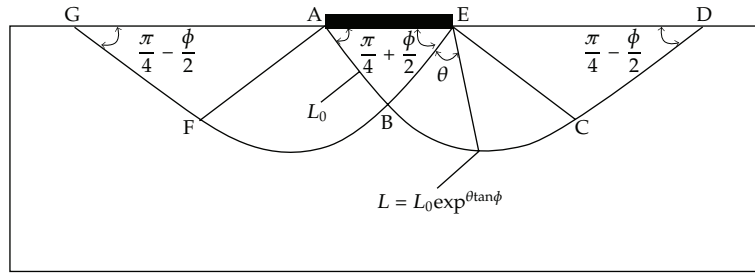


Figure 12: Prandtl solution of homogeneous footing.

The ultimate bearing capacities and locations of critical slip surfaces for the typical cases ($\phi = 25^\circ$) achieved by the FELEM and the theoretical results determined by (5.1) with different friction angles of the slopes are presented in Table 6 and Figure 13

$$P_u = c \cdot \left(\tan^2 \left(\frac{\pi}{4} + \frac{\phi}{2} \right) e^{\pi \tan \phi} - 1 \right) \cdot \cot \phi. \quad (5.1)$$

It can be seen from Table 6 and Figure 13 that the differences concerning the ultimate bearing capacity, the minimum factors of safety, and locations of associated failure surfaces are fairly minor between the FELEM and the analytical method. Thus, it is proven that the FELEM can lead to good estimation on the ultimate bearing capacity and capture the potential failure surface for the soil footing in geotechnical practices.

6. Summary

In the present study, the finite element limit equilibrium method (FELEM) in conjunction with a modified particle swarm optimization algorithm for slope stability evaluation is proposed. A number of remarkable features of this approach are highlighted. It is clearly

Table 6: The results of ultimate bearing capacity (kPa).

Methods		$\phi/(^{\circ})$				
		5	10	15	20	25
FELEM	P_u	66.3	85.3	111.8	149.6	204.5
	F_s	1.006	1.010	1.022	1.028	1.038
LEM	P_u	64.9	83.5	109.8	148.5	207.2
	F_s	1.0	1.0	1.0	1.0	1.0

**Figure 13:** Comparisons of failure surfaces of the FELEM and LEM for Example 5.5.

shown that (i) the definition of factor in the FELEM is suitable for noncircular slip surfaces; (ii) concerning the physical meaning, the factor of safety in the FELEM is the average value of the shear strength reduction coefficient along the sliding surface; (iii) it is still built on the basis of strength reserving theory as that in the LEM and SSRM; (iv) the FELEM in conjunction with the modified particle swarm optimization algorithm can be applied to the determination of non-circular failure surfaces accurately and efficiently; (v) satisfactory agreement on the minimum factors of safety and locations of associated critical surfaces between the LEM, SSRM, and FELEM can be achieved. Consequently, it is proven that the FELEM coupled with the modified particle swarm algorithm can be performed in general geotechnical engineering practice as a beneficial reinforcement for the LEM and SSRM.

Acknowledgments

The financial support by the Foundation of the State Key Laboratory of Coastal and Offshore Engineering (LP1016), the National Nature Science Foundation of China (51009021), and Special Scientific Research Foundation of China Institute of Water Resources and Hydropower Research (Yanji1211) and experimental data and technological supports from Professor Shao Longtan and Dr. Zhao Jie are gratefully acknowledged.

References

- [1] Y. M. Cheng, "Location of critical failure surface and some further studies on slope stability analysis," *Computers and Geotechnics*, vol. 30, no. 3, pp. 255–267, 2003.
- [2] Z. Teng, J. He, A. J. Degnan et al., "Critical mechanical conditions around neovessels in carotid atherosclerotic plaque may promote intraplaque hemorrhage," *Atherosclerosis*, vol. 223, no. 2, pp. 321–326, 2012.

- [3] S. Chen, Y. Wang, and C. Cattani, "Key issues in modeling of complex 3D structures from video sequences," *Mathematical Problems in Engineering*, vol. 2012, Article ID 856523, 17 pages, 2012.
- [4] S. Y. Chen, J. Zhang, Q. Guan, and S. Liu, "Detection and amendment of shape distortions based on moment invariants for active shape models," *IET Image Processing*, vol. 5, no. 3, pp. 273–285, 2011.
- [5] F. Kang, J. Li, and Q. Xu, "Damage detection based on improved particle swarm optimization using vibration data," *Applied Soft Computing*, vol. 12, no. 8, pp. 2329–2335, 2012.
- [6] F. Kang, J. Li, and Z. Ma, "An artificial bee colony algorithm for locating the critical slip surface inslope stability analysis," *Engineering Optimization*. In press.
- [7] O. C. Zienkiewicz, C. Humpheson, and R. W. Lewis, "Associated and non-associated visco-plasticity and plasticity in soil mechanics," *Geotechnique*, vol. 25, no. 4, pp. 671–689, 1975.
- [8] D. V. Griffiths and P. A. Lane, "Slope stability analysis by finite elements," *Geotechnique*, vol. 49, no. 3, pp. 387–403, 1999.
- [9] Y. M. Cheng, T. Lansivaara, and W. B. Wei, "Two-dimensional slope stability analysis by limit equilibrium and strength reduction methods," *Computers and Geotechnics*, vol. 34, no. 3, pp. 137–150, 2007.
- [10] J.-Z. Zou, D. J. Williams, and W.-L. Xiong, "Search for critical slip surfaces based on finite element method," *Canadian Geotechnical Journal*, vol. 32, no. 2, pp. 233–246, 1995.
- [11] J. Y. Kim and S. R. Lee, "An improved search strategy for the critical slip surface using finite element stress fields," *Computers and Geotechnics*, vol. 21, no. 4, pp. 295–313, 1997.
- [12] H. T. V. Pham and D. G. Fredlund, "The application of dynamic programming to slope stability analysis," *Canadian Geotechnical Journal*, vol. 40, no. 4, pp. 830–847, 2003.
- [13] T. Yamagami and Y. Ueta, "Search for critical slip lines in finite element stress fields by dynamic programming," in *Proceedings of the 6th International Conference on Numerical methods in Geomechanics*, pp. 1347–1352, Innsbruck, Austria, 1988.
- [14] L. T. Shao, H. X. Tang, and G. C. Han, "Finite element method for slope stability analysis with its applications," *Chinese Journal of Computational Mechanics*, vol. 18, no. 1, pp. 81–87, 2001.
- [15] Y. M. Cheng, L. Li, S.-C. Chi, and W. B. Wei, "Particle swarm optimization algorithm for the location of the critical non-circular failure surface in two-dimensional slope stability analysis," *Computers and Geotechnics*, vol. 34, no. 2, pp. 92–103, 2007.
- [16] V. R. Greco, "Efficient Monte Carlo technique for locating critical slip surface," *Journal of Geotechnical Engineering*, vol. 122, no. 7, pp. 517–525, 1996.
- [17] A. I. H. Malkawi, W. F. Hassan, and S. K. Sarma, "Global search method for locating general slip surface using Monte Carlo techniques," *Journal of Geotechnical and Geoenvironmental Engineering*, vol. 127, no. 8, pp. 688–698, 2001.
- [18] S. Chen, Y. Zheng, C. Cattani, and W. Wang, "Modeling of biological intelligence for SCM system optimization," *Computational and Mathematical Methods in Medicine*, vol. 2012, Article ID 769702, 10 pages, 2012.
- [19] P. Lu, S. Chen, and Y. Zheng, "Artificial intelligence in civil engineering," *Mathematical Problems in Engineering*, vol. 2013, Article ID 145974, 20 pages, 2013.
- [20] Z. Jie, *The research of some application problems in finite element method for slope stability analysis [Ph.D. thesis]*, Dalian University of Technology, Dalian, China, 2006.
- [21] D. V. Griffiths, "Computation of bearing capacity factors using finite elements," *Geotechnique*, vol. 32, no. 3, pp. 195–202, 1982.

Research Article

Freshwater Algal Bloom Prediction by Support Vector Machine in Macau Storage Reservoirs

Zhengchao Xie,¹ Inchio Lou,¹ Wai Kin Ung,² and Kai Meng Mok¹

¹ Faculty of Science and Technology, University of Macau, Taipa, Macau

² Laboratory & Research Center, Macao Water Supply Co. Ltd., Conselheiro Borja, Macau

Correspondence should be addressed to Inchio Lou, iclou@umac.mo

Received 26 August 2012; Accepted 11 November 2012

Academic Editor: Sheng-yong Chen

Copyright © 2012 Zhengchao Xie et al. This is an open access article distributed under the Creative Commons Attribution License, which permits unrestricted use, distribution, and reproduction in any medium, provided the original work is properly cited.

Understanding and predicting dynamic change of algae population in freshwater reservoirs is particularly important, as algae-releasing cyanotoxins are carcinogens that would affect the health of public. However, the high complex nonlinearity of water variables and their interactions makes it difficult to model the growth of algae species. Recently, support vector machine (SVM) was reported to have advantages of only requiring a small amount of samples, high degree of prediction accuracy, and long prediction period to solve the nonlinear problems. In this study, the SVM-based prediction and forecast models for phytoplankton abundance in Macau Storage Reservoir (MSR) are proposed, in which the water parameters of pH, SiO₂, alkalinity, bicarbonate (HCO₃⁻), dissolved oxygen (DO), total nitrogen (TN), UV₂₅₄, turbidity, conductivity, nitrate, total nitrogen (TN), orthophosphate (PO₄³⁻), total phosphorus (TP), suspended solid (SS) and total organic carbon (TOC) selected from the correlation analysis of the 23 monthly water variables were included, with 8-year (2001–2008) data for training and the most recent 3 years (2009–2011) for testing. The modeling results showed that the prediction and forecast powers were estimated as approximately 0.76 and 0.86, respectively, showing that the SVM is an effective new way that can be used for monitoring algal bloom in drinking water storage reservoir.

1. Introduction

Freshwater algal bloom is one of water pollution problems that occurs in eutrophic lakes or reservoirs due to the presence of excessive nutrients. It has been found that most species of algae (also called phytoplankton) can produce various cyanotoxins including *microcystins*, *cylindrospermopsis*, and *nodularin*, which have a direct impact on the water treatment processes and consequently the health of public [1]. Thus, it is of great importance to understand the population dynamics of algae in the raw water storage units. However, modeling the algae population in such a complicated system is a challenge, as the physical, chemical,

and biological processes as well as the interaction among them are involved, resulting in the highly nonlinear relationship between phytoplankton abundance and various water parameters.

Computational artificial intelligence techniques have been developed as the efficient tools in recent years for predicting (without considering time series effect) or forecasting (considering time series effect) algal bloom. Previous studies [2] have used the principle component regression (PCR), that is, principal component analysis (PCA) followed by multiple linear regression (MLR), to predict chlorophyll-a levels, the fundamental index of phytoplankton. However, the intrinsic problem of PCR is that the variables dataset used as the input of the model has high complex nonlinearity, expecting that PCR alone is inadequate for prediction, and the prediction results were unsatisfactory. With the development of artificial intelligence models, artificial neural network (ANN) such as backpropagation (BP) was applied to predict the algal bloom by assessing the eutrophication and simulating the chlorophyll-a concentration. ANN is a well-suited method with self-adaptability, self-organization, and error tolerance, which is better than PCR for nonlinear simulation. However, this method has such limitations as requirement of a great amount of training data, difficulty in tuning the structure parameter that is mainly based on experience, and its "black box" nature that makes it difficult to understand and interpret the data [2, 3].

Considering the drawbacks of both the methods, recently support vector machine (SVM) started to be used for predicting the chlorophyll concentration. It is a new machine-learning technology based on statistical theory and derived from instruction risk minimization, which can enhance the generalization ability and minimize the upper limit of generalization error. Compared to ANN, SVM has advantages of only requiring a small amount of samples, high degree of prediction accuracy, and long prediction period by using kernel function to solve the nonlinear problems. It is believed that SVM will provide a new approach for predicting the phytoplankton abundance in the reservoirs [4]. Also, this black box model can be applied in other locations and other cases such as red tide.

In this study, we attempted to develop an SVM-based predictive model to simulate the dynamic change of phytoplankton abundance in Macau Reservoir given a variety of water variables. The measured data from 2001 to 2011 were used to train and test the model. The present study will lead to a better understanding of the algal problems in Macau, which will help to develop later guidelines for forecasting the onset of algae blooms in raw water resources.

2. Materials and Methods

Macau is situated 60 km southwest of Hong Kong and experiences a subtropical seasonal climate that is greatly influenced by the monsoons. The difference of temperature and rainfall between summer and winter is significant though not great. Macau Main Storage Reservoir (MSR) (Figure 1), located in the east part of Macau peninsula, is the biggest reservoir in Macau with the capacity of about 1.9 million m³ and the water surface area of 0.35 km². It is a pumped storage reservoir that receives raw water from the West River of the Pearl River network and can provide water supply to the whole areas of Macau for about one week. MSR is particularly important as the temporary water source during the salty tide period when high salinity concentration is caused by intrusion of sea water to the water intake location. In recent years, there were reports (Macao Water Supply Co. Ltd, unpublished data) that the reservoir experienced algal blooms, and the situation appeared to be worsening.

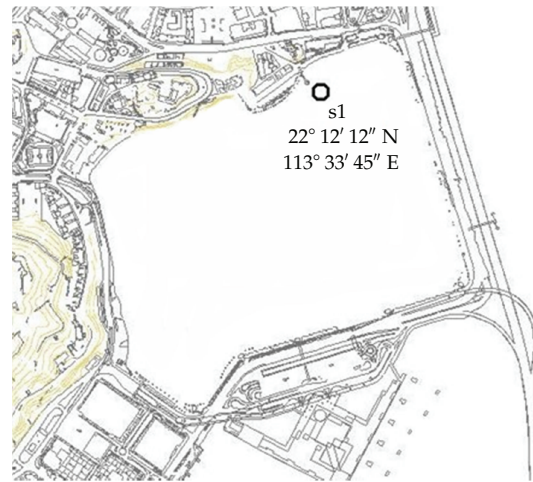


Figure 1: Location of the MSR.

Macau Water Supply Co. Ltd. is responsible for water-quality monitoring and management. Location in the inlet of the reservoir was selected for sampling. Samples were collected in duplicate monthly from May 2001 to February 2011 at 0.5 m from the water surface. A total of 23 water quality parameters, including hydrological, physical, chemical, and biological parameters, were monitored monthly. Precipitation was obtained from Macau Meteorological Center (http://www.smg.gov.mo/www/te_smgmail.php). Imported volume, exported volume, and water level were recorded by the inlet and outlet flow meters, based on which the hydraulic retention time (HRT) can be calculated. Turbidity, temperature, pH, conductivity, chloride (Cl^-), sulfate (SO_4^{2-}), silicon (SiO_2), alkalinity, bicarbonate (HCO_3^-), dissolved oxygen (DO), ammonium (NH_4^+), nitrite (NO_2^-), nitrate (NO_3^-), total nitrogen (TN), phosphorus (PO_4^{3-}), total phosphorus (TP), suspended solid, total organic carbon (TOC) and UV_{254} , and iron (Fe) were measured according to the standard methods [5]. The phytoplankton samples were fixed using 5% formaldehyde and transported to laboratory for microscopic counting.

In this work, correlation analysis was conducted to identify the water parameters which were significantly correlated with phytoplankton abundance (Table 1). Only the parameters with the correlation coefficients greater than 0.3 are selected as inputs in the SVM models. It was also noted that the parameters selected in forecast models are different from those in the prediction models, as the water parameters in previous data were also used in the correlation analysis.

As a prediction algorithm, SVM was firstly proposed by Vapnik [6] and is an effective tool for data classification and regression. The SVM is fundamentally based on Mercer core expansion theorem which maps sample space to a higher-dimension or even unlimited dimension feature space by nonlinear mapping functions (kernel function) [7]. In SVM, it transforms the problem of searching for an optimal linear regression hyperplane to a convex programming problem of solution for a convex restriction condition. Moreover, SVM can provide the global optimum solution because the problem in SVM is transformed to finding the solution to the quadratic programming.

SVM is selected in this work because of its advantages over other “black box” modeling approaches such as ANN as listed as follows [8].

- (1) The architecture of the estimated function does not have to be determined before training. Input data of any arbitrary dimensionality can be treated with only linear costs in the number of input dimensions.
- (2) SVM treats the regression as a quadratic programming problem of minimizing the data-fitting error plus regularization, which produces a global (or even unique) solution.
- (3) SVM combines the advantages of multivariate nonlinear regression in that only a small amount of data is required to produce a good generalization. In addition, the weakness of the transformational models in multivariate nonlinear regression can be overcome by mapping the data points to a sufficiently high-dimensional feature space.
- (4) Results obtained from SVM are easy to interpret.

In SVM, the whole process consists of several layers. The input vectors are put in the first layer. Suppose that the training datasets are

$$(x_1, y_1), (x_2, y_2), \dots, (x_N, y_N). \quad (2.1)$$

A nonlinear mapping $\psi(\cdot)$ is used to map samples from former space R^n to feature space [9]:

$$\psi(x) = (\phi(x_1), \phi(x_2), \dots, \phi(x_N)). \quad (2.2)$$

Then, in this higher-dimension feature space, optimal decisions function is

$$f(x) = w\phi(x) + b, \quad (2.3)$$

where b is the bias constant or the threshold which can be calculated as introduced in [8].

In this way, nonlinear prediction function is transformed to linear prediction function in higher-dimension feature space [9]. Note that parameters used in equations will be introduced later in this section. The SVM needs to find out the solution to minimize the following functional:

$$\begin{aligned} & \frac{1}{2} \|w\|^2 + C \sum_{i=1}^N (\xi_i + \xi_i^*), \\ \text{s.t. } & \begin{cases} y_i - w^T \phi(x_i) - b \leq \varepsilon + \xi_i \\ w^T \phi(x_i) + b - y_i \leq \varepsilon + \xi_i^* \\ \xi_i, \xi_i^* \geq 0. \end{cases} \end{aligned} \quad (2.4)$$

As introduced previously, SVM can provide the global optimum solution because the problem in SVM is transformed to finding the solution to the quadratic programming. So,

Table 1: Correlation analysis of prediction and forecast model.

Parameters	Prediction model	Forecast model		
		Time lagged (month)		
		$t-1$	$t-2$	$t-3$
Turbidity	−0.03	0.00	−0.01	−0.06
Temperature	0.19	0.21	0.19	0.14
pH	0.49	0.42	0.38	0.33
Conductivity	−0.08	0.01	0.14	0.21
Cl [−]	0.01	0.10	0.22	0.28
SO ₄ ^{2−}	−0.03	0.03	0.14	0.22
SiO ₂	0.33	0.31	0.16	0.04
Alkalinity	−0.34	−0.30	−0.21	−0.12
HCO ₃ [−]	−0.46	−0.40	−0.32	−0.24
DO	0.39	0.35	0.34	0.31
NO ₃ [−]	−0.29	−0.22	−0.22	−0.15
NO ₂ [−]	−0.10	−0.08	−0.02	0.03
NH ₄ ⁺	0.11	0.10	0.08	0.25
TN	0.68	0.60	0.53	0.46
UV ₂₅₄	0.56	0.55	0.48	0.47
Fe	−0.14	−0.06	−0.04	−0.08
PO ₄ ^{3−}	0.02	0.06	0.06	0.03
TP	0.08	0.05	0.02	0.00
Suspended solid	0.31	0.35	0.31	0.23
TOC	0.38	0.33	0.29	0.35
HRT	−0.12	−0.11	−0.13	−0.16
Water level	0.13	0.05	0.01	−0.02
Precipitation	−0.09	0.05	0.11	0.06
Phytoplankton abundance	—	0.82	0.71	0.62

the minimization problem shown in (2.4) could be transformed to finding the solution to maximize the following equation [5, 9–11]:

$$\begin{aligned}
 \max_{\alpha, \alpha^*} &= -\frac{1}{2} \sum_{i=1, l=1}^N (\alpha_i - \alpha_i^*) (\alpha_l - \alpha_l^*) \langle \phi(x_i), \phi(x_l) \rangle - \varepsilon \sum_{i=1}^N (\alpha_i - \alpha_i^*) + \sum_{i=1}^N y_i (\alpha_i - \alpha_i^*) \\
 \text{s.t.} &\begin{cases} \sum_{i=1}^N (\alpha_i - \alpha_i^*) = 0, \\ \alpha_i, \alpha_i^* \in [0, C]. \end{cases}
 \end{aligned} \tag{2.5}$$

where $\alpha, \alpha^*, \eta, \eta^* \geq 0$ are Lagrange multipliers.

According to Mercer's condition, in SVM the inner product $\langle \phi(x), \phi(x_i) \rangle$ can be defined through a kernel function $K(x, x_i)$. There are several kernel functions that are available as follows:

- (1) linear: $K(x_i, x_j) = x_i^T x_j$,
- (2) polynomial: $K(x_i, x_j) = (\gamma x_i^T x_j + r)^d$,
- (3) radial basis function: $K(x_i, x_j) = \exp(-\gamma \|x_i - x_j\|^2)$,
- (4) sigmoid: $K(x_i, x_j) = \tanh(\gamma a_i^T + r)$.

For these four kernel functions, in general, the RBF kernel function is a reasonable first choice [9]. This kernel function nonlinearly maps samples into a higher-dimensional space. So, unlike the linear kernel, it can handle the case when the relation between class labels and attributes is nonlinear. The second reason is that the RBF kernel function has a less number of hyperparameters which influences the complexity of model selection. Finally, the RBF kernel has fewer numerical difficulties [12–16].

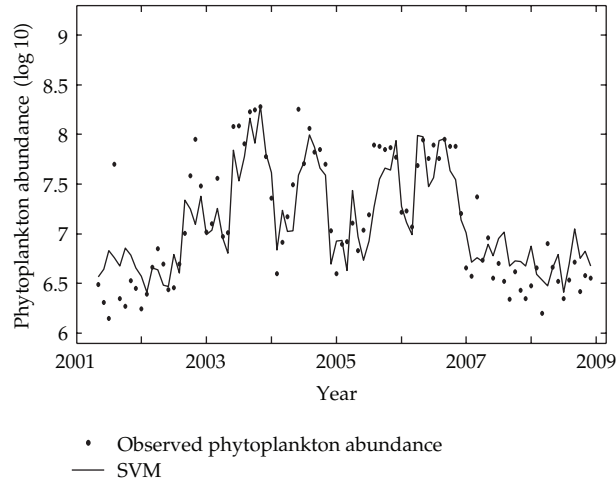
As shown in the kernel function mentioned previously, there are three parameters which need to be specified in the application of SVM: (1) capacity parameter C that controls the trade-off between maximizing the margin and minimizing the training error. If C is too small, then insufficient stress will be placed on fitting the training data. If C is too large, then the algorithm will overfit the training data. (2) RBF width parameter γ : the γ value is important in the RBF model and can lead to under- or over-fitting in prediction. A very large value of γ may lead to overfitting, and all the support vectors distances are taken into account, while in case of a very small γ , the machine will ignore most of the support vectors leading to failure in the trained point prediction [9]. (3) Insensitive loss function ε : if ε is too large, then it will result in less support vectors, and consequently, the resulting regression model may yield large prediction errors on unseen future data [10]. In this work, in order to prevent overtraining, an internal cross-validation [11] during construction of SVR models is adopted to have a good combination of the three parameters C , γ , and ε . Now, after the introduction of SVM, the following section gives the numerical results from the application of SVM.

With the above introduction of SVM, it is necessary to present performance indicators. The performance of models was evaluated using the following indicators: square of correlation coefficient (R^2) that provides the variability measure for the data reproduced in the model; mean absolute error (MAE) and root mean square error (RMSE) that measure residual errors, providing a global idea of the difference between the observation and modeling. The indicators were defined as follows:

$$\begin{aligned}
 R^2 &= 1 - \frac{F}{F_o}, \\
 F &= \sum (\hat{Y}_i - Y_i)^2, \\
 F_o &= \sum (Y_i - \bar{Y})^2, \\
 \text{MAE} &= \frac{1}{n} \sum_{i=1}^n (\hat{Y}_i - Y_i), \\
 \text{RMSE} &= \sqrt{\frac{1}{n} \sum_{i=1}^n (\hat{Y}_i - Y_i)^2},
 \end{aligned} \tag{2.6}$$

Table 2: Performance indexes of the prediction and forecast models.

Performance index	Prediction model				Forecast model			
	Accuracy performance		Generalization performance		Accuracy performance		Generalization performance	
	(training set)		(testing set)		(training set)		(testing set)	
	ANN	SVM	ANN	SVM	ANN	SVM	ANN	SVM
R^2	0.752	0.760	0.749	0.758	0.758	0.863	0.760	0.863
RMSE	0.307	0.307	0.316	0.351	0.299	0.229	0.306	0.264
MAE	0.238	0.243	0.243	0.274	0.229	0.127	0.247	0.226

**Figure 2:** Observed and predicted phytoplankton level for the training and validation dataset of the prediction models.

where n is the number of data; Y_i and \bar{Y}_i are observation data and the mean of observation data, respectively, and \hat{Y}_i is the modeling results.

3. Results and Discussion

The correlation of \log_{10} phytoplankton and water parameters for forecast model and prediction model was shown in Table 2. Parameters with correlation coefficients greater than 0.3 (highlighted in bold) will be retained in the models. It was also noted that the parameters selected in forecast models are different from those in the prediction models, as the water parameters in previous data (past record) were also used in the correlation analysis. In the forecast models of SVM, phytoplankton abundance (t) is a function of water parameter ($t-1$), water parameter ($t-2$), and water parameters ($t-3$), where $t-1$, $t-2$, and $t-3$ represent the 1 month, 2 months, and 3 months prior to time t . Thus, there were only 9 parameters used in the prediction models and 23 time-lagged parameters selected for the forecast models.

After the correlation analysis, it comes to the testing of the models invoked two parts, the accuracy performance and the generalization performance. Accuracy performance is to test the capability of the model to predict the output for the given input set that is originally used to train the model, while generalization performance is to test the capability of the model to predict the output for the given input sets that were not in the training set. In order

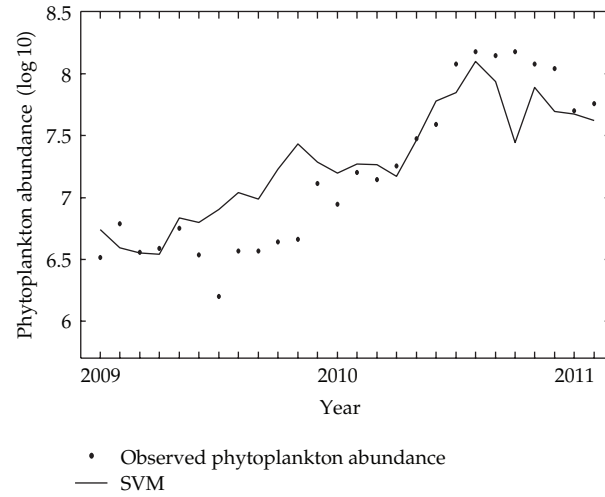


Figure 3: Observed and predicted phytoplankton level for the testing dataset of the prediction models.

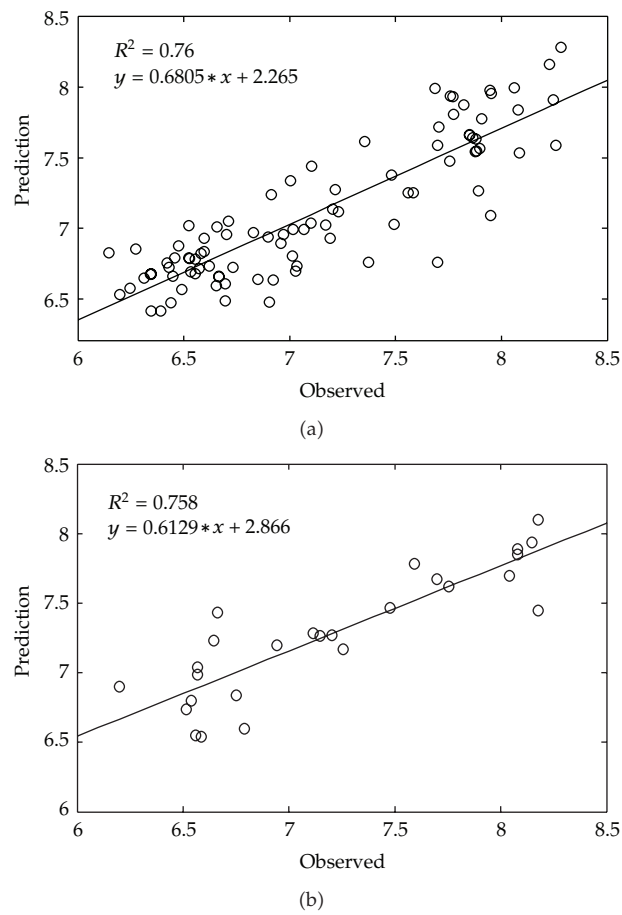


Figure 4: SVM result for the training and validation (a) and testing (b) data set.

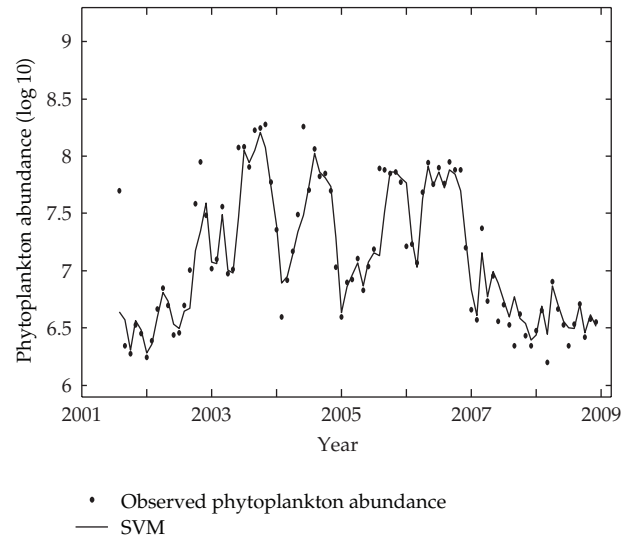


Figure 5: Observed and predicted phytoplankton level for the training and validation dataset of the forecast models.

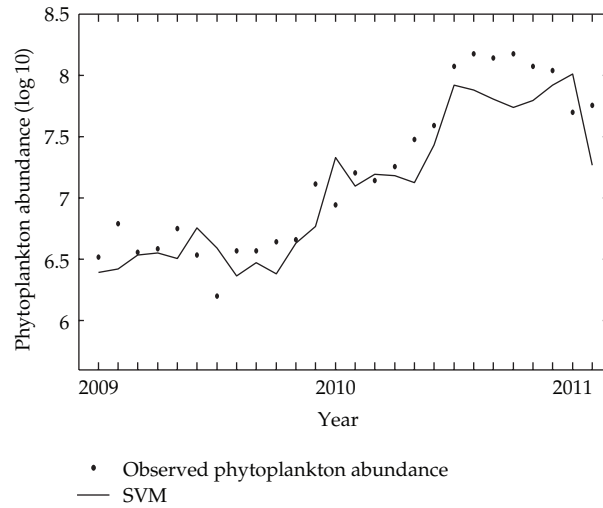


Figure 6: Observed and predicted phytoplankton level for the testing dataset of the forecast models.

to prevent the model that is memorizing the inputs instead of generalized learning, both performance checks need to be considered. In the present research, the performance indexes for SVM-based models were averaged with 50 runs.

In the application of SVM in this work, for the predication model, after the correlation analysis, 9 parameters such as pH, SiO_2 are selected as the independent variables, and phytoplankton abundance is selected as the induced variable (target value). Then, the data from May 2005 to December 2008 are used to train the model, and data from January 2009 to February 2011 are used to test the model. In the training process, the cross-validation approach as mentioned previously is adopted to obtain the optimal combination of parameters for the testing. Specifically, the training data are divided into 10 about the same

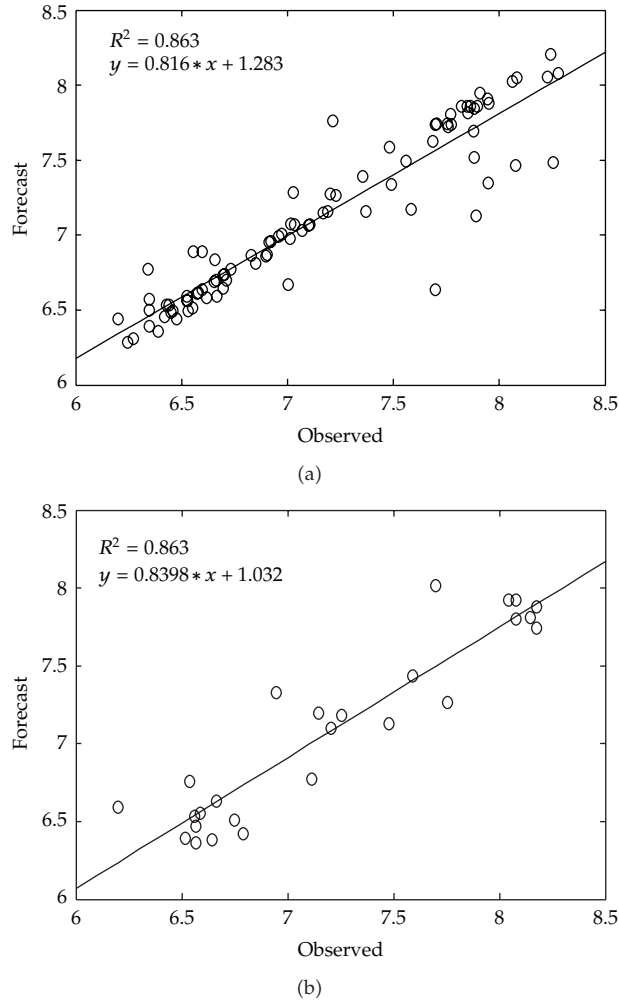


Figure 7: SVM result for the training and validation (a) and testing (b) data set.

size groups that are 9 groups for training, and the rest 1 group is used to test the model trained by the previous 9 groups' data. Then, this (9 groups training and 1 group testing) is repeated for 9 times (10 times in total). And then, parameters of the one process which has the best testing performance in these 10 repeats will be used as the optimal parameters combination in the "real" testing process which has the data from January 2009 to February 2011. The forecast model basically follows the same steps of the prediction model, while the only difference between these two models is that effect of time series which is included in the forecast model. So, in the forecast model, only the previous three months' data are included in the training process.

The performance of prediction and forecast models was shown in Table 2. Compared to our previous studies using ANN, the SVM has a similar performance for prediction model with R^2 of 0.758, RMSE of 0.351, and MAE of 0.274, while it has much better performance for forecast model with R^2 of 0.863, RMSE of 0.229, and MAE of 0.127, for testing. To balance the R^2 in training and testing, we defined the equal values for both data sets as the performance of the models. The observed data versus the modeling data were shown in Figures 4 and 7,

and the observed and modeling phytoplankton abundance changes over time were listed in Figures 2, 3, 5, and 6.

These results confirmed that SVM can handle well the nonlinear relationship between water parameters and phytoplankton abundance.

4. Conclusions

The SVM-based prediction and forecast models for phytoplankton abundance in MSR are proposed in this study. 15 water parameters with the correlation coefficients against phytoplankton abundance greater than 0.3 were selected, with 8-year (2001–2008) data for training and cross-validation and the most recent 3 years (2009–2011) for testing. The results showed that the forecast model has better performance with the R^2 of 0.863 than prediction model with the R^2 of 0.760, implying that the algal bloom problem is a complicated nonlinear dynamic system that is affected not only by the water variables in current month, but also by those in a couple of previous months. In addition, compared to ANN in our previous studies, SVM in the study showed superior forecast power, while similar prediction power in terms of regression coefficient. These results will provide an effective way for water quality monitoring and management of drinking water storage reservoirs. In addition, additional numerical approaches and optimization algorithms can be applied to enhance the performance [17–19].

Acknowledgments

The authors thank Macao Water Supply Co. Ltd. for providing historical data of water quality parameters and phytoplankton abundances. The financial support from the Fundo para o Desenvolvimento das Ciências e da Tecnologia (FDCT) (Grant no. FDCT/016/2011/A) and Research Committee at University of Macau is gratefully acknowledged.

References

- [1] Z. Selman, S. Greenhalgh, and R. Diaz, *Eutrophication and Hypoxia in Coastal Areas: A Global Assessment of the State of Knowledge*, World Resources Institute, Washington, DC, USA, 2008.
- [2] J. Pallant, I. Chorus, and J. Bartram, "Toxic cyanobacteria in water," in *SPSS Survival Manual*, 2007.
- [3] R. Hecht-Nielsen, "Kolmogorov's mapping neural network existence theorem," in *Proceedings of the 1st IEEE International Joint Conference of Neural Networks*, New York, NY, USA, 1987.
- [4] L. L. Rogers and F. U. Dowla, "Optimization of groundwater remediation using artificial neural networks with parallel solute transport modeling," *Water Resources Research*, vol. 30, no. 2, p. 457, 1994.
- [5] APHA, *Standard Methods for the Examination of Water and Wastewater*, American Public Health Association (APHA), American Water Works Association (AWWA) & Water Environment Federation (WEF), 2002.
- [6] V. Vapnik, *The Nature of Statistical Learning Theory*, Springer, New York, NY, USA, 1995.
- [7] T. A. Stolarski, "A system for wear prediction in lubricated sliding contacts," *Lubrication Science*, vol. 8, no. 4, pp. 315–351, 1996.
- [8] K. Li, *Automotive engine tuning using least-square support vector machines and evolutionary optimization [Ph.D. thesis]*, University of Macau, 2011.
- [9] Z. Liu, X. Wang, L. Cui, X. Lian, and J. Xu, "Research on water bloom prediction based on least squares support vector machine," in *Proceedings of the WRI World Congress on Computer Science and Information Engineering (CSIE '09)*, pp. 764–768, April 2009.
- [10] A. J. Smola and B. Scholkopf, 2003, <http://alex.smola.org/papers/2003/SmoSch03b.pdf>.

- [11] H. Wang and D. Hu, "Comparison of SVM and LS-SVM for regression," in *Proceedings of the International Conference on Neural Networks and Brain Proceedings (ICNNB '05)*, pp. 279–283, October 2005.
- [12] C. W. Hsu and C. C. Chang, *A Practical Guide to Support Vector Classification*, 2003.
- [13] U. Çaydaş and S. Ekici, "Support vector machines models for surface roughness prediction in CNC turning of AISI 304 austenitic stainless steel," *Journal of Intelligent Manufacturing*, vol. 23, pp. 639–650, 2012.
- [14] E. Avci, "A new expert system for diagnosis of lung cancer: GDA-LS-SVM," *Journal of Medical Systems*, vol. 36, pp. 2005–2009, 2012.
- [15] E. Çomak and A. Arslan, "A biomedical decision support system using LS-SVM classifier with an efficient and new parameter regularization procedure for diagnosis of heart valve diseases," *Journal of Medical Systems*, vol. 36, pp. 549–556, 2012.
- [16] Y. Xu, X. Chen, and Q. Li, "INS/WSN-integrated navigation utilizing LS-SVM and H_∞ filtering," *Mathematical Problems in Engineering*, vol. 2012, Article ID 707326, 19 pages, 2012.
- [17] C. Cattani, S. Chen, and G. Aldashev, "Information and modeling in complexity," *Mathematical Problems in Engineering*, vol. 2012, Article ID 868413, 3 pages, 2012.
- [18] S. Chen, Y. Zheng, C. Cattani, and W. Wang, "Modeling of biological intelligence for SCM system optimization," *Computational and Mathematical Methods in Medicine*, vol. 2012, Article ID 769702, 10 pages, 2012.
- [19] P. Lu, S. Chen, and Y. Zheng, "Artificial intelligence in civilengineering," *Mathematical Problems in Engineering*. In press.

Review Article

Artificial Intelligence in Civil Engineering

Pengzhen Lu,¹ Shengyong Chen,² and Yujun Zheng²

¹ Faculty of Civil Engineering & Architecture, Zhejiang University of Technology, Hangzhou 310023, China

² College of Computer Science & Technology, Zhejiang University of Technology, Hangzhou 310023, China

Correspondence should be addressed to Shengyong Chen, sy@ieee.org

Received 3 October 2012; Accepted 5 November 2012

Academic Editor: Fei Kang

Copyright © 2012 Pengzhen Lu et al. This is an open access article distributed under the Creative Commons Attribution License, which permits unrestricted use, distribution, and reproduction in any medium, provided the original work is properly cited.

Artificial intelligence is a branch of computer science, involved in the research, design, and application of intelligent computer. Traditional methods for modeling and optimizing complex structure systems require huge amounts of computing resources, and artificial-intelligence-based solutions can often provide valuable alternatives for efficiently solving problems in the civil engineering. This paper summarizes recently developed methods and theories in the developing direction for applications of artificial intelligence in civil engineering, including evolutionary computation, neural networks, fuzzy systems, expert system, reasoning, classification, and learning, as well as others like chaos theory, cuckoo search, firefly algorithm, knowledge-based engineering, and simulated annealing. The main research trends are also pointed out in the end. The paper provides an overview of the advances of artificial intelligence applied in civil engineering.

1. Introduction

The research of artificial intelligence has been developed since 1956, when the term “Artificial Intelligence, AI” was used at the meeting hold in Dartmouth College. Artificial intelligence, a comprehensive discipline, was developed based on the interaction of several kinds of disciplines, such as computer science, cybernetics, information theory, psychology, linguistics, and neurophysiology. Artificial intelligence is a branch of computer science, involved in the research, design and application of intelligent computer [1, 2].

The goal of this field is to explore how to imitate and execute some of the intelligent function of human brain, so that people can develop technology products and establish relevant theories [3]. The first step: artificial intelligence’s rise and fall in the 1950s. The second step: as the expert system emerging, a new upsurge of the research of artificial intelligence appeared from the end of 1960s to the 1970s. The third step: in the 1980s, artificial intelligence made a great progress with the development of the fifth generation computer.

The fourth step: in the 1990s, there is a new upsurge of the research of artificial intelligence: with the development of network technology, especially the international internet technology, artificial intelligence research by a single intelligent agent began to turn to the study of distributed artificial intelligence based on network environment. People study not only the same goal-based distributed problem solving, but also the multiply intelligent agents problem solving, which made the artificial intelligence more practical. Additionally, a thriving scene of artificial neural network research and application emerged and it had been deep into all areas of life as the Hopfield multilayer neural network model put forward. The main theories and methods of artificial intelligence are summarized as symbolism, behaviorism, and connectionism approach [4]. Since the appearance of artificial intelligence AI in the 1950s, a lot of hopes and dreams about it have been generated. Now we will elaborate the latest progress of artificial intelligence technology in all aspects of civil engineering and their relationship as follows.

The objective of this paper is to present highlights of references pertaining to artificial intelligence in civil engineering that have been published prior to 2012. Such papers will complement previously published literature survey articles that (1) would provide the theoretical foundation or may play an important role in the development of artificial intelligence in civil engineering; (2) would represent the levels and hotspots of current research of artificial intelligence in civil engineering; and (3) would facilitate continued research efforts. The rest of the paper is synthesized as follows: Section 2 describes artificial intelligence in civil engineering, Section 3 depicts reasoning classification, and learning of artificial intelligence in civil engineering, Section 4 introduces some other theories and methods. Finally we discuss some future trends in Section 5 and conclude in Section 6.

2. Intelligent Optimization Methods in Civil Engineering

Artificial intelligence is a science on the research and application of the law of the activities of human intelligence. It has been a far-reaching cross-frontier subject, after the 50 years' advancement. Nowadays, this technology is applied in many fields such as expert system, knowledge base system, intelligent database system, and intelligent robot system. Expert system is the earliest and most extensive, the most active and most fruitful area, which was named as "the knowledge management and decision-making technology of the 21 century." In the field of civil engineering, many problems, especially in engineering design, construction management, and program decision-making, were influenced by many uncertainties which could be solved not only in need of mathematics, physics, and mechanics calculations but also depend on the experience of practitioners. This knowledge and experience are illogically incomplete and imprecise, and they cannot be handled by traditional procedures. However, artificial intelligence has its own superiority. It can solve complex problems to the levels of experts by means of imitate experts. All in all, artificial intelligence has a broad application prospects in the practice of civil engineering.

Adam and Smith [5] presented progress in the field of adaptive civil-engineering structures. Self-diagnosis, multi-objective shape control, and reinforcement-learning processes were implemented within a control framework on an active tensegrity structure. Among artificial intelligence-based computational techniques, adaptive neuro-fuzzy inference systems were particularly suitable for modelling complex systems with known input-output data sets. Such systems can be efficient in modelling nonlinear, complex, and ambiguous behaviour of cement-based materials undergoing single, dual, or multiple damage factors

of different forms in civil engineering. Bassuoni and Nehdi [6] developed neuro-fuzzy based prediction of the durability of self-consolidating concrete to various sodium sulfate exposure regimes. Prasad et al. [7] presented an artificial neural network (ANN) to predict a 28-day compressive strength of a normal and high strength self-compacting concrete (SCC) and high performance concrete (HPC) with high volume fly ash. Lee et al. [8] used an artificial intelligence technique of back-propagation neural networks to assess the slope failure. The numerical results demonstrate the effectiveness of artificial neural networks in the evaluation of slope failure potential. Shaheen et al. [9] presented a proposed methodology for extracting the information from experts to develop the fuzzy expert system rules, and a tunneling case study was used to illustrate the features of the integrated system. Das et al. [10] described two artificial intelligence techniques for prediction of maximum dry density (MDD) and unconfined compressive strength (UCS) of cement stabilized soil. Forcael et al. [11] presented the results of a study that incorporates computer simulations in teaching linear scheduling concepts and techniques, in a civil engineering course "Construction Planning and Scheduling." To assess the effect of incorporating computer simulation in teaching linear scheduling, the students' evaluations and answers to the questionnaire were statistically compared. Krcaronemen and Kouba [12] proposed a methodology for designing ontology-backed software applications that make the ontology possible to evolve while being exploited by one or more applications at the same time. The methodology relies on a contract between the ontology and the application that is formally expressed in terms of integrity constraints. In addition, a reference Java implementation of the methodology and the proof-of-concept application in the civil engineering domain was introduced.

Due to a lot of uncertain factors, complicated influence factors in civil engineering, each project has its individual character and generality; function of expert system in the special links and cases is a notable effect. Over the past 20 years, in the civil engineering field, development and application of the expert system have made a lot of achievements, mainly used in project evaluation, diagnosis, decision-making and prediction, building design and optimization, the project management construction technology, road and bridge health detection and some special field, and so forth.

2.1. Evolutionary Computation

Evolutionary computation (EC) is a subfield of artificial intelligence, which uses iterative process (often inspired by biological mechanisms of evolution) to evolve a population of solution to a desired end. EC has been applied to the domain of civil engineering for several decades, mainly served as an effective method for solving complex optimization problems.

2.1.1. Genetic Algorithms

Genetic algorithms (GAs) [13] are one of the famous evolutionary algorithms which simulate the Darwinian principle of evolution and the survival of the fittest in optimization. It has extensive application value in the civil engineering field, but in many aspects it needs to be further studied and improved.

According to the research progress above the genetic algorithm in civil engineering, due to genetic algorithm developed rapidly, so there are still a lot of improvement measures not included in this paper. In general, the improvement of genetic algorithm approaches include change the genetic algorithm component or the use of technology, the hybrid genetic

algorithm, the dynamic adaptive technology, using nonstandard genetic operators, and the parallel genetic algorithm.

In recent years, the improvement of the genetic algorithm introduced many new mathematical tools and absorbed civil engineering as the latest achievement of applications. We can expect, along with the computer technology, the genetic algorithm in civil engineering application will be more general and more effective.

Senouci and Al-Derham [14] presented a genetic-algorithm-based multiobjective optimization model for the scheduling of linear construction projects. The model allows construction planners to generate and evaluate optimal/near-optimal construction scheduling plans that minimize both project time and cost.

2.1.2. Artificial Immune Systems

Provoked by the theoretical immunology, observed immune functions, principles, and models, artificial immune system (AIS) stimulates the adaptive immune system of a living creature to unravel the various complexities in real-world engineering optimization problems [15]. In this technique, a combination of the genetic algorithm and the least-squares method was used to find feasible structures and the appropriate constants for those structures. The new approach overcomes the shortcomings of the traditional and artificial neural network-based methods presented in the literature for the analysis of civil engineering systems.

Dessalegne and Nicklow employed an artificial life algorithm, derived from the artificial life paradigm [16]. The resulting multi-reservoir management model was successfully applied to a portion of the Illinois River Waterway.

According to characteristics of diversity of the immune system, a variety of immune algorithms have proposed by realization form. But since the immune system characteristics of the application exploration is still in its initial stage, the algorithm design has many aspects for improvement, such as the realization of the algorithm, parameter selection, the theory discussion, and the immune system in civil engineering application, still needing further development.

2.1.3. Genetic Programming

Genetic programming is a model of programming which uses the ideas of biological evolution to handle complex optimization problems [17]. Aminian et al. [18] presented a new empirical model to estimate the base shear of plane steel structures subjected to earthquake load using a hybrid method integrating genetic programming (GP) and simulated annealing (SA), called GP/SA. Hsie et al. [19] proposed a novel approach, called "LMGOT," that integrates two optimization techniques: the Levenberg Marquardt (LM) Method and the genetic operation tree (GOT). The GOT borrows the concept from the genetic algorithm, a famous algorithm for solving discrete optimization problems, to generate operation trees (OTs), which represent the structures of the formulas. Results show a concise formula for predicting the length of pavement transverse cracking and indicate that the LMGOT was an efficient approach to building an accurate crack model.

Cevik and Guzelbey [20] presented two plate strength formulations applicable to metals with nonlinear stress-strain curves, such as aluminum and stainless steel alloys, obtained by neural networks and Genetic Programming. The proposed formulations enable

determination of the buckling strength of rectangular plates in terms of Ramberg-Osgood parameters.

2.1.4. Other Evolutionary Algorithms

Caicedo and Yun [21] proposed an evolutionary algorithm that was able to identify both global and local minima. The proposed methodology was validated with two numerical examples.

Khalafallah and Abdel-Raheem [22] developed a novel evolutionary algorithm named Electimize and applied it to solve a hard optimization problem in construction engineering. The algorithm mimics the behavior of electrons flowing, through electric circuit branches with the least electric resistance. On the test problem, solutions are represented by electric wires and are evaluated on two levels: a global level, using the objective function, and a local level, evaluating the potential of each generated value for every decision variable. The experimental results show that Electimize has good ability to search the solution space extensively, while converging toward optimality.

Ahangar-Asr et al. [23] presented a new approach, based on evolutionary polynomial regression (EPR), for analysis of stability of soil and rock slopes. Rezanian et al. presented another method based on EPR for capturing nonlinear interaction between various parameters of civil engineering systems [24].

2.2. Swarm Intelligence

Metaheuristics based on swarm intelligence, which simulates a population of simple individuals evolving their solutions by interacting with one another and with the environment, have shown promising performance on many difficult problems and have become a very active research area in recent years.

2.2.1. Particle Swarm Optimization

Particle swarm optimization (PSO) is another population-based global optimization technique that enables a number of individual solutions, called particles, to move through a hyper dimensional search space to search for the optimum. Each particle has a position vector and a velocity vector, which are adjusted at iterations by learning from a local best found by the particle itself and a current global best found by the whole swarm. Modeling a system where multiple candidate solution coexists and collaborate simultaneously, PSO approaches embed problem-solving attempts in a social network and are suitable in nature for the optimization of very complex systems, and thus have been successfully applied. Solihin et al. [25] proposed a novel method for tuning PID controller of automatic gantry crane control using particle swarm optimization (PSO). This work presents in detail how to apply PSO method in finding the optimal PID gains of gantry crane system in the fashion of min-max optimization. The simulation results show that with proper tuning a satisfactory PID control performance can be achieved to drive nonlinear plant.

To overcome disadvantage, prove mathematical model accurate, and identify parameters full, Wang et al. used the group control. PSO algorithm was used to calculate the final value of every joint point [26]. The PD control based on the gravity compensation

for concrete pump truck boom was used. Through the simulation examples analysis, the conclusion was that the method of combination PSO and gravity compensation was suitable for concrete pump truck boom control. Wang et al. [27] analyses and compares the solution performances of genetic algorithms (GA), particle swarm optimization (PSO), and ant colony algorithms (ACA) from the three aspects, respectively, convergence, speed, and complexity of algorithm. The research result shows that compared with the other two algorithms, the ACA manifests its superiority for better convergence, satisfactory speed, and relatively small algorithm complexity, which were very suitable for solving the problems of sewer optimal design. Shayeghi et al. [28] give the application of the Particle Swarm Optimization (PSO) to design and optimize the parameters of the Tuned Mass Damper (TMD) control scheme for achieving the best results in the reduction of the building response under earthquake excitations. The analysis results reveals that the designed PSO based TMD controller had an excellent capability in reduction of the seismically excited example building. Ali and Ramaswamy [29] presented an optimal fuzzy logic control algorithm for vibration mitigation of buildings using magneto-rheological (MR) dampers. A microgenetic algorithm (μ -GA) and a particle swarm optimization (PSO) were used to optimize the FLC parameters. The present approach provided a better vibration control for structures under earthquake excitations. Filiberto et al. [30] proposed a method that combines the methaheuristic Particle Swarm Optimization (PSO) with the Rough Set Theory (RST) to carry out the prediction of the resistant capacity of connectors (Q) in the branch of civil engineering. At the same time, the k-NN method was used to calculate this value. Experimental results show that the algorithm k-NN, PSO, and the method for calculating the weight of the attributes constitute an effective technique for the function approximation problem. Schmidt [31] presented the synthesis of an active control system using a modified particle swarm optimization method. The system's controller design was analyzed as a minimization of the building stories' acceleration. The proposed fitness function was computationally efficient and incorporates the constraints on the system's stability and the maximum output of actuators.

Zheng and Liu [32] analyzed the various impact factors of project progress, and developed the mathematical model of schedule control based on the quantitative description of the relationship between impact factors with the schedule control of the project. In order to improve the speed and accuracy of solving, authors used the particle swarm algorithm to solve the above model. The empirical research showed that the method is effective in the field of project schedule control.

To calculate appropriate network coefficients, Tsai [33] designed a center-unified particle swarm optimization (CUPSO) approach, composed of a center particle and global and local variants, which is quite effective for optimization tasks. Marinaki et al. [34] proposed particle swarm optimization (PSO) for the calculation of the free parameters in active control systems and tested. The usage of PSO with a combination of continuous and discrete variables for the optimal design of the controller was proposed. Numerical applications on smart piezoelectric beams were presented. Nejadfard et al. [35] introduced a novel approach based on multi-robot cooperation for inspection and repair of dome structures. The simulation results prove that there exists a stable path to fully sweep the surface of a dome. The experimental results on a small scale prototype validate these findings. Raju et al. [36] represented the development of dynamic model of flexible beam structure using finite difference (FD) method. The simulated model was validated by comparing the resonance modes with the theoretical values. A nature inspired intelligence method, the Particle Swarm Optimization (PSO), was used for the vibration control of the beam and

the results were compared with genetic algorithm (GA) approach. The numerical simulation shows that sufficient vibration suppression can be achieved by means of these methods.

2.2.2. Ant Colony Optimization

Ant colony optimization (ACO) algorithm mimics the behavior of real ants living in colonies that communicate with each other using pheromones in order to accomplish complex tasks such as establishing a shortest path from the nest to food sources. In a very recent work, Moncayo-Martinez and Zhang studied the multi-objective ACO for supply chain optimization. They considered the problem for minimizing the total cost while keeping the total lead-times within required delivery due dates. They formulated the design problem into an ACO optimization form, and implemented a number of ant colonies in a sequence to explore the solution space and search for successively better non-dominated set of supply chain designs. Ant colony algorithm is proposed as a new bionic heuristic optimization algorithm. Although just a few years and, it is solving many complex combination optimization problems and showed obvious advantage.

Kaveh and Talatahari [37] presented an improved ant colony optimization (IACO) for constrained engineering design problems, and applied to optimal design of different engineering problems. Doerner et al. [38] introduced Pareto Ant Colony Optimization as an especially effective meta-heuristic for solving the portfolio selection problem and compares its performance to other heuristic approaches by means of computational experiments with random instances. Furthermore, authors provided a numerical example based on real world data.

Although ant colony algorithm has strong robustness, general parallel search and other advantages, but there is also search for a long time, in the algorithm model convergence and theoretical basis, and so forth have a lot of work remains to be further in-depth study. In addition, according combining optimization method of the ant colony algorithm and genetic algorithm and immune algorithm, it is effective way to improve the performance of ant colony algorithm. With the deepening of the research on ant colony algorithm, it will get more extensive application.

2.3. Neural Networks

Flood [39] applied artificial neural networks to stimulate interest within the civil engineering research community for developing the next generation results show that this approach requires the design of some very sophisticated genetic coding mechanisms in order to develop the required higher-order network structures and utilize development mechanisms observed in nature such as growth, self-organization, and multi-stage objective functions. Sharma and Das [40] used an artificial neural network (ANN) as a tool for backcalculation. Bendaña et al. [41] presents a fuzzy-logic-based system for selecting contractors. As part of the validation process, a neural network was developed to prove that the fuzzy-control tool has a behavior that can be recognized by a neural network. Bilgil and Altun [42] introduced an efficient approach to estimate the friction coefficient via an artificial neural network, which was a promising computational tool in civil engineering. The estimated value of the friction coefficient was used in Manning Equation to predict the open channel flows in order to carry out a comparison between the proposed neural networks based approach and the conventional ones. Results show that the proposed approach was in good

agreement with the experimental results when compared to the conventional ones. Z. Q. Gu, and S. O. Gu [43] presented numerical studies of multiple degrees-of-freedom (MDOF) structural vibration control based on the approach of the back propagation algorithm to the DRNN control method. Research results show that the structural vibration responses of linear and nonlinear MDOF structures are reduced by between 78% and 86%, and between 52% and 80%, respectively, when they are subjected to El Centro, Kobe, Hachinohe, and Northridge earthquake processes. Laflamme and Connor [44] proposed an adaptive neural network composed of Gaussian radial functions for mapping the behavior of civil structures controlled with magnetorheological dampers. The proposed controller is simulated using three types of earthquakes. Lee et al. [45] used an artificial intelligence technique of back-propagation neural networks to assess the slope failure. The numerical results demonstrate the effectiveness of artificial neural networks in the evaluation of slope failure potential based on five major factors, such as the slope gradient angle, the slope height, the cumulative precipitation, daily rainfall, and strength of materials.

Xiao and Amirkhania [46] develop a series of ANN models to simulate the resilient modulus of rubberized mixtures (ambient and cryogenic rubbers) using seven input variables including material components such as rubber and RAP percentages as well as the rheological properties of modified binders (i.e., viscosity, $G^*\sin \delta$, stiffness, and m -values). The results indicated that ANN-based models were more effective than the regression models and can easily be implemented in a spreadsheet, thus making it easy to apply.

Flood [39] stimulated interest within the civil engineering research community for developing the next generation of applied artificial neural networks. In particular, it identifies what the next generation of these devices needs to achieve, and provides direction in terms of how their development may proceed.

Benchmark and Narasimhan [47] presented a direct adaptive control scheme for the active control of the nonlinear highway bridge benchmark. The control force was calculated using a single hidden layer nonlinearly parameterized neural network in conjunction with a proportional-derivative type controller. The results show that the proposed controller scheme can achieve good response reductions in the structure, without the need for the exact description of the nonlinearities, or extensive structural system information.

Zhang and Haghighat [48] described the development of an Artificial Neural Network based Heat Convection (ANN-HC) algorithm to predict local average Nusselt Numbers along the duct surfaces. It was shown that the method can very well simulate the interactions between an ETAHE and its environment. Yveras [49] explore the possibility of using a tool based on artificial intelligence and real-life data. The results of this study indicate that this was an approach that could usefully be developed and investigated further. The tool managed to predict smell 100%, mold 76%, and rot 92% correctly. Rahman et al. [50] outlined the application of the multi-layer perceptron artificial neural network (ANN), ordinary kriging (OK), and inverse distance weighting (IDW) models in the estimation of local scour depth around bridge piers. It was shown that the artificial neural network model predicts local scour depth more accurately than the kriging and inverse distance weighting models. It was found that the ANN with two hidden layers was the optimum model to predict local scour depth.

Based on the BP neural network, Wang et al. [51] set up the model of cost estimation of highway engineering. It shows the promising perspective of BP Neural Network in cost estimate of construction engineering. Parhi and Dash [52] analyses the dynamic behavior of a beam structure containing multiple transverse cracks using neural network

controller. Results from neural controller have been presented for comparison with the output from theoretical, finite-element, and experimental analysis. From the evaluation of the performance of the neural network controller it was observed that the developed method can be used as a crack diagnostic tool in the domain of dynamically vibrating structures. Gui et al. [53] summarizes the structural optimization applications in civil engineering design and development of the situation based on the characteristics of the bridge structure design process was proposed for the bridge project to the genetic algorithm, neural network, expert system technology as the basis for combining automated design and optimization of structural design of the system. Alacali et al. [54] presented an application of Neural Network (NN) simulation in civil engineering science. The approach adapted in this study was shown to be capable of providing accurate estimates of lateral confinement coefficient, $K(s)$ by using the six design parameters.

Li et al. [55] presented a non-destructive, global, vibration-based damage identification method that utilizes damage pattern changes in frequency response functions (FRFs) and artificial neural networks (ANNs) to identify defects. Liu et al. [56] show possible applicability of artificial neural networks (ANN) to predict the compressive strength. The results showed that ANN is a feasible tool for predicting compressive strength. Cheng et al. [57] developed an evolutionary fuzzy hybrid neural network (EFHNN) to enhance the effectiveness of assessing subcontractor performance in the construction industry. The developed EFHNN combines neural networks (NN) and high order neural networks (HONN) into a hybrid neural network (HNN), which acts as the major inference engine and operates with alternating linear and nonlinear NN layer connections. Cachim [58] used artificial neural networks for predicting the temperatures in timber under fire loading. The artificial neural network model had been trained and tested using available numerical results obtained using design methods of Eurocode 5 for the calculation of temperatures in timber under fire loading. The training and testing results in the neural network model had shown that neural networks can accurately calculate the temperature in timber members subjected to fire. Arangio and Beck [59] used a historical overview of the probability logic approach and its application in the field of neural network models, the existing literature was revisited and reorganized according to the enunciated four levels. Then, this framework was applied to develop a two-step strategy for the assessment of the integrity of a long-suspension bridge under ambient vibrations.

As an analysis and solve complex problems, especially in the nonlinear problem, neural network is an important tool, and the neural network potential is realized more and more in engineering technology and information technology by the researchers. The neural network will be very broad used in the civil engineering field application prospect. The neural network still belongs to the new cross science, itself not perfect. As for neural network structure and algorithm, its improvement research has been in progress. And its application studies, there are still some problems, especially in the combination method of the neural network, fuzzy logic genetic algorithm, and expert system, and it will be a very attractive research field.

2.4. Fuzzy Systems

Zarandi et al. [60] develop fuzzy polynomial neural networks (FPNN) to predict the compressive strength of concrete. The results show that FPNN-Type1 has strong potential as a feasible tool for prediction of the compressive strength of concrete mix-design.

Hossain et al. presented an investigation into the comparative performance of intelligent system identification and control algorithms within the framework of an active vibration control (AVC) system [61]. A comparative performance of the algorithms in implementing system identification and corresponding AVC system using GAs and ANFIS is presented and discussed through a set of experiments.

Cheng et al. [62] developed an evolutionary fuzzy neural inference system (EFNIS) to imitate the decision-making processes in the human brain in order to facilitate geotechnical expert decision making.

Sobhani and Ramezani pour [63] developed a soft computing system to estimate the service life of reinforced concrete bridge deck as one of the most important issues in the civil engineering. The proposed system utilizes four fuzzy interfaces to quantify the exposure condition, required cover thickness, corrosion current density, and pitting corrosion ratio. The results showed that the proposed system could effectively predict the service life; however, it estimated longer service life in comparison with the probabilistic method.

Guo et al. [64] proposed a fuzzy control strategy based on a neural network forecasting model of the building structure with MR dampers, in which a neural network forecasting model is developed to predict dynamic responses of the system with MR dampers and a fuzzy controller is then designed to determine control currents of MR dampers. Choi et al. [65] investigated the applicability of the magnetorheological (MR) damper-based smart passive control system with the electromagnetic induction (EMI) part to the seismic protection of base-isolated building structures with nonlinear isolation systems such as friction pendulum bearings and lead-rubber bearings. Omurlu et al. [66] introduced the application of cluster control on viaduct roads composed of flat parts. Analysis of the performance of cluster control along with the individual effects of the controller parameters on system frequency response is discussed and presented. Guclu and Yazici [67] designed fuzzy logic and PD controllers for a multi-degree-of freedom structure with active tuned mass damper (ATMD) to suppress earthquake-induced vibrations. Fuzzy logic controller (FLC) was preferred because of its robust character, superior performance and heuristic knowledge use effectively and easily in active control. The results of the simulations show a good performance by the fuzzy logic controllers for different loads and the earthquakes. Ozbulut and Hurlbaas [68] proposed a neuro-fuzzy model of NiTi shape memory alloy (SMA) wires that was capable of capturing behavior of superelastic SMAs at different temperatures and at various loading rates while remaining simple enough to realize numerical simulations. It was shown that SMA damping elements can effectively decrease peak deck displacement and the relative displacement between piers and superstructure in an isolated bridge while recovering all the deformations to their original position. Shaheen et al. [69] demonstrates how fuzzy expert systems can be integrated within discrete event simulation models to enhance their modeling and predictive capabilities for construction engineering applications. A proposed methodology was presented for extracting the information from experts to develop the fuzzy expert system rules. Chen et al. [70] examines the feasibility of applying adaptive fuzzy sliding mode control (AFSMC) strategies to reduce the dynamic responses of bridges constructed using a lead rubber bearing (LRB) isolation hybrid protective system. The results demonstrate the viability of the presented methods. The attractive control strategy derived there-from was applied to seismically excited bridges using LRB isolation.

Bianchini and Bandini [71] propose a neuro-fuzzy model to predict the performance of flexible pavements using the parameters routinely collected by agencies to characterize the condition of an existing pavement. The results of the neuro-fuzzy model were superior to those of the linear regression model in terms of accuracy in the approximation. The proposed

neuro-fuzzy model showed good generalization capability, and the evaluation of the model performance produced satisfactory results, demonstrating the efficiency and potential of these new mathematical modeling techniques. Ozbulut and Hurlebaus [72] propose two fuzzy logic controllers (FLCs) for operating control force of piezoelectric friction dampers used for seismic protection of base-isolated buildings against various types of earthquake excitations. Results for several historical ground motions show that developed fuzzy logic controllers can effectively reduce isolation system deformations without the loss of potential advantages of seismic base isolation. Meng et al. [73] used a new fuzzy control arithmetic based on mode identification in semi-active control is put forward. Different fuzzy control strategy is applied. Nieto-Morote and Ruz-Vila [74] presented a risk assessment methodology based on the Fuzzy Sets Theory, which is an effective tool to deal with subjective judgment, and on the Analytic Hierarchy Process (AHP), which was used to structure a large number of risks. The proposed methodology incorporates knowledge and experience acquired from many experts, since they carry out the risks identification and their structuring, and also the subjective judgments of the parameters which are considered to assess the overall risk factor. Rosko [75] dealt with the structural topology optimization with fuzzy constraint. Presented study was applicable in engineering and civil engineering. Example demonstrates the presented theory. Gonzalez-Jorge et al. [76] proposed a methodology for extracting information about the presence of biological crusts on concrete structures using terrestrial laser scanners. The goal of this methodology was to integrate all the available information, range, intensity and color, into the extraction work-flow. The methodology is based primarily on two algorithms.

Yakut and Alli [77] designed neural based fuzzy sliding mode control algorithm by putting advantageous specifications of sliding mode control and artificial intelligence techniques and applied to 8 storey sample building with active tendon. The obtained results also show that the controller provides quite successful control under earthquake effects having different characteristics.

Mahjoobi et al. [78] presented alternative hindcast models based on Artificial Neural Networks (ANNs), Fuzzy Inference System (FIS), and Adaptive-Network-based Fuzzy Inference System (ANFIS). Wind speed, wind direction, fetch length, and wind duration were used as input variables, while significant wave height, peak spectral period, and mean wave direction were the output parameters. Results indicated that error statistics of soft computing models were similar, while ANFIS models were marginally more accurate than FIS and ANNs models.

According to above overview, research of the fuzzy system approximation theory is more than 10 years. From the initial approximation existence theorem to all kinds of sufficient conditions for the establishment of the necessary conditions, mechanism of fuzzy system approximation continuous function was revealed. The number of fuzzy rules is the universal approximation of the essence for fuzzy system. The fuzzy approximation theory has not been developed to the point of perfect, to be research work includes the following several aspects: fuzzy system approximation error analysis; the effective fuzzy system structure algorithm of suitable for the engineering application.

2.5. Expert System

An expert system is relying on human experts existing knowledge based on set up knowledge system; the expert system develops the earliest, the most effective in the artificial

intelligence research field. The expert system is widely used in road and bridge, construction engineering, geotechnical engineering, underground engineering, disaster prevention project, material engineering, geological exploration and petroleum chemical industry, and so forth. An expert system is in a particular area, and it has the corresponding knowledge and it has the corresponding knowledge and experience in the programming system. The application of artificial intelligence simulates human experts in solving the problem of the thinking process in the field and reaches or approaches the level of experts.

Golroo and Tighe [79] develop performance models for PCP for the first time by using an integrated Markov chain technique (combination of homogenous and non-homogenous techniques) through incorporation of expert knowledge. Both deterministic and stochastic approaches are applied to build up Markov models by using expected values and the Latin hypercube simulation technique, respectively. Grau et al. [80] summarize research addressing the question of what, when, and how much on-site design is appropriate to favorably influence project performance. On the basis of the analysis of data representative of 115 capital facility projects with \$9 billion in total installed costs, a database expert planning system was investigated to reliably compute the specific design activities that, when on-site executed, increase the chances for project success. In the civil engineering, the determination of concrete mix design is so difficult and usually results in imprecision. Fuzzy logic is a way to represent a sort of uncertainty which is understandable for human. Neshat and Adeli [81] is to design a Fuzzy Expert System to determine the concrete mix design. Sariyar and Ural [82] discussed soil-structure interaction (SSI) by using expert systems, namely, neural network (NN) approaches. This method provides a new point of view for evaluations of SSI and land use. Artificial neural networks (ANNs) have been applied to many civil engineering problems with some degree of success. Gupta et al. [83] used ANN as an attempt to obtain more accurate concrete strength prediction based on parameters like concrete mix design, size and shape of specimen, curing technique and period, environmental conditions, and so forth.

Chau and Albermani [84] describe a coupled knowledge-based system (KBS) for the design of liquid-retaining structures, which can handle both the symbolic knowledge processing based on engineering heuristics in the preliminary synthesis stage and the extensive numerical crunching involved in the detailed analysis stage. The prototype system is developed by employing blackboard architecture and a commercial shell VISUAL RULE STUDIO. Zain et al. [85] describes a prototype expert system called HPCMIX that provides proportion of trial mix of High Performance Concrete (HPC) and recommendations on mix adjustment. The knowledge was acquired from various textual sources and human experts. The system was developed using hybrid knowledge representation technique. Kazaz [86] considered the application of expert system as a sub-branch of the artificial intelligence systems. For overcoming this bottleneck as well as to enhance the knowledge of the supervisory staff, an expert-system on the fracture mechanics of concrete had been developed.

Expert system technology provides a new opportunity for organizing and system atising the available knowledge and experience in the structural selection domain. With the application of artificial intelligence method, the expert system in civil engineering application is also expanding. A civil engineering activity place will have intelligence technology including the application of expert system. The expert system will become construction management tools and assistant in civil engineering intelligent for 21st century humans.

3. Reasoning, Classification, and Learning

Göktepe et al. [87] presented the applicability of a fuzzy rule-based system for choosing swelling/shrinkage factors affecting the precision of earthwork optimization. This approach may assist in any highway alignment procedure to handle cut and fill volumes more accurately. Zanaganah et al. [88] developed a hybrid genetic algorithm-adaptive network-based FIS (GA-ANFIS) model in which both clustering and rule base parameters were simultaneously optimized using GAs and artificial neural nets (ANNs). Results indicate that GA-ANFIS model is superior to ANFIS and Shore Protection Manual (SPM) methods in terms of their prediction accuracy. Bianchini and Bandini [89] proposed a neuro-fuzzy model to predict the performance of flexible pavements using the parameters routinely collected by agencies to characterize the condition of an existing pavement. The proposed neuro-fuzzy model showed good generalization capability, and the evaluation of the model performance produced satisfactory results, demonstrating the efficiency and potential of these new mathematical modeling techniques.

Eliseo et al. [90] presented a case study showing the potential of the ontology to reasoning about temporal changes in architectural space. This work shows a domain ontology with temporal relations to record changes in a building throughout time and shows how this ontology can be used as a support for learning in History of Architecture class to motivate students. Lee and Mita [91] proposed a moving sensor agent robot with accelerometers and a laser range finder LRF. To achieve this purpose the robot frame was modified to move down to the ground and to provide enough rigidity to obtain good data.

El-Sawalhi et al. introduced an evolved hybrid genetic algorithm and neural network (GNN) model [92]. The results revealed that there was a satisfactory relationship between the contractor attributes and the corresponding performance in terms of contractor's deviation from the client objectives. Lee and Bernold [93] presented the result of an effort to test the functionality of ubiquitous communication applications over a wireless fidelity infranet installed on an unfriendly construction site. Its value was the lessons learned and the outcome of a variety of field tests with the prototype system. Kovacevic et al. [94] developed a question-and-answer (Q-A) system (reported elsewhere). To support this system, authors developed an automated crawler that permits the establishment of a bank of relevant pages, and adopted to the needs of this particular industry-user community. O'Brien et al. [95] describes an architecture informed by a working first generation prototype. Details of the prototype, lessons learned, and specific advancements were detailed. Future commercial implementation of the architecture will make construction-specific visions for ubiquitous computing possible by enabling flexible and robust discovery and use of data in an ad hoc manner. Luna et al. [96] developed a geographic information system (GIS) learning tool using a series of learning objects. These learning objects were designed to support supplemental instruction in GIS and were integrated seamlessly into the course curriculum. Singh et al. [97] propose the use of a novel image-based machine-learning (IBML) approach to reduce the number of user interactions required to identify promising calibration solutions involving spatially distributed parameter fields. The IBML approach was tested and demonstrated on a groundwater calibration problem and was shown to lead to significant improvements, reducing the amount of user interaction by as much as half without compromising the solution quality of the IMOGA.

Civil engineering students need to learn how to deliver practical sustainable solutions for engineering projects. Thompson [98] demonstrated that applied assessment and award techniques can be usefully used as teaching tools. Overall the case study work certainly

appears to fulfill the main learning objective of giving students an understanding of a breadth of practical solutions in sustainability. Obonyo [99] describe the deployment of an e-learning environment for construction courses based on enhancing virtual computing technologies using agent-based techniques. The proposed agent-oriented methodology and resulting application organizes construction knowledge into a structure that enables the students to undertake more self-directed, systematic and scientific exploration. Zhu et al. [100] explore the effectiveness of using simulation as a tool for enhancing classroom learning in the Civil Engineering Department of the University of Minnesota at Twin Cities. Findings in this research could have significant implications for future practice of simulation-based teaching strategy. Das et al. [101] describes two artificial intelligence techniques for prediction of maximum dry density (MDD) and unconfined compressive strength (UCS) of cement stabilized soil. Newson and Delatte [102] described the differences between two of the most familiar types: "case-histories" and "case-studies." These methods are presented using the Kansas City Hyatt Regency walkway collapse as an exemplar.

4. Others

4.1. Chaos Theory

Lu et al. [103] develop conceptual frameworks that approach the current model methodologies and applications from the theoretical perspective provided by chaos theory. Though the proposed applications as well as the illustrative example are weighted towards phenomena suggesting chaos, there was no intent here to make a case for the relative importance between chaotic and traditional models. Authors do not propose to replace current approaches to theory generation by one based on chaos theory, rather authors suggest extending current theory by introducing a chaos layer. Kardashov et al. [104] proposed a unit analytical approach that could be associated with real ECG and pressure pulses signal processing. Results shows that analytical dynamic models coupled with the available signal processing methods could be used for describing the self-organization and chaos degree in the heartbeats propagation and pressure pulses in ventricular at ejection phase. Enterprise Architecture (EA) models capture the fundamental elements of organizations and their relationships to serve documentation, analysis and planning purposes. As the elements and their relationships change over time, EA planning becomes increasingly complex. An analysis of existing methods shows that the complexity of dynamics is not sufficiently addressed.

4.2. Cuckoo Search

Durgun and Yildiz [105] introduced a new optimization algorithm, called the Cuckoo Search (CS) algorithm, for solving structural design optimization problems. This research was the first application of the CS to the shape design optimization problems in the literature. The CS algorithm is applied to the structural design optimization of a vehicle component to illustrate how the present approach can be applied for solving structural design problems. Results show the ability of the CS to find better optimal structural design. A new robust optimization algorithm, which can be regarded as a modification of the recently developed cuckoo search by Walton et al. [106], was presented. The modification involves the addition of information exchange between the top eggs, or the best solutions. In particular the modified cuckoo search shows a high convergence rate to the true global minimum even at high numbers

of dimensions. Li and Yin used an orthogonal learning cuckoo search algorithm used to estimate the parameters of chaotic systems [107]. This algorithm can combine the stochastic exploration of the cuckoo search and the exploitation capability of the orthogonal learning strategy. The proposed algorithm was used to estimate the parameters for these two systems.

4.3. Firefly Algorithm

Gandomi et al. [108] used a recently developed metaheuristic optimization algorithm, the Firefly Algorithm (FA), for solving mixed continuous/discrete structural optimization problems. FA mimics the social behavior of fireflies based on their flashing characteristics. The results of a trade study carried out on six classical structural optimization problems taken from literature confirm the validity of the proposed algorithm. Lukasik and Zak [109] provided an insight into the improved novel metaheuristics of the Firefly Algorithm for constrained continuous optimization tasks. Some concluding remarks on possible algorithm extensions are given, as well as some properties of the presented approach and comments on its performance in the constrained continuous optimization tasks. Xin-She [110] intend to formulate a new metaheuristic algorithm by combining L'evy flights with the search strategy via the Firefly Algorithm. Numerical studies and results suggest that the proposed L'evy-flight firefly algorithm is superior to existing metaheuristic algorithms. Implications for further research and wider applications were discussed.

4.4. Knowledge-Based Engineering

Sapuan [111] studies various work on the development of computerized material selection system. The importance of knowledge-based system ŽKBS. In the context of concurrent engineering was explained. The study of KBS in material selection in an engineering design process was described. Lovett et al. [112] describes a Knowledge Based Engineering (KBE) project currently in progress at Coventry University. The need for a methodology for KBE system development was examined, as are the differing requirements in this respect of small and large organizations. Chapman and Pinfold [113] discussed the current limitations of Computer Aided Design (CAD) tools and reports on the use of knowledge Based Engineering (KBE) in the creation of a concept development tool, to organize information flow and as an architecture for the effective implementation of rapid design solutions. These design solutions can then represent themselves in the correct form to the analysis systems. Kulon et al. developed a knowledge-based engineering (KBE) system for hot forging design using state-of-the-art technology and the Internet [114]. The benefits of a KBE approach over a traditional design process are emphasized. The aim of the proposed KBE system was to integrate the hot forging design process into a single framework for capturing knowledge and experience of design engineers.

4.5. Simulated Annealing

Mahfoud and Goldberg [115] introduced and analyzed a parallel method of simulated annealing. Borrowing from genetic algorithms, an effective combination of simulated annealing and genetic algorithms, called parallel recombinative simulated annealing, was developed. Dekkers and Aarts [116] presented a stochastic approach which was based on

the simulated annealing algorithm. The approach closely follows the formulation of the simulated annealing algorithm as originally given for discrete optimization problems. The mathematical formulation was extended to continuous optimization problems, and we prove asymptotic convergence to the set of global optima. Bouleimen and Lecocq described new simulated annealing (SA) algorithms for the resource-constrained project scheduling problem (RCPSP) and its multiple mode version (MRCPSP) [117]. The objective function considered was minimization of the makespan. Chen and Aihara [118] proposed a neural network model with transient chaos, or a transiently chaotic neural network (TCNN) as an approximation method for combinatorial optimization problems, by introducing transiently chaotic dynamics into neural networks.

4.6. Synthetic Intelligence

Prada and Paiva [119] described a model to improve the believability of groups of autonomous synthetic characters in order to promote user collaboration with such groups. This model was successfully used in the context of a collaborative game. The experiment conducted in this scenario demonstrated the positive effect that the model can have on the user's interaction experience. The development of engineered systems having properties of autonomy and intelligence had been a visionary research goal of the twentieth century. These developments inspire the proposal of a paradigm of engineered synthetic intelligence as an alternative to artificial intelligence, in which intelligence is pursued in a bottom-up way from systems of molecular and cellular elements, designed and fabricated from the molecular level and up.

5. Future Trends

We have summarized the main bio-inspired methods for SCM system design and optimization. It is deserved to note that swarm-based methods and artificial immune systems are not yet mature and thus are expected to gain more research interests. In civil engineering field, in the present situation, the research and development of artificial intelligence is only just starting, so far failing to play its proper role. The combination including Artificial intelligence technology and object-oriented and the Internet is the artificial intelligence technology the general trend of development. Artificial intelligence is in its development for civil engineering in the following aspects.

- (1) Fuzzy processing, integrated intelligent technology, intelligent emotion technology in the civil engineering.
- (2) To deepen the understanding of the problems of uncertainty and to seek appropriate reasoning mechanism is the primary task. To develop practical artificial intelligence technology, only to be developed in the field of artificial intelligence technology, and the knowledge to have a thorough grasp.
- (3) According to application requirements of civil engineering practical engineering, the research and development of artificial intelligence technology in civil engineering field were carried out continually. Many questions in civil engineering field need to used artificial intelligence technology. Due to the characteristics of civil engineering field, artificial intelligence technology was used in many areas for civil engineering field, such as civil building engineering, bridge engineering,

geotechnical engineering, underground engineering, road engineering, geological exploration and structure of health detection, and so forth.

- (4) Hybrid intelligence system and a large civil expert system research.
- (5) With the development of artificial intelligence technology, some early artificial intelligence technology need enhance and improve for knowledge, reasoning mechanism and man-machine interface optimization, and so forth.
- (6) To some related problems, many single function of artificial intelligent system integration can carry out, integrated as a comprehensive system of artificial intelligence, and expand the artificial intelligence system to solve the question ability.
- (7) Artificial intelligence technology was used in the actual application, only in the practical application of artificial intelligence technology, to test the reliability and give full play to the role of the artificial intelligence technology and to make artificial intelligence technology to get evolution and commercialize. In the commercialization of artificial intelligence technology, there are many successful examples abroad, for enterprise and socially brought considerable benefit.

6. Conclusion

This paper summarizes and introduces the intelligent technologies in civil engineering with recent research results and applications presented. All aspects of applications of the artificial intelligence technology in civil engineering were analyzed. On the basis of the above research results, prospects of the artificial intelligence technology in civil engineering field application and development trend were represented. Artificial intelligence can help inexperienced users solve engineering problems, can also help experienced users to improve the work efficiency, and also in the team through the artificial intelligence technology to share the experience of each member. Artificial intelligence technology will change with each passing day, as the computer is applied more and more popularly, and in civil engineering field will have a broad prospect.

Acknowledgments

This work was supported by the National Natural Science Foundation of China (61105073, 61173096, and 60870002), the Doctoral Fund of Ministry of Education of China (20113317110001), and Zhejiang Provincial Natural Science Foundation (R1110679).

References

- [1] Artificial intelligence, 2012, http://en.wikipedia.org/wiki/Artificial_intelligence.
- [2] Y. Kao, M. H. Chen, and Y. T. Huang, "A hybrid algorithm based on ACO and PSO for capacitated vehicle routing problems," *Mathematical Problems in Engineering*, vol. 2012, Article ID 726564, 2012.
- [3] S. Y. Chen, Y. Zheng, C. Cattani, and W. Wang, "Modeling of biological intelligence for SCM system optimization," *Computational and Mathematical Methods in Medicine*, vol. 2012, Article ID 769702, 30 pages, 2012.
- [4] History of Artificial Intelligence, 2012, http://en.wikipedia.org/wiki/History_of_artificial_intelligence.
- [5] B. Adam and I. F. C. Smith, "Active tensegrity: a control framework for an adaptive civil-engineering structure," *Computers and Structures*, vol. 86, no. 23-24, pp. 2215–2223, 2008.

- [6] M. T. Bassuoni and M. L. Nehdi, "Neuro-fuzzy based prediction of the durability of self-consolidating concrete to various sodium sulfate exposure regimes," *Computers and Concrete*, vol. 5, no. 6, pp. 573–597, 2008.
- [7] B. K. R. Prasad, H. Eskandari, and B. V. V. Reddy, "Prediction of compressive strength of SCC and HPC with high volume fly ash using ANN," *Construction and Building Materials*, vol. 23, no. 1, pp. 117–128, 2009.
- [8] T. L. Lee, H. M. Lin, and Y. P. Lu, "Assessment of highway slope failure using neural networks," *Journal of Zhejiang University: Science A*, vol. 10, no. 1, pp. 101–108, 2009.
- [9] A. A. Shaheen, A. R. Fayek, and S. M. Abourizk, "Methodology for integrating fuzzy expert systems and discrete event simulation in construction engineering," *Canadian Journal of Civil Engineering*, vol. 36, no. 9, pp. 1478–1490, 2009.
- [10] S. K. Das, P. Samui, and A. K. Sabat, "Application of artificial intelligence to maximum dry density and unconfined compressive strength of cement stabilized soil," *Geotechnical and Geological Engineering*, vol. 29, no. 3, pp. 329–342, 2011.
- [11] E. Forcael, C. R. Glagola, and V. Gonzalez, "Incorporation of computer simulations into teaching linear scheduling techniques," *Journal of Professional Issues in Engineering Education and Practice*, vol. 138, no. 1, pp. 21–30, 2012.
- [12] P. Krcaronemen and Z. Kouba, "Ontology-driven information system design," *IEEE Transactions on Systems, Man and Cybernetics C*, vol. 42, no. 3, 2012.
- [13] J. H. Holland, *Adaptation in Natural and Artificial Systems*, The University of Michigan Press, Ann Arbor, Mich, USA, 1975.
- [14] A. Senouci and H. R. Al-Derham, "Genetic algorithm-based multi-objective model for scheduling of linear construction projects," *Advances in Engineering Software*, vol. 39, no. 12, pp. 1023–1028, 2008.
- [15] J. D. Farmer, N. H. Packard, and A. S. Perelson, "The immune system, adaptation, and machine learning," *Physica D*, vol. 22, no. 1–3, pp. 187–204, 1986.
- [16] T. Dessalegne and J. W. Nicklow, "Artificial life algorithm for management of multi-reservoir river systems," *Water Resources Management*, vol. 26, no. 5, pp. 1125–1141, 2012.
- [17] W. Banzhaf, P. Nordin, R. E. Keller, and F. D. Francone, *Genetic Programming: An Introduction: On the Automatic Evolution of Computer Programs and Its Applications*, Morgan Kaufmann, 1998.
- [18] P. Aminian, M. R. Javid, A. Asghari, A. H. Gandomi, and M. A. Esmaili, "A robust predictive model for base shear of steel frame structures using a hybrid genetic programming and simulated annealing method," *Neural Computing and Applications*, vol. 20, no. 8, pp. 1321–1332, 2011.
- [19] M. Hsieh, Y. F. Ho, C. T. Lin, and I. C. Yeh, "Modeling asphalt pavement overlay transverse cracks using the genetic operation tree and Levenberg-Marquardt Method," *Expert Systems with Applications*, vol. 39, no. 5, pp. 4874–4881, 2012.
- [20] A. Cevik and I. H. Guzelbey, "A soft computing based approach for the prediction of ultimate strength of metal plates in compression," *Engineering Structures*, vol. 29, no. 3, pp. 383–394, 2007.
- [21] J. M. Caicedo and G. Yun, "A novel evolutionary algorithm for identifying multiple alternative solutions in model updating," *Structural Health Monitoring—An International Journal*, vol. 10, no. 5, pp. 491–501, 2011.
- [22] A. Khalafallah and M. Abdel-Raheem, "Electimize: new evolutionary algorithm for optimization with application in construction engineering," *Journal of Computing in Civil Engineering*, vol. 25, no. 3, pp. 192–201, 2011.
- [23] A. Ahangar-Asr, A. Faramarzi, and A. A. Javadi, "A new approach for prediction of the stability of soil and rock slopes," *Engineering Computations (Swansea, Wales)*, vol. 27, no. 7, pp. 878–893, 2010.
- [24] M. Rezaia, A. A. Javadi, and O. Giustolisi, "An evolutionary-based data mining technique for assessment of civil engineering systems," *Engineering Computations (Swansea, Wales)*, vol. 25, no. 6, pp. 500–517, 2008.
- [25] M. I. Solihin, Wahyudi, M. A. S. Kamal, and A. Legowo, "Optimal PID controller tuning of automatic gantry crane using PSO algorithm," in *Proceedings of the 5th International Symposium on Mechatronics and its Applications (ISMA '08)*, May 2008.
- [26] T. Wang, G. Wang, K. Liu, and S. Zhou, "Simulation control of concrete pump truck boom based on PSO and gravity compensation," in *Proceedings of the 2nd International Symposium on Intelligent Information Technology Application (IITA '08)*, pp. 494–497, December 2008.
- [27] L. Wang, Y. Zhou, and W. Zhao, "Comparative study on bionic optimization algorithms for sewer optimal design," in *Proceedings of the 5th International Conference on Natural Computation (ICNC '09)*, pp. 24–29, August 2009.

- [28] H. Shayeghi, H. Eimani Kalasar, H. Shayanfar, and A. Shayeghi, "PSO based TMD design for vibration control of tall building structures," in *Proceedings of the International Conference on Artificial Intelligence (ICAI '09)*, 2009.
- [29] S. F. Ali and A. Ramaswamy, "Optimal fuzzy logic control for MDOF structural systems using evolutionary algorithms," *Engineering Applications of Artificial Intelligence*, vol. 22, no. 3, pp. 407–419, 2009.
- [30] Y. Filiberto, R. Bello, Y. Caballero, and R. Larrua, "Using PSO and RST to predict the resistant capacity of connections in composite structures," *Studies in Computational Intelligence*, vol. 284, pp. 359–370, 2010.
- [31] A. Schmidt, *The Design of an Active Structural Vibration Reduction System Using a Modified Particle Swarm Optimization*, 2010.
- [32] X. Zheng and Z. Liu, "The schedule control of engineering project based on particle swarm algorithm," in *Proceedings of the 2nd International Conference on Communication Systems, Networks and Applications (ICCSNA '10)*, pp. 184–187, July 2010.
- [33] H. C. Tsai, "Predicting strengths of concrete-type specimens using hybrid multilayer perceptrons with center-unified particle swarm optimization," *Expert Systems with Applications*, vol. 37, no. 2, pp. 1104–1112, 2010.
- [34] M. Marinaki, Y. Marinakis, and G. E. Stavroulakis, "Fuzzy control optimized by PSO for vibration suppression of beams," *Control Engineering Practice*, vol. 18, no. 6, pp. 618–629, 2010.
- [35] A. Nejadfard, H. Moradi, and M. Ahmadabadi, "A multi-robot system for dome inspection and maintenance: concept and stability analysis," in *Proceedings of the IEEE International Conference on Robotics and Biomimetics (ROBIO '11)*, 2011.
- [36] V. Raju, D. Maheswari, and S. Patnaik, "Active vibration control of piezo actuated cantilever beam using PSO," in *Proceedings of the IEEE Students' Conference on Electrical, Electronics and Computer Science (SCEECS '12)*, 2012.
- [37] A. Kaveh and S. Talatahari, "An improved ant colony optimization for constrained engineering design problems," *Engineering Computations (Swansea, Wales)*, vol. 27, no. 1, pp. 155–182, 2010.
- [38] K. Doerner, W. J. Gutjahr, R. F. Hartl, C. Strauss, and C. Stummer, "Pareto ant colony optimization: a metaheuristic approach to multiobjective portfolio selection," *Annals of Operations Research*, vol. 131, no. 1-4, pp. 79–99, 2004.
- [39] I. Flood, "Towards the next generation of artificial neural networks for civil engineering," *Advanced Engineering Informatics*, vol. 22, no. 1, pp. 4–14, 2008.
- [40] S. Sharma and A. Das, "Backcalculation of pavement layer moduli from falling weight deflectometer data using an artificial neural network," *Canadian Journal of Civil Engineering*, vol. 35, no. 1, pp. 57–66, 2008.
- [41] R. Bendaña, A. Del Caño, and M. P. De La Cruz, "Contractor selection: Fuzzy-control approach," *Canadian Journal of Civil Engineering*, vol. 35, no. 5, pp. 473–486, 2008.
- [42] A. Bilgil and H. Altun, "Investigation of flow resistance in smooth open channels using artificial neural networks," *Flow Measurement and Instrumentation*, vol. 19, no. 6, pp. 404–408, 2008.
- [43] Z. Q. Gu and S. O. Gu, "Diagonal recurrent neural networks for MDOF structural vibration control," *Journal of Vibration and Acoustics, Transactions of the ASME*, vol. 130, no. 6, Article ID 061001, 2008.
- [44] S. Laflamme and J. J. Connor, "Application of self-tuning Gaussian networks for control of civil structures equipped with magnetorheological dampers," in *Active and Passive Smart Structures and Integrated Systems 2009*, vol. 7288 of *Proceedings of the SPIE*, The International Society for Optical Engineering, March 2009.
- [45] T. L. Lee, H. M. Lin, and Y. P. Lu, "Assessment of highway slope failure using neural networks," *Journal of Zhejiang University: Science A*, vol. 10, no. 1, pp. 101–108, 2009.
- [46] F. Xiao and S. N. Amirkhania, "Effects of binders on resilient modulus of rubberized mixtures containing RAP using artificial neural network approach," *Journal of Testing and Evaluation*, vol. 37, no. 2, pp. 129–138, 2009.
- [47] B. Benchmark and S. Narasimhan, "Robust direct adaptive controller for the nonlinear highway," *Structural Control and Health Monitoring*, vol. 16, no. 6, pp. 599–612, 2009.
- [48] J. Zhang and F. Haghighat, "Development of Artificial Neural Network based heat convection algorithm for thermal simulation of large rectangular cross-sectional area Earth-to-Air Heat Exchangers," *Energy and Buildings*, vol. 42, no. 4, pp. 435–440, 2010.
- [49] V. Yveras, "Performance prediction method in the early design stage for outdoor ventilated crawl spaces based on artificial neural networks," *Journal of Building Physics*, vol. 34, no. 1, pp. 43–56, 2010.

- [50] H. Rahman, K. Alireza, and G. Reza, "Application of artificial neural network, kriging, and inverse distance weighting models for estimation of scour depth around bridge pier with bed sill," *Journal of Software Engineering and Applications*, vol. 3, no. 10, 2010.
- [51] X. Z. Wang, X. C. Duan, and J. Y. Liu, "Application of neural network in the cost estimation of highway engineering," *Journal of Computers*, vol. 5, no. 11, pp. 1762–1766, 2010.
- [52] D. R. Parhi and A. K. Dash, "Application of neural networks and finite elements for condition monitoring of structures," *Proceedings of the Institution of Mechanical Engineers C*, vol. 225, no. 6, pp. 1329–1339, 2011.
- [53] X. Gui, X. Zheng, J. Song, and X. Peng, "Automation bridge design and structural optimization," *Applied Mechanics and Materials*, vol. 63-64, pp. 457–460, 2011.
- [54] S. N. Alacali, B. Akba, and B. Doran, "Prediction of lateral confinement coefficient in reinforced concrete columns using neural network simulation," *Applied Soft Computing Journal*, vol. 11, no. 2, pp. 2645–2655, 2011.
- [55] J. Li, U. Dackermann, Y. L. Xu, and B. Samali, "Damage identification in civil engineering structures utilizing PCA-compressed residual frequency response functions and neural network ensembles," *Structural Control and Health Monitoring*, vol. 18, no. 2, pp. 207–226, 2011.
- [56] J. Liu, H. Li, and C. He, "Predicting the compressive strength of concrete using rebound method and artificial neural network," *ICIC Express Letters*, vol. 5, no. 4, pp. 1115–1120, 2011.
- [57] M. Y. Cheng, H. C. Tsai, and E. Sudjono, "Evaluating subcontractor performance using evolutionary fuzzy hybrid neural network," *International Journal of Project Management*, vol. 29, no. 3, pp. 349–356, 2011.
- [58] P. B. Cachim, "Using artificial neural networks for calculation of temperatures in timber under fire loading," *Construction and Building Materials*, vol. 25, no. 11, pp. 4175–4180, 2011.
- [59] S. Arangio and J. Beck, "Bayesian neural networks for bridge integrity assessment," *Structural Control & Health Monitoring*, vol. 19, no. 1, pp. 3–21, 2012.
- [60] M. H. Fazel Zarandi, I. B. Türksen, J. Sobhani, and A. A. Ramezani-pour, "Fuzzy polynomial neural networks for approximation of the compressive strength of concrete," *Applied Soft Computing Journal*, vol. 8, no. 1, pp. 488–498, 2008.
- [61] M. A. Hossain, A. A. M. Madkour, K. P. Dahal, and H. Yu, "Comparative performance of intelligent algorithms for system identification and control," *Journal of Intelligent Systems*, vol. 17, no. 4, pp. 313–329, 2008.
- [62] M. Y. Cheng, H. S. Peng, Y. W. Wu, and T. L. Chen, "Estimate at completion for construction projects using evolutionary support vector machine inference model," *Automation in Construction*, vol. 19, no. 5, pp. 619–629, 2010.
- [63] J. Sobhani and A. A. Ramezani-pour, "Service life of the reinforced concrete bridge deck in corrosive environments: A soft computing system," *Applied Soft Computing Journal*, vol. 11, no. 4, pp. 3333–3346, 2011.
- [64] Y. Q. Guo, S. M. Fei, and Z. D. Xu, "Simulation analysis on intelligent structures with magnetorheological dampers," *Journal of Intelligent Material Systems and Structures*, vol. 19, no. 6, pp. 715–726, 2008.
- [65] K. M. Choi, H. J. Jung, H. J. Lee, and S. W. Cho, "Seismic protection of base-isolated building with nonlinear isolation system using smart passive control strategy," *Structural Control and Health Monitoring*, vol. 15, no. 5, pp. 785–796, 2008.
- [66] V. E. Omurlu, S. N. Engin, and I. Yükek, "Application of fuzzy PID control to cluster control of viaduct road vibrations," *JVC/Journal of Vibration and Control*, vol. 14, no. 8, pp. 1201–1215, 2008.
- [67] R. Guclu and H. Yazici, "Vibration control of a structure with ATMD against earthquake using fuzzy logic controllers," *Journal of Sound and Vibration*, vol. 318, no. 1-2, pp. 36–49, 2008.
- [68] O. E. Ozbulut and S. Hurlebaus, "A temperature- and strain-rate-dependent model of NiTi shape memory alloys for seismic control of bridges," in *Sensors and Smart Structures Technologies for Civil, Mechanical, and Aerospace Systems 2009*, usa, March 2009.
- [69] A. A. Shaheen, A. R. Fayek, and S. M. Abourizk, "Methodology for integrating fuzzy expert systems and discrete event simulation in construction engineering," *Canadian Journal of Civil Engineering*, vol. 36, no. 9, pp. 1478–1490, 2009.
- [70] C. W. Chen, K. Yeh, and K. F. R. Liu, "Adaptive fuzzy sliding mode control for seismically excited bridges with lead rubber bearing isolation," *International Journal of Uncertainty, Fuzziness and Knowledge-Based Systems*, vol. 17, no. 5, pp. 705–727, 2009.
- [71] A. Bianchini and P. Bandini, "Prediction of pavement performance through neuro-fuzzy reasoning," *Computer-Aided Civil and Infrastructure Engineering*, vol. 25, no. 1, pp. 39–54, 2010.

- [72] O. E. Ozbulut and S. Hurlebaus, "Fuzzy control of piezoelectric friction dampers for seismic protection of smart base isolated buildings," *Bulletin of Earthquake Engineering*, vol. 8, no. 6, pp. 1435–1455, 2010.
- [73] Q. Meng, M. Zhang, and J. Ye, "Fuzzy control strategy based on mode identification Used in semi-active control," *Applied Mechanics and Materials*, vol. 71–78, pp. 3975–3982, 2011.
- [74] A. Nieto-Morote and F. Ruz-Vila, "A fuzzy approach to construction project risk assessment," *International Journal of Project Management*, vol. 29, no. 2, pp. 220–231, 2011.
- [75] P. Rosko, "Structural topology optimization with fuzzy constraint," in *4th International Conference on Machine Vision (ICMV '11): Computer Vision and Image Analysis; Pattern Recognition and Basic Technologies*, vol. 8350 of *Proceedings of the SPIE*, The International Society for Optical Engineering, 2011.
- [76] H. Gonzalez-Jorge, D. Gonzalez-Aguilera, P. Rodriguez-Gonzalvez, and P. Arias, "Monitoring biological crusts in civil engineering structures using intensity data from terrestrial laser scanners," *Construction and Building Materials*, vol. 31, pp. 119–128, 2012.
- [77] O. Yakut and H. Alli, "Application of neural based fuzzy logic sliding mode control with moving sliding surface for the seismic isolation of a building with active tendon," *Journal of Intelligent & Fuzzy Systems*, vol. 20, no. 6, pp. 235–256, 2009.
- [78] J. Mahjoobi, A. Etemad-Shahidi, and M. H. Kazeminezhad, "Hindcasting of wave parameters using different soft computing methods," *Applied Ocean Research*, vol. 30, no. 1, pp. 28–36, 2008.
- [79] A. Golroo and S. L. Tighe, "Development of pervious concrete pavement performance models using expert opinions," *Journal of Transportation Engineering-Asce*, vol. 138, no. 5, pp. 634–648, 2012.
- [80] D. Grau, W. E. Back, and J. R. Prince, "Database expert planning system for on-site design strategies," *Journal of Computing in Civil Engineering*, vol. 26, no. 1, pp. 64–75, 2012.
- [81] M. Neshat and A. Adeli, "Designing a fuzzy expert system to predict the concrete mix design," in *Proceedings of the IEEE International Conference on Computational Intelligence for Measurement Systems and Applications (CIMSAS '11)*, pp. 80–85, 2011.
- [82] O. Sariyar and D. N. Ural, "Expert system approach for soil structure interaction and land use," *Journal of Urban Planning and Development*, vol. 136, no. 2, pp. 135–138, 2010.
- [83] R. Gupta, M. A. Kewalramani, and A. Goel, "Prediction of concrete strength using neural-expert system," *Journal of Materials in Civil Engineering*, vol. 18, no. 3, pp. 462–466, 2006.
- [84] K. W. Chau and F. Albermani, "A coupled knowledge-based expert system for design of liquid-retaining structures," *Automation in Construction*, vol. 12, no. 5, pp. 589–602, 2003.
- [85] M. F. M. Zain, M. N. Islam, and I. H. Basri, "An expert system for mix design of high performance concrete," *Advances in Engineering Software*, vol. 36, no. 5, pp. 325–337, 2005.
- [86] A. Kazaz, "Application of an expert system on the fracture mechanics of concrete," *Artificial Intelligence Review*, vol. 19, no. 2, pp. 177–190, 2003.
- [87] A. B. Göktepe, A. H. Lav, S. Altun, and G. Altıntaş, "Fuzzy decision support system to determine swell/shrink factor affecting earthwork optimization of highways," *Mathematical and Computational Applications*, vol. 13, no. 1, pp. 61–70, 2008.
- [88] M. Zanaganeh, S. J. Mousavi, and A. F. Etemad Shahidi, "A hybrid genetic algorithm-adaptive network-based fuzzy inference system in prediction of wave parameters," *Engineering Applications of Artificial Intelligence*, vol. 22, no. 8, pp. 1194–1202, 2009.
- [89] A. Bianchini and P. Bandini, "Prediction of pavement performance through neuro-fuzzy reasoning," *Computer-Aided Civil and Infrastructure Engineering*, vol. 25, no. 1, pp. 39–54, 2010.
- [90] M. Eliseo, J. Parente de Oliveira, and S. Pellegrino, "Domain ontology with temporal descriptions for architectural buildings as a support for learning history of architecture," *IEEE Multidisciplinary Engineering Education Magazine*, vol. 6, no. 2, 2011.
- [91] N. Lee and A. Mita, "Sensor agent robot with servo-accelerometer for structural health monitoring," *Sensors and Smart Structures Technologies for Civil, Mechanical, and Aerospace Systems*, vol. 8345, parts 1 and 2, 2012.
- [92] N. El-Sawalhi, D. Eaton, and R. Rustom, "Forecasting contractor performance using a neural network and genetic algorithm in a pre-qualification model," *Construction Innovation*, vol. 8, no. 4, 2008.
- [93] J. Lee and L. E. Bernold, "Ubiquitous agent-based communication in construction," *Journal of Computing in Civil Engineering*, vol. 22, no. 1, pp. 31–39, 2008.
- [94] M. Kovacevic, J. Y. Nie, and C. Davidson, "Providing answers to questions from automatically collected web pages for intelligent decision making in the construction sector," *Journal of Computing in Civil Engineering*, vol. 22, no. 1, pp. 3–13, 2008.

- [95] W. J. O'Brien, C. Julien, S. Kabadayi, X. Luo, and J. Hammer, "An architecture for decision support in ad hoc sensor networks," *Electronic Journal of Information Technology in Construction*, vol. 14, pp. 309–327, 2009.
- [96] R. Luna, R. Hall, M. Hilgers, and G. E. Louis, "GIS learning tool for civil engineers," *International Journal of Engineering Education*, vol. 26, no. 1, pp. 52–58, 2010.
- [97] A. Singh, B. S. Minsker, and P. Bajcsy, "Image-based machine learning for reduction of user fatigue in an interactive model calibration system," *Journal of Computing in Civil Engineering*, vol. 24, no. 3, pp. 241–251, 2010.
- [98] P. Thompson, "Teaching sustainability in civil engineering using Ceequal," *Proceedings of the Institution of Civil Engineers: Engineering Sustainability*, vol. 163, no. 4, pp. 209–217, 2010.
- [99] E. Obonyo, "An agent-based intelligent virtual learning environment for construction management," *Construction Innovation*, vol. 11, no. 2, 2011.
- [100] S. Zhu, F. Xie, and D. Levinson, "Enhancing transportation education through online simulation using an agent-based demand and assignment model," *Journal of Professional Issues in Engineering Education and Practice*, vol. 137, no. 1, pp. 38–45, 2011.
- [101] S. K. Das, P. Samui, and A. K. Sabat, "Application of artificial intelligence to maximum dry density and unconfined compressive strength of cement stabilized soil," *Geotechnical and Geological Engineering*, vol. 29, no. 3, pp. 329–342, 2011.
- [102] T. A. Newson and N. J. Delatte, "Case methods in civil engineering teaching," *Canadian Journal of Civil Engineering*, vol. 38, no. 9, pp. 1016–1030, 2011.
- [103] X. Lu, D. Clements-Croome, and M. Viljanen, "Integration of chaos theory and mathematical models in building simulation—part II: conceptual frameworks," *Automation in Construction*, vol. 19, no. 4, pp. 452–457, 2010.
- [104] V. Kardashov, S. Einav, Y. Okrent, and T. Kardashov, "Nonlinear reaction-diffusion models of self-organization and deterministic chaos: theory and possible applications to description of electrical cardiac activity and cardiovascular circulation," *Discrete Dynamics in Nature and Society*, vol. 2006, 2006.
- [105] I. Durgun and A. R. Yildiz, "Structural design optimization of vehicle components using cuckoo search algorithm," *Materials Testing*, vol. 54, no. 3, pp. 185–188, 2012.
- [106] S. Walton, O. Hassan, K. Morgan, and M. Brown, "Modified Cuckoo Search: a new gradient free optimisation algorithm," *Chaos Solitons & Fractals*, vol. 44, no. 9, pp. 710–718, 2011.
- [107] X. T. Li and M. H. Yin, "Parameter estimation for chaotic systems using the cuckoo search algorithm with an orthogonal learning method," *Chinese Physics B*, vol. 21, no. 5, Article ID 050507, 2012.
- [108] A. H. Gandomi, X. S. Yang, and A. H. Alavi, "Mixed variable structural optimization using Firefly Algorithm," *Computers & Structures*, vol. 89, no. 23–24, pp. 2325–2336, 2011.
- [109] S. Lukasik and S. Zak, *Firefly Algorithm for Continuous Constrained Optimization Tasks*, 2009.
- [110] Y. Xin-She, "Firefly algorithm, stochastic test functions and design optimisation," *International Journal of Bio-Inspired Computation*, vol. 2, no. 2, pp. 78–84, 2010.
- [111] S. M. Sapuan, "A knowledge-based system for materials selection in mechanical engineering design," *Materials and Design*, vol. 22, no. 8, pp. 687–695, 2001.
- [112] P. J. Lovett, A. Ingram, and C. N. Bancroft, "Knowledge-based engineering for SMEs—a methodology," *Journal of Materials Processing Technology*, vol. 107, no. 1–3, pp. 384–389, 2000.
- [113] C. B. Chapman and M. Pinfold, "Design engineering—a need to rethink the solution using knowledge based engineering," *Knowledge-Based Systems*, vol. 12, no. 5–6, pp. 257–267, 1999.
- [114] J. Kulon, P. Broomhead, and D. J. Mynors, "Applying knowledge-based engineering to traditional manufacturing design," *International Journal of Advanced Manufacturing Technology*, vol. 30, no. 9–10, pp. 945–951, 2006.
- [115] S. W. Mahfoud and D. E. Goldberg, "Parallel recombinative simulated annealing: a genetic algorithm," *Parallel Computing*, vol. 21, no. 1, pp. 1–28, 1995.
- [116] A. Dekkers and E. Aarts, "Global optimization and simulated annealing," *Mathematical Programming B*, vol. 50, no. 3, pp. 367–393, 1991.
- [117] K. Bouleimen and H. Lecocq, "A new efficient simulated annealing algorithm for the resource-constrained project scheduling problem and its multiple mode version," *European Journal of Operational Research*, vol. 149, no. 2, pp. 268–281, 2003.
- [118] L. Chen and K. Aihara, "Chaotic simulated annealing by a neural network model with transient chaos," *Neural Networks*, vol. 8, no. 6, pp. 915–930, 1995.
- [119] R. Prada and A. Paiva, "Teaming up humans with autonomous synthetic characters," *Artificial Intelligence*, vol. 173, no. 1, pp. 80–103, 2009.

Research Article

Optimum Design of Gravity Retaining Walls Using Charged System Search Algorithm

**S. Talatahari,¹ R. Sheikholeslami,² M. Shadfaran,³
and M. Pourbaba⁴**

¹ Marand Faculty of Engineering, University of Tabriz, Tabriz, Iran

² Department of Civil and Environmental Engineering, Amirkabir University of Technology, Tehran, Iran

³ Department of Civil Engineering, University of Tabriz, Tabriz, Iran

⁴ Department of Civil Engineering, Islamic Azad University, Maragheh Branch, Maragheh, Iran

Correspondence should be addressed to S. Talatahari, talatahari@tabrizu.ac.ir

Received 6 June 2012; Accepted 11 September 2012

Academic Editor: Sheng-yong Chen

Copyright © 2012 S. Talatahari et al. This is an open access article distributed under the Creative Commons Attribution License, which permits unrestricted use, distribution, and reproduction in any medium, provided the original work is properly cited.

This study focuses on the optimum design retaining walls, as one of the familiar types of the retaining walls which may be constructed of stone masonry, unreinforced concrete, or reinforced concrete. The material cost is one of the major factors in the construction of gravity retaining walls therefore, minimizing the weight or volume of these systems can reduce the cost. To obtain an optimal seismic design of such structures, this paper proposes a method based on a novel meta-heuristic algorithm. The algorithm is inspired by the Coulomb's and Gauss's laws of electrostatics in physics, and it is called charged system search (CSS). In order to evaluate the efficiency of this algorithm, an example is utilized. Comparing the results of the retaining wall designs obtained by the other methods illustrates a good performance of the CSS. In this paper, we used the Mononobe-Okabe method which is one of the pseudostatic approaches to determine the dynamic earth pressure.

1. Introduction

Every time a product is created or designed to satisfy human needs, the creator tries to achieve the best solution for the task in hand and therefore performs optimization. This process is often manual, time consuming and involves a step by step approach to identify the right combination of the product and associated process parameters for the best solution. Often the manual approach does not allow a thorough exploration of the solution space to find the optimum design, resulting in suboptimal designs [1–3]. Therefore experienced engineers may be able to come up with solutions that fulfill some of the requirements

on structural response, cost, aesthetics, and manufacturing but they will seldom be able to come up with the optimal structure.

One type of optimization methods is known as metaheuristic algorithms. These methods are suitable for global search due to their capability of exploring and finding promising regions in the search space at an affordable time. Meta-heuristic algorithms tend to perform well for most of the optimization problems [4–7]. As a new meta-heuristic approach, this paper utilizes charged system search algorithm (CSS) for the optimum design of gravity retaining walls subjected to seismic loading. Retaining walls is generally classified as gravity, semigravity (or conventional), nongravity cantilevered, and anchored. Gravity retaining walls are the walls which use their own weight to resist the lateral earth pressures. The main forces acting on gravity retaining walls are the vertical forces from the weight of the wall, the lateral earth pressure acting on the back face and the seismic loads. These forces are used herein to illustrate the design principles. If other forces are encountered, such as vehicular loads, they must also be included in the analysis. The lateral earth pressure is usually calculated by the Coulomb equation.

The paper is structured as follows. After this introduction, Section 2 recalls the optimization problem statement. Then review of CSS is presented in Section 3. Test case is presented in Section 4 while optimization and sensitivity analysis results are reported and discussed. Finally, Section 5 summarizes the main findings of this study, and conclusion is drawn based on the reported results.

2. The Optimization Problem

Gravity walls derive their capacity to resist lateral loads through dead weight of the wall. The earliest method for determining the combined static and dynamic earth pressure on a retaining wall was developed by Okabe [8] and Mononobe [9]. This method, generally referred to as the Mononobe-Okabe method, is based on plasticity theory and is essentially an extension of the Coulomb sliding wedge theory in which the transient earthquake forces are represented by an equivalent static force. Therefore the effect of the earthquake motion can be represented as inertial forces $K_h W$ and $K_v W$ acting at the centre of gravity of the mass [10]. The principle of this method is illustrated in Figure 1. The Mononobe-Okabe method was originally developed for a dry cohesion less material with the following two assumptions.

- (1) The wall yields sufficiently such that a triangular soil wedge behind the wall is formed at the point of incipient failure, with the maximum shear strength mobilized along the sliding surface.
- (2) The wall and the soil behave as a rigid body with the shear wave travelling at an infinite speed such that the acceleration effectively becomes uniform throughout the mass of the soil wedge.

The expression of the total dynamic force, P_{AE} (Figure 1) is given below:

$$P_{AE} = \frac{1}{2} \gamma H^2 (1 + K_v) C_{AE},$$

$$C_{AE} = \frac{\cos^2(\phi' - \theta - \beta)}{\cos \theta \cos^2 \beta \cos(\delta + \beta + \theta) \left[1 + \sqrt{\sin(\phi' + \delta) \sin(\phi' - \theta - i) / \cos(\delta + \beta + \theta) \cos(i - \beta)} \right]^2}. \quad (2.1)$$

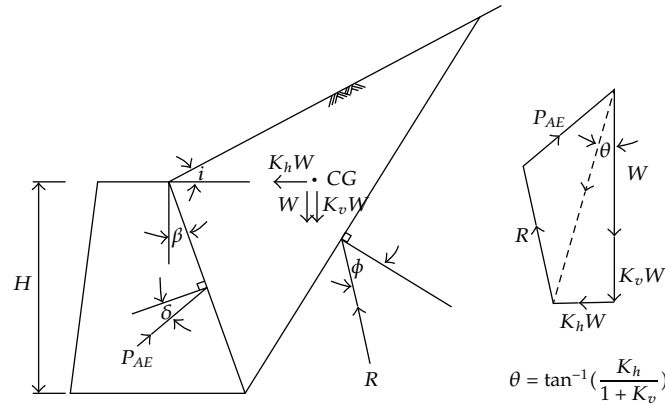


Figure 1: The Mononobe-Okabe method.

The pseudostatic approach can be visualized as effectively tilting the ground profile and wall geometry by an angle θ (defined as above), with a new gravity, g' , given by the following equation:

$$g' = \sqrt{(1 + K_v)^2 + K_h^2} g. \quad (2.2)$$

It should be noted that the Mononobe-Okabe equation is applicable for retaining walls where the angle i is less than or equal to $(\phi' - \theta)$. This is because if the angle i is greater than $(\phi' - \theta)$, the sloping backfill behind the wall will be unstable unless the soil has sufficient cohesive strength. In the latter case, the more versatile analysis approaches should be adopted.

More advanced methods, such as dynamic response analysis and finite element method, are capable of allowing for the dynamic characteristics of the soil-structure system. However, these advanced methods are usually not justified for the analysis of conventional gravity retaining walls subjected to earthquake loading and the above simple methods are generally adequate as shown in [11]. Therefore, Mononobe-Okabe method is used herein to determine the dynamic earth pressure.

On the other hand, there are three different modes of instabilities, namely sliding, overturning, and bearing capacity, which should be checked [12]. The procedure for computing the dynamic factors of safety against sliding and overturning is same as that for static calculations, except that the inertia of the gravity wall itself must also be included when earthquake loading is considered [13]. Thus, the optimal seismic design problem of gravity retaining walls may be expressed as

Design variables

$$\mathbf{X} = [x_1, x_2, \dots, x_6] \quad (2.3)$$

minimize

$$W(\mathbf{X}) = A_{cs} \cdot \gamma \quad (2.4)$$

constraints

$$\begin{aligned} FS_o &\geq 2, \\ FS_s &\geq 1.2, \\ FS_b &\geq 3, \end{aligned} \quad (2.5)$$

where \mathbf{X} is the vector containing the design variables (see Figure 2); W is the weight of a unit length of wall; A_{cs} is the wall cross-section area; γ is the density of the material; FS_o , FS_s , and FS_b are the factors of safety against overturning, sliding, and bearing capacity, respectively.

3. Charged System Search Algorithm

The Charged System Search (CSS) algorithm is based on the Coulomb and Gauss laws from electrical physics and the governing laws of motion from the Newtonian mechanics. This algorithm can be considered as a multiagent approach, where each agent is a Charged Particle (CP). Each CP is considered as a charged sphere with radius a , having a uniform volume charge density and is equal to

$$q_i = \frac{\text{fit}(i) - \text{fitworst}}{\text{fitbest} - \text{fitworst}} \quad i = 1, 2, \dots, N. \quad (3.1)$$

CPs can impose electric forces on the others, and its magnitude for the CP located in the inside of the sphere is proportional to the separation distance between the CPs, and for a CP located outside the sphere is inversely proportional to the square of the separation distance between the particles. The kind of the forces can be attractive or repelling, and it is determined by using ar_{ij} , the kind of force parameter, defined as

$$ar_{ij} = \begin{cases} +1 & \text{w.p. } k_t, \\ -1 & \text{w.p. } 1 - k_t, \end{cases} \quad (3.2)$$

where ar_{ij} determines the type of the force, $+1$ represents the attractive force, -1 denotes the repelling force, and k_t is a parameter to control the effect of the kind of force. In general, the attractive force collects the agents in a part of search space and the repelling force strives to disperse the agents. Therefore, the resultant force is redefined as

$$\mathbf{F}_j = q_j \sum_{i, i \neq j} \left(\frac{q_i}{a^3} r_{ij} \cdot i_1 + \frac{q_i}{r_{ij}^2} \cdot i_2 \right) ar_{ij} p_{ij} (\mathbf{X}_i - \mathbf{X}_j) \quad \begin{cases} j = 1, 2, \dots, N \\ i_1 = 1, i_2 = 0 \iff r_{ij} < a \\ i_1 = 0, i_2 = 1 \iff r_{ij} \geq a \end{cases} \quad (3.3)$$

the separation distance between two charged particles defined as

$$r_{ij} = \frac{\|\mathbf{X}_i - \mathbf{X}_j\|}{\|(\mathbf{X}_i + \mathbf{X}_j)/2 - \mathbf{X}_{\text{best}}\| + \varepsilon}, \quad (3.4)$$

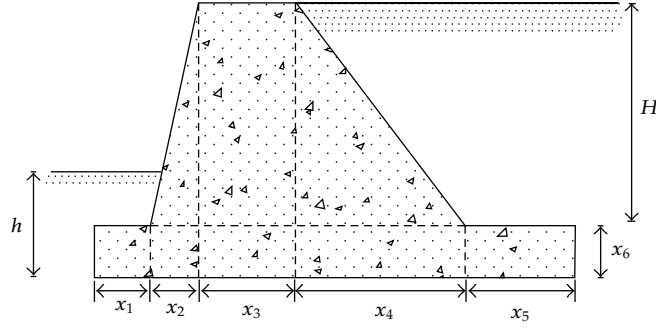


Figure 2: The design variables.

where ε is a small positive number to avoid singularity. The initial positions of CPs are determined randomly in the search space and the initial velocities of charged particles are assumed to be zero. P_{ij} determines the probability of moving each CP toward the others as

$$p_{ij} = \begin{cases} 1 & \frac{\text{fit}(i) - \text{fitbest}}{\text{fit}(j) - \text{fit}(i)} > \text{rand} \vee \text{fit}(j) < \text{fit}(i). \\ 0 & \text{otherwise.} \end{cases} \quad (3.5)$$

The resultant forces and the laws of the motion determine the new location of the CPs. At this stage, each CP moves towards its new position under the action of the resultant forces and its previous velocity as

$$\begin{aligned} \mathbf{X}_{j,\text{new}} &= \text{rand}_{j1} \cdot k_a \cdot \frac{\mathbf{F}_j}{m_j} \cdot \Delta t^2 + \text{rand}_{j2} \cdot k_v \cdot \mathbf{V}_{j,\text{old}} \cdot \Delta t + \mathbf{X}_{j,\text{old}}, \\ \mathbf{V}_{j,\text{new}} &= \frac{\mathbf{X}_{j,\text{new}} - \mathbf{X}_{j,\text{old}}}{\Delta t}, \end{aligned} \quad (3.6)$$

where k_a is the acceleration coefficient; k_v is the velocity coefficient to control the influence of the previous velocity; rand_{j1} and rand_{j2} are two random numbers uniformly distributed in the range $(0, 1)$. If each CP moves out of the search space, its position is corrected using the harmony search-based handling approach as described in [14]. In addition, to save the best design, a memory (charged memory) is utilized. The flowchart of the CSS algorithm is shown in Figure 3.

4. Numerical Example

In this section, an example is optimized with the proposed method. The final result is compared to the solution of the particle swarm optimization (PSO), big bang-big crunch algorithm (BB-BC), and heuristic big bang-big crunch (HBB-BC) [15] methods to demonstrate the efficiency of the present approach. For the example presented in this paper, the CSS algorithm parameters were set as follows: $k_a = 2.0$, $k_v = 1.5$, the number of agents is taken as 20, and the maximum number of searches is set to 500. The algorithms are coded in

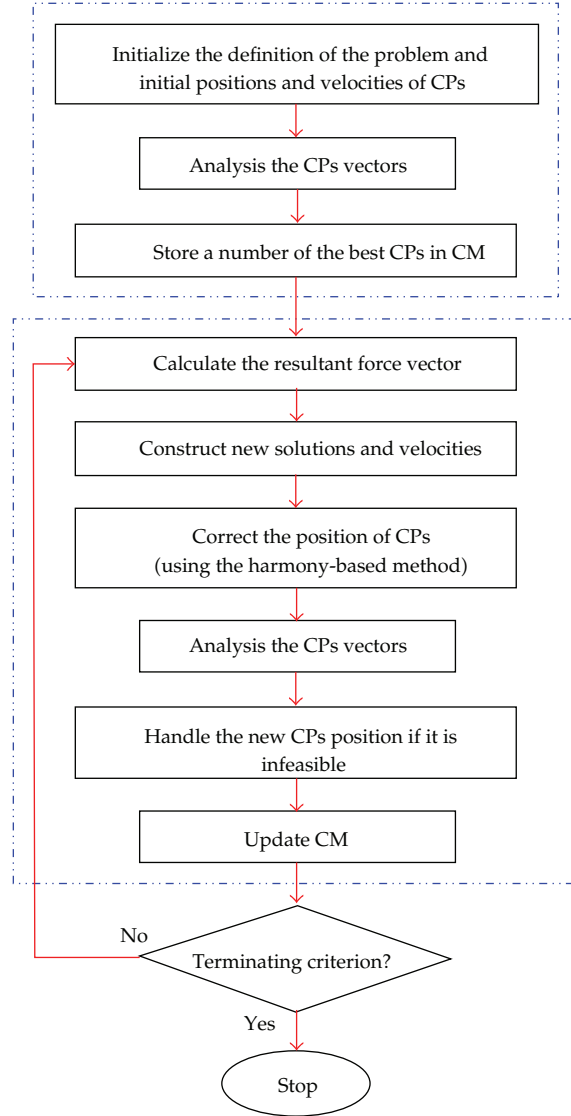


Figure 3: The flowchart for the CSS algorithm.

Matlab and in order to handle the constraints, a penalty approach is utilized. If the constraints are between the allowable limits, the penalty is zero; otherwise, the amount of penalty is obtained by dividing the violation of allowable limit to the limit itself.

The problem is the optimum seismic design of a wall with $H = 5.5$ m and $h = 1$ m. The backfill has shear strength parameters of $c' = 0$, $\phi' = 30^\circ$, and $\gamma = 16$ kN/m³. The wall is founded on a soil with c' equals zero, $\phi' = 38^\circ$, and $\gamma = 18.5$ kN/m³. The horizontal and vertical ground acceleration coefficient (K_h and K_v) is 0.35 and 0.0. Also the material's density is 24 kN/m (concrete wall). In this example, the angle of wall friction is 15° and the inclination of ground surface behind wall to horizontal is zero.

The results of the seismic design optimization process for the CSS algorithm and the PSO, BB-BC, and HBB-BC are summarized in Table 1. As shown in this table, the result for

Table 1: The optimum seismic designs comparison for the gravity retaining wall.

Design variable	Optimal values (m)			
	CSS	HBB-BC [15]	BB-BC [15]	PSO [15]
x_1	1.137	1.734	0.903	0.566
x_2	0.440	0.553	0.650	2.000
x_3	0.353	0.467	0.689	0.200
x_4	3.200	3.014	2.691	2.000
x_5	2.261	0.719	0.515	0.645
x_6	0.200	0.200	0.200	0.200
Best weight (kN)	322.293	328.297	337.607	344.700
Average weight (kN)	329.893	337.860	345.652	351.189
Number of analysis	4,400	10,000	10,000	10,000
FS_o	2.152	2.504	2.003	2.097
FS_s	1.200	1.200	1.200	1.200
FS_b	7.154	7.459	5.921	7.182

the CSS algorithm is 322.293 kN, which is lighter than the result of the PSO, standard BB-BC, and HBB-BC algorithm. In addition, the average weight of 20 different runs for the CSS algorithm is 2.3%, 4.8%, and 6.1% lighter than the average results of the HBB-BC, BB-BC, and PSO algorithms, respectively. Comparing these results shows that the new algorithm not only improves the reliability property due to decrease in the mean of results but also enhances the quality of the results due to the decrease in the best of results. The convergence history for the CSS gravity retaining wall design is shown in Figure 4.

Among the design constraints, the safety factor of sliding is the active one and almost for all design of different studied algorithms, it is the most important while the factor of safety against bearing capacity is not active and it will not affect the optimum design.

Any optimum design problem involves a design vector and a set of problem parameters. In many cases, we would be interested in knowing the sensitivities or derivatives of the optimum design (design variables and objective function) with respect to the problem parameters because this is very useful to the designer, to know which data values are more influential on the design. Sensitivity of optimal responses to these parameters is one of the important issues in the optimum design of retaining walls.

Here, using sensitivity analysis, the effect of changes on the safety factor for sliding on optimum weight of a wall was studied. The factor of safety for sliding of the wall is defined as the resisting forces divided by the driving force, or

$$FS_s = \frac{\text{Sliding resistance force} + \text{Allowable passive resultant force}}{\text{Active earth pressure resultant force}}. \quad (4.1)$$

If the wall is found to be unsafe against sliding, shear key below the base is provided. Such a key develops passive pressure which resists completely the sliding tendency of the wall. The customary minimum safety factor against sliding is 1.2, with some agencies requiring more. In the determination of the, FS_s , the effect of passive lateral earth pressure resistance in front of a wall footing or a wall footing key will only be considered when competent soil or rock exists which will not be removed or eroded during the structure life.

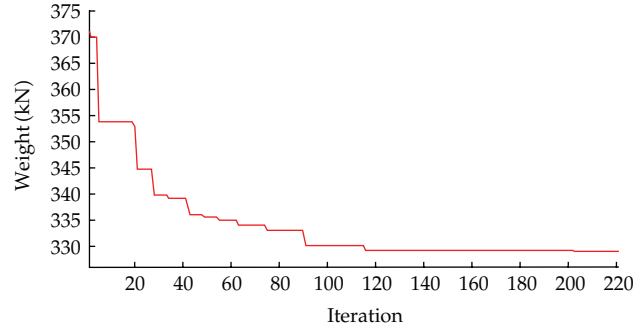


Figure 4: The convergence history of CSS algorithm (average of 20 different runs).

Not more than 50 percent of the available passive lateral earth pressure will be considered in determining the FS_s . In Figure 5, optimum weight variation against safety factor of sliding is depicted. It is interesting to emphasize that a small coefficient for $FS_s = 1.2$ causes an average decrease in cost of 43% as compared to a coefficient for $FS_s = 2$.

5. Concluding Remarks

Determining optimum weight and sensitivity analysis of gravity retaining walls subject to seismic loading is presented in detail, using the CSS algorithm. This algorithm contains three levels: initialization, search, and controlling the terminating criterion. In the initialization level, the parameters of the CSS algorithm, the primary location of the CPs, and their initial velocities are defined. Also in this level, a memory to store a number of the best CPs is introduced. The search level starts after the initialization level, where each CP moves toward the others considering the probability function, the magnitude of the attracting force vector, and the previous velocities. The moving process is defined in a way that it not only can perform more investigation in the search space, but also can improve the results. To fulfill this goal, some laws of physics containing the Coulomb and Gauss laws, and the governing laws of motion from Newtonian mechanics are utilized. The last level consists of controlling the termination.

Comparing the results of the retaining wall designs obtained by other meta-heuristic algorithms such as the PSO and the BB-BC shows a good balance between the exploration and exploitation abilities of the CSS; hence, its superior performance becomes evident. Both CSS and PSO are population-based algorithms in which the position of each agent is obtained by adding the agent's movement to its previous position; however, the movement strategies are different. The PSO algorithm utilizes a velocity term being a combination of the previous velocity movement in the direction of the local best, and movement in the direction of the global best, while the CSS approach uses the governing laws from electrical physics and the governing laws of motion from the Newtonian mechanics to determine the amount and the direction of a charged particle's movement. The potency of the PSO is summarized to find the direction of an agent's movement and therefore determining the acceleration constants becomes important. Similarly in the CSS method, updating is performed by considering the quality of the solutions and the separation distances between CPs. Therefore, not only the directions but also the amounts of movements are determined.

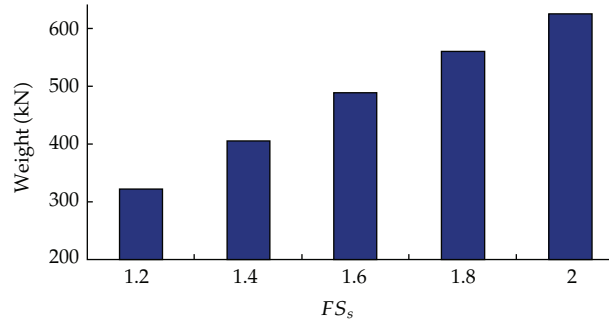


Figure 5: Weight variation against different FS_s .

Also a sensitivity analysis is performed for the optimum seismic design of gravity retaining wall parameters using the CSS algorithm in which the safety factor for sliding is concerned. The results related to the influence of the safety factors of sliding show that as expected, a large safety factor causes a costly wall compared to a small one.

Notation

W :	Weight of the sliding wedge
K_h :	Horizontal ground acceleration coefficient
K_v :	Vertical ground acceleration coefficient
P_{AE} :	Total dynamic force on the retaining wall
R :	Reaction on soil wedge from the surrounding ground
H :	Height of the wall
ϕ' :	Angle of shearing resistance of the soil
δ :	The angle of wall friction
i :	Inclination of ground surface behind wall to horizontal
β :	Inclination of the back of wall to vertical
θ :	Inclination of the resultant inertial force to the vertical = $\tan^{-1}(K_h/(1 + K_v))$
C_{AE} :	Horizontal seismic coefficient
fitbest:	Best fitness of all the particles
fitworst:	Worst fitness of all the particles
fit(i):	Fitness of the agent i
N :	Total number of CPs
F_j :	Resultant force acting on the j th CP
r_{ij} :	Separation distance between two charged particles
X_i :	Positions of the i th CPs
X_{best} :	Position of the best current CP.

References

- [1] R. Roy, S. Hinduja, and R. Teti, "Recent advances in engineering design optimisation: challenges and future trends," *CIRP Annals*, vol. 57, no. 2, pp. 697–715, 2008.
- [2] M. Li, S. C. Lim, and S. Chen, "Exact solution of impulse response to a class of fractional oscillators and its stability," *Mathematical Problems in Engineering*, vol. 2011, Article ID 657839, 9 pages, 2011.

- [3] S. Chen, Y. Wang, and C. Cattani, "Key issues in modeling of complex 3D structures from video sequences," *Mathematical Problems in Engineering*, vol. 2012, Article ID 856523, 17 pages, 2012.
- [4] A. H. Gandomi, X.-S. Yang, and A. H. Alavi, "Mixed variable structural optimization using firefly algorithm," *Computers and Structures*, vol. 89, no. 23-24, pp. 2325–2336, 2011.
- [5] A. H. Gandomi, X.-S. Yang, and A. H. Alavi, "Cuckoo search algorithm: a metaheuristic approach to solve structural optimization problems," *Engineering Computations*. In press.
- [6] A. H. Gandomi and A. H. Alavi, "Krill Herd: A new bio-inspired optimization algorithm," *Communications in Nonlinear Science and Numerical Simulation*, vol. 17, no. 12, pp. 4831–4845, 2012.
- [7] S. Chen, Y. Zheng, C. Cattani, and W. Wang, "Modeling of biological intelligence for SCM system optimization," *Computational and Mathematical Methods in Medicine*, vol. 2012, Article ID 769702, 30 pages, 2012.
- [8] S. Okabe, "General theory of earth pressure," *Japanese Society of Civil Engineers*, vol. 2, no. 1, 1926.
- [9] N. Mononobe, "Earthquake proof construction of masonry dams," in *Proceedings of the World Engineering Congress*, pp. 275–293, Tokyo, Japan, 1929.
- [10] P. N. Psarropoulos, G. Klonaris, and G. Gazetas, "Seismic earth pressures on rigid and flexible retaining walls," *Soil Dynamics and Earthquake Engineering*, vol. 25, no. 7–10, pp. 795–809, 2005.
- [11] Y. Yeung and K. Ho, *Gravity Retaining Walls Subject to Seismic Loading*, Civil Engineering Department, Hong Kong, China, 1994.
- [12] A. Kaveh and A. Shakouri Mahmud Abadi, "Harmony search based algorithms for the optimum cost design of reinforced concrete cantilever retaining walls," *International Journal of Civil Engineering*, vol. 9, no. 1, pp. 1–8, 2011.
- [13] A. C. Trandafir, T. Kamai, R. C. Sidle, and M. Popescu, "Seismic retrofit of gravity retaining walls for residential fills using ground anchors," *Geotechnical and Geological Engineering*, vol. 25, no. 6, pp. 679–691, 2007.
- [14] A. Kaveh and S. Talatahari, "Optimal design of skeletal structures via the charged system search algorithm," *Structural and Multidisciplinary Optimization*, vol. 41, no. 6, pp. 893–911, 2010.
- [15] A. Kaveh, S. Talatahari, and R. Sheikholeslami, "Optimum seismic design of gravity retaining walls using the heuristic big bang-big crunch algorithm," in *Proceedings of the 2nd International Conference on Soft Computing Technology in Civil, Structural and Environmental Engineering*, B. H. V. Topping and Y. Tsompanakis, Eds., Paper 4, Civil-Comp Press, 2011.

Research Article

Investment Decision Support for Engineering Projects Based on Risk Correlation Analysis

Yan Liu,¹ Ting-Hua Yi,² and Cui-Qin Wang¹

¹ College of Architectural Engineering, Qingdao Agricultural University, Qingdao 266109, China

² School of Civil Engineering, Dalian University of Technology, Dalian 116023, China

Correspondence should be addressed to Ting-Hua Yi, yth@dlut.edu.cn

Received 2 October 2012; Accepted 31 October 2012

Academic Editor: Fei Kang

Copyright © 2012 Yan Liu et al. This is an open access article distributed under the Creative Commons Attribution License, which permits unrestricted use, distribution, and reproduction in any medium, provided the original work is properly cited.

Investment decisions are usually made on the basis of the subjective judgments of experts subjected to the information gap during the preliminary stages of a project. As a consequence, a series of errors in risk prediction and/or decision-making will be generated leading to out of control investment and project failure. In this paper, the variable fuzzy set theory and intelligent algorithms integrated with case-based reasoning are presented. The proposed algorithm manages the numerous fuzzy concepts and variable factors of a project and also sets up the decision-making process in accordance with past cases and experiences. Furthermore, it decreases the calculation difficulty and reduces the decision-making reaction time. Three types of risk correlations combined with different characteristics of engineering projects are summarized, and each of these correlations is expounded at the project investment decision-making stage. Quantitative and qualitative change theories of variable fuzzy sets are also addressed for investment risk warning. The approach presented in this paper enables the risk analysis in a simple and intuitive manner and realizes the integration of objective and subjective risk assessments within the decision-makers' risk expectation.

1. Introduction

The purpose of engineering investment is to obtain satisfactory returns; such decisions however are affected by considerable uncertainties. Expected revenue largely depends on the analysis and control of these incertitudes. These uncertainties have been a constant from the perspective of the entire investment process, and investment decision-making plays a fundamental role because it is the starting point of the entire investment process. According to the expert estimation and case studies of major projects, early decision-making exerts a magnitude of influence of 70% or higher over an entire project. A large number of projects fail due to the errors in initial investment decisions. In the investment decision-making process of large-scale projects, many risk factors can cause decision failure. The most crucial factors

are the change of expected investment income, the increase of investment opportunity costs, the change of taxes imposed, the variations of market supply and demand relationships, the deficiencies of construction funding, and the backward technology. For the longest time, however, the construction phase has been accorded more attention in comparison with the investment decision-making stage despite the latter's significance in project management. Risk identification, assessment, and management should be initiated early at the project decision-making stage to substantially reduce the investment risks and provide the scientific basis for improvement of the success rate.

Research efforts have been devoted towards risk management; nevertheless, the risk structure, the risk analysis, and the prevention methods remain in dispute in academia. A gap still exists between the actual and expected effects of risk control. Many decisions are based on the intuition, experiences, and subjective judgments. Project risk factors are complicated and the clarification of the correlation among these factors is difficult. Implicit assumptions suggest that risk factors are treated as isolated aspects in the investigation of comprehensive effects. Other studies focus only on static links such as qualitative influencing factors, the index weight, and so forth, instead of concentrating on the correlations especially the dynamic correlations among attributes and the dependence between targets and attributes. Risk correlations are found in a large number of projects. Case-based reasoning (CBR) is an effective data mining application in engineering project studies. It solves new problems by analyzing similar problems that have been encountered and resolved in the past. When faced with new problems, the management team can determine suitable solutions by searching for recorded cases of a similar nature, in effect, reusing past experiences. Should the cases found be deemed unsatisfactory, the team can modify the cases to suit the current situation and then record it in a case database to serve as a future reference; such an approach is a self-learning technique. It is a useful tool in handling anticipated complex problems, which are difficult to model in theoretical terms.

Marcous et al. [1] investigated the CBR to provide bridge management systems with a deterioration model that eliminates the shortcoming of Markovian model. Chua et al. [2] described a case-based reasoning bidding system that helps contractors with the dynamic information varying with the specific features of the job and the new situation. Chua and Goh [3] used the CBR to assist safety-planning teams in developing and improving safety plans for construction activities through the reuse of safety knowledge during the past time. Cheng and Melhem [4] combined the CBR with fuzzy to predict the future health condition of a bridge deck and recommended the appropriate maintenance, rehabilitation, and replacement actions. Ozorhon et al. [5] constructed the CBR decision support to demonstrate how the experiences of competitors can be used by contractors in the international markets, to support the market segment decisions. Ryu et al. [6] presented the CBR as a construction planning tool for various types of construction projects. Goh and Chua [7] used the CBR approach to utilize past knowledge in the form of past hazard identification and incident cases to improve the efficiency and quality of new hazard identification.

The diversity of cases can provide high reliability for summarizing correlations, but at the same time may interfere in the decision-making process. Therefore, encapsulating risk correlation rules of a certain confidence level using various CBRs and risk management cases is essential. Moreover, understanding risk rules not only reduces risks by shedding light on the essence of uncertainty, but also plays a key role in investment decision-making and risk prediction. We uncover risk correlations that can provide decision support for investment decision-making by combining research trends with the characteristics of engineering projects.

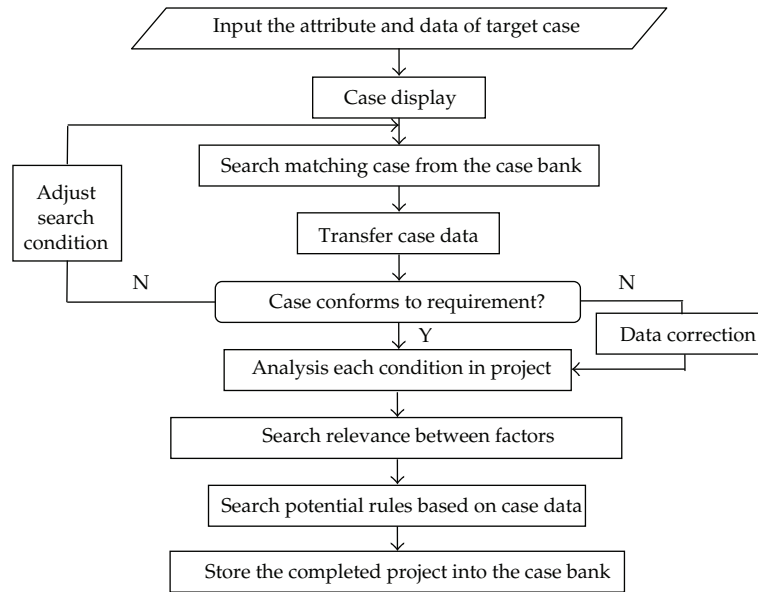


Figure 1: Analysis flow based on CBR technique.

2. Risk Correlation of Project Investment Decision-Making

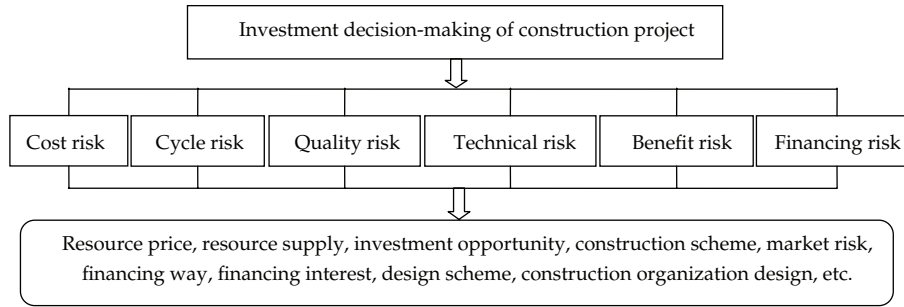
As a sub-branch of artificial intelligence, the CBR is a mode of reasoning that generates solutions to current problems by studying solutions to past problems of a similar nature stored in a knowledge database [8]. The method reuses past cases and experiences to solve new problems, evaluates new problems, explains abnormal conditions, and understands new conditions. Figure 1 shows the analysis flow in project investment.

The more cases stored, the more comprehensive the reference value. The research focus of the CBR is mainly on case storage, case retrieval, and similarity algorithm. However, it takes each case as independent items for research, rather than thoroughly studying the correlation between cases and attributes. Not only can it exclude the particularity of individual cases, but also reflects the essential characteristics of a wide range of cases to explore, at a certain confidence level, risk-inherent correlations using a large number of cases. Currently, the application of CBR in engineering projects is at its initial stage; thus, few studies on risk correlation mining have been conducted. However difficult, the key to exploring risk correlations and the factors relevant to these correlations is to determine the process involved in investment decision-making in engineering projects. On the basis of these insights, we uncover and compile three kinds of risk correlations (see Table 1) by combining the correlation mining methods applied in other domains and the risk factors present in engineering projects. The process is described as follows.

(1) An existing qualitative correlation is always existed as an influencing factor and index set, and it is also found in risk identification links. It has been accepted knowledge and this type of correlation is the one most easily identified. For example, as we know, investment decision-making composed of a series of first, second, and even multigrade risk indexes (see Figure 2). In risk prediction, the risk factors affecting target sets are first listed. Subsequently, these factors are divided into two grades or more according to the category they belong to. Subjective scoring methods, such as Analytic Hierarchy Process, fuzzy comprehensive

Table 1: Risk correlation classes of engineering project investment decision-making.

Risk Correlation Classification	Content
Existing qualitative correlation	(1) Risks classification
	(2) Risk influencing factors
	(3) Risk index set
Derivation correlation
	(1) Resource value
	(2) Operation price
	(3) Demand quantity
	(4) Construction period
	(5) Financing amount
Correlation mining through objective and subjective data
	(1) Investment deviation prediction
	(2) Schedule deviation prediction
	(3) Quantitative and qualitative change of risk
	(4) Risk factors dynamic correlation
	(5) Threshold of risk warning
	(6) Incremental and self-adaptive correlation

**Figure 2:** Risk indexes of investment decision-making.

evaluation, and so on, are typically used to calculate the degree of influence of each risk factor, that is, the weight that it carries [9–11]. As far as qualitative correlation is concerned, weight and method cannot be considered, although many risk factors can be listed by subjective experiences rather than by scientific methods. Confidence levels can even reach 100%.

(2) Derivation correlation mainly comprises type derivation, influence degree derivation, causality derivation, optimum derivation, and formula derivation. This paper provides examples of the above-mentioned derivations based on CBR, risk prediction, and risk management at the investment decision-making stage. The types of derivation correlations are discussed as follows.

(a) Type Derivation Uses the Clustering Method to Classify Existing Project Cases

It uncovers risk events, risk occurrence probabilities, and risk solutions of each type and summarizes these to serve as individual category markers. In new projects, cases can be searched and similarity can be calculated based on this derivation. It also can learn from the risk data

and risk measures of its category for decision-making. When a new project is completed, it stores information in a case database for future project risk management. This approach is a process of self and incremental learning.

Take variable fuzzy clustering iterative model as an example. Suppose n samples to be clustered compose a set, m is the sample index number, $m \times n$ is the eigenvalue matrix given in (2.1) that can be used for sample set clustering:

$$X = \begin{bmatrix} x_{11} & x_{12} & \cdots & x_{1n} \\ x_{21} & x_{22} & \cdots & x_{2n} \\ \vdots & \vdots & \ddots & \vdots \\ x_{m1} & x_{m2} & \cdots & x_{mn} \end{bmatrix} = (x_{ij}), \quad (2.1)$$

where x_{ij} is the eigenvalue of index i of the clustering sample j , $i = 1, 2, \dots, m$; $j = 1, 2, \dots, n$.

Each index has a different dimension and magnitude which means that there are positive and negative indicators. Therefore, the original data must be normalized, and the normalized number must be in $[0, 1]$ range. Different normalized methods can be used according to specific problems. Matrix X can be used after the normalized transfers into the index eigenvalue normalization matrix in

$$R = \begin{bmatrix} r_{11} & r_{12} & \cdots & r_{1n} \\ r_{21} & r_{22} & \cdots & r_{2n} \\ \vdots & \vdots & \ddots & \vdots \\ r_{m1} & r_{m2} & \cdots & r_{mn} \end{bmatrix} = (r_{ij}), \quad (2.2)$$

where r_{ij} = the index eigenvalue normalization number, $r_j = (r_{1j}, r_{2j}, \dots, r_{mj})$ is the index eigenvalue vector of sample j .

Suppose the sample set is divided into c classes, $s_j = (s_{1h}, s_{2h}, \dots, s_{mh})$ is the fuzzy clustering center vector of class h , where $h = 1, 2, \dots, c$; $0 \leq s_{ih} \leq 1$, p is the distance parameter, α is the optimal criteria parameter, and $\omega = (\omega_1, \omega_2, \dots, \omega_m)$ is the index weight vector. Equation (2.3) are the optimal fuzzy clustering matrix u_{hj}^* and the fuzzy clustering center matrix s_{ih}^* :

$$u_{hj} = \left\{ \left| \frac{\sum_{i=1}^c \sum_{i=1}^m [\omega_i (r_{ij} - s_{ih})]^p}{\sum_{i=1}^m [\omega_i (r_{ij} - s_{ik})]^p} \right|^{\alpha/p} \right\}^{-1}, \quad (2.3)$$

$$s_{ih} = \frac{\sum_{j=1}^n u_{hj}^{2/(p-1)} r_{ij}}{\sum_{j=1}^n u_{hj}^{2/(p-1)}}, \quad \frac{\alpha}{p} = 1.$$

In this model, the sample weights, relative membership degree, and cluster centers tend to be stable in the dynamic iteration. And the advantage of this model is that it not only considers the index weight but also the relative membership degree u_{hj} . Thus, the sample j belongs to the class h as another weight, resulting in a developed and perfect weight distance. And based on that, to some extent, the accuracy of type derivation could also be improved.

(b) Influence Degree Derivation Mainly Aims at Weight and Risk Consequence

Suppose risk event A is more important or has more serious consequences compared with event B , and B is more important than C . Certainly, A is more important than C . That is $A > B$ and $B > C$, so $A > C$. Thus, in the risk prediction and risk control of a new project, A should be paid more attention to than B and C to avoid risk losses.

(c) Causality Derivation Is Similar to Influence Degree Derivation

Suppose that in some link, risk event C is directly caused by event B , and B is directly caused by A . Meanwhile, event C is more serious than B , and B is more serious than A . Hence, when event A occurs, the transformation condition from A to B and B to C should be controlled in a timely manner to prevent a more serious C from occurring. A causal correlation can be revealed from a wide range of existent cases, and this correlation can resolve the risk loss before it escalates.

(d) Optimum Derivation Consists of Project Time Optimization, Cost Optimization, Resource Optimization, Bi-Objective Optimization, and Multi-Objective Optimization

Combined with the construction period, cost, and resource allocation of completed projects, optimal project duration, and optimal cost interval can be summarized based on existent cases in each category. The construction period, cost, and resources of a new project can be reasonably controlled, based on category data. It can effectively reduce certain risks.

(e) Formula Derivation Mainly Uses the Western Economic Principles Associated with Mathematical Statistics Methods

It can be used as a reference value for improving risk assessment of investment decision-making to reasonably deduce the risk quantitative correlations. Because of the difficulties involved in risk quantitative analysis, there are a few investigations in such type of correlation which only limited to macroeconomic and financial risks. At present this type of correlation only includes the relationship between a single risk factor and the investment target. We should study not only on comprehensive effect of risk factors, but also on exploring quantitative relationship among risk factors. Because this type involves quantitative analyses, along with some potential assumptions in the derivation process, this correlation has inferior confidences but with better interestingness than the first type. Moreover it is on the basis of economics rigorous formulas and statistical inference; therefore it provides some scientific reference values. Because of the difficulties involved in risk quantitative analysis, this paper focuses only on risk measurement derivation. Risk measurement is one of the indicators in determining risk intensity. Risks are understood differently, bringing forth varied risk measurement techniques as well. Equation (2.4) is one representation of this type of derivation.

If the probability distribution of risk event X is unknown, the empirical distribution of X can be obtained through statistical analysis. Thus, the risk intensity of event X is

$$F = \frac{\sigma_x}{E[X]} = \frac{\sqrt{V[X]}}{E[X]}, \quad (2.4)$$

where $E[X]$ is the mean value of sample X which is expressed as

$$E[X] = \frac{1}{n} \sum_{i=1}^n X_i, \quad (2.5)$$

where n is the sample size, X_i is the value of sample i th sample point, and $V[X]$ is the sample variance.

This derivation correlation process combines basic economics and statistics formulas with investment risk factors. Fluctuations in the prices of project resources or supply volume exert some influence on total investment. According to the western economics, a relationship exists between the resource price and the supply volume, depicted as follows [12]:

$$E_S = \frac{\Delta Q/Q}{\Delta P/P}, \quad (2.6)$$

where E_S is the elasticity of supply price, P is the resource price, Q represents the supply volume, ΔP is the incremental price of resource, and ΔQ denotes the incremental volume of supply.

Suppose $X = \Delta P/P$ and $Y = \Delta Q/Q$, respectively, represent the rate of change in the resource price and the supply volume. Combined with (2.6), it is expressed as

$$Y = E_S * X. \quad (2.7)$$

Suppose X is a random variable, E_S is the constant while the market condition is stable, and Y is also a random variable with mean and variance as follows:

$$E[Y] = E_S * E[X], \quad V[Y] = E_S^2 * V[X]. \quad (2.8)$$

Calculating the risk degree of Y using (2.4), we obtain

$$F_Y = \frac{\sqrt{V[Y]}}{E[Y]} = \frac{\sqrt{V[X]}}{E[X]} = F_X. \quad (2.9)$$

From (2.9), the risk degree F_Y of Y is equal to the risk degree F_X of X . Because of the market risk, the maximum resource price is as follows:

$$P_{\max} = E[P] + \sqrt{V[P]} = E[P](1 + F_P). \quad (2.10)$$

- (i) If $F_P = 0$ does not consider the market risk, the initial value of the resource price would be $P_0 = E[P]$.
- (ii) If $F_P \neq 0$ has taken the market risk into account, then the mean of the incremental resource price would be $\Delta \bar{P} = (1/2)(P - P_0) = (1/2)P_0 \bullet F_P$.

- (iii) Because of fixed costs, the increment of total investment caused by risks is equal to that of the resource value consumption. Thus, the average increase rate of total investment induced by risks is

$$\varepsilon = \frac{\sum_{i=1}^n \Delta \bar{P} * Q_i}{B_0} * 100\% = \frac{(1/2) \sum_{i=1}^n \Delta \bar{P} * Q_i * F_{pi}}{B_0} \bullet 100\%, \quad (2.11)$$

where Q_i is the consumption of i th resource, P_{0i} is the initial value of i th resource price, F_{pi} represents the risk degree of i th resource price, and B_0 denotes the initial estimation of total investment.

Such correlation study based on CBR is still relatively rare. In traditional project management, experiential knowledge is often lost at the end of the project. CBR, therefore, is not only a repository of existing cases, but also provides a platform for case summaries and knowledge mining. Because the derivation of such correlation assumptions and fault tolerance is allowed, the subsequent correlation presents lower confidence but is more interesting. Moreover, this correlation is based on CBR and concrete data of completed projects; thus, it is of scientific reference value.

(3) People are often interested in potential correlations hidden under data. Therefore, correlation mining through objective and subjective methods presents the highest interest of all the three correlations. Currently, research on such correlations is divided into two types: one focuses mainly on algorithm improvement and computer programming for algorithms; this approach has few applications in engineering. The other employs practical analysis, but targets only individuality and not generality. However, theory has to be indispensable for practical use. We therefore uncover six correlations that can provide decision support for investment decision-making in engineering projects. These are investment deviation prediction, schedule deviation prediction, quantitative and qualitative risk change, dynamic correlation of risk factors, risk warning threshold, and incremental and self-adaptive correlation. According to different sources of data, this type of correlation mining is divided into two categories: one is derived from qualitative data, and the other from quantitative data.

(a) Qualitative Data

Qualitative data is obtained mainly from expert scoring, Boolean values, characteristic values, and so forth. For example, index weight is a form of this correlation. It mainly depends on expert scoring, indicating that the important relationship among all the risk factors. Many studies on weight determination and improvement have been carried out. This paper focuses on studying the relationship among risk factors with a certain confidence level based on variable fuzzy sets, rough sets, Bayesian, decision tree and support vector machines, and so forth. A fuzzy set usually has variability of time, space, and conditions, particularly in the engineering project investment. Because of the uncertainties that characterize a given project and its environment variables in the investment stage, fuzzy theory in engineering project research needs to upgrade mathematical theories, models, and methods. We use variable fuzzy sets for a better fit. To yield sound, adaptive, and heuristic investment decisions, as well as improve forecast quality and reduce reaction time in actual situations, the decision-maker would require intelligent algorithms other than CBR, such as rough sets, to mathematically address fuzziness and uncertainties. The decisions or classification rules can be derived through knowledge reduction based on the premise of invariable classification ability.

Table 2: Attributes used in CBR prediction model.

Input Attribute Number	Attribute	Class	Range
R_1	Total area of the building	3	[330 m ² , 1381 m ²) [1381 m ² , 2432 m ²) [2432 m ² , 3484 m ²]
R_2	Ratio of the typical floor area to the total area of the building	2	[0.07, 0.16] (0.16, 0.26]
R_3	Ratio of the footprint area to the total area of the building	2	[0.07, 0.19] (0.19, 0.30]
R_4	Number of floors	2	(4, 5, 6) (7, 8)
R_5	Type of overhang design	2	No overhang or one way
R_6	Foundation system	3	Pier, wall, slab
R_7	Type of floor structure	2	Cast in situ concrete, precast concrete
R_8	Location of the core	2	At the sides, in the middle
Output	Cost of the structural system per m ²	5	(\$30/m ² , \$56/m ²)
			(\$56/m ² , \$82/m ²)
			(\$82/m ² , \$108/m ²)
			(\$108/m ² , \$134/m ²)
			(\$134/m ² , \$160/m ²)

Table 3: Classes specified for output attribute of cost per m².

Input Case No.	Input Casebase								Output Attribute
	Input Attribute								
	R_1	R_2	R_3	R_4	R_5	R_6	R_7	R_8	
1	1	2	1	1	One-way	Sides	Precast	Wall	1
2	3	1	1	2	No cons	Middle	RC	Slab	2
3	1	2	2	1	No cons	Sides	RC	Wall	1
4	2	2	2	1	No cons	Sides	RC	Wall	1
5	1	2	1	1	One-way	Middle	RC	Slab	3
6	1	1	1	1	No cons	Sides	RC	Wall	1
7	3	1	1	1	No cons	Middle	RC	Wall	2
8	1	2	1	1	No cons	Sides	RC	Pier	2
9	2	2	2	1	No cons	Middle	RC	Slab	3
10	3	1	1	1	No cons	Middle	RC	Slab	1
11	2	1	1	2	No cons	Sides	RC	Wall	1

Eleven practical cases of the same category are analyzed, and their unit prices are mainly constrained by eight influencing factors. The eight factors and their grade distributions are enumerated in Table 2. The attribute classifications of each case are shown in Table 3 [13]. The rough sets method does not require any prior knowledge other than the dataset that requires processing; thus, we adopt this method to reduce the attributes that influence construction unit price based on the practical data shown in Table 3.

In rough sets, $U \neq \emptyset$ indicates that the universe is the finite set of objects. Suppose R is an equivalence relationship in U , and U/R represents the set of all equivalence classes

without \mathbf{R} . If $\mathbf{P} \in \mathbf{R}$ and $\mathbf{P} \neq \emptyset$, then $\cap \mathbf{P}$ denotes the intersection of all equivalence relationships in \mathbf{P} . $\mathbf{P} \cdot \mathbf{P}$ is also an equivalence relationship. $\cap \mathbf{P}$ is the indiscernibility relationship in \mathbf{P} , denoted by $\text{ind}(\mathbf{P})$. Therefore, $U/\text{ind}(\mathbf{P})$ denotes the knowledge related to the equivalence relationship with family \mathbf{P} ; it is usually denoted by U/\mathbf{P} .

Suppose $U = \{\mathbf{R}, \mathbf{D}\}$, $\mathbf{R} = \{R_1, R_2, R_3, R_4, R_5, R_6, R_7, R_8\}$ is the condition attribute set, and $\mathbf{D} = \{\text{Output}\}$ is the target set. Their respective equivalence relationships based on attribute values are as follows:

$$\begin{aligned}
 \frac{U}{R_1} &= \{(1, 3, 5, 6, 8)(4, 9, 11)(2, 7, 10)\}; \\
 \frac{U}{R_2} &= \{(2, 6, 7, 10, 11)(1, 3, 4, 5, 8, 9)\}; \\
 \frac{U}{R_3} &= \{(1, 2, 5, 6, 7, 8, 10, 11)(3, 4, 9)\}; \\
 \frac{U}{R_4} &= \{(1, 3, 4, 5, 6, 7, 8, 9, 10)(2, 11)\}; \\
 \frac{U}{R_5} &= \{(1, 5)(2, 3, 4, 6, 7, 8, 9, 10, 11)\}; \\
 \frac{U}{R_6} &= \{(1, 3, 4, 6, 8, 11)(2, 5, 7, 9, 10)\}; \\
 \frac{U}{R_7} &= \{(1)(2, 3, 4, 5, 6, 7, 8, 9, 10, 11)\}; \\
 \frac{U}{R_8} &= \{(1, 3, 4, 6, 7, 11)(2, 5, 9, 10)(8)\}; \\
 \frac{U}{\mathbf{D}} &= \{(1, 3, 4, 6, 10, 11)(2, 7, 8)(5, 9)\}.
 \end{aligned} \tag{2.12}$$

Calculating whether $\text{ind}(\mathbf{R})$ is equal to $\text{ind}(\mathbf{R} - \{R\})$ yields attribute cores R_1 , R_4 , and R_8 . Non-reduction attributes are not unique, and these are $\{R_1, R_3, R_4, R_7, R_8\}$, $\{R_1, R_2, R_4, R_7, R_8\}$, $\{R_1, R_2, R_4, R_5, R_8\}$, $\{R_1, R_3, R_4, R_5, R_8\}$, $\{R_1, R_3, R_4, R_6, R_8\}$, and $\{R_1, R_2, R_4, R_6, R_8\}$. The rough sets method decreases the condition attributes to five, which substantially reduces computational complexity and improves decision-making efficiency. In actual forecasts, the more practical cases there are, the better the scientific decision support for the project. However, as the number of cases increases, the dependence among risk factors may change. It is practical, therefore, to study incremental correlation, which allows for certain error rates in the investment decision-making stage.

(b) Quantitative Data

The primary sources of quantitative data are the objective data of each project. There are two approaches to process these data. In the first scheme, quantitative data are transformed into qualitative form by triangular fuzzy or trapezoidal fuzzy method, and then the correlations are derived from the qualitative data. In the second scheme, objective data are directly analyzed to explore correlations [14–16]. In accordance with the second processing method,

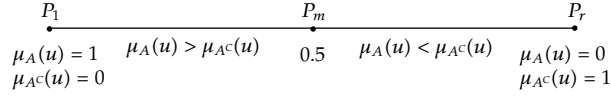


Figure 3: Schematic diagram of opposite fuzzy sets.

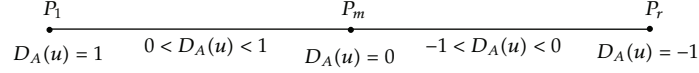


Figure 4: Schematic diagram of relative difference function.

we analyze the comprehensive effects of risk factors on risk monitoring and risk warning via quantitative and qualitative change theories of the variable fuzzy sets method.

The fuzzy sets concept was proposed by Zadeh in 1965, which was then developed into a new mathematical discipline—fuzzy sets theory. However, fuzzy sets are a static theory that cannot describe the dynamic variability of fuzziness, fuzzy events, or fuzzy concepts. Theoretically, using static fuzzy sets theory to study the dynamics of fuzziness is an insufficient approach. Contradictions exist between theoretical studies and research objectives. Chen [17] proposed the relative membership degree and relative membership function in the 1990s. He established engineering fuzzy sets theory [18]. In the early 21st century, Chen [18–21] created the variable fuzzy sets theory, which was a breakthrough in static concepts and theory of fuzzy sets.

Using variable fuzzy sets with the relative membership function to describe intermediate transition is a dynamic demonstration of fuzziness by precise mathematical language. Suppose U is a universe, and u is the element of U , $u \in U$. A and A^c is a pair of opposite fuzzy concept in u . At any point in the continuum number axis of the relative membership function, $\mu_A(u)$ is a relative membership degree of u to A , and $\mu_{A^c}^c(u)$ is a relative membership degree of u to A^c , where A^c is opposite A . $\mu_A(u) + \mu_{A^c}^c(u) = 1$, where $0 \leq \mu_A(u) \leq 1$ and $0 \leq \mu_{A^c}^c(u) \leq 1$. Seen from Figure 3, on left pole P_l : $\mu_A(u) = 1$, $\mu_{A^c}^c(u) = 0$; and on right pole P_r : $\mu_A(u) = 0$, $\mu_{A^c}^c(u) = 1$; P_m is the gradual qualitative change point whose continuum is $[1, 0]$ to A and $[0, 1]$ to A^c , and $\mu_A(u) + \mu_{A^c}^c(u) = 0.5$.

Suppose $D_A(u)$ is the relative difference degree of u to A , and $D_A(u) = \mu_A(u) - \mu_{A^c}^c(u)$. It is seen from Figure 4 that point P_m is where $D_A(u) = 0$ denotes the point at which dynamic balance with gradual qualitative change is reached. Points P_l and P_r are where $D_A(u) = 1$ and -1 represent the points at which mutational qualitative change is reached. Thus, the two forms of qualitative change, that is, gradual change and mutation, can be completely and clearly expressed by the relative difference degree.

Suppose C is one variable factor set of V , and $C = \{C_A, C_B, C_C, C_D, C_E, C_F\}$.

C_A is the variable factor set, C_B represents the variable spatial factor set, C_C denotes the variable condition factor set, C_D is the variable model set, C_E stands for the variable parameter set, and C_F is the other variable factor set.

The standard models for evaluating quantitative or qualitative change in a variable fuzzy set are as follows:

- (i) The criterion for quantitative change is $D_A(u) \cdot D_A(C(u)) > 0$.
- (ii) The criterion for gradual qualitative change is $D_A(u) \cdot D_A(C(u)) < 0$.

Table 4: Basic data from Feb. 2003 to Sep. 2003 of section F in the contract.

Time	No. of Month	Monthly Plan (million Yuan)	Monthly Completion (million Yuan)	Overall Completion (million Yuan)	Completion Rate	Contract Price after Change (million Yuan)
2003.2	14	880.1126	597.9812	5991.5486	0.6800	8695.2054
2003.3	15	938.5220	717.9559	6709.5045	0.7650	8555.2054
2003.4	16	918.4406	530.2455	7239.7500	0.5800	8555.2054
2003.5	17	959.0213	630.8527	7820.6027	0.6578	8655.2054
2003.6	18	766.6541	218.3175	8029.8021	0.2848	9021.8495
2003.7	19	766.6541	259.7389	8219.0000	0.3388	9221.8495
2003.8	20	68.6561	391.8619	8611.4029	0.5860	9221.8495
2003.9	21	593.3010	182.7692	8774.9369	0.3080	9141.8495

Table 5: Calculation of investment cost risk of section F in the contract.

Time	Volum Change This Month (million Yuan)	Cumulative Investment Deviation (million Yuan)	Net Value (million Yuan)	Offset Ratio from Total Investment	Offset Ratio from Schedule
2003.2		-1614.1201	7605.6690	-0.2122	-0.1856
2003.3	-140	-1754.1201	8463.6250	-0.2073	-0.2050
2003.4	0	-1754.1201	8993.8700	-0.1950	-0.2050
2003.5	100	-1654.1201	9474.7230	-0.1746	-0.1911
2003.6	366.6441	-1287.4760	9317.2780	-0.1382	-0.1427
2003.7	200	-1087.4760	9306.4760	-0.1169	-0.1179
2003.8	0	-1087.4760	9698.8790	-0.1121	-0.1179
2003.9	-80	-1167.4760	9942.4130	-0.1174	-0.1277

(iii) Two criteria are assigned to mutational qualitative change:

- (a) if the change occurs not through the gradual qualitative change point,
 $D_A(u) \cdot D_A(C(u)) = |D_A(u)|;$
- (b) if the change occurs through the gradual qualitative change point, $D_A(u) \cdot D_A(C(u)) = -|D_A(u)|.$

The data in Tables 4 and 5 were taken from a highway construction project [22]. We analyze the quantitative and qualitative changes in risk factors during the construction period to provide reference for determining the risk threshold value.

$D_A(u) = ((x_i - b_i) / (a_i - b_i))$, where $x_i \in [a_i, b_i]$ and $D_A(u) = ((x_i - b_i) / (d_i - b_i))$, where $x_i \in [b_i, d_i]$ is the linear equation of relative difference degree [23].

X_1 is the deviation rate of the total investment cost, and X_2 is the deviation rate of the schedule. This work comprehensively evaluates risks based on these two deviation rates. The relative difference degree of investment cost and schedule from February 2003 to September 2003 is calculated according to eigenvalues of $[a, b]$ and $[b, d]$ (see Table 6), respectively.

Suppose the weight vector of the two indexes is $\omega = [0.5, 0.5]$, and the risk relative difference degree of each month is $D_A(u) = \sum_{i=1}^2 \omega_i D_A(u)_i$. The relative difference degree of comprehensive risk of each month is shown in Table 7.

Table 6: The eigenvalues of $[a, b]$ and $[b, d]$ of the deviation index.

X_1	X_2
$[a_1, b_1] \quad [b_1, d_1]$	$[a_2, b_2] \quad [b_2, d_2]$
$[-0.1, -0.18] \quad [-0.18, -0.25]$	$[-0.1, -0.18] \quad [-0.18, -0.25]$

Table 7: Relative difference degrees from Feb. 2003 to Sep. 2003 of section F in the contract.

Time	2003.2	2003.3	2003.4	2003.5	2003.6	2003.7	2003.8	2003.9
$D_A(u)$	-0.27	-0.37	-0.27	0.26	0.26	0.78	0.80	0.76

The tendency of the value of $D_A(u)$ to move closer to -1 indicates high risk. By contrast, its tendency to move closer to 1 indicates low risk. Table 7 shows that the changes occurring from April 2003 to May 2003 are gradual qualitative changes, whereas the other continuous intervals are quantitative changes. The result in Table 7 is simple and intuitionistic. In addition, the decision-maker can combine the results with his own risk tolerance to determine the risk threshold required to implement appropriate measures. Our proposed method combines objective and subjective evaluations.

3. Conclusions

Research on risk correlation remains a bottleneck in current risk management in engineering project investment decision-making. We divide risk correlation into three types and elucidate the third correlation using actual data. The proposed approach combines data mining and variable fuzzy sets with investment decision-making, yielding simple, intuitionistic, and easily explainable results. Findings generated from this study provide reference value because it comprehensively considers risk prediction, risk management, and cost reduction analysis. Dynamics correlation and incremental correlation are the directions for further study.

Acknowledgments

This research work was jointly supported by the Science Fund for Creative Research Groups of the NSFC (Grant no. 51121005), the National Natural Science Foundation of China (Grant no. 51222806), and the Program for New Century Excellent Talents in University (Grant no. NCET-10-0287).

References

- [1] G. Morcous, H. Rivard, and A. Hanna, "Case-based reasoning system for bridge management," *Journal of Computing in Engineering*, pp. 1363–1370, 2000.
- [2] D. K. H. Chua, D. Z. Li, and W. T. Chan, "Case-based reasoning approach in bid decision making," *Journal of Construction Engineering and Management*, vol. 127, no. 1, pp. 35–45, 2001.
- [3] D. K. H. Chua and Y. M. Goh, "Application of case based reasoning in construction safety planning," in *Proceedings of the International Workshop on Information Technology in Civil Engineering: Computing in Civil Engineering*, pp. 298–307, Washington, DC, USA, November 2002.
- [4] Y. Cheng and H. Melhem, "Application of fuzzy case-based reasoning to bridge management," *Journal of Construction Engineering and Management*, pp. 1–12, 2005.
- [5] B. Ozorhon, I. Dikmen, and M. T. Birgonul, "Case-based reasoning model for international market selection," *Journal of Construction Engineering and Management*, vol. 132, no. 9, pp. 940–948, 2006.

- [6] H. G. Ryu, H. S. Lee, and M. Park, "Construction planning method using case-based reasoning (CONPLA-CBR)," *Journal of Computing in Civil Engineering*, vol. 21, no. 6, pp. 410–422, 2007.
- [7] Y. M. Goh and D. K. H. Chua, "Case-based reasoning for construction hazard identification: case representation and retrieval," *Journal of Construction Engineering and Management*, vol. 135, no. 11, pp. 1181–1189, 2009.
- [8] M. Galushka and D. Patterson, "Intelligent index selection for case-based reasoning," *Knowledge-Based Systems*, vol. 19, no. 8, pp. 625–638, 2006.
- [9] S. Y. Chen, J. Zhang, H. Zhang, N. M. Kwok, and Y. F. Li, "Intelligent lighting control for vision-based robotic manipulation," *IEEE Transactions on Industrial Electronics*, vol. 59, no. 8, pp. 3254–3263, 2012.
- [10] S. Wen, W. Zheng, J. Zhu, X. Li, and S. Chen, "Elman fuzzy adaptive control for obstacle avoidance of mobile robots using hybrid force/position incorporation," *IEEE Transactions on Systems, Man and Cybernetics Part C*, vol. 42, no. 4, pp. 603–608, 2011.
- [11] S. Chen, Y. Zheng, C. Cattani, and W. Wang, "Modeling of biological intelligence for SCM system optimization," *Computational and Mathematical Methods in Medicine*, vol. 2012, Article ID 769702, 10 pages, 2012.
- [12] W. P. Xiao, W. P. Ou, and Y. G. Ou, "Practical methods of investment risk analysis at construction project," *Journal of Chongqing Jianzhu University*, vol. 19, no. 6, pp. 7–14, 1997.
- [13] S. Z. Doğan, D. Arditi, and H. Murat Günaydin, "Using decision trees for determining attribute weights in a case-based model of early cost prediction," *Journal of Construction Engineering and Management*, vol. 134, no. 2, pp. 146–152, 2008.
- [14] S. Chen, W. Huang, C. Cattani, and G. Altieri, "Traffic dynamics on complex networks: a survey," *Mathematical Problems in Engineering*, Article ID 732698, 23 pages, 2012.
- [15] S. Y. Chen, H. Tong, Z. Wang, S. Liu, M. Li, and B. Zhang, "Improved generalized belief propagation for vision processing," *Mathematical Problems in Engineering*, vol. 2011, Article ID 416963, 12 pages, 2011.
- [16] S. C. Lim, C. H. Eab, K. H. Mak, M. Li, and S. Y. Chen, "Solving linear coupled fractional differential equations by direct operational method and some applications," *Mathematical Problems in Engineering*, vol. 2012, Article ID 653939, 28 pages, 2012.
- [17] S. Y. Chen, "Philosophical basis of systemic dialectical theory of relative subordinate function," *Journal of Systemic Dialectics*, vol. 4, no. 2, pp. 26–29, 1996.
- [18] S. Y. Chen, "Philosophical foundation of variable fuzzy sets theory," *Journal of Dalian University of Technology*, vol. 25, no. 1, pp. 53–57, 2005.
- [19] S. Y. Chen, "Theory and model of engineering variable fuzzy set—mathematical basis for fuzzy hydrology and water resources," *Journal of Dalian University of Technology*, vol. 45, no. 2, pp. 308–312, 2005.
- [20] S. Y. Chen, "Theory of variable fuzzy sets and variable model sets," *Mathematics in Practice and Theory*, vol. 38, no. 18, pp. 146–153, 2008.
- [21] S. Y. Chen, "Quantity change and quality change criterion models of variable fuzzy sets theory and their application," *Systems Engineering and Electronics*, vol. 30, no. 10, pp. 1879–1882, 2008.
- [22] G. P. Zhou, "Research on early-warning threshold values for investment risk of infrastructure projects," *Highway*, no. 2, pp. 100–103, 2006.
- [23] S. Y. Chen and J. X. Yuan, "Variable fuzzy sets model and demonstration of inaccuracy of extensible methods applied in water science," *Water Resources Protection*, vol. 23, no. 6, pp. 1–6, 2007.

Research Article

Histogram Modification and Wavelet Transform for High Performance Watermarking

**Ying-Shen Juang,¹ Lu-Ting Ko,² Jwu-E Chen,² Yaw-Shih Shieh,³
Tze-Yun Sung,³ and Hsi Chin Hsin⁴**

¹ Department of Business Administration, Chung Hua University, Hsinchu 30012, Taiwan

² Department of Electrical Engineering, National Central University, Chungli 32001, Taiwan

³ Department of Electronics Engineering, Chung Hua University, Hsinchu 30012, Taiwan

⁴ Department of Computer Science and Information Engineering, National United University,
Miaoli 36003, Taiwan

Correspondence should be addressed to Tze-Yun Sung, bobsung@chu.edu.tw

Received 15 September 2012; Accepted 16 October 2012

Academic Editor: Sheng-yong Chen

Copyright © 2012 Ying-Shen Juang et al. This is an open access article distributed under the Creative Commons Attribution License, which permits unrestricted use, distribution, and reproduction in any medium, provided the original work is properly cited.

This paper proposes a reversible watermarking technique for natural images. According to the similarity of neighbor coefficients' values in wavelet domain, most differences between two adjacent pixels are close to zero. The histogram is built based on these difference statistics. As more peak points can be used for secret data hiding, the hiding capacity is improved compared with those conventional methods. Moreover, as the differences concentricity around zero is improved, the transparency of the host image can be increased. Experimental results and comparison show that the proposed method has both advantages in hiding capacity and transparency.

1. Introduction

Digital watermarking is a technique to embed imperceptible, important data called watermark into the host image for the purpose of copyright protection, integrity check, and/or access control [1–9]. However, it might cause the distortion problem regarding the recovery of the original host image. In order to protect the host image from being distorted, a reversible watermarking technique has been reported in the literature. The reversible watermarking technique does not only hide the secret data but also the host image that can be exactly reconstructed in a decoder. Therefore, it can be used in those applications where the host images, such as medical images, military maps, and remote sensing images, must be completely recovered [10–14].

Recent reversible watermarking techniques can be divided into spatial domain, transform domain, and compressed domain methods. In spatial domain based methods [15–19], the secret data is embedded by pixels' value modification. In the transform domain methods [20, 21], reversible-guaranteed transforms, such as integer discrete cosine transform and integer wavelet transform, are exploited and data embedding is depending on coefficient modulation. In the compressed domain methods [22, 23], image compression techniques like vector quantization and block truncation coding are involved.

Most spatial domain reversible watermarking techniques are developed based on three principles, they are difference expansion [15, 16] and histogram modification [17–19, 24]. Zhao et al. proposed a reversible data hiding based on multilevel histogram modification [19]. In this scheme, the inverse “S” order is adopted to scan the image pixels for difference generation. The embedding capacity is determined by two factors, the embedding level and the number of histogram bins around 0. However, with a better pixel scan path can provide a higher capacity with the embedding level not changing.

Wavelet transform provides an efficient multiresolution representation with various desirable properties such as subband decompositions with orientation selectivity and joint space-spatial frequency localization. In wavelet domain, the higher detailed information of a signal is projected onto the shorter basis function with higher spatial resolution; the lower detailed information is projected onto the larger basis function with higher spectral resolution. This matches the characteristics of a better situation for scanning the image pixels for difference generation [25, 26].

In this paper, we propose a reversible watermarking technique based on histogram modification and discrete wavelet transform. The remainder of the paper proceeds as follows. In Section 2, the reversible watermarking based on histogram modification is reviewed briefly. Section 3 describes the reversible watermarking based on histogram modification and discrete wavelet transform. Experimental results and comparison are presented in Section 4. Finally, conclusion is given in Section 5.

2. Histogram Modification for Reversible Watermarking

Zhao et al. proposed a reversible data hiding based on histogram modification in [19]. In this scheme, the inverse “S” order is adopted to scan the image pixels for difference generation. The integer parameter called embedding level EL ($EL \geq 0$) controls the hiding capacity and transparency of the marked image. A higher EL indicates that more watermark can be embedded but leads more distortion to a watermarked image.

The data embedding process of $EL = 0$ is as follows, and the histogram modification strategy is shown in Figure 1. First, the image is inverse “S” scanned and the difference histogram is constructed. Next, the histogram shifting is performed. The secret bit “1” can be hidden by changing the difference of the pixel value from 0 to 1, and the “0” is hidden by keeping the difference of the pixel value not changed. Each marked pixel can be produced by its left neighbor subtracting the modified difference. Finally, rearrange these marked pixels to produce the watermarked image.

The process of data extraction and image recovery is as follows. The watermarked image is also inverse “S” scanned into a sequence first. As the first pixel value is not changed during embedding, we have the first pixel value. Second, the difference of the first pixel value and second pixel value can be obtained. If the difference is 0, one bit watermark “0” is extracted. If the difference is 1, one bit watermark “1” is extracted and the original difference is 0. Thus the original pixel associated with the difference can be obtained. If the difference

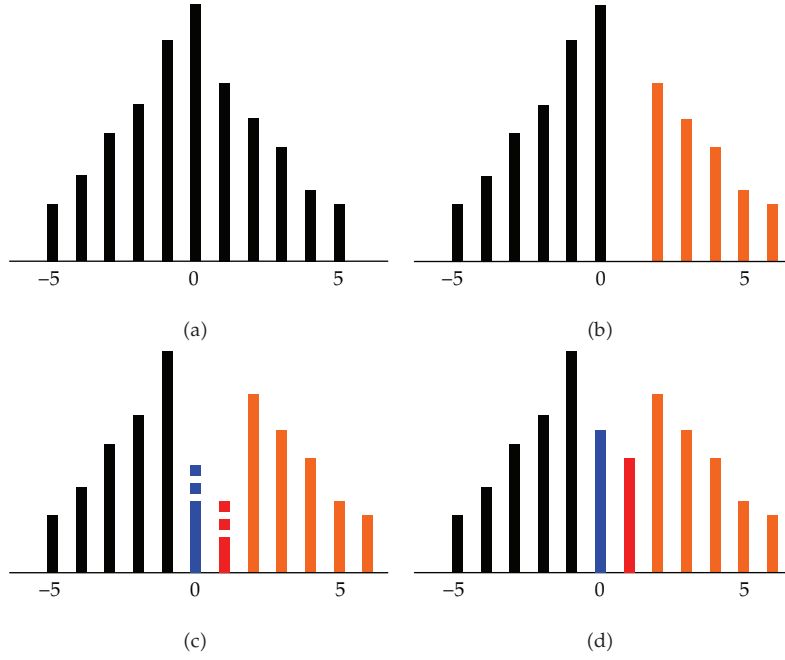


Figure 1: The histogram modification strategy: (a) the original histogram and (b) the histogram shifting: shift bins larger than 0 rightward (orange bins). (c) Secret data embedding: embed secret data “0” by keeping the difference of the pixel value not changed (blue bin) and embed secret data “1” by changing the difference of the pixel value from 0 to 1 (red bin). (d) The modified histogram.

is larger than 1, subtract 1 from the difference and recover the original pixel. Repeat these operations for the remained watermarked sequence and all the host pixels are recovered. Finally, rearrange these recovered pixels to produce the original host image.

The embedding capacity is determined by two factors, the embedding level and the number of histogram bins around 0. As mentioned before, a higher EL indicates that more watermark can be embedded, but leads more distortion to a watermarked image. However, with a better pixel scan path can provide a higher capacity with the embedding level not changing. Thus, we proposed an appropriate method to reach a higher capacity with embedding level $EL = 0$.

3. The Proposed Method

In this section, we proposed a novel reversible data hiding based on histogram modification and discrete wavelet transform. According to the similarity of neighbor coefficients' values in wavelet domain, most differences between two adjacent pixels are close to zero. The histogram is built based on these difference statistics. As more peak points can be used for secret data hiding, the hiding capacity is improved compared with those conventional methods.

3.1. Discrete Wavelet Transform

Discrete wavelet transform (DWT) provides an efficient multiresolution analysis for signals, specifically, any finite energy signal $f(x)$ can be written by

$$f(x) = \sum_n S_J(n) \phi_{Jn}(x) + \sum_{\ell \leq J} \sum_n D_\ell(n) \psi_{\ell n}(x), \quad (3.1)$$

where ℓ denotes the resolution index with larger values meaning coarser resolutions, n is the translation index, $\psi(x)$ is a mother wavelet, $\phi(x)$ is the corresponding scaling function, $\psi_{\ell n}(x) = 2^{-\ell/2}\psi(2^{-\ell}x - n)$, $\phi_{\ell n}(x) = 2^{-\ell/2}\phi(2^{-\ell}x - n)$, $S_J(n)$ is the scaling coefficient representing the approximation information of $f(x)$ at the coarsest resolution 2^J , and $D_\ell(n)$ is the wavelet coefficient representing the detail information of $f(x)$ at resolution 2^ℓ . Coefficients $S_\ell(n)$ and $D_\ell(n)$ can be obtained from the scaling coefficient $S_{\ell-1}(n)$ at the next finer resolution $2^{\ell-1}$ by using 1-level DWT, which is given by

$$\begin{aligned} S_\ell(n) &= \sum_k S_{\ell-1}(k)h(2n-k), \\ D_\ell(n) &= \sum_k S_{\ell-1}(k)g(2n-k), \end{aligned} \quad (3.2)$$

where $h(n) = \langle \phi, \phi_{-1,-n} \rangle$, $g(n) = \langle \psi, \phi_{-1,-n} \rangle$, and $\langle \cdot, \cdot \rangle$ denote the inner product. It is noted that $h(n)$ and $g(n)$ are the corresponding low-pass filter and high-pass filter, respectively. Moreover, $S_{\ell-1}(n)$ can be reconstructed from $S_\ell(n)$ and $D_\ell(n)$ by using the inverse DWT, which is given by

$$S_{\ell-1}(n) = \sum_k S_\ell(k)\tilde{h}(n-2k) + \sum_k D_\ell(k)\tilde{g}(n-2k), \quad (3.3)$$

where $\tilde{h}(n) = h(-n)$ and $\tilde{g}(n) = g(-n)$.

For image applications, 2D DWT can be obtained by using the tensor product of 1D DWT. Among wavelets, Haar's wavelet is the simplest one, which has been widely used for many applications. The low-pass filter and high-pass filter of Haar's wavelet are as follows

$$\begin{aligned} h(0) &= 0.5; & h(1) &= 0.5, \\ g(0) &= 0.5; & g(1) &= -0.5. \end{aligned} \quad (3.4)$$

Figures 2 and 3 show the row decomposition and the column decomposition using Haar's wavelet, respectively. Notice that the column decomposition may follow the row decomposition, or vice versa, in 2D DWT.

As a result, 2D DWT with Haar's wavelet is as follows:

$$\begin{aligned} LL &= \frac{A+B+C+D}{4}, \\ LH &= \frac{A+B-C-D}{4}, \\ HL &= \frac{A-B+C-D}{4}, \\ HH &= \frac{A-B-C+D}{4}, \end{aligned} \quad (3.5)$$

where A, B, C , and D are pixels values, and LL, LH, HL , and HH denote the approximation, detail information in the horizontal, and vertical and diagonal orientations, respectively, of the input image. Figure 4 shows 1-level, 2D DWT using Haar's wavelet.

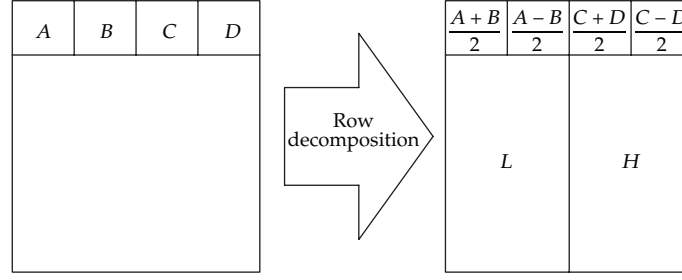


Figure 2: The row decomposition using Haar's wavelet (A, B, C , and D are pixels values).

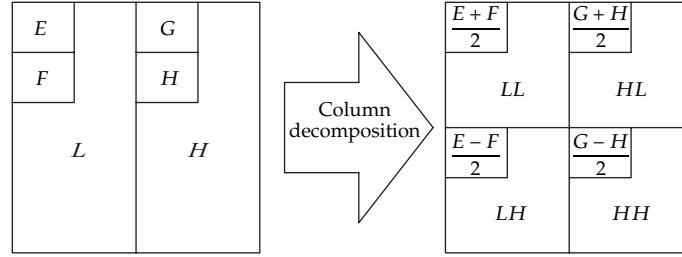


Figure 3: The column decomposition using Haar's wavelet (E, F, G , and H are pixel values).

The LL subband of an image can be further decomposed into four subbands: $LLLL$, $LLLH$, $LLHL$, and $LLHH$ at the next coarser resolution, which together with LH , HL , and HH forms the 2-level DWT of the input image. Thus, higher level DWT can be obtained by decomposing the approximation subband in the recursive manner.

3.2. Watermarking Scheme

Figure 5 shows the proposed embedding process; the details are described below. First, decompose the host $M \times N$ image I via 2D DWT into four 1-level subbands: LL , LH , HL , and HH . Then decompose these 1-level subbands again into sixteen 2-level subbands: $LLLL$, $LLLH$, $LLHL$, $LLHH$, $LHLL$, $LHLH$, $LHHL$, $LHHH$, $HLLL$, $HLLH$, $HLHL$, $HLHH$, $HHLL$, $HHLH$, $HHHL$, and $HHHH$, as shown in Figures 5(a) and 5(b). Second, generate a random sequence for these subbands. Third, select a random starting location in the first subbands. Fourth, pick a random scanning direction and scan the first subband into pixel sequence $p_1, p_2, \dots, p_{M \times N/16}$. Next, compute the difference d_i ($1 \leq i \leq M \times N/16$) according to (3.6) and construct a histogram based on d_i ($2 \leq i \leq M \times N/16$)

$$d_i = \begin{cases} p_1, & i = 1, \\ p_{i-1} - p_i, & 2 \leq i \leq M \times N/16. \end{cases} \quad (3.6)$$

Then shift the histogram bins which are larger than 1 rightward one level as

$$d'_i = \begin{cases} p_1, & \text{if } i = 1, \\ d_i, & \text{if } d_i < 1, \ 2 \leq i \leq M \times N/16, \\ d_i + 1, & \text{if } d_i \geq 1, \ 2 \leq i \leq M \times N/16. \end{cases} \quad (3.7)$$

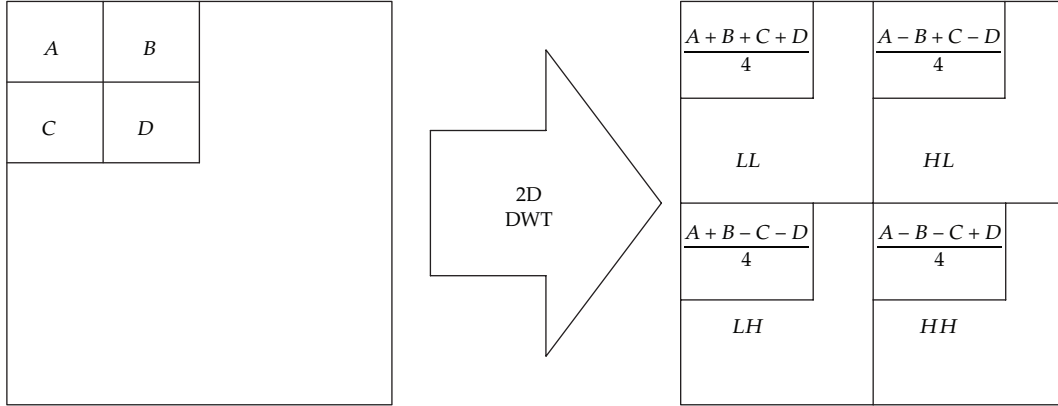


Figure 4: 1-level 2D DWT using Haar's wavelet (A , B , C , and D are pixel values).

Examine $d'_i = 0$ ($2 \leq i \leq M \times N/16$) one by one. Each difference less than 1 can be used to hide one secret bit (pixels with green color in Figure 5(f) of the difference sequence d'_i). If the corresponding watermark bit $w = 0$, it is not changed (pixels with blue color in Figure 5(f) of the difference sequence d'_i). And if $w = 1$, add the difference by 1 (pixels with red color in Figure 5(f) of the difference sequence d'_i). The operation is as

$$d''_i = \begin{cases} p_1, & \text{if } i = 1, \\ d'_i + w, & \text{if } d'_i < 1, w = 1, 2 \leq i \leq M \times N/16, \\ d'_i, & \text{if } d'_i < 1, w = 0, 2 \leq i \leq M \times N/16, \\ d'_i, & \text{if } d'_i \geq 1, 2 \leq i \leq M \times N/16, \end{cases} \quad (3.8)$$

and generate watermarked pixel sequence p'_i by this operation:

$$p'_i = \begin{cases} p_1, & i = 1, \\ p_{i-1} - d''_i, & 2 \leq i \leq M \times N/16. \end{cases} \quad (3.9)$$

Rearrange p'_i and the first 2-level watermarked subband is obtained. Repeat these operations for the remained subbands.

Pick the 2-level watermarked subbands $LLLL'$, $LLLH'$, $LLHL'$, and $LLHH'$ and perform the 2D inverse DWT to get the 1-level watermarked subband LL' . Repeat this operation for the remained 2-level watermarked subbands to get the 1-level watermarked subbands LH' , HL' , and HH' . Finally, perform the 2D inverse DWT to get the watermarked image I' .

The data extraction and image recovery is the inverse process of data embedding, and the process is as follows. First, decompose the watermarked image I' via 2D DWT into four 1-level watermarked subbands: LL' , LH' , HL' , and HH' . Then decompose these watermarked subbands again into sixteen 2-level watermarked subbands: $LLLL'$, $LLLH'$, $LLHL'$, $LLHH'$, $LHLL'$, $LHLH'$, $LHHL'$, $LHHH'$, $HLLL'$, $HLLH'$, $HLHL'$, $HLHH'$, $HHLL'$, $HHLH'$, $HHLH'$, and $HHLH'$.

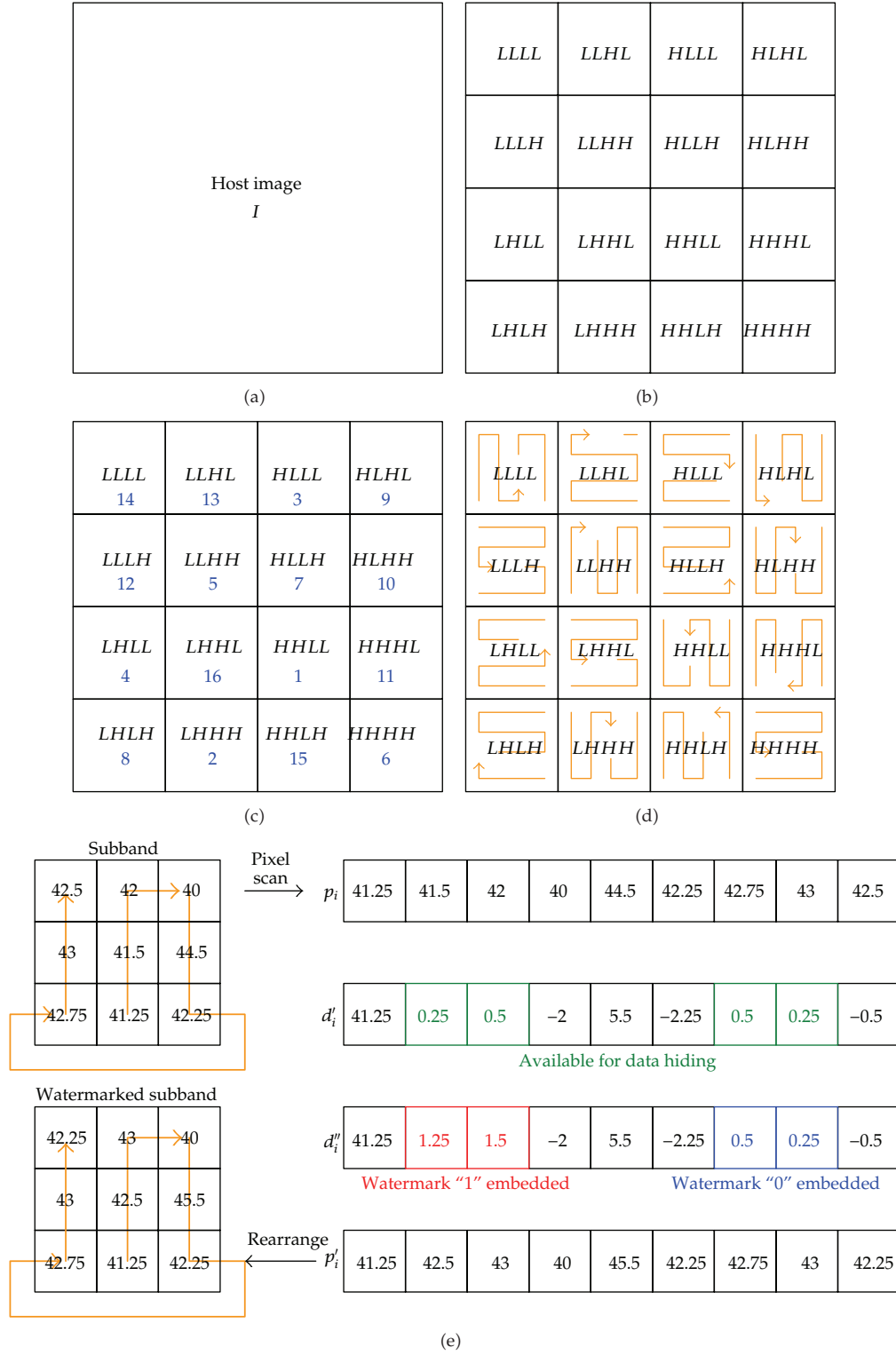


Figure 5: Continued.

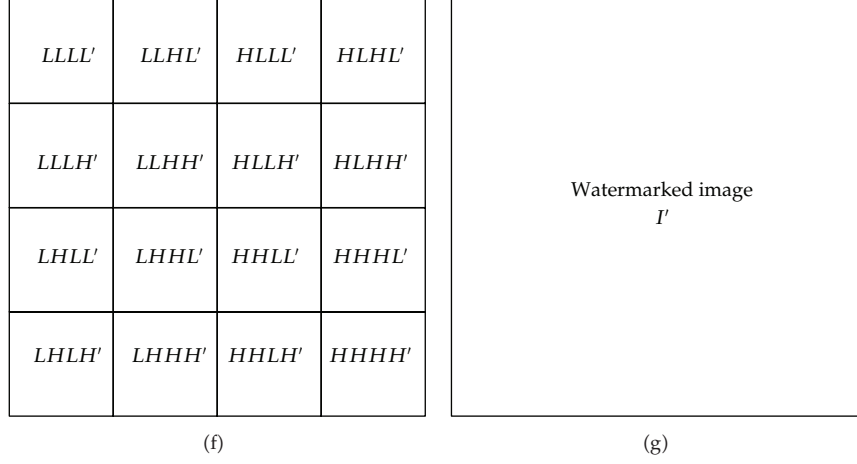


Figure 5: The proposed data embedding principle: (a) the original host image (b) decomposes into sixteen subbands, (c) generates the random sequence of the subbands, (d) selects the random starting location and direction of each subbands (e) An example of embedding watermark into pixel sequence; (f) rearranged watermarked subbands; (g) the watermarked image.

$HHHL'$, and $HHHH'$. Second, get the subband sequence of the watermark, starting location, and scanning direction of each watermarked subbands. Third, scan the first watermarked subband into watermarked pixel sequence $p'_1, p'_2, \dots, p'_{M \times N/16}$. Then recover the original pixel sequence based on the following:

$$p_i = \begin{cases} p'_1, & \text{if } i = 1, \\ p'_i, & \text{if } p_{i-1} - p'_i \leq 1, \ 2 \leq i \leq M \times N, \\ p'_i - 1, & \text{if } p_{i-1} - p'_i > 1, \ 2 \leq i \leq M \times N. \end{cases} \quad (3.10)$$

Figure 6 shows an example of secret data extracting and original pixel sequence recovering.

Rearrange the original pixel sequence and the original 2-level subband can be recovered. Repeat those operations until all 2-level subbands are recovered and perform 2D inverse DWT to get the 1-level subbands. Finally, perform 2D inverse DWT again and the original host image can be obtained.

The secret data is extracted as

$$w = \begin{cases} 0, & \text{if } 0 \leq p_{i-1} - p'_i < 1, \ 2 \leq i \leq M \times N, \\ 1, & \text{if } 1 \leq p_{i-1} - p'_i < 2, \ 2 \leq i \leq M \times N. \end{cases} \quad (3.11)$$

Rearrange these extracted bits and the original watermark can be obtained.

4. Experimental Results

Figure 7 shows our test images, six 256×256 with 256 gray levels are selected as test images; they are Lena, Baboon, Barbara, Boat, Board, and Peppers. Table 1 lists the average capacity

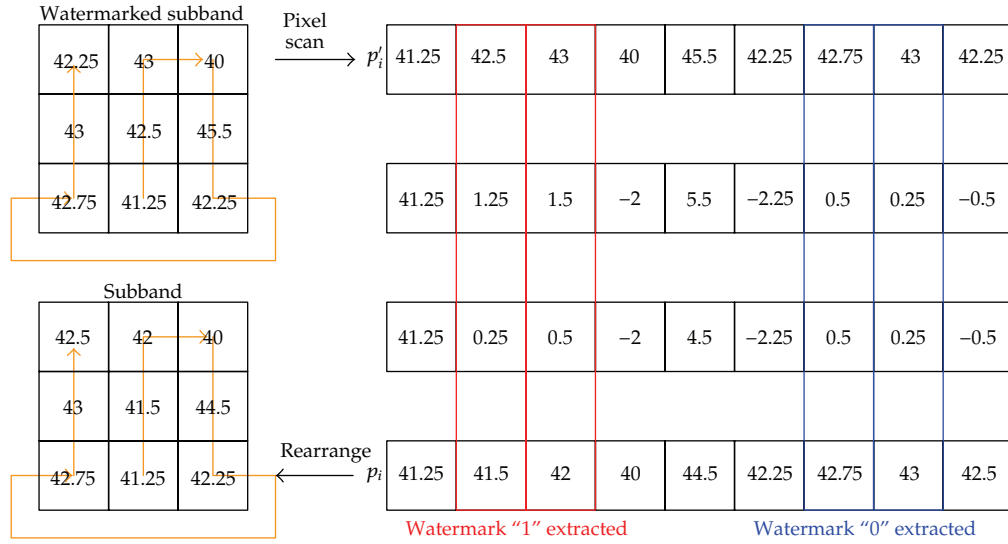


Figure 6: An example of secret data extracting and original pixel sequence recovering.

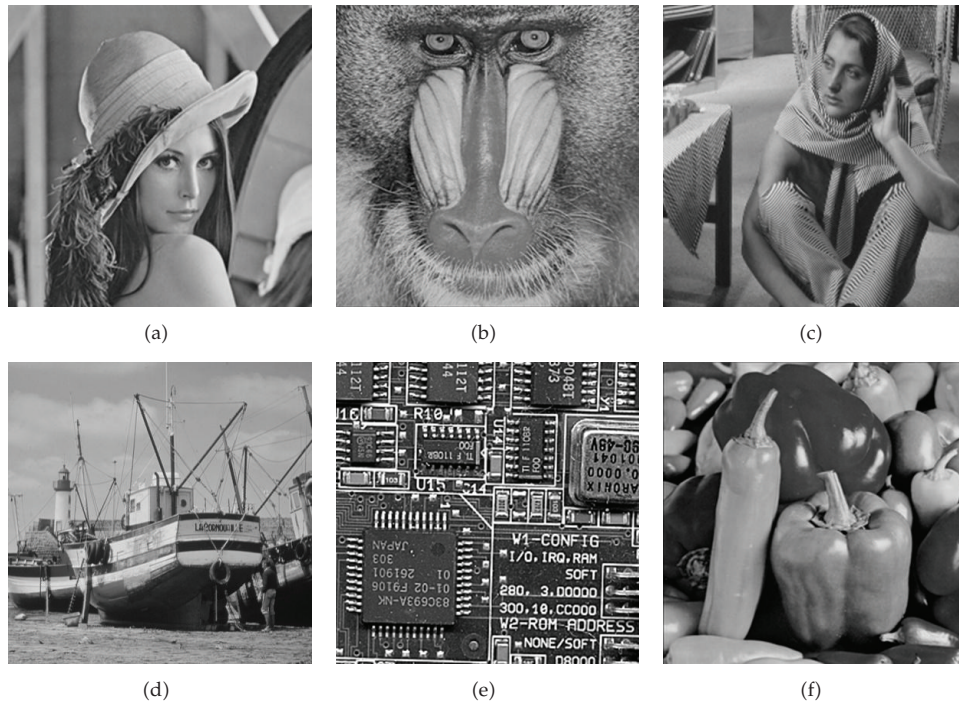


Figure 7: Test images: (a) Lena, (b) Baboon, (c) Barbara, (d) Boat, (e) Board, and (f) Peppers. The six watermarked images obtained by our scheme and Zhao et al.'s method are shown in Figures 8–13. Note that all of the bits of the watermarks embedded inside are "1" which leads to a maximum distortion. All these results demonstrate not only the capacities but also the PSNRs in our method which are improved. In other words, even though more secret data embedded in our scheme and leads more distortion, the marked images quality is still better.



Figure 8: Watermarked Lena image obtained by our scheme ((a) 10580 bits hidden, 69.51 dB) and Zhao et al.'s scheme ((b) 8239 bits hidden, 50.65 dB) with EL = 0.

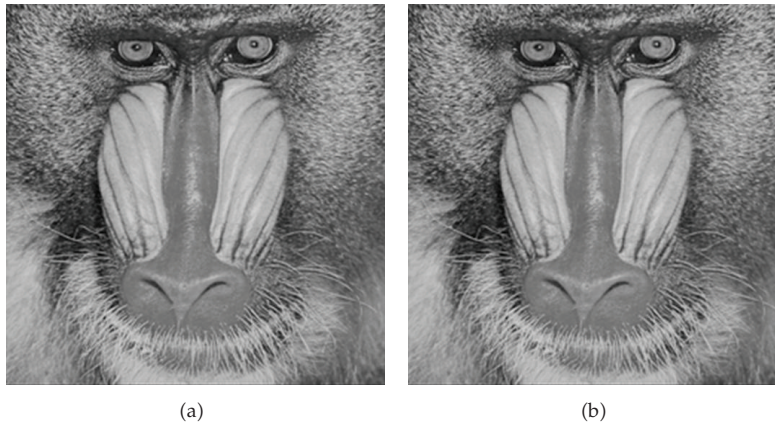


Figure 9: Watermarked Baboon's image obtained by our scheme ((a) 5900 bits hidden, 60.86 dB) and Zhao et al.'s scheme ((b) 2161 bits hidden, 51.01 dB) with EL = 0.

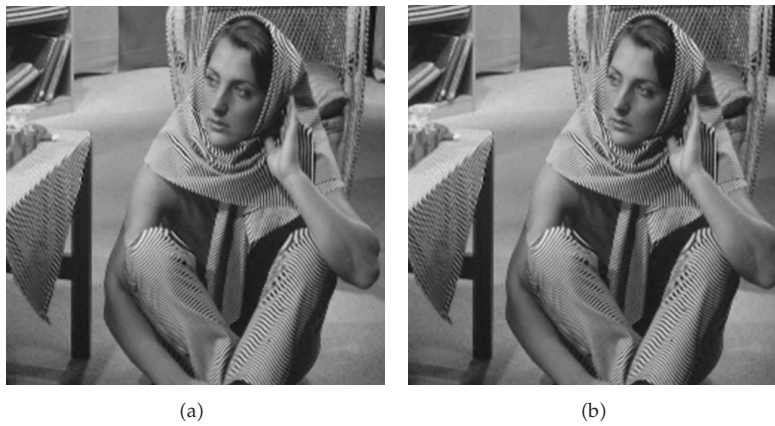


Figure 10: Watermarked Barbara's image obtained by our scheme ((a) 7446 bits hidden, 69.81 dB) and Zhao et al.'s scheme ((b) 3959 bits hidden, 50.91 dB) with EL = 0.



Figure 11: Watermarked Boat image obtained by our scheme ((a) 8257 bits hidden, 72.39 dB) and Zhao et al.'s scheme ((b) 5628 bits hidden, 50.79 dB) with EL = 0.

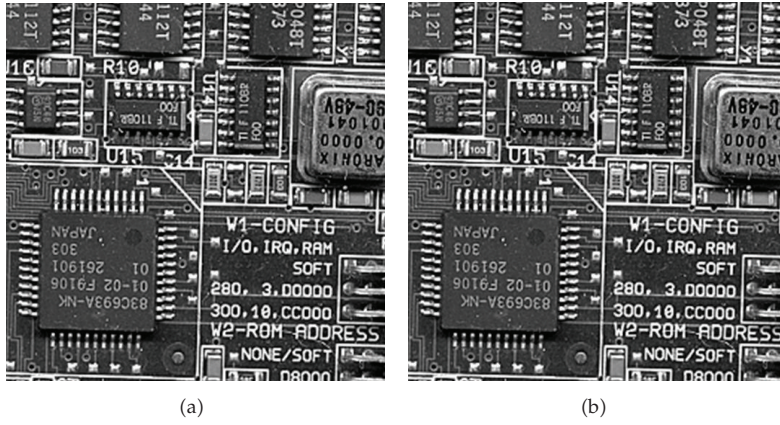


Figure 12: Watermarked Board image obtained by our scheme ((a) 4888 bits hidden, 55.11 dB) and Zhao et al.'s scheme ((b) 3589 bits hidden, 50.92 dB) with EL = 0.

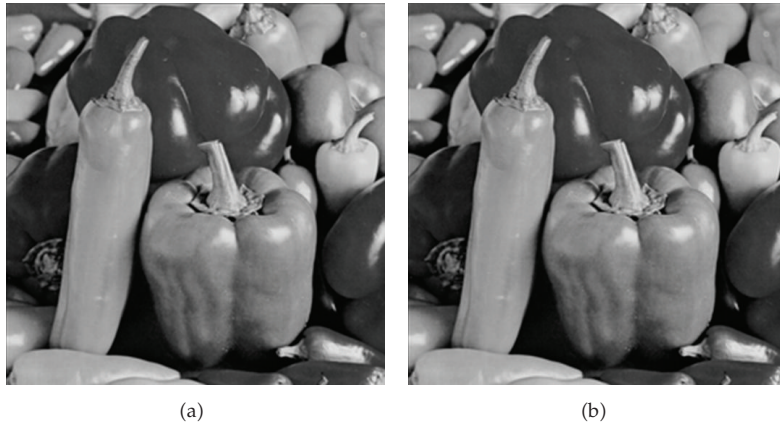


Figure 13: Watermarked Peppers image obtained by our scheme ((a) 9456 bits hidden, 66.41 dB) and Zhao et al.'s scheme ((b) 7299 bits hidden, 54.12 dB) with EL = 0.

Table 1: Performance comparison of Zhao et al.'s method and the proposed method.

Test images	Items	Zhao et al. [19]	This work
Lena	Capacity	0.1257	0.1511
	PSNR (dB)	50.65	69.51
Baboon	Capacity	0.0329	0.0847
	PSNR (dB)	51.01	60.86
Barbara	Capacity	0.0604	0.1069
	PSNR (dB)	50.91	69.81
Boat	Capacity	0.0858	0.1186
	PSNR (dB)	50.79	72.39
Board	Capacity	0.0547	0.0702
	PSNR (dB)	50.92	55.11
Peppers	Capacity	0.1113	0.1371
	PSNR (dB)	54.12	66.41

(bit per pixel) and PSNR (db) values of the proposed scheme. The peak signal to noise ratio (PSNR) is used to evaluate the image quality [27], which is defined as

$$\text{PSNR} = 20 \log \left(\frac{255}{\sqrt{\text{MSE}}} \right), \quad (4.1)$$

where MSE denotes the mean square error.

The six watermarked images obtained by our scheme and Zhao et al.'s method are shown in Figures 8, 9, 10, 11, 12, and 13. Note that all of the bits of the watermarks embedded inside are "1" which leads to a maximum distortion. All these results demonstrate that not only the capacities but also the PSNRs in our method are improved. In other words, even though more secret data embedded in our scheme and leads more distortion, the marked images quality is still better.

5. Conclusion

In this paper, a reversible watermarking based on the histogram modification has been proposed. The transparency of the watermarked image can be increased by taking advantage of the proposed watermarking. As the host image can be exactly reconstructed, it is suitable especially for medical images, military maps, and remote sensing images. The proposed reversible watermarking based on multilevel histogram modification and discrete wavelet transform is preferable and provides a higher capacity and higher transparency compared with other histogram modification based methods.

Acknowledgment

This work is supported by the National Science Council of Taiwan, under Grants NSC100-2628-E-239-002-MY2 and NSC100-2410-H-216-003.

References

- [1] I. J. Cox, J. Kilian, F. T. Leighton, and T. Shamoan, "Secure spread spectrum watermarking for multimedia," *IEEE Transactions on Image Processing*, vol. 6, no. 12, pp. 1673–1687, 1997.

- [2] M. D. Swanson, M. Kobayashi, and A. H. Tewfik, "Multimedia data-embedding and watermarking technologies," *Proceedings of the IEEE*, vol. 86, no. 6, pp. 1064–1087, 1998.
- [3] S. Chen, J. Zhang, Y. Li, and J. Zhang, "A hierarchical model incorporating segmented regions and pixel descriptors for video background subtraction," *IEEE Transactions on Industrial Informatics*, vol. 8, no. 1, pp. 118–127, 2012.
- [4] M. Barni, F. Bartolini, and A. Piva, "Improved wavelet-based watermarking through pixel-wise masking," *IEEE Transactions on Image Processing*, vol. 10, no. 5, pp. 783–791, 2001.
- [5] X. Zhang, Y. Zhang, J. Zhang, S. Chen, D. Chen, and X. Li, "Unsupervised clustering for logo images using singular values region covariance matrices on Lie groups," *Optical Engineering*, vol. 51, no. 4, Article ID 047005, 8 pages, 2012.
- [6] G. C. Langelaar, I. Setyawan, and R. L. Lagendijk, "Watermarking digital image and video data," *IEEE Signal Processing Magazine*, vol. 17, no. 5, pp. 20–46, 2000.
- [7] C. I. Podilchuk and E. J. Delp, "Digital watermarking: algorithm and application," *IEEE Signal Processing Magazine*, vol. 18, no. 4, pp. 33–46, 2001.
- [8] S. Chen, H. Tong, Z. Wang, S. Liu, M. Li, and B. Zhang, "Improved generalized belief propagation for vision processing," *Mathematical Problems in Engineering*, vol. 2011, Article ID 416963, 12 pages, 2011.
- [9] C. S. Lu and H. Y. M. Liao, "Multipurpose watermarking for image authentication and protection," *IEEE Transactions on Image Processing*, vol. 10, no. 10, pp. 1579–1592, 2001.
- [10] L. T. Ko, J. E. Chen, H. C. Hsin, Y. S. Shieh, and T. Y. Sung, "Haar wavelet based just noticeable distortion model for transparent watermark," *Mathematical Problems in Engineering*, vol. 2012, Article ID 635738, 14 pages, 2012.
- [11] S. Y. Chen, J. Zhang, Q. Guan, and S. Liu, "Detection and amendment of shape distortions based on moment invariants for active shape models," *IET Image Processing*, vol. 5, no. 3, pp. 273–285, 2011.
- [12] L. T. Ko, J. E. Chen, Y. S. Shieh, H. C. Hsin, and T. Y. Sung, "Nested quantization index modulation for reversible watermarking and its application to healthcare information management systems," *Computational and Mathematical Methods in Medicine*, vol. 2102, Article ID 839161, 8 pages, 2012.
- [13] H. Liu, S. Y. Chen, and N. Kubota, "Guest editorial special section on intelligent video systems and analytics," *IEEE Transactions on Industrial Informatics*, vol. 8, no. 1, p. 90, 2012.
- [14] L.-T. Ko, J.-E. Chen, Y.-S. Shieh, M. Scalia, and T.-Y. Sung, "A novel fractional-discrete-cosine-transform-based reversible watermarking for healthcare information management systems," *Mathematical Problems in Engineering*, vol. 2012, Article ID 757018, 17 pages, 2012.
- [15] A. M. Alattar, "Reversible watermark using the difference expansion of a generalized integer transform," *IEEE Transactions on Image Processing*, vol. 13, no. 8, pp. 1147–1156, 2004.
- [16] D. C. Lou, M. C. Hu, and J. L. Liu, "Multiple layer data hiding scheme for medical images," *Computer Standards and Interfaces*, vol. 31, no. 2, pp. 329–335, 2009.
- [17] Z. Ni, Y. Q. Shi, N. Ansari, and W. Su, "Reversible data hiding," in *Proceedings of the IEEE International Symposium on Circuits and Systems (ISCAS '03)*, vol. 2, pp. II912–II915, May 2003.
- [18] Y. C. Li, C. M. Yeh, and C. C. Chang, "Data hiding based on the similarity between neighboring pixels with reversibility," *Digital Signal Processing*, vol. 20, no. 4, pp. 1116–1128, 2010.
- [19] Z. Zhao, H. Luo, Z. M. Lu, and J. S. Pan, "Reversible data hiding based on multilevel histogram modification and sequential recovery," *AEU*, vol. 65, no. 10, pp. 814–826, 2011.
- [20] B. Yang, M. Schmucker, X. Niu, C. Busch, and S. Sun, "Integer DCT based reversible image watermarking by adaptive coefficient modification," in *Security, Steganography, and Watermarking of Multimedia Contents VII*, vol. 5681 of *Proceedings of SPIE*, pp. 218–229, January 2005.
- [21] G. Xuan, Q. Yao, C. Yang et al., "Lossless data hiding using histogram shifting method based on integer wavelets," in *Proceedings of the 5th International Workshop on Digital Watermarking (IWDW '06)*, vol. 4283 of *Lecture Notes in Computer Science*, pp. 323–332, 2006.
- [22] C. C. Chang, C. Y. Lin, and Y. H. Fan, "Lossless data hiding for color images based on block truncation coding," *Pattern Recognition*, vol. 41, no. 7, pp. 2347–2357, 2008.
- [23] B. G. Mobasseri and D. Cinalli, "Lossless watermarking of compressed media using reversibly decodable packets," *Signal Processing*, vol. 86, no. 5, pp. 951–961, 2006.
- [24] N. M. Kwok, X. Jia, D. Wang, S. Y. Chen, G. Fang, and Q. P. Ha, "Visual impact enhancement via image histogram smoothing and continuous intensity relocation," *Computers and Electrical Engineering*, vol. 37, no. 5, pp. 681–694, 2011.

- [25] M. Li, C. Cattani, and S. Y. Chen, "Viewing sea level by a one-dimensional random function with long memory," *Mathematical Problems in Engineering*, vol. 2011, Article ID 654284, 13 pages, 2011.
- [26] S. Y. Chen, H. Tong, and C. Cattani, "Markov models for image labeling," *Mathematical Problems in Engineering*, vol. 2012, Article ID 814356, 18 pages, 2012.
- [27] B. Chen and G. W. Wornell, "Quantization index modulation: a class of provably good methods for digital watermarking and information embedding," *IEEE Transactions on Information Theory*, vol. 47, no. 4, pp. 1423–1443, 2001.

Research Article

Down-Hole Heat Exchangers: Modelling of a Low-Enthalpy Geothermal System for District Heating

M. Carlini,¹ S. Castellucci,² E. Allegrini,¹ and A. Tucci²

¹ Department of Agriculture, Forest, Nature and Energy (D.A.F.N.E), University of Tuscia,
Via Camillo de Lellis, 01100 Viterbo, Italy

² CIRDER, University of Tuscia, Via Camillo de Lellis, 01100 Viterbo, Italy

Correspondence should be addressed to S. Castellucci, sonia.castellucci@unitus.it

Received 30 July 2012; Accepted 11 September 2012

Academic Editor: Sheng-yong Chen

Copyright © 2012 M. Carlini et al. This is an open access article distributed under the Creative Commons Attribution License, which permits unrestricted use, distribution, and reproduction in any medium, provided the original work is properly cited.

In order to face the growing energy demands, renewable energy sources can provide an alternative to fossil fuels. Thus, low-enthalpy geothermal plants may play a fundamental role in those areas—such as the Province of Viterbo—where shallow groundwater basins occur and conventional geothermal plants cannot be developed. This may lead to being fuelled by locally available sources. The aim of the present paper is to exploit the heat coming from a low-enthalpy geothermal system. The experimental plant consists in a down-hole heat exchanger for civil purposes and can supply thermal needs by district heating. An implementation in MATLAB environment is provided in order to develop a mathematical model. As a consequence, the amount of withdrawable heat can be successfully calculated.

1. Introduction

The Directive 2009/28/CE—implemented in Italy in 2010—set ambitious targets in order to ensure a clean and sustainable future. Its aim is to reduce greenhouse gases emissions by 20%, to produce 20% of energy from renewable sources and to decrease the consumption by 20% improving the energy efficiency. These goals must be reached by 2020 [1].

The above-mentioned regulation led the public administrations and private stakeholders to investigate new technologies which may face the growing energy demands by the use of renewable sources alternative to fossil fuels. Thus, energy supply might change from being predominantly fossil fuelled to being fuelled by locally available sources. In this scenario, low-enthalpy geothermal plants for heating and cooling buildings can be successfully used [2].

Basically, ground source heat pump systems can be distinguished in two different types: earth-coupled or closed-loop and groundwater or open-loop. In the first case, heat exchangers are underground and located horizontally (known as GSHP, acronym for “ground source heat pump”), vertically (known as DHE, acronym for “down-hole heat exchanger”) or obliquely. Heat is transferred from or to the ground thanks to a heat-carrying which circulates within the exchanger [2].

In the present paper, the use of DHE is taken into account. The exploitation of geothermal resources by DHEs is not characterized by mass withdrawal from the aquifer: more precisely, they permit heat transfer without extracting any fluid from the ground. This is to avoid the depletion of the aquifer, as requested by legislative restrictions. However, an important aspect has to be considered: the amount of withdrawable heat may be limited (usually less than 100 kW). This phenomenon is mainly due to the interaction between heat exchanger, well, and aquifer. As a consequence, DHEs are mostly used in small applications, such as buildings, greenhouses, and thermal baths [3, 4].

In order to increase vertical circulation of water and the natural mass transfer between aquifer and well, promoters can be used [5]. The exchangers consist in pipes or tubes which are located within the well. Because of the low capacity, these systems are successful up to 150 m of depth. Several designs are nowadays available but the most common one is a U-tube which extends to near the bottom of the well. Multiple tubes can be alternatively used [6].

Several studies were carried out in the past and led to the reconstruction of the stratigraphy, the evaluation of heat flow, the probable origin of hot waters and the chemical properties of gas and hydrothermal emissions. Della Vedova et al. developed a new heat flow map as shown in Figure 1: it can be seen how the highest values (red and orange areas) are mostly located in the Tyrrhenian Sea and in Central Italy (western coastline, especially in Tuscany and northern Latium) [7].

In the province of Viterbo hydrogeological settings and shallow groundwater basins seem to be particularly suitable for a wide implementation of DHE systems. Moreover, performances of geothermal heat pumps are significantly limited since groundwater basin temperatures vary from 40°C up to 90°C. Thus, their use is not recommended and implemented in the area.

The province of Viterbo is located in northern Latium and hosts several thermal springs in its territory. They had been already known by Romans who used them for therapeutic purposes. Bullicame Spring is one of the most famous hydrothermal source and is even mentioned by the poet Dante Alighieri. Nowadays, thermal waters are exploited for direct use or to supply spas and pools. Figure 2 shows the location of Viterbo hydrothermal area (dotted circle) within the regional geological picture. The investigated area lies between the Tyrrhenian coastline and the Apennines. From a geological point of view, the region is characterized by sedimentary basins belonging to the upper Miocene-Pleistocene age, elongated between ridges of Mesozoic-Paleogene rocks, which overlay a Paleozoic-Triassic metamorphic basement. Within this geological framework, Cimini volcanic complex consists of quartzolatic domes and ignimbrites and lavas. The Vico complex is characterized by explosive activity and is a typical stratovolcano. The substrate beneath them is made of sedimentary rocks [8].

The province of Viterbo is characterized by overlapped interacting aquifers. More precisely, the shallow volcanic aquifer has fresh waters which come from the area around Cimini Mountains. It is limited at the bottom by the semiconfining marly-calcareous-arenaceous complex and low-permeability clays. Vertical upflows of thermal waters—consisting in sulphate-chloride-alkaline-earth type and gases—occur westwards of Viterbo.

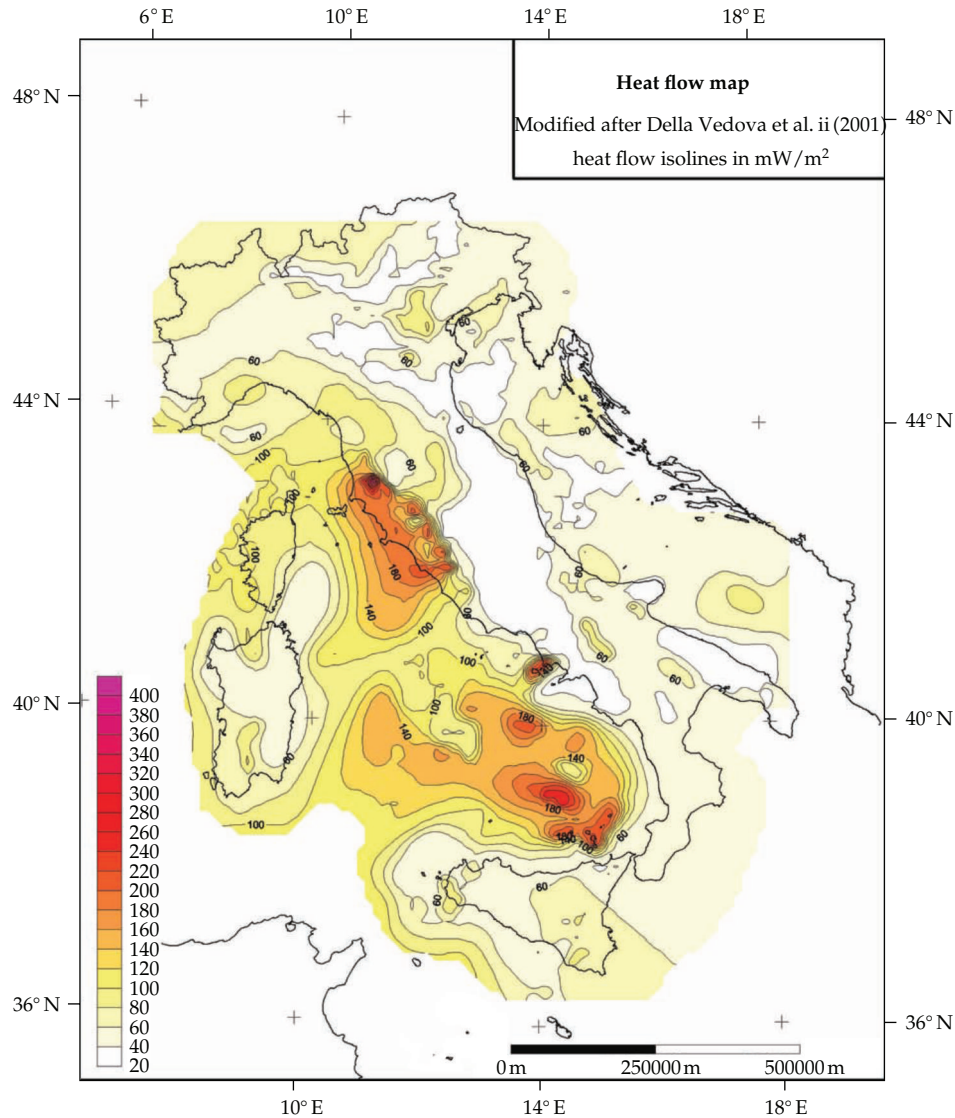


Figure 1: Heat flow map in Italy [7].

This phenomenon is mainly due to the uplifted carbonate reservoir, the limited thickness of the semiconfining layer, and the high local geothermal gradient. Hot waters are characterized by temperatures varying between 30 and 60°C thanks to the deep circulation in carbonate rocks. The minimum upward flow is 0.1 m³/sec. Springs and deep wells are fed by it [8].

An appropriate interpretation of the stratigraphy is successfully reached by drilling wells. Moreover, it can be correlated to surface geology in order to get the reconstruction of the hydrostratigraphy of the thermal area. Formations of Cimini and Vico complexes occur from the first 10 m down to 100 m. The shallow unconfined aquifer consists in these rocks and its thickness decreases where there are more layers of travertine. Plio-Pleistocene deposits lie beneath the volcanic aquifer and marly-calcareous-arenaceous flysh occurs below them [8].

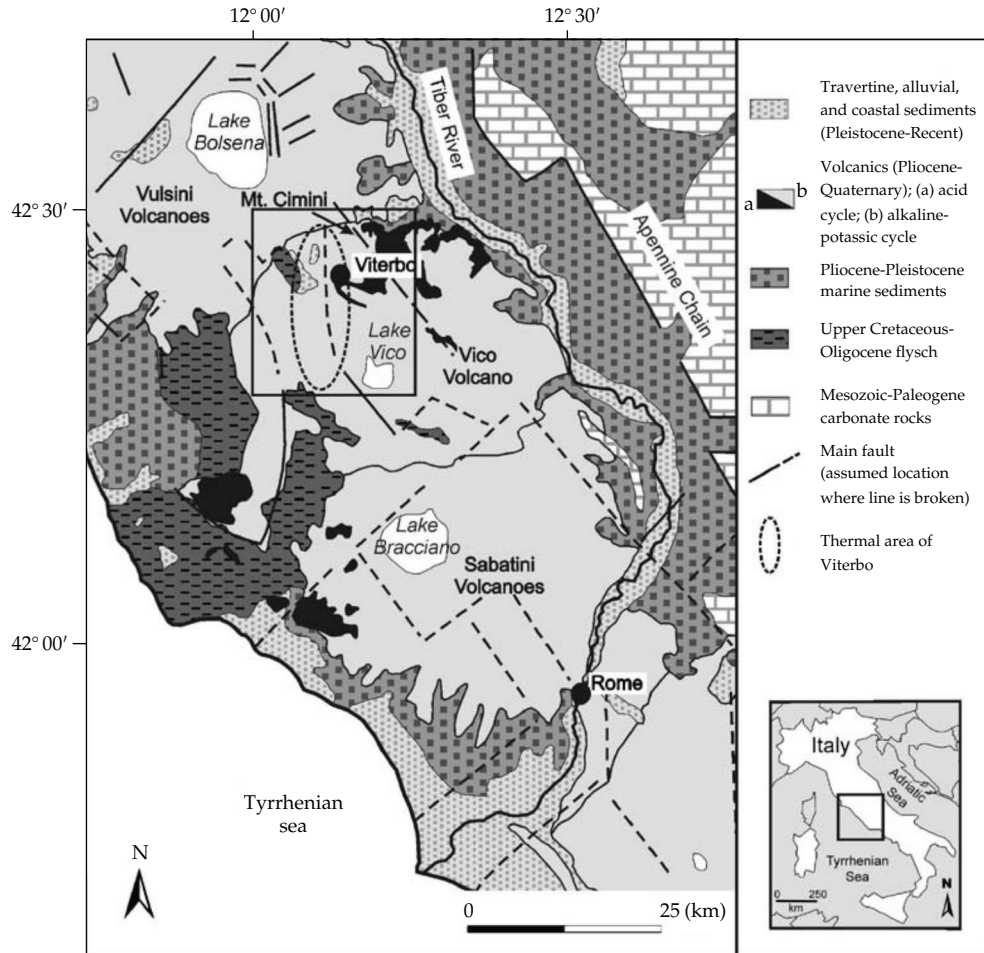


Figure 2: Viterbo Hydrothermal area within the regional geological picture [8].

A high concentration of wells and thermal springs occurs in the central area of the province of Viterbo. Data—such as elevation, discharge, and temperature—are available. With specific regard to the most important thermal springs in the province, the data are given in Table 1 [8].

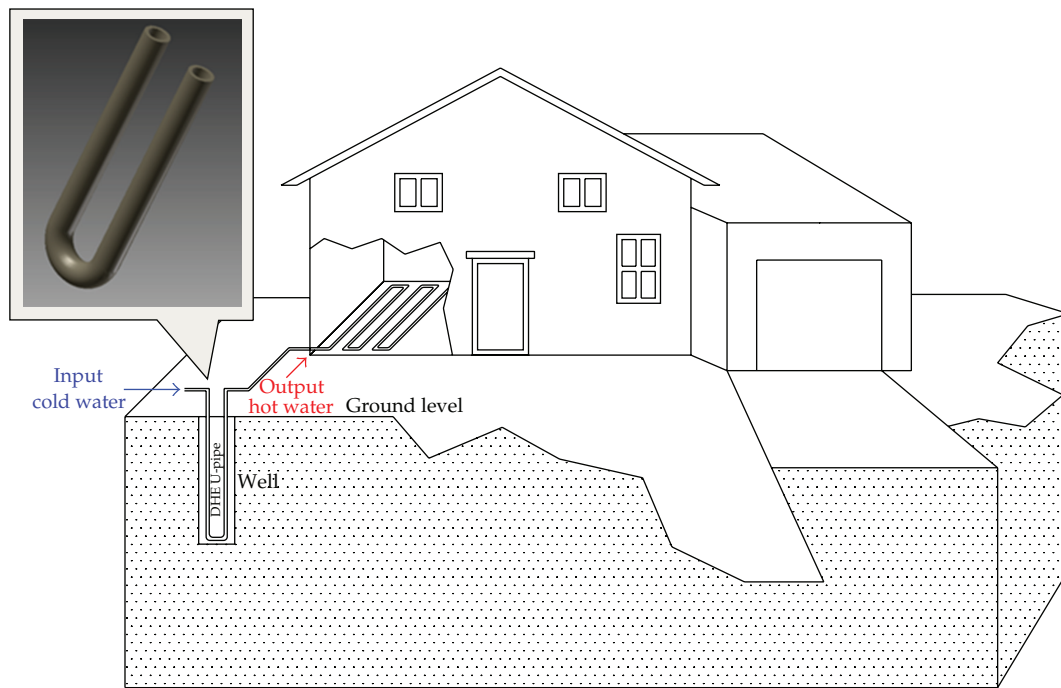
The aim of the present paper is to exploit the heat coming from a low-enthalpy geothermal plant for civil purposes, that is, district heating, as shown in Figure 3. In order to evaluate the withdrawable amount of heat, an implementation in MATLAB environment is developed. The goal is reached using real data which have been obtained by specific measurements *in situ*.

2. Models and Methods

The experimental plant is located in the central thermal area of Figure 2 and has been provided by Mr. Daniele Cortese, who owns the company “Plants and Bulbs”. Since regulations discourage the drilling of new wells, an existing one is chosen to develop the

Table 1: Data of the main thermal springs in the province of Viterbo [8].

Spring or group of springs	Name	Elevation (m a.s.l.)	Discharge (l/s)	Temperature (°C)
3	Bagnaccio	310–390	10	38–64
4	Monterozzo	305–319	5	27–51
7-8	Zitelle	289–308	6.5	39–65
9	Carletti	285	1.5	57
10	Bullicame	298	10.4	57
17	S. Cristoforo	245	0.1	53
21	S. Sisto	230	3	57
26	Bacucco	315–320	2	36–49
27	Urcionio	305–319	20	28–60

**Figure 3:** Low-enthalpy geothermal plant for civil purposes.

system. Moreover, the well is linked to the volcanic aquifer which is characterized by low hydraulic gradients and lays between swampy deposits and travertine. The local substratum is more than 50 m deep and consists in marly-calcareous-arenaceous complex [8].

The low-enthalpy geothermal system can be easily drafted as a reservoir which contains hot water and a pipe. Measurements of temperature in the groundwater basin were carried out at different depths: 2, 22, and 44 m, respectively. The temperature inside the well can be considered as constant and equal to 60°C, since the range of its variability is limited. According to the drilling log, the well is 60 m deep below the ground level. Its diameter is 150 mm and reaches the bottom of the aquifer. Moreover, a steel flanged pipe is located on the top of the well in order to contain the upflow water, which is generated by gases pressure

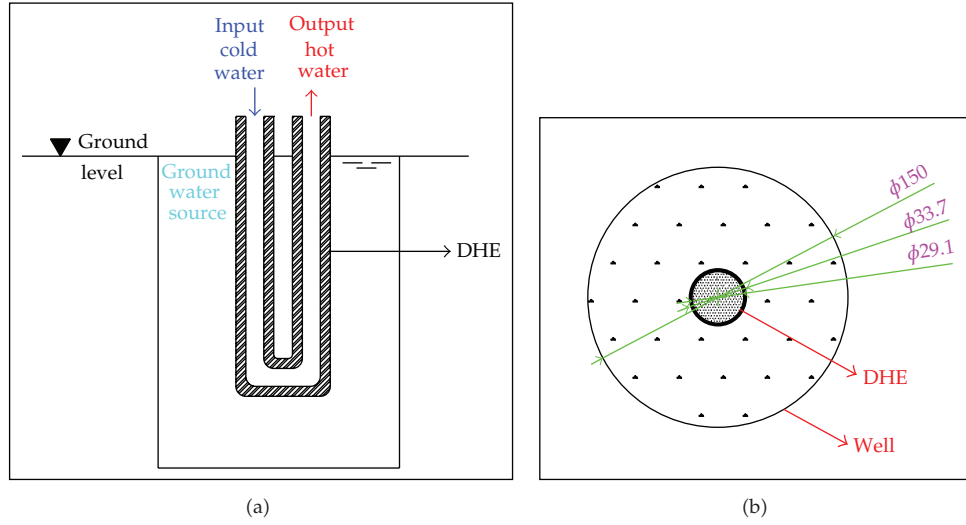


Figure 4: Schematic model (a) and size of the heat exchanger within the well (b).

and reaches 1.5 m above ground level. The heat exchanger consists in a vertical single U-pipe, as shown in Figure 4: the internal and external diameters are 29.1 mm and 33.7 mm, respectively and the total length is 110 m. The pipe is made of steel and its thickness is 4.6 mm. Three different modes of heat transfers occur: natural convection in the ground water basin, conduction within the wall of the pipe, and forced convection inside the heat exchanger. The latter is due to the pumping of water. The groundwater within the well is characterized by convective motions which are due to differences of density and consequently cause heat transfers [9].

In order to evaluate the total amount of withdrawable heat using the above-described system, an implementation in MATLAB is developed. The overall heat transfer rate Q is formally represented by [9–11]

$$Q = A \cdot U_D \cdot \Delta T_{LM}, \quad (2.1)$$

where A : overall heat exchange area (m^2); U_D : overall heat transfer coefficient ($\text{W}/\text{m}^2/\text{K}$); ΔT_{LM} : logarithmic mean temperature difference (K). U_D can be successfully calculated using the following formula [9–11]:

$$\frac{1}{U_D} = \frac{1}{h_{i0}} = \frac{d_{\text{ext}}}{2k} \cdot \ln\left(\frac{d_{\text{int}}}{d_{\text{ext}}}\right) + \frac{1}{h_{e0}} + R, \quad (2.2)$$

where h_{i0} : heat transfer coefficient inside the pipe ($\text{W}/\text{m}^2/\text{K}$); h_{e0} : heat transfer coefficient in the groundwater basin ($\text{W}/\text{m}^2/\text{K}$); d_{ext} : external diameter of the pipe (m); d_{int} : internal diameter of the pipe (m); k : thermal conductivity of the wall ($\text{W}/\text{m}/\text{K}$); R : fouling factor (dimensionless).

The second term in the definition of U_D is related to conduction but can be neglected since the thickness of the tube is limited. Moreover, k results from the type of material and R is tabulated depending on type of fluid, heat exchangers, and temperature. Figure 5 shows

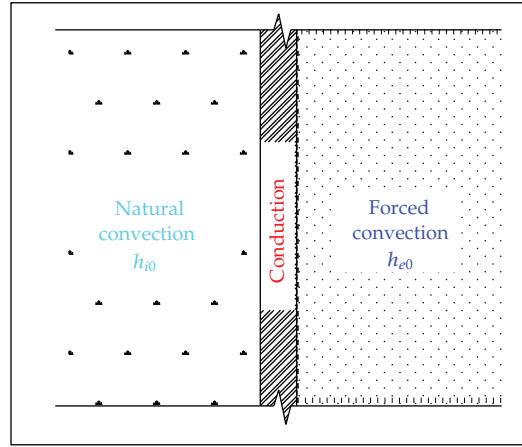


Figure 5: Heat transfers and heat transfer coefficients.

a schematic model with the different modes of heat transfers and the heat transfer coefficient related to them [12–15].

MATLAB is a high-level language and interactive environment which enables you to perform numerical computations and intensive tasks. It is an abbreviation for “MATrix LABoratory” and is designed to operate primarily on matrices and arrays [16].

With specific regard to the above-described plant, an implementation in MATLAB allows to develop a mathematical model for the DHE in the shallow groundwater basin. The model results from measurements *in situ* so that it is possible to evaluate its quality, repeatability, and use in other areas [17–24].

In (2.2), h_{i0} can be calculated using Reynolds number and the heat transfer coefficient J_h which depends on fluid motion conditions inside the pipe. The so called “laminar flow” occurs when Reynolds number is less than 2100. When its value is higher than 10000, the flow becomes “turbulent”. If it is in the range between 2100 and 10000, the motion is in transition conditions. Furthermore, Reynolds number is related with water speed inside the heat exchanger. The latter can be easily calculated using the values of flow rate at the entrance of the pipe and the cross section. h_{e0} depends on several parameters—such as the density of the fluid in the groundwater basin and the coefficient of thermal expansion—which result from the temperature of the film (T_{film}) between the thermal water and the wall of the heat exchanger. Thus, (T_{film}) is linked to the water temperature inside the well (T_{ext}) and the temperature of the wall (T_{wall}). (T_{wall}) is obtained using ($T_{\text{m,fluid}}$) (mean temperature of the fluid in the pipe) and (T_{ext}). In order to calculate ($T_{\text{m,fluid}}$) the values of water temperature at the beginning (T_{in})—which is known—and at the end (T_{out}) of the tube are required [9, 10]. The mean temperature profile within the pipe (Figure 6) can be defined by the following equation:

$$T_{\text{out}}(x) = T_{\text{ext}} - (T_{\text{ext}} - T_{\text{in}}) \cdot \exp\left(\frac{p \cdot U_D}{m \cdot C_p} \cdot x\right), \quad (2.3)$$

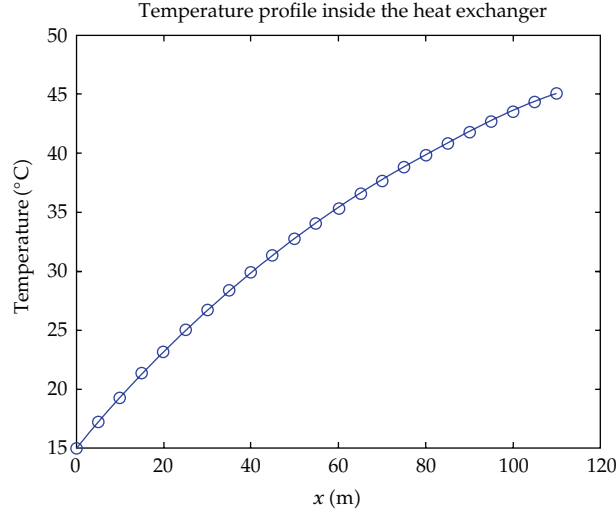


Figure 6: Temperature profile of the water within the heat exchanger.

Table 2: Output values.

	Output
Re	34543
$T_{m,\text{fluid}}$	30
T_{wall}	31
T_{film}	45.5
T_{out}	45
h_{i0}	4269
J_h	137.61
h_{e0}	146
U_D	138
A	11.65
ΔT_{LM}	27.31
Q	43386

where T_{ext} water temperature inside the well (K); T_{in} : water temperature at the beginning of the pipe (K); P : perimeter (m); m : flow rate (m^3/sec); c_p : specific heat at constant pressure (joule/kg/K).

Since T_{out} depends on U_D which results from h_{i0} and h_{e0} , an iteration loop is developed in MATLAB: an initial value for T_{out} and h_{e0} is adopted and the iteration process continues until the convergence is reached.

3. Results and Discussions

The results in Table 2 are given by the implementation in MATLAB environment.

The low-enthalpy geothermal system can be successfully used for civil purposes, such as district heating, which provides energy to supply thermal needs. The total energy demand to heat a building depends on the so called “heat degree days”, whose acronym is “HDDs”.



Figure 7: Heating degree day map in Italy according to [25].

The heating requirements for a given structure at a specific location are considered to be directly proportional to the number of HDDs at that location. HDDs are defined relative to a base temperature which is the outside temperature above which a building does not need heating. In order to evaluate HDDs, an approximation method is to take the average temperature on any given day and to subtract it from the base temperature. If the value is less than or equal to zero, that day has zero HDDs; if the value is positive, that number represents the number of HDDs on that day. Thus, only the positive differences of temperature must be considered. HDDs are calculated as follows:

$$\text{HDD} = \sum_{i=1}^{\text{nhd}} (T_0 - T_i), \quad (3.1)$$

where i : value varying from 1 to the number of heating days nhd ; T_0 : base temperature ($^{\circ}\text{C}$); T_i : mean daily external temperature ($^{\circ}\text{C}$).

According to the value given by (3.1), Italy is divided into six different areas—from “zone A” (the hottest one) to “zone F” (the coldest one), as Figure 7 shows. More precisely, HDD increases when the climate becomes colder. Viterbo belongs to “zone D” [25].

Table 3: Area heated by the down-hole heat exchanger in the experimental plant.

Classes of buildings	Energy supply (W/m^3)	Area heated by DHE (m^2)
A	10	1446
B	15	964
C	20	723

The total amount of withdrawable heat Q —which comes from the implementation in MATLAB—leads to the determination of the thermal needs of a specific building. Buildings can be distinguished in seven classes considering the level of consumption of primary energy. Since the energy supply to heat the house is known for each class, the area—which can be heated by the DHE in the experimental plant—can be calculated. The results are shown in Table 3 and are referred to the lowest consumption buildings.

4. Conclusion

The mathematical model—provided by the useful implementation in MATLAB environment—leads to the evaluation of withdrawable heat using a DHE in a low-enthalpy geothermal plant. As a consequence, the thermal needs, supplied by the system, can be calculated. As it can be seen in Table 3, buildings of different sizes can be heated by low-temperature systems, such as radiant floors or thermoconvectors. The surface area depends on the energy class: 1446 m^2 —which approximately corresponds to 14 flats, 100 m^2 each—can be heated if the building belongs to class A. The amount of surface—heated by DHE—decreases from class A to class C. In the latter case, it is equal to 723 m^2 .

Moreover, other situations can be easily considered in the model by simply changing the input data, such as geometry of the heat exchangers (d_{int} , d_{ext} and L), T_{in} , or considering the variability of T_{ext} in the well.

It is important to underline that the implemented model can be successfully used in those areas where shallow thermal ground basins occur and if their temperature is close to 60°C . Furthermore, the result of modelling is a correct sizing of DHEs for civil purposes, that is district heating.

References

- [1] Directive 2009/28/EC of the European Parliament and of the Council.
- [2] S. Lo Russo, C. Boffa, and M. V. Civita, “Low-enthalpy geothermal energy: an opportunity to meet increasing energy needs and reduce CO_2 and atmospheric pollutant emissions in Piemonte, Italy,” *Geothermics*, vol. 38, no. 2, pp. 254–262, 2009.
- [3] A. Carotenuto, C. Casarosa, and L. Vanoli, “Optimizing the position of the tube casing slotted section for geothermal wells with a downhole heat exchanger,” *Geothermics*, vol. 30, no. 1, pp. 133–157, 2001.
- [4] A. Carotenuto, N. Massarotti, and A. Mauro, “A new methodology for numerical simulation of geothermal down-hole heat exchangers,” *Applied Thermal Engineering*, vol. 48, pp. 225–236, 2012.
- [5] A. Carotenuto, C. Casarosa, M. Dell’isola, and L. Martorano, “An aquifer-well thermal and fluid dynamic model for downhole heat exchangers with a natural convection promoter,” *International Journal of Heat and Mass Transfer*, vol. 40, no. 18, pp. 4461–4472, 1997.
- [6] J. W. Lund, “The use of down-hole heat exchangers,” no. 97601, Geo-Heat Center, Oregon Institute of Technology, Klamath Falls, Ore, USA.
- [7] D. Scrocca, C. Doglioni, and F. Innocenti, “Vincoli per una interpretazione della geodinamica italiana: una revisione,” *Memorie Descrittive della Carta Geologica d’Italia*, vol. 62, pp. 15–46, 2003.

- [8] V. Piscopo, M. Barbieri, V. Monetti et al., "Hydrogeology of thermal waters in Viterbo area, central Italy," *Hydrogeology Journal*, vol. 14, no. 8, pp. 1508–1521, 2006.
- [9] M. Carlini and S. Castellucci, "Efficient energy supply from ground coupled heat transfer source," in *Proceedings of the ICCSA*, vol. 6017 of *Lecture Notes in Computer Science Part 2*, pp. 177–190, Springer, Berlin, Germany, 2010.
- [10] M. Carlini and S. Castellucci, "Modelling the vertical heat exchanger in thermal basin," in *Proceedings of the ICCSA*, vol. 6785 of *Lecture Notes in Computer Science Part 4*, pp. 277–286, Springer, Berlin, Germany, 2011.
- [11] M. Carlini, D. Monarca, P. Biondi, T. Honorati, and S. Castellucci, "A simulation model for the exploitation of geothermal energy for a greenhouse in the viterbo province," in *Proceedings of the International Conference Ragusa SHWA, Work Safety and Risk Prevention in Agro-food and Forest Systems*, pp. 621–629, Ragusa Ibla Campus, Italy, 2010.
- [12] P. A. Østergaard and H. Lund, "A renewable energy system in Frederikshavn using low-temperature geothermal energy for district heating," *Applied Energy*, vol. 88, no. 2, pp. 479–487, 2011.
- [13] A. Michopoulos, K. T. Papakostas, and N. Kyriakis, "Potential of autonomous ground-coupled heat pump system installations in Greece," *Applied Energy*, vol. 88, no. 6, pp. 2122–2129, 2011.
- [14] P. Cui, X. Li, Y. Man, and Z. Fang, "Heat transfer analysis of pile geothermal heat exchangers with spiral coils," *Applied Energy*, vol. 88, no. 11, pp. 4113–4119, 2011.
- [15] Z. Shengjun, W. Huaixin, and G. Tao, "Performance comparison and parametric optimization of subcritical Organic Rankine Cycle (ORC) and transcritical power cycle system for low-temperature geothermal power generation," *Applied Energy*, vol. 88, no. 8, pp. 2740–2754, 2011.
- [16] <http://www.mathworks.com/>.
- [17] S. Castellucci, M. Carlini, M. Guerrieri, and T. Honorati, "Stability and control for energy production parametric dependence," *Mathematical Problems in Engineering*, vol. 2010, Article ID 842380, 21 pages, 2010.
- [18] S. Castellucci and M. Carlini, "Modelling and simulation for energy production parametric dependence in greenhouses," *Mathematical Problems in Engineering*, vol. 2010, Article ID 590943, 28 pages, 2010.
- [19] M. Carlini and S. Castellucci, "Efficient energy supply from ground coupled heat transfer source," in *Proceedings of the ICCSA*, vol. 6017 of *Lecture Notes in Computer Science Part 2*, pp. 177–190, 2010.
- [20] C. Cattani, S. Chen, and G. Aldashev, "Information and modeling in complexity," *Mathematical Problems in Engineering*, vol. 2012, Article ID 868413, 4 pages, 2012.
- [21] S. Chen, Y. Zheng, C. Cattani, and W. Wang, "Modeling of biological intelligence for SCM system optimization," *Computational and Mathematical Methods in Medicine*, vol. 2012, Article ID 769702, 10 pages, 2012.
- [22] M. Li, S. C. Lim, and S. Chen, "Exact solution of impulse response to a class of fractional oscillators and its stability," *Mathematical Problems in Engineering*, vol. 2011, Article ID 657839, 9 pages, 2011.
- [23] S. Chen, Y. Wang, and C. Cattani, "Key issues in modeling of complex 3D structures from video sequences," *Mathematical Problems in Engineering*, vol. 2012, Article ID 856523, 17 pages, 2012.
- [24] S. C. Lim, C. H. Eab, K. H. Mak, M. Li, and S. Y. Chen, "Solving linear coupled fractional differential equations by direct operational method and some applications," *Mathematical Problems in Engineering*, vol. 2012, Article ID 653939, 28 pages, 2012.
- [25] Legislative Decree 29/12/2006 n. 311 published on Gazzetta Ufficiale 01/02/2007 no. 26.

Research Article

Real-Time Simulation of Fluid Scenes by Smoothed Particle Hydrodynamics and Marching Cubes

Weihong Wang,^{1,2} Zhongzhou Jiang,¹ Honglin Qiu,¹ and Wei Li¹

¹ College of Computer Science, Zhejiang University of Technology, Hangzhou 310023, China

² State Key Laboratory of Software Development Environment, Beijing 100083, China

Correspondence should be addressed to Weihong Wang, wwh@zjut.edu.cn

Received 2 August 2012; Accepted 26 September 2012

Academic Editor: Fei Kang

Copyright © 2012 Weihong Wang et al. This is an open access article distributed under the Creative Commons Attribution License, which permits unrestricted use, distribution, and reproduction in any medium, provided the original work is properly cited.

Simulating fluid scenes in 3D GIS is of great value in both theoretical research and practical applications. To achieve this goal, we present an algorithm for simulation of fluid scenes based on smoothed particle hydrodynamics. A 3D spatial grid partition algorithm is proposed to increase the speed for searching neighboring particles. We also propose a real-time interactive algorithm about particle and surface topography. We use Marching Cubes algorithm to extract the surface of free moving fluids from particles data. Experiments show that the algorithms improve the rate of rendering frame in realtime, reduce the computing time, and extract good real effects of fluid surface.

1. Introduction

Simulation of fluid scenes has a wide range of applications in the movie special effects, computer animation, game production, virtual reality, and many other fields [1–4]. At first, most studies of fluid simulation are based on the nonphysical procedural modeling method which generates scene by parameterized surface. Although the simulation is faster, these methods are not based on physical principles, thus lack of authenticity, and can't simulate some detailed effects, such as the effect of wave overturning. At the same time these methods are based on random functions, it is difficult to achieve solid-liquid interaction. So most researchers focused on fluid simulation based on physical methods.

At present, physics-based fluid simulation methods are mainly divided into two types [5]: one is grid-based Euler method, the other is particle-based Lagrange method. Smoothed particle hydrodynamics (SPH) is a new method based on particle-based Lagrange method, which is mainly used in astrophysics at first. J. Monaghan is the first one to apply SPH into simulation of free surface flow. Stam and Fiume [6] brought in SPH method

into fluid simulation to achieve the effect of gas and flame. And then, the researches on fluid simulation mainly adopt particle-based Lagrange method. Harada et al. [7] made the searching adjacent particle feasible by constructing uniform spatial grid. Under this circumstances, fluid particles are relatively dispersed and lots of idle grid units would appear. Therefore, Grahm [8] made the fast searching adjacent particle of arbitrary size scene possible by constructing the space uniform grids with Hash function through GPU. Kolb and Cuntz [9] made use of GPU to achieve the whole process of SPH. However, this method calculates in the grids and interpolates in the particles, which leads to physical discontinuousness and simulation results distorted. David Lopez et al. [10] made use of SPH to build the physical pressure modal on river basin of the Villar Del Rey Dam, and it simulated the fluid scene of discharge floodwater. The way to deal with boundary interaction is too simple. So it simplified the terrain boundary to regular area, but the terrain surface is rugged in 3D GIS.

Although there are many SPH methods to simulate fluid in literature, they can't apply to simulate fluid in real-time and high efficiency in complex scene [11–13], such as simulating debris flow and flood and other process of fluid evolution in the 3D GIS. This paper improves 3D spatial grid partition algorithm to increase speed of neighboring particles searching, and we also propose a real-time interactive algorithm on particle and terrain surface. The results show that this method can calculate in real-time and has a good rendering rate.

2. Smoothed Particle Hydrodynamics

The basic idea of SPH makes fluid as a series of discrete particles, through the role of the smooth, which has certain radius of kernel functions to a particle physics scalar (such as density, pressure, etc.) assigning to the adjacent particles, as shown in Figure 1. Physical scalar A of any particle $X(x, y, z)$ can be calculated by

$$A(x) = \sum_j m_j \frac{A_j}{\rho_j} W(X - X_j, h), \quad (2.1)$$

$$\nabla A(x) = \sum_j m_j \frac{A_j}{\rho_j} \nabla W(X - X_j, h), \quad (2.2)$$

where ρ_j is density of the particle X_j , m_j is quality of the particle X_j , and h is radius of smoothing kernel. If the distance from the particle X to particle X_j , that is, $|X - X_j| < h$, the particles X_j is in smooth domain of the particle X , we can get the weight of particle X_j by smoothing kernel function $W(X)$. Otherwise $|X - X_j| > h$, the weight of the particles X_j is zero. In the solution of fluid equations, we often need to take derivatives of the physical scalar, and this operation only affects smoothing kernel function in SPH method. Therefore gradient of physical scalar value A can be expressed as (2.2).

3. Grid-Based Neighboring Particles Search

The existing neighboring particle search algorithms mostly adopt to traverse all particles directly, with time complexity of $O(n^2)$ and n stands for the number of fluid particles. Chen et al. [14] constructed an index table of two-dimensional array of particle and spatial grid by dividing the three-dimensional space grid with grid number being the primary key and

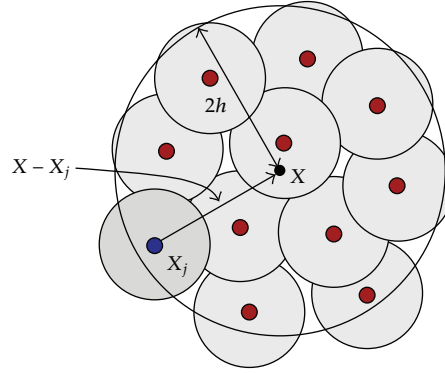


Figure 1: The basic principle of SPH.

the index table being radix sorted (algorithm complexity of radix sort is $O(n)$). The index numbers of the first particle which corresponds to each grid are obtained so that each grid in the particle is identified.

In this paper, the improved neighboring particle search algorithm doesn't need to create the index table of particle and grid but divide grids, which saves memory space. It also doesn't need to sort the particles and the index table, so it reduces the complexity of algorithm. The algorithm steps are as follows.

Step 1. Divide the three-dimensional spatial grid. In this paper, bounding box of the three-dimensional terrain space is divided into cube grid with length of h . h stands for the radius of smoothing kernel. The Standard Template Library `std::vector < Particle > m_Grid` is used to store information of particles of each spatial grid. Particle is a class which stores density, velocity, spatial coordinates, and other physical information of fluid particle, and a Particle* pointer pointing to next particle.

Step 2. Put the fluid particles into three-dimensional spatial grid. Insert all the particles $X_i(x, y, z)$ ($1 \leq i \leq n$) into the corresponding spatial grid number (x_i, y_i, z_i) by (3.1). That is to insert the current particle pointer into the spatial grid:

$$\text{Grid}(x_i, y_i, z_i) = \{\min_int(x/h), \min_int(y/h), \min_int(z/h)\}, \quad (3.1)$$

where x, y, z stands for the particle X_i in x, y, z axis coordinate, respectively, `min_int` is the positive integer function that get the minimum value, and $\text{grid}(x_i, y_i, z_i)$ represents spatial grid number.

Step 3. Calculate the neighboring particles of each particle. In SPH method, particles are only affected by other particles in radius of smoothing kernel, so we will find the scope for particle located in the neighborhood of 27 spatial grids. Firstly, calculate the spatial grid number $\text{Grid}(x_i, y_i, z_i)$ of particle X_i by (3.1); then calculate index number of $\text{Grid}(x_i, y_i, z_i)$ by

$$\text{Gindex} = y_i * \text{GridWidth} * \text{GridHeight} + z_i * \text{GridWidth} + x_i. \quad (3.2)$$

GridWidth, GridDepth, and GridHeight, respectively, stand for the dimension on direction X, Y, Z of spatial grid, then the contained particles of $m_Grid(Gindex)$ are stored in pointer array. Finally, visit all the particles in Grid $\{x_i \pm 1, y_i \pm 1, z_i \pm 1\}$ and calculate current particle of density and physical pressure and so on by using the equations derivated from (2.1) and (2.2).

4. Interaction between the Fluid Particles and the Boundary

The simplest algorithm is exhaustive algorithm on dealing with interaction between fluids and boundary. Assuming that there are M geometric facets and N fluid particles in the scene, its time complexity is $O(M*N)$. In the 3D GIS, the number of triangular patches of terrain mostly ranges from 10^5 to 10^7 and the number of fluid particles is generally between 10^3 and 10^6 . If the exhaustive algorithm is adopted, the computation will be too huge to be accepted. In this regard, [14] proposed a boundary interaction algorithm based on spatial mesh, which inserts information of the terrain boundary and obstacle into the spatial grid, then judges whether the fluid particles are intersected with boundary geometry patches and obstacle in spatial grid when the fluid particles pass through. The algorithm requires geometry patches of boundaries to be small enough; if geometry patches are large, the number of grid number each grid space occupied will increase, which will lead to reduced efficiency of algorithm.

Because the number of triangular grids of terrain is huge in the 3D GIS, if the above algorithms are adopted for boundary interaction, the amount of calculation will be too huge and the efficiency of real-time rendering will be degenerated. Regarding this, this paper proposes a real-time interaction method of the boundary bounce particles, where the time complexity of algorithms is $O(N)$ and N is the number of fluid particles. Interaction between the fluid particles and the terrain is mainly used in interaction between the fluid particles and the terrain surface to prevent fluid particles from penetrating through the terrain surface, shown in Figure 2 The basic idea of algorithm is as follows.

Step 1. Calculate intersection T_i of the ray and triangular grid of the terrain surface. The origin of the rays is $X_i(x_i, y_i, z_i)$ and direction is straight down $(-y)$. As DEM data is regular grid data, two-dimension array can be used for storage. Spatial coordinate Vex1 of the triangle patches of terrain surface can be calculated by (4.1). Ver2 is $(m * x_step, m_height[m][n + 1], (n + 1) * x_step)$. In a similar way, coordinates of Ver3 and Ver4 can be calculated. The x and z axis's coordinates of T_i and X_i are equal, if $(z_i - z)/(x_i - x) \geq 1$, then calculate the elevation of T_i by bilinear interpolation of triangle 1. Otherwise, calculate the elevation of T_i by bilinear interpolation of triangle 2, x_i and z_i are the coordinates of V_i , x and z are coordinates of Ver1. x, y, z , respectively, stands for the particle X_i on x, y, z axis coordinate. x_step and z_step , respectively, stands for space interval on x, z axis coordinate of the terrain elevation. m_height stands for the two-dimension array which stores the terrain data:

$$\begin{aligned}
 m &= \text{int_min}\left(\frac{x_i}{x_step}\right), \\
 n &= \text{int_min}\left(\frac{z_i}{z_step}\right), \\
 y &= m_height[m][n], \\
 \text{Ver1}(x, y, z) &= \{m * x_step, y, n * z_step\}.
 \end{aligned} \tag{4.1}$$

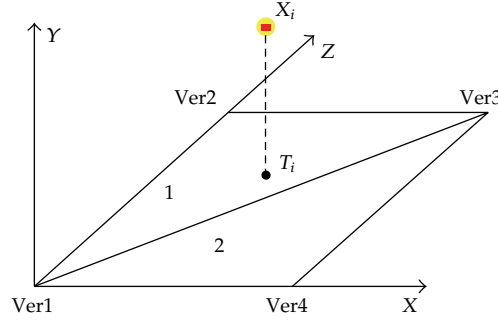


Figure 2: Interaction between the fluid particles and the terrain surface.

Step 2. Judge whether the particle X_i is in the area that rebounded by the terrain. First, calculate the spatial distance $|X_i - T_i|$ from particles X_i to T_i . If $|X_i - T_i| > R$, then the particle X_i is not in rebound area, so go to Step 1, and deal with particle X_{i+1} . Otherwise, $|X_i - T_i| \leq R$, then enter Step 3, R values for h which is the radius of the smoothed particle.

Step 3. Calculate force of rebound boundary. When fluid particle X_i is close to terrain, the particle X_i will be rebounded by the terrain surface. The rebound force f_i can be calculated by (4.2), where u_i is speed of the particle, K_{stiff} is the hardness parameters of the terrain, K_{damp} is deceleration parameter of terrain to the particle, and n is the normal unit vector of the triangular patches that include the intersection T_i . When the fluid particles gradually approach the terrain surface, the rebound force increases gradually until the velocity of the particle decreases to zero. At this time, the particle is still subjected to the effect of rebound which increases the velocity of the particle, thus preventing fluid particles to penetrate through the terrain. The direction of the rebound force is normal direction of the triangular mesh plane. Note that the rendering system only renders the clockwise triangular patches; we adopt clockwise triangles for the calculation of the normal unit vector of triangular patches that the particles locate in:

$$f_i = \begin{cases} K_{\text{stiff}} * (2R - d) - u_i * n * K_{\text{damp}} * n, & R > d, \quad d = |X_i - T_i|, \\ 0, & \text{otherwise.} \end{cases} \quad (4.2)$$

5. Visualization of the Fluid Surface

The fluid surface reconstruction is important for fluid simulation. Lighting and texture rendering of the fluid surface will improve the fidelity of fluid scene. Iwasaki et al. [15] proposed Point Splatting method to build the surface rendering, and this method has highly real-time rendering efficiency, but emptiness appears where fluid particles are relatively sparse [16–20]. In this paper, Marching Cubes algorithm is proposed to be applied in constructing fluid surface of free moving, which has the advantages of simple operation and fast drawing. The process is as follows.

Step 1. The 3D space is evenly divided into spatial grids. Traverse all the particles in the fluid region, calculate minimum coordinates (Ver_{\min}) and maximum coordinates (Ver_{\max}) of

the particles which are bounding box of fluid region, and divide the box into homogeneous spatial grids.

Step 2. Calculate the density of the vertices of each spatial grids. Then use the divided grids as the sampling points of fluid scenes to get fluid density field data. Calculate the density value of each grid of the 8 vertices by using (2.1) and SPH interpolation on particles of each grid.

Step 3. Determine the threshold value of density isosurface of the fluid surface. According to the fluid pressure equal to atmospheric pressure, and the state equation of an ideal atmosphere, threshold value of density isosurface of the fluid surface can be obtained as follows:

$$\rho_{\text{surface}} = \frac{p}{k}, \quad (5.1)$$

where ρ_{surface} stands for the fluid surface density, p for atmospheric pressure, and k for gaseous constant.

Step 4. Compare each vertex density value of spatial grid with threshold value of isosurface. If the vertex density value is greater or equal to the isosurface value, vertex value is 1 and the vertex is in the isosurface; otherwise is 0 and the vertex is outside of isosurface. According to the result of the comparison, structure the grid state table.

Step 5. Calculate the vertex of density isosurface coordinates of each spatial grid. If a vertex of a side of a grid is in the isosurface, while the other vertex is out of the isosurface, then, this side inevitably intersects with the desired isosurface. Firstly, according to the grid state table, get the grid's sides which intersect with the isosurface. Then calculate the intersection of grid's side and isosurface by linear interpolation method.

Step 6. Draw density isosurface. By using the central difference method and the linear interpolation method, calculate vertex normal of each triangle. Finally according to the coordinate values of each triangle vertex and normal vector, draw density isosurface.

6. Experiment Results

In this paper, the experiment platform is Intel Core 2 Duo CPU T6670@2.2GHZ. Main memory is 2 G, and graphic card is NVIDIA GeForce 9300GS with memory of 256 M, and operating system is Windows XP, and the drawing SDK is OSG (OpenSceneGraph).

Figure 3 shows fluid outflowing from a topographic position in 3D GIS, and its dynamic process of evolution on the terrain surface. The fluid particle number is 30000. Figure 4 shows the Figure 3 Scene by Marching Cube algorithm to construct the effect of fluid surface of free moving.

As this algorithm applies Marching Cube algorithm which is the same as [8] to construct the fluid surface and field particle search and complex boundary interaction algorithm which are used in this algorithm are different to [12], thus they are comparable. Table 1 shows the comparison of simulation speed of the algorithm and two other kinds of algorithm. Figure 5 shows comparison of computing time per frame. Table 1 and Figure 5 show that this algorithm reduces the computation time per frame.



Figure 3: Fluid in the dynamic evolution process of particle simulation (particle number 30000).



Figure 4: Effect of reconstruction of fluid surface mesh reconstruction (particle number 30000).

Table 1: Comparison of the three algorithms on simulation rate.

This paper algorithm		[12] Algorithm		[8] Algorithm	
Particle number	FPS	Particle number	FPS	Particle number	FPS
2000	153.4	3000	68	4000	33
4000	94.3	8000	26	20000	10
8000	45.2	20000	12.7	30000	6.7
16000	26.4				
32000	14.5				
64000	8.2				
128000	3.8				

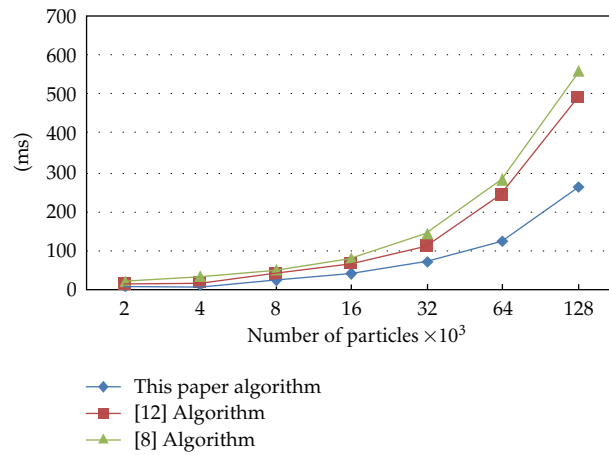


Figure 5: Comparison of the three algorithms on simulation rate.

7. Conclusion

In order to simulate the fluid scene in 3D GIS, this paper proposed an SPH algorithm for fluid scene simulation. The experiment results show that this algorithm can calculate in real-time and has a good real-time rate of rendering frame, and achieve the desired goals. In near future we intend to further improve the algorithms of extracting fluid surface and enhance reconstruction speed and accuracy of the fluid surface mesh.

Acknowledgments

This paper is supported by the National Natural Science Foundation of China (60873033), the Natural Science Foundation of Zhejiang Province (R1090569), and the State Key Laboratory of Software Development Environment Open Fund (SKLSDE-2012KF-05).

References

- [1] M. Carlini and S. Castellucci, "Modelling and simulation for energy production parametric dependence in greenhouses," *Mathematical Problems in Engineering*, vol. 2010, Article ID 590943, 28 pages, 2010.
- [2] M. Li, C. Cattani, and S. Y. Chen, "Viewing sea level by a one-dimensional random function with long memory," *Mathematical Problems in Engineering*, vol. 2011, Article ID 654284, 13 pages, 2011.
- [3] Carlo Cattani, Shengyong Chen, and Gani Aldashev, "Information and Modeling in Complexity," *Mathematical Problems in Engineering*, vol. 2012, Article ID 868413, 4 pages, 2012.
- [4] S. Chen, H. Tong, and C. Cattani, "Markov models for image labeling," *Mathematical Problems in Engineering*, vol. 2012, Article ID 814356, 18 pages, 2012.
- [5] Y. Liu, X. Liu, H. Zhu, and E. Wu, "Physically based fluid simulation in computer animation," *Journal of Computer-Aided Design and Computer Graphics*, vol. 17, no. 12, pp. 2581–2589, 2005.
- [6] J. Stam and E. Fiume, "Depicting fire and other gaseous phenomena using diffusion processes," in *Proceedings of the 22nd Annual ACM Conference on Computer Graphics and Interactive Techniques*, pp. 129–135, Los Angeles, Calif, USA, August 1995.
- [7] T. Harada, S. Koshizuka, and Y. Kawaguchi, "Smoothed particle hydrodynamics on GPU," in *Proceedings of The Computer Graphics International*, pp. 63–70, Rio de Janeiro, Brazil, 2007.
- [8] A. Grahm, "Interactive simulation of contrast fluid using smoothed particle," *Hydrodynamics*, pp. 1–69, 2008.
- [9] A. Kolb and N. Cuntz, "Dynamic particle coupling for GPU based fluid simulation," in *Proceedings of the 18th Symposium on Simulation Technique*, pp. 722–727, Erlangen, Germany, 2005.
- [10] D. Lopez, R. Marivela, and F. Aranda, "SPH model calibration using data from pressure of the prototype still basin of Villar Del Rey Dam, Spain," in *Proceedings of the 33rd IAHR Congress, Water Engineering for a Sustainable Environment*, pp. 187–198, 2009.
- [11] S. Y. Chen, "Kalman filter for robot vision: a survey," *IEEE Transactions on Industrial Electronics*, vol. 59, no. 11, pp. 4409–4420, 2012.
- [12] P. Kipfer and R. Westermann, "Realistic and interactive simulation of rivers," in *Proceedings of the 32nd Annual Conference on Computer Graphics (SIGGRAPH '06)*, pp. 1–8, New York, NY, USA, June 2006.
- [13] S. Chen, Y. Wang, and C. Cattani, "Key issues in modeling of complex 3D structures from video sequences," *Mathematical Problems in Engineering*, vol. 2012, Article ID 856523, 17 pages, 2012.
- [14] X. Chen, Z. Wang, J. He, H. Yan, and Q. Peng, "An integrated algorithm of real-time fluid simulation on GPU," *Journal of Computer-Aided Design and Computer Graphics*, vol. 22, no. 3, pp. 396–405, 2010.
- [15] K. Iwasaki, Y. Dobashi, F. Yoshimoto, and T. Nishita, "Real-time rendering of point based water surfaces," *Advances in Computer Graphics*, vol. 4035, pp. 102–114, 2006.
- [16] C. Cattani, "Shannon wavelets for the solution of integro-differential equations," *Mathematical Problems in Engineering*, vol. 2010, Article ID 408418, 22 pages, 2010.

- [17] E. G. Bakhoun and C. Toma, "Specific mathematical aspects of dynamics generated by coherence functions," *Mathematical Problems in Engineering*, vol. 2011, Article ID 436198, 10 pages, 2011.
- [18] S. Y. Chen and Z. J. Wang, "Acceleration strategies in generalized belief propagation," *IEEE Transactions on Industrial Informatics*, vol. 8, no. 1, pp. 41–48, 2012.
- [19] N. M. Kwok, X. Jia et al., "Visual impact enhancement via image histogram smoothing and continuous intensity relocation," *Computers & Electrical Engineering*, vol. 37, no. 5, pp. 681–694, 2011.
- [20] S. C. Lim, C. H. Eab, K. H. Mak, M. Li, and S. Y. Chen, "Solving linear coupled fractional differential equations by direct operational method and some applications," *Mathematical Problems in Engineering*, vol. 2012, Article ID 653939, 28 pages, 2012.

Research Article

Numerical Solution of Nonlinear Volterra Integral Equations System Using Simpson's 3/8 Rule

**Adem Kılıçman,¹ L. Kargaran Dehkordi,²
 and M. Tavassoli Kajani²**

¹ Department of Mathematics and Institute for Mathematical Research, University Putra Malaysia, 43400 Serdang, Malaysia

² Department of Mathematics, Islamic Azad University, Khorasgan Branch, Isfahan 81595-158, Iran

Correspondence should be addressed to Adem Kılıçman, akilicman@putra.upm.edu.my

Received 30 April 2012; Accepted 31 July 2012

Academic Editor: Sheng-yong Chen

Copyright © 2012 Adem Kılıçman et al. This is an open access article distributed under the Creative Commons Attribution License, which permits unrestricted use, distribution, and reproduction in any medium, provided the original work is properly cited.

The Simpson's 3/8 rule is used to solve the nonlinear Volterra integral equations system. Using this rule the system is converted to a nonlinear block system and then by solving this nonlinear system we find approximate solution of nonlinear Volterra integral equations system. One of the advantages of the proposed method is its simplicity in application. Further, we investigate the convergence of the proposed method and it is shown that its convergence is of order $O(h^4)$. Numerical examples are given to show abilities of the proposed method for solving linear as well as nonlinear systems. Our results show that the proposed method is simple and effective.

1. Introduction

We consider the system of second kind Volterra integral equations (VIE) given by

$$f(x) = g(x) + \int_0^x K(x, s, f(s)) ds, \quad 0 \leq s \leq x \leq X, \quad (1.1)$$

where

$$f(x) = [f_1(x), f_2(x), \dots, f_n(x)]^T, \quad g(x) = [g_1(x), g_2(x), \dots, g_n(x)]^T, \quad (1.2)$$

$$K(x, s, f(s)) = \begin{bmatrix} k_{1,1}(x, s, f_1, \dots, f_n) & \cdots & k_{1,n}(x, s, f_1, \dots, f_n) \\ \vdots & \ddots & \vdots \\ k_{n,1}(x, s, f_1, \dots, f_n) & \cdots & k_{n,n}(x, s, f_1, \dots, f_n) \end{bmatrix}.$$

Numerical solution of Volterra integral equations system has been considered by many authors. See for example [1–5].

In recent years, application of HPM (Homotopy Perturbation Method) and ADM (Adomian Decomposition Method) in nonlinear problems has been undertaken by several scientists and engineers [6–8]. HPM [8] was proposed by He in 1999 for the first time and recently Yusufoglu has proposed this method [9] for solving a system of Fredholm-Volterra type integral equations. Block by block method was suggested by Young [10] for the first time in connection with product integration techniques. On the other side, the engineers are facing certain challenges to deal with complexity and efficient mathematical modeling. Thus, there are several research have being carried out related to these problems. For example, more details on the modeling of complexity we refer to [11], direct operational method to solve a system of linear in-homogenous couple fractional differential equations, see [12] and for a class of fractional oscillatory system, see [13].

In this paper, we consider block by block method by using Simpson's 3/8 rule for solving linear and nonlinear systems of Volterra integral equations. And we make a block by block method comparison between our method and HPM.

This paper is organized as follow: in Section 2, we present some background material on the use of this method. In Section 3, we prove the convergence result. Finally, numerical results are given in Section 4.

2. Starting Method

Consider a system of nonlinear Volterra integral equations in (1.1) and further, we suppose that the system equation (1.1) has a unique solution. However, the necessary and sufficient conditions for existence and uniqueness of the solution of (1.1) can be found in [14]. The idea behind the block by block methods is quite general but is most easily understood by considering a specific. Let us assume that $m = 2$ in (1.1) and use the Simpson's 3/8 rule as a numerical integration formulae. Let $F_{i,j} \simeq f_i(x_j)$ then

$$\begin{aligned} F_{1,3} &\simeq f_1(x_3) = g_1(x_3) + \int_0^{x_3} k_{1,1}(x_3, s, f_1(s))ds + \int_0^{x_3} k_{1,2}(x_3, s, f_2(s))ds, \\ F_{2,3} &\simeq f_2(x_3) = g_2(x_3) + \int_0^{x_3} k_{2,1}(x_3, s, f_1(s))ds + \int_0^{x_3} k_{2,2}(x_3, s, f_2(s))ds, \end{aligned} \quad (2.1)$$

approximating the integrals by Simpson's 3/8 rule, we have

$$\begin{aligned} F_{1,3} &= g_1(x_3) + \frac{3h}{8} \\ &\times \{k_{1,1}(x_3, x_0, F_{1,0}) + 3k_{1,1}(x_3, x_1, F_{1,1}) + 3k_{1,1}(x_3, x_2, F_{1,2}) + k_{1,1}(x_3, x_3, F_{1,3})\} + \frac{3h}{8} \\ &\times \{k_{1,2}(x_3, x_0, F_{2,0}) + 3k_{1,2}(x_3, x_1, F_{2,1}) + 3k_{1,2}(x_3, x_2, F_{2,2}) + k_{1,2}(x_3, x_3, F_{2,3})\}, \end{aligned}$$

$$\begin{aligned}
F_{2,3} = & g_2(x_3) + \frac{3h}{8} \\
& \times \{k_{2,1}(x_3, x_0, F_{1,0}) + 3k_{2,1}(x_3, x_1, F_{1,1}) + 3k_{2,1}(x_3, x_2, F_{1,2}) + k_{2,1}(x_3, x_3, F_{1,3})\} + \frac{3h}{8} \\
& \times \{k_{2,2}(x_3, x_0, F_{2,0}) + 3k_{2,2}(x_3, x_1, F_{2,1}) + 3k_{2,2}(x_3, x_2, F_{2,2}) + k_{2,2}(x_3, x_3, F_{2,3})\},
\end{aligned} \tag{2.2}$$

where

$$F_{1,0} = g_1(x_0), \quad F_{2,0} = g_2(x_0). \tag{2.3}$$

Further we also get

$$\begin{aligned}
F_{1,2} \simeq f_1(x_2) &= g_1(x_2) + \int_0^{x_2} k_{1,1}(x_2, s, f_1(s))ds + \int_0^{x_2} k_{1,2}(x_2, s, f_2(s))ds, \\
F_{2,2} \simeq f_2(x_2) &= g_2(x_2) + \int_0^{x_2} k_{2,1}(x_2, s, f_1(s))ds + \int_0^{x_2} k_{2,2}(x_2, s, f_2(s))ds.
\end{aligned} \tag{2.4}$$

In order to evaluate the integrals on the right hand sides, we introduce the points $x_{2/3} = 2h/3$, $x_{4/3} = 4h/3$ and the corresponding values $F_{2/3}$, $F_{4/3}$ and use the Simpson's 3/8 rule with step size $2h/3$, then we gain

$$\begin{aligned}
F_{1,2} = & g_1(x_2) + \frac{h}{4} \\
& \times \{k_{1,1}(x_2, x_0, F_{1,0}) + 3k_{1,1}(x_2, x_{2/3}, F_{1,2/3}) + 3k_{1,1}(x_2, x_{4/3}, F_{1,4/3}) + k_{1,1}(x_2, x_2, F_{1,2})\} \\
& + \frac{h}{4} \{k_{1,2}(x_2, x_0, F_{2,0}) + 3k_{1,2}(x_2, x_{2/3}, F_{2,2/3}) + 3k_{1,2}(x_2, x_{4/3}, F_{2,4/3}) + k_{1,2}(x_2, x_2, F_{2,2})\}, \\
F_{2,2} = & g_2(x_2) + \frac{h}{4} \\
& \times \{k_{2,1}(x_2, x_0, F_{1,0}) + 3k_{2,1}(x_2, x_{2/3}, F_{1,2/3}) + 3k_{2,1}(x_2, x_{4/3}, F_{1,4/3}) + k_{2,1}(x_2, x_2, F_{1,2})\} \\
& + \frac{h}{4} \{k_{2,2}(x_2, x_0, F_{2,0}) + 3k_{2,2}(x_2, x_{2/3}, F_{2,2/3}) + 3k_{2,2}(x_2, x_{4/3}, F_{2,4/3}) + k_{2,2}(x_2, x_2, F_{2,2})\},
\end{aligned} \tag{2.5}$$

where $F_{1,2/3}$, $F_{1,4/3}$, $F_{2,2/3}$, $F_{2,4/3}$ have unknown values, which can be estimated by Lagrange interpolation points x_0, x_1, x_2, x_3 . Therefore we obtain

$$\begin{aligned}
l_0(x_{2/3}) &= \frac{14}{81}, & l_1(x_{2/3}) &= \frac{28}{27}, & l_2(x_{2/3}) &= -\frac{7}{27}, & l_3(x_{2/3}) &= \frac{4}{81}, \\
l_0(x_{4/3}) &= -\frac{5}{81}, & l_1(x_{4/3}) &= \frac{20}{27}, & l_2(x_{4/3}) &= \frac{10}{27}, & l_3(x_{4/3}) &= -\frac{4}{81}.
\end{aligned} \tag{2.6}$$

Thus,

$$\begin{aligned}
 F_{1,2/3} &= \frac{14}{81}F_{1,0} + \frac{28}{27}F_{1,1} - \frac{7}{27}F_{1,2} + \frac{4}{81}F_{1,3}, \\
 F_{1,4/3} &= -\frac{5}{81}F_{1,0} + \frac{20}{27}F_{1,1} + \frac{10}{27}F_{1,2} - \frac{4}{81}F_{1,3}, \\
 F_{2,2/3} &= \frac{14}{81}F_{2,0} + \frac{28}{27}F_{2,1} - \frac{7}{27}F_{2,2} + \frac{4}{81}F_{2,3}, \\
 F_{2,4/3} &= -\frac{5}{81}F_{2,0} + \frac{20}{27}F_{2,1} + \frac{10}{27}F_{2,2} - \frac{4}{81}F_{2,3}.
 \end{aligned} \tag{2.7}$$

Substituting from (2.7) into (2.5) we obtain the following values for $F_{1,2}$, $F_{2,2}$

$$\begin{aligned}
 F_{1,2} &= g_1(x_2) + \frac{h}{4} \\
 &\times \left\{ k_{1,1}(x_2, x_0, F_{1,0}) + 3k_{1,1} \times \left(x_2, x_{2/3}, \frac{14}{81}F_{1,0} + \frac{28}{27}F_{1,1} - \frac{7}{27}F_{1,2} + \frac{4}{81}F_{1,3} \right) \right. \\
 &\quad \left. + 3k_{1,1} \left(x_2, x_{4/3}, -\frac{5}{81}F_{1,0} + \frac{20}{27}F_{1,1} + \frac{10}{27}F_{1,2} - \frac{4}{81}F_{1,3} \right) + k_{1,1}(x_2, x_2, F_{1,2}) \right\} + \frac{h}{4} \\
 &\times \left\{ k_{1,2}(x_2, x_0, F_{2,0}) + 3k_{1,2} \left(x_2, x_{2/3}, \frac{14}{81}F_{2,0} + \frac{28}{27}F_{2,1} - \frac{7}{27}F_{2,2} + \frac{4}{81}F_{2,3} \right) \right. \\
 &\quad \left. + 3k_{1,2} \left(x_2, x_{4/3}, -\frac{5}{81}F_{2,0} + \frac{20}{27}F_{2,1} + \frac{10}{27}F_{2,2} - \frac{4}{81}F_{2,3} \right) + k_{1,2}(x_2, x_2, F_{2,2}) \right\},
 \end{aligned} \tag{2.8}$$

$$\begin{aligned}
 F_{2,2} &= g_2(x_2) + \frac{h}{4} \\
 &\times \left\{ k_{2,1}(x_2, x_0, F_{1,0}) + 3k_{2,1} \times \left(x_2, x_{2/3}, \frac{14}{81}F_{1,0} + \frac{28}{27}F_{1,1} - \frac{7}{27}F_{1,2} + \frac{4}{81}F_{1,3} \right) \right. \\
 &\quad \left. + 3k_{2,1} \left(x_2, x_{4/3}, -\frac{5}{81}F_{1,0} + \frac{20}{27}F_{1,1} + \frac{10}{27}F_{1,2} - \frac{4}{81}F_{1,3} \right) + k_{2,1}(x_2, x_2, F_{1,2}) \right\} \\
 &+ \frac{h}{4} \left\{ k_{2,2}(x_2, x_0, F_{2,0}) + 3k_{2,2} \left(x_2, x_{2/3}, \frac{14}{81}F_{2,0} + \frac{28}{27}F_{2,1} - \frac{7}{27}F_{2,2} + \frac{4}{81}F_{2,3} \right) \right. \\
 &\quad \left. + 3k_{2,2} \left(x_2, x_{4/3}, -\frac{5}{81}F_{2,0} + \frac{20}{27}F_{2,1} + \frac{10}{27}F_{2,2} - \frac{4}{81}F_{2,3} \right) + k_{2,2}(x_2, x_2, F_{2,2}) \right\}.
 \end{aligned}$$

Also we get

$$\begin{aligned}
 F_{1,1} &\simeq f_1(x_1) = g_1(x_1) + \int_0^{x_1} k_{1,1}(x_1, s, f_1(s))ds + \int_0^{x_1} k_{1,2}(x_1, s, f_2(s))ds, \\
 F_{2,1} &\simeq f_2(x_1) = g_2(x_1) + \int_0^{x_1} k_{2,1}(x_1, s, f_1(s))ds + \int_0^{x_1} k_{2,2}(x_1, s, f_2(s))ds,
 \end{aligned} \tag{2.9}$$

to evaluate the integrals on the right-hand sides, we introduce points $x_{1/3} = h/3$, $x_{2/3} = 2h/3$ and the corresponding values $F_{1/3}$, $F_{2/3}$ and use the Simpson's 3/8 rule with step size $h/3$. Therefore we have

$$\begin{aligned}
 F_{1,1} &= g_1(x_1) + \frac{h}{8} \\
 &\quad \times \{k_{1,1}(x_1, x_0, F_{1,0}) + 3k_{1,1}(x_1, x_{1/3}, F_{1,1/3}) + 3k_{1,1}(x_1, x_{2/3}, F_{1,2/3}) + k_{1,1}(x_1, x_1, F_{1,1})\} \\
 &\quad + \frac{h}{8} \{k_{1,2}(x_1, x_0, F_{2,0}) + 3k_{1,2}(x_1, x_{1/3}, F_{2,1/3}) + 3k_{1,2}(x_1, x_{2/3}, F_{2,2/3}) + k_{1,2}(x_1, x_1, F_{2,1})\}, \\
 F_{2,1} &= g_2(x_1) + \frac{h}{8} \\
 &\quad \times \{k_{2,1}(x_1, x_0, F_{1,0}) + 3k_{2,1}(x_1, x_{1/3}, F_{1,1/3}) + 3k_{2,1}(x_1, x_{2/3}, F_{1,2/3}) + k_{2,1}(x_1, x_1, F_{1,1})\} \\
 &\quad + \frac{h}{8} \{k_{2,2}(x_1, x_0, F_{2,0}) + 3k_{2,2}(x_1, x_{1/3}, F_{2,1/3}) + 3k_{2,2}(x_1, x_{2/3}, F_{2,2/3}) + k_{2,2}(x_1, x_1, F_{2,1})\},
 \end{aligned} \tag{2.10}$$

where $F_{1,1/3}$, $F_{1,2/3}$, $F_{2,1/3}$, $F_{2,2/3}$ have unknown values, similarly, that can be estimated by Lagrange interpolation points x_0, x_1, x_2, x_3 . As a result we obtain

$$\begin{aligned}
 l_0(x_{1/3}) &= \frac{40}{81}, & l_1(x_{1/3}) &= \frac{20}{27}, & l_2(x_{1/3}) &= -\frac{8}{27}, & l_3(x_{1/3}) &= \frac{5}{81}, \\
 l_0(x_{2/3}) &= \frac{14}{81}, & l_1(x_{2/3}) &= \frac{28}{27}, & l_2(x_{2/3}) &= -\frac{7}{27}, & l_3(x_{2/3}) &= \frac{4}{81},
 \end{aligned} \tag{2.11}$$

and so

$$\begin{aligned}
 F_{1,1/3} &= \frac{40}{81}F_{1,0} + \frac{20}{27}F_{1,1} - \frac{8}{27}F_{1,2} + \frac{5}{81}F_{1,3}, \\
 F_{1,2/3} &= \frac{14}{81}F_{1,0} + \frac{28}{27}F_{1,1} - \frac{7}{27}F_{1,2} + \frac{4}{81}F_{1,3}, \\
 F_{2,1/3} &= \frac{40}{81}F_{2,0} + \frac{20}{27}F_{2,1} - \frac{8}{27}F_{2,2} + \frac{5}{81}F_{2,3}, \\
 F_{2,2/3} &= \frac{14}{81}F_{2,0} + \frac{28}{27}F_{2,1} - \frac{7}{27}F_{2,2} + \frac{4}{81}F_{2,3}.
 \end{aligned} \tag{2.12}$$

Substituting (2.12) into (2.10), we obtain the following values for $F_{1,1}$ and $F_{2,1}$:

$$\begin{aligned}
 F_{1,1} = & g_1(x_1) + \frac{h}{8} \\
 & \times \left\{ k_{1,1}(x_1, x_0, F_{1,0}) + 3k_{1,1} \times \left(x_1, x_{1/3}, \frac{40}{81}F_{1,0} + \frac{20}{27}F_{1,1} - \frac{8}{27}F_{1,2} + \frac{5}{81}F_{1,3} \right) \right. \\
 & \quad \left. + 3k_{1,1} \times \left(x_1, x_{2/3}, \frac{14}{81}F_{1,0} + \frac{28}{27}F_{1,1} - \frac{7}{27}F_{1,2} + \frac{4}{81}F_{1,3} \right) + k_{1,1}(x_1, x_1, F_{1,1}) \right\} \\
 & + \frac{h}{8} \left\{ k_{1,2}(x_1, x_0, F_{2,0}) + 3k_{1,2} \times \left(x_1, x_{1/3}, \frac{40}{81}F_{2,0} + \frac{20}{27}F_{2,1} - \frac{8}{27}F_{2,2} + \frac{5}{81}F_{2,3} \right) \right. \\
 & \quad \left. + 3k_{1,2} \times \left(x_1, x_{2/3}, \frac{14}{81}F_{2,0} + \frac{28}{27}F_{2,1} - \frac{7}{27}F_{2,2} + \frac{4}{81}F_{2,3} \right) + k_{1,2}(x_1, x_1, F_{2,1}) \right\}, \tag{2.13}
 \end{aligned}$$

$$\begin{aligned}
 F_{2,1} = & g_2(x_1) + \frac{h}{8} \\
 & \times \left\{ k_{2,1}(x_1, x_0, F_{1,0}) + 3k_{2,1} \times \left(x_1, x_{1/3}, \frac{40}{81}F_{1,0} + \frac{20}{27}F_{1,1} - \frac{8}{27}F_{1,2} + \frac{5}{81}F_{1,3} \right) \right. \\
 & \quad \left. + 3k_{2,1} \times \left(x_1, x_{2/3}, \frac{14}{81}F_{1,0} + \frac{28}{27}F_{1,1} - \frac{7}{27}F_{1,2} + \frac{4}{81}F_{1,3} \right) + k_{2,1}(x_1, x_1, F_{1,1}) \right\} \\
 & + \frac{h}{8} \left\{ k_{2,2}(x_1, x_0, F_{2,0}) + 3k_{2,2} \times \left(x_1, x_{1/3}, \frac{40}{81}F_{2,0} + \frac{20}{27}F_{2,1} - \frac{8}{27}F_{2,2} + \frac{5}{81}F_{2,3} \right) \right. \\
 & \quad \left. + 3k_{2,2} \times \left(x_1, x_{2/3}, \frac{14}{81}F_{2,0} + \frac{28}{27}F_{2,1} - \frac{7}{27}F_{2,2} + \frac{4}{81}F_{2,3} \right) + k_{2,2}(x_1, x_1, F_{2,1}) \right\}.
 \end{aligned}$$

Equations (2.2), (2.8), and (2.13) are three pairs of simultaneous equations in terms of unknowns $F_{1,1}$, $F_{2,1}$, $F_{1,2}$, $F_{2,2}$, $F_{1,3}$, and $F_{2,3}$ for the nonlinear system of VIE. The solutions of these equations may be found by the method of successive approximation or by a suitable software package such as Maple. For the linear system of VIE a direct method can be used for solving system of linear algebraic equations.

3. The General Scheme

Consider the system of VIE

$$f(x) = g(x) + \int_0^x K(x, s, f(s)) ds, \quad 0 \leq x \leq a. \tag{3.1}$$

Let $0 = x_0 < x_1 < \dots < x_N = a$ be a partition of $[0, a]$ with the step size h , such that $x_i = ih$ for $i = 0, 1, \dots, N$. Then we can construct a block by block approach so that a system

of p simultaneous equations is obtained and thus a block of p values of F is also obtained simultaneously. We put $p = 6$ for simplicity. Setting $x = x_{3m+1}$ in (3.1) we get

$$\begin{aligned} F_{1,3m+1} &\simeq f_1(x_{3m+1}) = g_1(x_{3m+1}) + \int_0^{x_{3m+1}} k_{1,1}(x_{3m+1}, s, f_1(s)) ds + \int_0^{x_{3m+1}} k_{1,2}(x_{3m+1}, s, f_2(s)) ds, \\ F_{2,3m+1} &\simeq f_2(x_{3m+1}) = g_2(x_{3m+1}) + \int_0^{x_{3m+1}} k_{2,1}(x_{3m+1}, s, f_1(s)) ds + \int_0^{x_{3m+1}} k_{2,2}(x_{3m+1}, s, f_2(s)) ds \end{aligned} \quad (3.2)$$

or equivalently

$$\begin{aligned} F_{1,3m+1} &= g_1(x_{3m+1}) + \int_0^{x_{3m}} k_{1,1}(x_{3m+1}, s, f_1(s)) ds + \int_0^{x_{3m}} k_{1,2}(x_{3m+1}, s, f_2(s)) ds \\ &\quad + \int_{x_{3m}}^{x_{3m+1}} k_{1,1}(x_{3m+1}, s, f_1(s)) ds + \int_{x_{3m}}^{x_{3m+1}} k_{1,2}(x_{3m+1}, s, f_2(s)) ds, \\ F_{2,3m+1} &= g_2(x_{3m+1}) + \int_0^{x_{3m}} k_{2,1}(x_{3m+1}, s, f_1(s)) ds + \int_0^{x_{3m}} k_{2,2}(x_{3m+1}, s, f_2(s)) ds \\ &\quad + \int_{x_{3m}}^{x_{3m+1}} k_{2,1}(x_{3m+1}, s, f_1(s)) ds + \int_{x_{3m}}^{x_{3m+1}} k_{2,2}(x_{3m+1}, s, f_2(s)) ds. \end{aligned} \quad (3.3)$$

Now, integration over $[0, x_{3m}]$ can be accomplished by Simpson's 3/8 rule and the integral over $[x_{3m}, x_{3m+1}]$ is computed by using a cubic interpolation. Hence

$$\begin{aligned} F_{1,3m+1} &= g_1(x_{3m+1}) + \frac{3h}{8} \\ &\quad \times \{ k_{1,1}(x_{3m+1}, x_0, F_{1,0}) + 3k_{1,1}(x_{3m+1}, x_1, F_{1,1}) \\ &\quad + 3k_{1,1}(x_{3m+1}, x_2, F_{1,2}) + 2k_{1,1}(x_{3m+1}, x_3, F_{1,3}) + \cdots + k_{1,1}(x_{3m+1}, x_{3m}, F_{1,3m}) \} \\ &\quad + \frac{3h}{8} \{ k_{1,2}(x_{3m+1}, x_0, F_{2,0}) + 3k_{1,2}(x_{3m+1}, x_1, F_{2,1}) \\ &\quad + 3k_{1,2}(x_{3m+1}, x_2, F_{2,2}) + 2k_{1,2}(x_{3m+1}, x_3, F_{2,3}) + \cdots + k_{1,2}(x_{3m+1}, x_{3m}, F_{2,3m}) \} \\ &\quad + \frac{h}{8} \left\{ k_{1,1}(x_{3m+1}, x_{3m}, F_{1,3m}) + 3k_{1,1} \right. \\ &\quad \times \left(x_{3m+1}, x_{3m+1/3}, \frac{40}{81} F_{1,3m} + \frac{20}{27} F_{1,3m+1} - \frac{8}{27} F_{1,3m+2} + \frac{5}{81} F_{1,3m+3} \right) \\ &\quad + 3k_{1,1} \left(x_{3m+1}, x_{3m+2/3}, \frac{14}{81} F_{1,3m} + \frac{28}{27} F_{1,3m+1} - \frac{7}{27} F_{1,3m+2} + \frac{4}{81} F_{1,3m+3} \right) \\ &\quad \left. + k_{1,1}(x_{3m+1}, x_{3m+1}, F_{1,3m+1}) \right\} + \frac{h}{8} \end{aligned}$$

$$\begin{aligned}
& \times \left\{ k_{1,2}(x_{3m+1}, x_{3m}, F_{2,3m}) + \right. \\
& + 3k_{1,2} \left(x_{3m+1}, x_{3m+1/3}, \frac{40}{81}F_{2,3m} + \frac{20}{27}F_{2,3m+1} - \frac{8}{27}F_{2,3m+2} + \frac{5}{81}F_{2,3m+3} \right) \\
& + 3k_{1,2} \left(x_{3m+1}, x_{3m+2/3}, \frac{14}{81}F_{2,3m} + \frac{28}{27}F_{2,3m+1} - \frac{7}{27}F_{2,3m+2} + \frac{4}{81}F_{2,3m+3} \right) \\
& \left. + k_{1,2}(x_{3m+1}, x_{3m+1}, F_{2,3m+1}) \right\},
\end{aligned} \tag{3.4}$$

and in a similar way the right-hand side is obtained for $F_{2,3m+1}$, where $F_{1,0} = g_1(x_0)$, $F_{2,0} = g_2(x_0)$.

By setting $x = x_{3m+2}$ in (3.1) we get

$$\begin{aligned}
F_{1,3m+2} & \simeq f_1(x_{3m+2}) = g_1(x_{3m+2}) + \int_0^{x_{3m+2}} k_{1,1}(x_{3m+2}, s, f_1(s)) ds \\
& + \int_0^{x_{3m+2}} k_{1,2}(x_{3m+2}, s, f_2(s)) ds, \\
F_{2,3m+2} & \simeq f_2(x_{3m+2}) = g_2(x_{3m+2}) + \int_0^{x_{3m+2}} k_{2,1}(x_{3m+2}, s, f_1(s)) ds \\
& + \int_0^{x_{3m+2}} k_{2,2}(x_{3m+2}, s, f_2(s)) ds
\end{aligned} \tag{3.5}$$

or equivalently

$$\begin{aligned}
F_{1,3m+2} & = g_1(x_{3m+2}) + \int_0^{x_{3m}} k_{1,1}(x_{3m+2}, s, f_1(s)) ds + \int_0^{x_{3m}} k_{1,2}(x_{3m+2}, s, f_2(s)) ds \\
& + \int_{x_{3m}}^{x_{3m+2}} k_{1,1}(x_{3m+2}, s, f_1(s)) ds + \int_{x_{3m}}^{x_{3m+2}} k_{1,2}(x_{3m+2}, s, f_2(s)) ds, \\
F_{2,3m+2} & = g_2(x_{3m+2}) + \int_0^{x_{3m}} k_{2,1}(x_{3m+2}, s, f_1(s)) ds + \int_0^{x_{3m}} k_{2,2}(x_{3m+2}, s, f_2(s)) ds \\
& + \int_{x_{3m}}^{x_{3m+2}} k_{2,1}(x_{3m+2}, s, f_1(s)) ds + \int_{x_{3m}}^{x_{3m+2}} k_{2,2}(x_{3m+2}, s, f_2(s)) ds.
\end{aligned} \tag{3.6}$$

Now, the integration over $[0, x_{3m}]$ can be accomplished by Simpson's 3/8 rule and the integral over $[x_{3m}, x_{3m+2}]$ is computed by using a cubic interpolation. Hence

$$\begin{aligned}
F_{1,3m+2} & = g_1(x_{3m+2}) + \frac{3h}{8} \\
& \times \{ k_{1,1}(x_{3m+2}, x_0, F_{1,0}) + 3k_{1,1}(x_{3m+2}, x_1, F_{1,1}) + 3k_{1,1}(x_{3m+2}, x_2, F_{1,2}) \\
& + 2k_{1,1}(x_{3m+2}, x_3, F_{1,3}) + \cdots + k_{1,1}(x_{3m+2}, x_{3m}, F_{1,3m}) \}
\end{aligned}$$

$$\begin{aligned}
& + \frac{3h}{8} \{ k_{1,2}(x_{3m+2}, x_0, F_{2,0}) + 3k_{1,2}(x_{3m+2}, x_1, F_{2,1}) + 3k_{1,2}(x_{3m+2}, x_2, F_{2,2}) \\
& \quad + 2k_{1,2}(x_{3m+2}, x_3, F_{2,3}) + \cdots + k_{1,2}(x_{3m+2}, x_{3m}, F_{2,3m}) \} \\
& + \frac{h}{4} \left\{ k_{1,1}(x_{3m+2}, x_{3m}, F_{1,3m}) + 3k_{1,1} \right. \\
& \quad \times \left(x_{3m+2}, x_{3m+2/3}, \frac{14}{81}F_{1,3m} + \frac{28}{27}F_{1,3m+1} - \frac{7}{27}F_{1,3m+2} + \frac{4}{81}F_{1,3m+3} \right) + 3k_{1,1} \\
& \quad \times \left(x_{3m+2}, x_{3m+4/3}, -\frac{5}{81}F_{1,3m} + \frac{20}{27}F_{1,3m+1} + \frac{10}{27}F_{1,3m+2} - \frac{4}{81}F_{1,3m+3} \right) \\
& \quad \left. + k_{1,1}(x_{3m+2}, x_{3m+2}, F_{1,3m+2}) \right\} + \frac{h}{4} \\
& \times \left\{ k_{1,2}(x_{3m+2}, x_{3m}, F_{2,3m}) + 3k_{1,2} \right. \\
& \quad \times \left(x_{3m+2}, x_{3m+2/3}, \frac{14}{81}F_{2,3m} + \frac{28}{27}F_{2,3m+1} - \frac{7}{27}F_{2,3m+2} + \frac{4}{81}F_{2,3m+3} \right) \\
& \quad + 3k_{1,2} \left(x_{3m+2}, x_{3m+4/3}, -\frac{5}{81}F_{2,3m} + \frac{20}{27}F_{2,3m+1} + \frac{10}{27}F_{2,3m+2} - \frac{4}{81}F_{2,3m+3} \right) \\
& \quad \left. + k_{1,2}(x_{3m+2}, x_{3m+2}, F_{2,3m+2}) \right\}, \tag{3.7}
\end{aligned}$$

and a similar right-hand side obtains for $F_{2,3m+2}$, where $F_{1,0} = g_1(x_0)$, $F_{2,0} = g_2(x_0)$. In a similar manner we obtain

$$\begin{aligned}
F_{1,3m+3} & \simeq f_1(x_{3m+3}) = g_1(x_{3m+3}) + \int_0^{x_{3m+3}} k_{1,1}(x_{3m+3}, s, f_1(s)) ds \\
& \quad + \int_0^{x_{3m+3}} k_{1,2}(x_{3m+3}, s, f_2(s)) ds, \\
F_{2,3m+3} & \simeq f_2(x_{3m+3}) = g_2(x_{3m+3}) + \int_0^{x_{3m+3}} k_{2,1}(x_{3m+3}, s, f_1(s)) ds \\
& \quad + \int_0^{x_{3m+3}} k_{2,2}(x_{3m+3}, s, f_2(s)) ds, \tag{3.8}
\end{aligned}$$

$$\begin{aligned}
F_{1,3m+3} & = g_1(x_{3m+3}) + \frac{3h}{8} \\
& \times \{ k_{1,1}(x_{3m+3}, x_0, F_{1,0}) + 3k_{1,1}(x_{3m+3}, x_1, F_{1,1}) \\
& \quad + 3k_{1,1}(x_{3m+3}, x_2, F_{1,2}) + 2k_{1,1}(x_{3m+3}, x_3, F_{1,3}) \\
& \quad + \cdots + k_{1,1}(x_{3m+3}, x_{3m+3}, F_{1,3m+3}) \} + \frac{3h}{8}
\end{aligned}$$

$$\begin{aligned}
& \times \{k_{1,2}(x_{3m+3}, x_0, F_{2,0}) + 3k_{1,2}(x_{3m+3}, x_1, F_{2,1}) \\
& \quad + 3k_{1,2}(x_{3m+3}, x_2, F_{2,2}) + 2k_{1,2}(x_{3m+3}, x_3, F_{2,3}) \\
& \quad + \cdots + k_{1,2}(x_{3m+3}, x_{3m+3}, F_{2,3m+3})\}, \\
F_{2,3m+3} &= g_2(x_{3m+3}) + \frac{3h}{8} \\
& \times \{k_{2,1}(x_{3m+3}, x_0, F_{1,0}) + 3k_{2,1}(x_{3m+3}, x_1, F_{1,1}) \\
& \quad + 3k_{2,1}(x_{3m+3}, x_2, F_{1,2}) + 2k_{2,1}(x_{3m+3}, x_3, F_{1,3}) \\
& \quad + \cdots + k_{2,1}(x_{3m+3}, x_{3m+3}, F_{1,3m+3})\} + \frac{3h}{8} \\
& \times \{k_{2,2}(x_{3m+3}, x_0, F_{2,0}) + 3k_{2,2}(x_{3m+3}, x_1, F_{2,1}) \\
& \quad + 3k_{2,2}(x_{3m+3}, x_2, F_{2,2}) + 2k_{2,2}(x_{3m+3}, x_3, F_{2,3}) \\
& \quad + \cdots + k_{2,2}(x_{3m+3}, x_{3m+3}, F_{2,3m+3})\}.
\end{aligned} \tag{3.9}$$

Equations (3.4)–(3.9) form a system with six unknowns for $m = 1, 2, \dots$. In fact, we have six simultaneous equations at each step.

4. Convergence Analysis

In this section we investigate the convergence of the proposed method. The following theorem shows that the order of convergence is at least four.

Theorem 4.1. *The approximate method given by the systems Equations (3.4), (3.7), and (3.9), is convergent and its order of convergence is at least four.*

Proof. We have

$$\begin{aligned}
|\varepsilon_{1,3m+1}| &= |F_{1,3m+1} - f_1(x_{3m+1})| \\
&= \left| h \sum_{i=0}^{3m} w_i k_{1,1}(x_{3m+1}, x_i, F_{1,i}) + h \sum_{i=0}^{3m} w_i k_{1,2}(x_{3m+1}, x_i, F_{2,i}) \right. \\
& \quad + \frac{h}{8} k_{1,1}(x_{3m+1}, x_{3m}, F_{1,3m}) + \frac{3h}{8} k_{1,1} \\
& \quad \times \left(x_{3m+1}, x_{3m+1/3}, \frac{40}{81} F_{1,3m} + \frac{20}{27} F_{1,3m+1} - \frac{8}{27} F_{1,3m+2} + \frac{5}{81} F_{1,3m+3} \right) \\
& \quad + \frac{3h}{8} k_{1,1} \left(x_{3m+1}, x_{3m+2/3}, \frac{14}{81} F_{1,3m} + \frac{28}{27} F_{1,3m+1} - \frac{7}{27} F_{1,3m+2} + \frac{4}{81} F_{1,3m+3} \right) \\
& \quad \left. + \frac{h}{8} k_{1,1}(x_{3m+1}, x_{3m+1}, F_{1,3m+1}) + \frac{h}{8} k_{1,2}(x_{3m+1}, x_{3m}, F_{2,3m}) \right|
\end{aligned}$$

$$\begin{aligned}
& + \frac{3h}{8} k_{1,2} \left(x_{3m+1}, x_{3m+1/3}, \frac{40}{81} F_{2,3m} + \frac{20}{27} F_{2,3m+1} - \frac{8}{27} F_{2,3m+2} + \frac{5}{81} F_{2,3m+3} \right) \\
& + \frac{3h}{8} k_{1,2} \left(x_{3m+1}, x_{3m+2/3}, \frac{14}{81} F_{2,3m} + \frac{28}{27} F_{2,3m+1} - \frac{7}{27} F_{2,3m+2} + \frac{4}{81} F_{2,3m+3} \right) \\
& + \frac{h}{8} k_{1,2}(x_{3m+1}, x_{3m+1}, F_{2,3m+1}) \\
& - \left| \int_0^{x_{3m+1}} k_{1,1}(x_{3m+1}, s, f_1(s)) ds - \int_0^{x_{3m+1}} k_{1,2}(x_{3m+1}, s, f_2(s)) ds \right|,
\end{aligned} \tag{4.1}$$

using the Lipschitz condition it can be written as

$$\begin{aligned}
|\varepsilon_{1,3m+1}| & \leq hc_1 \sum_{i=0}^{3m} |\varepsilon_{1,i}| + hc_2 \sum_{i=0}^{3m} |\varepsilon_{2,i}| + hc_3 |\varepsilon_{1,3m+1}| + hc_4 |\varepsilon_{2,3m+1}| \\
& + hc_5 |\varepsilon_{1,3m+2}| + hc_6 |\varepsilon_{2,3m+2}| + hc_7 |\varepsilon_{1,3m+3}| + hc_8 |\varepsilon_{2,3m+3}| \\
& + |R_{1,3m+1}| + |R_{2,3m+1}| + |R_{1,3m+2}| + |R_{2,3m+2}|,
\end{aligned} \tag{4.2}$$

where $R_{i,3m+1}, R_{i,3m+2}$ ($i = 1, 2$) are the errors of integration rule. Without loss of generality, we assume that

$$\|\varepsilon_{l,j}\|_{\infty} = \max_{l=1,2} \max_{j=3m+1,3m+2,3m+3} |\varepsilon_{l,j}| = |\varepsilon_{1,3m+1}|, \tag{4.3}$$

then let $R = \max_i [|R_{1,i}|, |R_{2,i}|]$, hence

$$\begin{aligned}
\|\varepsilon_{l,j}\|_{\infty} & \leq hc \sum_{i=0}^{3m} (|\varepsilon_{1,i}| + |\varepsilon_{2,i}|) + 6hc' \|\varepsilon_{l,j}\|_{\infty} + 4R, \\
\|\varepsilon_{l,j}\|_{\infty} & \leq \frac{hc}{1-6hc'} \sum_{i=0}^{3m} (|\varepsilon_{1,i}| + |\varepsilon_{2,i}|) + \frac{4R}{1-6hc'},
\end{aligned} \tag{4.4}$$

then from Gronwall inequality, we have

$$\|\varepsilon_{l,j}\|_{\infty} \leq \frac{4R}{1-6hc'} e^{(c/(1-6hc'))x_n}. \tag{4.5}$$

For functions k and f with at least fourth-order derivatives, we have $R = o(h^4)$ and so $\|\varepsilon_m\|_{\infty} = o(h^4)$ and the proof is completed. \square

5. Numerical Results

In this section, some examples are given to certify the convergence and error bounds of the presented method. All results are computed using the well-known symbolic software

Table 1: Numerical results of Example 5.1.

x	e_{HPM} in [9]		$h = 0.1$		$h = 0.05$	
	$e(f_1)$	$e(f_2)$	$e(f_1)$	$e(f_2)$	$e(f_1)$	$e(f_2)$
0.1	$9.678e^{-07}$	$4.711e^{-05}$	0	0	0	0
0.2	$3.002e^{-05}$	$7.111e^{-04}$	0	0	0	0
0.3	$2.211e^{-04}$	$3.399e^{-03}$	0	0	0	0
0.4	$9.053e^{-04}$	$1.015e^{-02}$	0	0	0	0
0.5	$2.687e^{-03}$	$2.346e^{-02}$	0	$1.0e^{-10}$	0	$1.0e^{-10}$
0.6	$6.511e^{-03}$	$4.605e^{-02}$	0	0	0	0
0.7	$1.372e^{-02}$	$8.084e^{-02}$	0	$1.0e^{-10}$	0	$1.0e^{-10}$
0.8	$2.609e^{-02}$	0.131	$1.0e^{-10}$	$1.0e^{-10}$	0	$1.0e^{-10}$
0.9	$2.929e^{-02}$	0.198	0	0	0	0
1.0	$7.601e^{-02}$	0.287	0	0	0	0

Table 2: Numerical results of Example 5.2.

x	$h = 0.1$		$h = 0.05$		$h = 0.025$	
	$e(f_1)$	$e(f_2)$	$e(f_1)$	$e(f_2)$	$e(f_1)$	$e(f_2)$
0.1	$8.76e^{-08}$	$5.4267e^{-07}$	$2.5e^{-09}$	$4.23e^{-09}$	$3.e^{-10}$	$5.3e^{-10}$
0.2	$1.582e^{-07}$	$1.721e^{-07}$	$1.93e^{-08}$	$1.96e^{-08}$	$1.1e^{-09}$	$3.0e^{-10}$
0.3	$9.821e^{-07}$	$1.480e^{-07}$	$5.86e^{-08}$	$9.1e^{-09}$	$3.6e^{-09}$	$6.0e^{-10}$
0.4	$1.279e^{-06}$	$9.462e^{-07}$	$7.26e^{-08}$	$2.73e^{-08}$	$6.0e^{-09}$	$2.1e^{-09}$
0.5	$1.5475e^{-06}$	$8.662e^{-07}$	$1.432e^{-07}$	$6.44e^{-08}$	$8.7e^{-09}$	$3.1e^{-09}$
0.6	$3.7774e^{-06}$	$1.2556e^{-06}$	$2.320e^{-07}$	$8.35e^{-08}$	$1.44e^{-08}$	$5.3e^{-09}$
0.7	$4.4688e^{-06}$	$2.7058e^{-06}$	$2.707e^{-07}$	$1.421e^{-07}$	$1.92e^{-08}$	$9.4e^{-09}$
0.8	$5.1935e^{-06}$	$3.4142e^{-06}$	$3.935e^{-07}$	$2.295e^{-07}$	$2.43e^{-08}$	$1.38e^{-08}$
0.9	$8.4753e^{-06}$	$4.7428e^{-06}$	$5.286e^{-07}$	$3.101e^{-07}$	$3.30e^{-08}$	$2.0e^{-08}$
1.0	$9.8341e^{-06}$	$7.3373e^{-06}$	$6.107e^{-07}$	$4.427e^{-07}$	$4.04e^{-08}$	$2.86e^{-08}$

Maple 12. Tables 1–3 show the obtained results for nonlinear examples and Tables 4–6 contain the results for linear examples. The results in Tables 1–6 show the absolute errors $|f(x_i) - F_i|$, $i = 1, 2, \dots, N$, where $f(x_i)$ is the exact solution evaluated at $x = x_i$ and F_i is the corresponding approximate solution.

Example 5.1. Consider the following system [9]:

$$\begin{aligned} x - x^2 + \int_0^x (f_1(s) + f_2(s)) ds &= f_1(x), \quad 0 \leq x \leq 1 \\ x - \frac{x^2}{2} - \frac{x^3}{3} + \int_0^x (f_1^2(s) + f_2(s)) ds &= f_2(x), \quad 0 \leq x \leq 1 \end{aligned} \quad (5.1)$$

with the exact solutions $f_1(x) = x$ and $f_2(x) = x$. In Table 1 we compare the errors $e(f_1)$ and $e(f_2)$ obtained using the present method and method in [9].

Table 3: Numerical results of Example 5.3.

x	$h = 0.1$		$h = 0.05$		$h = 0.025$	
	$e(f_1)$	$e(f_2)$	$e(f_1)$	$e(f_2)$	$e(f_1)$	$e(f_2)$
0.1	$3.398e^{-06}$	$3.4931e^{-06}$	$3.4e^{-08}$	$8.21e^{-08}$	$3.0e^{-09}$	$1.49e^{-08}$
0.2	$1.853e^{-06}$	$3.2536e^{-06}$	$1.36e^{-07}$	$5.302e^{-07}$	$2.0e^{-09}$	$2.76e^{-08}$
0.3	$1.934e^{-06}$	$1.55679e^{-05}$	$8.8e^{-08}$	$9.580e^{-07}$	$5.0e^{-09}$	$5.88e^{-08}$
0.4	$1.0510e^{-05}$	$2.52780e^{-05}$	$2.53e^{-07}$	$1.0938e^{-06}$	$1.7e^{-08}$	$9.17e^{-08}$
0.5	$1.1155e^{-05}$	$2.21338e^{-05}$	$6.96e^{-07}$	$2.3675e^{-06}$	$2.9e^{-08}$	$1.245e^{-07}$
0.6	$1.7852e^{-05}$	$6.29575e^{-05}$	$9.93e^{-07}$	$3.9457e^{-06}$	$6.0e^{-08}$	$2.441e^{-07}$
0.7	$6.2599e^{-05}$	$1.201563e^{-04}$	$2.259e^{-06}$	$4.5288e^{-06}$	$1.44e^{-07}$	$4.090e^{-07}$
0.8	$8.9572e^{-05}$	$9.5467e^{-05}$	$5.569e^{-06}$	$1.2368e^{-05}$	$2.90e^{-07}$	$6.01e^{-07}$
0.9	$1.70559e^{-04}$	$3.70854e^{-04}$	$1.0249e^{-05}$	$2.4445e^{-05}$	$6.51e^{-07}$	$1.533e^{-06}$
1.0	$7.91069e^{-04}$	$1.185001e^{-03}$	$2.6732e^{-05}$	$3.0637e^{-05}$	$1.730e^{-06}$	$3.391e^{-06}$

Table 4: Numerical results of Example 5.4.

x	$h = 0.1$		$h = 0.05$		$h = 0.025$	
	$e(f_1)$	$e(f_2)$	$e(f_1)$	$e(f_2)$	$e(f_1)$	$e(f_2)$
0.1	$2.848e^{-07}$	$2.375e^{-07}$	$2.39e^{-08}$	$9.0e^{-10}$	$4.7e^{-09}$	$2.0e^{-10}$
0.2	$7.777e^{-07}$	$3.0e^{-10}$	$1.835e^{-07}$	$5.0e^{-09}$	$1.07e^{-08}$	$9.0e^{-10}$
0.3	$5.6610e^{-06}$	$5.69e^{-08}$	$3.433e^{-07}$	$2.75e^{-08}$	$2.13e^{-08}$	$2.3e^{-09}$
0.4	$5.5049e^{-06}$	$7.029e^{-07}$	$3.371e^{-07}$	$8.39e^{-08}$	$2.36e^{-08}$	$5.6e^{-09}$
0.5	$5.5930e^{-06}$	$2.1033e^{-06}$	$4.788e^{-07}$	$1.254e^{-07}$	$2.96e^{-08}$	$1.30e^{-08}$
0.6	$1.03890e^{-05}$	$2.115e^{-06}$	$6.279e^{-07}$	$1.97e^{-07}$	$3.86e^{-08}$	$1.3e^{-08}$
0.7	$1.00566e^{-05}$	$5.211e^{-06}$	$6.128e^{-07}$	$4.05e^{-07}$	$4.12e^{-08}$	$2.4e^{-08}$
0.8	$1.01662e^{-05}$	$9.770e^{-06}$	$7.676e^{-07}$	$6.02e^{-07}$	$4.56e^{-08}$	$3.9e^{-08}$
0.9	$1.56375e^{-05}$	$1.2629e^{-05}$	$9.480e^{-07}$	$9.28e^{-07}$	$5.81e^{-08}$	$6.2e^{-08}$
1.0	$1.60249e^{-05}$	$2.3160e^{-05}$	$9.813e^{-07}$	$1.592e^{-06}$	$6.54e^{-08}$	$1.03e^{-07}$

Example 5.2. Consider the following system [7]:

$$\begin{aligned} \cos(x) - \frac{1}{2}\sin^2(x) + \int_0^x (f_1(s)f_2(s))ds &= f_1(x), \quad 0 \leq x \leq 1 \\ \sin(x) - x + \int_0^x f_1^2(s)ds + \int_0^x f_2^2(s)ds &= f_2(x), \quad 0 \leq x \leq 1 \end{aligned} \quad (5.2)$$

the exact solutions are $f_1(x) = \cos(x)$ and $f_2(x) = \sin(x)$. The errors are given in Table 2.

Example 5.3. Consider the following system [15]:

$$\begin{aligned} \sec(x) - x + \int_0^x (f_1^2(s) - f_2^2(s))ds &= f_1(x), \quad 0 \leq x \leq 1 \\ 3 \tan(x) - x - \int_0^x (f_1^2(s) + f_2^2(s))ds &= f_2(x), \quad 0 \leq x \leq 1, \end{aligned} \quad (5.3)$$

where the exact solutions are $f_1(x) = \sec(x)$ and $f_2(x) = \tan(x)$.

Table 5: Numerical results of Example 5.5.

x	$h = 0.1$		$h = 0.05$		$h = 0.025$	
	$e(f_1)$	$e(f_2)$	$e(f_1)$	$e(f_2)$	$e(f_1)$	$e(f_2)$
0.1	$3.671e^{-07}$	$2.9894e^{-07}$	$1.30e^{-08}$	$1.057e^{-08}$	$7.0e^{-10}$	$2.11e^{-09}$
0.2	$4.491e^{-07}$	$3.780e^{-07}$	$8.39e^{-08}$	$7.33e^{-08}$	$5.0e^{-09}$	$4.6e^{-09}$
0.3	$2.1364e^{-06}$	$2.0417e^{-06}$	$1.439e^{-07}$	$1.335e^{-07}$	$1.07e^{-08}$	$8.4e^{-09}$
0.4	$3.1803e^{-06}$	$2.5989e^{-06}$	$1.946e^{-07}$	$1.627e^{-07}$	$1.22e^{-08}$	$1.17e^{-08}$
0.5	$3.8590e^{-06}$	$3.0494e^{-06}$	$2.841e^{-07}$	$2.441e^{-07}$	$1.82e^{-08}$	$1.54e^{-08}$
0.6	$5.3109e^{-06}$	$5.0008e^{-06}$	$3.539e^{-07}$	$3.262e^{-07}$	$2.28e^{-08}$	$2.06e^{-08}$
0.7	$7.0863e^{-06}$	$5.9892e^{-06}$	$4.518e^{-07}$	$3.856e^{-07}$	$2.86e^{-08}$	$2.52e^{-08}$
0.8	$8.5579e^{-06}$	$7.0265e^{-06}$	$5.596e^{-07}$	$4.947e^{-07}$	$3.55e^{-08}$	$3.15e^{-08}$
0.9	$9.9840e^{-06}$	$9.3934e^{-06}$	$6.597e^{-07}$	$6.118e^{-07}$	$4.28e^{-08}$	$3.89e^{-08}$
1.0	$1.29156e^{-05}$	$1.10909e^{-05}$	$8.334e^{-07}$	$7.207e^{-07}$	$5.42e^{-08}$	$4.64e^{-08}$

Table 6: Numerical results of Example 5.6.

x	e_{HPM}		$h = 0.1$		$h = 0.05$	
	$e(f_1)$	$e(f_2)$	$e(f_1)$	$e(f_2)$	$e(f_1)$	$e(f_2)$
0.2	$3.947e^{-04}$	$6.333e^{-05}$	0	$4.0e^{-09}$	$6.7e^{-08}$	$6.0e^{-09}$
0.4	$6.060e^{-03}$	$1.962e^{-03}$	$4.445e^{-06}$	$8.83e^{-07}$	$2.25e^{-07}$	$1.23e^{-07}$
0.6	$2.855e^{-02}$	$1.409e^{-02}$	$1.3e^{-08}$	$7.150e^{-06}$	$2.0e^{-09}$	$5.69e^{-07}$
0.8	$8.088e^{-02}$	$5.465e^{-02}$	$1.4583e^{-05}$	$1.5812e^{-05}$	$3.62e^{-07}$	$1.199e^{-06}$
1.0	$1.685e^{-01}$	$1.483e^{-01}$	$1.3989e^{-05}$	$3.2971e^{-05}$	$7.27e^{-07}$	$2.346e^{-06}$
1.2	$2.770e^{-01}$	$3.135e^{-01}$	$2.173e^{-06}$	$7.3764e^{-05}$	$1.51e^{-07}$	$4.865e^{-06}$
1.4	$3.567e^{-01}$	$5.369e^{-01}$	$3.4677e^{-05}$	$9.9081e^{-05}$	$1.006e^{-06}$	$7.222e^{-06}$
1.6	$3.034e^{-01}$	$7.325e^{-01}$	$3.5568e^{-05}$	$1.62912e^{-04}$	$2.002e^{-06}$	$1.0807e^{-05}$
1.8	$6.562e^{-02}$	$6.821e^{-01}$	$2.7768e^{-05}$	$2.77606e^{-04}$	$1.765e^{-06}$	$1.7732e^{-05}$
2.0	1.043	$4.961e^{-02}$	$9.6763e^{-05}$	$3.46228e^{-04}$	$4.258e^{-06}$	$2.4040e^{-05}$

Example 5.4. Consider the following system [7]:

$$\begin{aligned} \cosh(x) + x \sin(x) - \int_0^x e^{x-s} f_1(s) ds - \int_0^x \cos(x-s) f_2(s) ds &= f_1(x), \quad 0 \leq x \leq 1 \\ 2 \sin(x) + x(\sin^2(x) + e^x) - \int_0^x e^{x+s} f_1(s) ds - \int_0^x x \cos(s) f_2(s) ds &= f_2(x) \quad 0 \leq x \leq 1, \end{aligned} \quad (5.4)$$

with the exact solutions $f_1(x) = e^{-x}$ and $f_2(x) = 2 \sin(x)$. Table 4 shows the errors.

Example 5.5. Consider the following Volterra system of integral equations [5]:

$$\begin{aligned} g_1(x) - \int_0^x (\sin(s-x) - 1) f_1(s) ds + \int_0^x (1-s \cos(x)) f_2(s) ds &= f_1(x), \quad 0 \leq x \leq 1 \\ g_2(x) + \int_0^x f_1(s) ds + \int_0^x (x-s) f_2(s) ds &= f_2(x), \quad 0 \leq x \leq 1 \end{aligned} \quad (5.5)$$

the functions $g_1(x)$ and $g_2(x)$ are chosen such that the exact solutions are to be $f_1(x) = \cos(x)$ and $f_2(x) = \sin(x)$. The errors are given in Table 5.

Example 5.6. Consider the following Volterra system of integral equations [5]

$$\begin{aligned} g_1(x) + \int_0^x (x-s)^3 f_1(s) ds + \int_0^x (x-s)^2 f_2(s) ds &= f_1(x), \quad 0 \leq x \leq 2 \\ g_2(x) + \int_0^x (x-s)^4 f_1(s) ds + \int_0^x (x-s)^3 f_2(s) ds &= f_2(x), \quad 0 \leq x \leq 2 \end{aligned} \quad (5.6)$$

the functions $g_1(x)$ and $g_2(x)$ are chosen such that the exact solutions are to be $f_1(x) = x^2 + 1$ and $f_2(x) = 1 - x^3 + x$. Table 6 compares errors.

6. Conclusion

Now let $E(h) = ch^q$ be error of the block by block using Simpson's 3/8 rule where c and q are, respectively, a constant and order of the error, then we have $q = \ln(E(h)/c) / \ln(h)$. By computing the order q from this formulae for the errors reported in Tables 1–6, we conclude that $q \geq 4$. This confirms the claim that was stated in introduction and was proved by the convergence analysis. For example in Table 2 for $x = 0.1$, $E(f_1(h)) = 0.876e^{-07}$ where $h = 0.1$, so we get $q = 8$ or in Table 4 for $x = 0.5$, $E(f_2(h)) = 0.130e^{-07}$ where $h = 0.025$, so we get $q = 4.14268$ or in Table 6 for $x = 0.6$, $E(f_1(h)) = 0.2e^{-08}$, $h = 0.05$ then $q = 6.148974$.

Note that in the Table 1 we compare the order of convergence between the results which were obtained by Yusufoglu [9] (by using HPM method) and block by block method. Further, the results of the Table 6 show that block by block method is efficient for the large values of x , whereas HPM method isn't applicable. Also, the time of computation in block by block method is less than HPM method whenever programming of both method is done in MAPLE package.

Acknowledgments

This paper was prepared when the third author visits the Institute for Mathematical Research (INSPER) thus the authors wish to thank the Institute for Mathematical Research (INSPER), University Putra Malaysia. The authors would also like to express their sincere thanks and gratitude to the reviewer(s) for their valuable comments and suggestions.

References

- [1] A. Akyüz-Daşcıoğlu, "Chebyshev polynomial solutions of systems of linear integral equations," *Applied Mathematics and Computation*, vol. 151, no. 1, pp. 221–232, 2004.
- [2] M. E. A. El Tom, "Application of spline functions to systems of Volterra integral equations of the first and second kinds," *Journal of the Institute of Mathematics and its Applications*, vol. 17, no. 3, pp. 295–310, 1976.
- [3] H. M. Liu, "Variational approach to nonlinear electrochemical system," *Chaos, Solitons Fractals*, vol. 23, no. 2, pp. 573–576, 2005.
- [4] K. Maleknejad and M. Shahrezaee, "Using Runge-Kutta method for numerical solution of the system of Volterra integral equation," *Applied Mathematics and Computation*, vol. 149, no. 2, pp. 399–410, 2004.
- [5] M. Rabbani, K. Maleknejad, and N. Aghazadeh, "Numerical computational solution of the Volterra integral equations system of the second kind by using an expansion method," *Applied Mathematics and Computation*, vol. 187, no. 2, pp. 1143–1146, 2007.

- [6] S. Abbasbandy, "Numerical solutions of the integral equations: homotopy perturbation method and Adomian's decomposition method," *Applied Mathematics and Computation*, vol. 173, no. 1, pp. 493–500, 2006.
- [7] J. Biazar and H. Ghazvini, "He's homotopy perturbation method for solving systems of Volterra integral equations of the second kind," *Chaos, Solitons and Fractals*, vol. 39, no. 2, pp. 770–777, 2009.
- [8] J.-H. He, "Homotopy perturbation technique," *Computer Methods in Applied Mechanics and Engineering*, vol. 178, no. 3-4, pp. 257–262, 1999.
- [9] E. Yusufoglu, "A homotopy perturbation algorithm to solve a system of Fredholm-Volterra type integral equations," *Mathematical and Computer Modelling*, vol. 47, no. 11-12, pp. 1099–1107, 2008.
- [10] A. Young, "The application of approximate product integration to the numerical solution of integral equations," *Proceedings of the Royal Society A*, vol. 224, pp. 561–573, 1954.
- [11] C. Cattani, S. Chen, and G. Aldashev, "Information and modeling in complexity," *Mathematical Problems in Engineering*, vol. 2012, Article ID 868413, 3 pages, 2012.
- [12] S. C. Lim, C. H. Eab, K. H. Mak, M. Li, and S. Y. Chen, "Solving linear coupled fractional differential equations by direct operational method and some applications," *Mathematical Problems in Engineering*, vol. 2012, Article ID 653939, 28 pages, 2012.
- [13] M. Li, S. C. Lim, and S. Chen, "Exact solution of impulse response to a class of fractional oscillators and its stability," *Mathematical Problems in Engineering*, vol. 2011, Article ID 657839, 9 pages, 2011.
- [14] L. M. Delves and J. L. Mohamed, *Computational Methods for Integral Equations*, Cambridge University Press, Cambridge, UK, 1985.
- [15] R. K. Saeed and C. Ahmed, "Approximate solution for the system of Non-linear Volterra integral equations of the second kind by using block-by-block method," *Australian Journal of Basic and Applied Sciences*, vol. 2, no. 1, pp. 114–124, 2008.

Research Article

Analysis of a T-Frame Bridge

Pengzhen Lu,^{1,2,3} Fangyuan Li,⁴ and Changyu Shao²

¹ Faculty of Civil Engineering and Architecture, Zhejiang University of Technology, Hangzhou 310014, China

² Shanghai Municipal Engineering Design and Research Institute, Shanghai 200092, China

³ Department of Civil Engineering, Zhejiang University, Hangzhou 310027, China

⁴ College of Civil Engineering, Tongji University, Shanghai 200092, China

Correspondence should be addressed to Fangyuan Li, fyli@tongji.edu.cn

Received 30 May 2012; Accepted 6 August 2012

Academic Editor: Sheng-yong Chen

Copyright © 2012 Pengzhen Lu et al. This is an open access article distributed under the Creative Commons Attribution License, which permits unrestricted use, distribution, and reproduction in any medium, provided the original work is properly cited.

The structural behavior of T-frame bridges is particularly complicated and it is difficult using a general analytical method to directly acquire the internal forces in the structure. This paper presents a spatial grillage model for analysis of such bridges. The proposed model is validated by comparison with results obtained from field testing. It is shown that analysis of T-frame bridges may be conveniently performed using the spatial grillage model.

1. Introduction

Rigid frame bridges are appearing in various exotic forms resulting in complex, efficient, and aesthetically pleasing structures, with graceful appearance, compact construction dimension, spacious room under bridge, and a broad eye view, and the plan can be applied to the construction of long span bridges. Because of T-frame bridge special advantages in the rigid frame bridge, more and more the T-frame bridges were used. The safety of the T-frame bridges presents an increasing important concern in design, construction, and service. This special type of flexible, large span T-frame bridges makes the structural analysis more complex and difficult [1–3].

Typically, the design of highway bridges in China must conform to the General Code for Design of Highway Bridges and Culverts (JTG D60-2004) specifications. The analysis and design of any highway bridge must consider truck and lane loadings. However, the structural behavior of T-frame bridge is particularly complicated, and many rigorous methods for analysis of T-frame bridges are quite tedious and often difficult.

Pan et al. [1] carried out uncertainty analysis of creep and shrinkage effects in long-span continuous rigid frame of Sutong Bridge. Azizi et al. [4] used spectral element method for analyzing continuous beams and bridges subjected to a moving load. Wang et al. [5] analyzed dynamic behavior of slant-legged rigid-frame Highway Bridge. Dicleli [6] presented a computer-aided approach of integral-abutment bridges, and an analysis procedure and a simplified structure model were proposed for the design of integral-abutment bridges considering their actual behavior and load distribution among their various components [7, 8]. There were several approximate analysis methods for bridge decks, which include the grillage method and the orthotropic plate theory [9]. Yoshikawa et al. [10] investigated construction of Benten Viaduct, rigid-frame bridge with seismic isolators at the foot of piers. Kalantari and Amjadian [11] reported a 3DOFs analytical model an approximate hand method was presented for dynamic analysis of continuous rigid deck.

Mabsout et al. [12] reported the results of parametric investigation using the finite-element analysis of straight, single-span, simply supported reinforced concrete slab bridges. The study considered various span lengths and slab widths, number of lanes, and live loading conditions for bridges with and without shoulders. Longitudinal bending moments and deflections in the slab were evaluated and compared with procedures recommended by AASHTO [13].

In a word, the above mentioned methods can not exactly deal with the structural mechanical behavior of the T-frame bridges what's worse, they may lead to insecurity of structural design. Grillage analysis is probably the most popular computer-aided method for analyzing bridge decks [14, 15]. This is because it is easy to comprehend and use, relatively inexpensive, and it has been proven to be reliably accurate for a wide variety of bridge types [16–19]. The method, pioneered for computer use by Lightfoot and Sawko [20] represented the deck by an equivalent grillage of beams. Based on the grillage method, Hambly [21] produced design charts for the analysis and design of bridge decks. Based on the structure characteristic and the grillage method, analysis of a T-frame bridge based on the grillage method will be represented.

This paper presents a spatial grillage model for the analysis of a T-frame bridge. Static and dynamic analysis results of spatial grillage model for the T-frame bridge are compared with results based on results obtained from field testing. The research results shown that analysis of T-frame bridges may be conveniently performed using the spatial grillage model.

2. Box-Girder Deck Analysis with Spatial Grillage Model

Spatial grillage model is a convenient method for analysis of box-girder bridges. In the model, the box-girder slab is represented by an equivalent grid of beams whose longitudinal and transverse stiffnesses are approximately the same as the local plate stiffnesses of the box-girder slab.

In the spatial grillage model analysis, the orientation of the longitudinal members should be always parallel to the free edges while the orientation of transverse members can be either parallel to the supports or orthogonal to the longitudinal beams. According to the grillage model, the output internal force resultants can be used directly. The grillage model involves a plane grillage of discrete interconnected beams. The representation of a bridge as a grillage is ideally suited for carrying out the necessary calculations associated with analysis and design on a digital computer and it gives the designer an idea about the structural behavior of the bridge.

The main challenge in the spatial grillage model is how to obtain an equivalent grillage based on the box-girder deck structure. The spatial grillage model for analyzing box-girder Slab bridge includes figuring out the grillage mesh and grillage member section properties.

2.1. Spatial Grillage Mesh

Determination of a suitable grillage mesh for a box-girder of rigid frame bridge is, as for a slab deck, best approached from a consideration of the structural behavior of the particular deck rather than from the application of a set of rules. Since the average longitudinal and transverse bending stiffness are comparable, the distribution of load is somewhat similar to that of a torsionally flexible slab, but with forces locally concentrated. The grillage simulates the prototype closely by having its members coincident with the centre lines of the prototypes beams. In addition, there is a diaphragm in the prototype such as over a support, and then a grillage member should be coincident. Based on section shape of the rigid frame bridge and support arrangements, a spatial grillage mesh should be represented by the above mentioned spatial grillage method. At the same time, according to the grillage equivalent theory, the following three important aspects have to be noted: according to mechanical behavior of a rigid frame bridge, one should place the grillage beams along the lines of designed strength; the longitudinal and transverse member spacing should be reasonably similar to permit sensible static distribution of loads; in addition, virtual longitudinal and transverse members are often employed for the sake of convenience in the analysis. The virtual members only offer stiffness, but its weight must be ignored.

2.2. Grillage Member Section Properties

Grillage member section properties include longitudinal grillage member section properties and transverse grillage member section properties. Based on rigid frame bridge structural features, the amount of each deck for prototype bridge is represented by the appropriate grillage member. The flexural inertia of each grillage member is calculated about the centroid of the section it represents. The section properties of a transverse grillage member, which solely represents slab, are calculated as for slab. For this

$$\begin{aligned} I &= \frac{bd^3}{12}, \\ c &= \frac{bd^3}{6}. \end{aligned} \tag{2.1}$$

When the grillage member also includes a diaphragm, an estimate must be made of the width of slab acting as flange. If the diaphragms are at close centres, the flanges of each can be assumed to extend to midway between diaphragms. It is usually conservative to assume that the effective flange is 0.3 of the distance between longitudinal members. The parameters of the grillage member section properties for box-girder are given by



Figure 1: A photo of Quhai T-frame bridge.

$$GJ_x = \frac{E}{2(1+m)}, \quad (2.2)$$

$$GJ_y = \frac{E}{2(1+m)},$$

where E is the modulus of elasticity, I_x , I_y the moments of inertia, J_x , J_y the moments of torsional inertia, and m the moment per unit width.

3. Illustrative Example

The Quhai rigid frame bridge is over the Qu river in Dongguang, Guangdong province, China. A photo of the bridge just before its opening is shown in Figure 1. The bridge has a single box with double chamber deck construction consisting of 29 spans with an overall length of 768.6 m ($19.3 \text{ m} + 12 \times 20 \text{ m} + 70 \text{ m} + 110 \text{ m} + 70 \text{ m} + 12 \times 20 \text{ m} + 19.3 \text{ m}$). The bridge was completed in 1995. The two-way roadway of the bridge deck is 32 m wide with six lanes. Figure 2 shows the general view of the Quhai rigid frame bridge with schematic plan, elevation, and typical cross section of the single box with double chamber deck.

The Quhai Bridge is a rigid frame design for a single box with double chamber bridge, with two main palaces with hang holes, T-frame of $2 \times 40 \text{ m}$, and two hung-girder spans is 30 m. Cantilever root height of box-girder for T-frame is 6 m, and end height is 2 m. A single box with double chamber and 32 m wide section was selected for the bridge superstructure. The design live load of the original bridge is vehicle load, and checking load is trailer-100 (loads specified in the Bridge Design Code of China). In order to increase the bearing capacity of the bridge, new loads specified (truck-20 and trailer-120) were employed for the bridge application.

3.1. Three-Dimensional Finite Element Modeling

Three-dimensional linear elastic finite element models of the spatial grillage model of the Quhai Bridge have been constructed using SAP2000 finite element analysis software. In the finite-element model, 3D beam4 elements were adopted to create the grillage model that will be used to determine the internal stress resultants, natural frequencies, and corresponding mode shapes. The spatial grillage model was shown in Figure 3, and the virtual beams only

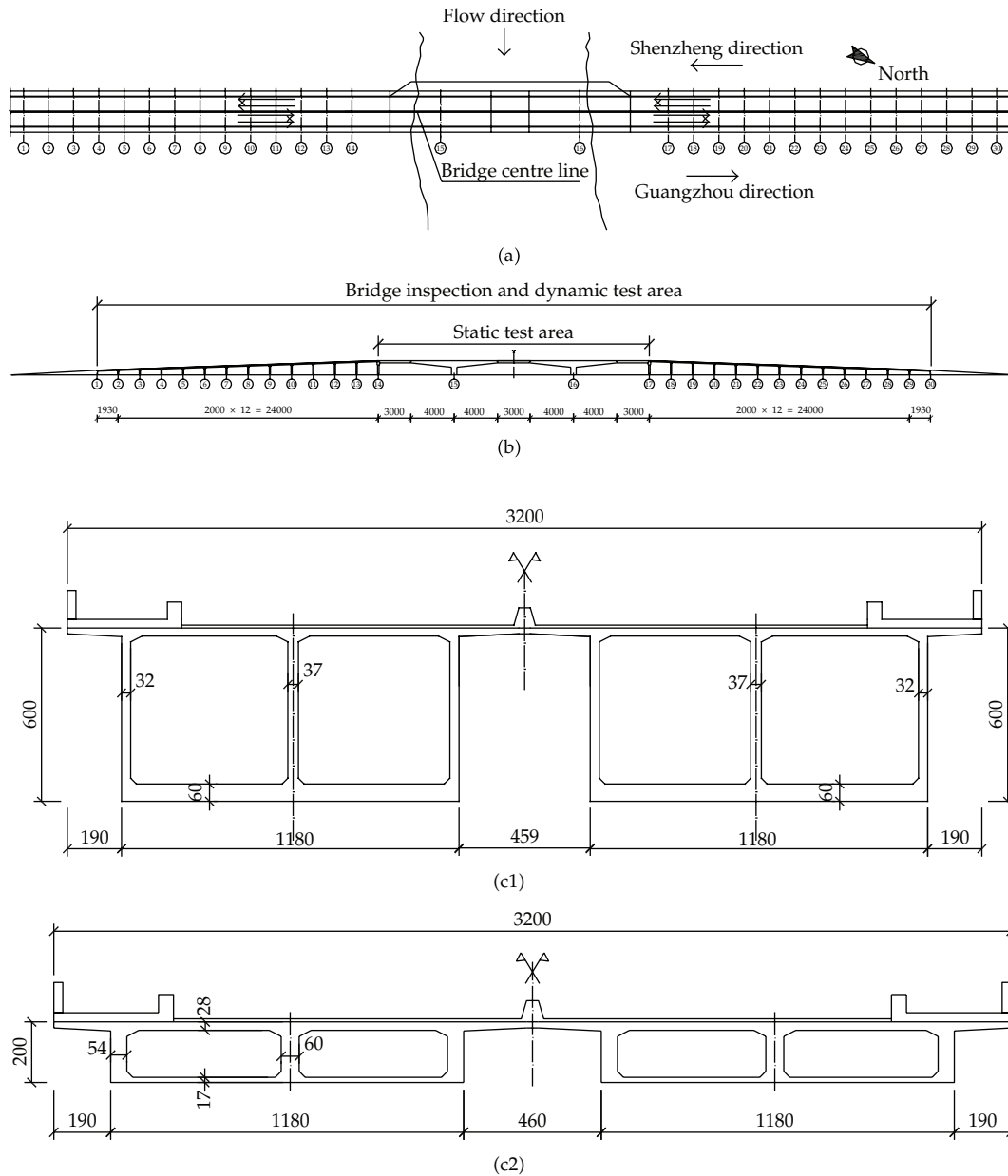


Figure 2: General view of Quhai T-frame bridge: (a) plan view; (b) elevation view; (c) typical cross-section of box-girder deck.

offer stiffness. In the finite-element model of the bridge, 3D 1104 elements (beam 4) and 817 nodes were used. The spatial grillage model of the bridge as a whole is shown in Figure 4.

3.2. Results of Static Analysis

According to the influence line method of the control section, internal forces of longitudinal and transverse grillage members were presented. Internal force values of the control section

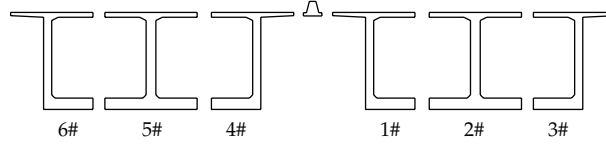


Figure 3: Equivalent grillage model.

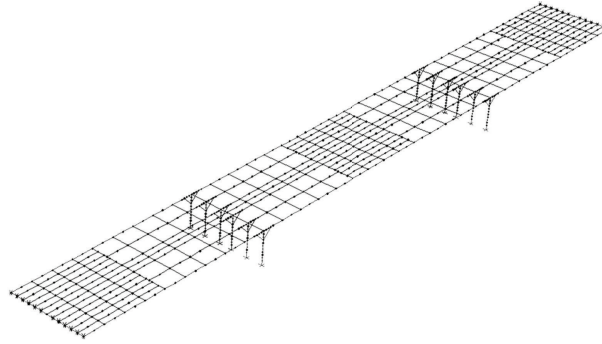


Figure 4: Grillage model of main bridge for Quhai Bridge.

for the grillage model were shown in Tables 1 and 2. In accordance with the analytical results of the longitudinal grillage, under trailer-120 load, the maximum normal moment of edge hang beam (1#) was obtained by the mid-span section of the grillage, and the maximum value is $2.0 \times 10^6 \text{ N} \cdot \text{m}$; the maximum normal moment of middle hang beam (1#) was obtained by the mid-span section of the grillage, and the maximum value is $2.13 \times 10^6 \text{ N} \cdot \text{m}$; under truck 20 and crowd load, the maximum negative moment was proposed by the abutments (15#) section of the grillage, and the maximum value is $2.06 \times 10^7 \text{ N} \cdot \text{m}$. In terms of the internal stress resultants, the moment and shear force envelope diagrams of the control grillage model were obtained and shown in Figures 5, 6, and 7.

3.3. Results of Dynamic Analysis

From the dynamic analysis using the spatial grillage model, the first natural frequency of the hang beam (14-15#) and T-frame is 3.6 Hz and 1.31 Hz, respectively, and vibration mode is symmetric vertical bending; the first natural frequency of the hang beam (16-17#) and T-frame is 3.6 Hz and 1.31 Hz, respectively, and vibration mode is symmetric vertical bending; the first natural frequency of the middle-span hang beam is 3.6 Hz, and vibration mode is symmetric vertical bending. The first mode shapes of the bridge are shown in Figure 8.

4. Description of Field Load Tests and Results

The field static or dynamic tests on bridges have been of great interest not only in investigating bridge fundamental behavior but also for calibrating finite-element models. Several results of field tests and correlated finite-element analyses have been presented for the Quhai Bridge. The field load tests on the Quhai Bridge employed the corresponding design load, to simulate the design live loads of the bridge. The field load tests on the Quhai Bridge

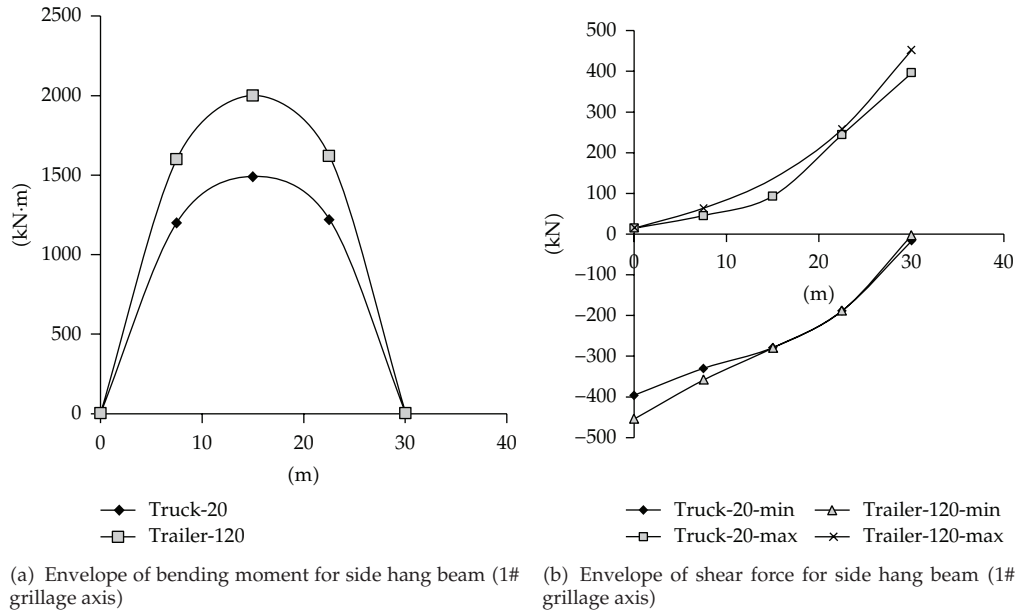


Figure 5: Envelope of internal force of grillage model for side hang beam (1# grillage).

Table 1: Moment under design live load (control sections of 1# grillage/N·m).

Section location	Trailer 120 max/min	Truck 20 max/min	Control moment
Pier (14#)	0/0	0/0	0/0
0.5 L	$3.9E + 6 / -2.4E + 4$	$2.9E + 6 / -3.1E + 5$	$3.9E + 6 / -3.1E + 5$
Corbel	0/0	0/0	0/0
Pier (15#)	$0 / -3.5E + 7$	$0 / -4.1E + 7$	$0 / -4.1E + 7$
Corbel	$0 / -5.6E + 3$	$0 / -1.1E + 4$	$0 / -1.1E + 4$
0.5 L	$4.2E + 6 / -2.4E + 4$	$3.2E + 6 / -3.3E + 5$	$4.3E + 6 / -3.3E + 5$
Corbel	0/0	0/0	0/0
Pier (16#)	$0 / -3.5E + 7$	$0 / -4.1E + 7$	$0 / -4.1E + 7$

Table 2: Shear force under design live load (control sections of 1# grillage/N).

Section location	Trailer 120 max/min	Truck 20 max/min	Control moment
Pier (14#)	$5.3E + 2 / -9.1E + 5$	$2.9E + 4 / -7.9E + 5$	$9.1E + 5$
0.5 L	$2.7E + 5 / -5.7E + 5$	$1.8E + 5 / -5.5E + 5$	$5.7E + 5$
Corbel	$9.1E + 5 / -6.1E + 3$	$7.9E + 5 / -3.3E + 4$	$9.1E + 5$
Corbel	$8.6E + 5 / 0$	$7.4E + 5 / 0$	$8.6E + 5$
Pier (15#)	$1.1E + 6 / 0$	$1.7E + 6 / 0$	$1.7E + 6$
Pier (15#)	$0 / -1.1E + 6$	$0 / -1.7E + 6$	$1.7E + 6$
Corbel	$0 / -8.6E + 5$	$0 / -7.5E + 5$	$8.6E + 5$
Corbel	$6.2E + 3 / -9.7E + 5$	$3.8E + 4 / -8.8E + 5$	$9.7E + 5$
0.5 L	$3.1E + 5 / -5.5E + 5$	$2.1E + 5 / -5.5E + 5$	$5.5E + 5$
Corbel	$9.1E + 5 / -6.1E + 3$	$7.9E + 5 / -3.5E + 4$	$9.1E + 5$
Corbel	$8.6E + 5 / 0$	$7.5E + 5 / 0$	$8.6E + 5$
Pier (16#)	$1.1E + 6 / 0$	$1.7E + 6 / 0$	$1.7E + 6$
Pier (16#)	$0 / -1.1E + 6$	$0 / -1.7E + 6$	$1.7E + 6$

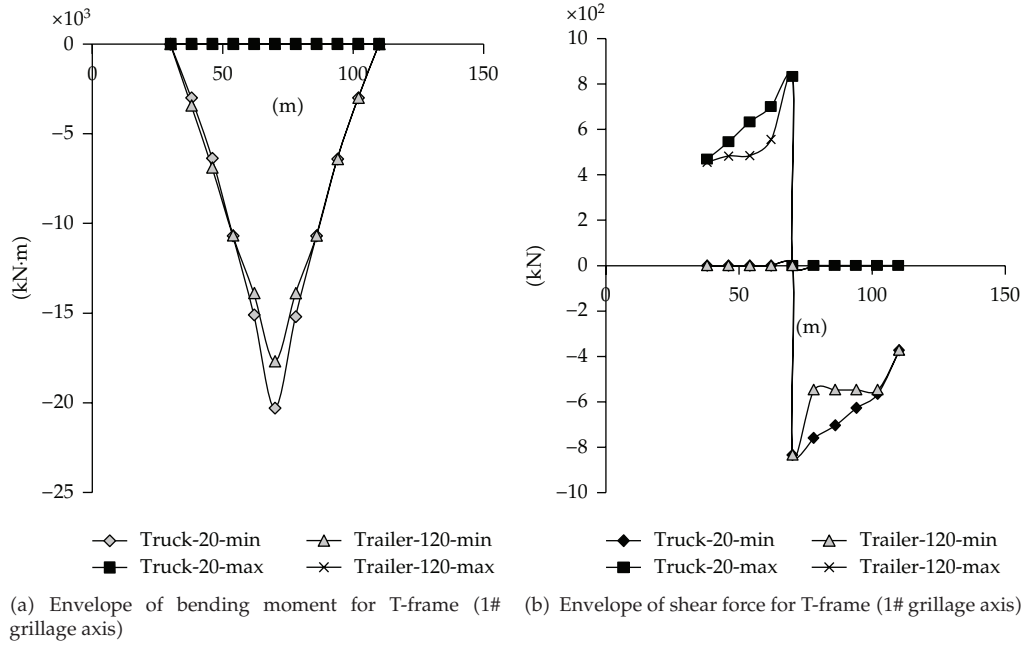


Figure 6: Envelope of internal force of grillage model for T-frame (1# grillage).

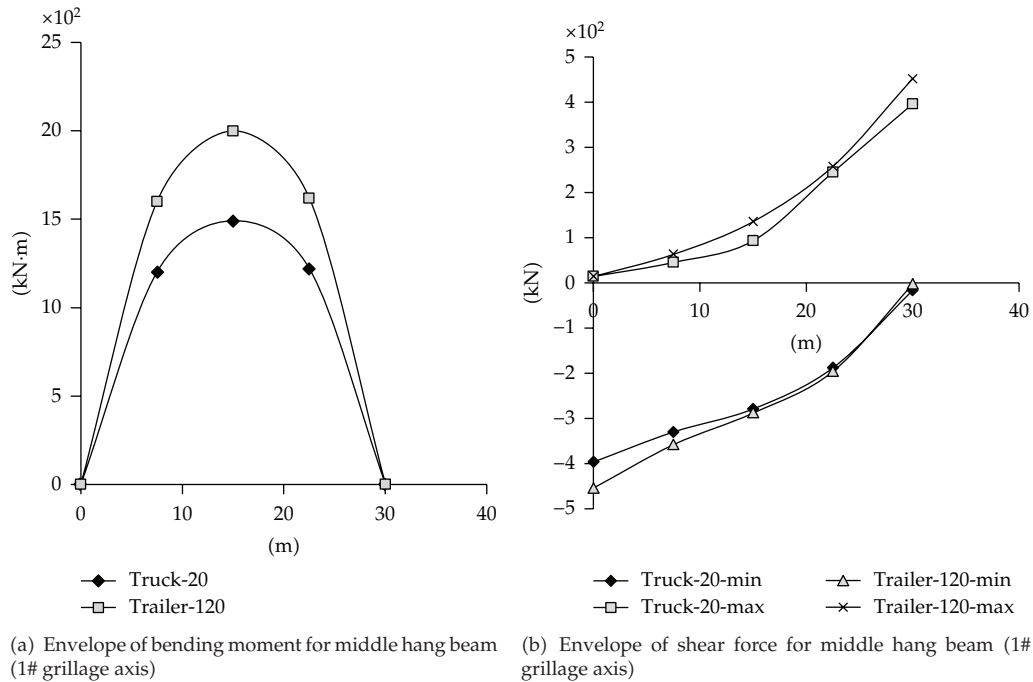


Figure 7: Envelope of internal force of grillage model for middle hang beam (1# grillage).

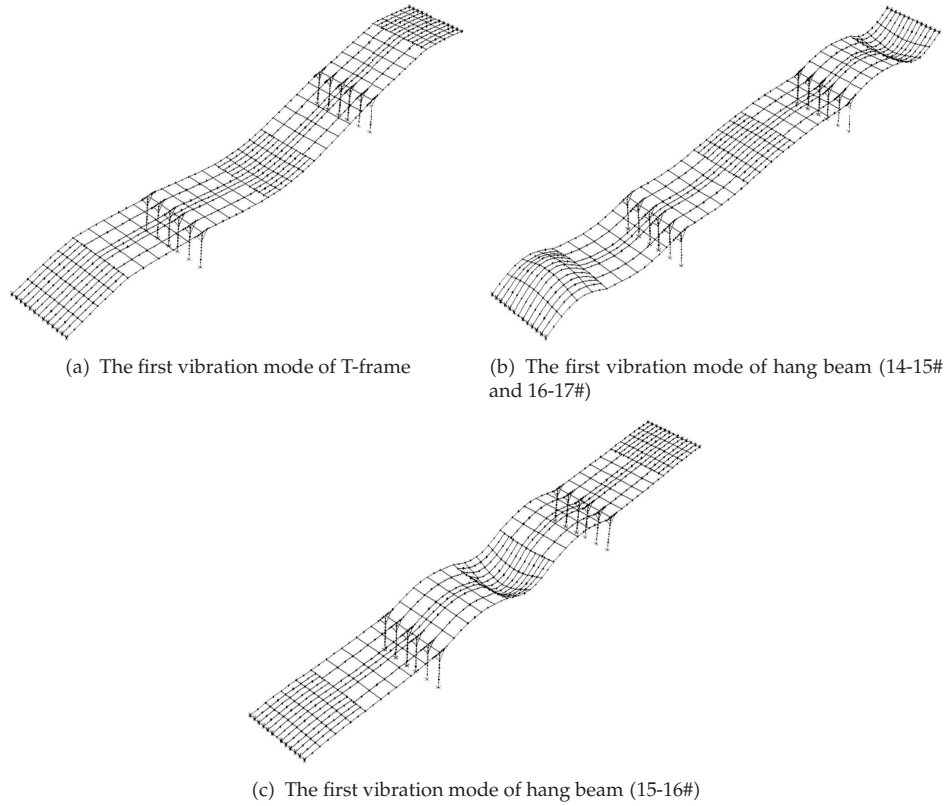


Figure 8: the first vibration mode of grillage model for hang beam and T-frame.

employed the heavily loaded dump trucks, each with approximately 30t weight, to simulate the design live loads of the bridge. Due to the difficulty to hire the same type of such heavy dump trucks in the area, there were, in total, 5 trucks employed during the static load tests. The individual axle load and spacing of each dump truck were carefully measured at the nearby weight station before it was moved to the bridge.

In addition, the applied test loads should be identical to the design live loads of the bridge. The applied test loads are normally designated by the static test load efficiency:

$$\eta = \frac{S_t}{S_d(1 + \mu)}, \quad (4.1)$$

where S_t is the resultant force at the specified section under the planned static test loads; S_d is the resultant force at the same specified section under the design live loads; μ is the impact factor used in the design of the bridge. All test load efficiency η values are within 0.8–1.05, which demonstrates the validity of the statically loaded tests on the bridge. As a result, a total of 27 measuring points of the deflection were set, and 54 strained measuring points were measured. The test setup included strained measurements and deflection measurements at control section. The three load cases during the field tests are shown in Figure 9.



Figure 9: Photos of three critical load cases: (a) field loading on the main span (16-17#); (b) field loading on the main span (14-15#); (c) field loading on the main span (15-16#).

4.1. Results of Deflection Test

Deflection values of the prototype bridge for the corresponding grillage under working condition I and working condition II are shown in Figure 10, and deflection values of the prototype bridge for the corresponding grillage under working condition III are shown in Figure 11. Measure point (5#) is a control point in the regions of the largest deformation cross-section and its corresponding maximum value is -23.6 mm. The maximum theoretic deformation of the measure point for control section is -26.3 mm, and the ratio α between the experimental and theoretical value is 0.9, and it is within the range of the national standard ($0.7 \leq \alpha \leq 1.05$). Maximum values of control section deflection of the field test are also in the range of national standard ($[f] \leq l/600 = 116.67$ mm). The results of measured deflection show that all values of measured deflections satisfied the design requirements. This indicates that the bridge possesses the adequate strength to resist the loadings.

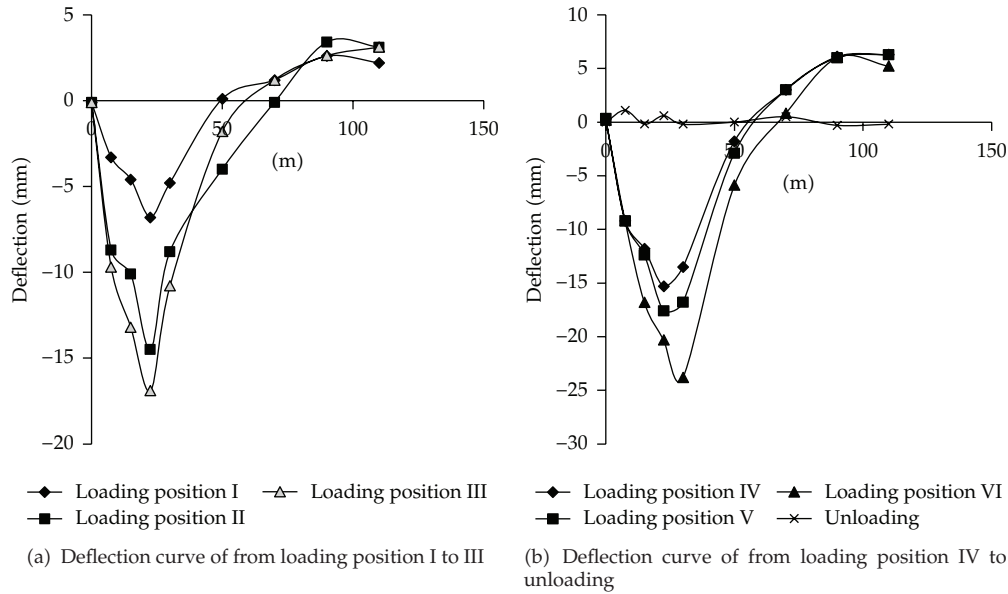


Figure 10: experimental deformations under working condition I and working condition II (14-15#).

4.2. Results of Strain Test

According to the comparative analysis of the strains between the field test and theoretical analysis, the ratio β of the strain between the experimental and theoretical value is found to be within the range of the national standard (i.e., $0.7 \leq \beta \leq 1.05$). The results of measured strains show that the bridge deck strains met the requirements of design, and all strains can resume completely when the applied field loads were removed. Based on the analysis of the Quhai Bridge, the internal force (bending moment and shear force) in the deck can be obtained directly by the proposed method. Hence, the proposed method is simple and convenient. Its use can lead to a significant reduction of the analytical workload associated with solid slab bridges.

4.3. Results of Dynamic Test

Dynamic properties can be obtained by measurement of vibrations produced by ambient loads and vehicle bump. The experimental program includes dynamic characterization of the structure in normal conditions and when a half of the bridge is covered by traffic. The response of the structure was measured at 7 selected points using accelerometers. Preliminary results obtained from an FE dynamic analysis were used to determine the optimum location of the sensors. The first mode shapes of the bridge according to field dynamic test and theoretical value are presented in Table 3. The results of measured dynamic properties show that the test values of fundamental frequency for T-frame is bigger than theoretic values, but the test values of fundamental frequency for middle-span hang beam is smaller than theoretic values. This indicates that middle-span stiffness is relatively weak.

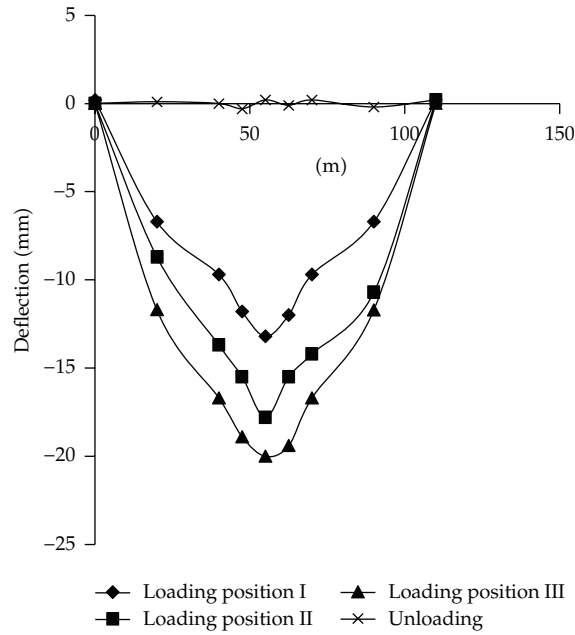


Figure 11: Experimental deformations under working condition III (15-16#).

Table 3: Experimental and theoretical base frequency (Hz).

Experiment location	Experiment	Theory	Vibration mode
15# T-frame	2.24	1.31	Symmetric vertical bending
Middle-span hang beam	2.70	3.60	Symmetric vertical bending
16# T-frame	2.22	1.30	Symmetric vertical bending

5. Conclusion

The static and dynamic behaviors of a rigid T-frame bridge were investigated analytically and experimentally. Based on the comparison study on analysis results obtained from the conventional and proposed analysis methods, one may obtain more economical designs using the spatial grillage model. Main contents of the grillage model include the grillage mesh and the grillage member section properties. The precision of the grillage model mainly lies on the simulation of the equivalent grillage stiffness and the element property. According to the comparative analysis, the bridge possesses a relatively small stiffness to resist the deformation. As a result, field test results have indicated that the bridge works in the elastic stage, but the bridge has a relatively smaller load-carrying capacity under the design load conditions. Therefore, some suggests of reinforcement or maintenance for the bridge were presented to increase bearing capacity, and prestressed outside were employed to solve deflection of beam, relatively smaller effective prestress and web shear crack. In addition, bearings of right and left hang beam were replaced to recover mechanical behavior of the original design.

Acknowledgments

The authors wish to thank the referees and Sheng-yong Chen for some helpful comments. Moreover, they are grateful for the financial support provided by the Science Foundation of China Postdoctor (Grant no. 20110490183), the Science Foundation of Ministry of Housing and Urban-Rural Development of the People's Republic of China (Grant no. 2012-K2-6), the Education Department Science Foundation of Zhejiang (Grant no. Y201122051), the Science Foundation of Zhejiang University of Technology (Grant no. 2011XY022).

References

- [1] Z. F. Pan, C. C. Fu, and Y. Jiang, "Uncertainty analysis of creep and shrinkage effects in long-span continuous rigid frame of Sutong Bridge," *Journal of Bridge Engineering*, vol. 16, no. 2, pp. 248–258, 2011.
- [2] C. Cattani, S. Chen, and G. Aldashev, "Information and modeling in complexity," *Mathematical Problems in Engineering*, vol. 2012, Article ID 868413, 4 pages, 2012.
- [3] S. Chen, Y. Wang, and C. Cattani, "Key issues in modeling of complex 3d structures from video sequences," *Mathematical Problems in Engineering*, vol. 2012, Article ID 856523, 17 pages, 2012.
- [4] N. Azizi, M. M. Saadatpour, and M. Mahzoon, "Using spectral element method for analyzing continuous beams and bridges subjected to a moving load," *Applied Mathematical Modelling*, vol. 36, no. 8, pp. 3580–3592, 2012.
- [5] T. L. Wang, D. Huang, and M. Shahawy, "Dynamic behavior of slant-legged rigid-frame highway bridge," *Journal of structural engineering*, vol. 120, no. 3, pp. 885–902, 1994.
- [6] M. Dicleli, "A rational design approach for prestressed-concrete-girder integral bridges," *Engineering Structures*, vol. 22, no. 3, pp. 230–245, 2000.
- [7] M. Carlini, S. Castellucci, M. Guerrieri, and T. Honorati, "Stability and control for energy production parametric dependence," *Mathematical Problems in Engineering*, vol. 2010, Article ID 842380, 21 pages, 2010.
- [8] S. Y. Chen and Q. Guan, "Parametric shape representation by a deformable NURBS model for cardiac functional measurements," *IEEE Transactions on Biomedical Engineering*, vol. 58, no. 3, pp. 480–487, 2011.
- [9] A. R. Cusens and R. P. Pama, *Bridge Deck Analysis*, Wiley, New York, NY, USA, 1975.
- [10] M. Yoshikawa, H. Hayashi, S. Kawakita, and M. Hayashida, "Construction of Benten viaduct, rigid-frame bridge with seismic isolators at the foot of piers," *Cement and Concrete Composites*, vol. 22, no. 1, pp. 39–46, 2000.
- [11] A. Kalantari and M. Amjadian, "An approximate method for dynamic analysis of skewed highway bridges with continuous rigid deck," *Engineering Structures*, vol. 32, no. 9, pp. 2850–2860, 2010.
- [12] M. Mabsout, K. Tarhini, R. Jabakhanji, and E. Awwad, "Wheel load distribution in simply supported concrete slab bridges," *Journal of Bridge Engineering*, vol. 9, no. 2, pp. 147–155, 2004.
- [13] AASHTO, *LRFD Design Specifications*, Washington, DC, USA, 3rd edition, 2004.
- [14] C. Cattani, "Shannon wavelets for the solution of integrodifferential equations," *Mathematical Problems in Engineering*, vol. 2010, Article ID 408418, 22 pages, 2010.
- [15] S. Y. Chen, J. Zhang, Q. Guan, and S. Liu, "Detection and amendment of shape distortions based on moment invariants for active shape models," *IET Image Processing*, vol. 5, no. 3, pp. 273–285, 2011.
- [16] E. C. Hambly and E. Pennells, "Grillage analysis applied to cellular bridge decks," *Structural Engineer*, vol. 53, no. 7, pp. 267–274, 1975.
- [17] M. P. Saka, "Theorems of structural variation for grillage systems," *Computers and Structures*, vol. 77, no. 4, pp. 413–421, 2000.
- [18] L. G. Jaeger and B. Bakht, "The grillage analogy in bridge analysis," *Canadian journal of civil engineering*, vol. 9, no. 2, pp. 224–235, 1982.
- [19] P. Z. Lu, J. P. Zhang, and A. R. Liu, "Structure analysis for Y-shape Bridge based on grillage theory," *Journal of Guangzhou University*, no. 2, pp. 67–72, 2006.

- [20] E. Lightfoot and F. Sawko, "Structural frame analysis by electronic computer: grid frameworks resolved by generalized slope deflection," *Engineering*, pp. 18–20, 1959.
- [21] E. C. Hambly, *Upper Part Bridge Structural Capability*, Communication Press, Beijing, China, 1982.

Research Article

Statistical Analysis and Calculation Model of Flexibility Coefficient of Low- and Medium-Sized Arch Dam

Su Huaizhi,^{1,2} You Ting,^{2,3} and Wen Zhiping⁴

¹ State Key Laboratory of Hydrology-Water Resources and Hydraulic Engineering, Hohai University, No. 1 Xikang Road, Nanjing 210098, China

² College of Water Conservancy and Hydropower Engineering, Hohai University, No. 1 Xikang Road, Nanjing 210098, China

³ National Engineering Research Center of Water Resources Efficient Utilization and Engineering Safety, No. 1 Xikang Road, Nanjing 210098, China

⁴ Department of Computer Engineering, Nanjing Institute of Technology, No. 1 Hongjing Avenue, Nanjing 211167, China

Correspondence should be addressed to Su Huaizhi, su_huaizhi@hhu.edu.cn

Received 8 June 2012; Accepted 20 July 2012

Academic Editor: Fei Kang

Copyright © 2012 Su Huaizhi et al. This is an open access article distributed under the Creative Commons Attribution License, which permits unrestricted use, distribution, and reproduction in any medium, provided the original work is properly cited.

The flexibility coefficient is popularly used to implement the macroevaluation of shape, safety, and economy for arch dam. However, the description of flexibility coefficient has not drawn a widely consensus all the time. Based on a large number of relative instance data, the relationship between influencing factor and flexibility coefficient is analyzed by means of partial least-squares regression. The partial least-squares regression equation of flexibility coefficient in certain height range between 30 m and 70 m is established. Regressive precision and equation stability are further investigated. The analytical model of statistical flexibility coefficient is provided. The flexibility coefficient criterion is determined preliminarily to evaluate the shape of low- and medium-sized arch dam. A case study is finally presented to illustrate the potential engineering application. According to the analysis result of partial least-squares regression, it is shown that there is strong relationship between flexibility coefficient and average thickness of dam, thickness-height ratio of crown cantilever, arc height ratio, and dam height, but the effect of rise-span ratio is little relatively. The considered factors in the proposed model are more comprehensive, and the applied scope is clearer than that of the traditional calculation methods. It is more suitable for the analogy analysis in engineering design and the safety evaluation for arch dam.

1. Introduction

As a superior type, arch dam has been extensively used in dam construction. But its design and calculation methods are more complex than that of earth dam and gravity dam. There

are the following problems. First of all, to implement the comparative analysis for different design schemes of arch dam, some shape data are lack of reference. Secondly, it is difficult to estimate the earthwork volume index of dam body which is used to determine the dam shape and assess the economy. The problem has an impact on selection of dam site and determination of project scale during engineering preplanning. With the help of flexibility coefficients, macroevaluation of arch dam's shape, security, and economy has recently become important research topic in the field of dam.

Lombardi [1], who is a famous dam expert in Swiss, first proposed the "flexibility coefficient" concept during researching the Kolnbrein dam heel cracking. The calculation equation of flexibility coefficient C was given as follows. $C = A^2/VH$, where A is the developed area of the arch dam in upstream face, m^2 ; V is the earthwork volume of dam, m^3 ; H is the arch dam height, m . And the above flexibility coefficient was used to assess the arch dam safety. Lombardi considered that in normal conditions, when the value of C is about 15, the arch is safe; in the higher concrete grouting technology and rational construction, the value of C can be up to 20. After that, many dam experts began to research the calculation models and functions. Many calculation models were built and its application scope got a great expansion. Lombardi damage line was proposed to distinguish empirically the cracking damage of the arch dam [2, 3]. The flexibility coefficient was introduced to estimate the reasonability on structure design of arch dam [4], implement the optimization design of arch dam shape [5], and assess the arch dam safety [6, 7].

On the whole, the existing definition and calculation method on the flexibility coefficient are accuracy and concision. They can embody the flexibility degree of arch dam at the horizontal direction. However, there are some questions to analyze and perfect. For example, the differences of flexibility coefficient between various canyon shapes are great which also have not some certain roles. In the condition of similar shape and height, a large difference in flexibility coefficient will affect engineering analogy analysis and arch shape design. Sometimes safety degree of the arch dam is unconscionable to reflect through Lombardi damage line building by flexibility coefficient.

Based on above problems in existing research, a large number of statistical data on low- and medium-sized arch dams are collected and implemented the regression analysis. The partial least-squares regression method is used to analyze the statistical data of the related factors on flexibility coefficient. The calculation model of flexibility coefficient is built. The statistical flexibility coefficient is proposed.

2. Analysis Method of Partial Least-Squares Regression

As a commonly multivariate statistical analysis method, PLSR (partial least-squares regression) combines the basic functions in multiple linear regression analysis, principal component analysis, and typical correlation analysis. It can be used to solve effectively the multicollinearity between the independent variables. After a partial least-squares regression analysis, the regression model between independent variable and dependent variable can be not only obtained but also the correlation between variables can be analyzed. It makes the analysis more richer and makes the interpretation of the regression model deeper.

(1) Basic Idea

A multiple linear regression model can be described as follows:

$$Y = XB + \varepsilon, \quad (2.1)$$

where Y is dependent-variable vector; X is independent variable matrix; B is regression coefficient vector; ε is residual vector.

The least-square estimation of regression coefficient vector B is

$$B = (X'X)^{-1}X'Y. \quad (2.2)$$

When multiple correlation is existed in factors belong to X , and $X'X$ is singular matrix or similar to singular, the least-square estimation will become invalid.

Partial least-squares regression extracts the principal component t_1 and u_1 from the X and Y . t_1 and u_1 as much as possible carry variability information from their own data table. At the same time, relevance of t_1 and u_1 reaches to maximum. After extraction, regression is carried out, respectively, through X to t_1 and Y to t_1 . If the regression equation is accuracy, the algorithm is terminated; otherwise, the second round of extraction is conducted making use of the residual information that X is explained by t_1 , Y by t_1 . It is reciprocating until it can reach a satisfactory accuracy.

(2) Simplified Algorithm of Partial Least Squares for Unit-Dependent Variable

Assumed that dependent variable is $y \in R^n$, a set of the dependent variable is $X = [x_1, \dots, x_p]$, $x_j \in R^n$, and F_0 is standardized variable of dependent variable y , it is found that $F_{0i} = (y_i - \bar{y})/s_y$, $i = 1, 2, \dots, n$, in which \bar{y} is mean value of y ; s_y is a standard deviation of y ; E_0 is standard matrix of a dependent-variable set X .

The data of F_0 and E_0 are known, due to the principal component of independent variable $u_1 = F_0$, it is gotten that

$$w_1 = \frac{E_0' F_0}{\|E_0' F_0\|}, \quad t_1 = E_0 w_1, \quad p_1 = \frac{E_0' t_1}{\|t_1\|^2}, \quad E_1 = E_0 - t_1 p_1'. \quad (2.3)$$

In the h step ($h = 2, \dots, m$), the data of E_{h-1} , F_0 is known, and it is gotten that

$$w_h = \frac{E_{h-1}' F_0}{\|E_{h-1}' F_0\|}, \quad t_h = E_{h-1} w_h, \quad p_h = \frac{E_{h-1}' t_h}{\|t_h\|^2}, \quad E_h = E_{h-1} - t_h p_h'. \quad (2.4)$$

At this moment, the m principal component t_1, t_2, \dots, t_m is obtained, the regression of F_0 on t_1, t_2, \dots, t_m , is implemented, it is gotten that

$$\hat{F}_0 = r_1 t_1 + \dots + r_m t_m. \quad (2.5)$$

Considering that t_1, t_2, \dots, t_m is linear combination of E_0 , that is,

$$t_h = E_{h-1} w_h = E_0 w_h^*, \quad (2.6)$$

where $w_h^* = E_0 \prod_{j=1}^{h-1} (I - w_j p_j') w_h$, so \hat{F}_0 could be written to linear combination style of E_0 . That is,

$$\hat{F}_0 = r_1 E_0 w_1^* + \cdots + r_m E_0 w_m^* = E_0 \left[\sum_{h=1}^m r_h w_h^* \right]. \quad (2.7)$$

Finally, it can be converted to regression equation y for x_1, x_2, \dots, x_p

$$\hat{y} = \alpha_0 + \alpha_1 x_1 + \cdots + \alpha_p x_p. \quad (2.8)$$

(3) Cross-Validation (CV)

All the n sample points are divided into two parts adopting the working style similar to sampling test method. The first part is a set of the rest sample points (containing $n-i$ sample points) removing a sample point i , and a regression equation is fitted by h principal components and these partial sample points; the second part is a sample point i which is substituted into regression equation, and a fitted value of regression equation $y_{h(-i)}$ has gotten. For each $i = 1, 2, \dots, n$, the above steps are repeated, and the forecasting error square sum for y PRESS _{h} can be obtained

$$\text{PRESS}_h = \sum_{i=1}^n (y_i - y_{h(-i)})^2. \quad (2.9)$$

Adopting all sample points, regression model is established fetching h principal components. The i sample point is substituted into regression mode, and then a fitted value of y_{hi} can be obtained. If all of sample points are substituted successively, error square sum SS _{h} for y is defined

$$\text{SS}_h = \sum_{i=1}^n (y_i - y_{hi})^2. \quad (2.10)$$

For the principal component t_h , CV is defined as

$$Q_h^2 = 1 - \frac{\text{PRESS}_h}{\text{SS}_{(h-1)}}. \quad (2.11)$$

A great amount of research indicates that when $Q_h^2 \geq 0.0975$, the contribution of the principal component t_h on regression is outstanding, namely, the increase of the principal component t_h is beneficial; otherwise, it should stop introducing the principal component.

(4) Precision Analysis

In the partial least-squares regression, the principal component t_h extracted from independent variable not only represents variability information in X as much as possible but also

associates with Y interpreting information in Y . In order to measure the t_h explanatory capacity $i = 1, 2, \dots, n$, it is defined as the following equations.

The explanatory capacity of t_h to x_j :

$$Rd(x_j; t_h) = r^2(x_j, t_h). \quad (2.12)$$

The explanatory capacity of t_h to X :

$$Rd(X; t_h) = \frac{1}{p} \sum_{j=1}^p Rd(x_j; t_h). \quad (2.13)$$

The cumulate explanatory capacity of t_1, t_2, \dots, t_m to X :

$$Rd(X; t_1, t_2, \dots, t_m) = \sum_{h=1}^m Rd(X; t_h). \quad (2.14)$$

The explanatory capacity of t_h to y :

$$Rd(y; t_h) = r^2(y, t_h). \quad (2.15)$$

The cumulate explanatory capacity of t_1, t_2, \dots, t_m to y :

$$Rd(y; t_1, t_2, \dots, t_m) = \sum_{h=1}^m Rd(y; t_h). \quad (2.16)$$

(5) The Effect of Independent Variable x_j in the Interpretation of y

In order to analyze the relationship between independent variable X and dependent variable y , and to understand the role of each independent variable in the system analysis, it is needed that explanatory capacity is to be discussed when x_j explains y . This is a question of common interest in the regression analysis.

The explanatory capacity can be measured by variable importance in the projection VIP_j . The definition VIP_j is

$$VIP_j^2 = \frac{p \sum_{h=1}^m Rd(y; t_h) w_{hj}^2}{\sum_{h=1}^m Rd(y; t_h)}, \quad (2.17)$$

where w_{hj} is the j component of the axis w_h ; p is the number of independent variables.

It can be seen from the partial least-square principle that interpretation of x_j to y is transmitted by t_h . If the explanatory capacity that t_h to y is very capable and x_j plays an important role in the construction of t_h , it is believed to be more power. Accordingly, if a value of w_{hj} in t_h principal component of a larger value of $Rd(y; t_h)$ is larger, it plays a vital role that x_j explains all of y . The definition of VIP_j reflects this idea.

In addition, the square sum p of VIP_j can also be deduced for all factors. Therefore, if the function is similar for p independent variables as interpretation, all of the VIP_j are 1. The greater the value of VIP_j is, the deeper the function of interpretation is.

3. Statistical Calculation Model of Flexibility Coefficient for Arch Dam Based on the Project Cases

3.1. Dependent Variable Selection of Flexibility Coefficient and Project Data

According to the definition and existing research results of flexibility coefficient, dependent variable factor set of flexibility coefficient is selected as follows: $X = \{x_1, x_2, \dots, x_{12}\}$ = (dam height, temperature drop, concrete volume of the dam, central plane area, average thickness of dam, thickness-height ratio of crown cantilever, arc-height ratio, chord length-height ratio, rise-span ratio, Top boom-bottom chord ratio of downstream face (this is also called valley shape factor), upstream face area of normal water level, dam water thrust of normal water level). The actual project data collected is shown in Figure 1. Data used in this paper are derived from actual dam projects. Data of the actual project cases above have the following characteristics.

- (1) Dam height is between 30 m–70 m.
- (2) According to the design code of concrete arch dam (SL282-2003), arch dam thickness is divided. The ratio of above arch dams is thin arch dam : medium arch dam : thick arch dam = 38% : 61% : 1%.
- (3) According to arch ring type, various types of arch dams above in the ratio are parabolic variable-thickness double-curved arch : double-curvature constant thickness arch dam with single-centered arc : others (such as mixture-type arch dam and circular variable thickness arch dam with five-centered arc) = 68% : 9% : 23%.
- (4) Dams of discharging through crest orifice, which account for 66% of the total, are usually used.

3.2. The PLSR Analysis of Flexibility Coefficient

3.2.1. Establishment of PLSR Equation for Flexibility Coefficient

According to (2.9)–(2.11), the principal component cross-validation of data is

$$\{Q_1^2, Q_2^2, Q_3^2, Q_4^2, Q_5^2\} = \{0.3581, 0.1965, 0.1496, 0.2161, -0.0802\}. \quad (3.1)$$

According to cross validation principle, when $Q_h^2 \geq 0.0975$, the contribution of principal component t_n to regression equation is significant. Then introducing t_n and the first four principal components are necessary.

Table 1: The explanatory capacity of main components to dependent variables and independent variables.

	x_1	x_2	x_3	x_4	x_5	x_6	x_7
t_1	0.631	0.223	0.308	0.226	0.400	0.001	0.181
t_2	0.258	0.029	0.546	0.729	0.248	0.012	0.230
t_3	0.038	0.004	0.117	0.022	0.303	0.869	0.447
t_4	0.012	0.165	0.003	0.000	0.005	0.032	0.103
	x_8	x_9	x_{10}	x_{11}	x_{12}	y	
t_1	0.156	0.061	0.190	0.191	0.276	0.488	
t_2	0.230	0.000	0.058	0.767	0.677	0.204	
t_3	0.441	0.003	0.011	0.011	0.000	0.119	
t_4	0.152	0.293	0.138	0.000	0.004	0.066	

Through calculating and analyzing, the PLSR equations of standardized data and raw data are (3.2) and (3.3), respectively,

$$\begin{aligned} \hat{F}_0 = & -8.307 \times 10^{-2}E_{01} + 2.874 \times 10^{-2}E_{02} - 0.168E_{03} + 0.260E_{04} - 0.753E_{05} \\ & - 0.507E_{06} + 0.378E_{07} + 0.416E_{08} - 0.186E_{09} + 0.220E_{10} + 0.280E_{11} + 0.178E_{12}, \end{aligned} \quad (3.2)$$

$$\begin{aligned} \hat{y} = & 21.770 - 3.610 \times 10^{-2}x_1 + 0.102x_2 - 4.362 \times 10^{-5}x_3 + 6.664 \times 10^{-4}x_4 - 1.872x_5 \\ & - 46.043x_6 + 2.186x_7 + 2.761x_8 - 6.863x_9 + 7.548x_{10} + 7.574 \times 10^{-4}x_{11} + 1.900 \times 10^{-5}x_{12}. \end{aligned} \quad (3.3)$$

Multiple correlation coefficients R and F of raw data PLSR equation are 0.936 and 21.384, respectively.

3.2.2. The Precision Analysis

According to (2.12)–(2.16), the explanatory capacity and the accumulative explanatory capacity of main components to dependent variables and independent variables are calculated. The results are shown in Tables 1 and 2.

- (1) As can be seen from Table 1, explanatory capacity of each component to independent variables is the capacity that how many variation information can be used in the analysis process. Sometimes the capacity is little, even nothing. This is mainly because that (1) the PLSR requires the covariance between main components and dependent variables be maximum. However, when it is maximal, explaining capacity of some main components to independent variables is low. (2) The contribution of certain independent variables to some main components is little or nothing.
- (2) As can be seen from Table 2, the total explaining capacity of dependent variable is 87.7% and that of independent variable is 81.7%.
- (3) The explaining capacity of t_1 to variation information in y is 48.8%, and the linear correlation coefficient between them is 0.7. There is a good linear correlation.

Based on the above analysis, the data have relatively good linear trend and the PLSR equation has high precision. They can well reflect the average law between X and y .

Table 2: The accumulative explanatory capacity of main components to dependent variables and independent variables.

	t_1	t_2	t_3	t_4
The explanatory capacity on X	0.237	0.315	0.189	0.076
The accumulative explanatory capacity on X	0.237	0.552	0.741	0.817
The accumulative explanatory capacity on Y	0.488	0.692	0.811	0.877

3.2.3. The Explanatory Role Analysis of Independent Variable to Dependent Variable

According to (2.17), variable importance in the projection VIP can be calculated, and the histogram can be drawn in Figure 2. From Figure 2, it shows the following.

- (1) The VIP values of x_5, x_6, x_7, x_8 are greater than 1 and that of x_1 is near 1. From the explanatory capability of independent variable x_j to dependent variable y , it can be known that all the VIP_j is 1 when the explanatory role of them to y is the same aiming at p independent variables. When the VIP_j value is bigger than 1, the capability of explaining y is bigger. It can be seen that these five factors (average thickness of the dam, thickness-height ratio, arc length-height ratio, chord length-height ratio, dam height) are significant in explaining y .
- (2) The VIP value of x_9 is smallest. It shows that the explanatory capability of x_9 to y is weakest.

From the dam structure, clearly, the average dam thickness and dam height have a great influence on the flexibility; the thickness-height ratio and the arc length-height ratio of crown cantilever, which reflect the thickness of arch dam and valley shape, have a major impact on the shape of arch dam, then affect the flexibility coefficient. The ratio of arc and chord of the dam crest is x_9 , which just reflects the bending degree of horizontal arch of dam crest and has a limited impact on the overall dam.

3.2.4. The Evaluation of Regression Equation Stability

According to the complexity of flexibility coefficient factors and the requirement of sample data, the method of stability in this paper is that after extracting a certain amount of the date, build the model by remaining data, make a coefficient compared, and judge stability of the equation. The specific implementation is to remove five sample points by three times and build the model with the remaining data.

After removing the extracted sample points and judging the main ingredients number of remaining data, the PLSR model can be made. In order to compare easily, the coefficient, result of regression model of the standardized data, can be used to be compared. The calculated specific factors are shown in Table 3. From the table it can be seen that the change of coefficient is within 5% excepting x_1, x_2 (dam height factor and temperature drop factor) by means of comparing each sampling factors and original factors. Stability of the whole coefficient is relatively good.

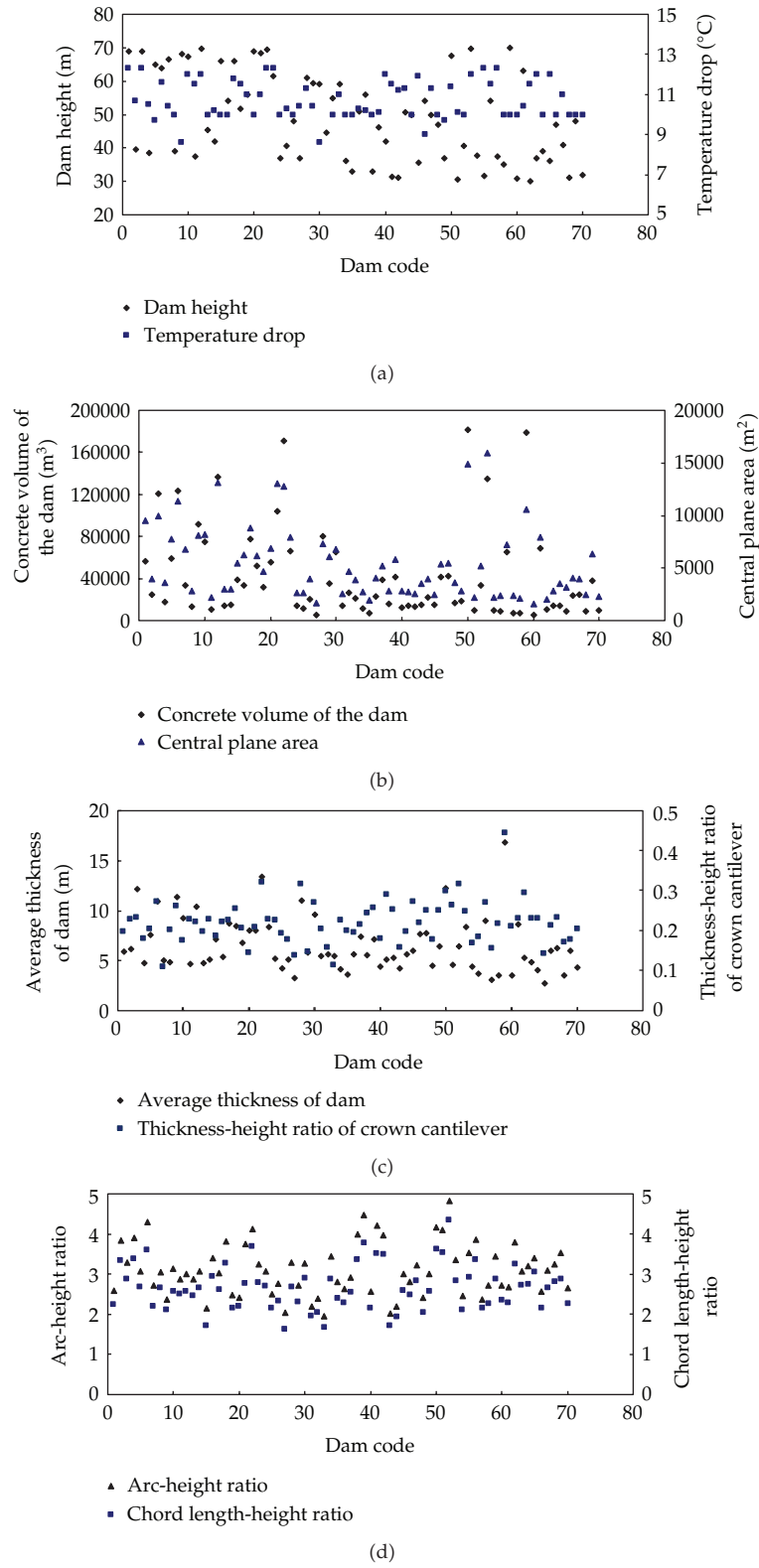


Figure 1: Continued.

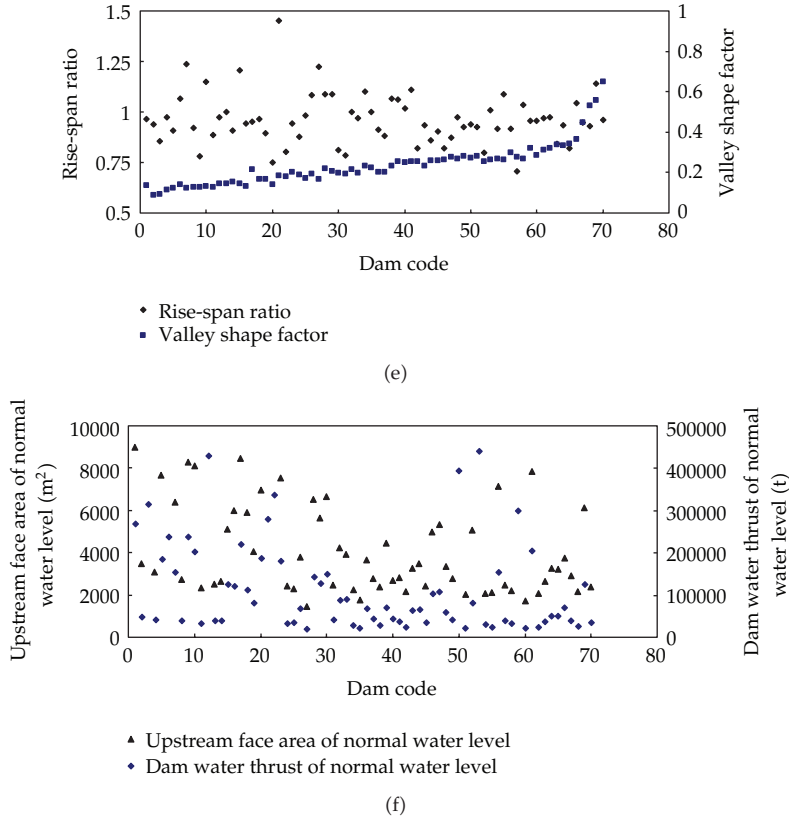


Figure 1: The actual project data of dependent variables for flexibility coefficient.

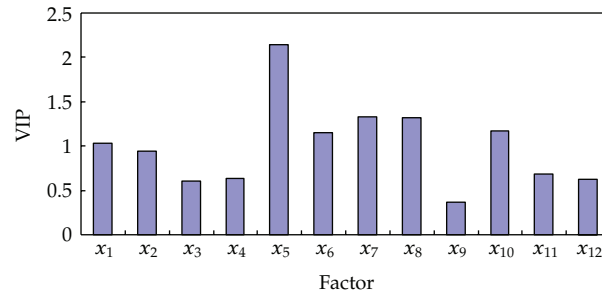


Figure 2: Variable importance in the projection.

3.2.5. The Statistical Calculation Model of Flexibility Coefficient

The above regression analysis is implemented to obtain the PLSR equation of flexibility coefficient in certain dam height range between 30 m and 70 m. From stability and regression

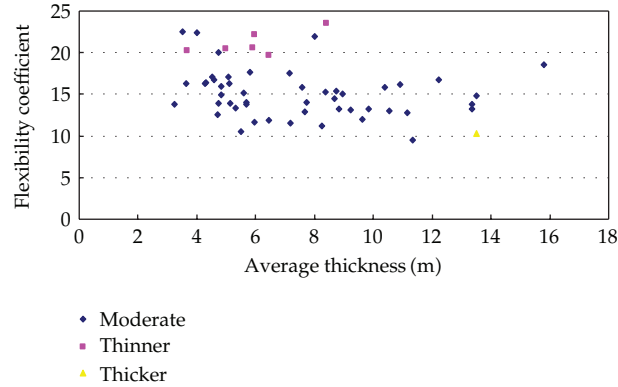


Figure 3: Scatter diagrams of flexibility coefficient and average thickness.

Table 3: The coefficients of regression equation based on original data and extracted sample data.

Variable	Group			
	Original coefficient	Coefficient of sample 1	Coefficient of sample 2	Coefficient of sample 3
x_1	-0.0831	-0.0887	-0.0976	-0.1084
x_2	0.0287	0.0352	0.0212	0.0271
x_3	-0.1681	-0.1656	-0.1690	-0.1518
x_4	0.2603	0.2560	0.2503	0.2426
x_5	-0.7530	-0.7343	-0.7346	-0.7157
x_6	-0.5071	-0.5159	-0.5185	-0.4716
x_7	0.3780	0.3668	0.3704	0.3498
x_8	0.4155	0.4030	0.4067	0.3851
x_9	-0.1859	-0.2082	-0.1933	-0.1900
x_{10}	0.2196	0.2250	0.2043	0.2144
x_{11}	0.2799	0.2771	0.2730	0.2672
x_{12}	0.1776	0.1726	0.1684	0.1730

accuracy, it can be seen that the PLSR equation is rational. Accordingly, calculation model of the flexibility coefficient C is proposed

$$\begin{aligned}
 C = & 21.770 - 3.610 \times 10^{-2}x_1 + 0.102x_2 - 4.362 \times 10^{-5}x_3 + 6.664 \times 10^{-4}x_4 - 1.872x_5 \\
 & - 46.043x_6 + 2.186x_7 + 2.761x_8 - 6.863x_9 + 7.548x_{10} + 7.574 \times 10^{-4}x_{11} + 1.900 \times 10^{-5}x_{12}.
 \end{aligned}
 \tag{3.4}$$

4. Examples

From the analysis of interpretation, it can be seen that explaining function of the average thickness of dam to the flexibility coefficient is strongest. According to [8], the scatter diagrams of flexibility coefficient and average thickness of dam are shown in Figure 3. It shows that flexibility coefficient of sample points, whose thickness for dam body is moderate, is almost distributed from 10 to 20. Therefore, this preliminary view is that the dam thickness

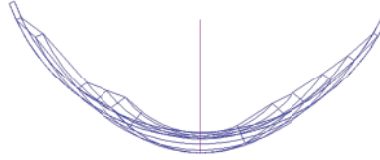


Figure 4: Arch dam plan.

Table 4: The calculated results of statistical factors for one arch dam.

x_1	x_2	x_3	x_4	x_5	x_6
34	12.1	13768	3824.11	3.6	0.206
x_7	x_8	x_9	x_{10}	x_{11}	x_{12}
5.129	3.965	1.336	0.263	3607.94	48453.13

is moderate, whose flexibility coefficient is from 10 to 20. When it is more than 20, the dam is thinner; when less than 20, the dam is thicker.

Based on the above evaluation criteria and the calculation model (3.4), the structural safety of an arch dam project is studied. With the help of the stress analysis results of this arch dam, the feasibility and reliability of the calculation model of flexibility coefficient and its criterion is verified.

4.1. Project Introduction

The arch dam project began in 1974 and basically completed in 1979. The dam is a concrete double-curvature masonry arch dam, whose total storage capacity is 120.5 ten thousand m^3 , crest elevation is 121.0 m, bottom elevation is 86.0 m, the maximum dam height is 35 m, thickness of the dam crest is 2 m, thickness of the dam bottom is 7 m, thickness-height ratio is 0.2, chord length of dam crest is 128.2 m, width-height ratio is 3.66, central angle of dam crest is 120° , and central angle of dam bottom is 60° . At the corresponding dam height of 4 m, setting a horizontal fracture, cutting beam-based, and using bridge-type rubber to stop water are to be done. The spill way whose net width is 30 m is arranged on the dam crest. Curved form of free jump is used to overflow.

4.2. Safety Evaluation of Arch Dam Structure Based on the Proposed Model and Criteria

The shape calculation of above arch dam is implemented. The results are shown in Table 4.

The values of factors in Table 4 are substituted into calculation model of flexibility coefficient (see (3.4)). The flexibility coefficient of the arch dam is 26.13, larger than 20. Therefore, the dam is deemed to be relatively thin and the structure safety is lower.

4.3. Safety Check for Arch Dam Based on the Calculation Results of Dam Stress

Dam stress is calculated and analyzed to check for the rationality of the above results.

Table 5: Characteristic elevation and water level (m).

Maximum dam height	35.0	Check water level	121.2
Crest elevation	121.0	Normal water level	119.5
Bottom elevation	86.0	Lowest operating water level	90.2
Sediment elevation	95	Design water level	120.95

Table 6: Physical and mechanical parameters of dam body and foundation.

	Dam foundation	Dam body
Deformation modulus	7.02×10^6 MPa	10^7 MPa
Poisson's ratio	0.28	0.225
Density	2.4 t/m^3	2.3 t/m^3
Concrete thermal diffusivity	/	$3.0 \text{ m}^2/\text{month}$
Coefficient of thermal expansion	/	$0.000008/^\circ\text{C}$

4.3.1. Calculation Conditions

(1) Arch Outline

The arch ring is a circular and single-centered ring with constant thickness. The dam is divided into 6 arches and 13 beams. Three of arches are located in the river bed. Analysis planar graph can be seen from Figure 4.

(2) Characteristic elevation and water level are shown in Table 5.

(3) Physical and mechanical parameters are given in Table 6.

(4) Temperature Parameters

The temperature considering perennial mean temperature and sunshine effects is 16°C ; the temperature considering annual temperature amplitude (temperature rise) and sunshine effects is 11.7°C ; the temperature considering surface temperature of reservoir water and sunshine effects is 16°C ; the temperature considering surface temperature of reservoir water (temperature drop) and sunshine effects is 11°C ; the temperature considering surface temperature of reservoir water (temperature rise) and sunshine effects is 10.6°C ; the water temperature of reservoir bottom is 11°C .

(5) Operating Conditions

The following six operational conditions are selected.

Case 1. Normal water level, sediment, and dead weight.

Case 2. Check water level, sediment, dead weight, and temperature rise.

Case 3. Lowest operating water level, sediment, dead weight, and temperature drop.

Case 4. Lowest operating water level, sediment, dead weight, and temperature drop.

Case 5. Normal water level, sediment, dead weight, and temperature rise.

Case 6. Design water level, sediment, dead weight, and temperature rise.

4.3.2. Calculation Results

(1) Maximum Dam Surface Stress

Maximum dam surface stress of every condition can be seen in Table 7.

(2) Contour Map of Principal Tensile Stress on the Dam Surface

For low and medium arch dam dominated by tensile stress, contour map of principal tensile stress is only given (see Figure 5).

4.3.3. Stress Analysis

The following can be seen from stress distributions.

- (1) For the first, second, and sixth conditions, the upstream tensile stress exceeds the allowed value. The stress value is largest at the first condition, which is at the normal water level, and is distributed approximately in the whole river bed of the upstream dam bottom. The downstream tensile stresses of three conditions meet the standard value.
- (2) For the third and fourth conditions, the upstream tensile stresses meet the standard value. But the downstream tensile stresses at the middle-lower part of the abutment exceed the standard value. The maximum tensile stress occurred at the fourth condition, up to 3.11 MPa, which is far more than the norms.
- (3) For the fifth condition, the upstream tensile stress at the bottom of dam exceeds the standard value, and the downstream tensile stress at the abutment exceeds the standard value.

In addition, the maximum radial displacement to the downstream is 17.2 mm, to the upstream is 8.47 mm, which is a little high for arch dams whose heights are 30 m–35 m. That shows that the overall stiffness of the arch dam is not high and the ability of deformation resistance is finite.

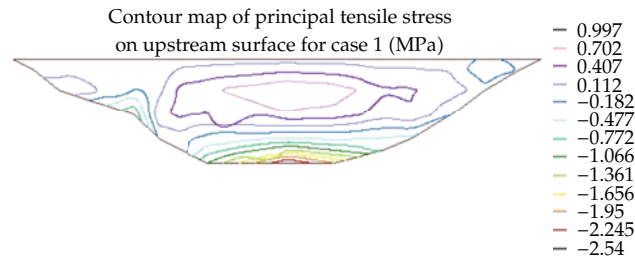
From the above analysis, they can be seen that stress distributions of this arch dam are not good, and the radial displacement is relatively large. It is reason that there are unreasonable shape design, relatively small average thickness of arch dam, and relatively small overall stiffness. They also have been proved from comparisons of arch dams that are the same height range to the case.

4.4. Results Comparison

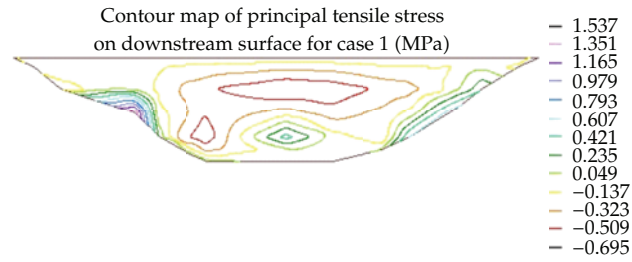
From the stress analysis, it can be known that the dam is relatively thin and lower structure safety keeping in step with the introduced model. In addition, during dam safety evaluation, experts also think that the dam is a little thin and has a limited overload capacity, which showed that it is feasible to evaluate arch dam safety with the introduced model once more.

Table 7: Maximum dam surface stress of every condition (MPa).

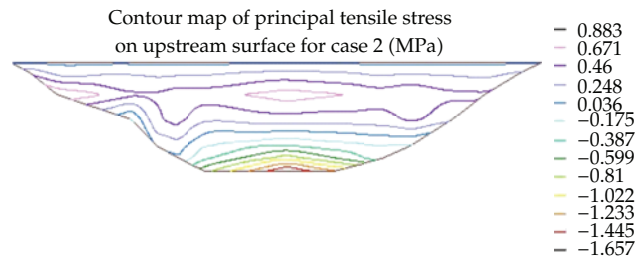
Case	Upstream surface			Downstream surface		
	Maximum principal tensile stress	Position	Maximum principal pressure stress	Position	Maximum principal pressure stress	Position
Case 1	2.54	7R 0C	1.88	3R 0C	0.69	3R 0C
Case 2	1.66	7R 0C	2.00	1R-7C	0.74	3R-5C
Case 3	0.66	1R-7C	2.24	6R-2C	1.42	6R-2C
Case 4	0.42	4R 0C	3.70	6R-2C	3.11	6R-2C
Case 5	1.34	7R 0C	1.77	1R-7C	1.16	3R-5C
Case 6	1.60	7R 0C	1.96	1R-7C	0.82	3R-5C



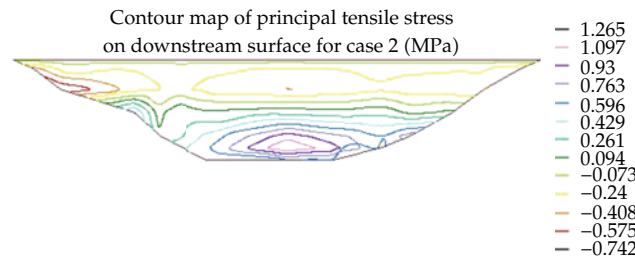
(a)



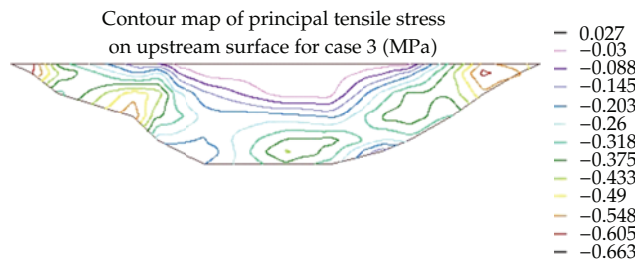
(b)



(c)

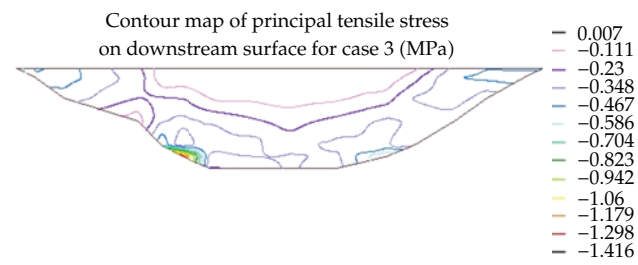


(d)

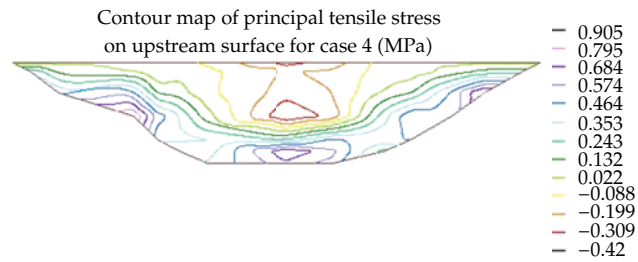


(e)

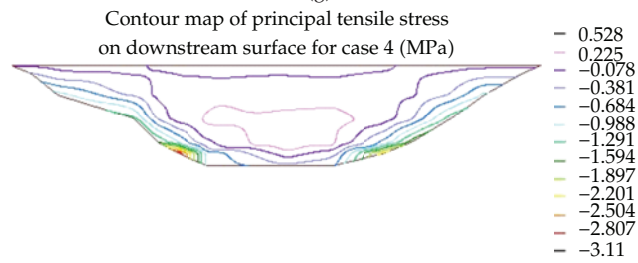
Figure 5: Continued.



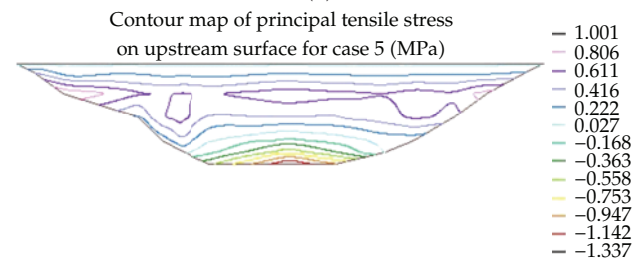
(f)



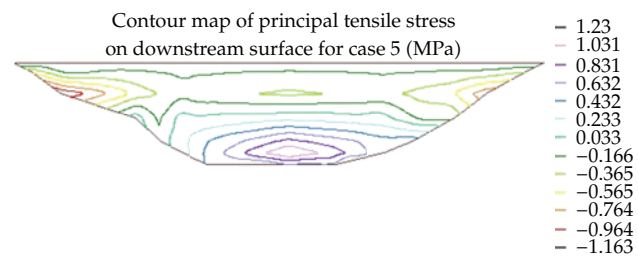
(g)



(h)



(i)



(j)

Figure 5: Continued.

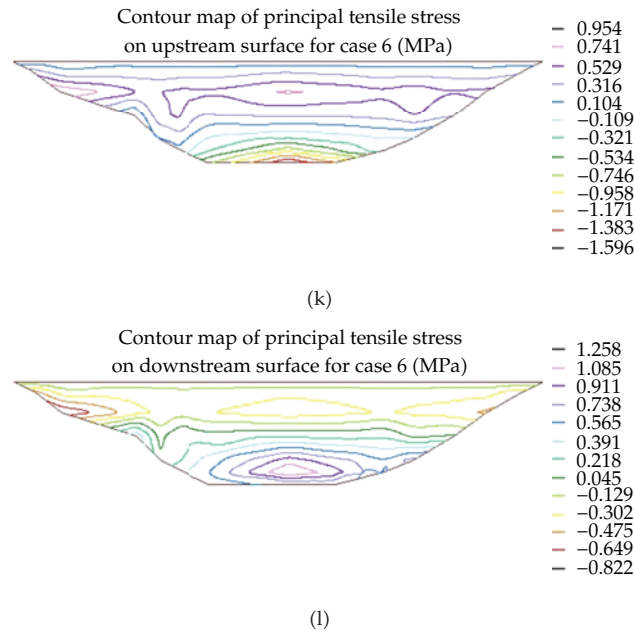


Figure 5: Contour map of principal tensile stress on the dam surface.

5. Conclusions

In recent years, flexibility coefficient, which is an objective index, is put forward to deal with problems, such as much subjective evaluation to the body safety of arch dam and lack of criteria of determining shape parameters of shape design. Flexibility coefficient has a unique advantage on the macroevaluation of arch dam shape, safety, and economy. According to large numbers of projects data, statistic rules of flexibility coefficient of arch dam are studied from the perspective of regression. The regressive equation of flexibility coefficient in certain height range, which is based on partial least-squares method, is established. Further, regressive precision and equation stability is analyzed deeply. And the calculation model of statistical flexibility coefficient is presented. A case application shows that the model has certain application value.

- (1) After analyzing explanatory capacity of factors to dependent variable, the result shows that average thickness of dam, thickness-height ratio of crown cantilever, arc-height ratio, and dam height have the higher explanation ability than others. The relation between them should be focused mainly when calculating flexibility coefficient.
- (2) Compared to traditional methods calculate of flexibility coefficient, the model in this paper has a comprehensive consideration, such as the valley shape coefficient that reflects the valley shape, thickness-height ratio that reflects arch dam thickness and thinness, and temperature-lowering load that has an important influence to arch dam stress, and the force of water and areas of upstream face in normal water level in the dam working. There is a wider application in calculating dam volume inversely. Traditional models do not distinguish dam height. But the rationality is worth to be discussed. It is because that the low- and medium-sized and the

high-sized arch dam have different stress conditions and methods. While statistical flexibility coefficient presented by this paper has a clear operating range, it is more suitable to analogy analysis and study on variation of flexibility coefficient.

- (3) Because the designing method of arch dam is more complex than gravity dam and earth dam. For specific valley conditions, project quantity can not be estimated quickly, which bring many difficulties to choose dam site and determine engineer scales during the preliminary planning. Now, we can apply calculation model introduced by this paper to select the specific flexibility coefficient. In coupled with the fitting values of other factors, the volume of dam body is inversely calculated. Choosing dam site and determine engineer scales preliminarily also provides certain references to shape data estimation.
- (4) For the arch dam shape which is designing and optimizing, after calculating shape data and values of corresponding factors, its flexibility coefficient can be gotten by the introduced calculation model of flexibility coefficient. Then, considering dam volume and dam safety, its reasonable shape can be chosen based on the flexibility coefficient.
- (5) The calculation model of statistical flexibility coefficient, which is based on PLSR, not only provides the more reasonable method to ascertain flexibility coefficient but also accomplishes some study related to principle component regression (PCR) and canonical correlation analysis (CCR). It can supply the better regressive equation that contains rich and deep data information. Moreover, it is studied that quadratic term and cubic term of related factors of flexibility coefficient affect the regressive equation on the basis of linear analysis. The result shows nonlinear parts of added factors have an unapparent influence to improve the precision of regressive analysis.

Acknowledgments

This research has been partially supported by National Natural Science Foundation of China (SN: 51179066, 51139001), Jiangsu Natural Science Foundation (SN: BK2012036), the Program for New Century Excellent Talents in University (SN: NCET-10-0359), the Special Fund of State Key Laboratory of China (SN: 2009586912), the Fundamental Research Funds for the Central Universities (Grant No. 2012B06614), Jiangsu Province "333 High-Level Personnel Training Project" (Grant No. BRA2011179) and the Priority Academic Program Development of Jiangsu Higher Education Institutions (PAPD) (SN: YS11001).

References

- [1] G. Lombardi, "Koelnbrein dam: an unusual solution for an unusual problem," *International Water Power and Dam Construction*, vol. 43, no. 6, pp. 31–34, 1991.
- [2] Q. W. Ren and B. L. Wang, "Discussion on slenderness coefficient of arch dams," *Journal of Hohai University (Natural Sciences)*, vol. 31, no. 1, pp. 1–4, 2003.
- [3] F. W. Xu and B. Tian, "Investigation on flexibility coefficient of arch dam," *Yangtze River*, vol. 38, no. 11, pp. 41–42, 2007.
- [4] H. L. Rao, "Arch dam configuration parameters statistic analysis," *Design of Hydroelectric Power Station*, vol. 20, no. 3, article 22, pp. 1–5, 2004.

- [5] Y. Jiang, X. T. Ding, and C. S. Gu, "Buckling analysis and modification of stress control index for super high and thin arc dam body," *Journal of Hohai University (Natural Sciences)*, vol. 36, no. 1, pp. 54–57, 2008.
- [6] B. F. Zhu, "Stress level coefficient and safety level coefficient for arch dams," *Dam Engineering*, vol. 11, no. 3, pp. 133–142, 2000.
- [7] H. Su, Z. Wu, Y. Gu, J. Hu, and Z. Wen, "Game model of safety monitoring for arch dam deformation," *Science in China E*, vol. 51, no. 2, pp. 76–81, 2008.
- [8] Y. C. Ma and S. C. Lou, "Discussion on flexibility and volume of arch dams," *Dam and Safety*, no. 6, pp. 1–3, 2005.